THE UNIVERSITY *of* EDINBURGH

The Role of Active Galactic Nuclei in Galaxy Evolution

David Nisbet

Doctor of Philosophy
The University of Edinburgh
2018

Abstract

It is now believed that most, if not all, galaxies contain a supermassive black hole (SMBH) and that these play a crucial role in their host galaxies' evolution. Whilst accreting material, a SMBH (known as an active galactic nucleus, AGN, during this growth phase) releases energy which may have the effect of quenching star formation and constraining the growth of the galaxy. It is believed that AGNs can be divided into two broad fundamental categories, each with its own feedback mechanism. The radiative-mode of feedback occurs in gas-rich galaxies when substantial star formation is occurring and their young AGNs are growing rapidly through efficient accretion of cold gas. A fraction of the energy released by an AGN is transferred into the surrounding gas, creating a thermal "energy-driven" wind or pressure "momentum-driven" wind. Gas and dust may be expelled from the galaxy, so halting star formation but also cutting off the fuel supply to the AGN itself. The jet-mode occurs thereafter. The SMBH has now attained a large mass, but is accreting at a comparatively low level as gas slowly cools and falls back into the galaxy. The accretion process generates two-sided jets that generate shock fronts, so heating the gas surrounding the galaxy and partially offsetting the radiative cooling. This restricts the inflow of gas into the galaxy, so slowing the growth of the galaxy and SMBH.

There are several convincing theoretical arguments to support the existence of these feedback mechanisms, although observational evidence has been hard to obtain. A new radio telescope – the Low Frequency Array (LOFAR) – recently started operations. LOFAR is especially suitable for investigating AGN feedback. It has been designed to allow exploration of low radio frequencies, between 10 and 240 MHz, which are particularly relevant for research into AGN activity. Also, with its large field-of-view and multi-beam capability, LOFAR is ideal for conducting extensive radio surveys. A project to image deeply the ELAIS-N1 field was started in May 2013.

This thesis uses a number of surveys at different wavelengths, but particularly the low-frequency radio observations of the ELAIS-N1 field, to improve our knowledge of jet-mode AGN feedback and hence of the interplay between the complicated processes involved in galaxy formation and evolution. The more important pieces of research within the thesis are as follows:

- A sample of 576 AGNs in the nearby universe was assembled and used to find a relationship between radio luminosity, X-ray luminosity and black hole mass. Moreover, the relationship is valid over at least 15 orders of magnitude in X-ray luminosity, strongly suggesting that the process responsible for the launching of radio jets is scale-invariant.

- The established "Likelihood Ratio" technique was refined to incorporate colour information in order to optimally match the radio sources in the ELAIS-N1 field with their host galaxies.

- The resulting catalogue was used to investigate ways in which radio sources can be matched automatically with their host galaxies (and so avoiding laborious visual examination of each source). The conclusions have helped the design of a pipeline for an extensive wide-area survey currently being conducted by the LOFAR telescope.

- The catalogue was also used to investigate the evolution of jet-mode AGNs. This involved: deriving source counts; obtaining redshifts for each object; classifying the radio sources into the different populations of radiative-mode AGNs, jet-mode AGNs and star-forming galaxies; and using the above preparatory work in order to derive a luminosity function for jet-mode AGNs.

- Key conclusions are that (1) feedback from jet-mode AGNs peaks at around a redshift of 0.75, (2) the space density of jet-mode AGNs declines steadily with redshift and (3) the typical luminosity of a jet-mode AGN increases steadily with redshift.

Declaration

I declare that this thesis was composed by myself, that the work contained herein is my own except where explicitly stated otherwise in the text, and that this work has not been submitted for any other degree or professional qualification except as specified.

Parts of this work have been published in Nisbet and Best (2016).

(*David Nisbet, 2018*)

Acknowledgements

Many, many people have provided invaluable advice, help and support over the past four years, including colleagues, collaborators and those in research teams who have worked to carry out the observations and generate the data on which this research has depended. Two people in particular have made the preparation of the thesis not only enjoyable but possible.

Professor Philip Best showed a seemingly endless knowledge of the subject, provided countless hours of help and, most importantly, displayed incredible patience in guiding me through the past four years - in all respects, far exceeding the role of a supervisor. Thank you so much, Philip.

And thanks to you, Joyce, for indulging my interest in astrophysics, taking an interest in my ramblings and providing so much support and encouragement (and so many cheese rolls). I shall always appreciate that you gave me the opportunity to study the most fascinating of subjects.

"The evolution of the universe can be likened to a display of fireworks that has just ended: some few red wisps, ashes, and smoke. Standing on a well-chilled cinder, we see the fading of the suns and try to recall the vanished brilliance of the origin of the worlds." Lemaître (1931)

Contents

List of Figures

List of Tables

Chapter 1

The Theory of AGN Feedback

1.1 The Cosmological Background

Over the past twenty years, the cold dark matter model with a cosmological constant (the ΛCDM model) has established itself as the "standard" model of cosmology (for example, Mo et al., 2010, Chapter 3). This postulates that the cosmic mass-energy density of the universe comprises $\sim 4\%$ baryons, $\sim 25\%$ dark matter and the remainder in the form of dark energy. Dark energy is assumed to be an unknown form of energy that permeates all of space, opposes gravity and is responsible for the expansion of the universe. The key properties of dark matter, according to the standard model, are that it is cold – the particles became non-relativistic very early in the history of the universe and so were unable to travel more than a negligible distance – and that the particles interact through gravity and the weak force, but do not interact with electromagnetic radiation.

The universe started, 13.8 billion years ago according to Planck data (Planck Collaboration et al., 2016), in an extremely dense, hot and almost, but not quite, homogeneous state. Quantum fluctuations in the density field of the dominant dark matter were amplified during a period of very rapid inflation to create small inhomogeneities that can now be detected via temperature fluctuations in the Cosmic Microwave Background. The background density decreased as the universe expanded, certain regions exceeded a critical over-density relative to the background and became gravitationally self-bound, allowing dark matter haloes to form. The resultant gravitational potential well attracted ordinary matter,

speeding up the structure formation process. The assumption that cold dark matter rather than baryons was responsible for the first formation of structure overcomes the problem that thermal and radiative pressures would have prevented the collapse of the baryonic matter. Cold dark matter was able to form these initial, gravitationally-bound subhaloes. Once formed, gravitational interaction with baryons would allow the thermal energy barriers to be overcome, resulting in a collapse into the first stars and galaxies.

CDM models predict that growth thereafter was hierarchical: small haloes formed first and then grew through a combination of mergers and accretion of gas not correlated with the assembly of the halo. N-body simulations have been able to closely replicate this scenario, and their output matches the structure that is observed from galactic surveys and the structure in the Cosmic Microwave Background; see, for example, the review by Somerville and Davé (2015). Additionally, research based on observations of Type Ia Supernovae, Cepheid stars, galaxy clusters and the Cosmic Microwave Background have placed constraints on the main cosmological parameters. Although there is some tension in the results, the differences are largely irrelevant when it comes to galaxy modelling. In summary, there is now a solid framework upon which to develop models that simulate the development and evolution of galaxies.

The modelling of galaxy formation is, however, extremely complex as there are many more ongoing physical processes other than just gravity. Baryonic matter interacts in a dissipational manner. Heating, cooling, shocks, star formation, stellar evolution and the effect of radiation are just some of the factors that need to be considered, as well as feedback effects. It has long been recognised that some form of feedback needs to play a part in the process of galaxy evolution. White and Rees (1978) were unable to reproduce the observed faint end of the luminosity function when running simulations of hierarchical cosmological models and argued that there must be some mechanism that lowers the efficiency of galaxy formation. Attention initially focussed mainly on supernovae, although a variety of other feedback processes were also considered; these included radiation pressure on dust, thermal conduction, cosmic ray pressure and photoionisation by the ultraviolet background. Following a study by Benson et al. (2003) that examined the impact of different feedback mechanisms on the shape of the bright end of the galaxy luminosity function, feedback from active galactic nuclei (AGNs) was increasingly seen as a prerequisite of a successful simulation. AGN feedback is the subject of this thesis. AGNs, discussed in more detail in Sections 1.3 and

1.4, are accreting supermassive black holes (SMBHs) at the heart of galaxies, that are capable of emitting copious amounts of radiation and/or powerful relativistic jets which are powered by accretion of material into the black hole.

1.2 The Arguments in Favour of AGN Feedback

There are several convincing arguments why AGN feedback must play a part in galaxy evolution. These are summarised in the following six sub-sections.

1.2.1 The Galaxy Luminosity Function

The luminosity function – the space density of sources as a function of luminosity – is a powerful tool when assessing the accuracy of simulations in matching observations. Early simulations using the ΛCDM cosmological model tended to generate a distribution of dark halo masses that was at variance with the observed galaxy luminosity function. This is illustrated in the upper chart in Figure 1.1. The observed luminosity function, as estimated by Eke et al. (2006) using data from the 2PIGG catalogue, is shown by the blue squares. The predicted luminosity function is shown by the red line in the chart; this has been calculated by converting the halo mass function derived by Jenkins et al. (2001) into a luminosity function for galactic systems by assuming a constant mass-to-luminosity ratio. The mass-to-luminosity ratio has been chosen so that the two lines coincide at the point of the break in the observed function. Clearly, there is little agreement between the predicted and observed functions: the simulation predicts too many faint galaxies and too many bright galaxies, and does not replicate the observed break in the luminosity function.

It is possible to discard the assumption of a constant mass to luminosity ratio and work backwards to derive a mass-to luminosity function that would produce the observed luminosity function. Baugh (2006) has shown that such a mass-to-luminosity function is physically implausible. The ratio would need to have a strong dependency on the mass of the haloes: it would have a minimum value at a mass of $10^{12}h^{-1}M_{\odot}$ and would increase by a factor of approximately six to both lower and higher masses. More recently, the same point emerges from research into the stellar mass – halo mass relationship, see Section 1.4.

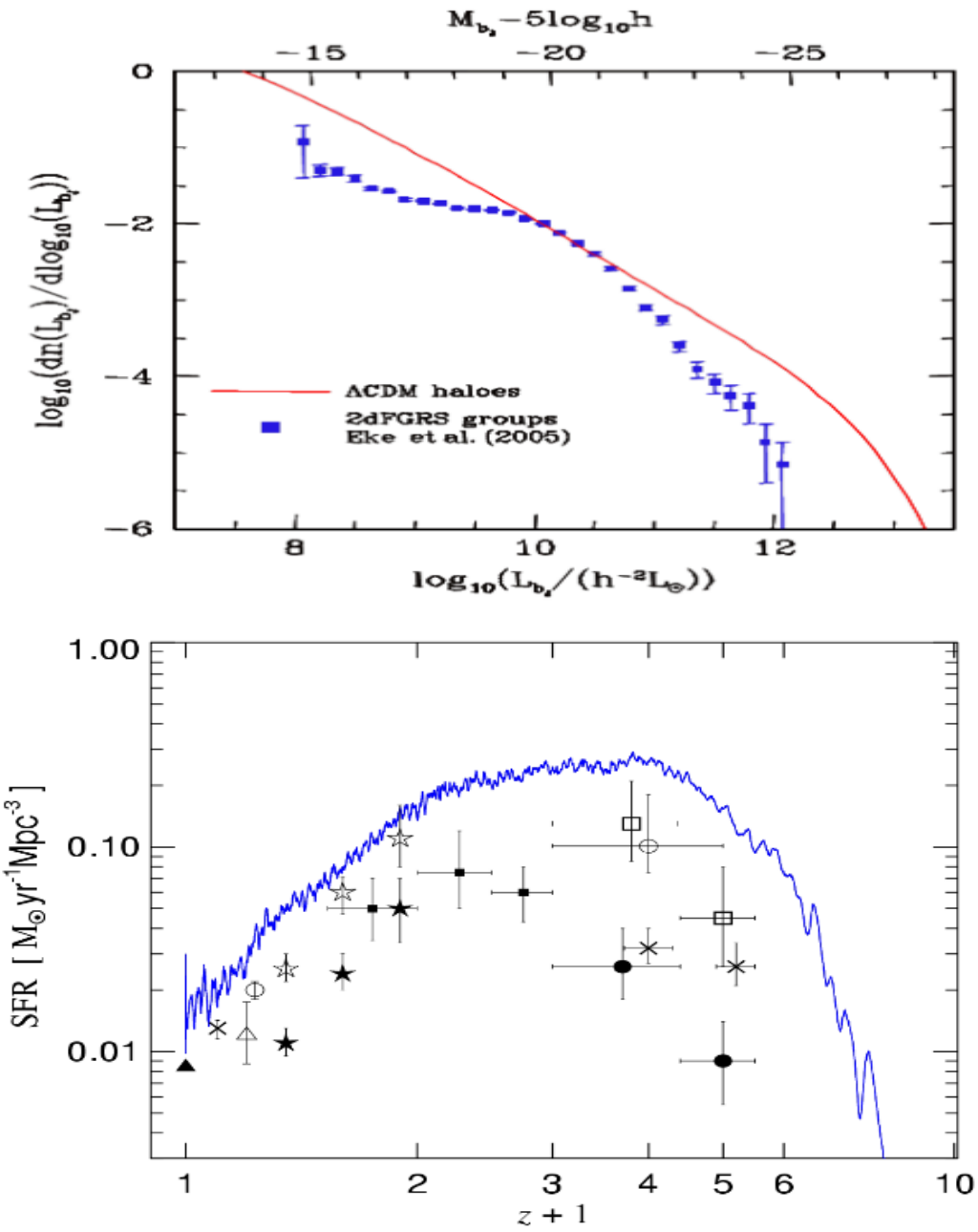

Figure 1.1 *Upper chart. A comparison of the observed galaxy luminosity function (blue squares) and the predicted luminosity function based on the ΛCDM model (red, solid line). The observed luminosity function has been estimated from the 2PIGG catalogue by Eke et al. (2006). The predicted luminosity function has been obtained by converting the halo mass function of Jenkins et al. (2001) using a constant mass to light ratio for each halo. Source: Baugh (2006). Lower chart. A comparison of star formation rates observed (black symbols) and those predicted from the ΛCDM model without incorporating AGN feedback (blue, solid line). Source: Springel (2011).*

Kay et al. (2002) investigated a variety of models of star formation and concluded that all of the algorithms resulted in too many bright galaxies unless some form of feedback were incorporated. Introducing feedback from supernovae allows simulations broadly to reproduce the faint end of the luminosity function, helped also by the fact that more precise observations have recently redefined the faint end of the luminosity function (for example, Bañados et al., 2010). However, this makes little difference at the bright end, given the deeper gravitational potential wells of more massive galaxies. Indeed, the introduction of supernova feedback can worsen the discrepancy in some simulations. As galaxy formation becomes less efficient in small galaxies, reheated gas is returned to the intercluster medium and then is attracted into the larger galaxies.

The same point is made in the lower chart in Figure 1.1, produced by Springel (2011): star formation in simulations based on the ΛCDM cosmological model is higher than that observed at all redshifts. Observational determinations of the star formation rate have been steadily improving in recent years, discussed in the review by Madau and Dickinson (2014), but the discrepancy remains.

It appears that only if an additional process in massive galaxies, such as AGN feedback, is included in models can the observed and simulated luminosity functions coincide.

1.2.2 Angular Momentum

Simulations also have a problem that, if no AGN feedback is included, then they have difficulty in reproducing the morphology of disk galaxies accurately. They tend to generate disks that are smaller than those observed. The discrepancy arises out of the treatment of angular momentum.

Observations suggest that the angular momentum of disk galaxies is similar to that of dark matter haloes of the same circular velocity. Given that baryons and dark matter should have had similar specific angular momentum before collapse, this implies that there has been little transfer of angular momentum from baryons to dark matter during the assembly of the luminous disk. By contrast, simulations historically built in the following scenario: gas cools very quickly early in a galaxy's lifetime due to the high densities involved; disks form by the coalescence of lumps of cold gas; dynamical friction drains them of angular momentum, which is then transferred out to dark matter in the halo; and so disks

of relatively small radii are formed.

This is illustrated in the upper chart in Figure 1.2, taken from Abadi et al. (2003). For our purposes, the key point from this figure is that simulated galaxies, the empty circles, possess less angular momentum than do the observed galaxies, the small pink dots. In order to bring the simulations into line with observations it is necessary to introduce a mechanism that prevents the gas from cooling rapidly. This requires some form of feedback.

Once feedback is included, the simulations produce results much more in accord with observations. The lower chart in Figure 1.2, produced from the Virgo Consortium's EAGLE project (Schaye et al., 2015) by Zavala et al. (2016), is one example. Although there are still some discrepancies from observations, particularly for disc-dominated galaxies, specific angular momentum from the simulations is in line with observations.

1.2.3 Entropy

The thermal history of the intracluster medium, with respect to both gravitational and non-gravitational processes, is embedded within its entropy. The entropy profiles are, therefore, a useful tool for examining the impact of AGN heating and radiative cooling.

Entropy within a cloud of gas has a linear dependence on temperature if the only source of heating has been gravitational contraction. A common definition of "entropy" in studies of galaxy clusters (useful since it comprises items that can be estimated from observations) is:

$$S = \frac{T}{n_e^{2/3}} \tag{1.1}$$

implying that S is proportional to the adiabats of a monoatomic gas. S is related to the traditional thermodynamic definition of entropy, s, by:

$$s = c_V \, log(S) + constant \tag{1.2}$$

where c_V is the constant-volume specific heat capacity.

If the only source of heating is due to gravitational contraction, then it can be

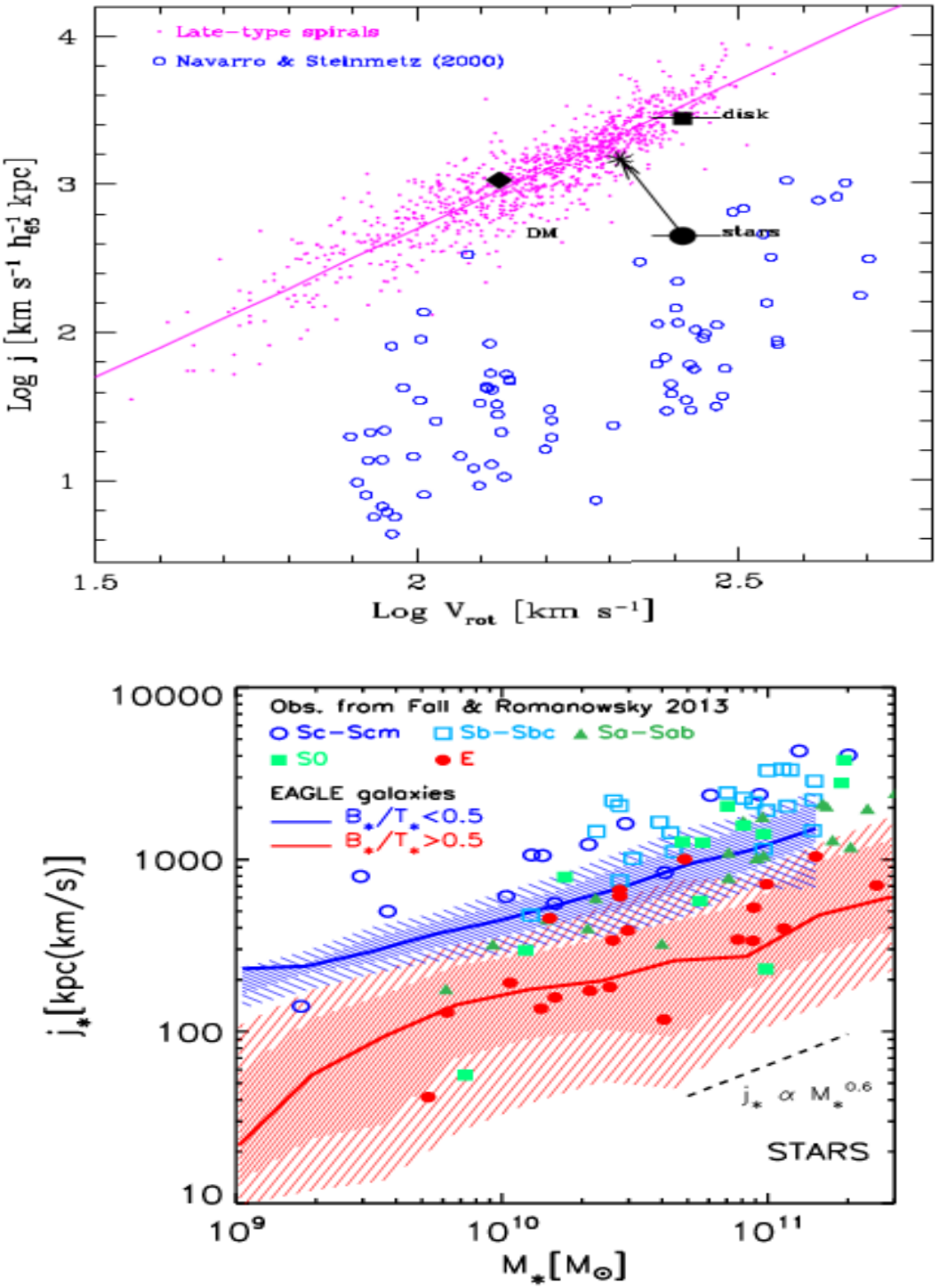

Figure 1.2 *Upper chart. A comparison of the observed angular momentum (empty blue circles) and that predicted using a model with no AGN feedback (pink dots). Source: Abadi et al. (2003). Lower chart. Specific angular momentum as a function of stellar mass, shown separately for bulge-dominated (coloured red) and disk-dominated (coloured blue) galaxies. The thick lines and accompanying uncertainty regions are simulated data using a model with AGN feedback – see text. The symbols are observed data from Fall and Romanowsky (2013). Source: Zavala et al. (2016)*

shown (Borgani et al., 2004) that at redshift, z:

$$S \propto \frac{T}{(E_z^2 \Delta_c)^{2/3}}, \tag{1.3}$$

where

$$E_z = [(1+z)^3 \Omega_m + 1 - \Omega_m]^{\frac{1}{2}} \tag{1.4}$$

measures the evolution of the Hubble constant and Δ_c is the overdensity, in units of the critical density, at which the entropy is measured. It follows that once Δ_c is fixed, there should be a linear relationship between the entropy of the gas and the temperature of the gas. In fact, the situation is slightly more complicated. Based on arguments set forward by Ponman et al. (1999) and Finoguenov et al. (2004), the linear relationship should trend into an entropy floor (a constant entropy value) at very low temperatures, but this is irrelevant to the present discussion.

The theoretical linear S $\propto$ T relationship is not, however, observed. Instead, an "entropy-ramp" is found, as shown in Figure 1.3 by the blue dashed line. Rather than following the linear S $\propto$ T scaling at hot systems with a flattening to a floor for cold systems, entropy seems to scale approximately as $T^{2/3}$. These observations are from Ponman et al. (2003), and were confirmed by Mushotzky et al. (2003). Finally, the entropy properties of simulated clusters do show excess entropy compared with the theoretical linear S $\propto$ T relationship, but only in the

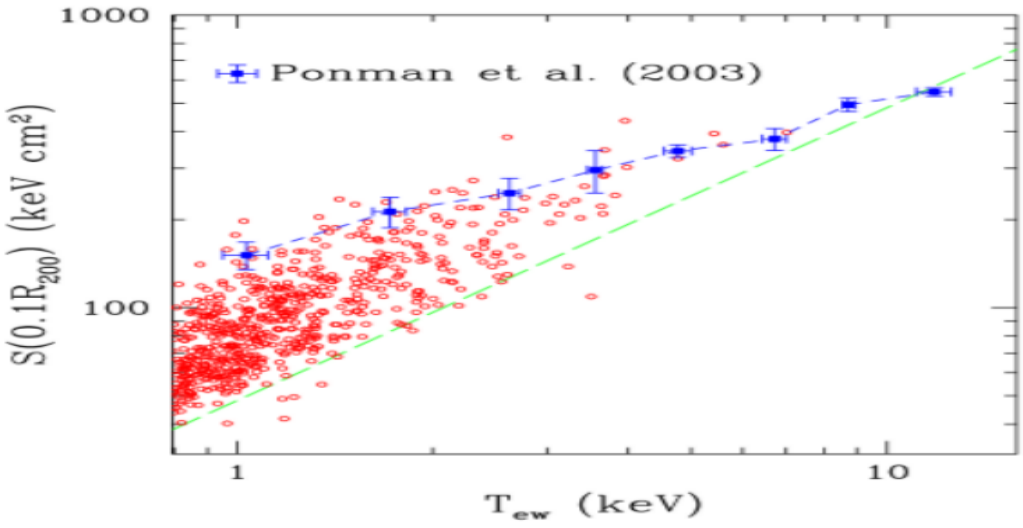

Figure 1.3 *Entropy vs (emission-weighted) temperature: observations are shown by the dashed blue line; the red circles show simulated results; and the dashed green line shows the theoretical linear $S \propto T$ relationship. Sources: Ponman et al. (2003) and Tornatore et al. (2003).*

most extreme cases do the results (red circles in Figure 1.3) match observations (for example, Tornatore et al., 2003).

A number of solutions have been proposed, including extreme radiation cooling and feedback from supernovae. None has succeeded in removing the discrepancy between theory, simulations and observations. However, studies, most recently by Chaudhuri et al. (2013) and Iqbal et al. (2017), show that AGN feedback is able to bridge the gap.

1.2.4 The Cooling Flow Problem

Galaxies, whether in isolation, in groups or in clusters, are enveloped in hot gas. The temperature of the gas can be estimated from X-ray spectra and this reveals that the gas is virially bound within dark matter haloes. The gas can cool through various processes including inverse Compton scattering, radiative decay following collisional excitement of atoms and Bremsstrahlung radiation as electrons are accelerated in an ionised plasma. From measurements of the X-ray emission, it is possible to estimate a cooling time for the gas by dividing the thermal energy of the gas by the cooling rate. The cooling time is often much shorter than the age of the system ("cool-core clusters"), which suggests that the gas should be cooling, flowing into the centre of the structure, condensing and turning into stars (a cooling flow, Fabian, 1994). However, measurements of star formation rates consistently find that they are at least an order of magnitude lower than expected: for example, Peterson et al. (2003) used X-ray spectrometry to demonstrate that very little of the gas cooled through a temperature one-third of that of the bulk of the gas. Many subsequent studies have also similarly found star-formation rates below those predicted from simple cooling and star-formation models, as reviewed by McNamara and Nulsen (2007). There needs to be some process that is heating the gas and largely offsetting the radiative losses.

1.2.5 The Magorrian Relationship

Over the past fifteen years, spectroscopic evidence of highly-peaked stellar velocity profiles in the core of a galaxy and, more locally, measurements of rapid orbital motions of individual stars have built a persuasive case that most, if not all, galactic bulges contain a SMBH. The arguments have been comprehensively

reviewed by Kormendy and Ho (2013). Furthermore, extensive observations in the local universe have revealed a tight correlation between the mass of a SMBH and the bulge mass of its host galaxy, initially propounded by Magorrian et al. (1998), or equivalently between the mass of a SMBH and the stellar velocity dispersion (Ferrarese and Merritt, 2000); these findings have subsequently been corroborated by many researchers. It follows that the mass of a SMBH, M_{BH}, is related to the spheroid stellar mass, M_S, by

$$M_{BH} = kM_S \tag{1.5}$$

A comparison of black hole mass with the bulge mass of the host galaxy is illustrated in Figure 1.4, taken from Kormendy and Ho (2013).

Estimates of k were at first closely grouped – for example, 0.14% ± 0.04% by Häring and Rix (2004) and 0.13%, quoted without an accompanying uncertainty, by Ferrarese and Ford (2005). More recent studies have argued that the relationship might be more complex, in three ways. First, the value of k may be higher than the initial estimates: Kormendy and Ho (2013) argue for a value of $0.49^{+0.06}_{-0.05}$ after omitting pseudobulges (because here the tight correlation breaks down), galaxies with uncertain SMBH mass measurements and mergers in progress. Second, k may evolve as a function of redshift, with results from, inter alia, Walter et al. (2004), McLure et al. (2006) and Bennert et al. (2011) suggesting that within a range of $0 < z < 2$:

$$k(z) \propto (1+z)^{\beta} \tag{1.6}$$

where β is of the order two, although Ding et al. (2017) argue for a much lower value of 0.06. Here, further research is needed to check that the apparent redshift dependency is not simply due to selection effects. Third, several researchers have found that there is a non-linear dependence on the bulge mass, such that:

$$\frac{M_{BH}}{10^9\, M_\odot} = k \left(\frac{M_{bulge}}{10^{11}\, M_\odot} \right)^{\alpha} \tag{1.7}$$

Estimates of α are reasonably consistent, with Häring and Rix (2004) finding 1.12 ± 0.06, McConnell and Ma (2013) quoting values between 1.05 ± 0.11 and 1.23 ± 0.16 depending on the conversion from velocity dispersion to black hole mass, and Kormendy and Ho (2013) finding 1.17 ± 0.08.

It is argued, for example by Peng (2007), Gaskell (2011) and Jahnke and Macciò

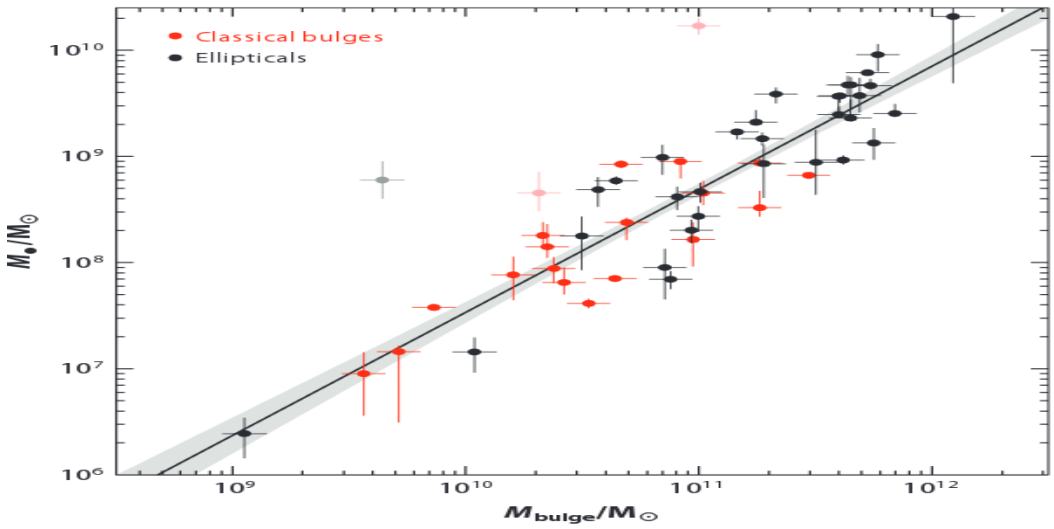

Figure 1.4 *The linear relationship between the mass of a black hole and the mass of the bulge of its host galaxy. Source: Kormendy and Ho (2013).*

(2011), that galaxy mergers contribute towards the Magorrian relationship. As a consequence of the Central Limit Theorem, the averaging that happens during mergers acts to tighten the correlation between the mass of a black hole and that of its host galaxy. Nevertheless, the closeness of the correlation between the mass of a SMBH and of its host galaxy suggests that mergers cannot be a complete explanation and that there needs to be some process that binds the growth of the SMBH to that of the galaxy. Kormendy and Ho (2013) extend the argument. Observations show that black hole masses correlate tightly with classical bulges and ellipticals, correlate very weakly with pseudo-bulges and dark haloes and do not correlate at all with disks. They suggest that (1) the correlation with pseudobulges and dark haloes is so weak that it suggests nothing other than black holes find it easier to grow in large galaxies which, by definition, contain more fuel, (2) the co-evolution between an AGN and its host galaxy that engineers the mass correlation occurs mostly at redshifts two to four when quasar activity was it its height and (3) processes thereafter act to preserve that correlation.

1.2.6 Downsizing

One of the puzzling aspects of galaxy formation is that of down-sizing. Star formation in recent times – redshifts less than one, say – is occurring mostly in intermediate-mass galaxies (for example, Kodama et al., 2004), whilst the most massive galaxies – typically ellipticals found in clusters – tend to be passive (Cowie

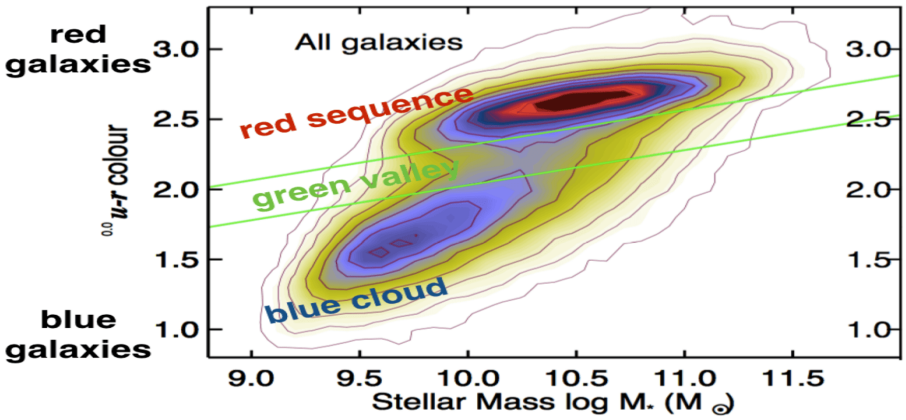

Figure 1.5 *The division of galaxies by mass and colour (i.e. temperature). The galaxy sample is based on data from the Sloan Digital Sky Survey Data Release 7 (Abazajian et al., 2009), with the sample selection described in Schawinski et al. (2010). The sample is restricted to a redshift range of $0.02 < z < 0.05$. The contours are linear and scaled to the highest value. Source: Schawinski et al. (2014).*

et al., 1996). Consequently, galaxies tend to separate into those that are young, blue and active and those that are old, red and dead, with the "green valley" in between being sparsely populated (Figure 1.5).

The implication is that today's massive galaxies must have experienced early and rapid star formation. Observations do, indeed, show that at high redshifts massive galaxies were forming stars at prodigious rates and that there were many massive galaxies already in existence at redshifts of over one (for example, Mortlock et al., 2015). This appears to conflict with the hierarchical growth of structure incorporated within the ΛCDM cosmogony. It seems that there must be some mechanism to shut off, or at least to reduce, star formation in galaxies once they attain a certain size. Simulations and semi-analytical modelling initially attempted to replicate the effect by incorporating supernova or starburst feedback, but these suffer the difficulty that they themselves arise out of star formation. It appears that feedback from AGNs is required. Croton et al. (2006) constructed their model around the assumption of radio feedback from those AGNs that lie at the centre of a quasi-static X-ray emitting atmosphere within a galaxy group or cluster. Their Millennium Run model seems to have the added advantage that if the parameters are set to solve the cooling flow problem, then it also leads to a cut-off in the luminosity function of galaxies which is

in agreement with observations. It is now standard practice to include AGN feedback within simulations.

1.3 The Energetics

There is convincing evidence that the energy source for all AGNs is a black hole. Firstly, the rapid variability of X-ray emission suggests that the power system must be an extremely compact object. Given that powers of up to 10^{41}W are generated by the most luminous quasars (Wu et al., 2015), then the only feasible mechanism is accretion onto such a compact object. Secondly, observations of stellar proper motions in the local universe reveal objects orbiting a compact central object at velocities of 500 - 1000 km/s, indicating a very high mass for that object. Thirdly, spectroscopic evidence comes from redshifted broad X-ray Fe lines (for example, Yaqoob et al., 1995): the profile of these lines is indicative of beaming, a transverse Doppler shift (time dilation of the moving light source) and gravitational redshift, all of which are consistent with the presence of a SMBH.

The arguments advanced in the previous sub-sections build a convincing case that AGN feedback must play a role in galaxy evolution. But how important a role? Consider the scales involved. If a black hole were the size of a table-tennis ball, then its host galaxy would be approximately twice the size of the Earth. How much influence can a black hole exert on its host galaxy? In fact, it is straightforward to show that the influence could be profound:

- As matter accretes onto a black hole, the energy released is in the range of 4% - 42% of the rest mass energy of the accreting material (see Peacock, 2010, chapter 2). The exact fraction depends on the rate of spin of the black hole, but a standard assumption is that, on average, around 10% of the rest mass energy is released (appropriate for a non-rotating black hole).
- Over the lifetime of the black hole, the energy that has been released is, therefore, $E_{BH} \approx 0.1 M_{BH} c^2$.
- The binding energy of a galaxy is $E_{gal} \approx M_{gal}\sigma^2$, where σ is the velocity dispersion of the galaxy.
- As discussed above, $M_{BH} \approx 0.005 M_{gal}$ using the relation found by Kormendy and Ho (2013).

- Combining the three expressions above, $\frac{E_{BH}}{E_{gal}} \approx 0.0005(\frac{c}{\sigma})^2$.
- The velocity dispersion of a galaxy would typically be below 400 km/s, implying that $E_{BH} > 280\ E_{gal}$.

The energy produced during the growth of a black hole would, therefore, be many times greater than the binding energy of the host galaxy. If even a small fraction of that energy were transferred into the gas, then the effect on a galaxy's behaviour could be significant.

1.4 The Classification of Active Galactic Nuclei

Active galaxies have traditionally been placed into a number of categories, according to their luminosity, spectral properties and ratio of nuclear to host galaxy stellar light; the categories include Seyfert galaxies, quasars, QSOs, LINERs, Blazars and radio galaxies. Progressively, however, the view has developed that AGNs can be more usefully divided into just two fundamental types, with the division dependent on how much material is being accreted onto the SMBH.

The theory underpinning the view that there are two types of AGNs, defined by the rate at which material is being accreted, has been developed principally by Narayan and Yi in the 1990's. The key paper, out of a series published, is Narayan and Yi (1995). The authors derived a suite of flow equations governing the accretion of material onto a black hole and, by imposing certain conditions, found a family of self-consistent solutions (their Section 2). Their conclusions can be summarised as follows:

- A critical factor is the fraction of viscously dissipated energy from the accretion inflow that is stored in the gas as entropy as opposed to being radiated away.
- If that fraction is small – that is, very little advection – then the solutions imply a standard, geometrically-thin accretion disk and, by construction, a high proportion of the energy is radiated away.
- By contrast, in the advection-dominated case the solutions imply that accretion is almost spherical, the gas is close to the virial temperature and

the gas is rotating at far below the Keplerian rate. This is more akin to Bondi accretion, discussed shortly in Section 1.4.2.

- The Bernouilli parameter is the sum of the kinetic energy, the potential energy and the enthalpy of the accreting gas and determines the probability that outflows or winds may occur spontaneously. In the advection-dominated case, this parameter is positive across most of the flow, and particularly so at angles close to the rotation axis. The implication is that bipolar outflows are likely along the rotation axis.

- Furthermore, the authors suggest that, while radiation and magnetic fields would help, the jets could be produced without these fillips provided that the material stays adiabatic during the initial acceleration phase of the outflow.

The threshold value that marks the division between the two types of AGNs is approximately 1% of the Eddington limit (Best and Heckman, 2012). The Eddington limit itself defines the maximum accretion rate (and hence maximum luminosity) that is possible, which occurs when the radiation force acting outwards exactly balances the gravitational force acting inwards. The reasons for a transition at this threshold are still imperfectly understood, and the exact fraction of the Eddington limit is believed to depend on, inter alia, the rate of spin of the SMBH and, especially, the viscosity of the accretion disk (Qiao and Liu, 2009).

Over the past ten years research into the relationship between stellar mass and halo mass has tended to validate the theory, to confirm the existence of two different feedback mechanisms and to provide further insights into the crossover point from the radiative- to the jet-mode. Figure 1.6, taken from Behroozi et al. (2010), plots the stellar mass to halo mass (SM–HM) relationship for the local universe. It illustrates the well-known point that high-mass galaxies have a significantly different scaling for the SM–HM relationship than do low-mass galaxies and suggests that the cross-over point is at a stellar mass of $10^{10.6}\,M\odot$, in broad agreement with the green valley shown in Figure 1.5. More interestingly, detailed analysis of the curve by the authors reveals that the SM–HM relation cannot be fitted with a power-law above that cross-over mass. They argue that the data are consistent with a transition region in which galaxies may be subject to multiple feedback mechanisms and further suggest that the width of the transition region may be influenced by the time taken for galaxies to gain stellar mass,

the fraction of stellar mass that arose from quiescent star formation as opposed to having been merger-driven and the extent of interaction between different feedback mechanisms.

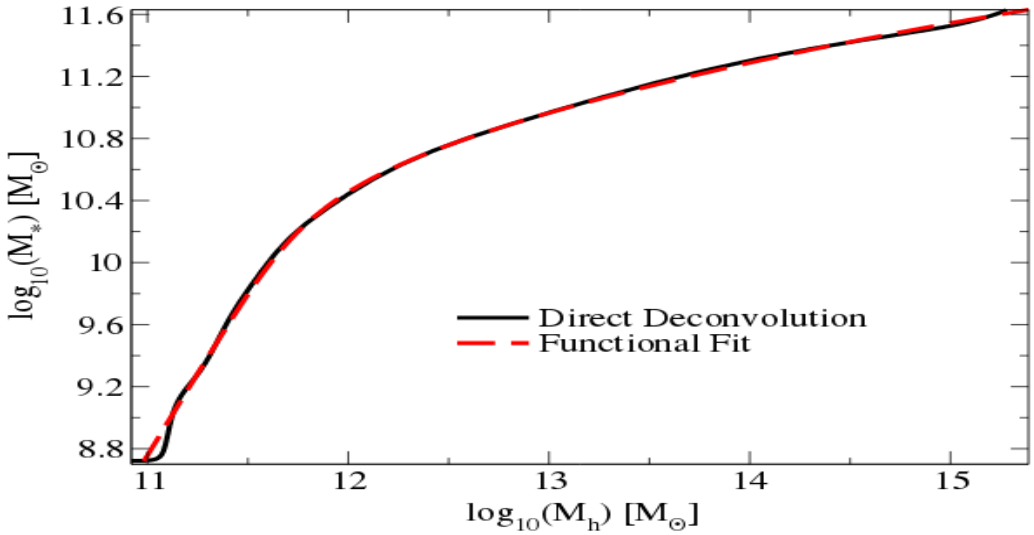

Figure 1.6 *The stellar mass – halo mass relation in the local universe, derived from the stellar mass function of Li and White (2009) matched to the simulated distribution of haloes. Source: Behroozi et al. (2010).*

Confusingly, the literature abounds with different names for the two classifications of AGNs. If the inflow is above the threshold fraction, then an AGN is said to be in cold, high-excitation, radiative, quasar or wind mode; if the inflow is lower than that threshold, then the names used are hot, low-excitation, jet, radio, kinetic or maintenance mode. Here, the nomenclature will follow that used by Heckman and Best (2014), with the two types referred to as radiative-mode AGNs and jet-mode AGNs.

Schematic diagrams of the the two types of AGNs are shown in Figure 1.7 and these are explained in the following two sections.

1.4.1 Radiative-mode AGNs

Radiative-mode AGNs are found in relatively young, growing galaxies, which implies that the peak of this activity occurred at redshifts of between two and three.

Infall onto a SMBH occurs through a geometrically-thin, but optically-thick, accretion disk that reaches in to within a few Schwarzschild radii of the SMBH

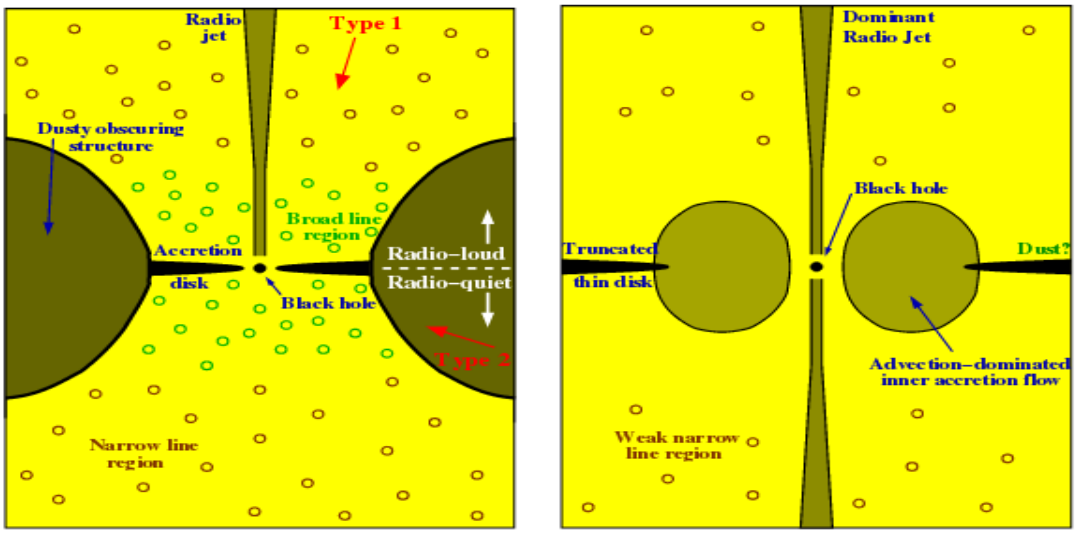

(a) *A radiative-mode AGN.* **(b)** *A jet-mode AGN.*

Figure 1.7 *Schematics, not to scale, of the two types of AGNs. (a) Radiative-mode AGNs have a geometrically thin, optically thick accretion disk. Luminous UV radiation from the disk illuminates the broad-line and narrow-line regions. An obscuring structure of gas and dust surrounds the central regions. (b) Accretion in jet-mode AGNs is through a geometrically-thick advection-dominated accretion flow; at larger radii, there may be a transition to an outer truncated thin disk. Most of the energetic output from these sources is released through radio jets. Source: Heckman and Best (2014).*

(shown schematically in the left-hand diagram in Figure 1.7). Thermal emission from the accretion disk is the dominant energy source of the AGN, with the radiation peaking in the optical and ultraviolet wavebands. The lower energy photons produced from this spectrum are scattered to higher energies by relativistic electrons in the surrounding corona. This inverse Compton scattering is surmised to cause the power law component in the X-ray spectrum (0.2-10 keV) of an AGN. Radiation from the accretion disk illuminates clouds that are very rapidly orbiting the SMBH at radii of a few light days; consequently, the lines emitted from these clouds are broad. Slower-moving gas clouds orbit the SMBH at greater distances, giving rise to narrower emission lines. An obscuring structure of gas and dust surrounds the central regions; the structure is often depicted as a torus although its exact geometry is not tightly constrained. The dusty structure is heated by radiation from the AGN and re-emits radiation in the mid- and far-infrared. Overall, therefore, radiative-mode AGNs emit right across the electromagnetic spectrum. A more detailed description is provided in Ho (2008).

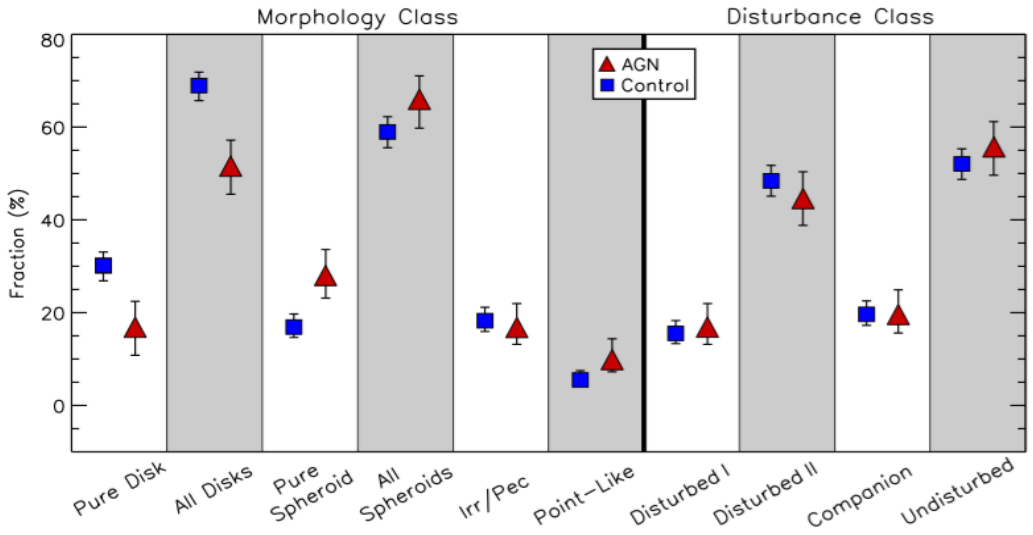

Figure 1.8 *The fraction of AGN hosts (red triangles) and control galaxies (blue squares) within different morphological and disturbance classes. Source: Kocevski et al. (2012).*

It is believed that the dusty structure prohibits a direct view of the central regions of an AGN from certain lines of sight and so the viewing angle can affect the observed spectrum; in particular, whether or not the broad lines are present. This factor is believed to explain differences between sub-categorisations of Seyfert galaxies (into Seyfert 1's and Seyfert 2's), and between QSOs and type-2 quasars; an early proponent of this orientation-based unification theorem was Antonucci (1993).

Theoretical arguments have been put forward to suggest that mergers may be the trigger for AGN activity. There is, however, little observational evidence to support that view except in the most luminous cases. Figure 1.8, taken from Kocevski et al. (2012), implies that there is no difference in the morphology of AGN hosts compared with quiescent galaxies. Sabater et al. (2015) reached a similar conclusion after reviewing recent research reports, arguing that all that is required to prompt "typical" AGN activity is a plentiful supply of cold gas in the central region of a galaxy, whatever the origin of the gas.

As matter accretes onto a SMBH, a fraction of the energy released is transferred into the surrounding gas. This can be through one of two processes. Radiated photons can heat the gas either by Compton scattering or by photoionising metals, so creating a thermal "energy-driven" wind. Alternatively, radiation pressure on dust (which has a much larger cross-section than gas) can cause a pressure "momentum-driven" wind. Both the processes described have large inefficiencies

(Cattaneo et al., 2009) and it is difficult to calculate theoretically the fraction of energy emitted from a SMBH that is deposited in gas and dust.

The transfer of energy into gas is the basis for the putative feedback process for radiative-mode AGNs. Simulations show that a galactic wind can significantly reduce star formation, particularly in lower mass systems; in a high-mass galaxy, the effect on star formation is less pronounced (for example, the EAGLE project described by Schaye et al., 2015). However, the expulsion of gas and dust from a galaxy, whilst quenching star formation, also cuts off the fuel to the AGN. Once the AGN activity has reduced, or ceased, gas is able to fall back into the galaxy, restarting the cycle. Hence, it is speculated that there are episodic periods of star formation coinciding with growth of a SMBH, leading to the correlation in the mass of a SMBH and its host galactic bulge.

Establishing a causal link between radiative-mode feedback and the quenching of star formation is fraught with difficulties for several reasons. There is the general point that the central regions of an AGN are likely to be obscured by a dusty torus. The radiative mode occurs mostly at higher redshifts. An AGN is likely to outshine its host galaxy, hindering the gathering of data on the galaxy. Furthermore, as mentioned above, a galaxy hosting a radiative-mode AGN is also likely to be experiencing substantial star formation (albeit at lower rates than would be theoretically expected without a feedback mechanism) which makes it hard to disentangle the effect of AGN feedback from that caused by stellar activity. The observational evidence is mostly circumstantial:

- It is known that AGNs do drive super-winds. Spectroscopic evidence in the form of blue-shifted absorption lines show that highly-ionised gas is outflowing with speeds (well) above 500 km/s (for example, Netzer, 2015), believed to be the upper limit for supernova-driven winds. It is not easy, however, to estimate accurately the masses of the gas involved in these winds, with uncertainties in estimates greater than an order of magnitude. This, in turn, makes it difficult to establish a causal link between the presence of a quasar wind and the cessation of star formation.

- Galaxies reside in dark matter haloes, with the total mass of the halo an order of magnitude greater than the stellar content. Silk and Nusser (2010) have argued that AGN feedback would not be sufficiently energetic to eject gas from the halo as well as the galaxy. This implies that gas would end up trapped in the halo, and it is possible that the squeezing of the gas

during ejection from the galaxy could trigger star formation in shells. Bieri et al. (2016) used simulations to show that such overpressurisation can boost a galaxy's star formation rate. There is some observational evidence: van Dokkum et al. (2010) found such a shell pattern in galaxies around a redshift of two, when quasar activity was at its peak. Also, observations by Salomé et al. (2015) and Rauch et al. (2013) in the local universe and at a redshift of 3.0 respectively appear to show evidence of AGN-induced star formation.

- The chemical composition of giant elliptical galaxies suggests that star formation occurred in a relatively short time (for example, Renzini, 2006), which argues in favour of some mechanism that could abruptly stop star formation.

There is still, therefore, considerable uncertainty in assessing the importance of quasar winds in quenching star formation. There is a pressing need to obtain better estimates for the masses, length scales and temperature structure of the winds.

1.4.2 Jet-mode AGNs

Jet-mode AGNs tend to be linked with more massive black holes that are found in older galaxies, those whose morphologies consist of classical bulges and massive ellipticals. Gas in these galaxies is hot and relatively little star formation is occurring. The AGN is accreting at significantly below – less than about 1% of – the Eddington limit in a radiatively inefficient process.

The structure of a jet-mode AGN is believed to differ from that of a radiative-mode AGN (Heckman and Best, 2014, and references therein). The accretion disk is either absent or truncated in the inner regions; instead, there is a geometrically-thick structure, which leads to an inflow time that is much shorter than the radiative cooling time (Ho 2008); this is shown in the right-hand diagram in Figure 1.7.

Bondi (1952) derived an accretion rate formula for hot gas surrounding a black hole:

$$\dot{M} = \frac{16\pi G^2 M_{BH}^2 \rho(r_a)}{c_s^3} \tag{1.8}$$

where $\rho(r_a)$ is the density of the gas at the accretion radius $r_a = 2GM_{BH}/c_s^2$ and c_s is the sound speed. The Bondi formula has tended to be used in numerical simulations. It is, however, based on an ideal set of assumptions – unperturbed and steady initial conditions, adiabaticity, the absence of magnetic fields, spherical symmetry – and it tends to generate infalls that are (much) lower than those required to fuel observed activity from the most luminous AGNs. Also, viscosity is ignored in the Bondi formula, yet infall of gas into a black hole requires a substantial transfer of angular momentum from the gas to stars or to dark matter and viscosity has a crucial role in that process. Gaspari et al. (2013) investigated the effect on the Bondi formula of a more realistic set of conditions. The key point from their analysis is that in a common astrophysical scenario the general clumpy medium and cooling flow lead to colder clumps, accretion is mainly cold and chaotic, filaments are created by turbulent and tidal forces and these allow accretion rates to be up to two orders of magnitude higher than those predicted by the Bondi formula. Such rates are sufficient even for the more powerful jet-mode AGNs.

The accretion of hot gas onto very massive black holes generates two-sided jets. The mechanism that produces the jets is not yet understood, but a leading hypothesis is that the mass and spin of a SMBH distort space and time, twisting magnetic field lines into a coil that propels material outwards (see the review by Romero et al., 2017). There is observational support for the theory. Firstly, Marscher et al. (2008) studied a comparatively nearby – at a distance of 300 million parsecs – blazar, BL Lacertae, during a period of extreme outburst. The observations from the National Science Foundation's Very Long Baseline Array (VLBA) radio telescope revealed material spiralling outwards, in line with predictions. Secondly, it follows that the greater the mass of a black hole, the greater the probability of jets (and, to a lesser extent, the greater the power of the jets). This has indeed been observed, with Best et al. (2005) finding that radio-AGN activity is a very strong function of black hole mass.

It appears that the distorted magnetic field lines pull charged particles off the geometrically-thick structure and accelerate them outwards at close to the speed of light. The jets can extend for mega-parsecs, far outside the galaxy itself. When launched, the particles travel at relativistic velocities. It is believed that, in most cases, the particles decelerate quickly once they hit the gaseous halo of the host galaxy and then dissipate into sub-sonic plumes. The jets generate expanding shock fronts where they impact the surrounding intergalactic medium (IGM) and,

as the shock fronts advance, the plasma builds up behind them within low-density cavities. These bubbles are sufficiently buoyant to rise through the intracluster medium (McNamara et al., 2000). At particularly high radio luminosities, the jets survive as highly-collimated structures until they terminate as bright shocks (hot spots) at the interface with the IGM. The bow shock associated with the expanding radio source means that, although the jets themselves are highly collimated, the radio jet energy is eventually transferred into the IGM in an isotropic manner, as illustrated in Figure 1.9.

Reviewing recent studies, Fabian (2012) concludes that, out of twenty clusters in which a cooling problem can be identified, bubbles are observed by Chandra in nineteen (the twentieth cluster is currently undergoing a merger). Given that bubbles would be difficult to observe if located exactly in our line of sight, the conclusion is that the bubbling fraction may be at least 95%. This implies that the bubbling process is not very episodic, but is fairly continuous, in the most extreme cooling flows

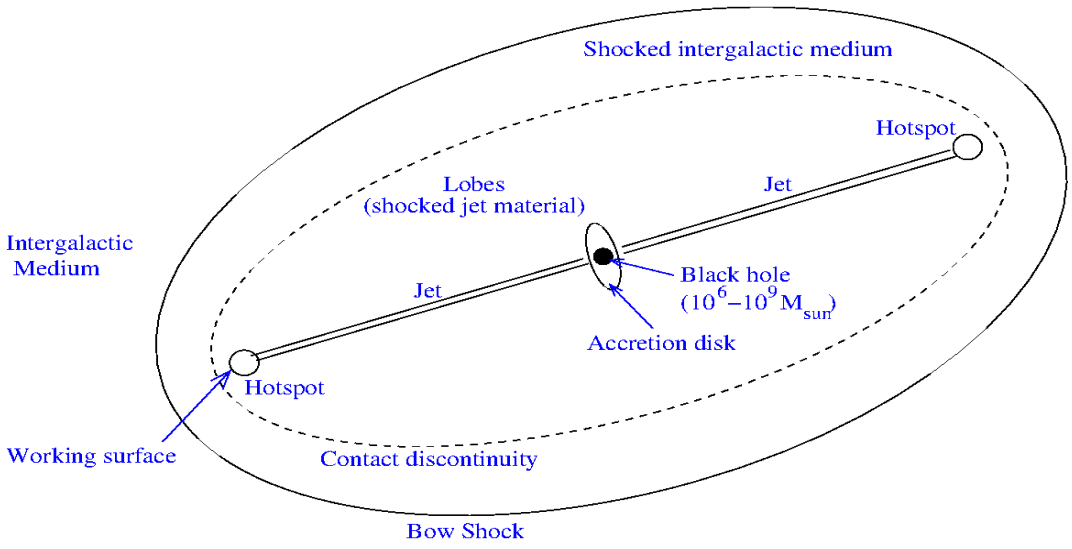

Figure 1.9 *A schematic diagram of a jet-mode AGN. Distorted magnetic field lines pull charged particles off the geometrically-thick structure and accelerate them outwards. When launched, the particles travel at relativistic velocities and the jets can extend for mega-parsecs. The particles are believed to decelerate quickly once they hit the gaseous halo of the host galaxy and then dissipate into sub-sonic plumes. The jets generate expanding shock fronts where they impact the surrounding intergalactic medium; as the shock fronts advance, plasma builds up behind them within low-density cavities. These bubbles are sufficiently buoyant to rise through the intracluster medium. Source: The University of Edinburgh, High Energy Astrophysics lecture notes.*

The X-ray cavities provide a direct means of quantifying the mechanical energy released by an AGN through measurements of the work done on the hot gaseous haloes. Cavity volumes can be estimated by combining their observed linear scale with assumptions about their geometry (Bîrzan et al., 2004). The pressure of the IGM can be obtained from measurements of its X-ray temperature and density. The energy of a cavity can then be calculated as $4pV$, the enthalpy of a cavity filled with relativistic gas. It is also possible to estimate the time over which the energy has been supplied by dividing the radial distance of the cavity from the SMBH by the assumed rising velocity of the bubble (normally taken as the speed of sound). This, in turn, allows the jet power to be estimated.

The accretion rate onto a SMBH is normally calculated from the Bondi spherical accretion model; as discussed earlier in this subsection, that may lead to a (substantial) underestimation, particularly if the measurements are made outside the Bondi radius. Assuming the standard 10% mass conversion efficiency, the energy output of the SMBH is obtained and can be compared with the jet power.

Initial studies, for example by Bîrzan et al. (2004) and Allen et al. (2006), found a close correlation between the accretion rate and the jet power. There is, however, considerable uncertainty attached to many of the assumptions underpinning the calculations described above and the closeness of that correlation has been called into question by subsequent studies (for example, Cavagnolo et al., 2010): different estimates for the energy in a cavity have been proposed, ranging from $E = pV$ up to $E = 10pV$; the validity of Bondi spherical accretion model has been questioned; and it has been suggested that energy from the spin of the black hole can also be channelled into the jet (for example, Benson and Babul, 2009). Nevertheless, it seems safe to conclude that much of the energetic output of a SMBH is channelled into the jets and that their power is eventually transferred into the IGM where it offsets the radiative cooling of the gas.

That leaves the question of whether the energy deposited by the jets into the gas is sufficient to solve the cooling problem described in Section 1.2.4. Best et al. (2005), Best et al. (2007) and Nulsen et al. (2007) have addressed the problem. The average rate of jet kinetic energy production of a black hole can be estimated from its radio luminosity. Jet production is believed to be episodic and the duty cycle can be estimated from the fraction of galaxies that host an AGN as a function of black hole mass. The cooling rate of the gas can be found from its X-ray luminosity, considering only that from within the cooling radius. The consensus view from these three papers is that the radio-AGN heating rate is at

least sufficient to balance the radiative losses in the most massive clusters and to exceed the heating rate by more than an order of magnitude when considering individual elliptical galaxies. Even allowing for the fact that, especially in smaller systems, part of the energy of the jet will be deposited outside the cooling radius and allowing for the approximations within the calculations, it seems safe to assume that jet-mode AGNs are a viable explanation for the lower-than-expected star formation.

Energy from an AGN is, therefore, deposited into the same gas that fuels the AGN - the ingredients are in place for a feedback cycle. Note that for a feedback process to be efficient, an AGN must be able to react quickly to changes in the environment so that the heating - cooling balance can be maintained. This is also an argument against Bondi accretion since Soker (2006) demonstrates that under Bondi accretion the infall of hot gas from the IGM into a SMBH occurs on timescales of over 1 Gyr; by contrast, Gaspari et al. (2013) argue that variations in the rate of cold clump accretion can occur on the much more rapid timescales demanded by an efficient feedback mechanism.

The synchrotron radiation generated by the jets and from the cavities can be observed at radio frequencies, while the cavities can also be viewed directly at X-ray frequencies. The gas surrounding a galaxy is hot, highly ionised and mostly transparent. There is, therefore, plenty of observational evidence to support the feedback theory. Despite that, the details of the feedback mechanism remain unclear. Current instruments do not have the sensitivity required to allow detailed study of individual elliptical galaxies: the X-ray luminosity of a single galaxy can be five orders of magnitude smaller than that of the brightest clusters. Also, inadequate resolution means that selection effects hinder research; as one example, large but not small bubbles are detectable.

1.5 Microquasars

There is an opportunity to study the accretion process and the launching of jets in objects that are located within our own galaxy.

Given that black holes are characterised simply by their mass and their spin, most of the ongoing processes should be scale-invariant. Support for that view is provided by microquasars, radio-emitting X-ray binaries. As the name suggests,

microquasars are scaled-down versions of quasars. Like quasars, they contain a spinning black hole (in this case, locked into a binary system with a companion star), an accretion disk and collimated jets of relativistic particles. The properties of the two types of object clearly differ: a microquasar's black hole has a mass that is typically a few tens of that of the sun; the temperature of its accretion disk is several million degrees compared with several thousand degrees for a quasar; its accretion disk is of the order of a few thousand kilometres in size compared with millions of kilometres for a quasar; and the particles in the jets travel a few parsecs instead of over a million parsecs for the more powerful quasars.

Nevertheless, the underlying physics that leads to the launching of the jets is believed to be the same. Jets from black holes that span nine orders of magnitude in mass are morphologically similar and the core emission tends to display the same flat power-law spectrum. The scale invariance leads to the concept of the Fundamental Plane of black hole activity — an empirical relationship between the black hole mass, radio luminosity (a probe for the radio jet) and X-ray luminosity. Black hole binaries in our own galaxy and AGNs both lie upon the same relationship. The tightest relationship for X-ray binaries is seen for those in the "low-hard" state; this implies binaries with low Eddington fractions and so the appropriate counterparts with which comparisons should be made are jet-mode AGNs such as LINERs. The Fundamental Plane, which is described more fully by, for example, Merloni and Heinz (2007) and Saikia et al. (2015), is investigated in detail in Chapter 2 of this thesis.

The study of microquasars has the potential to improve our understanding of the physics of accretion disks and the formation of jets near the horizon of a black hole. Jets produced by microquasars are easier to study because their apparent motions in the sky are approximately two orders of magnitude faster than those from quasars (Mirabel and Rodriguez, 1995). Timescales associated with jets are broadly proportional to the mass of the black hole, so variations that might last centuries for a quasar may be experienced in a day for a microquasar. There has, however, been a drawback: paradoxically, it is easier to find extragalactic jet-mode AGNs than to find microquasars in the Milky Way. Accretion disks in AGNs emit strongly in the optical and ultraviolet, whereas those of microquasars need to be identified by their X-ray emission. This has meant that the number of known microquasars is still not large, although it should grow rapidly with the development of new X-ray wide-field surveys. For the moment at least, the study of jet-mode AGNs is likely to provide the greatest insights into the physics

involved in the launching of relativistic jets.

1.6 The Radio Luminosity Function

The luminosity function can provide valuable insights into the structure and evolution of AGNs. Investigations into the luminosity function tend to support the division of AGNs into the two categories defined by different accretion modes. It was discovered fifty years ago by Longair (1966) that radio AGN sources exhibit luminosity-dependent evolution, with the space density of the high-luminosity population rising strongly with redshift, but with much less evidence of cosmic evolution at lower luminosities. There have been many later works investigating radio luminosity function evolution that have confirmed this picture, for example Dunlop and Peacock (1990) and Rigby et al. (2011). This supports the two-population classification of AGN: radiative-mode AGNs dominate at only the highest luminosities and evolve rapidly with redshift, whereas jet-mode AGNs evolve more slowly.

Until recently, however, the lack of precise classification of AGNs as jet-mode or radiative-mode has meant that this has been an inferred result, rather than one that has been directly measured. To investigate this in more detail Best and Heckman (2012), Best et al. (2014) and Pracy et al. (2016) assembled samples of jet-mode and radiative-mode AGNs and constructed luminosity functions for the local universe and out to redshifts of 1.0 and 0.75 respectively. The luminosity functions of the radiative-mode and jet-mode AGNs were found to have breaks at significantly different luminosities, providing further evidence that the accretion modes are different for the two categories of AGNs. All teams of researchers confirmed that the radiative-mode population evolved quickly through the redshift range under examination, consistent with these AGNs being hosted by young star-forming galaxies. The result also provides support for the view that both radiative-mode AGNs and star-formation activity are dependent on the available supply of cold gas to the galaxy.

These studies found little evolution in the jet-mode population, consistent with jet-mode AGNs evolving broadly in line with the stellar mass function of massive quiescent galaxies. There were slight differences in the detail of the luminosity functions of the jet-mode AGNs: Pracy et al. (2016) found little or no evolution up to redshift $z = 0.75$, whereas Best et al. (2014) found slow positive evolution

out to a redshift of 0.6 and a decline thereafter. Not only that, but Best et al. (2014) found that the positive evolution was driven by the highest-luminosity jet-mode AGNs and there was a slight negative evolution for the lowest-luminosity objects. To explain that, they considered several possible models:

- The evolution is driven simply by the change in redshift of the space density of their host galaxies, which are massive quiescent galaxies.
- The model above is adapted to incorporate a time delay between the formation of quiescent galaxies and the onset of jet-mode AGN activity.
- An assumption is made that the typical luminosity of jet-mode AGNs increases with redshift possibly due, for example, to subtle changes in the halo hot gas fraction, the cooling function or the average density of the medium into which the jets are expanding.
- The jet-mode population is contaminated by a population linked to the radiative-mode AGNs: accretion onto an AGN is a stochastic process and accretion rates may temporarily fluctuate across the critical Eddington fraction, resulting in radiative-mode AGNs being classified in the jet-mode.

These models can lead to similar evolution patterns up to a redshift of around z = 1, but the luminosity functions are expected to diverge thereafter. Extending measurement of the jet-mode luminosity function out to redshift z = 2 is a key part of the work described in Chapter 5 of this thesis, where the luminosity function is discussed in more detail.

1.7 A Summary of AGN Feedback

The overall picture that emerges can be summarised as follows. The radiative mode occurs when a galaxy and its AGN are comparatively young. At that stage, the galaxy contains huge volumes of cold molecular gas, substantial star formation is occurring and an AGN is accreting at a significant fraction of the Eddington limit. Stellar feedback is important in such galaxies; by contrast, AGN feedback, arising from radiation-induced expulsion of gas and dust from the galaxy, is likely to be a significant factor only when the AGN becomes particularly powerful. At that time, the SMBH turns into a quasar and may blow away surrounding gas and dust, leading to the cessation of each of star formation, growth in the galaxy

and growth in the AGN. This is the phase that links the mass of an AGN with that of its host galaxy. The jet-mode phase occurs thereafter when the SMBH has attained a large mass, but is accreting at less than 1% of the Eddington limit as gas cools slowly and falls back into the galaxy. The jet-mode feedback maintains a comparatively constant flow of infalling gas, which allows the galaxy and SMBH to grow in tandem and so preserves the mass correlation.

Direct observational evidence of the radiative-mode feedback has been hard to obtain. Not only does this phase occur mainly at higher redshifts, but, by definition, it is taking place in a dusty environment and so obscuration is a major problem. By contrast, the jet mode can be more easily observed, at radio and X-ray frequencies, since it is occurring now in nearby massive objects; nevertheless, our understanding of the advection-dominated accretion process and the mechanism(s) responsible for the launching of jets remains imperfect.

There remain many unanswered questions. Fabian (2012) and Kormendy and Ho (2013) summarised a number. How many radiative-mode phases does a galaxy undergo - one or several? What is the relative importance of starburst-driven feedback and AGN feedback in driving cold gas out of early-type galaxies? Are observations of local AGNs representative of powerful quasars around a redshift of two? Can radio-jet energy be thermalised and is it confined within individual galaxies? How important is the spin of a SMBH in determining the energy released in the collimated jets? Is AGN feedback the main energy source that keeps gas hot? Alternatives include a shock process from the infall of gas from the cosmological web (Dekel and Birnboim, 2008) and gas recycled from dying stars that is injected into the halo at the kinetic temperature of stellar motions. Also, critically, how does jet-mode feedback evolve over cosmic time?

A number of new radio facilities have recently, or are about to, come on stream which should help to resolve some of these issues. Low-frequency radio observations from the LOw-Frequency ARray (LOFAR) and the Square Kilometre Array will provide information on the electron populations in the bubbles of cluster cores and, by mapping parts of the sky at a redshift of two, will provide an insight into the relative importance of AGN feedback and the environments in which it has taken place. At GHz radio frequencies, the Jansky Very Large Array will study the interactions of jets with plasma and examine the plasma's magnetic field structure. The Atacama Large Millimetre/submillimetre Array should offer the spatial and spectral resolution necessary to penetrate the high absorption around radiative-mode AGNs.

1.8 The Structure of this Report

This thesis uses a number of surveys at different wavelengths, but particularly low-frequency (150 MHz) radio observations from LOFAR of the ELAIS-N1 field, to improve our knowledge of jet-mode AGN feedback and hence of the interplay between the complicated processes involved in galaxy formation and evolution. The structure is as follows.

In Chapter 2, the Fundamental Plane of black hole activity is investigated and the relationship derived using a sample of 576 X-ray selected LINERs. The remainder of the main body of the thesis is based on LOFAR observations of the ELAIS-N1 field. Chapter 3 describes the matching of the radio sources to their host galaxies and, importantly, sets out a new likelihood ratio method of achieving the cross-match. A collaborative effort is currently developing a pipeline that will standardise and, as much as possible, automate the extraction of radio sources from a LOFAR image and allow the identification of their optical counterparts. The catalogue produced in Chapter 3 was used to assist in the development of that pipeline and these inputs are set out in Chapter 4. Chapter 5 describes the science results extracted from the ELAIS-N1 catalogue, in particular by extending the luminosity function of jet-mode AGNs out to a redshift of 2. Chapter 6 summarises the key conclusions from the thesis and outlines future avenues that can be explored. A separate project used radio observations to examine the Schmidt-Kennicutt relationship at higher redshifts. This topic, which is distinct from the work in the main thesis, is described in Appendix A. Finally, the catalogues produced for the work in Chapter 2 and in Chapters 3 to 5 are shown in Appendices B and C respectively.

The cosmology used throughout this thesis assumes parameter values of $\Omega_m = 0.3$, $\Omega_\Lambda = 0.7$ and $\mathrm{H}_0 = 70\,\mathrm{km\,s^{-1}\,Mpc^{-1}}$. Also, when discussing the spectral index of radio sources, α is defined from $S_\nu \propto \nu^{-\alpha}$ and, unless otherwise stated, an index of $\alpha = 0.75$ is assumed.

Chapter 2

The Fundamental Plane and Mass Function of LINERs

2.1 Introduction

The research contained in this chapter has been published in Nisbet and Best (2016).

This thesis focuses on jet-mode AGNs. As discussed in the previous chapter, there are a number of areas where our understanding of these objects is limited. These include the mechanism that causes the launching of the jets and details of the way in which AGNs restrict star formation in their host galaxy. In order to investigate these issues, a sample of 576 LINERs (Low-Ionisation Nuclear Emission-line Regions) was assembled, with the AGNs selected on the basis of their hard (2 – 12 keV) X-ray luminosity. Note that not all LINERs are believed to host an AGN (for example, Sturm et al., 2006), but the hard X-ray selection limit implies that the LINERs in this sample do. X-rays provide one of the most direct evidences of nuclear activity and are fundamental to the study of the accretion process. The sample was used to investigate the fraction of galaxies hosting a LINER as a function of both stellar mass and black hole mass, and also to investigate the Fundamental Plane of black hole activity – the scale-invariant relationship between black hole mass, X-ray luminosity and radio luminosity described in the previous chapter.

This chapter is structured as follows. A brief description is given in Section 2.2

of the catalogues used to construct the sample of X-ray selected LINERs and a fuller description is provided on how the sample was constructed from these in Section 2.3. The methodology used to calculate the mass-dependent fraction of galaxies hosting an X-ray LINER is then described in Section 2.4 and the results shown. The Fundamental Plane relationship for the sample of LINERs is derived in Section 2.5 and the relationship tested against a sample of X-ray binaries. In Section 2.6, the Fundamental Plane was used to convert from an X-ray-selected to a pseudo radio-selected sample of LINERs, the mass-dependent fraction of galaxy hosts was re-examined, and then this was compared with determinations from radio-selected galaxies. The implications of the results obtained in the analysis are then discussed in Section 2.7, followed by a summary of the key conclusions in Section 2.8.

2.2 The Catalogues

This work has been carried out on a database of LINERs, for which both X-ray and radio luminosity information and black hole mass estimates are available. The sample was constructed by crossmatching the fourth data release of the 3XMM Serendipitous Source catalogue of X-ray sources (released by the XMM-Newton Survey Science Centre; XMM-SSC 2013) with the seventh data release from the Sloan Digital Sky Survey ((SDSS-DR7; Abazajian et al., 2009) and then adding in radio luminosity data obtained from the Faint Images of the Radio Sky at Twenty-cm (FIRST) catalogue (Becker et al., 1995).

2.2.1 The SDSS Spectroscopic Sample

The SDSS (York et al., 2000) is a major multi-filter optical imaging and spectroscopic survey conducted on a dedicated 2.5-metre telescope at the Apache Point Observatory, New Mexico. This study used the seventh data release (SDSS-DR7), produced from a survey area that covers approximately one-quarter of the extragalactic sky. The spectra span an observed wavelength range of
3800 – 9200 Å.

The work used only galaxies selected to be in the main galaxy sample. The selection process of these is described in Strauss et al. (2002). In summary, the objects must have a signal / noise of more than 5, they must not exceed

certain saturation, brightness or blending thresholds, they must have a Petrosian magnitude of $r < 17.77$ and they must be spectroscopically confirmed as galaxies. The median redshift of galaxies in the main sample is 0.104.

For each of the galaxies in the catalogue, a large number of physical parameters have been estimated from the photometric and spectroscopic information in the MPA-JHU value-added catalogues (Brinchmann et al., 2004). The parameters used within this research are the redshift, total stellar mass, 4000Å break strength, Hδ absorption measure, accurate emission-line fluxes and galaxy velocity dispersion from which the black hole mass is estimated (described later in this chapter). The methods used to derive the parameters are described in Kauffmann et al. (2003a,b,c) and Heckman and Kauffmann (2004).

2.2.2 The 3XMM Catalogue of X-ray Sources

3XMM-DR4 is the latest catalogue of serendipitous X-ray sources from the European Space Agency's (ESA) XMM-Newton observatory, and has been created by the XMM-Newton Survey Science Centre (SSC) on behalf of ESA (Rosen et al., 2016). The catalogue contains source detections drawn from a total of 7427 observations taken by the XMM-Newton European Photon Imaging Camera (EPIC) between 2000 and 2012 inclusive. For net exposure time $\geq$ 1ksec, the total area of the catalogue fields is $\sim$1397 square degrees. Taking account of the substantial overlaps between observations, the net sky area covered independently is $\sim$794 square degrees.

The catalogue contains 531,261 detections, of which 372,728 are unique X-ray sources. Due to intrinsic features of the instrumentation as well as some shortcomings in the source detection process, some detections are considered to be spurious or their parameters are considered to be unreliable. Just over 80% of the sources are considered to be clean (marked in the catalogue with a summary flag < 3).

This research is interested in AGNs that are selected in the hard energy range. In this energy range, LINERs are dominated by a hard power-law component that shows little intrinsic absorption, whereas at lower energies ($\leq$ 2keV) an additional soft component is often present (for example, Ho, 2008, and references therein). The 3XMM catalogue provides fluxes in the 2.0 – 4.5 keV and 4.5 – 12.0 keV bands. The median flux obtained by summing these two bands is

$\sim 1.3 \times 10^{-14}$ erg/cm^2/s, and around 20% of sources have fluxes below 1.0×10^{-14} erg/cm^2/s. The flux values from the three EPIC cameras are, overall, in agreement to $\sim$10%. The positional accuracy of the catalogue point source detections is generally < 3 arcseconds (90% confidence radius) and 90% of point sources have 1-sigma positional uncertainties < 2.4 arcseconds.

2.2.3 Faint Images of the Radio Sky at Twenty-cm

FIRST is a project designed to produce a catalogue of radio sources from a survey area of over 10,000 square degrees (Becker et al., 1995). Approximately 80% of the sky observed is in the north Galactic cap, and 20% is in the south Galactic cap. Both regions are covered by the Sloan Digital Sky Survey. Using the Very Large Array (VLA) in its B-configuration, an atlas of maps was produced by coadding the twelve images adjacent to each pointing centre. These maps have 1.8 arcseconds pixels, a typical rms of 0.16 mJy, and an angular resolution of 5 arcseconds. The noise in the coadded maps varies by only 15% from the best to the worst places in the maps, except in the vicinity of bright sources (> 100 mJy) where sidelobes can lead to an increased noise level. At the 1 mJy source detection threshold, there are $\sim$90 sources per square degree, $\sim$35% of which have resolved structure on scales from 2 – 30 arcseconds. The astrometric reference frame of the maps is accurate to 0.05 arcseconds, and individual sources have 90% confidence error circles of radius < 0.5 arcseconds at the 3 mJy level and 1 arcsecond at the survey threshold.

2.3 The Construction of the Sample of LINERs

The construction of the database of LINERs is described below and is summarised in Table 2.1.

2.3.1 The Parent X-ray Sample

Three filters were applied to the list of 372,728 unique sources in the 3XMM-DR4 catalogue.

First, extended X-ray sources, defined as those with a radius of more than

6 arcseconds, were excluded in order to remove sources dominated by the Bremsstrahlung emission of the hot gas in galaxy groups and clusters. 11% of the sources are extended, leaving 332,637 point sources.

Second, those X-ray sources whose detections were considered to be unreliable (those with a summary flag of higher than two) were filtered out; this left 290,396 X-ray sources.

Third, this research was interested in selecting LINERs, in particular looking at the hard X-ray emission from the AGN. Accordingly, the selection criterion was based on hard X-ray flux, obtained by summing the fluxes in the 2.0 - 4.5 keV and 4.5 - 12.0 keV bands. Sources were accepted only if there was a reliable signal in both of these X-ray bands. 258,675 galaxies passed this test. Results were also tested using stricter signal / noise criteria and the results were found to be consistent within the errors.

In order to facilitate comparisons with literature values, the analysis defined the X-ray flux to be that in the rest-frame 2.0 – 10.0 keV range. It was assumed that the X-ray spectrum followed a $\nu^{-\alpha}$ relationship with $\alpha = 1$; hence the 2.0 – 12.0 keV flux was reduced by 10% to convert it onto the 2.0 – 10.0 keV range. A redshift K-correction was also applied.

2.3.2 Matching with the SDSS Catalogue

There are 914,694 galaxies in the MPA-JHU SDSS-DR7 catalogue. Two cuts were applied to this list. As mentioned above, it was decided to include only sources that are in the main galaxy sample in order to avoid the introduction of biases into the sample of LINERs; for example, the luminous red galaxy sample, which probes only a range of galaxy parameter space, was thus excluded. This restriction reduced the number of galaxies by 21%, leaving 725,094. To ensure that evolutionary effects did not distort the analysis, galaxies with spectroscopic redshifts of over 0.30 were rejected. A further 1178 galaxies failed this test, leaving 723,916. The analysis was also carried out using narrower redshift ranges and no significant differences in results were found.

Three positional cross-matches of the 3XMM and SDSS catalogues were performed; these used separation distances of less than or equal to 3 arcseconds, 5

3XMM-DR4		Sources Remaining	
Total Number of X-ray Sources		531261	
After removing:	Non-unique Sources	372728	
	Extended Sources	332637	
	Unreliable Detections	290396	
	Sources with insufficient signal in either band	258675	
SDSS-DR7			
Total Number of Galaxies		914694	
After removing:	Galaxies not in Main Sample	725094	
	Galaxies with z > 0.30	723916	
Cross-match 3XMM-DR4 with SDSS-DR7		1172	
After removing:	Galaxies with no Black Hole Mass Data	1094	
Split into Categories		Classified via BPT	Selected in LINER sample
	LINERs	170	170
	Unclassified Objects	363	340
	Transition Objects	157	45
	Narrow-line AGNs	40	34
	Seyferts	214	0
	Star-forming Galaxies	150	0
	Total	1094	589
After removing:	LINERs with no Radio Flux Data		576

Table 2.1 *A summary of the filtration process used to construct the sample of LINERs (see text for details).*

arcseconds or 8 arcseconds as the criterion for deciding whether a successful match was found. They generated 980, 1172 and 1338 cross-matches respectively. The probabilities of a false match, estimated by randomising the coordinates of the X-ray sources and then performing the cross match, were found to be 2.1%, 4.1% and 8.0% respectively. Given the need to maximise the number of cross-matches but to minimise the number of false detections, a separation distance of less than or equal to 5 arcseconds was selected as the most suitable criterion for deciding whether a successful match was found. For comparison, the positional accuracy of the 3XMM catalogue is under 3 arcseconds as measured by the 90% confidence radius. The research was checked using separation distances of both 3 arcseconds and 8 arcseconds in the cross-matching process in order to ensure that the results were not dependent on the choice of separation distance; no significant differences were found. It is noted that a likelihood ratio crossmatching algorithm, along the lines of that developed in Chapter 3, could have been adopted here. This was not, however, considered critical for the scientific outcome, as shown by the similarity in results when different crossmatching radii were used.

Black hole masses for the galaxies were determined from the velocity dispersions,

using the traditional correlation in the form:

$$\log\left(\frac{M_{BH}}{M_{\odot}}\right) = \alpha + \beta \log\left(\frac{\sigma}{200\,\mathrm{km/s}}\right) \tag{2.1}$$

Estimates of the intercept, α, and the slope, β, have varied. Tremaine et al. (2002) found values of 8.13 ± 0.06 and 4.02 ± 0.32 respectively and these values have been used in much of the research conducted with the SDSS catalogue. More recent estimates have tended to find higher values of beta; for example, McConnell and Ma (2013) estimated the intercept and slope to be 8.32 ± 0.05 and 5.64 ± 0.32 respectively. In this research the McConnell & Ma values have been adopted throughout when calculating the black hole masses, and in one part of the analysis (see Section 2.5.2) it is shown that the results arising from the use of the McConnell & Ma relationship provide a better match when extended to X-ray binaries than would be obtained by using the Tremaine et al relationship.

78 of the 3XMM-SDSS matches were removed because no reliable velocity dispersion, and hence no black hole mass, information was available. This left 1094 sources.

2.3.3 Diagnostic Tests to Select LINERs

LINERs are characterised by weak, small-scale radio jets, luminosities that are weaker than Seyfert galaxies and quasars, and optical spectra that are dominated by emission lines from low-ionisation species – primarily [OI] λ6300, [OII] λλ3726,9 and [SII] λλ6717, 31 (Ho et al., 1997). A classification scheme using optical emission line ratios was first put forward by Heckman (1980) and subsequently amendments have been proposed by, inter alia, Baldwin et al. (1981), Kewley et al. (2001, 2006) and Kauffmann et al. (2003a). In this research, a two-pronged approach was adopted to identify LINERs.

The sources were first categorised, where possible, following the emission line ratio diagnostic method described in detail by Kewley et al. (2006)(their Section 3). Three diagnostic tests based on pairs of emission line ratios were prepared; the tests compared log([OIII]/Hβ) with (i) log([NII]/Hα), (ii) log([SII]/Hα) and (iii) log([OI]/Hα). The sources were split into six categories based on their locations in these diagrams (or by the absence of the relevant lines). In those cases where the three tests produced different classifications, the general principle used was to give the greatest precedence to the third test and the least precedence to the

first test. The 1094 sources were found to divide into 150 star-forming galaxies, 214 Seyferts, 170 LINERs, 157 transition objects (sources with characteristics intermediate between those of star-forming galaxies and those of LINERs and Seyferts), 40 narrow-line AGN (a mixture of type 2 Seyferts and LINERs, but with insufficient data to permit a classification) and 363 objects for which an unambiguous classification was not possible due to the absence of sufficient emission lines. Those objects classified as LINERs were accepted and those classified as Seyferts or star-forming galaxies were rejected. There are likely to be large numbers of LINERs within the transition objects, narrow-line AGN and unclassified objects and so objects in these three categories were subjected to two further diagnostic tests to sift out the LINERs.

Firstly, the Hα luminosity was compared with the X-ray luminosity in order to separate out star-forming galaxies from the AGNs within these three categories. This test exploits the fact that for star-forming galaxies the X-ray emission is expected to scale with Hα emission (for example, Kennicutt et al., 1994) and the ratio of X-ray emission to Hα emission is likely to be considerably lower than for LINERs. Sources were considered to be star-forming galaxies, and so rejected, if:

$$\log \mathrm{L_{H\alpha}} > 0.525 \log \mathrm{L_X} - 12.6 \tag{2.2}$$

The diagnostic line was set by deriving the upper limit to the star-forming population (the 150 star-forming galaxies) in our sample and, given that a second test would follow, was set at a conservative level. The test could be carried out only for those sources for which Hα information was available. Out of these, 73 sources failed the test and were rejected: 6 unclassified objects, 66 transition objects and 1 narrow-line AGN.

Secondly, the 4000Å break strength was compared with $\log(\mathrm{L[OIII]}/\sigma^4)$, where σ is the galaxy velocity dispersion; $\mathrm{L[OIII]}/\sigma^4$ is a proxy for the ratio of the luminosity to the Eddington luminosity (Kewley et al., 2006) and is therefore a fundamental property that divides LINERs from Seyferts since jet-mode and radiative-mode AGNs separate in Eddington-scaled accretion rates (as discussed in Chapter 1). The 4000Å break strength provides a measure of specific star formation within a galaxy, which also typically differs between LINERs and Seyferts. A comparison of the break strength against the proxy for the Eddington ratio should, therefore, provide an effective means of identifying LINERs from the unclassified objects, transition objects and narrow-line AGNs: the LINERs should be characterised by a relatively high break strength and

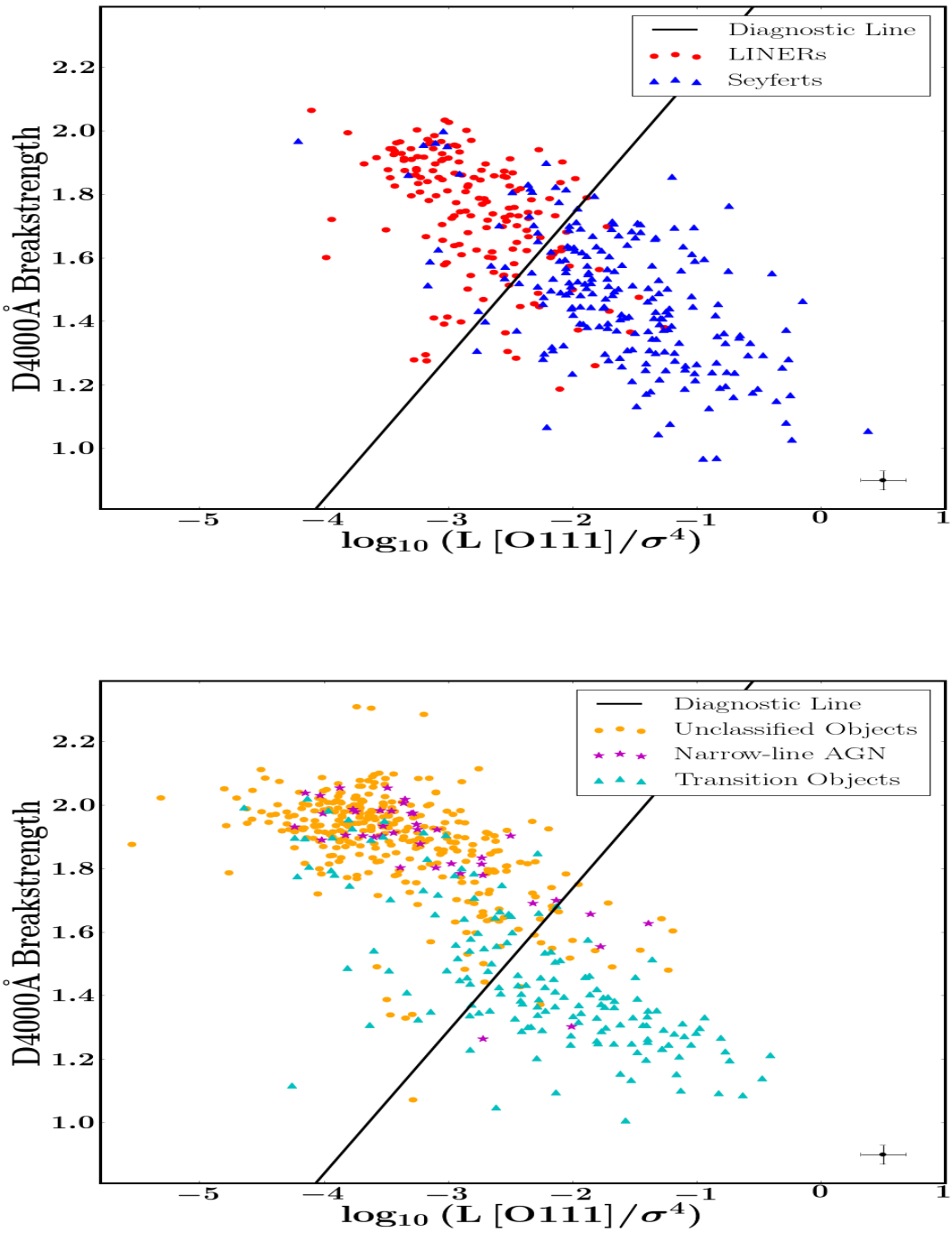

Figure 2.1 *Using a diagnostic based on the 4000Å break strength vs log(L[OIII]/σ^4) to identify LINERs amongst the unclassified objects, with L[OIII]/σ^4 measured in solar luminosities /(km/s)^4. The separating line is defined from the top panel according to Equation 2.3 and is used to classify sources in the lower panel. Typical error bars are shown in the bottom right of the diagrams.*

low Eddington ratio. There is, indeed, a comparatively clean demarcation between those X-ray AGNs classified as LINERs and Seyferts (Figure 2.1, upper). An optimisation procedure was used to select the most suitable diagnostic line – that which maximises the completeness of the sample of LINERs and minimises contamination rates. Specifically, the division line was optimised to minimise f_{wrong}, where $f^2_{wrong} = f^2_{wrong-LINER} + f^2_{wrong-Seyfert}$, and $f_{wrong-LINER}$ and $f_{wrong-Seyfert}$ are the fractions of wrongly-diagnosed LINERs and Seyferts respectively. The diagnostic line was found to be:

$$D_{4000} = 0.45 \log \left(\frac{L[OIII]}{\sigma^4} \right) + 2.64 \,, \tag{2.3}$$

where $\frac{L[OIII]}{\sigma^4}$ is measured in Solar luminosities / $(km/s)^4$. Using the diagnostic line, it can be seen that the majority of unclassified objects can be categorised as LINERs as well as a majority of narrow-line AGNs and minority of transition objects (Figure 2.1, lower). This is consistent with the facts that the narrow-line AGNs tend to be in the same area as the LINERs in the BPT diagrams (although not unambiguously so) and the unclassified objects are mostly weak-lined and hence likely to be LINERs, whereas the transition objects have associated star formation and are more likely to be Seyferts.

After both diagnostic tests, the number of selected objects was found to be 589: all 170 LINERs, 340 out of 363 unclassified objects, 45 out of 157 transition objects and 34 out of 40 narrow-line AGNs (see Table 2.1).

As discussed above, a cross-match with the SDSS catalogue was conducted using randomised coordinates for the X-ray sources and this generated 48 cross-matches; black hole mass data were available for 42 of these. These 42 sources were subjected to the same diagnostic tests and the results are shown in Table 2.2. 25 LINERs were identified, of which 24 had valid radio flux data. That represented 57% of the original 42 sources. For comparison, the corresponding proportion was 53% for the main LINER sample. The overall contamination of the LINER sample due to mismatches is $\leqslant 4\%$.

2.3.4 The Radio Properties

Radio flux densities for the sources were then obtained from the FIRST Survey. Radio data were unavailable for 13 of the 589 galaxies, either because they

Categorised into:	via BPT	of which LINERs
LINERs	5	5
Unclassified Objects	22	18
Transition Objects	3	0
Narrow-line AGNs	2	2
Seyferts	0	0
Star-forming Galaxies	10	0
Total	42	25

Table 2.2 *The classification of a sample generated by a randomised cross-match.*

were located outside of the FIRST coverage (there is not a perfect overlap with the SDSS survey area) or because the galaxies were located in regions of noisy radio flux close to bright sources. These 13 sources were discarded from the sample. Catalogue values existed for 104 of the remaining 576 LINERs. Radio flux densities for the other 472 LINERs were obtained by extracting image cut-outs from FIRST at the location of each source, fitting these with a Gaussian of FWHM 5 arcseconds at the location of the SDSS host galaxy and determining the best-fit normalisation. It was checked that this approach produced results that were consistent with the catalogue values, where they existed; it was also checked that the approach was consistent with using just the peak value.

The radio flux density was converted to an integrated luminosity using the calculated redshift for each source, the assumed cosmological model and the formula $L_R = \nu L_\nu$, where $\nu = 1.4$ GHz for the FIRST data.

2.3.5 The Final Sample

The final sample, therefore, consists of 576 LINERs. X-ray, optical and radio data, as well as estimates of redshift, stellar mass and black hole mass, are available for each of these objects. The properties of the 576 LINERs are set out in a catalogue in Appendix B.

2.4 The Fraction of Galaxies that host LINERs

The fraction of galaxies that host LINERs was investigated as a function of both stellar and black hole mass.

2.4.1 Areal Sky Coverage

The 3XMM catalogue and SDSS-DR7 catalogue cover different areas of sky. The 3XMM pointings cover a net sky area of 794 square degrees. The SDSS-DR7 spectroscopy covers 8032 square degrees, but a small part of that area corresponds to areas of noisy or absent radio data. That proportion was estimated from the fact that radio data were unavailable for 13 out of 589 LINERs, suggesting that the "missing" area is approximately 2.2%. The effective area was, therefore, taken to be 7855 square degrees. Very approximately, one quarter of the 3XMM area overlaps with the SDSS area. This implies that the 3XMM pointings within the SDSS survey area cover, very crudely, around 2% of that area. The fraction, however, varies strongly with the flux limit, because different observations have different depths and because the sensitivity varies with the location of the source within an XMM pointing.

In order to estimate the fraction as a function of flux limit (which can then be converted to a function of luminosity and redshift), the following procedure was adopted. The sky density of X-ray sources allows an estimation of the average sky area surrounding each X-ray source according to its flux. By combining this information with the number of 3XMM sources within the SDSS survey area, it is possible to estimate the fraction of the SDSS survey area covered by the XMM pointings, again as a function of flux. After binning the LINERs by flux, their number can be divided by the relevant fraction to permit a like-for-like comparison with the number of SDSS galaxies. The methodology in detail is described below.

The space density of X-ray sources, split by flux, was taken from the parameterisation derived by Georgakakis et al. (2008). They found that the number of X-ray sources above a flux level, f_x, per square degree was given by the expression:

$$N = \begin{cases} -K' \frac{f_{ref}}{1+\beta_2} \left(\frac{f_x}{f_{ref}}\right)^{1+\beta_2}, & \text{if } f_x < f_b, \\ K \frac{f_{ref}}{1+\beta_1} \left[\left(\frac{f_b}{f_{ref}}\right)^{1+\beta_1} - \left(\frac{f_x}{f_{ref}}\right)^{1+\beta_1} \right] & \\ \quad -K' \frac{f_{ref}}{1+\beta_2} \left(\frac{f_x}{f_{ref}}\right)^{1+\beta_2}, & \text{otherwise,} \end{cases} \tag{2.4}$$

where the normalisation constants K and K′ are related by $K' = K(\frac{f_b}{f_{ref}})^{\beta_1-\beta_2}$, f_b is the X-ray flux of the break of the double power law, $f_{ref} = 10^{-14}$ erg s^{-1} cm^{-2} is the normalisation flux and β_1, β_2 are the power-law indices for fluxes

fainter and brighter than the break flux respectively. For the 2.0 - 10.0 keV X-ray band, Georgakakis et al found values for β_1, β_2, f_b and K of -1.56, -2.52, $10^{0.09}$ (in units of 10^{-14} erg s^{-1} cm^{-2}) and 3.79 (in units of 10^{16} deg^{-2}/(erg s^{-1} cm^{-2})) respectively.

The number of sources per square degree was then inverted to obtain an estimate of the average area per X-ray source based on its flux.

All the 3XMM sources within 5 arcminutes of an SDSS spectroscopic source were found. There are just over 70,000 of them and this was taken as a close estimate of the number of 3XMM galaxies within the SDSS survey area. These sources were binned into 47 flux bands, spanning the range $10^{-15.85}$ to $10^{-11.15}$ erg s^{-1} cm^{-2}. For each flux band, the number of sources was multiplied by the average area per source. It was assumed that, given the wide sky coverage, clustering effects and edge effects would cancel out. The resulting estimate of areal coverage as a function of flux limit is plotted in Figure 2.2 (the blue points).

Targeting of specific sources could affect this estimation method, and this is expected to be most prevalent at the highest fluxes (as also suggested by the upturn in Figure 2.2 at these fluxes). This can be tested using the assumption that all those sources within 20 arcseconds of the centre of a pointing were targeted. The green triangles in Figure 2.2 reveal that at fluxes above $10^{-13.0}$ erg s^{-1} cm^{-2} the fraction of centred sources rises sharply. Datapoints in the flux bands above $10^{-13.0}$ erg s^{-1} cm^{-2} were, therefore, discarded when finding the best-fit polynomial. A polynomial of order five was fitted to the datapoints, shown as the blue line. The formula of the line is:

$$\log(\text{Area}) = -0.001003\,F_X{}^5 - 0.04914\,F_X{}^4 - 0.7954\,F_X{}^3 - 3.542\,F_X{}^2 + 22.91\,F_X + 186.1 \tag{2.5}$$

where the areal coverage of the 3XMM – SDSS overlap is in square arcminutes and F_X is the $\log_{10}$ flux in erg s^{-1} cm^{-2}. The log(Area) was assumed to remain constant above $F_X = -12.0$ erg s^{-1} cm^{-2}, as would be expected at these bright fluxes which should be detectable in all observations.

The average area per X-ray source based on its flux could then be divided by the total area covered by the SDSS survey to find the fraction of areal coverage at each flux density. So, it is possible to determine, for an SDSS galaxy at a given redshift, what the probability is that it will have been observed in 3XMM pointings with sufficient sensitivity to detect it down to any given luminosity.

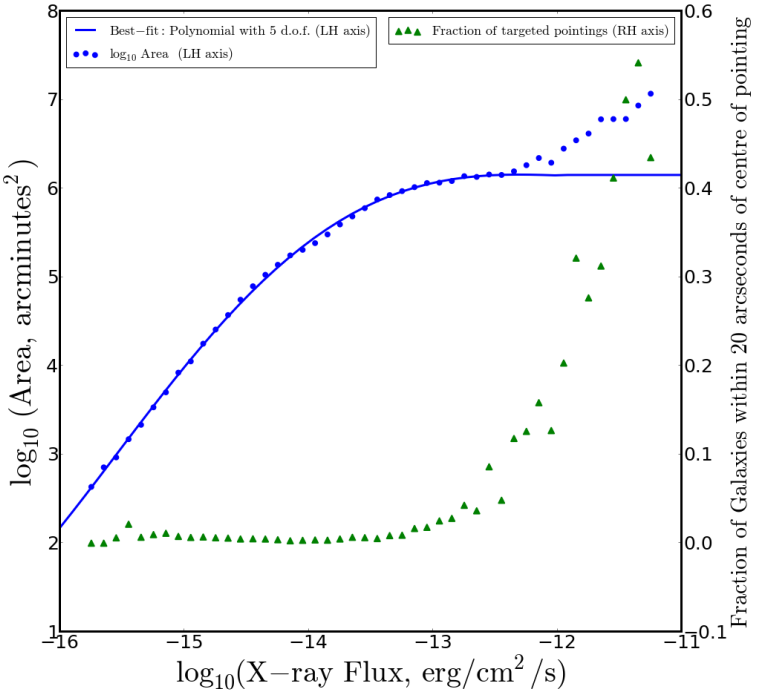

Figure 2.2 *The blue dots show the areal coverage of the 3XMM – SDSS-DR7 overlap region as a function of flux limit. The green triangles, which show the fraction of galaxies within 20 arcseconds of the centre of a pointing (right-hand axis), indicate the targeting of those sources with fluxes above* 10^{-13} *erg* $\mathrm{cm}^{-2}\mathrm{s}^{-1}$. *Data points below that flux level are fitted with a polynomial of order 5 (shown by the solid blue line); the polynomial gives the average area surrounding each X-ray source as a function of its flux.*

2.4.2 Deriving the Mass Function

It was now possible to proceed to derive the mass fraction of LINERs. The fraction of galaxies hosting a LINER at luminosity L was evaluated as:

$$f_{LINER}(L) = \frac{\sum_z N_{LINER}(z, L)}{\sum_z (fract(z, L) \times N_{SDSS}(z))} \tag{2.6}$$

where $\mathrm{N_{LINER}(z, L)}$ is the number of LINERs in the sample at redshift z and X-ray luminosity L, $\mathrm{N_{SDSS}(z)}$ is the number of SDSS galaxies at redshift z and fract(z, L) is the (luminosity-dependent) areal-coverage fraction that must be applied to ensure a like-for-like comparison between the LINERs and SDSS galaxies. Expression 2.6 was calculated in narrow bins of luminosity which could then be summed to give the overall fraction of galaxies that host a LINER. In

order to perform the calculations, the LINERs and SDSS galaxies were divided into 18 luminosity bins, ranging from $10^{40.0}$ to $10^{44.5}$ erg/s in widths of 0.25 dex. In each of the luminosity bins, the LINERs were further subdivided into redshift bins of width z = 0.01.

Datapoints were considered reliable only if the denominator – the number of potential hosts – in a given luminosity bin exceeded 20. This is to minimise any distortion caused by targeting biases. The calculation of the number of potential hosts assumes random pointings. The analysis risks distortion when the number of potential hosts is small and so a single targeted pointing has the potential to significantly affect the result. Hence, datapoints were removed from the analysis if the number of potential hosts in any relevant luminosity bin was below the specified threshold. This had the consequence of removing datapoints at low luminosities. It was checked that the results were insensitive to a change in the threshold to 10 or to 30 potential hosts.

Errors were calculated assuming a Poisson distribution for the number of LINERs. If there were no LINERs in a particular luminosity bin, the upper limit was calculated assuming a single LINER.

2.4.3 The Results

Having developed the procedure to calculate the fraction of galaxies hosting a LINER, the mass-dependent LINER fraction could now be obtained. First, three subsamples of LINERs were constructed – those with luminosity above $10^{40.0}$, $10^{41.0}$ and $10^{42.0}$ erg/s. These represent, therefore, the lowest X-ray luminosity at which the objects in each subsample could have been detected. Second, the LINERs and SDSS galaxies were further divided into bins according to stellar mass, ranging from $10^{7.5}$ to $10^{12.0}$ solar masses. For each of the three luminosity samples, the fraction of galaxies that host a LINER was then calculated for each stellar mass bin in which the number of potential hosts criterion was met. The results, which are plotted in the upper chart of Figure 2.3, show that the fraction of galaxies hosting a LINER increases significantly with the stellar mass of a galaxy for all three luminosity limits.

The slopes of the best-fitting straight lines through the three sets of points are 1.32 $\pm$ 0.05 (L > 40.0 erg/s), 1.89 $\pm$ 0.08 (L > 41.0 erg/s) and 1.70 $\pm$ 0.17 (L > 42.0 erg/s). Although the gradients are not tightly constrained because of the paucity

of datapoints and the size of the error bars, it is clear that the fraction of galaxies hosting a LINER is strongly dependent on stellar mass. It can also be seen that at low X-ray luminosities and high stellar masses, the fraction approaches unity – in other words, essentially all high-mass galaxies host a LINER. Finally, we note that a change of 1 dex in the X-ray luminosity leads to a change in the fraction of approximately 1 dex in the opposite direction.

There have been a number of studies examining the fraction of galaxies displaying X-ray AGN activity. A summary is provided by Brandt and Alexander (2015) in their Section 5.4. It is of interest to compare the results of these studies with the results from this work, although they are not directly comparable: whereas this work investigated the proportion of galaxies hosting a LINER at redshifts of below 0.30, the other studies have considered the fraction of galaxies hosting any class of AGN within wider redshift ranges. All studies have found, like this one, that the fraction is a strong function of stellar mass. However, the results of these previous studies show flatter slopes and higher normalisations than are found here. For example, Aird et al. (2012) found a slope of $\sim$0.75 that was independent of the X-ray luminosity compared with a slope in this research of 1.6 $\pm$ 0.2. For normalisation, at an X-ray luminosity threshold of $10^{42.0}$ erg/s and stellar mass of $10^{11.0}$ solar masses, Aird et al found a fraction of $\sim$0.07 compared with this study's value of $\sim$0.004. Both differences are unsurprising: the fraction of galaxies hosting a LINER is clearly lower than the fraction hosting any AGN, especially at relatively high luminosities where Seyferts dominate; and, given that LINERs tend to reside in older, high-mass galaxies, it is expected that the proportion of galaxies hosting a LINER should have a stronger dependence on stellar mass.

The analysis was repeated, but now using black hole masses rather than stellar masses. Once again, the fraction of galaxies hosting a LINER shows a strong dependence on mass (Figure 2.3, lower chart), albeit to a lesser extent than for stellar mass. The slopes of the best-fitting straight lines through the three sets of points are 0.57 $\pm$ 0.07 (L $>$ 40.0 erg/s), 0.71 $\pm$ 0.04 (L $>$ 41.0 erg/s) and 0.56 $\pm$ 0.07 (L $>$ 42.0 erg/s). The normalisation remains the same, with an increase of 1 dex in the X-ray luminosity leading to around a 1 dex decrease in the fraction of galaxies hosting a LINER, and vice versa. There is also a faint suggestion that the fractions tend to level off at higher black hole masses, but there are insufficient data to investigate this.

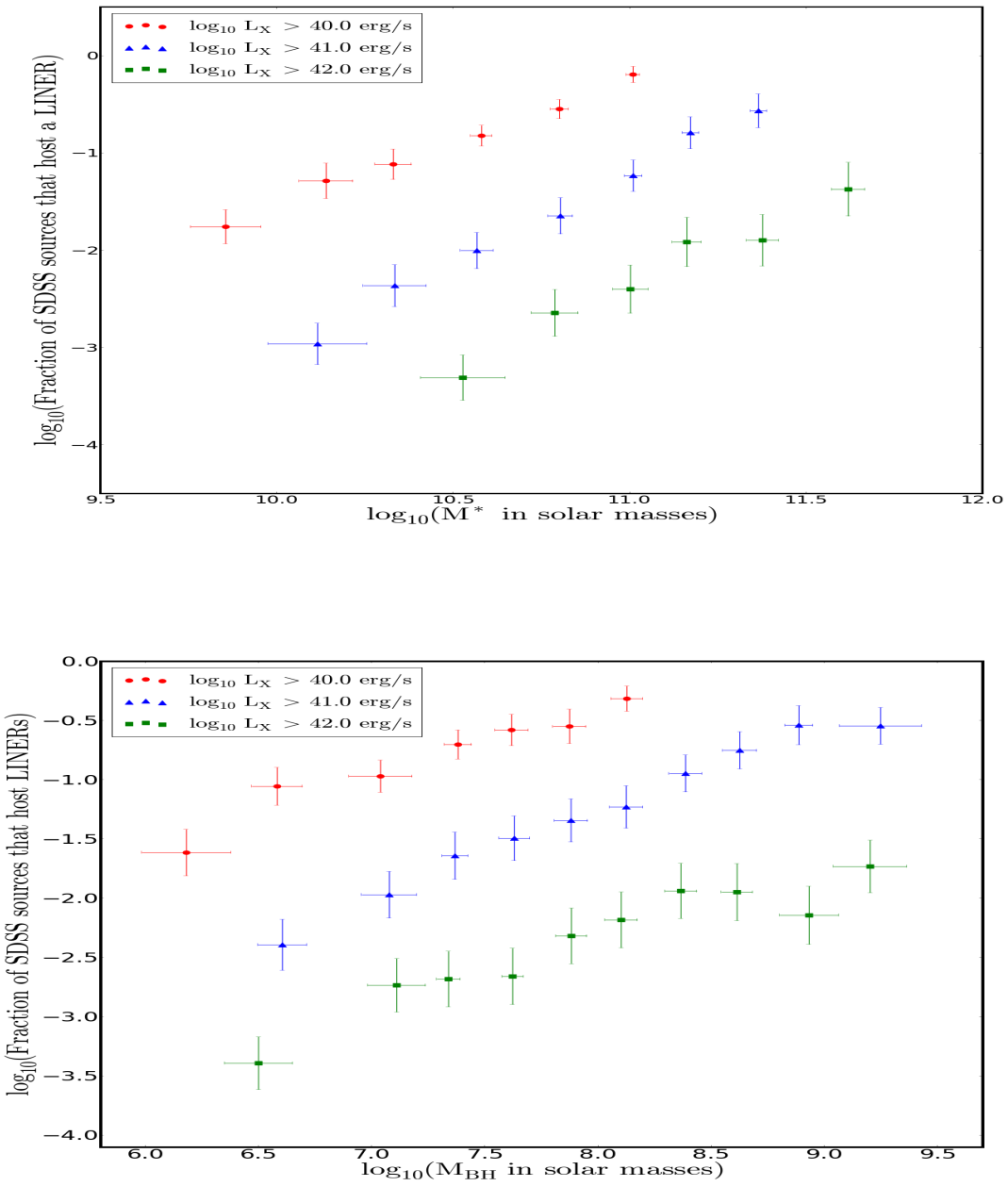

Figure 2.3 *The fraction of galaxies hosting a LINER according to stellar mass (upper chart) and black hole mass (lower chart). Three subsamples of LINERs are considered - those with X-ray luminosity above $10^{40.0}$ (red dots), $10^{41.0}$ (blue triangles) and $10^{42.0}$ (green squares) erg/s.*

2.5 The Fundamental Plane of Black Hole Activity

It has been postulated that black hole accretion and jet formation is a scale-invariant process; this implies that there will be a relationship between radio luminosity, X-ray luminosity and black hole mass that spans the complete mass range of black holes, from supermassive black holes to stellar X-ray binaries. Such a relationship, defining the Fundamental Plane of black hole activity, was derived empirically first by Merloni et al (2003) and then by a number of researchers (Table 2.3 below lists a selection). Most have derived the relationship using both AGNs and X-ray binaries; a minority have used just AGNs, but normally relatively small and heterogeneous samples of AGNs.

The scale invariance implied by the Fundamental Plane is valid only when the accretion properties are the same (see Heinz and Sunyaev, 2003, who derive different scalings for different accretion modes). The tightest relationship for X-ray binaries is seen for those genuinely in the "low-hard" state, which is for low Eddington fractions. It follows that a valid comparison with "low-hard" X-ray binaries requires a sample of jet-mode (LINER) AGN. This sample of 576 LINERs is large enough to investigate whether the fundamental plane relationship holds within AGNs alone.

The distribution of the LINERs' radio flux densities, which is shown in Figure 2.4, reveals the following points. 196 LINERs (34% of the total) have a flux density greater than 3× the rms of the FIRST survey and can, therefore, be considered to be reasonably secure detections. A further 251 LINERs (44%) have positive flux densities lower than 3× the rms. 129 of the LINERs (22%) have a negative flux density. The median and mean flux densities are respectively 0.22 mJy and 6.29 mJy. This implies that there is a lot of information contained in the flux densities of the "non-detections" and so it is important to make full use of the data, including low signal / noise detections and indeed negative values. In this case, however, standard stacking techniques are not appropriate because of the wide range of redshifts in the sample. The methodology described below does utilise all of the available information.

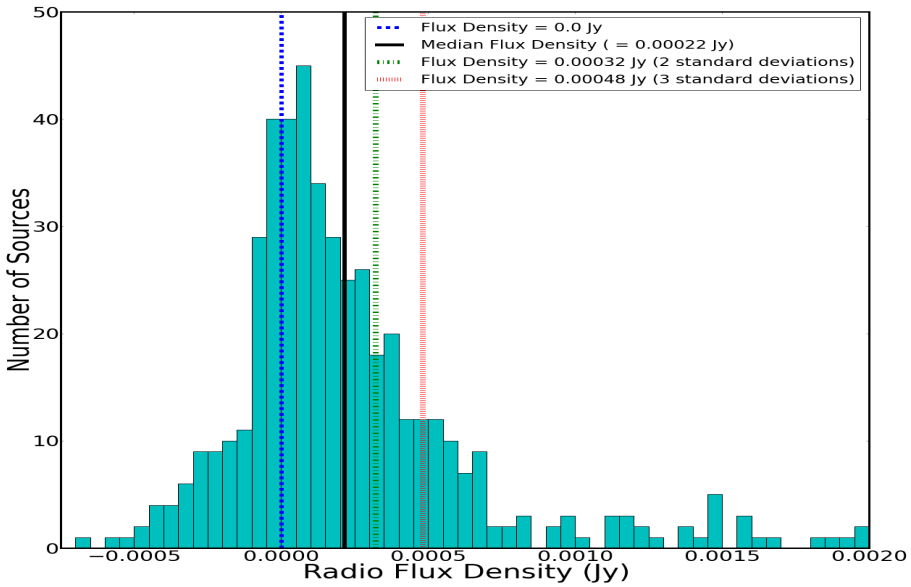

Figure 2.4 *The distribution of radio flux densities for the sample of 576 LINERs. Note that 29 LINERs have flux densities greater than 0.002 Jy and are not shown in the diagram. The black dashed line shows the median flux density. The green and red dashed vertical lines show the flux densities at 2x and 3x the FIRST survey rms respectively.*

2.5.1 The L_X – L_R Relationship

The relationship between the X-ray and radio luminosities was investigated, first with the black hole mass ignored and then including a dependency on the black hole mass. In deriving the best-fit parameters, two sources of uncertainty in the radio luminosity are considered. The first results from the uncertainty in the measurement of the radio flux densities from the FIRST data, which is assumed to be 0.16 mJy. The second effect to be accounted for is the inherent scatter within the X-ray luminosity / radio luminosity / black hole mass relationship. This scatter arises from both measurement errors due to, for example, source peculiarities, timing differences in the measurements of the X-ray, radio and optical data for variable sources, beaming effects, absorption and the calculation of the black hole masses. It also arises from intrinsic sources of scatter caused by, for example, black hole spin and the fact that the X-ray emission may not be generated solely from the jets. The inherent scatter is unknown and so was modelled as part of the optimisation process.

Ignoring a possible dependency on black hole mass, the required relationship is

expressed in the form:

$$\log\left(\frac{L_R}{\mathrm{erg/s}}\right) = a\,\log\left(\frac{L_X}{10^{42}\,\mathrm{erg/s}}\right) + c \tag{2.7}$$

where the denominator under the X-ray luminosity is introduced in order to try and ensure that a and c are largely uncorrelated in the minimisation procedure. The variables to be found are a, c and σ (the inherent scatter, as measured by the standard deviation, in the X-ray luminosity / radio luminosity relationship). The procedure was as follows:

- For a given value for each of a, c and σ, the predicted radio luminosity of every source was calculated from its X-ray luminosity using the above expression.

- To allow for the intrinsic scatter in the relation, an addition of N_1 times σ was applied to the predicted radio luminosity, where N_1 was allowed to vary in small steps between -10.0 and +10.0. So, for each set of values of a, c and σ, a large number of predicted radio luminosities were generated.

- All of these predicted radio luminosities were converted to flux densities. Each one was compared with the actual radio flux density. From this, N_2, the number of standard deviations in the offset, was calculated, given the uncertainty in the radio flux density of 0.16 mJy.

- N_1 and N_2 were combined in quadrature. The minimum value, N_{min}, for each source was then found for those values of a, c and σ. This represents the combined number of standard deviations that the radio flux density is away from the prediction. For bright radio sources the dominant contribution to the offset comes from the intrinsic scatter (i.e. N_1), whereas for faint sources it is the uncertainty on the FIRST flux density that dominates.

- Having determined N_{min} for each source for a given a, c and σ, the best-fit values to those parameters were then found by a maximum likelihood analysis where the log likelihood function is given by:

$$\ln L = -0.5 \sum_i (N_{min,i}^2 + \ln(2\pi\sigma^2)) \tag{2.8}$$

  where i is the sum over all sources.

The values of a, c and σ that maximised the log likelihood function were a = 0.70, c = 38.55 and σ = 0.85, yielding the expression:

$$\log\left(\frac{L_R}{\mathrm{erg/s}}\right) = 0.70\,\log\left(\frac{L_X}{10^{42}\mathrm{erg/s}}\right) + 38.55 \tag{2.9}$$

The errors on the slope and intercept were calculated via the inversion of the Hessian matrix and emerged as $\pm$ 0.09 and $\pm$ 0.12 respectively. The error on the scatter was $\pm$ 0.02. The upper panel of Figure 2.5 shows the radio luminosity plotted against the X-ray luminosity, with the best-fit shown as the orange line.

2.5.2 The Fundamental Plane

The exercise was repeated, but now including black hole mass as a dependency. A fourth variable, the multiple applied to the black hole mass, now also needed to be found through the optimisation procedure. The expression obtained was:

$$\log\left(\frac{L_R}{\mathrm{erg/s}}\right) = 0.65\,\log\left(\frac{L_X}{10^{42}\mathrm{erg/s}}\right) + 0.69\,\log\left(\frac{M_{BH}}{10^8\,M_\odot}\right) + 38.35 \tag{2.10}$$

The variables with their associated uncertainties were found to be 0.65 $\pm$ 0.07, 0.69 $\pm$ 0.10 and 38.35 $\pm$ 0.10. The value of the scatter, σ, emerged as 0.73 $\pm$ 0.03. The best-fit line is plotted as a black solid line in the lower chart in Figure 2.5.

Including black hole mass as a dependency gave a better fit to the data. The scatter, σ, dropped from 0.85 (fitting without black hole mass dependency) to 0.73 (fitting with black hole mass dependency) which indicates that the black hole mass dependency accounts for some of the scatter in the L_X – L_R relationship. A likelihood ratio test was used to investigate whether the improvement is statistically significant once account is taken of the extra degree of freedom. The result was finely balanced. The χ^2 value, computed as -2 $\times$ the natural log of the ratio of the likelihoods, emerged as 2.20. The χ^2 distribution has one degree of freedom, implying that the observed value is at the 86% confidence interval. This suggests that there is still a 14% probability that the fit with no black hole mass dependency is the better one. However, as discussed below, the black hole mass dependency is required in order to allow the fundamental plane to fit black holes in a much lower mass range than encountered in LINERs alone (that is, in galactic X-ray binaries).

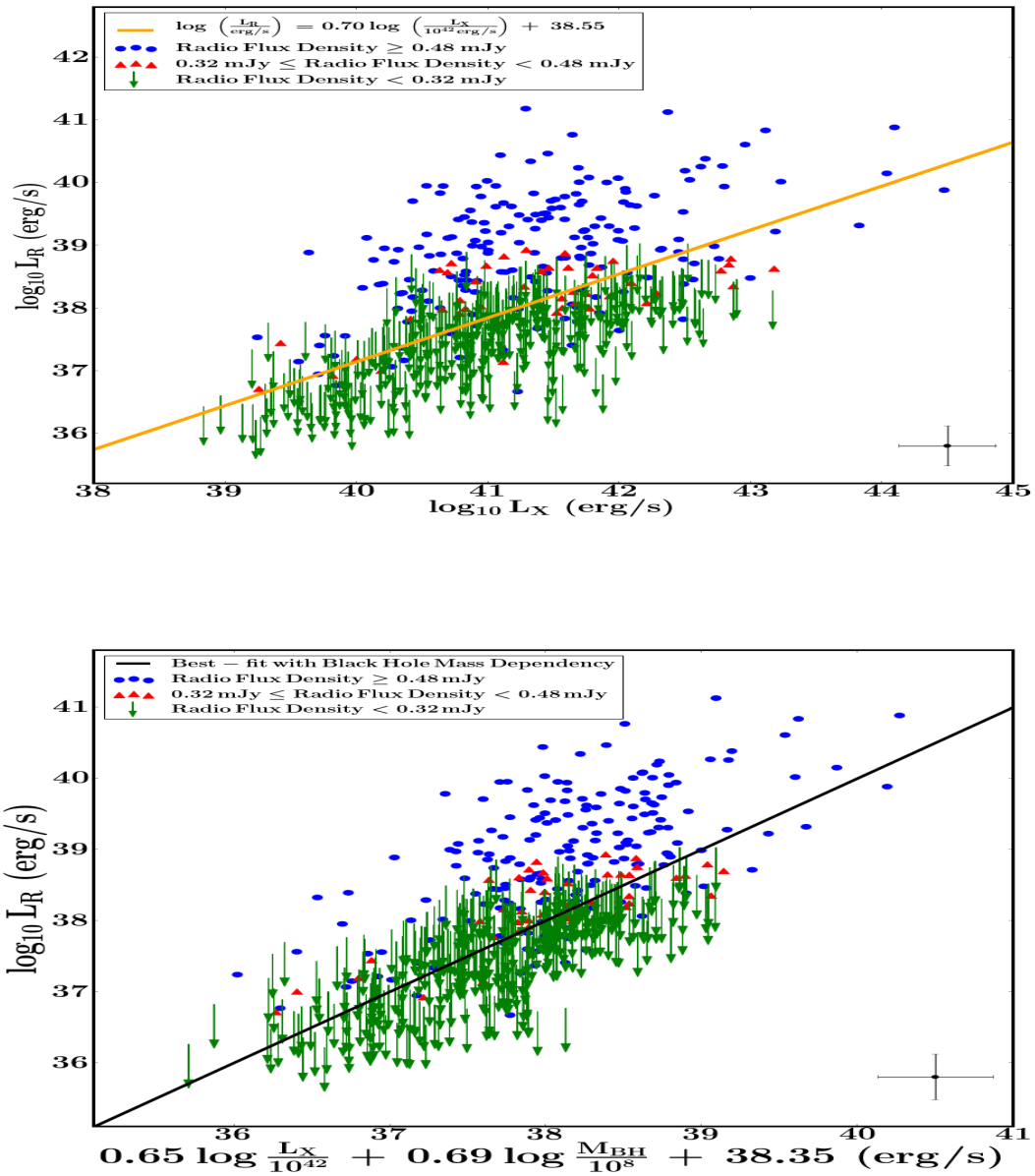

Figure 2.5 *The Fundamental Plane relationship calculated without black hole mass dependency (upper chart) and with black hole mass dependency (lower chart). In the upper chart, the x-axis shows the log X-ray luminosity and the y-axis shows the log radio luminosity evaluated as* νL_ν. *In the lower chart, the x-axis shows the predicted log radio luminosity and the y-axis shows the actual log radio luminosity. In both panels, galaxies with a radio flux density above 0.48 mJy (3× the FIRST survey rms) have secure radio luminosities and are plotted as blue dots. Galaxies with radio flux densities in the range 0.32 - 0.48 mJy are marginal radio detections and are plotted as red triangles. Galaxies with radio flux densities below 0.32 mJy are plotted as limits, with the base of the arrow corresponding to a radio flux density of 0.32 mJy. Note though, as described in the text, the full radio information was used in the fitting process. Typical error bars are shown in the bottom right of both diagrams.*

Research Paper	Parameters			Size of Sample		Description of AGNs Sample
	a	b	c	AGNs	XRBs	
Nisbet & Best (1)	$0.65^{+0.07}_{-0.07}$	$0.69^{+0.10}_{-0.10}$	$38.35^{+0.10}_{-0.10}$	576	0	576 LINERs
Nisbet & Best (2)	$0.70^{+0.09}_{-0.09}$		$38.55^{+0.12}_{-0.12}$	576	0	576 LINERs
Nisbet & Best (3)	$0.65^{+0.05}_{-0.05}$	$0.96^{+0.10}_{-0.10}$	$38.42^{+0.07}_{-0.07}$	576	0	576 LINERs
Merloni et al 2003	$0.60^{+0.11}_{-0.11}$	$0.78^{+0.11}_{-0.09}$	38.42	99	8	14 Quasars, 58 Seyferts, 24 LINERs, 3 Transition Objects
Körding et al 2006	$0.63^{+0.4}_{-0.4}$	$0.75^{+0.3}_{-0.3}$	38.47	41	5	41 LINERs
Körding et al 2006	$0.57^{+0.07}_{-0.07}$	$0.78^{+0.18}_{-0.18}$	38.01	92	11	14 Quasars, 56 Seyferts, 22 LINERs
Gültekin et al 2009	$0.67^{+0.12}_{-0.12}$	$0.78^{+0.27}_{-0.27}$	38.65	18	0	13 Seyferts, 3 Transition Objects, 2 Unclassified Objects
Gültekin et al 2009	$0.62^{+0.10}_{-0.10}$	$0.82^{+0.08}_{-0.08}$	38.55	18	3	13 Seyferts, 3 Transition Objects, 2 Unclassified Objects
Bonchi et al 2013	$0.39^{+0.03}_{-0.06}$	$0.68^{+\text{n.a.}}_{-\text{n.a.}}$	38.43	1268	0	Mixture of both Type 1 and Type 2 AGNs
Saikia et al 2015	$0.64^{+0.4}_{-0.4}$	$0.61^{+0.2}_{-0.2}$	n.a.	39	4	12 Seyferts, 20 LINERs, 7 Transition Objects
Saikia et al 2015	$0.83^{+0.3}_{-0.3}$	$0.82^{+0.2}_{-0.2}$	37.72	39	0	12 Seyferts, 20 LINERs, 7 Transition Objects

Table 2.3 *A selection of Fundamental Plane relationships derived by different researchers. The parameters are defined from equation 2.11. The three models from this research are defined as follows: (1) fitting with black hole mass dependency and using the McConnell & Ma (2013) relationship between velocity dispersion and black hole mass; (2) fitting without black hole mass dependency; (3) fitting with black hole mass dependency and using the* $M_{BH} - \sigma$ *relationship derived by Tremaine et al (2002).*

Table 2.3 sets out different derivations of the Fundamental Plane relationship, summarising the samples used in each attempt and showing the Fundamental Plane relationships obtained. The relationships have all been manipulated into the same format:

$$\log \mathrm{L_R} = \mathrm{a} \log \left(\frac{\mathrm{L_X}}{10^{42}} \right) + \mathrm{b} \log \left(\frac{\mathrm{M_{BH}}}{10^{8}} \right) + \mathrm{c} \tag{2.11}$$

and the values obtained for the three parameters are shown in columns 2, 3 and 4 of Table 2.3. As such, the parameter values derived from different studies should be suitable for comparison since they are largely uncorrelated. There are, however, differences in the definitions of radio luminosity: Merloni et al. (2003), Körding et al. (2006) and Gültekin et al. (2009) calculated the radio luminosity from an observing frequency of 5 GHz (using νL_ν) and Saikia et al. (2015) used an observing frequency of 15 GHz. In this study and that of Bonchi et al. (2013) the radio luminosity was obtained from an observing frequency of 1.4 GHz. All results in Table 2.3 have been brought into line with an observing frequency of 1.4 GHz. An analysis conducted by de Gasperin et al. (2011) on low-luminosity AGNs similar to those studied here concluded that $< \log \mathrm{P_{5GHz}} > - < \log \mathrm{P_{1.4GHz}} >= 0.35$ and so a reduction of 0.35 in parameter c was applied to bring the results from Merloni et al, Körding et al and Gültekin et al onto an equivalent footing to those in this study. This adjustment corresponds to a mean spectral slope of $\alpha = 0.4$, which is reasonable for these small-scale (core-dominated) sources. On the assumption that this spectral index remains relevant up to a frequency of 15 GHz, parameter c found by Saikia et al has been similarly reduced by 0.62. There were also small differences in the methods used by the different researchers to calculate the black hole masses; no attempt has been made to adjust for this.

Körding et al (2006) performed the analysis with a number of different combinations of AGN-type and X-ray binaries; the results of only two are shown here – a sample that contains only LINERs for the AGN population (and so is consistent with this work) and a sample that closely replicates that used by Merloni et al. (2003). In five cases shown in Table 2.3, the researchers have derived their relationship using a database consisting of both AGNs and also a small number of galactic X-ray binaries (but using several different observations for each of these binaries, which change with time to provide pseudo independent measurements). In the remaining cases, including the Fundamental Plane relationships derived in this study, only AGNs were used in the analysis.

The parameters derived in this work agree with those in the literature, with the values typically within one standard deviation of those derived elsewhere (Table 2.3).

A useful test of the relationships found in this study is to extrapolate them to lower black hole masses and investigate whether there is agreement with a sample of X-ray binaries. The sample of X-ray binaries was constructed using data from Merloni et al. (2003) and Saikia et al. (2015). Following the arguments put forward by Körding et al. (2006), two of the X-ray binaries in the Merloni et al sample were excluded: Cyg X-1, because it changes its state frequently (Gallo et al., 2003), and GRS 1915 + 105, because it seemingly remains for most of its time in a very high state (Reig et al., 2003). In addition, those datapoints that were limits were excluded. The Saikia et al sample was included without adjustment. That produced an overall sample of 130 observations from seven X-ray binaries. For comparison, Sgr A* is also included on the plots.

As expected, the Fundamental Plane relationship does need to include the black hole mass dependency in order to fit the X-ray binaries. In Figure 2.6 the observed radio luminosity is plotted against the predicted radio luminosity, calculated using the derived relationships. The upper chart illustrates that when black hole mass is included as a dependency the Fundamental Plane does indeed straddle the datapoints of the X-ray binaries for parameters derived only from a fit of the LINER AGN distribution. That is clearly not the case when black hole mass is excluded (middle chart).

As discussed earlier, the black hole masses have been estimated using the McConnell and Ma (2013) black hole mass – velocity dispersion relationship. It is of interest to repeat the whole analysis, but now using the relationship derived by Tremaine et al. (2002) to calculate the black hole masses. This generates a Fundamental Plane defined by the parameters $a = 0.65^{+0.05}_{-0.05}$, $b = 0.96^{+0.10}_{-0.10}$ and $c = 38.42^{+0.07}_{-0.07}$. The increase in parameter b from 0.69 (using a power of 5.64 in the black hole mass – velocity dispersion relation) to 0.96 (using a power of 4.02) is consistent with the fact that, given $M_{BH} \propto \sigma^{x}$, then it is expected that $b \propto \left(\frac{1}{x}\right)$. The plane now undershoots the X-ray binaries (Figure 2.6, lower chart). The analysis provides support for the steeper black hole mass – velocity dispersion relationship derived by McConnell & Ma.

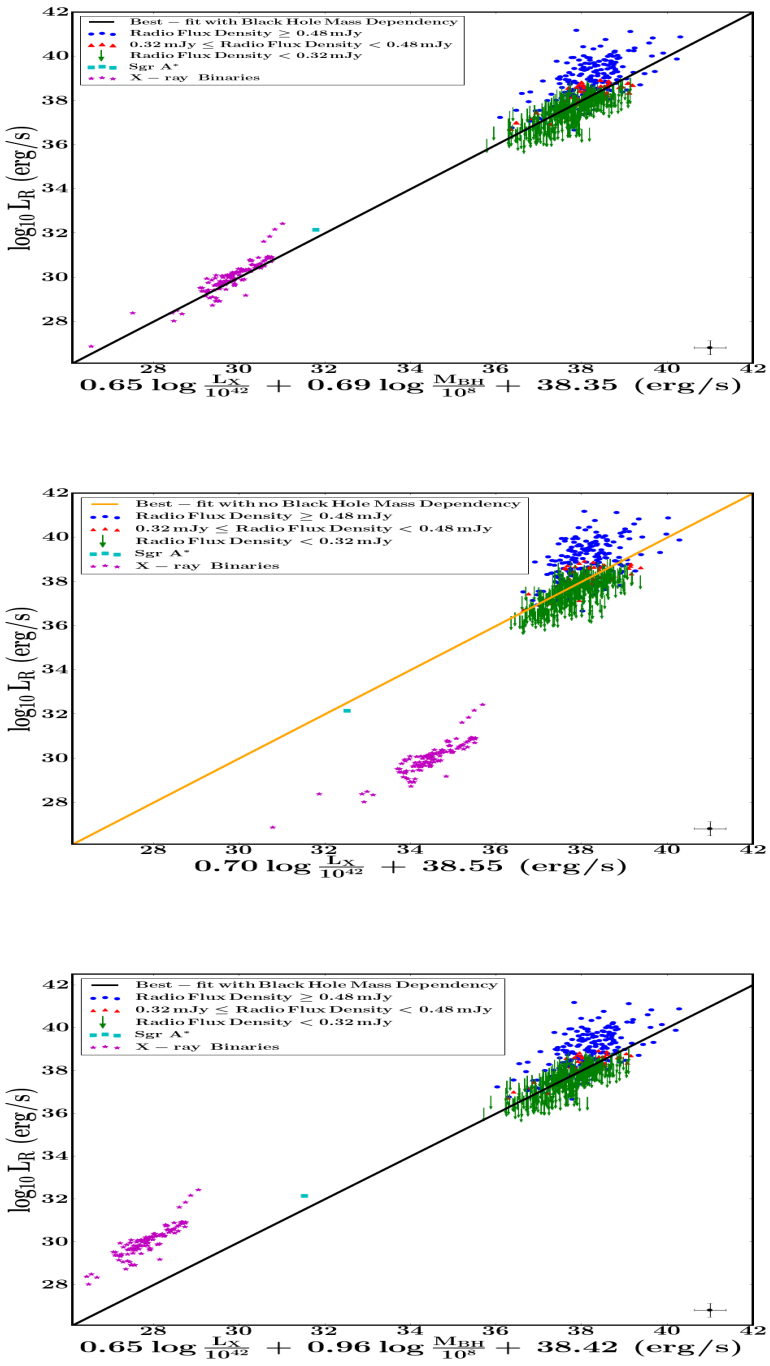

Figure 2.6 *The observed radio luminosity at 1.4 GHz is plotted against the radio luminosity predicted by the Fundamental Plane relationship. In the upper chart, the relationship includes black hole mass dependency. In the middle chart, the relationship has no black hole mass dependency. In the lower chart, the relationship includes black hole mass dependency, but in this case the black hole masses of the LINERs have been calculated using the black hole mass – velocity dispersion relationship derived by Tremaine et al. (2002). Typical error bars for the LINERs are shown in the bottom right of the three diagrams.*

2.6 A Comparison with the Radio-selected LINER fraction

Best et al. (2005) demonstrated that the fraction of galaxies hosting a radio-loud AGN is a strong function of both stellar and black hole mass. Having derived the Fundamental Plane relationship between X-ray luminosity, radio luminosity and black hole mass, it is now possible to convert from an X-ray selected sample of LINERs to a pseudo-radio-selected sample, so allowing a comparison between the results obtained in Section 2.4 and those of Best et al.

Again, three subsamples were examined, consisting of LINERs with X-ray luminosities corresponding (according to the Fundamental Plane relationship derived above) to radio luminosities above $10^{38.0}$, $10^{38.5}$ and $10^{39.0}$ erg/s. In practice, this means evaluating down to a different L_X limit at each black hole mass. The fraction of galaxies hosting each of these subsamples, as a function of black hole mass, was found. The results are shown in Figure 2.7. The comparison is made against a radio-selected sample of AGNs, also from SDSS-DR7, drawn from the analysis of Best and Heckman (2012). For this analysis, their radio sample was restricted to only jet-mode AGNs, re-evaluated for only core radio flux and selected above $10^{39.0}$ erg/s. Due to radio flux density limits, the sample had to be restricted to $z < 0.1$, which gives a slightly different redshift coverage to this X-ray selected sample.

A key result is that the slopes found in the two analyses are in reasonable agreement. For the three subsamples in this analysis, the best-fitting straight lines through the datapoints had slopes of 1.9 ± 0.2 ($L_R > 10^{38.0}$ erg/s), 1.7 ± 0.1 ($L_R > 10^{38.5}$ erg/s) and 1.1 ± 0.3 ($L_R > 10^{39.0}$ erg/s). It is noted that these subsamples contain only between four and six datapoints each and so the gradients are not tightly constrained. The best-fitting slope for the jet-mode AGNs radio-selected sample is 1.3. There is, however, an indication that for this sample the best fit turns over at around $10^{9.0}$ solar masses and if a straight line is fitted just through the points below that level then the slope emerges as 1.6. Overall, therefore, the analysis tends to support the conclusions of Best et al. (2005), and also those of Janssen et al. (2012), that the fraction of galaxies hosting a jet-mode AGN scales approximately as $M_{BH}^{1.6}$. This provides reassurance that the results in Section 2.4 – the fraction of galaxies hosting a LINER as a function of black hole mass – are reasonable, as are the parameter values a =

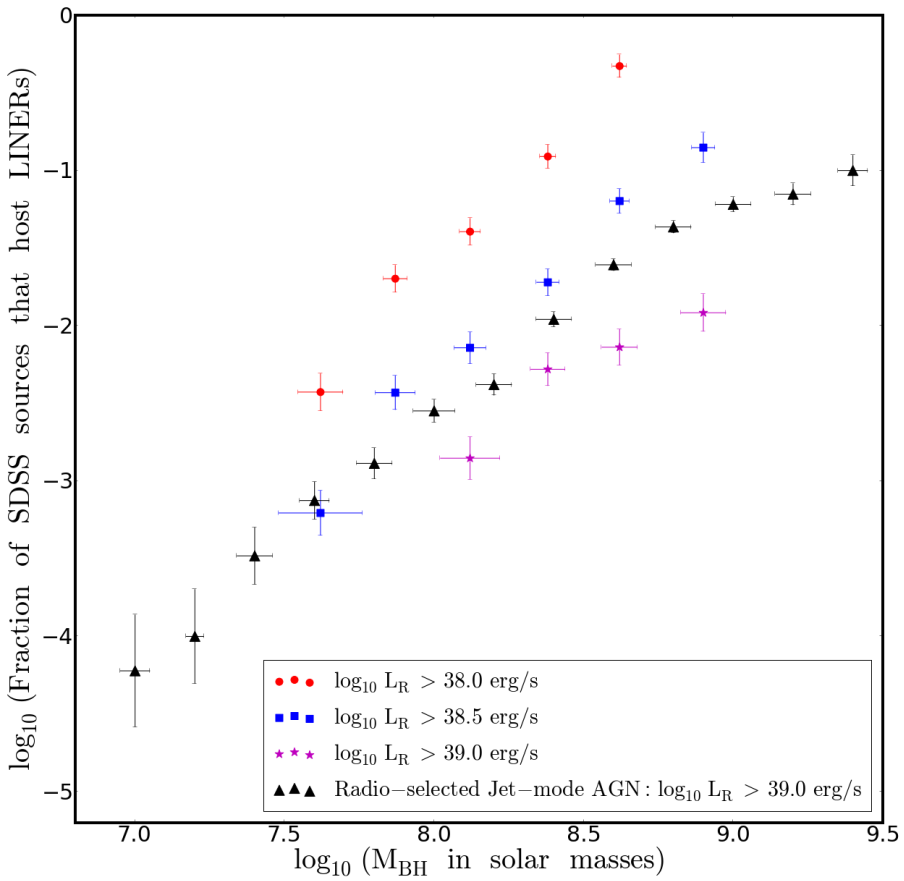

Figure 2.7 *A comparison of the fraction of galaxies hosting LINERs calculated using a radio-selected sample of LINERs (black triangles) with a sample of X-ray-selected LINERs that have been converted into a pseudo-radio-selected sample using the Fundamental Plane relationship (red, blue and magenta symbols). The radio sample consists only of jet-mode AGNs and uses core radio luminosities. All samples use the McConnell and Ma (2013) relationship to estimate the black hole mass.*

0.65 and b = 0.69 found for the Fundamental Plane relationship.

Figure 2.7 also reveals that there is a small but non-negligible disagreement in the normalisation: results for the radio-selected subsample with radio luminosity above $10^{39.0}$ erg/s are between the results for the subsamples of X-ray selected LINERs with converted radio luminosity above $10^{38.5}$ erg/s and those with radio luminosity above $10^{39.0}$ erg/s, but are slightly closer to the former. There is an offset of approximately 0.3 dex between the two sets of results, suggesting

that there may be a discrepancy in the derived value of the intercept in the Fundamental Plane relationship. Even allowing for the fact that small uncertainties in the Fundamental Plane parameters magnify up into changes in the predicted radio luminosity, a discrepancy of 0.3 dex does appear large in the context of the calculated error of 0.10 in the intercept.

There are several factors that might contribute to the offset. The different redshift regimes (an upper limit of z = 0.30 in this research and upper limit of z = 0.10 for the radio-selected sample) might be a factor. It seems unlikely, though, that this would have a major effect, especially since there was no significant difference in the results when the X-ray-selected sample was restricted to redshifts of below 0.20.

The possible inclusion of misclassified Seyferts in the sample and the possibility of incorrect X-ray matches with the SDSS galaxies could both affect the normalisation. To test the former, those LINERs with a ratio of $\log([\mathrm{OIII}]/\mathrm{H}\beta) > 3.0$ – that is, those closest to Seyferts in the diagnostic diagrams – were removed from the sample. There were eight of them. This made no difference to the results. Nor is the latter point likely to be significant. Based on a potential contamination of 24 mis-matched sources (see Section 2.3.3), the 24 sources with upper limits of radio luminosity most outlying from the $L_X - L_R$ relationship were removed and the analysis repeated. The change in the intercept value was less than the 0.1 dex uncertainty.

The explanation for the disagreement in the normalisations is more likely to lie in one or both of the following factors. First, scatter in the Fundamental Plane relation means that the X-ray cuts and radio cuts are not identical: a vertical (X-ray) cut on Figure 2.5 generates a subsample of LINERs that mostly lie below the best-fit line, whereas a horizontal (radio) cut will generate a different subsample of LINERs that will be biased to be above the best-fit line. This introduces a discrepancy between the two approaches which could lead to a difference in the results if the scatter is asymmetric. Indeed, for the $L > 10^{39.0}$ erg/s cut studied, this samples the very upper end of the distribution (see the upper panel in Figure 2.5) where such an asymmetric scatter is seen.

Second, there could be an error in the Fundamental Plane parameters. As discussed above, this would need to be at the $\sim 3\sigma$ level given the formally-calculated uncertainties. As a further investigation of this, the $L_X - L_R$ relationship was re-examined as a function of M_{BH}. It was assumed that at a

given M_{BH} the slope of the relationship and the scatter were fixed at the best-fit values of 0.65 and 0.73 respectively. The LINERs were then divided into bins according to black hole mass and an optimisation procedure was conducted on each of the binned subsamples; the process was as described in Section 2.5.1, but in this case only one free parameter, the intercept, needed to be found.

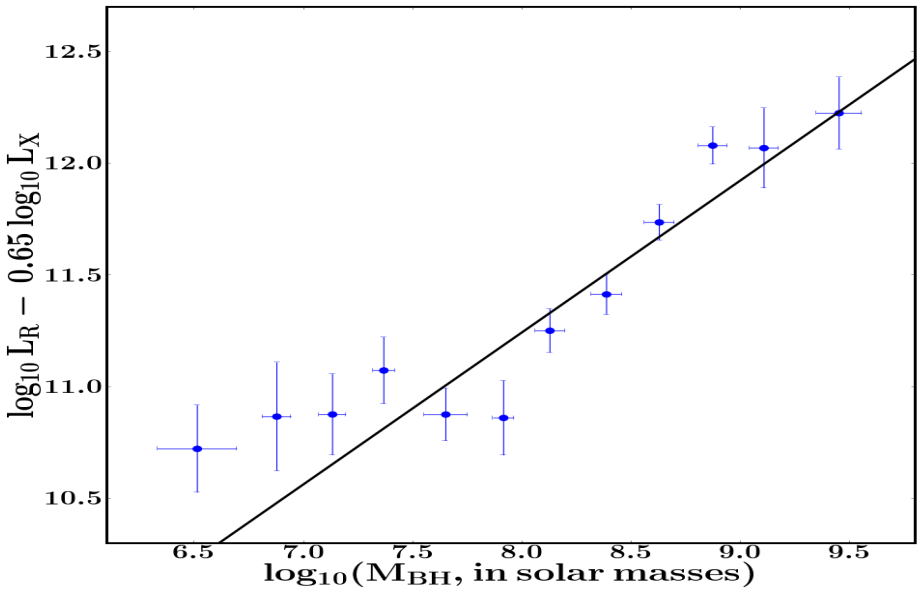

Figure 2.8 *The values of the intercept of the* $L_X - L_R$ *relationship have been obtained by dividing the LINERs into bins of black hole mass, keeping parameters a and* σ *constant and then finding the optimal value of parameter c in each bin. The blue points show the results obtained; the best-fit straight line is shown in black.*

The results are shown in Figure 2.8, with the values of the intercept found in each mass bin plotted against black hole mass. The best-fit straight line is plotted in black. The slope of this line is 0.68, which is reassuringly consistent with the slope determined for the Fundamental Plane. However, although the large error bars prevent definitive conclusions, there are indications that the straight line does not fit the data well. The values of the intercept remain fairly constant at black hole masses below $10^{8.0}$ solar masses and then rise steeply thereafter. A number of functions were tested as a fit to the data. Two that provided statistically better fits to the data points than did the straight line (using a reduced chi-squared approach as the test) were: an exponential curve; and a horizontal line up to a break point of a black hole mass equal to $10^{7.9}$ solar masses followed by a straight line with slope of 1.02 above the break point. Interestingly, Gültekin et al. (2009)

also found a steeper Fundamental Plane slope when they examined high M_{BH} objects, but later Gultekin et al. (2014) found a plane consistent with the X-ray binaries when they included AGNs with $M_{BH} \sim 10^6$ – that concords with the pattern of datapoints in Figure 2.8. Further investigation into this matter will require a larger sample and is outside the scope of this thesis, but for this analysis the key point is that the scatter around the straight line seems larger than the formal 0.1 dex error which might help to explain the issues seen.

2.7 Discussion

The key points emerging from the results obtained in this research are described in the following subsections.

2.7.1 The Fundamental Plane of Black Hole Activity

Most derivations of the Fundamental Plane relationship have included both X-ray binaries and AGNs within the analysis. The large difference in both radio and X-ray luminosity between these two subsamples constrains the slope of the plane into a narrow range, implying that the information within the AGNs subsamples is not being fully utilised. Similarly, the information contained within the subsamples of X-ray binaries is limited; the number of objects in each subsample is small and multiple observations of the same object are clearly not independent (for example, if black hole spin is a factor). There is also the question of whether the Fundamental Plane relationship is genuine, or whether the fact that the two populations scale together masks variations within these populations.

This sample of 576 LINERs has the advantage of being large enough to allow the Fundamental Plane to be derived from the AGNs datapoints alone, and then the X-ray binaries can be used as an independent test of the result. Additionally, this sample is restricted to jet-mode AGNs, the correct type of AGNs to provide consistency with the X-ray binaries. A fit was found that goes through the binaries. The fit is similar to those obtained in other studies and comfortably within the uncertainties, providing corroboration for their results which have been derived using different approaches to the construction of the sample. It is noted, however, that the estimate of the slope (parameter a) from this work is towards the top end of the range and the estimate of the dependence on black hole mass

(parameter b) is towards the lower end of the range: in any flux-limited sample, these two parameters are expected to be weakly anti-correlated, a fact confirmed by the calculated covariance matrix.

It is of interest that the value of 0.73 dex for the scatter around the relationship, the "thickness" of the Fundamental Plane, is in the middle of the range found by other researchers. Such a value suggests that there may indeed be inherent scatter within the relationship, an interesting topic for future research. It has been suggested that the Fundamental Plane could be used as a means of estimating black hole mass from observations of radio and X-ray luminosity (for example, Gültekin et al., 2009); the size of the scatter appears to limit the practicality of such an approach unless the origin of the scatter can be identified and associated with an observable. A variety of parameters was tested – [OIII] line luminosity, the Hα line luminosity, the Hβ line luminosity and the 4000Å break strength – without finding a correlation.

2.7.2 XBONGs

One of the discoveries coming out of recent X-ray surveys is the existence of X-ray Bright Optically-Normal Galaxies (XBONGs); these are objects that display luminous hard X-ray emission – typically $L_{2-10keV}$ over 10^{42}erg/s – but whose optical spectra resemble quiescent normal galaxies with no indication of nuclear activity; see, for example, Comastri et al. (2002) and Trump et al. (2009). XBONGs, therefore, show the characteristics of an AGN hosted by a "normal" galaxy. A number of explanations have been put forward, including: dilution from the host galaxy light; Compton-thick sources, with X-ray photons having sufficient energy to pass through the torus surrounding the accretion disk, but optical photons unable to do so; and diffuse emission associated with small galaxy groups. One favoured option is that the spectra of XBONGs are due to an advection-dominated accretion flow – that is, a jet-mode AGN – in which the X-ray emission, emerging from the base of the jet and the nucleus, has been boosted by a beaming effect along the viewing angle (cf. Hart et al., 2009).

This work demonstrates that a significant fraction of point-like X-ray sources matched to SDSS galaxies are LINER-like, possessing weak low-ionisation lines. These extend to high X-ray luminosities, with $L_{2-10keV} \sim 10^{42}$ erg/s. They can, therefore, explain some, or all, of the XBONG population. The study also shows that these sources obey the Fundamental Plane, which implies that there is

no evidence of strong beaming. This, in turn, rules out beaming as a general explanation for the XBONG population as a whole. It is possible that the more extreme examples of XBONGs could be boosted by beaming. Indeed, if the origin of the X-ray emission is the jet rather than the advection dominated accretion flow itself, then a proportion of beamed sources would be expected. Further discussion of that topic is beyond the scope of this thesis.

It is also noted that the sources in this sample all lie at redshifts of under 0.3, suggesting that dilution is also unlikely to be a general explanation for all XBONGs.

2.7.3 AGN Feedback

The Fundamental Plane relationship implies that the AGNs in this sample are experiencing accretion flows with the characteristics of the low-hard state of the X-ray binaries, implying radiatively inefficient accretion flows. This can be investigated by examining the ratio of the mechanical luminosity to the bolometric luminosity. The relationship found for low-luminosity (LINER-like) AGNs by Ho (2009):

$$\mathrm{L_{bol}} \approx 15.8\,\mathrm{L_{2-10keV}}\ \mathrm{erg/s} \tag{2.12}$$

allows an estimate of the bolometric luminosity to be obtained from the X-ray luminosity, while the relationship found by Cavagnolo et al. (2010):

$$\mathrm{L_{mech}} \approx 5.8 \times 10^{43} \left(\frac{\mathrm{L_{radio}}}{10^{40}}\right)^{0.70}\ \mathrm{erg/s} \tag{2.13}$$

allows an estimate of the mechanical energy to be obtained from the radio luminosity. The scatter in both these relationships prohibits too much to be drawn from any simple measurement, but they should provide a reasonable guide to the population. Figure 2.9 plots the (log) ratio of the mechanical to bolometric luminosity observed for the X-ray selected LINERs. Also shown on the diagram are a series of dashed lines which show the theoretical (log) ratio for a selection of Eddington fractions for sources that follow the Fundamental Plane relationship. These model lines have been calculated by combining equations 2.10, 2.12 and 2.13 with:

$$\mathrm{f_{Edd}} = \frac{\mathrm{L_{mech}} + \mathrm{L_{bol}}}{\mathrm{L_{Edd}}} = \frac{\mathrm{L_{mech}} + \mathrm{L_{bol}}}{1.26 \times 10^{38}\,\mathrm{M_{BH}}} \tag{2.14}$$

to give:

$$\left(\frac{L_{mech}}{L_{bol}}\right)^{-0.83} + \left(\frac{L_{mech}}{L_{bol}}\right)^{-1.83} = 1523 \times f_{Edd} \times (M_{BH})^{0.12} \qquad (2.15)$$

where f_{Edd} is the Eddington fraction. Although there is a lot of scatter and a little over half of all the datapoints are limits (from those LINERs with a radio flux density below 0.32 mJy), the diagram does make several points of interest:

- For the LINERs, a significant proportion (over half on average for this sample) of the energy is released in the jets.
- The data indicate that the fraction of energy released in mechanical form increases with black hole mass – that is, higher black hole mass objects not only have a higher "on" fraction, but are also more efficient at radio-jet feedback.
- The negative slope of the model lines shows that, for a fixed Eddington ratio, the ratio of mechanical to bolometric luminosity decreases (gently) with increasing black hole mass. Since the data indicate that the fraction of energy released in mechanical form increases with black hole mass, this implies that black holes with the highest masses tend to have low Eddington ratios.
- The model lines show that mechanical luminosity becomes progressively more dominant at lower Eddington fractions, as found by, for example, Merloni and Heinz (2007).
- The LINERs mostly lie within a range bounded by Eddington fractions of 10^{-6} and 10^{-2}. This confirms that these sources are in the jet-mode regime, with Eddington fractions of below 10^{-2} (cf. Best and Heckman, 2012).
- Intriguingly, there is a suggestion that the fraction of mechanical to bolometric luminosity rises more sharply above a black hole mass of around 10^8 solar masses. This provides (weak) support for the argument from Figure 2.8 that some change occurs at that black hole mass threshold, possibly in the accretion flow, in the properties of the black hole or in the properties of the host galaxy. In view of both the large uncertainties in the derivation of the data in Figure 2.9 and of the scatter within that diagram, it is emphasised again that this point is made only in order to indicate an area where further research may be of interest.

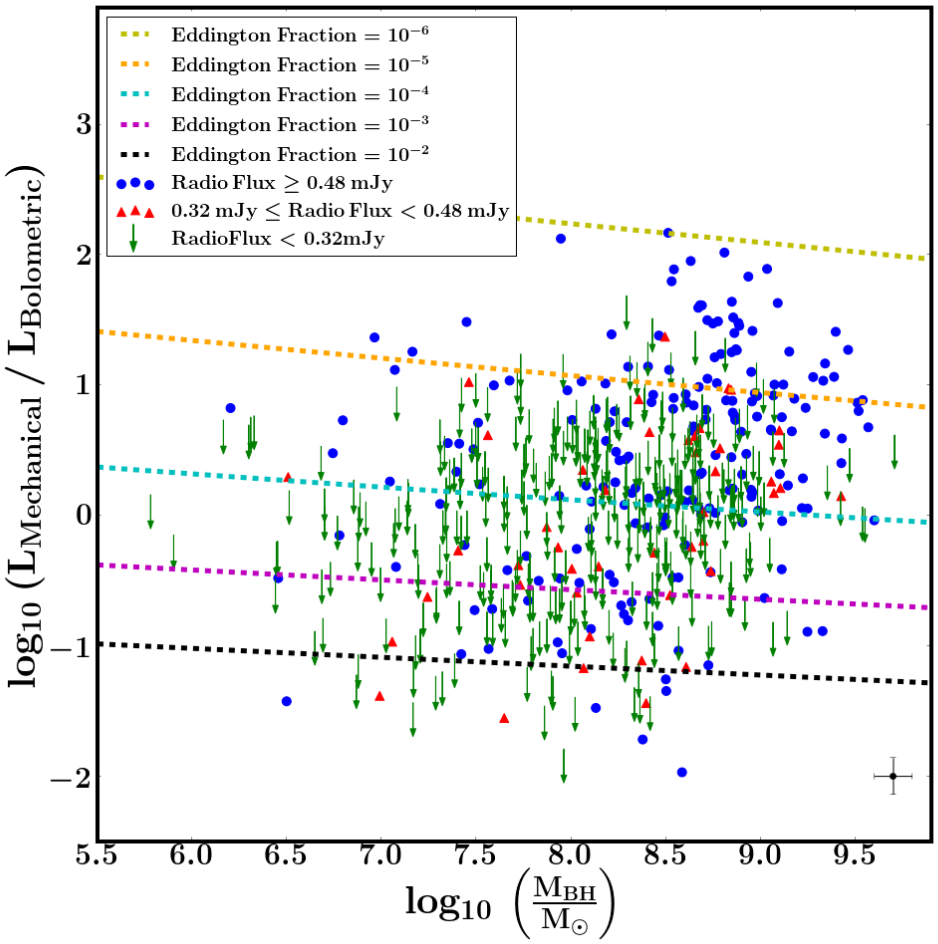

Figure 2.9 *An analysis of the ratio of the mechanical luminosity to the bolometric luminosity, as a function of black hole mass. LINERs with radio flux density above 0.48 mJy (3× rms) are represented by blue dots. Those with radio flux density between 0.32 mJy and 0.48 mJy (between 2× rms and 3× rms) are represented by red triangles. LINERs with radio flux density below 0.32 mJy are represented by green arrows, the base of which is plotted at the luminosity corresponding to 0.32 mJy. The dashed lines show the theoretical ratio as a function of black hole mass for a selection of different Eddington fractions for sources obeying the Fundamental Plane – the derivation is described in the text. Typical error bars are shown in the bottom right of the diagram.*

2.8 Conclusions

The main conclusions from this chapter are:

- The fraction of galaxies hosting a LINER is a strong function of stellar mass and also of black hole mass. The scaling factors are approximately $f_{LINER} \propto M_*^{1.6\pm0.2}$ and $f_{LINER} \propto M_{BH}^{0.6\pm0.1}$ respectively. These are shallower than found for radio selection (but are consistent once the Fundamental Plane is considered) and demonstrate that $\frac{L_{rad}}{L_X}$ scales with M_{BH}.
- By studying a sample of jet-mode AGNs (radiatively inefficient), a Fundamental Plane is found which matches X-ray binaries in the low-hard state (and so in the same accretion mode as the AGNs). The analysis confirms the results from previous studies that a scale-invariant Fundamental Plane does exist, and one that spans at least 15 orders of magnitude in X-ray luminosity. The Fundamental Plane was found to be $\log\left(\frac{L_R}{erg/s}\right) = 0.65^{+0.07}_{-0.07} \log\left(\frac{L_X}{10^{42} erg/s}\right) + 0.69^{+0.10}_{-0.10} \log\left(\frac{M_{BH}}{10^8\,M_\odot}\right) + 38.35^{+0.10}_{-0.10}$.
- The relationship does, however, have a significant scatter. No simple observable was found that could account for this which argues against the Fundamental Plane being used to estimate accurately black hole mass from observations of X-ray and radio luminosity.
- For consistency of the Fundamental Plane derivation with the X-ray binary population, this work favours a steep gradient in the relationship between black hole mass and velocity dispersion, as suggested by recent studies.
- It has been argued that the anomalously high X-ray luminosity of XBONGs can be explained by a beaming effect along the line of sight. This sample of LINERs, which share the same characteristics as XBONGs, display no evidence of strong beaming. The implication is that beaming cannot be a general explanation for all XBONGs.
- It is found that for the LINERs a significant proportion of the energy is released in the jets, and that the proportion rises with increasing black hole mass.
- Rather more speculatively, it is of interest to note that there are hints of a change in the properties of a black hole or in the accretion flow at a mass of around 10^8 solar masses, as indicated in both Figure 2.8 and Figure 2.9.

Chapter 3

Identification of a Sample of LOFAR sources in ELAIS-N1

3.1 The Low-Frequency Array

The remainder of this thesis is based on observational data obtained from LOFAR, the LOw-Frequency ARray. LOFAR is a new-generation radio interferometer, designed to operate at low radio frequencies — those between 10 and 240 MHz — and so opening up a section of the spectrum that has hitherto been comparatively neglected.

The telescope consists of an array of dipole antennas which are grouped into stations. The core 38 stations are located in the Netherlands, with a further twelve stations in Germany, France, Sweden, Poland and the UK. An additional station is under construction in Ireland. Each station in the Netherlands consists of 96 low-band and 48 high-band antennas; the international stations (those outside the Netherlands) have 96 of each type. In contrast to earlier radio telescopes, the LOFAR antennas are static; pointing and tracking are accomplished by using beam-forming techniques to combine the signal from each antenna into a phased array. The signals from different stations are then sent to a central GPU cluster and correlated. This system requires high-power and high-throughput computing resources both centrally and at each station, but confers the twin advantages of agility and flexibility. Also, relevant for this thesis, it offers the scope for multiple, simultaneous observations from a station which, when combined with the large

field of view at such low frequencies, means that LOFAR is a very effective survey instrument. A (much) more detailed description of LOFAR is provided by van Haarlem et al. (2013).

LOFAR is capable of producing sensitive high-resolution observations; a depth of 0.1 mJy per beam at a resolution of 5 arcseconds is expected from a standard 8-hour scan using the high-band antennas. There are, however, a number of very challenging issues that need to be overcome to achieve this. First, the ionosphere leads to delay differences between the stations which distort the phases of the measured visibilities. The extent of the phase change depends on the observing frequency and the viewing path through the ionosphere; hence the phase errors are direction dependent within the large field-of-view of each station and also vary from station to station. Second, the beam shapes vary with time, a consequence of the fact that the delays between dipole elements are adjusted in order to track sources as they move across the sky. Small errors in modelling the station beams can amplify into significant distortions in the image. This means that even after applying a series of calibration steps designed to remove the various distortions present in the images from traditional radio telescopes, there remain significant artifacts in LOFAR images. These artifacts are centred around sources, particularly bright sources. Improper calibration of bright sources leads to extensive residuals across the entire image, increasing the rms noise to typically between 5 and 10 times the level expected.

In order to remove the above distortions and produce images with the targeted depth and resolution, a new method of calibration has been developed — direction-dependent facet calibration. The techniques have been developed by van Weeren et al. (2016), building upon earlier work carried out by, for example, Noordam (2004) and Intema et al. (2009). A high-level summary of the steps is as follows:

- Observations of calibrator sources before and after the target field are used to calibrate slowly-varying effects, such as separating the consequences of clock errors from those of the ionosphere.
- The image is divided into facets, with the tessellation scheme designed to ensure that each facet has a bright source near its centre.
- For each facet in turn, the sources from other facets are subtracted from the raw data and then a self-calibration cycle is conducted on the defining

Table 3.1 *Multiband data in ELAIS-N1*

Survey / Telescope	Reference	Abbreviation	Data	Wavebands
Galaxy Evolution Explorer	Martin et al. (2005)	GALEX	ultraviolet	fuv (1539 Å) and nuv (2316 Å)
Sloan Digital Survey	York et al. (2000)	SDSS	optical	u, g, r, i and z
Isaac Newton Telescope	Laing and Jones (1985)	INT	optical	u, g, r, i and z
Panoramic Survey Telescope and Rapid Response System	Huber et al. (2017)	PanSTARRS	optical	g, r, i, z and y
UKIRT Infrared Deep Sky Survey	Lawrence et al. (2007)	UKIDSS	infrared	J and K
Two Micron All-Sky Survey	Skrutskie et al. (2006)	2MASS	infrared	J, H and K
Spitzer Wide-area Infrared Extragalactic Survey	Surace et al. (2005)	SWIRE	infrared	3.6, 4.5, 5.8 and 8.0 microns
Spitzer Extragalactic Representative Volume Survey	Mauduit et al. (2012)	SERVS	infrared	3.6 and 4.5 microns
Wide-field Infrared Survey	Wright et al. (2010)	WISE	infrared	3.4, 4.6, 12.0 and 22.0 microns
Spitzer Multiband Imaging Photometer for SIRTF	Rieke et al. (2004)	MIPS	infrared	24, 70 and 160 microns
Herschel Multi-Tiered Extragalactic Survey	Tanaka et al. (2017)	HERMES	infrared	24 and 250 microns
VLA Faint Images of the Sky at Twenty-centimetres Survey	Becker et al. (1995)	FIRST	radio	21 cm

A selection of the observational data available for the ELAIS-N1 field. The abbreviations are those used throughout the rest of this thesis.

bright source in order to obtain a set of direction-dependent corrections for that facet.

- It is then assumed that the direction-dependent corrections that have been found for the central area of the facet containing the bright source are applicable for the facet as a whole; the corrections are applied direction by direction.
- Once each facet has been calibrated, they are then imaged in turn.

In this way, an image for the field is obtained. Note that alternative direction-dependent calibration and imaging methods are also under development, such as those of Tasse (2014) and Tasse et al (2017, in prep).

3.2 ELAIS-N1

The LOFAR telescope was used to conduct an in-depth survey of the European Large Area ISO Survey North 1 region (the ELAIS-N1 field). ELAIS-N1 benefits from low galactic cirrus contamination, a high ecliptic latitude and a low column of foreground material. For these reasons, the field was chosen by ESO to be part of a deep wide angle survey, conducted between March 1996 and April 1998. Subsequent surveys have built up a wealth of multiband data for the field. The survey data that were used, to a greater or lesser extent, in this thesis are set out in Table 3.1.

Around 250 hours of observations of ELAIS-N1 have been taken by LOFAR. The bulk of the bandwidth was placed on the central beam, but different observations adopted a variety of strategies for using the remaining $\sim 25\%$ of the bandwidth. Focus here will be on the central beam. Details of the observational strategy are set out in Table 3.2.

3.3 A Description of the Observations

This thesis uses a first ELAIS-N1 catalogue involving a preliminary direction-dependent reduction of a single dataset; the dataset was obtained from a single eight-hour observation. The frequency range was 115–176 MHz, with a central

Table 3.2 *Observation parameters*

Observation Period	February 2013 onwards
Observation Time	$\sim$ 250 hours
Stations	61 core and remote stations in HBA _ InnerMode
Integration Time	1 second, averaged to 2 seconds in pre-processing
Correlations	XX, XY, YX, YY
Sampling Mode	8 bit
Sampling Clock Frequency	200 MHz
Frequency Range	115 – 176 MHz and 179 – 189 MHz
Central Frequency	150 MHz
Bandwidth	72 MHz
Sub-bands	371 (1 discarded)
Bandwidth per sub-band	195 kHz
Channels per sub-band	64 (4 discarded), averaged to 15 in pre-processing

frequency of 150 MHz. The imaging of ELAIS-N1 was carried out by Dr Jose Sabater and is described in detail in Sabater et al (in preparation). Sources were extracted from the image using the Python Blob Detection and Source Measurement (PyBDSM) software, as described in Mohan and Rafferty (2015) (note that the name has since been updated to Python Blob Detector and Source Finder). PyBDSM was developed specifically to serve the needs of LOFAR (although it can be used with images from any radio interferometric telescope) and, in particular, to deal with the wide range of scales of emission within the LOFAR images. After experimenting with different sets of parameters for PyBDSM, it was decided to adopt those used by Williams et al. (2016). The more important parameters were given the following values:

- rms_box = (160, 50): a sliding box size of 160 pixels every 50 pixels was used to create the rms map.
- rms_box_bright = (60,15): a smaller box size was used near bright sources.
- adaptive_thresh = 150: bright sources were defined to be those with a peak of more than 150x the sigma-clipped rms across the whole field.
- group_tol = 10: PyBDSM breaks up the image into islands containing one or more Gaussians and this parameter helps to determine the number of Gaussians inside an island that may be subsequently combined into a single source – a large value of group_tol results in larger sources.

Table 3.3 *The number of LOFAR sources in each facet.*

Facet Number	Number of LOFAR Sources	Number in PanSTARRS area	Number in PanSTARRS / UKIDSS / SWIRE area
1	195	195	195
2	173	0	0
3	221	0	0
4	155	81	81
5	145	144	140
6	198	152	135
7	117	93	58
8	167	158	148
9	153	131	117
10	170	82	82
11	125	0	0
12	121	0	0
13	223	65	55
14	156	13	11
15	135	108	79
16	168	168	168
17	174	41	31
18	204	0	0
19	176	0	0
Total	3176	1431	1300

The last point is important. It means that the radio emission sources identified by PyBDSM may be point-like (formed out of one Gaussian) or extended; this is relevant for the analysis that follows.

The image was divided into 19 facets and within these facets the chosen PyBDSM parameter set allowed 3176 LOFAR sources to be detected. The sources, split by facet, are shown in the upper chart in Figure 3.1. The overall aim was to find multiband counterparts of the LOFAR sources and so the sample was restricted to those LOFAR sources within the region covered by the PanSTARRS, UKIDSS and SWIRE surveys. There are 1300 such LOFAR sources, with the split by facet shown in the final column of Table 3.3. Six of the facets contain no LOFAR sources within the relevant area. A second imaging of the entire field was subsequently carried out using a slightly improved calibration procedure which identified a further 57 LOFAR sources in the relevant area, bringing the total sample size to 1357. These 1357 LOFAR sources are shown in the lower chart in Figure 3.1.

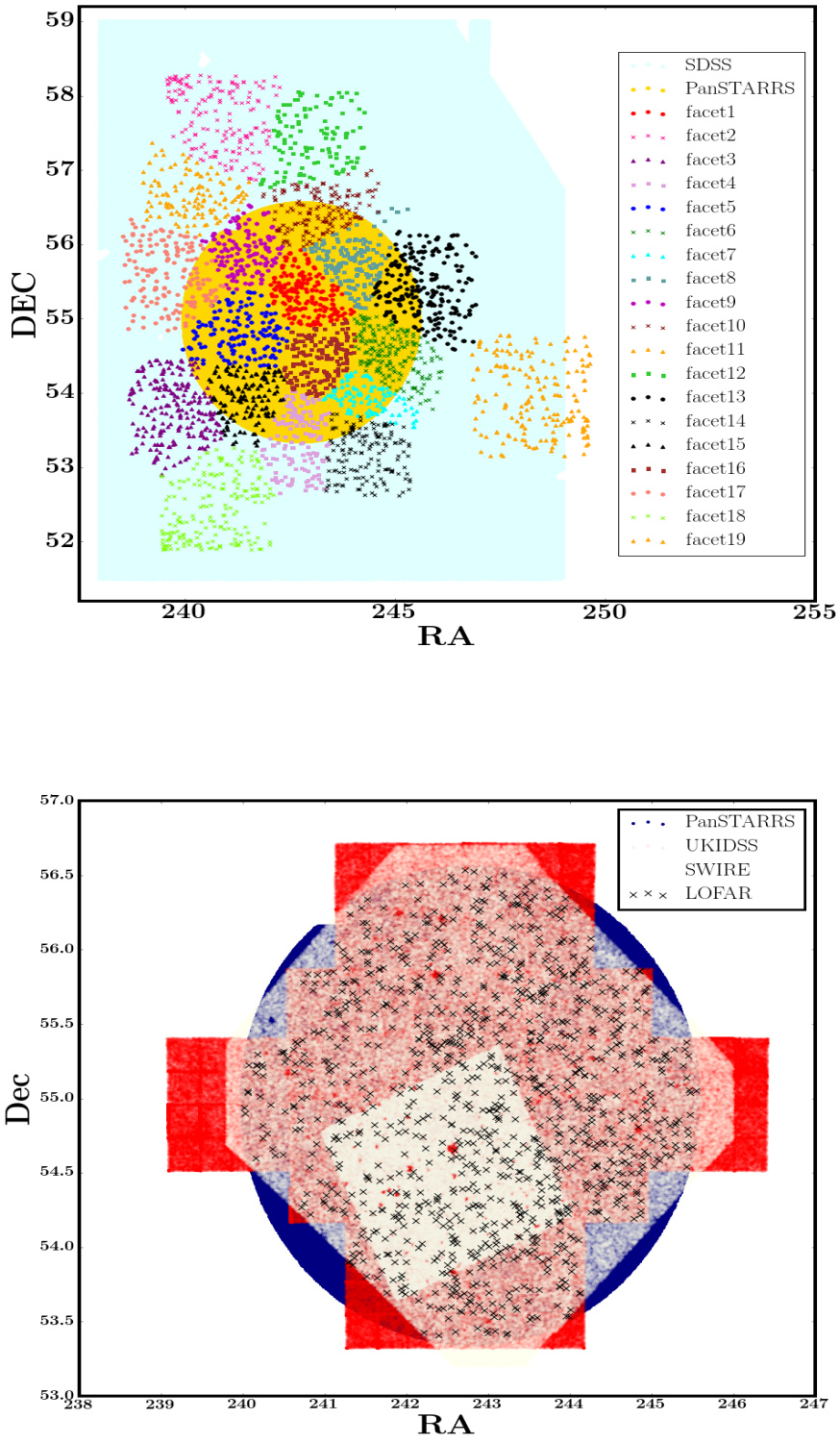

Figure 3.1 *Upper figure: the LOFAR sources split by facet, and the area of the PanSTARRS (yellow shading) and SDSS (blue shading) surveys. Lower figure: the 1357 LOFAR sources within the area covered by the PanSTARRS (blue), UKIDSS (red) and Spitzer (ivory) surveys; note that the area of the SERVS survey can be recognised by the greater density of the Spitzer sources (the white square).*

3.4 Astrometry

An important first step was to check the astrometry in each of the facets; although the LOFAR data are formally on the International Celestial Reference Frame, astrometric errors might be introduced by the low-resolution input model and by self-calibration phase shifts. The facet-by-facet reduction process means that different astrometrical corrections might be required for each facet. A possible approach would be to check positions against the VLA FIRST radio sources, but the comparatively low depth of that survey and hence low number of matches coupled with the difficulty of pinpointing the exact centre of radio emission both suggest that this would not produce accurate results. A better method is to take advantage of deeper optical data and to check the positional accuracy against the astrometry of the PanSTARRS deep i-band catalogue and the SDSS DR10 catalogue. The PanSTARRS catalogue has a positional accuracy of 0.07 arcseconds and the SDSS catalogue has an accuracy of 0.045 arcseconds per coordinate for sources brighter than r = 20. The SDSS survey area covered completely the first 18 facets and covered approximately two-thirds of the 19th facet (upper chart, Figure 3.1). By contrast, only two of the facets are completely within the PanSTARRS area and eleven of the facets are partially within that area. The other six facets are completely outside the PanSTARRS area and so are irrelevant for the sample studied in this thesis; for completeness, however, the astrometrical adjustments for all 19 facets were calculated and are shown below.

The PanSTARRS objects have a significantly greater density than those from the SDSS survey – approximately 232700 per square degree compared with 40100 respectively – and so the former were used, where possible, to calculate the coordinate adjustments; the SDSS catalogue was then used as a check on the results. The facets where this approach was used were 1, 4, 5, 6, 7, 8, 9, 10, 13, 15 and 16. Facets 14 and 17 contained just 13 and 41 sources within the PanSTARRS survey area and so the comparison was made initially against the SDSS sources and the results checked against PanSTARRS. For the remaining six facets, the coordinate adjustments were, by necessity, calculated in relation to the SDSS catalogue alone.

To ensure that consistent results would be provided irrespective of whether the comparison was against PanSTARRS or SDSS, the astrometry of the PanSTARRS catalogue relative to the SDSS catalogue was first examined. The nearest SDSS neighbour to each PanSTARRS source was found, provided that

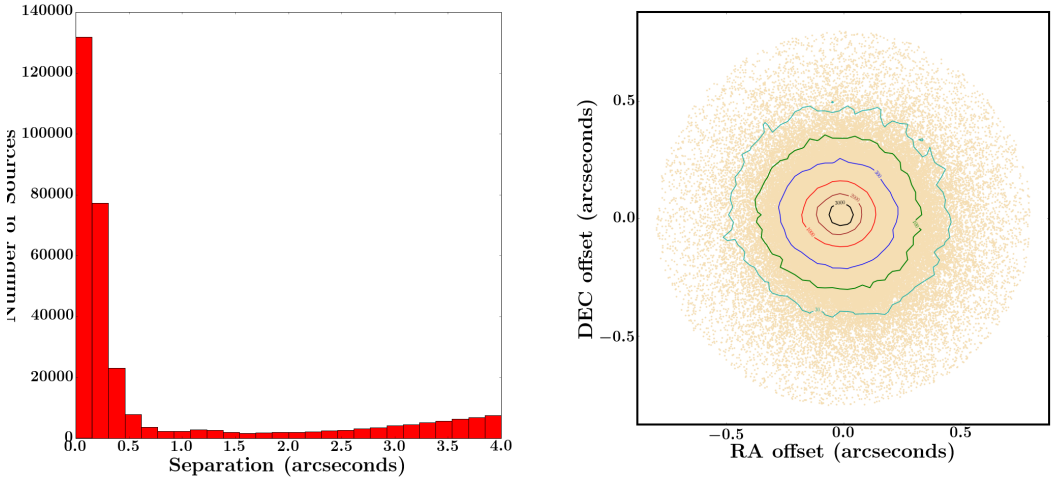

Figure 3.2 *A comparison of the astrometry of PanSTARRS and SDSS. Left-hand chart: The nearest SDSS neighbour to each PanSTARRS source was found and the distribution of separations is plotted. Right-hand chart: The RA and Dec offsets are plotted (PanSTARRS minus SDSS), with the contours showing the density of sources.*

the separation was less than 0.8 arcseconds, and the Right Ascension (RA) and Declination (Dec) offsets calculated. That separation threshold was obtained by examining the distribution of closest matches (Figure 3.2, left-hand side) and taking the minimum of the distribution; the implication is that random matches start to dominate at separations higher than the 0.8 arcsecond threshold. The offsets between the PanSTARRS and SDSS coordinates were plotted in the right-hand chart in Figure 3.2 and, as can be seen, there was very close agreement. The mean offsets were found to be $+0.0191 \pm 0.0003$ arcseconds in the RA and -0.0167 ± 0.0003 in the Dec (in both cases, PanSTARRS less SDSS). It appears that it is appropriate to compare the astrometry of the facets against either catalogue.

The method used to calculate the coordinate adjustments necessary for the LOFAR sources was as follows:

- For a given facet, the nearest PanSTARRS source to each LOFAR source was identified and the separations recorded.
- The number of matches declined with increasing separation up until 5 arcseconds; for offsets greater than 5 arcseconds, the number of nearest neighbours started to increase again as random sources rather than matches

were picked up. This was consistent with the density of the PanSTARRS sources.

- For the purposes of this exercise, it was assumed that all matches between LOFAR and PanSTARRS sources for all facets could be considered to be genuine if the separation were less than 5 arcseconds.

- For simplicity, the same 5 arcsecond threshold was used when comparing the LOFAR astrometry with that of SDSS.

- In each of facets 1, 4, 5, 6, 7, 8, 9, 10, 13, 15 and 16, the mean RA offsets and mean Dec offsets were found for "genuine" matches between the LOFAR sources and the PanSTARRS catalogue.

- These adjustments were applied to the LOFAR coordinates. Again, the nearest matches within 5 arcseconds were found and the mean offsets calculated. This step was necessary because the coordinate adjustments bring a number of new matches within the 5 arcsecond threshold and push a number outside the threshold. The iterative process was continued until there was agreement in the adjustments between two successive iterations (typically, no more than three iterations were required).

- The exercise was repeated for all 19 facets using SDSS sources as the counterparts.

- As a final check, the adjustments were recalculated by repeating the whole process, but now after removing those LOFAR sources estimated to have extended emission and hence have a relatively high positional uncertainty. Only sources based on a single Gaussian were considered (those flagged as S = single in the PyBDSM output). A further crude test was used to try and filter out extended radio sources. The ratios of A = Peak Flux / Total Flux and B = Maximum Axis / Minimum Axis were calculated and a source was deemed to be point-like, and included in the analysis, if $A/B > 0.2$. 69% of sources satisfied these two criteria. In no case did this additional step lead to a change of more than 0.26 arcseconds in the solution.

The results are set out in Table 3.4.

For the eleven facets where the comparison could be made against both PanSTARRS and SDSS, the coordinate adjustments were similar under both

Table 3.4 *The coordinate adjustments per facet, as calculated by different methods.*

Facet Number	Comparison with PanSTARRS all LOFAR sources		Comparison with PanSTARRS point-like LOFAR sources		Comparison with SDSS all LOFAR sources		Comparison with SDSS point-like LOFAR sources	
	RA offset arcsec	Dec offset arcsec	RA offset arcsec	Dec offset arcsec	RA offset arcsec	Dec offset arcsec	RA offset arcsec	Dec offset arcsec
1	+3.95	+4.04	+3.96	+3.96	+3.97	+4.18	+3.97	+4.14
2					-1.58	+0.12	-1.68	+0.20
3					-6.08	-10.19	-6.42	-10.47
4	+3.54	+0.84	+3.76	+0.93	+3.28	+0.68	+3.42	+0.75
5	-2.65	-1.34	-2.64	-1.32	-2.71	-1.19	-2.69	-1.44
6	+3.10	-4.21	+3.10	-4.24	+3.11	-4.26	+3.11	-4.24
7	+1.03	-3.46	+0.97	-3.39	+1.18	-3.41	+1.08	-3.49
8	+3.96	+3.74	+3.97	+3.73	+3.84	+3.98	+3.83	+3.91
9	+4.29	+1.22	+4.39	+ 1.19	+3.94	+1.12	+3.99	+1.08
10	+2.12	+2.12	+2.28	+2.08	+1.95	+2.15	+2.17	+2.06
11					-3.44	+0.52	-3.18	+0.57
12					-2.02	+0.28	-1.87	+0.28
13	+5.61	+3.49	+5.35	+3.49	+5.50	+3.71	+5.63	+3.55
14					-2.62	-7.64	-2.52	-7.83
15	-2.32	-4.93	-2.32	-5.09	-2.42	-4.88	-2.18	-5.01
16	+4.00	+1.74	+4.02	+1.71	+3.87	+1.69	+3.87	+1.63
17					-0.08	+1.52	-0.29	+1.57
18					+1.56	-0.21	+1.81	-0.19
19					+5.77	+ 2.25	+5.11	+2.22

approaches, with a mean difference of 0.19 arcseconds in the positional adjustments (calculated by combining the RA and Dec adjustments in quadrature). Similarly, it mattered little whether or not the LOFAR sample was restricted to point-like sources, with a mean difference of 0.11 arcseconds in the results from the two approaches. The coordinate adjustments derived from the comparison with PanSTARRS using all LOFAR sources were adopted. As a final check, the adjustments were applied to the LOFAR coordinates, the offsets to the nearest PanSTARRS neighbours were calculated and plotted, and a histogram of the separations was also produced. This confirmed that the offsets were clustered around zero and that the distribution of separations declined out to a distance of 5 arcseconds. The two charts for Facet 1 are shown in Figure 3.3 (when viewing the histogram, it must be remembered that the area of the annulus represented by each bin rises with increasing separation).

For facets 14 and 17, the analysis was made against the SDSS catalogue. The required corrections were comparatively small in facet 17 and there was close alignment when the results were checked against PanSTARRS. Facet 14 was more problematic. The SDSS analysis showed that large corrections were needed to the RA and, particularly, the Dec coordinates. There were only 13 LOFAR sources in Facet 14 within the PanSTARRS area. When the adjustments were applied to their coordinates and the astrometry compared with PanSTARRS, the Dec coordinates were closely aligned but there was a mean RA discrepancy of approximately one arcsecond. It was decided to adopt the adjustments found

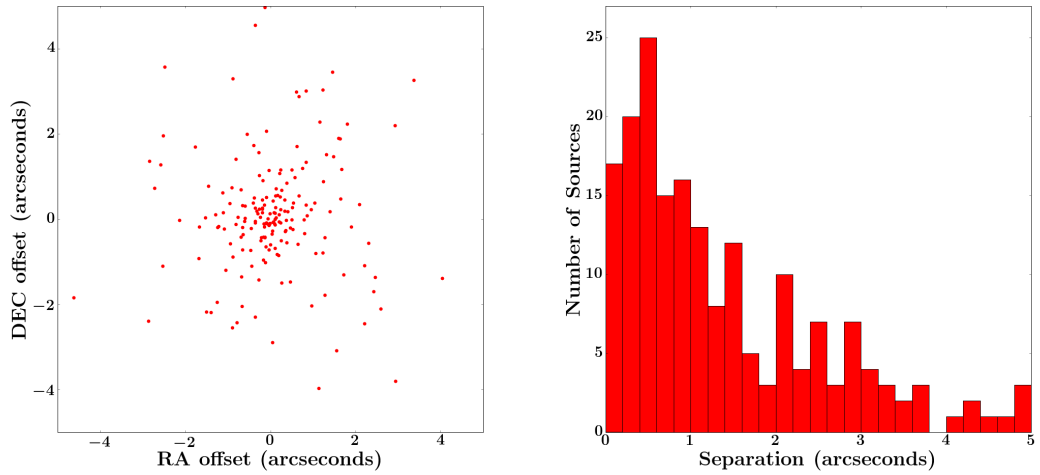

Figure 3.3 *Both charts apply to Facet 1. After applying the coordinate adjustments to the coordinates of the LOFAR sources, the offsets to the nearest PanSTARRS neighbour are clustered around zero (left-hand figure). The distribution of separations declines out to a distance of 5 arcseconds (right-hand figure).*

through the SDSS comparisons, but all eleven of the facet 14 sources within the PanSTARRS/UKIDSS/SWIRE area were checked visually later in the analysis to ensure that any inaccuracy in the astrometric adjustments did not lead to a false match (in fact, in all eleven cases examination of the images suggested that the correct counterpart had been found).

Finally, the coordinate adjustments in facet 3 were very large, with an RA offset of -6.08 arcseconds and a Dec offset of -10.19 arcseconds. The analysis was repeated for this facet using the FIRST catalogue to derive the adjustments; the results were in close agreement, with an RA offset of -6.34 arcseconds and Dec offset of -10.16 arcseconds.

The final adjustments for each facet are shown in Table 3.5, together with their rms errors.

3.5 The Catalogues used to Cross-match

Five catalogues were used to find counterparts. The optical data were taken from a four-year observational programme conducted by PanSTARRS. One-quarter of

Table 3.5 *The coordinate adjustments for each facet.*

Facet Number	RA Adjustment arcseconds	Dec adjustment arcseconds	RA adj. Error arcseconds	Dec adj. Error arcseconds
1	+3.95	+4.04	0.09	0.10
2	-1.58	+0.12	0.17	0.14
3	-6.08	-10.19	0.11	0.09
4	+3.54	+0.84	0.10	0.17
5	-2.65	-1.34	0.13	0.13
6	+3.10	-4.21	0.12	0.10
7	+1.03	-3.46	0.15	0.14
8	+3.96	+3.74	0.11	0.10
9	+4.29	+1.22	0.14	0.14
10	+2.12	+2.12	0.16	0.16
11	-3.44	+0.52	0.18	0.15
12	-2.02	+0.28	0.16	0.20
13	+5.61	+3.49	0.19	0.16
14	-2.62	-7.64	0.15	0.15
15	-2.32	-4.93	0.14	0.14
16	+4.00	+1.74	0.11	0.11
17	-0.08	+1.52	0.13	0.13
18	+1.56	-0.21	0.15	0.17
19	+5.77	+2.25	0.21	0.18

the survey time was allocated to a Medium Deep Survey of ten fields, one of which, MD08, was ELAIS-N1; the Medium Deep Survey is described in Huber et al. (2017). Observations were taken through g, r, i, z and y filters. This thesis used sources extracted from the MD08 Medium Deep Field Catalogue, with g-band and i-band data used in the cross-matching procedure. K-band sources were obtained from UKIDSS conducted using the UKIRT Wide Field Camera, as described in Lawrence et al. (2007). The UKIDSS survey had five components; the sources in this work were obtained from the Deep Extragalactic Survey, DXS, and using the deep stacks data. Longer wavelength near-infrared data at 3.6 micron were obtained from Spitzer surveys, using both SWIRE and Spitzer Extragalactic Representative Volume Survey (SERVS) catalogues. These are described in Surace et al. (2005) and Mauduit et al. (2012) respectively. The SERVS survey was deeper, but covered only part of the area under investigation. All of the SERVS sources within a quadrilateral whose vertices are defined by the following four coordinates are included: (240.955138, 54.77832), (243.12906, 55.359262), (244.015507, 54.213811) and (241.888356, 53.643521). The actual area covered by the SERVS survey is fractionally larger, but defining a regular area ensured a clean separation between the use of the SERVS and SWIRE catalogues. 751 SERVS sources, representing under 0.5% of the total SERVS catalogue, were outside of the quadrilateral and so were omitted. Outside the quadrilateral, SWIRE sources were used to provide the 3.6 micron data.

Each catalogue was cleaned in order to remove sources (1) that have no valid magnitude, (2) are outside the relevant area and (3) are considered to be duplicates (particularly relevant for surveys where the catalogue had been built up from observations of many individual overlapping frames). Sources that were within 1 arcsecond of each other were treated as duplicates, as were those that failed the following test:

$$\mathrm{abs}(\mathrm{M}_1 - \mathrm{M}_2) + \mathrm{separation}[\mathrm{source1}, \mathrm{source2}] < 2.0 \tag{3.1}$$

where M_1 and M_2 are the apparent magnitudes of the two sources being compared and separation[source1, source2] is their angular separation in arcseconds. When a pair of duplicate sources was found, the one with the brighter magnitude was retained and the other discarded. There is a chance of removing genuine pairs from the analysis, but visual tests confirmed that the vast majority are indeed duplicate entries. Cleaning these from the catalogues is essential for the colour-based likelihood ratio analysis that is described later in this chapter.

Table 3.6 *The number of sources in the cleaned catalogues*

Catalogue	Band	Number of Sources (cleaned)
PanSTARRS	g	1,192,656
PanSTARRS	i	1,319,071
UKIDSS	K	547,052
Spitzer:SWIRE	3.6 micron	171,759
Spitzer:SERVS	3.6 micron	158,738

The numbers of sources remaining after the filtration process are shown in Table 3.6. Up to 20% of the sources may be stars rather than galaxies: for example, 120442 of the K-band sources are shown with pGalaxy < 0.35 in the UKIDSS catalogue, where pGalaxy indicates the probability that a source is a galaxy and is calculated by combining individual detection classifications in each waveband into a merged score according to Bayesian classification rules. Consideration was given to removing such sources or alternatively including them as a separate category. A subsequent investigation, however, found that neither approach worked well. If the probabilities in the catalogue are accurate, then 5700 of these sources will in fact be galaxies and the investigation revealed that both approaches led to a significant number of genuine matches being missed. Consequently, it was decided to include these sources and allow the likelihood ratio analysis, described later in this chapter, to prevent the occurrence of false matches with stars.

3.5.1 Grouping the Counterparts

In preparation for matching the LOFAR sources with their host galaxies, the sources from the five optical and infrared catalogues were combined into likely groupings - that is, where it is believed that the entries from each catalogue refer to the same galaxy.

The groupings were formed by starting with the PanSTARRS i-band sources and finding the nearest source from each of the other catalogues, provided that the separation was less than one arcsecond. Those K-band sources that had not been linked with an i-band source were then examined to find counterparts from the g-band and Spitzer catalogues using the same search criterion (and considering only g-band and Spitzer sources that had not already found an i-band match). Finally, the remaining g-band sources were compared with the remaining Spitzer

sources to identify matches. This method does mean that there is a risk that a small number of groupings might be mis-identified, but it was felt that the effect would be too small to be of concern.

The procedure produced 1527544 groupings. A problem was, however, discovered later in the analysis: there were a large number of K-band only detections (those without a corresponding i-band, g-band or 3.6 micron detection) that were spurious. The false detections were either due to interference caused by a nearby bright source or due to crosstalk interference resulting from bulk read-out from infrared detectors.

In the first case, the effect can be seen in Figure 3.4, which shows the distribution of the offsets from bright K-magnitude sources for the giK-detections (blue line) compared with that of K-only sources (red histogram). The giK-detections give a guide to the expected shape of the radial distribution for genuine K-only detections. The actual distribution is far different, indicating the presence of a large number of spurious detections close to bright sources. To alleviate the problem, all K-only detections were removed from the list of groupings if they were within 30 arcseconds of a <12 magnitude source, within 20 arcseconds of a 12 - 14 magnitude source or within 13 arcseconds of a 14 - 16 magnitude source. The charts in Figure 3.4 illustrate why these particular radii were chosen; they mark the points where the two distributions most clearly start to diverge. This is a crude method of removing spurious sources – some genuine galaxies will be removed and some spurious detections outside the chosen radii will remain –

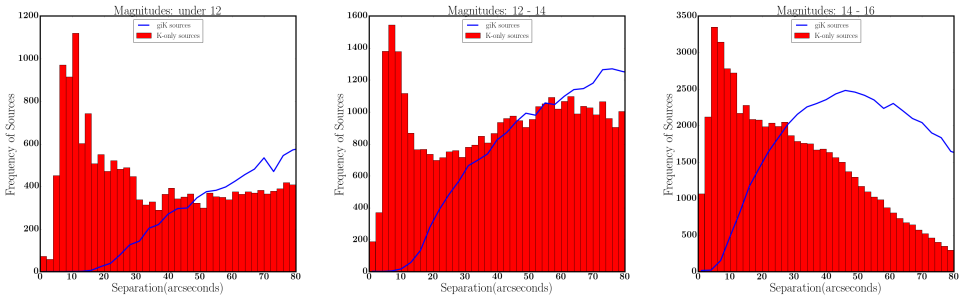

Figure 3.4 *The charts show the distribution of the offsets of K-only detections (red histogram) and giK-detected sources (blue line) from bright K-magnitude sources. The bright K-magnitude sources are those with magnitudes below 12 (left-hand chart), magnitudes between 12 and 14 (middle chart) and magnitudes between 14 and 16 (right-hand chart).*

but is effective for the likelihood ratio analysis (the reason why these spurious detections need to be removed is discussed later in this chapter). However, to ensure that a genuine match to a LOFAR source was not erroneously excluded by this filtering process, no K-only detection within 5 arcseconds of a LOFAR source was removed.

In the second case, the need to remove false crosstalk detections can be seen from Figure 3.5. There are spikes in the distribution of offsets at distances around 51 arcseconds and 102 arcseconds away from bright sources (defined as those with a K-magnitude less than 16). All K-only detections were removed if they were between 50 and 52 arcseconds or between 101 and 103 arcseconds away from a bright source along the right ascension or along the declination (that is, approximately 51 arcseconds or 102 arcseconds "northwards", "eastwards", "southwards" or "westwards" of a bright source).

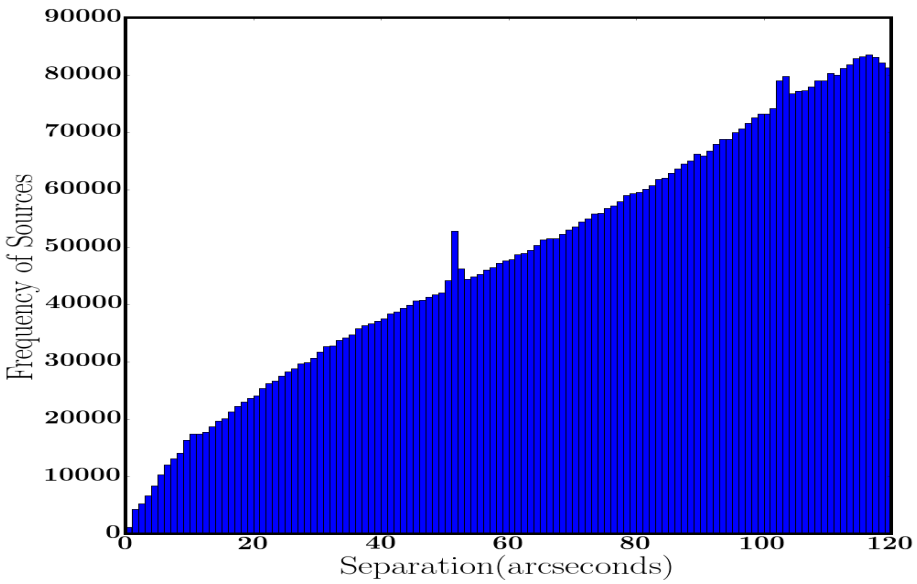

Figure 3.5 *The distribution of offsets of K-only detections from bright (<16 magnitude in K-band) sources. The presence of false crosstalk detections is highlighted by the two spikes in the distribution.*

These two filtration procedures removed 34506 (hopefully) spurious K-only detections. Any LOFAR source that was subsequently matched with a K-only detection was visually examined to confirm the reliability of the K-band emission. There were 38 K-only matches and all were found to be genuine.

The final split of the groupings is set out in Table 3.7; an underscore indicates no

Table 3.7 *The breakdown of the groupings*

Category	Number of Groupings in Category
giKs	225,163
giK_	169,769
gi_s	48,030
gi__	688,607
g_Ks	1120
g_K_	1,639
g__s	788
g___	49,595
_iKs	9,810
_iK_	8,258
_i_s	3,085
_i__	165,741
__Ks	23,152
__K_	40,006
___s	58,275
Total	1,493,038

identification in that particular band and s (= Spitzer) is used to denote the 3.6 micron detections.

3.6 Identifying the Multiband Counterparts

A difficulty in cross-matching object catalogues at different wavelengths is how to differentiate between those objects that are true counterparts and those that are unrelated foreground or background objects. The difficulty is accentuated when matching to a radio catalogue, given the uncertainty in positioning the centre of the radio source. In an attempt to overcome the problem, a likelihood ratio technique has been developed over the past forty years, with refinements introduced most recently by Sutherland and Saunders (1992), Ciliegi et al. (2003), Fleuren et al. (2012) and McAlpine et al. (2012). The basic principle, described in more detail later in this chapter, is that the choice is based on the distance between the centre of the radio flux and the possible counterpart galaxy, modified by a factor determined by the magnitude or colour of the putative counterpart. The technique is not suitable for use with all radio sources, but the likelihood ratio procedure provides a useful, automated route to determine the likeliest host galaxies for those radio sources where the expected host galaxy position can be

estimated accurately – for example, those that are single, isolated and without extended emission. A high-level description of the process is as follows:

- The LOFAR sources were visually examined to identify those that were obviously unsuitable for the likelihood ratio technique to be used.
- For the small minority of LOFAR sources that were unsuitable for likelihood ratio analysis, the probable counterparts were determined by visual examination of the images.
- For the remaining LOFAR sources, a likelihood ratio test was applied to select the most probable host galaxy.

These stages are now described in more detail.

3.6.1 The Visual Categorisation

In order to decide which of the LOFAR sources were suitable to be matched using the likelihood ratio technique, all were examined visually. This was a practical option given the comparatively small number of radio sources. It would, however, be impractical for larger surveys and suggestions to help in automating the process are presented in Chapter 4. By viewing the images, the radio sources could be placed into four categories. The first category contained those sources where the choice of counterpart would be determined by the likelihood ratio process - there were 1117 sources in this category. The second category contained those sources that had either extended emission or appeared to be part of a complex system, meaning that the position of the host galaxy may not be easily identified - there were 100 sources in this category. The third category contained those sources that were believed to be one component in a double or triple system, and hence the galaxy centre would be positioned between this source and its partner - there were 22 sources in this category. Note that the lobes of a jet-mode AGN may be widely separated (over 100 arcseconds is not unusual) and so are difficult to differentiate from two isolated sources; subsequent analysis, described later in this chapter, revealed that this first visual examination had significantly underestimated the number of double systems. The fourth category contained those sources where the visual examination cast doubt on the authenticity of the source; typically, these would be located close to brighter radio emission. There were 118 in this category.

The division into categories was accomplished by a team of four people. Each LOFAR source was viewed by the author and at least one other person independently. Where their categorisations differed, the decision was discussed. If there was still disagreement, then a third opinion was sought.

Examples of the four categories are shown in Figure 3.6. The two images in the first row show sources that are single, isolated and with point-like emission and so were passed through to the likelihood ratio analysis. The images in the second row show examples of an extended-emission source. The third row shows multi-component radio sources. Image (f) shows a double source: the PyBDSM extraction software identified the two lobes but not the centre. The bottom row shows examples where the source identified by PyBDSM is not genuine, either because it is related to (or noise created by) a nearby bright source or because the flux is only slightly higher than the surrounding noise; in both cases, the absence of detections in the optical / near-infrared bands provides further confirmation that these are not genuine sources.

When deciding on the categorisation of each source, use was made of the Faint Images of the Radio Sky at Twenty-cm (FIRST) catalogue. This survey had a source detection threshold of around 1 mJy at 1.4 GHz and so is not as deep as the LOFAR survey for typical spectral indices of $\alpha \approx +0.7$ ($S_\nu \propto \nu^{-\alpha}$). Nevertheless, the position of the objects in the FIRST catalogue provided a useful check on the location of the brighter LOFAR sources and can also be useful to highlight any flatter spectrum components which may indicate the radio core. FIRST galaxies are present in four of the images in Figure 3.6 – image (b), image (d), image(e) and image(g) – where they are marked by red crosses.

3.6.2 A Visual Examination of the LOFAR Sources unsuitable for Likelihood Ratio Analysis

The broad principles followed when matching those LOFAR sources that were considered unsuitable for likelihood ratio analysis with their host galaxies are described in this section.

The main issue with sources whose emission is extended is uncertainty over the exact position of the centre. Such sources typically comprise more than one Gaussian and the averaging process used by PyBDSM to estimate the location of the centre may not necessarily provide the optimum position. Head-and-tail

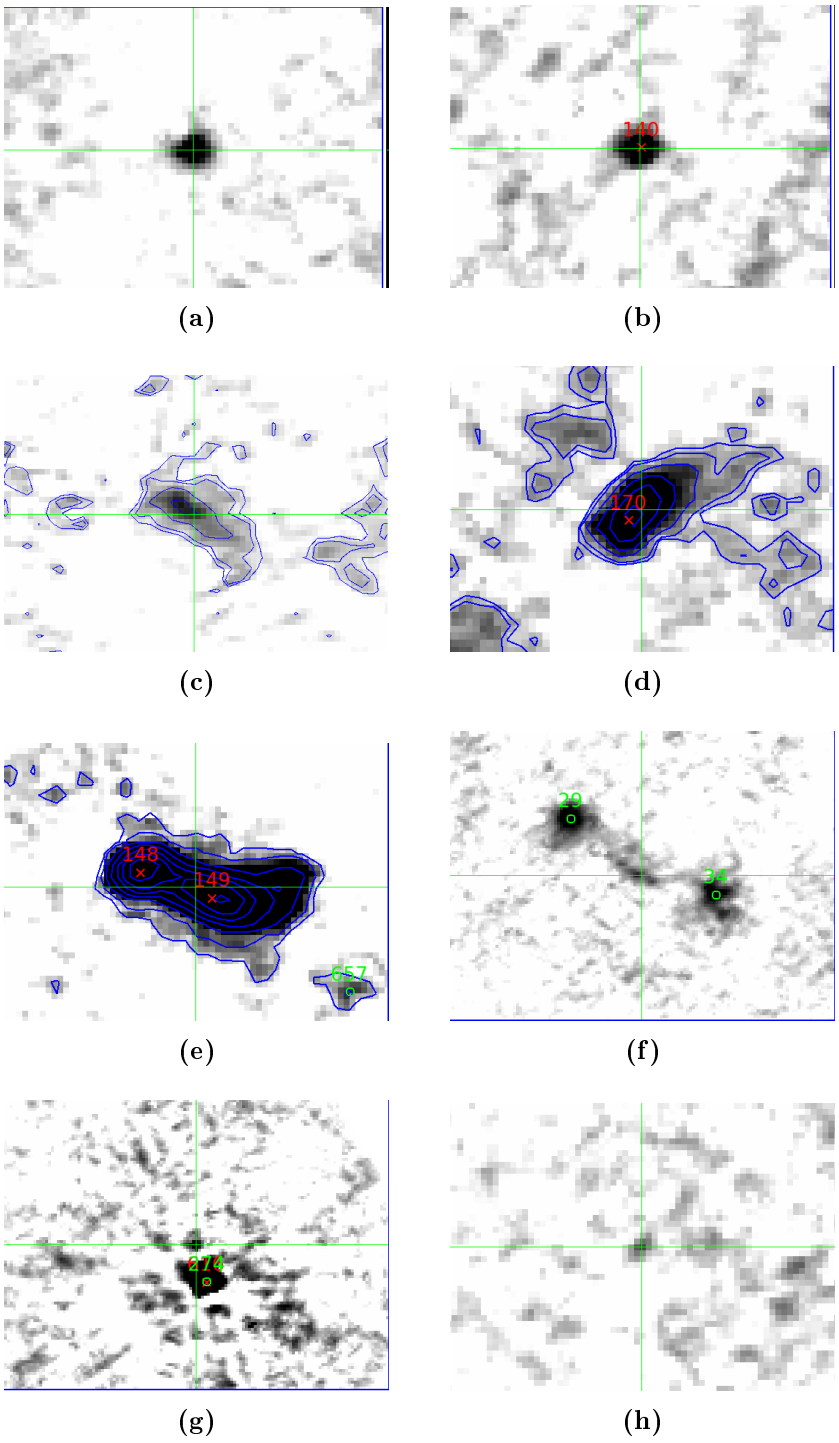

(a) (b) (c) (d) (e) (f) (g) (h)

Figure 3.6 *Images (a) and (b) show LOFAR sources that are suitable for the likelihood ratio analysis. The other six images show sources that were deemed unsuitable, either because the emission is extended (second row), the source is part of a double system (third row) or the "source" may be spurious (bottom row). The images are 100 arcseconds by 75 arcseconds, apart from image (f) which is 200 arcseconds by 150 arcseconds. The crosshair shows the position of the LOFAR source, a red cross shows the position of any FIRST sources in the image and the green circles show the position of any nearby LOFAR sources. Radio flux contours are shown where they are considered to be helpful.*

sources are examples of this: image (d) in Figure 3.6 shows that the centre estimated by PyBDSM (the green crosshair) has been pulled away from the position of the host galaxy which, in this case, is marked by the FIRST source (the red cross). The location of the flux peak is a useful indicator of the position of the host galaxy for head-and-tail sources. A second type of extended emission is from "compact doubles", where the lobes are identified by two of the Gaussians that comprise the source. In these cases, the host galaxy is likely to be in a line (approximately) between the two peaks, with the position based on the ratio of the fluxes. In image (e) in Figure 3.6, the two lobes happen to be shown by two FIRST sources (148 and 149). The host galaxy does indeed lie between these Gaussian peaks, but closer to FIRST 148 than the centre of the flux found by PyBDSM (shown by the green crosshair) which has been influenced by the extended emission to the "west" of the system.

Likelihood ratio techniques have been adapted for such compact double sources (for example, Best et al., 2003) by using a flux-weighted mean position and allowing for larger positional errors. This approach may be suitable for large LOFAR surveys (see Chapter 4), but the relatively small number of sources in this field makes visual analysis a practical alternative.

For the vast majority of the extended sources, the host galaxy could be identified straightforwardly. In a small number of cases, two possible candidates were identified. In these cases, the position of the centre of the radio emission was adjusted by visually identifying a core component from either the LOFAR or FIRST data and the likelihood ratio analysis was then allowed to make the final selection. Finally, there were eight LOFAR sources where no counterpart could be satisfactorily identified, sometimes because there was no suitable match and other times because it was impossible to distinguish between multiple candidates.

The approach was similar for the double sources. Estimating the position of the host galaxy was complicated for the largest of these by the extensive distances between the lobes, but the knowledge that the host galaxy is likely to be massive and red in colour helped the matching decision.

There were nine cases where PyBDSM had combined more than one Gaussian into a single source, but where a visual inspection suggested that there were, in fact, two distinct radio sources with matching host galaxies. These were separated into two entries in the final catalogue, with the flux allocated appropriately between the two new sources.

3.6.3 The Likelihood Ratio Analysis

A likelihood ratio test was now applied to the 1117 LOFAR sources deemed suitable to be passed through this analysis in order to determine the groupings that are their likely counterparts. The traditional approach is that the likelihood ratio (LR) is given by the expression:

$$LR = \frac{f(r, \sigma) \times q(m)}{n(m)}, \tag{3.2}$$

where f(r, σ) is the radial probability distribution of the offsets, r, between the LOFAR and counterpart sources and σ is the uncertainty in the measurement of the offset; n(m) is the sky surface density of the full counterpart population as a function of magnitude, m; and q(m) is the expected distribution of the true counterparts as a function of m. Note that it is possible to incorporate n(m) and q(m) into the likelihood ratio analysis either as density functions or as cumulative distribution functions. In this work, the latter were chosen since a cumulative magnitude distribution is better behaved at faint magnitudes and can be more convenient in its treatment of non-detections as limits. Also, use of a cumulative distribution reduces the problem of small sample sizes within bins. Hereafter, these functions are written as n(<m) and q($< m$).

The probability that a counterpart is a genuine match is, therefore, determined by the separation between the two objects in units of the standard deviation on the offset, modified by a factor that depends on the magnitude of the counterpart. This is the method outlined by, for example, Sutherland & Saunders (1992), Ciliegi et al (2003), McAlpine et al (2012) and Fleuren et al (2012).

The methodology was, however, refined in this research for two reasons. Firstly, colour as well as magnitude was used to provide a better guide to whether or not a galaxy is a true counterpart of a radio source. Hence, equation (3.2) is modified to:

$$LR = \frac{f(r, \sigma) \times q(< m, c)}{n(< m, c)}, \tag{3.3}$$

where c is colour, and q(<m,c) and n(<m,c) give the cumulative magnitude distributions within colour bins of the counterparts. Secondly, radio sources tend to reside in relatively dense areas of the sky and this needs to be carefully incorporated into the estimation of q(<m,c) to avoid distortions to the results. In order to allow for both of these factors a three-stage process was developed.

A high-level description is given below, with the detail provided in the following sections.

The LOFAR sources are first subjected to a likelihood ratio analysis with the modifying factor based on magnitude alone. This analysis was designed to make allowance for the clustering of galaxies around radio sources during the estimation of q(<m).

The results of this first run are used to calibrate a second likelihood ratio test in which the modifying factor is now based on colour as well as magnitude. The matches to the LOFAR sources and the overall population of galaxies are each divided into colour categories, which fix the prior distribution within the analysis.

A third likelihood ratio test, again with the modifying factor based on both colour and magnitude, is applied to obtain the final matches (subject to visual checking for matches with a low likelihood ratio).

The three-stage likelihood ratio analysis might appear cumbersome, but is necessary in order to take appropriate account of clustering. Visual investigation of the results suggests that this approach does improve significantly the accuracy of the matching process.

A more detailed description of how the methodology is implemented is as follows, with a full explanation of the key parts of the process given in the remainder of this section:

- All counterpart groupings within 10 arcseconds of each radio source are identified; the probability of a valid counterpart beyond that search radius is negligible.
- The function f(r, $\boldsymbol{\sigma}$) is calculated for each of these potential counterparts; the details of the calculation are explained in the following subsection.
- Each counterpart grouping is now passed through the first run of the likelihood ratio analysis. The functions n(<m) and q(<m) are calculated separately for each of the i, g, K and 3.6 micron wavebands at which that galaxy has been detected; a detailed description of the calculation is provided later in this section.
- For each counterpart grouping, a likelihood ratio is calculated for each detected waveband.

- An overall likelihood ratio is then assigned to each grouping based on the highest individual likelihood ratio from each of its detected wavebands.
- The source with the highest likelihood ratio is considered a provisional match to the radio source, provided that the ratio exceeds a threshold value.
- The six counterparts with the highest likelihood ratios are now carried forward to the analysis that incorporates colour information.
- The functions n(<m,c) and q(<m,c) are calculated for each colour bin; the latter function is determined from the provisional matches defined in the first run of the likelihood ratio analysis.
- The likelihood analysis is rerun using both magnitude and colour, and each potential counterpart grouping can then be assigned a single likelihood ratio according to its colour and magnitude; the rules for determining how the colour and magnitude are defined are described below.
- The function q(<m,c) is recalibrated based on the matches from the second likelihood ratio analysis.
- A new likelihood ratio is then calculated for each counterpart grouping based on the refined q(<m,c) functions.
- The galaxy with the highest likelihood ratio, again provided that the value exceeds a threshold value, is regarded as the genuine counterpart to the radio source subject to a final visual check.
- The final visual check is carried out for those matches with likelihood ratios either below or just above the threshold value, and also for those cases where the two likeliest counterparts emerge from the analysis with similar likelihood ratios.

The process is now described in greater detail.

The Determination of f(r, σ)

f(r, σ) is the probability that a counterpart at a separation of r arcseconds in a particular direction is a genuine match. The function depends on the separation between the LOFAR source and its possible counterpart and the uncertainty in the measurement of the separation, designated as σ. In its turn, σ depends on:

(i) the uncertainty in the position of the LOFAR source resulting mainly from errors in the estimation of the source size along its major and minor axes

(ii) the orientation of the major axis in relation to the direction between the LOFAR and counterpart sources

(iii) the uncertainty in the location of the counterpart object; this tends to contribute little to the overall value of σ

(iv) the uncertainty because of discrepancies between the astrometry of the LOFAR facet and the astrometry of the counterpart survey.

In the discussion that follows, the first three items are combined into the value σ_1 and the fourth item is designated as σ_2.

The methodology and assumptions described in Condon (1997), summarised below, are used to calculate σ_1. Define

- E_{maj} = 1σ error on the FWHM of the major axis of the LOFAR source
- E_{min} = 1σ error on the FWHM of the minor axis of the LOFAR source
- δx_0 = uncertainty in the position of the LOFAR source along its major axis
- δy_0 = uncertainty in the position of the LOFAR source along its minor axis
- θ = angle of orientation between the major axis of the LOFAR source and its putative counterpart (measured anticlockwise from the vector joining the radio source and the counterpart)
- δx_1 = uncertainty in the RA position of the counterpart source
- δy_1 = uncertainty in the Dec position of the counterpart source
- ϕ = angle between the vector joining the radio source and the putative counterpart and RA
- Err_{LOFAR} = uncertainty in the position of the LOFAR source projected along the vector joining the radio and counterpart sources
- $Err_{counterpart}$ = uncertainty in the position of the counterpart source along the same direction.

It is first assumed that:

$$\delta x_0 = \frac{1}{8\ ln(2)}\ E_{maj} \tag{3.4}$$

and

$$\delta y_0 = \frac{1}{8\ ln(2)}\ E_{min} \tag{3.5}$$

The $8\,ln(2)$ factor is simply a conversion from FWHM to standard deviation. These expressions, as discussed by Condon (1997), are true only in the limit of a high signal to noise ratio and with uncorrelated noise. Neither of these apply here and so both δx_0 and δy_0 need to be increased by an adjustment factor. A factor of $\sqrt{2}$ was chosen, similar to the adjustments used when constructing the NRAO VLA Sky Survey and Westerbork Northern Sky Survey catalogues, as described by Condon et al. (1998) and Rengelink et al. (1997) respectively.

It is then straightforward to show that, when measuring the separation between a LOFAR source and its counterpart, the value of σ_1 can be found through the following expressions:

$$Err_{LOFAR} = \sqrt{\delta x_0^2\ cos^2\theta\ +\ \delta y_0^2\ sin^2\theta} \tag{3.6}$$

$$Err_{counterpart} = \sqrt{\delta x_1^2\ cos^2\phi\ +\ \delta y_1^2\ sin^2\phi} \tag{3.7}$$

and, therefore, that the overall error on the separation, σ_1, is:

$$\sigma_1 = \sqrt{Err_{LOFAR}^2\ +\ Err_{counterpart}^2} \tag{3.8}$$

The difficulty is in estimating the last component of σ, designated as σ_2. To overcome this problem, the following method was used.

First, the LOFAR sources were restricted to those 1117 that were regarded as single, isolated and without extended emission. The separation between each LOFAR source and its most likely i-band neighbour was measured. The separations were placed into bins of width 0.25 arcseconds; the subsequent analysis was repeated using bins of different width and it was confirmed that the final results were robust against a change in bin size.

Second, for each LOFAR galaxy the uncertainty in the measurement of the separation, σ_1, was calculated by the method described above.

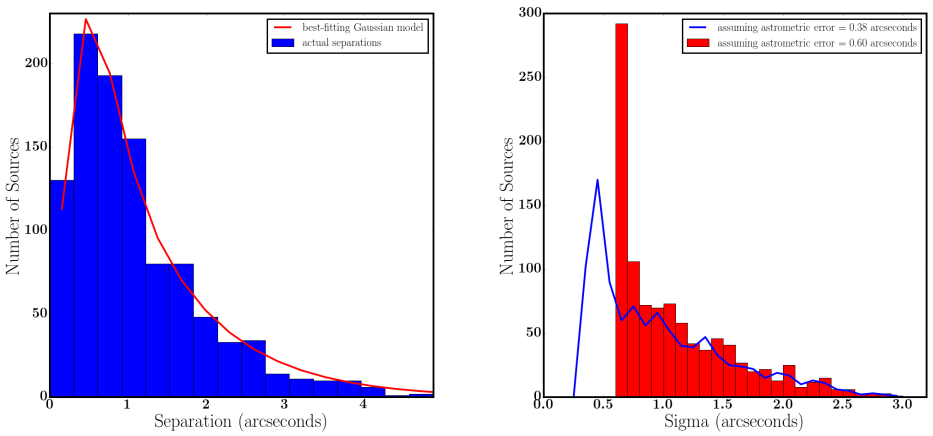

(a) **(b)**

Figure 3.7 *(a) The blue histogram shows the distribution of the offsets between the LOFAR galaxies and their nearest i-band counterparts. The red line shows the best-fitting Gaussian distribution, which has a value of σ_2 = 0.38 arcseconds — see text. (b) Shown is the distribution of uncertainties in the separation between each LOFAR source and its nearest i-band neighbour after assuming values of σ_2 of 0.38 arcseconds (blue line) and 0.6 arcseconds (red histogram).*

Third, σ_1 needs to be added in quadrature to the uncertainty caused by the errors in the astrometry between the LOFAR facets and the PanSTARRS i-band survey. It is this latter item, σ_2, that needs to be determined. In order to do so, it was assumed that the distribution of separations can be modelled by a Gaussian distribution. For each LOFAR source, therefore, there is a unique expected Gaussian distribution based on its particular value of σ_1 combined in quadrature with the global value of σ_2. Each of the 1117 Gaussian distributions was converted into a histogram with bins of width 0.25 arcseconds (after allowing for the different areas in the annuli represented by each bin). The values could then be summed across each LOFAR source to permit a comparison with the histogram of actual offsets.

Fourth, a minimisation procedure was used to find the value of σ_2 that produces the best-fitting match between the two distributions.

A value of $\sigma_2 = 0.38$ arcseconds provided the best-fit. The left-hand plot in Figure 3.7 shows the actual distribution of offsets (blue histogram) and the modelled distribution (red line).

However, there are several objections to this approach. Each facet has its own astrometric error and so there is an implicit assumption that it is possible to sum each facet's Gaussian distribution to create a Gaussian that can be used across the whole survey area; that is theoretically incorrect. A value of $\sigma_2 = 0.38$ arcseconds appears low when compared with the 1σ uncertainties for the facet-by-facet coordinate adjustments (shown in Table 3.5). There is also a practical problem that when a value of $\sigma_2 = 0.38$ arcseconds was incorporated into the likelihood ratio process, there were a number of LOFAR sources, particularly those with very low positional errors output from PyBDSM, where apparently valid matches were rejected because the analysis appeared to unduly favour proximity. It was, therefore, decided to increase the value of σ_2. Trial values of 0.5, 0.6, 0.8 and 1.0 were incorporated into the likelihood ratio analysis and a visual examination of those LOFAR sources where the counterpart changed suggested that $\sigma_2 = 0.6$ is an appropriate choice. The consequent distribution of uncertainties in the offsets between the LOFAR galaxies and their nearest i-band neighbours is shown in the right-hand chart in Figure 3.7. The fact that almost 300 sources are placed in the lowest bin – that is, having a value of σ of just over 0.6 and hence having an extremely low value of σ_1 – highlights the need to impose a value of $\sigma_2 = 0.6$.

The Determination of n(<m) and q(<m)

The functions n(<m) and q(<m) were derived for each of the i, g, K and 3.6 micron wavebands.

The n(<m) term, the cumulative magnitude distribution of the population per square arcsecond, was obtained by binning and counting sources within a rectangle defined by the four coordinates (RA, Dec) = (241.5, 53.8), (241.5, 56.3), (244.0, 53.8) and (244.0, 56.3). The known area of the rectangle allows an accurate normalisation. The rest of the analysis is based on the full area under investigation.

The q(<m) term is the cumulative magnitude distribution of the genuine counterparts to the LOFAR sources. Note that q(<m) is a probability and would scale to unity if the match to every radio source were contained in the counterpart catalogues. q(<m) was estimated using the method described by Ciliegi et al. (2003). First, the cumulative magnitude distribution was obtained of all possible counterpart sources within 5 arcseconds of each LOFAR source, whether or

not they are thought to be genuine matches. The distribution, designated as total(<m), was smoothed using a polynomial of order seven; if necessary, the two tails were adjusted to ensure that the endpoints of the distribution ran smoothly into 0 and 1. The background count as a function of magnitude was estimated by applying n(<m) to an area of a circle of radius 5 arcseconds and then deducting it from the smoothed distribution. Finally, the resulting function needs to be normalised and multiplied by Q_0, an estimate of the fraction of LOFAR sources that have a genuine counterpart within the counterpart catalogue. Hence, using the nomenclature of Ciliegi et al. (2003),

$$real(< m) = total(< m) \; - \; n(< m) \; \times \; N_{radio\,sources} \; \times \; \pi \; \times \; radius^2 \qquad (3.9)$$

and

$$q(< m) = \frac{real(< m)}{real(< \infty)} \; \times \; Q_0 \qquad (3.10)$$

where the summation gives the total number of objects in the real(<m) distribution.

There are different methods of calculating Q_0 described in the literature. The method used here is that described by Fleuren et al. (2012). The key point is that this method is designed to estimate $1 - Q_0$ rather than Q_0 itself, which has the advantage of minimising the risk of overestimating Q_0 because of clustering around the radio sources. The method is as follows:

- A search radius, r, was chosen.
- The proportion of LOFAR sources that do not have a counterpart within the specified search radius was found using a simple positional crossmatch.
- A randomised catalogue of 1117 (that is, equal to the number of LOFAR sources) pseudo radio sources within the survey area was created.
- A positional crossmatch identified the number of pseudo radio sources from the randomised catalogue that do not have a match.
- Q_0 for the specified search radius can then be estimated from

$$Q_0\, F(r) = 1 - \frac{number\ of\ observed\ blanks}{number\ of\ blanks\ at\ randomised\ positions}. \qquad (3.11)$$

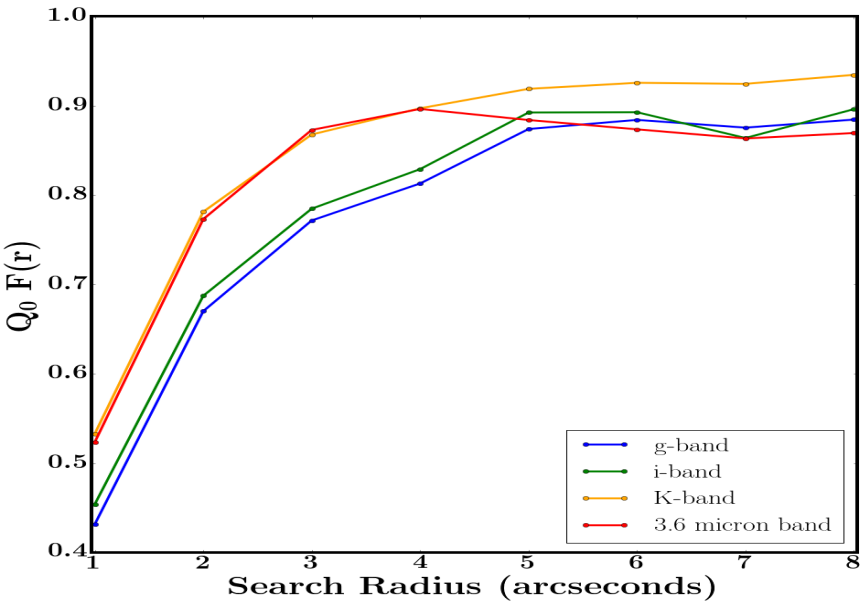

Figure 3.8 *The values of Q_0 derived at different search radii for the four counterpart catalogues.*

where $F(r) = 1 - e^{-\frac{r^2}{2\sigma^2}}$. The derivation is provided by Fleuren et al. (2012).

- The procedure was repeated at different search radii from 1 arcsecond up to 10 arcseconds. Above a search radius of 5 arcseconds, the values of F(r) approach one and stable values of Q_0 are found, as illustrated in Figure 3.8.

- The value of Q_0 was chosen to be the mean of the results at search radii 5, 6, 7 and 8 arcseconds.

Values of Q_0 of 0.89, 0.89, 0.93 and 0.87 were calculated for the g, i, K and 3.6 micron bands respectively.

The distributions of n(<m) and q(<m) for the i-band are shown in Figure 3.9 for illustration. As can be seen, the magnitude distribution of the host galaxies, as measured by q(<m), differs considerably from that of the overall population, n($< m$).

Two final adjustments were required. Firstly, the ratio of q(<m) / n(<m) was constrained to ensure that it progressed smoothly; that might not be the case at the extremities of the distribution where small numbers might make the progression in this ratio volatile. Secondly, the likelihood ratios were

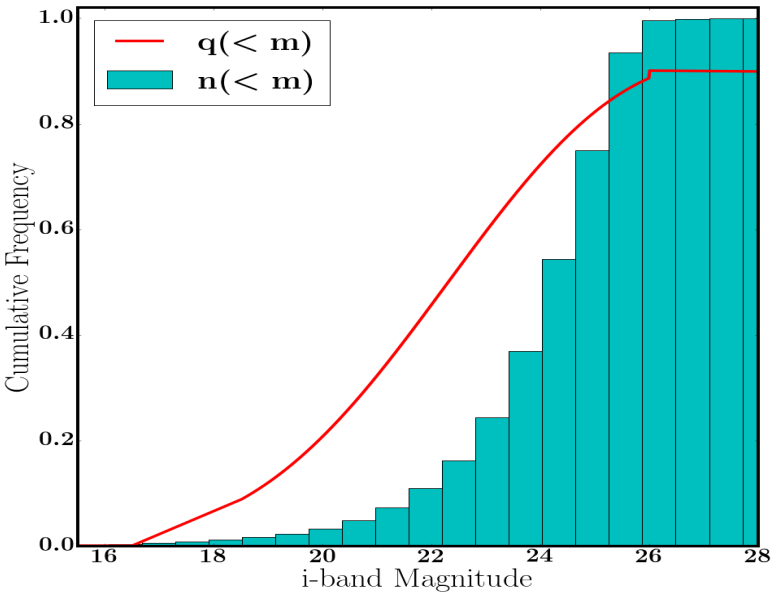

Figure 3.9 *The cumulative magnitude distributions of the n(<m) and q(<m) functions for the i-band demonstrate that there is a clear distinction between the distribution for the host galaxies (red line) and that of the overall population of galaxies (cyan histogram).*

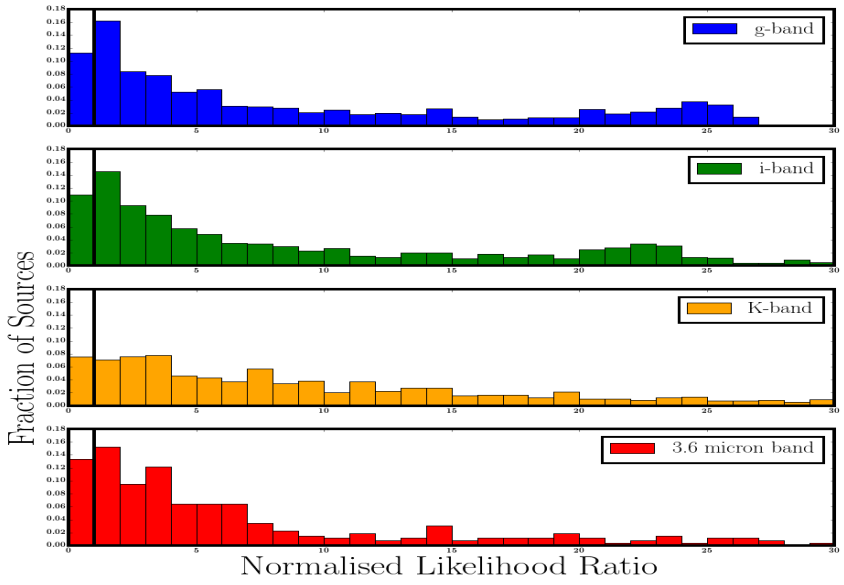

Figure 3.10 *The distribution of the normalised likelihood ratios for each waveband; genuine matches are deemed to be those with a likelihood ratio above the threshold (to the right of the vertical line).*

normalised to allow a like-for-like comparison between different wavebands. The normalisation was carried out by dividing the raw likelihood ratios by the value at the $(1 - Q_0)$th percentile; these values, which were 16.1, 12.6, 2.9 and 26.8 for the g-band, i-band , K-band and 3.6 micron band respectively, define the likelihood ratio where completeness and reliability align. Consequently, a normalised likelihood ratio of 1.0 acted as the threshold for deciding whether a genuine match had been found; that is, a match is deemed to be correct if the normalised likelihood ratio is over 1.0. The distributions of the normalised likelihood ratios for each of the four wavebands are shown in Figure 3.10; as can be seen, the distributions are broadly similar apart from a broadening in the K-band because of its higher value of Q_0. There are arguments both for and against normalising the likelihood ratios in the way described, but it is noted that this should make no difference to the final set of matches: the first run of the likelihood ratio analysis generates a set of provisional matches and a full completeness and reliability analysis is carried out at the end of the matching process to determine which of the final matches are genuine.

Having created the infrastructure, it was now possible to perform the first run of the likelihood ratio analysis. For each LOFAR source, all groupings within 10 arcseconds were found. A likelihood ratio was assigned to each grouping, based on the highest normalised likelihood ratio out of the components of the grouping; that is, if a grouping has detections in each of g, i, K and 3.6 micron bands, then the highest of the four resulting likelihood ratios is adopted. The grouping with the highest likelihood ratio was provisionally accepted as a match, provided that the likelihood ratio exceeded the threshold of 1.0.

Incorporating Colour into the Likelihood Ratio Analysis

Having obtained a set of provisional matches to the LOFAR sources, it is now practical to incorporate colour into the analysis. To do this, it is necessary to estimate a value of $Q_0(c)$ and distributions of q(<m,c) and n(<m,c) for different colour bins. Here it is important to note that the technique developed by Fleuren et al. (2012) to determine Q_0, and adopted in 3.6.3, would not work when considering different colour bins. This is because a radio source match in one colour bin may have companion galaxies in other colour bins, which would bias the determination of the number of blank fields in those other colours and hence bias the calculation of their values of $Q_0(c)$. The potential overestimation of $Q_0(c)$

is significant – it was calculated to be of the order of 40% for the cross-matches presented here. The first-pass analysis described in the previous section bypasses, or at least minimises, this problem by providing a set of provisional matches from which q(<m,c) and $Q_0(c)$ could be directly extracted, and which are an unbiased starting point towards an iterative solution.

The modifying factor will, therefore, now be based on colour as well as magnitude and the LOFAR sources and groupings need to be binned according to colour. The upper chart in Figure 3.11 shows that the galaxies that match LOFAR sources tend to be redder than the population as a whole. This is shown more clearly in the lower chart. The proportion of matched galaxies in relation to the overall population increases by a factor of almost 10 between an $i - K$ colour of 3.0 and 4.5, suggesting that this particular colour has considerable discriminatory power. Note that the matches in both sub-figures are taken to be those at the end of the likelihood ratio process. As is suggested by the upper chart in Figure 3.11 and will be more obvious shortly, the $g - i$ colour is less effective in deciding whether a galaxy is a genuine match to a LOFAR source.

The division into colour bins was effected in the following way. All groupings where the g, i and K magnitudes had been measured, or could be estimated through interpolation, were combined; these groupings were giKs, giK_, gi_s, g_Ks, g_K_ and g__s. Three other categories, _iKs, _iK_ and _i_s, were also added in, with the g-magnitude being taken as an upper limit of 25.4. The limit was chosen as the point at which the distribution of g-magnitudes in the PanSTARRS catalogue turns over and so indicates the point at which detections start to be significantly limited by the depth of the survey. Note that the $g - i$ colour is only broadly used and so the analysis is largely unaffected by the precise value chosen. The groupings in these nine categories were then placed into ten $i - K$ bins that were further sub-divided into two according to the $g - i$ colour. The $g - i$ division point was chosen to divide the population of galaxies into approximately equal halves. This meant that the division point varied as a function of $i - K$, increasing from 1.039 at the bluest $i - K$ bin to 1.632 at the reddest bin (see Table 3.8).

From Figure 3.11, the ratio of matches to the total population varies by less than 50% for values of $i - K$ over 4.0. The analysis is, therefore, broadly insensitive into which colour bin K-only sources are placed. For K-only sources, an $i - K$ colour was adopted corresponding to i = 25.0 (the PanSTARRS limit), but, after noting that a few very faint K-only sources were placed at the blue end with this

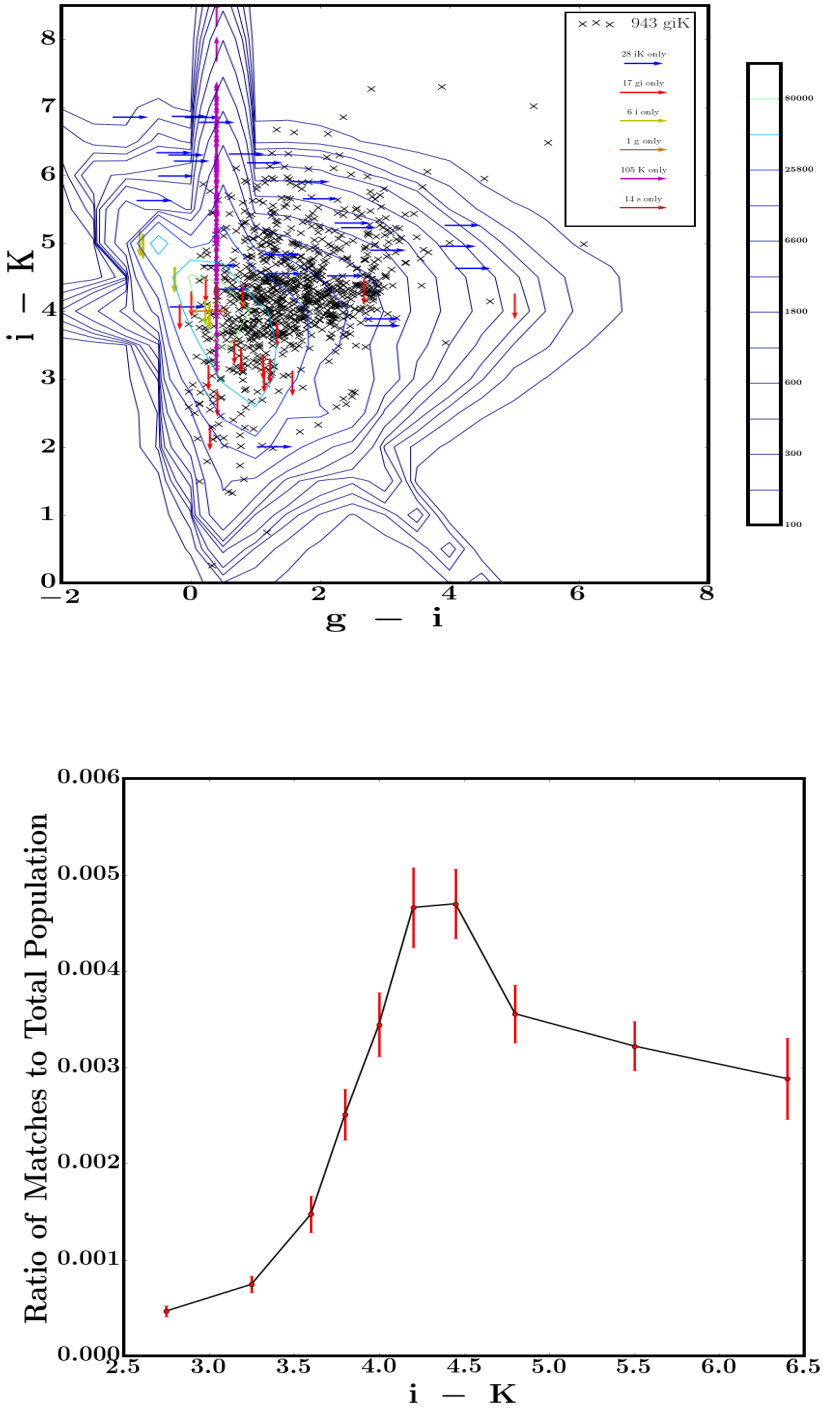

Figure 3.11 *Upper Figure: Those galaxies that are matched with a radio source are plotted on a colour-colour diagram. The contours show the distribution of all galaxies in the survey area. If there is no detection in one of the bands, then the magnitude is estimated by interpolation or by using the limits of 25.4, 25.0 and 21.0 for g, i and K bands respectively. Lower Figure: The proportion of matched galaxies to the overall population is shown in $i - K$ bins.*

assumption, a limit of $i - K$ >4.0 was also imposed. Consequently, the K-only and Ks groupings were divided into six $i - K$ colour bins – the same as those described in the previous paragraph, but excluding the four bluest bins. The K-only and Ks-only groupings were not subdivided by $g-i$ colour given the absence of detections in these bands.

The remaining four categories could not be split by $i - K$ colour because of the absence of K-detections. The i-only and gi_ _ groupings were combined into one category, with the final two categories comprising the g-only and s-only groupings.

That meant that a total of 29 colour categories were used. The numbers of groupings in each colour bin are shown in Table 3.8. A $Q_0(c)$ factor was determined for each colour category by calculating the ratio of the number of provisionally matched galaxies in that category (that is, including only those matches that surpassed the likelihood ratio threshold) by the total number of radio sources being matched. Hence, $\sum_c Q_0(c) = Q_0$. 90% of galaxies passed the threshold, consistent with the Q_0 factors for each waveband. The benefit of removing spurious K-band sources from the sample earlier in the process can now be seen; otherwise, the n(<m,c) values for the K-only categories risked being erroneously increased by an artificially inflated population size, which would suppress their likelihood ratios and also distort the fractions in the lower chart of Figure 3.11. In order to ensure that there was a measurable probability of a match in each category, a minimum value of 0.001 was imposed. Having calculated the $Q_0(c)$ factors, the n(<m,c) and q(<m,c) distributions were also computed for all 29 colour categories. The magnitudes were defined as those for the i-band, where available; otherwise, the K-band magnitudes were used for the K-only and Ks-only categories, the g-band magnitude used for the g-only category and the 3.6 micron magnitude for the s-only category. A single likelihood ratio could now be calculated for each possible counterpart galaxy based on its separation, its colour and its magnitude. A revised set of matches was thus generated.

In 77 cases (7%), the match from the second likelihood ratio run differed from that found in the first run. The matches should now be more accurate than those produced in the initial run and, in theory, a revised, lower likelihood ratio threshold could now be justified. However, from a practical standpoint it was simpler to continue to accept 90% of the matches and to allow a full completeness and reliability analysis, described below, to determine the likelihood threshold at the end of the process. Refined $Q_0(c)$ factors were now recalculated using the new set of matched galaxies and the likelihood ratio analysis was repeated. On

this occasion, 14 sources found a different match. Convergence had now been achieved: a further recalculation of the $Q_0(c)$ factors and a fourth likelihood ratio run produced no further changes in the set of matched galaxies.

The $Q_0(c)$ factors after the second run, together with the exact colour divisions, are set out in Table 3.9. It can be seen that there is a strong progression in the

Table 3.8 *Total number of groupings by colour category*

Category	i - K	g - i	All giK categories		K, Ks only
		Midpoint	Blue Half	Red Half	
1	< 3.0	1.04	76261	77489	0
2	3.0 - 3.5	1.08	50322	51137	0
3	3.5 - 3.7	1.19	19615	19614	0
4	3.7 - 3.9	1.32	17495	17222	0
5	3.9 - 4.1	1.44	14253	13714	6433
6	4.1 - 4.3	1.53	11787	11232	4020
7	4.3 - 4.6	1.58	14282	13186	7872
8	4.6 - 5.0	1.65	14296	12315	11930
9	5.0 - 6.0	1.80	17249	11654	21439
10	> 6.0	1.63	3147	1392	11464
gi, i only			854787		
g only			49595		
s only			57836		

Table 3.9 $Q_0(c)$ *factors by colour category*

Category	i - K	g - i	All giK categories		K, Ks only
		Midpoint	Blue Half	Red Half	
1	< 3.0	1.04	0.031	0.002	
2	3.0 - 3.5	1.08	0.027	0.017	
3	3.5 - 3.7	1.19	0.023	0.025	
4	3.7 - 3.9	1.32	0.044	0.035	
5	3.9 - 4.1	1.44	0.039	0.058	0.004
6	4.1 - 4.3	1.53	0.051	0.057	0.001
7	4.3 - 4.6	1.58	0.072	0.075	0.003
8	4.6 - 5.0	1.65	0.052	0.057	0.012
9	5.0 - 6.0	1.80	0.073	0.054	0.030
10	> 6.0	1.63	0.014	0.011	0.019
gi, i only			0.001		
g only			0.001		
s only			0.012		

factors moving from the blue i-K bins to the red i-K bins, as was shown in Figure 3.11; for direct comparison those numbers should strictly be moderated by the number of sources in each i - K colour bin (Table 3.8). By contrast, there is no apparent pattern comparing the $Q_0(c)$ factors across the red and blue g-i bins; note that since the sample was divided in half in the parent population, these numbers are directly comparable.

3.7 Analysing the Results

Having found the likelihood ratios for potential matches for all of the radio sources, it was now necessary to decide which of these matches could be trusted. The first step is to carry out a completeness and reliability analysis in order to determine the likelihood ratio threshold above which a match could be considered to be genuine. Completeness and reliability functions were both calculated as a function of the likelihood ratio threshold, T, according to the following formulae that are described in Best et al. (2003):

$$Completeness(T) = 1 - \frac{1}{Q_0\,N} \sum_{LR_i < T} \frac{Q_0 \times LR_i}{Q_0 \times LR_i + (1 - Q_0)} \tag{3.12}$$

$$Reliability(T) = 1 - \frac{1}{Q_0\,N} \sum_{LR_i > T} \frac{1 - Q_0}{Q_0 \times LR_i + (1 - Q_0)} \tag{3.13}$$

where the summation is for all matches below the likelihood ratio threshold under consideration in equation 3.12 and for all matches above the threshold in equation 3.13, N is the total number of radio sources and Q_0 has been set at 0.93. This value for Q_0 was chosen initially after a visual examination of all low-likelihood matches, but was later confirmed to be reasonable by the analysis that follows. The results of the completeness and reliability analysis are shown in the upper chart of Figure 3.12.

An alternative method of determining an appropriate choice of likelihood ratio threshold is to consider the probability that the incremental matches that would be accepted as the threshold is progressively lowered are, in fact, genuine. This probability, again as a function of the likelihood ratio threshold, can be estimated using the following derivation:

$$Number\ of\ genuine\ matches\ using\ threshold\ T_1 = N\ Q_0\ C(T_1) \quad (3.14)$$
$$Number\ of\ genuine\ matches\ using\ threshold\ T_2 = N\ Q_0\ C(T_2) \quad (3.15)$$
$$Total\ number\ of\ matches\ using\ threshold\ T_1 = N\ Q_0\ \frac{C(T_1)}{R(T_1)} \quad (3.16)$$
$$Total\ number\ of\ matches\ using\ threshold\ T_2 = N\ Q_0\ \frac{C(T_2)}{R(T_2)} \quad (3.17)$$

So, if the threshold is lowered from T_1 to T_2, then

$$Number\ of\ genuine\ additional\ matches = N\ Q_0\ (C(T_1)\ -\ C(T_2)) \quad (3.18)$$
$$Number\ of\ additional\ matches = N\ Q_0\ (\frac{C(T_1)}{R(T_1)}\ -\ \frac{C(T_2)}{R(T_2)}) \quad (3.19)$$
$$Probability\ that\ additional\ matches\ are\ genuine = \frac{C(T_1)\ -\ C(T_2)}{\frac{C(T_1)}{R(T_1)}\ -\ \frac{C(T_2)}{R(T_2)}} \quad (3.20)$$

The probability, as a function of the likelihood ratio threshold, is plotted in the lower chart in Figure 3.12. Both charts suggest that a threshold around 0.2 is sensible: the completeness and reliability ratios are then 0.992 and 0.985 respectively and the probability that additional sources are genuine at that threshold is 0.75. There are 1046 radio sources with a match above this likelihood ratio threshold, representing 93.6% of the total (and justifying the choice of Q_0 adopted for the completeness and reliability analysis).

The 71 sources that returned a match with a likelihood ratio below the threshold of 0.2 were examined visually and could be categorised as follows:

- In 10 cases, the radio source appeared to be spurious, with the emission due to interference.
- In 16 cases, the radio emission was from the lobe of a larger system.
- In 15 cases, the radio emission was either extended (13 sources) or a compact double (2 sources), causing the PyBDSM software to misplace the centre of the emission. The correct match was still achieved in 10 out of these cases, albeit with a low likelihood; in the other 5 cases, the misplacement resulted in the wrong match being identified.
- In 30 cases, it was not possible to identify securely a genuine counterpart either because there was no obvious candidate or, more rarely, because there was a close choice between two or more low-likelihood matches.

There were 35 matches with a likelihood ratio between 0.2 and 1.0. These were also checked visually. In 26 cases, the correct counterpart had been identified. In

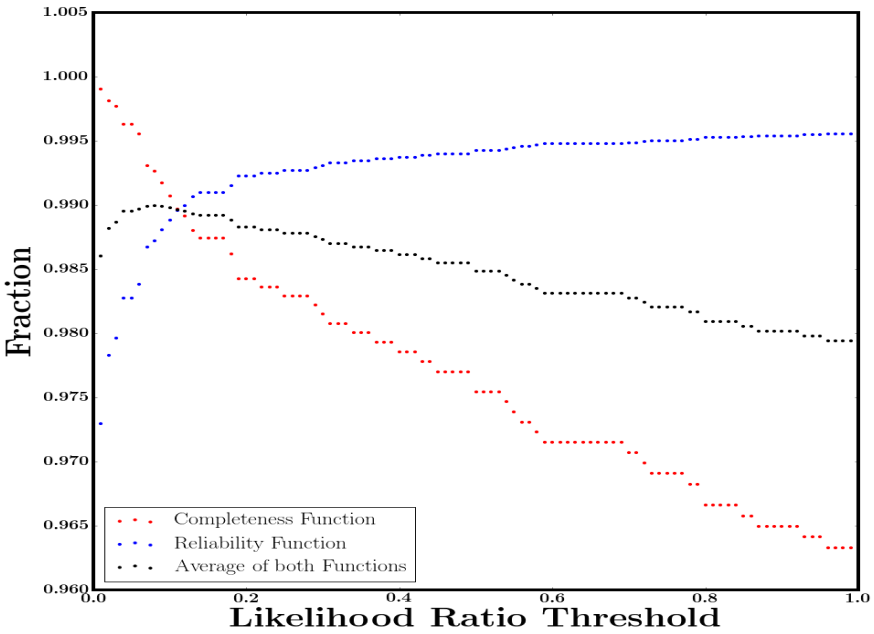

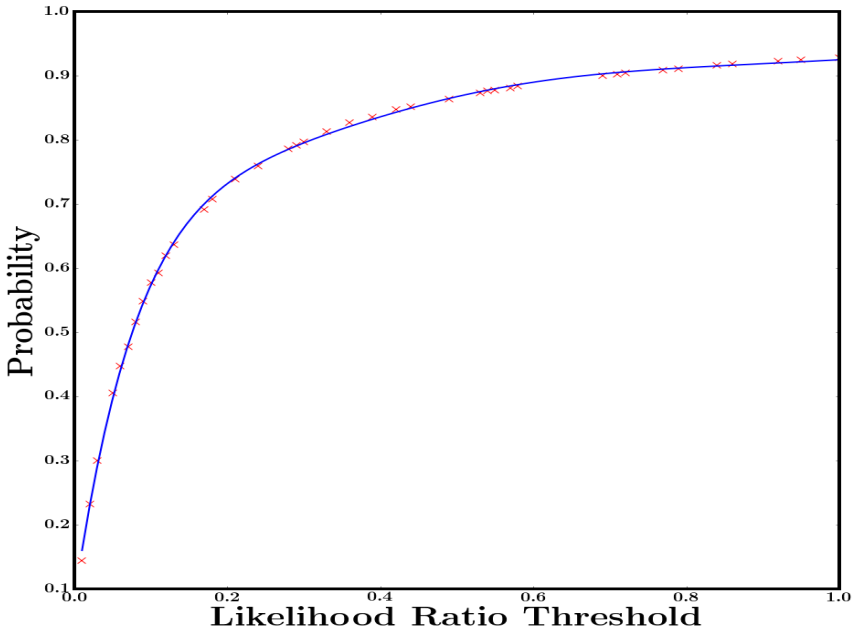

Figure 3.12 *Upper Figure: the completeness and reliability ratios as a function of the likelihood ratio threshold. Lower Figure: the probability that an additional source is genuine as a function of the likelihood ratio threshold.*

6 cases, the emission was from the lobe of a larger system. 2 of the sources were deemed to be spurious, The final source was extended (a head-and-tail system), with the centre of the source wrongly positioned and a false match identified.

Finally, another 74 sources were examined visually where the best two matches had similar likelihood ratios, defined as the highest likelihood ratio being less than four times that of the second likeliest. The likelihood ratio analysis had found the "correct" match in 67 cases; these matches either appeared to be genuine when checked visually or, if it was difficult to choose between two competing candidates, there was no reason to disfavour the match chosen by the likelihood ratio analysis. In 3 cases, the emission was extended and, when that was taken into account, a visual check clearly preferred the matching galaxy with the second highest likelihood ratio. Two of the sources appeared to be spurious, so neither match was correct. In one case, the emission was from the lobe of a double system. In the final case, the likelihood analysis selected the wrong match because the g-band and i-band emission from the genuine counterpart had been omitted from the PanSTARRS catalogues (obscured by a bright nearby foreground galaxy).

The catalogue was amended to incorporate the mis-identifications and re-categorisations discovered by the visual examination. Ideally, these sources would be removed from the likelihood ratio analysis, the values of $Q_0(c)$ recalculated and the likelihood ratio analysis re-run. However, due to the small changes involved, this was not done since it would have no impact on the identifications, only on the quoted $Q_0(c)$ factors. As suggested by Table 3.10 below, Q_0 ($= \sum_c Q_0(c)$) would then equal 0.97.

A valid question is whether the initial examination of the LOFAR sources could have identified that most of the sources discussed above were unsuitable to be passed through the likelihood ratio analysis. With respect to the spurious sources, the approach taken in the initial examination was to reject an object only if it appeared highly probable that it was spurious (rather than to risk discarding genuine objects); a decision to discard a source could be made with much greater confidence if the subsequent analysis failed to identify a plausible host galaxy. As already mentioned, it is often impractical to differentiate a lobe of a double system from a stand-alone radio source in an initial visual examination. In those cases where the radio emission is extended, it was a matter of judgement when to allow a source to proceed through the likelihood ratio analysis. The cross-comparison with the optical data provides additional information that could have helped the initial judgement. Having now constructed a catalogue of matches that is

believed to be highly accurate, it was possible to address this question – how to accurately separate the radio sources into those requiring visual examination and those able to be assessed automatically through the likelihood ratio route – in a more analytic way and this is discussed in the following chapter.

In summary, the visual examination of low-likelihood or similar-likelihood sources makes three points. Firstly, the fractions of genuine counterparts above and below the likelihood ratio threshold of 0.2 are broadly consistent with those expected from the completeness and reliability analysis; this corroborates the choice of threshold. Secondly, the likelihood ratio analysis appears to make sensible choices based on the information input into it, suggesting that both the methodology and the choice of parameters are defensible. Thirdly, the false matches highlight the importance of developing a sensible, systematic procedure to identify as many as possible of the extended, double and spurious radio sources before running the likelihood ratio analysis.

The final radio catalogue with the optical / infrared counterparts is listed and described in Appendix C. A summary of the statistics is shown in Table 3.10; this table was constructed after excluding spurious sources and the 58 lobes of double or triple sources. There are 1221 stand-alone radio sources listed in the catalogue, with a match having being identified for 1180 of them. Of these, 1030 found a host galaxy match through the likelihood ratio analysis alone. The distribution of their likelihood ratios (in log format for clarity) is shown in Figure 3.13. The red vertical line marks the likelihood ratio threshold; identified in the chart – to the left of the line and coloured green – are those ten sources where a visual examination confirmed that the low-likelihood match was indeed correct. The key point from the distribution, however, is that the vast majority of the matches appear secure, with likelihood ratios well above the threshold. As stated above, the proportion of genuine matches found through the likelihood ratio analysis was 94%. Table 3.10 makes the point that the analysis would have correctly identified the host of 97% of the radio sources if the analysis had been conducted on a perfectly cleaned-up catalogue (that is, containing neither spurious sources nor lobes).

Table 3.10 *Statistics of the final catalogue*

Source Type	Classification Method	Number	Number of Optical IDs	ID Fraction
Singles	Likelihood Ratio	1060	1030	97%
Extended Singles	Visual	129	121	94%
Multi-components	Visual	32	29	91%
Total		1221	1180	97%

The statistics are shown after the removal of spurious sources and the lobes of multi-component sources.

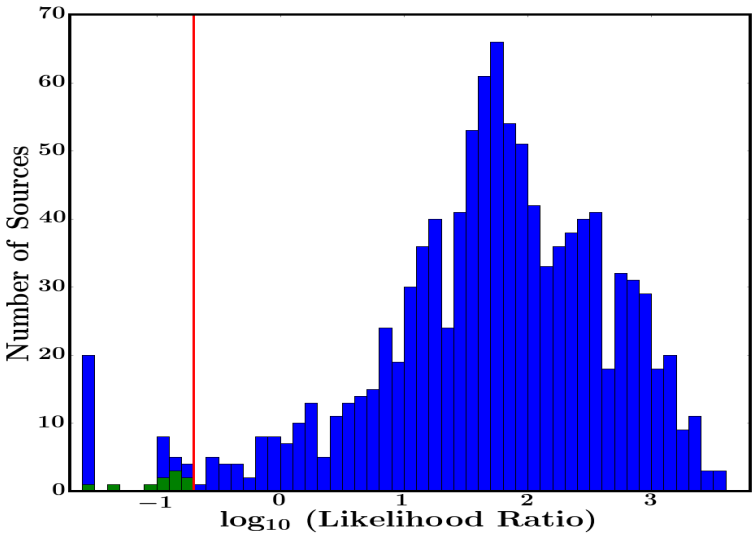

Figure 3.13 *The distribution of log likelihood ratios for the 1070 radio sources matched through the maximum likelihood process. The red line shows the likelihood ratio threshold. All likelihood ratios below 0.03 are grouped into the leftmost bin. The ten sources where a visual examination confirmed that the low-likelihood match was indeed correct are shown in green.*

Chapter 4

The Development of Automated Survey Cross-matching

4.1 Introduction

The likelihood ratio technique described in the previous chapter was developed in order to facilitate the matching of the LOFAR sources within the ELAIS-N1 field with their optical counterparts. It was also developed as part of a collaborative effort which has the aim of standardising and, as much as possible, automating a pipeline from LOFAR image to optical identification of the LOFAR sources. This is in preparation for the large amount of data that is being generated by a wide-area survey currently being undertaken by the LOFAR telescope; the LOFAR Two-metre Sky Survey (LoTSS) is described in Shimwell et al. (2017).

The combination of the likelihood ratio analysis supplemented by extensive visual checking has produced accurate matches for a large sample of radio sources in the ELAIS-N1 field. As demonstrated by the completeness and reliability investigation described in Chapter 3, the number of erroneous matches is believed to be very small. This means that the database is ideal for providing input into several of the decisions required to construct the pipeline. These inputs are described in this chapter.

4.2 The Separation of Radio Sources into those suitable for Likelihood Ratio Analysis

Given the very many sources that will be detected in the wide-area survey, it is important to minimise the number being sent for visual examination. Equally, the analysis described in Chapter 3 highlights the importance of identifying as accurately as possible those radio sources that are not suitable for likelihood ratio analysis. The ELAIS-N1 dataset was used to try to identify the criteria that might be used to separate LOFAR sources into those suitable for likelihood ratio analysis and those that would need to be examined visually.

First, however, some datapoints needed to be removed from the ELAIS-N1 sample. The collaboration has now recommended a standardised set of parameters to be used within the PyBDSM image reduction and hence to which the tuning of automated techniques needs to be applied. The reduction used for the ELAIS-N1 image had been made many months before the standardised set had been prepared and had used a slightly different set of parameters. In a small number of cases, the change in parameters led to either a different source being detected or to a shift in the central position of a radio source which in turn led to a different match being found through the likelihood ratio analysis. Such sources were removed from the analysis that follows (since it is not known which match is correct), leaving 1141 LOFAR sources in the final sample.

The investigation considered separately LOFAR sources that were associated with a single Gaussian from PyBDSM and those that had more than one Gaussian component.

Single-component Sources

There were 892 sources that emanated from single Gaussians. Radio sources suitable for likelihood ratio analysis are likely to be compact and isolated, and so the distance to the nearest neighbouring LOFAR source and the deconvolved size of the LOFAR source are promising parameters to consider. Accordingly, the LOFAR sources were binned by each of these properties. A likelihood ratio analysis was conducted and the fraction of correct matches recorded in each bin. A match was deemed to be correct if it agreed with the galaxy previously identified as the genuine counterpart. In those cases where the original choice was made

through the likelihood ratio analysis, the matches must, by definition, tally; in those cases where the original choice was made through a visual examination, there may or may not be agreement and this is what is being investigated.

The results are illustrated in Figure 4.1. The upper left-hand chart shows the proportion of correct matches as a function of the distance to the nearest neighbour and the upper right-hand chart shows the fraction of correct matches as a function of deconvolved size. In both charts the red line shows the cumulative number of sources at each bin. The lower two charts show the same information, but now the left-hand chart has been produced after restricting the LOFAR sources to those with a deconvolved size of less than 15 arcseconds. In the right-hand chart, the LOFAR sources have been restricted to those more than 50 arcseconds from their nearest neighbour.

The charts suggest that approximately 76% of single-Gaussian LOFAR sources satisfy both criteria (deconvolved size of less than 15 arcseconds and more than 50 arcseconds to the nearest neighbour) and that these can be sent through the likelihood ratio route with a 99.0% probability of selecting a genuine match. Tables 4.1 and 4.2 below illustrate the trade-off between maximising the number of sources sent through the likelihood ratio route and minimising the resulting fraction of incorrect matches. So, for example, selecting LOFAR sources with a deconvolved size of less than 24 arcseconds and a distance to the nearest neighbour of at least 30 arcseconds would allow 90% of sources to be sent through the likelihood ratio route, with a 1.7% probability of erroneous matches.

These tables provide useful input into the decision process of the pipeline.

Multi-component Gaussians

The 249 sources associated with more than one Gaussian were then considered. A likelihood ratio analysis was conducted on both the source itself and also on each of the individual Gaussians, allowing the sources to be divided into two categories according to the results:

- Category 1: The likelihood ratio (LR) of the best match to the overall source position exceeded each of the best-match LRs of the component Gaussians.
- Category 2: The LR of the source was less than the LR of at least one of the component Gaussians.

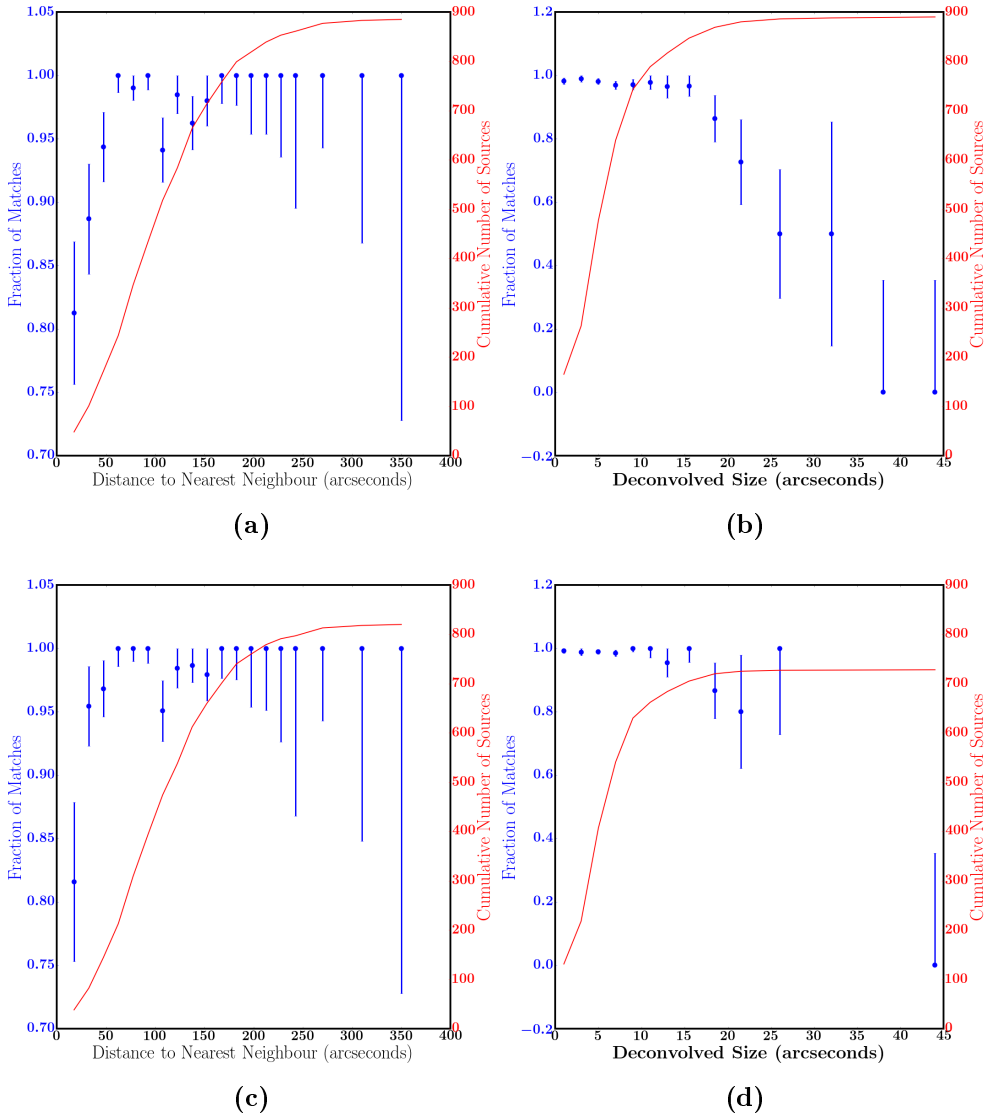

Figure 4.1 *The upper two charts show the fraction of correct matches as a function of the distance from the LOFAR source to its nearest LOFAR neighbour (left-hand chart) and as a function of the deconvolved size of the LOFAR source (right-hand chart). The lower two charts repeat the analyses, but now with the LOFAR sources restricted to those with a deconvolved size of less than 15 arcseconds (left-hand chart) and restricted to those more than 50 arcseconds from their nearest neighbour (right-hand chart). In all four charts, the red line shows the cumulative number of LOFAR sources at each bin, as indicated by the right-hand axis.*

Table 4.1 *The fraction of LOFAR sources split by deconvolved size and distance to nearest neighbour*

Distance to Nearest Neighbour (arcseconds)	Deconvolved Size (arcseconds)									
	<3	<6	<9	<12	<15	<18	<21	<24	<27	<30
>0	0.22	0.53	0.79	0.88	0.91	0.95	0.96	0.97	0.98	0.98
>10	0.21	0.53	0.79	0.87	0.91	0.95	0.96	0.97	0.98	0.98
>20	0.21	0.52	0.77	0.86	0.89	0.93	0.94	0.95	0.96	0.96
>30	0.20	0.50	0.74	0.82	0.85	0.88	0.89	0.90	0.90	0.90
>40	0.19	0.48	0.72	0.79	0.82	0.86	0.86	0.87	0.87	0.87
>50	0.17	0.45	0.67	0.74	0.76	0.79	0.80	0.80	0.81	0.81
>60	0.17	0.43	0.65	0.71	0.74	0.77	0.77	0.77	0.78	0.78
>70	0.16	0.40	0.60	0.66	0.68	0.71	0.71	0.71	0.72	0.72
>80	0.14	0.36	0.54	0.59	0.61	0.63	0.64	0.64	0.64	0.64
>90	0.12	0.32	0.47	0.52	0.54	0.56	0.57	0.57	0.57	0.57

Table 4.2 *The percentage of wrong matches (out of number tested)*

Distance to Nearest Neighbour (arcseconds)	Deconvolved Size (arcseconds)									
	<3	<6	<9	<12	<15	<18	<21	<24	<27	<30
>0	1.6%	1.7%	2.1%	2.0%	2.2%	2.4%	2.6%	2.8%	3.0%	3.0%
>10	1.0%	1.5%	2.0%	1.9%	2.1%	2.2%	2.5%	2.7%	2.9%	2.9%
>20	1.1%	1.5%	1.9%	1.8%	2.0%	2.2%	2.4%	2.6%	2.8%	2.8%
>30	1.1%	1.3%	1.4%	1.2%	1.3%	1.5%	1.6%	1.7%	1.9%	1.9%
>40	1.2%	1.2%	1.3%	1.1%	1.2%	1.4%	1.6%	1.7%	1.7%	1.7%
>50	0.6%	1.0%	1.0%	0.9%	1.0%	1.3%	1.3%	1.4%	1.4%	1.4%
>60	0.7%	1.0%	1.0%	0.9%	1.1%	1.3%	1.3%	1.4%	1.4%	1.4%
>70	0.7%	1.1%	1.1%	1.0%	1.2%	1.4%	1.4%	1.6%	1.6%	1.6%
>80	0.8%	1.2%	1.3%	1.1%	1.3%	1.6%	1.6%	1.7%	1.7%	1.7%
>90	1.0%	1.4%	1.4%	1.3%	1.4%	1.8%	1.8%	1.8%	1.8%	1.8%

There were 106 sources in Category 1 and 143 in Category 2. The two categories can be further subdivided according to the success of the match, as set out in Table 4.3. If the analysis were restricted to those sources where the original match was found through the likelihood ratio analysis (rather than through visual examination), then the numbers in Category 1 and Category 2 would drop to 72 and 63 respectively as shown in the first column of Table 4.3.

These latter results highlight that the key challenge is to determine which LOFAR sources are suitable for likelihood ratio analysis. If a strategy is adopted of using the highest likelihood ratio, irrespective of whether it is for a source or a component Gaussian, to select the host galaxy, then only two out of the 135 sources that were originally assessed by the likelihood ratio analysis are wrongly matched. There are a further 46 cases where the original decision was based on visual examination and the likelihood ratio analysis now selects the wrong galaxy. It is instructive to examine these 48 cases to try to identify properties of the source that might indicate why it was unsuitable to be sent through the likelihood ratio route. The results are summarised in Table 4.4.

Table 4.3 *The sub-division of categories 1 and 2 by type of match*

	Number of Sources		
	Likelihood Ratio	Visual	Total
Category 1			
Both Source and Gaussian find correct id	49	12	61
Source finds wrong id; Gaussian finds correct id	0	3	3
Source finds correct id; Gaussian finds wrong id	23	10	33
Both find wrong id	0	9	9
Category 2			
Both Source and Gaussian find correct id	61	17	78
Source finds wrong id; Gaussian finds correct id	0	29	29
Source finds correct id; Gaussian finds wrong id	2	13	15
Both find wrong id	0	21	21

The number of sources in each category is split into those for which the original match was found through the likelihood ratio analysis and those for which the match was found through visual examination.

Table 4.4 *A breakdown of the incorrect matches*

	Category 1	Category 2
Lobe of Double	2	8
Compact Double	5	12
Extended Source	5	14
No Secure id	0	2
Total	12	36

The categories are described in the text.

In ten of the cases, the radio emission emanates from the lobe of a double system and a coincident galaxy is mistakenly identified as the match. Seventeen are compact doubles (both lobes within the area covered by the Gaussians) and the likelihood ratio analysis is unable to identify the galaxy at the centre of the system due to uncertainty over its position. There are nineteen extended LOFAR sources, where the matching galaxy was originally identified through visual examination and now one of the Gaussians is close enough to a random galaxy to make a false match. Finally, there are two cases where neither the original likelihood ratio analysis nor subsequent visual examination was able to make a secure identification, but one of the Gaussians has picked up an erroneous match.

There are 30 cases where both the source and the Gaussian select a wrong match (9 in Category 1 and 21 in Category 2). In only one of these cases do the source and the Gaussian find the same wrong match; the LOFAR emission is for the lobe of a double system and a random galaxy within that lobe is wrongly identified as the match. The interesting corollary is that, in this sample at least, whenever the source and Gaussian select the same galaxy it is highly likely to be a genuine match.

The breakdown in Table 4.4 hints at properties that might be capable of determining which multi-Gaussian sources can be safely sent for likelihood ratio analysis. Properties that might be relevant for a decision tree are:

- The distance to the nearest neighbouring LOFAR source, indicating the probability that the radio emission is part of a larger system.
- The number of Gaussian components: two components might indicate a

higher probability of the source being a compact double; by contrast, a higher number of Gaussians increases the probability of an erroneous match.

- The likelihood ratio of the source (Category 1) or the best Gaussian (Category 2).
- The ratio of the likelihood ratio of the source to the likelihood ratio of the best Gaussian.
- The maximum separation of the Gaussians, indicating the extent to which the radio emission is extended.
- The deconvolved size of the largest Gaussian.
- The deconvolved size of the Gaussian with the highest likelihood ratio.
- The flux ratio of the brightest Gaussians: a ratio close to one might indicate a compact double.

Each of these was examined in turn. The distribution of correct matches as a function of the relevant property was compared with the distribution of incorrect matches in the hope that there would be a clear division between the two distributions. There was an insignificant difference for two of the properties – the distance to the nearest neighbour and the flux ratio of the two brightest Gaussians – and so these properties were disregarded.

Charts for the remaining six properties are shown in Figures 4.2 to 4.7. There are two charts in each case, apart from Figure 4.7 which is relevant only for Category 2. The left-hand chart shows the distributions for Category 1 and the right-hand chart shows the distributions for Category 2. These charts in turn are subdivided into three: the top sub-figure shows the cumulative distribution for the correct and wrong matches, the middle sub-figure shows the distribution for the correct matches and bottom sub-figure shows the distribution for the wrong matches. The correct matches are shown in blue and the wrong matches in red.

As can be seen, there are clear offsets in the distributions, but in these one-dimensional plots there is no clear point where it would be possible to automate without giving large numbers of wrong answers. It is possible that some combination of these properties might provide a guide to which of the multi-Gaussian sources can be sent for likelihood ratio analysis. The offsets are most pronounced in Figures 4.2 and 4.7, suggesting that the application of a minimum

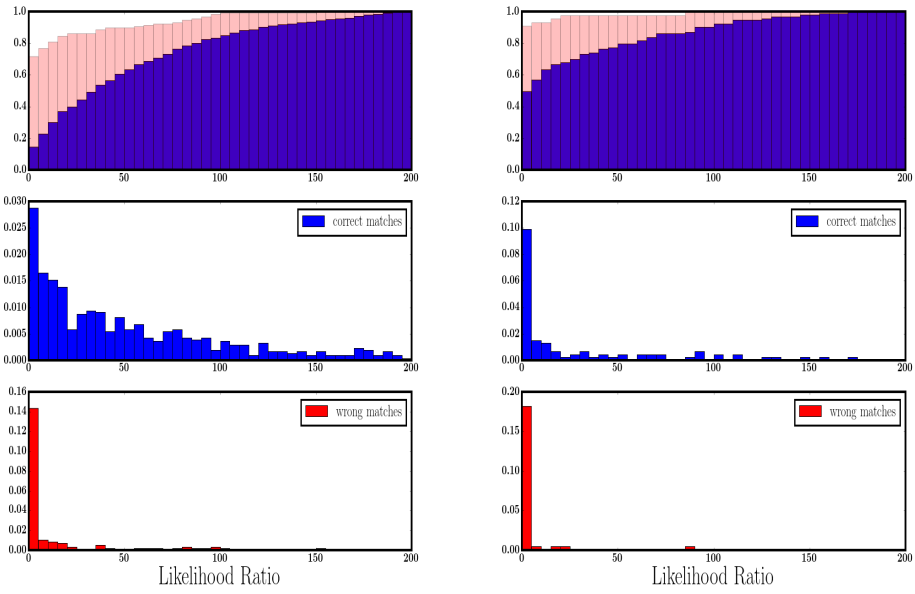

(a) **(b)**

Figure 4.2 *The fraction of correct matches as a function of the likelihood ratios of the source (Category 1 — left-hand chart) and the best Gaussian (Category 2 — right-hand chart).*

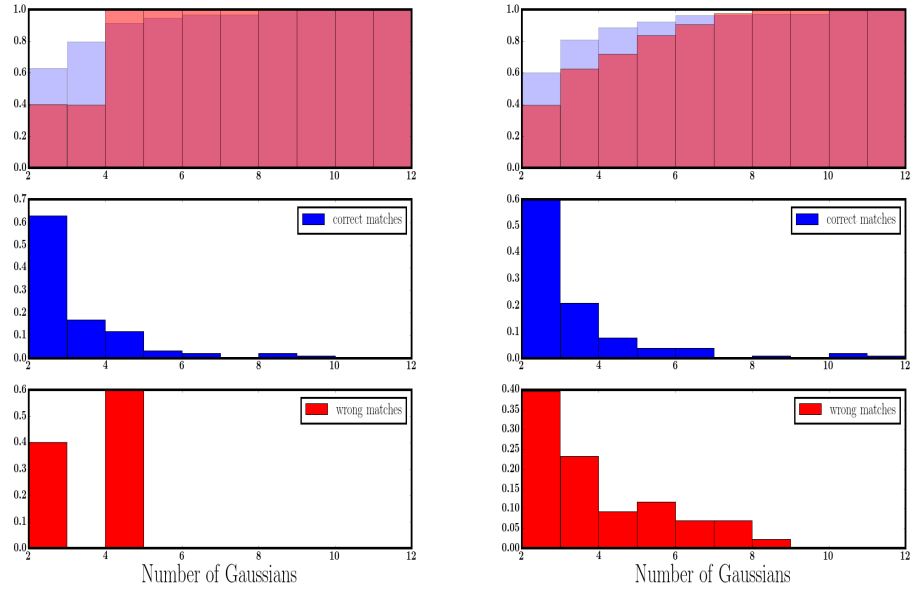

(a) **(b)**

Figure 4.3 *The fraction of correct matches as a function of the number of Gaussian components (Category 1 — left-hand chart; Category 2 — right-hand chart).*

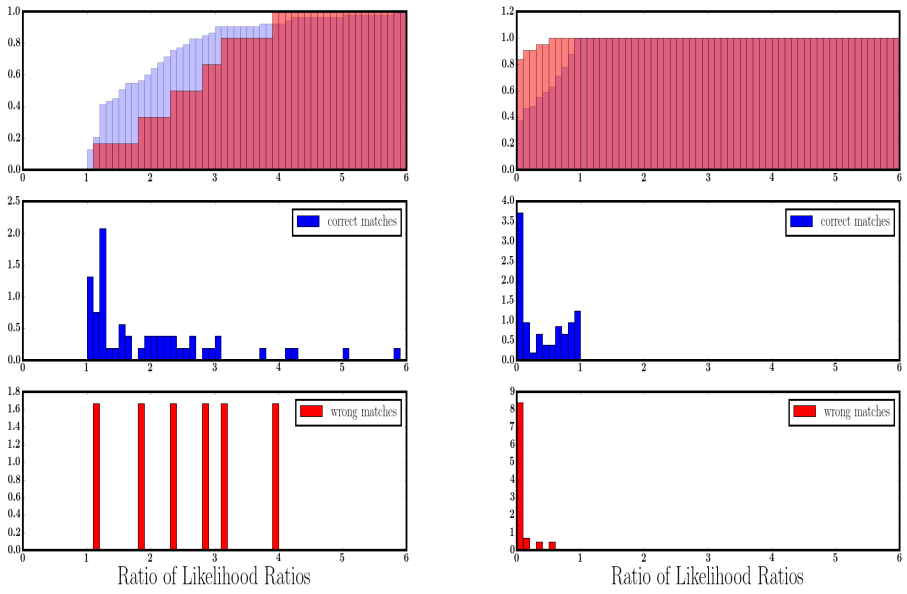

(a) **(b)**

Figure 4.4 *The fraction of correct matches as a function of the ratio of the likelihood ratio of the source to the likelihood ratio of the best Gaussian (Category 1 — left-hand chart; Category 2 — right-hand chart).*

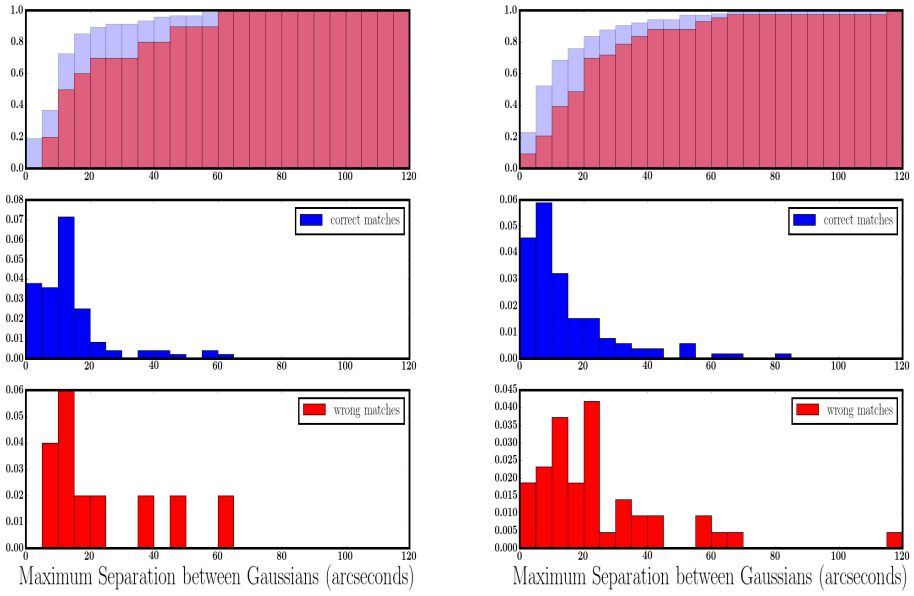

(a) **(b)**

Figure 4.5 *The fraction of correct matches as a function of the maximum separation between the Gaussian components (Category 1 — left-hand chart; Category 2 — right-hand chart).*

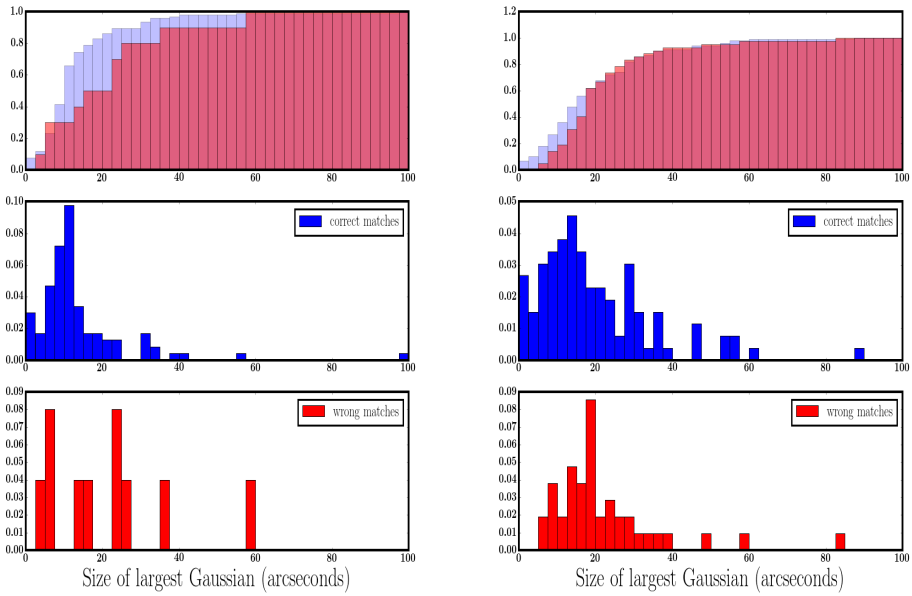

(a) **(b)**

Figure 4.6 *The fraction of correct matches as a function of the deconvolved size of the largest Gaussian component (Category 1 — left-hand chart; Category 2 — right-hand chart).*

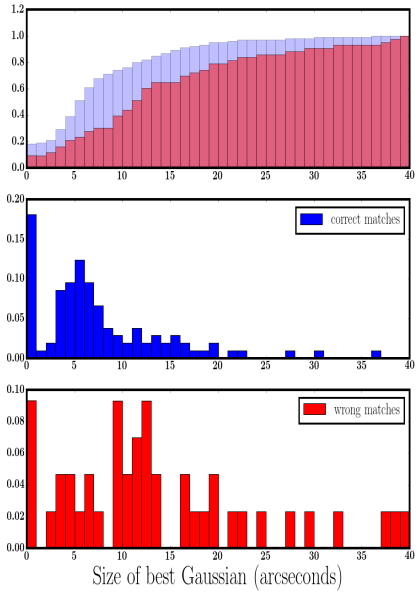

(a)

Figure 4.7 *The fraction of correct matches as a function of the size of the Gaussian component with the highest likelihood ratio (Category 2 only).*

likelihood ratio threshold coupled with a maximum size might prove a promising avenue. This, however, requires further analysis using a larger sample.

In summary, the analysis in this section suggests that a viable strategy to the problem of separating radio sources into those that can be sent through the likelihood ratio route and those that require visual identification of the host galaxy might be as follows. Single-Gaussian sources are sent through the likelihood ratio path provided that their deconvolved size is under 15 arcseconds and that the distance to their nearest neighbour is more than 30 arcseconds. All multi-Gaussian sources are initially sent through the likelihood ratio route, with the analysis performed on both the source itself and also on each individual Gaussian. If the match found for the source coincides with that found for the Gaussian with the highest-likelihood match, then the identification is accepted. Otherwise, the source is sent for visual investigation. Based on the statistics from the sample in this research (which will not necessarily be valid for the LoTSS survey, but should provide a reasonable guide), Table 4.5 shows the results produced by this approach for a population of 100,000 radio sources (note that the number of detections expected in the LoTSS survey is in the order of 10^7!); the figures in the table are rounded to avoid spurious accuracy. The key figures are that:

- in 82,700 cases (83%), the match is found through the likelihood ratio route
- an erroneous match will be found in 1,300 of these
- the number of sources requiring visual examination is 17,300, split into 7,800 and 9,500 single- and multi- Gaussian sources respectively.

The number of visual examinations is still uncomfortably high. It is hoped that further analysis using a larger sample of sources than available in this study will confirm that the combination of a minimum likelihood ratio threshold and maximum size threshold will allow a proportion of the 9,500 multi-Gaussians, currently shown as needing visual examination, to be processed automatically. It is also worth noting that source sizes in existing LOFAR images have been found to be larger than expected, due to imperfect calibration and imaging techniques. New techniques, under development by Tasse et al (in prep.) may produce smaller source sizes and so allow a higher fraction of single Gaussians to pass through the likelihood ratio analysis.

Table 4.5 *The division of a sample of 100,000 radio sources*

	Total	Likelihood Ratio			Visual
	Number	Total	Correct	Wrong	Examination
Single-Gaussian	78200	70400	69200	1200	7800
Multi-Gaussian:					
LR matches coincide	12300	12300	12200	100	
other	9500				9500
Total	100000	82700	81400	1300	17300

The division of a sample of 100,000 radio sources into those able to be matched via likelihood ratio analysis and those requiring visual examination. The likely number of erroneous matches is also shown.

4.3 Accurate Positioning of a Fibre

Spectroscopic follow-up of the galaxy matches allows accurate redshifts to be obtained for the radio sources and is an important part of the subsequent analysis. The WEAVE-LOFAR project (Smith et al., 2016) has been designed to obtain the follow-up for of order a million LOFAR radio sources using the new WEAVE multi-object and multi-field unit fibre-fed spectrograph (Dalton et al., 2012). WEAVE will have 1000 fibres of 0.65 arcsecond radius.

The ELAIS-N1 dataset allowed tests to be performed in order to judge whether there would be a problem if the location of the radio source were to be used to position the fibres. This would be relevant if, for example, the depth of a counterpart catalogue was insufficient for a host galaxy to be detected and so the positioning of the fibre would need to depend on the coordinates of the LOFAR source. The WISE and PanSTARRS 3pi surveys, described in Wright et al. (2010) and Chambers et al. (2016) respectively, will be used to find host galaxies for the LOFAR wider-area LoTSS survey: these have the necessary sky coverage, but are not as deep as, for example, the PanSTARRS Medium-Deep, UKIDSS and SWIRE data.

The upper left-hand chart in Figure 4.8 shows the distribution of offsets from the radio position to the position of the host galaxy for sources that do not appear in the WISE catalogues (but are in the deeper data in ELAIS-N1): these are likely to be the ones that will not find an infrared counterpart in the wide-area

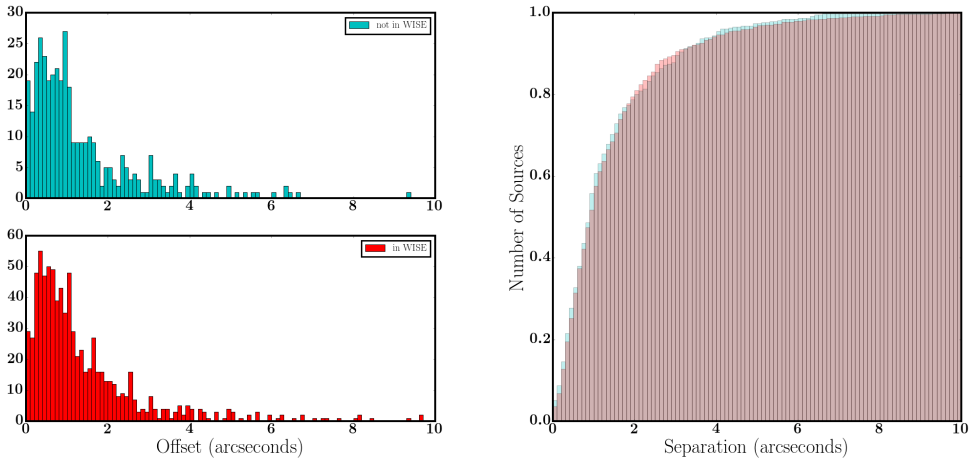

(a)

(b)

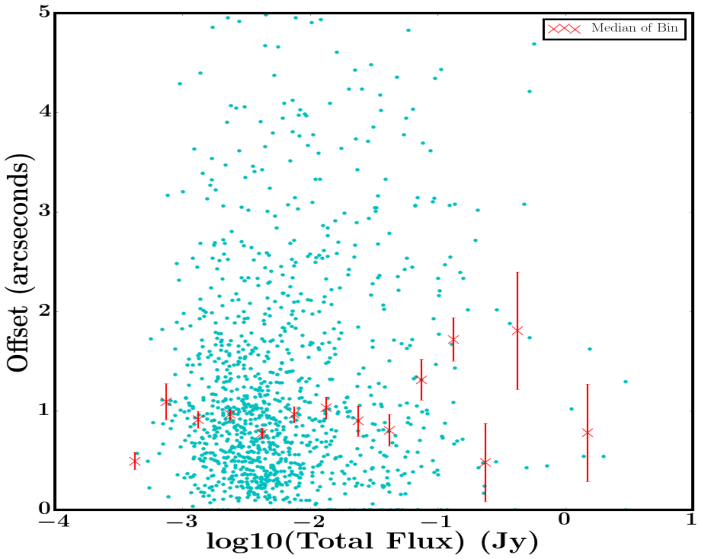

(c)

Figure 4.8 *Chart(a) shows the distribution of offsets between the radio position and that of the host galaxy for sources that do not appear in the WISE catalogue (upper sub-chart) and those that do (lower sub-chart). Chart(b) shows the cumulative distributions. Chart(c) demonstrates that the positional accuracy of a LOFAR source has not a strong dependency on radio flux. The chart plots the offset against radio flux for sources both in and not in the WISE catalogue; individual points are plotted in blue, while red points show the median in flux bins.*

survey. There are 380 such sources. For comparison, the lower panel shows the same information for sources that are in WISE (829 sources) and is actually very similar – as can be seen more clearly in the upper right chart, which shows that the two cumulative distributions almost exactly coincide.

The positional accuracy needs to be (ideally, much) better than 0.65 arcseconds, the fibre radius. The cumulative distribution shows that this is achieved only for approximately 40% of sources. The bottom chart suggests that the positional accuracy of the LOFAR source is not a strong function of radio flux. That the accuracy does not get dramatically worse towards low fluxes is partly because such sources are likely to be low-luminosity AGNs or star-forming galaxies and are, therefore, intrinsically compact. The main conclusion from the chart is that the inaccuracy is due mainly to the intrinsically extended nature of radio sources and to astrometric errors. The implication is that if the LOFAR survey is deeper than that used for the ELAIS-N1 field, then the higher signal / noise that will be achieved will not significantly improve the situation. A brief investigation was made to try and identify properties of the radio sources, such as size, that might indicate which sources are likely to have positional accuracy better than 0.65 arcseconds; nothing obvious was found.

4.4 Adaption of the Likelihood Ratio Method to the LoTSS Survey

The ELAIS-N1 field benefits from a wealth of high-quality multiband data, whereas the LoTSS survey covers a much wider area of the sky which restricts the choice of counterpart catalogues. As mentioned in the previous section, the infrared data will be taken from the Wide-field Infrared Survey Explorer (WISE) catalogue; although not as deep as UKIDSS and SWIRE/SERVS, WISE has the requisite coverage. The optical i-band data will be taken from the PanSTARRS 3pi survey in Data Release 1 (DR1), as described in Chambers and Pan-STARRS Team (2017), rather than the Medium-Deep Survey. The difference in depth between the two i-band datasets is approximately 3.5 magnitudes: the 3pi survey i-band magnitudes turn over at $\sim$ 21.4 whereas the turn-over point is $\sim$ 25.0 for the Medium-Deep Survey. This section considers how the likelihood ratio methodology can be adapted for use with the LoTSS survey.

The critical point that needs investigation is whether the colour of a galaxy, as defined by the magnitude difference between the optical and WISE infrared bands, has the same discriminatory power in matching with radio sources as that provided by the i - K colour used in the ELAIS-N1 field. There is an important consideration when conducting this investigation. When colour was incorporated into the likelihood ratio analysis for the ELAIS-N1 field, there was no problem arising from the use of limits because of the depth of the data. If a source was undetected in the K-band, then it was definitely in the "blue" region of the curve (see the lower chart in Figure 3.9); that is, the i - K colour would be under 4.0. Similarly, a source undetected in the i-band would be firmly in the "red" region, with an i - K colour of at least 4.0. The use of limits will not necessarily give such a clean demarcation when analysing the shallower data applicable to the LoTSS survey.

The investigation was conducted using the ELAIS-N1 data in order to examine the fraction of matched galaxies to the overall population, as a function of (i - 3.4 micron) colour. The overall strategy was to use this dataset unadjusted in order to obtain the "true" distribution. The distribution could then be recalculated after amending the dataset in order to replicate the shallower PanSTARRS and WISE data that will be used to find the LoTSS counterparts. A comparison of the two distributions would indicate whether a colour-based likelihood ratio approach is possible for the LoTSS survey.

Figure 4.9 shows the results of the analysis using the deep data unadjusted. Details of the calculation are as follows:

- The i-band data were taken from the PanSTARRS Medium Deep catalogue.
- The 3.4 micron data were obtained from the SWIRE 3.6 micron catalogue, with an adjustment of -0.0663 to convert it onto a 3.4 micron equivalent. The adjustment factor was calculated from the mean difference between the SWIRE 3.6 micron magnitude and WISE 3.4 magnitude for 100747 galaxies in the ELAIS-N1 field with detections in both bands.
- The black line in Figure 4.9 shows the progression in the fraction of galaxies that are matches for those sources with detections in both bands. The red line shows the fraction after also including sources that are detected in only one band, and using upper limits of 25.5 for the i-band magnitudes and 20.5 for the 3.4 micron magnitudes to calculate the colour. The fact that

the two lines closely align confirms the point made above that the use of limits does not cause a problem for the deeper data.

The analysis was now repeated, but amending the data to replicate the shallower surveys that will be used to find the LoTSS host galaxies. It was initially assumed that all i-band detections with magnitudes above 21.4 would not be detected in the shallower PanSTARRS 3pi survey and similarly all WISE 3.4 micron detections would be at magnitudes below 20.25. A second analysis was then carried out using limits of 21.9 and 20.75 respectively. There was very little difference between the two sets of results and, to aid clarity, only the second set is plotted (as the blue line) in Figure 4.10. The black line in the chart again shows the progression of the fraction for the deep data. Several conclusions can be drawn:

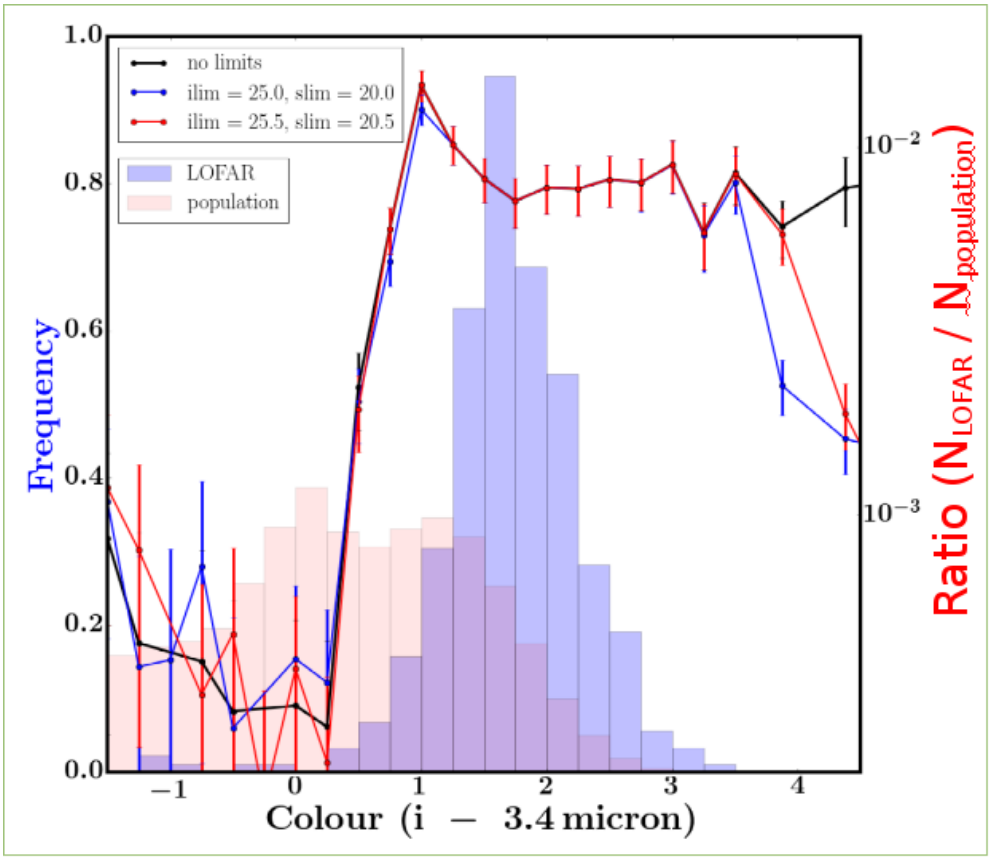

Figure 4.9 *The blue and red histograms show the distribution by (i - 3.4 micron) colour of the matched galaxies and all galaxies respectively (left-hand axis). The proportion of matched galaxies to the overall population is shown in (i - 3.4 micron) colour bins (right-hand axis). The chart is based on the deep data used for the ELAIS-N1 field.*

- There are some discrepancies in the results at (i - 3.4 micron) colours below 2.0; above 2.0, the fractions for the deep and shallow data closely align.
- However, the key point is that the shallow data also sees a strong increase in the fraction of matches above a colour of zero: between a colour of zero and three, the fraction increases by an order of magnitude.
- Below a colour of zero, the trends for both sets of data appear to reverse, but this is of limited importance given that there are very few matches within this colour region.
- Figure 4.10 suggests a strategy for categorising the LoTSS data by colour in the likelihood ratio analysis. Below an (i - 3.4 micron) colour of zero and also above a colour of 3, comparatively few bins are needed: in both regimes, not only is there little change in the fraction of matches but there are also few matches. The matches mostly have colours of between zero and 3.0 and here the fraction rises rapidly, suggesting that tight binning is appropriate.

Overall, the analysis in this sub-section supports the view that a colour-based likelihood ratio procedure is practical, and indeed desirable, for the LoTSS survey.

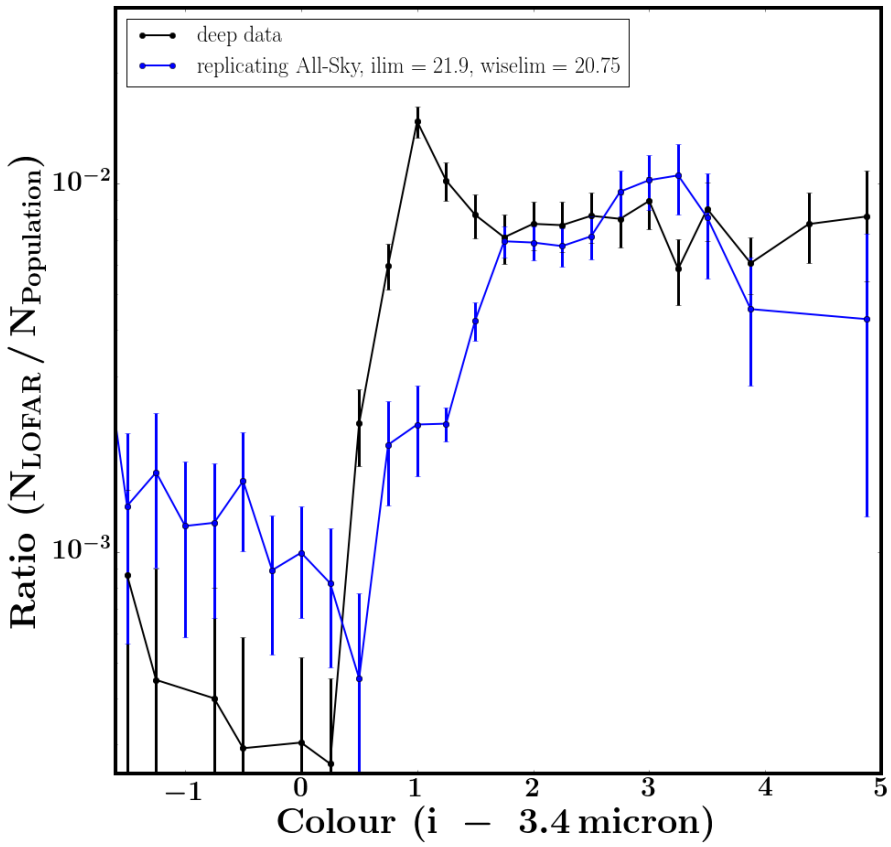

Figure 4.10 *The proportion of matched galaxies to the overall population is shown in (i - 3.4 micron) colour bins for the deep data used for the ELAIS-N1 field (black line), and also amended to replicate the shallower surveys used to find the LoTSS counterparts (blue line). It shows that a colour-based likelihood ratio analysis is advisable for the LoTSS data and suggests that tight binning is appropriate between a colour of zero and three.*

Chapter 5

The Evolution of Jet-mode AGNs

5.1 Introduction

The description of jet-mode AGN feedback described in Chapter 1 has been extensively studied and tested in the local universe, but research into its validity at earlier times is still in its infancy. The catalogue of ELAIS-N1 radio sources assembled for this thesis offers an opportunity to study the space density of jet-mode AGNs out to a redshift of two and provide insights into the feedback mechanism.

5.2 Flux Calibration

A necessary first step is to check the accuracy of the LOFAR flux densities. It is possible that systematic errors have been embedded in the flux density measurements due to the transfer of amplitudes from proxy calibrators observed at different elevations to the target field coupled with errors in the LOFAR station beam models (Heald et al., 2015) and also due to the more general calibration challenges faced by radio interferometers operating at low frequencies. A comparison was made with the flux densities calculated from seven other low-frequency surveys that covered all or part of the ELAIS-N1 field; details of these surveys are set out in Table 5.1.

Figure 5.1 allows an initial check of the accuracy of the flux densities. Eleven

Table 5.1 *Surveys of ELAIS-N1*

Telescope	Frequency MHz	Reference	Angular Resolution arcseconds	Minimum Flux Density mJy
VLSS	74	Cohen et al. (2007)	80	700
TGSS	150	Intema et al. (2017)	25	60
GMRT	325	Sirothia et al. (2009)	15	0.5
WSRT	350	de Bruyn, private communication	45	2.8
GMRT	610	Garn et al. (2008)	5	0.5
VLA-FIRST	1400	Becker et al. (1995)	5	1.4
VLA-NVSS	1400	Condon et al. (1998)	45	2.5

The seven surveys used to check the accuracy of the flux density measurements. The Minimum Flux Density indicates the flux density at which the survey is sufficiently complete for the purpose of this analysis (see text).

LOFAR sources were chosen and their fluxes compared with those derived from the other surveys. The shallow depth of the VLSS survey means that there are very few matches with LOFAR sources (fewer than ten across the whole ELAIS-N1 field) and only three of these have counterparts in at least two of the other surveys. These three sources were chosen. The other eight LOFAR sources shown in Figure 5.1 were selected because they are compact and isolated, and because there is a match from at least three of the surveys. The flux densities of the LOFAR sources are marked by crosses in the chart; the lines simply join the flux densities of the counterparts and do not represent best fits; and error bars are not shown for clarity (given that the points align vertically) but tend to be of the order of 10%. The flux densities plotted at 1400 MHz are those from the VLA-FIRST survey rather than from VLA-NVSS.

It is hard to draw definitive conclusions from Figure 5.1 given the small sample size, but the following points are worth making. There is a suggestion from the chart that the VLSS flux densities might be biased low, although this could be caused by low-frequency spectral flattening as first proposed by Israel and Mahoney (1990). Even disregarding the VLSS flux densities, there is a suggestion of curvature in the spectral shape around the frequency of the LOFAR observations. The eye is drawn to a comparison with the TGSS 150 MHz flux density values which are very broadly consistent with the LOFAR flux densities. Overall, the chart hints that any discrepancy in the flux density measurements is

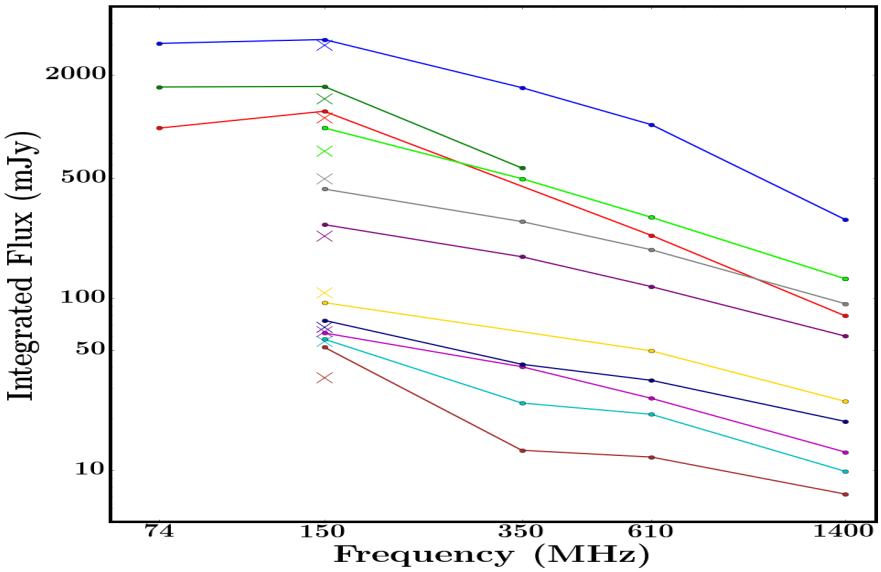

Figure 5.1 *A comparison of the flux densities in the LOFAR survey (the crosses) and in other low-frequency surveys (the filled circles) for eleven sources. The comparisons are against the VLSS, TGSS, WSRT, GMRT and VLA-FIRST surveys at 74, 150, 350, 610 and 1400 MHz respectively, as detailed in Table 5.1. The chart suggests that any discrepancy in the flux density measurements of the LOFAR sources is not too pronounced.*

not too pronounced.

A more detailed investigation was now conducted. The LOFAR sources were compared with each of the other seven surveys in turn, the typical flux ratio calculated for each of these seven comparisons and the results plotted. It is obviously desirable to maximise the number of sources when carrying out each comparison, but this must be tempered by the necessity of avoiding the introduction of biases into the results due either to the variable effective depths of the different surveys or to different angular resolutions. The LOFAR sources were first put through a filtration process, with the criteria tailored to the properties of each survey. The procedure is illustrated by following through the filtration process for the comparison with the VLA-FIRST survey at 1400 MHz.

First, the flux density distribution of the VLA-FIRST sources (the left-hand chart in Figure 5.2) suggests that incompleteness starts to become significant at flux densities under 1.4 mJy. Assuming a typical spectral index of $\alpha = 0.7$, this corresponds to a LOFAR flux density of 5.6 mJy. It was, therefore, decided to

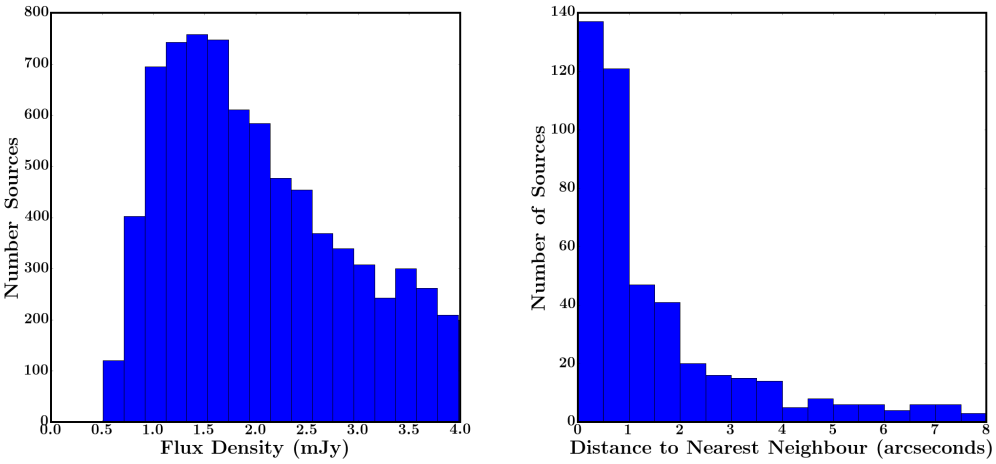

(a) **(b)**

Figure 5.2 *Left-hand chart: the flux density distribution of the VLA-FIRST sources, suggesting that incompleteness becomes significant below 1.4 mJy. Right-hand chart: a cross-match of the LOFAR and VLA-FIRST catalogues, showing the distance to the nearest neighbour.*

restrict the LOFAR sources to those with a flux density of at least 6.0 mJy.

Second, it is desirable to restrict the sample to compact LOFAR sources in order to avoid resolution effects. The VLA-FIRST survey has a high angular resolution, similar to that of LOFAR, but has poor sensitivity to extended structures, suggesting that this needs to be a tight restriction. LOFAR sources were limited to those with a major axis size of under 10 arcseconds. It was possible to relax this restriction when comparing against those surveys with poorer resolution.

Third, the LOFAR sources should be isolated, although this is less important for comparatively high resolution surveys such as VLA-FIRST. LOFAR sources were accepted provided that the distance to the nearest LOFAR neighbour was at least 10 arcseconds. The threshold was allowed to increase to as much as 60 arcseconds for the lower resolution surveys where there is a risk of contamination of flux densities by nearby sources.

Fourth, it was checked that each counterpart survey covered the whole of the area of the LOFAR catalogue (as was the case for VLA-FIRST). The two GMRT surveys did not and so the LOFAR sources were, in these two cases, restricted to the intersecting areas.

Fifth, the remaining LOFAR sources could now be crossmatched with the VLA-

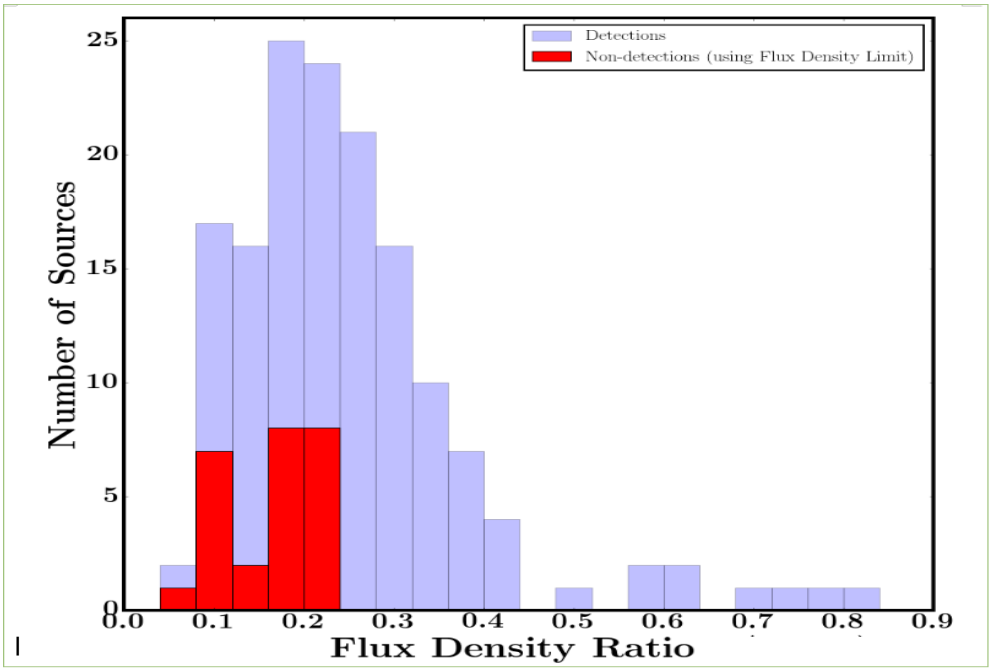

Figure 5.3 *The ratio of the flux densities (VLA-FIRST flux density / LOFAR flux density). The sources where a limit was used for the VLA-FIRST flux density are shown in red.*

FIRST catalogue. An examination of the distance from each LOFAR source to its nearest VLA-FIRST neighbour (the right-hand plot in Figure 5.2) indicates that accepting all matches within 4 arcseconds is a sensible choice. This threshold was higher for shallower surveys with lower densities of sources.

The filtration process, steps 1 – 4 above, left 158 LOFAR sources available to be matched with the VLA-FIRST catalogue. 132 matches were found and the ratio of the VLA-FIRST flux density to the LOFAR flux density was calculated for each of them. The remaining 26 cases were assumed to be non-detections within the VLA-FIRST survey and the VLA flux density was taken as an upper limit of 1.4 mJy in order to calculate an upper limit to the ratios. The distribution of the ratios (the VLA-FIRST flux density divided by the LOFAR flux density) is shown in Figure 5.3. The median value of the distribution – 0.225 in the case of VLA-FIRST – was taken as the typical ratio of the fluxes between the LOFAR and counterpart survey. Note that this value is higher than the ratios emanating from sources using upper limits, so is unbiased by the non-detections and thus justifies the choice of the LOFAR minimum flux threshold.

One further issue arose during the analysis in relation to the GMRT 610MHz survey. After passing them through the four filtration steps, over a quarter of

Table 5.2 *Criteria used to match LOFAR sources with those of the other surveys*

Telescope	Minimum LOFAR Flux Density mJy	Maximum Size of Major Axis arcsec	Distance to Nearest Neighbour arcsec	Maximum Crossmatch Separation arcsec	Number of Sources	
					Detected	Non-detected
VLSS(74MHz)	530	25	60	10	6	1
TGSS(150MHz)	65	20	60	5	27	0
GMRT(325MHz)	1.2	20	40	8	240	7
WSRT(350MHz)	5.5	10	60	6	143	4
GMRT(610MHz)	1.5	10	10	4	150	28
VLA-FIRST(1400MHz)	6.0	10	10	4	132	26
VLA-NVSS(1400MHz)	14	15	60	10	94	16

the remaining LOFAR sources failed to find a match with a GMRT source. Some of these were undoubtedly genuine non-detections, with the GMRT flux density below the detection level for that survey. However, the depth of the GMRT survey appears to be somewhat patchy and it is likely that the number of non-detections had consequently been artificially increased. The rms image confirmed that there were areas within that survey suffering from high levels of noise (and hence low levels of detections) – a problem due to residual calibration errors near the brightest sources. To minimise the problem, those LOFAR sources lying in a region of high noise within the GMRT image – defined as having a rms flux density of over 0.12 mJy –were removed from the analysis. This brought the fraction of non-detections within the matches down to a level closer to, albeit still above, those found in the other surveys.

The criteria used in the matching process for each survey together with the resulting number of matches are shown in Table 5.2.

Finally, the uncertainty on the median was estimated as follows. The error on the mean value was calculated in the normal way and the resulting uncertainty was multiplied by 1.253 to obtain the error on the median (Ivezić et al., 2014). This approach is valid only for large samples and for normally-distributed populations; neither is strictly correct here, but the approximation will be adequate for this analysis. The median value also has some sensitivity to the criteria used to select the LOFAR sources. The analysis was repeated by adjusting the minimum flux threshold by $\pm$ 10% and the maximum size threshold by $\pm$ 2 arcseconds; this produced four values, which were taken to give a measure of the uncertainty caused by the filtration process. Again, this is a crude approach, but should be

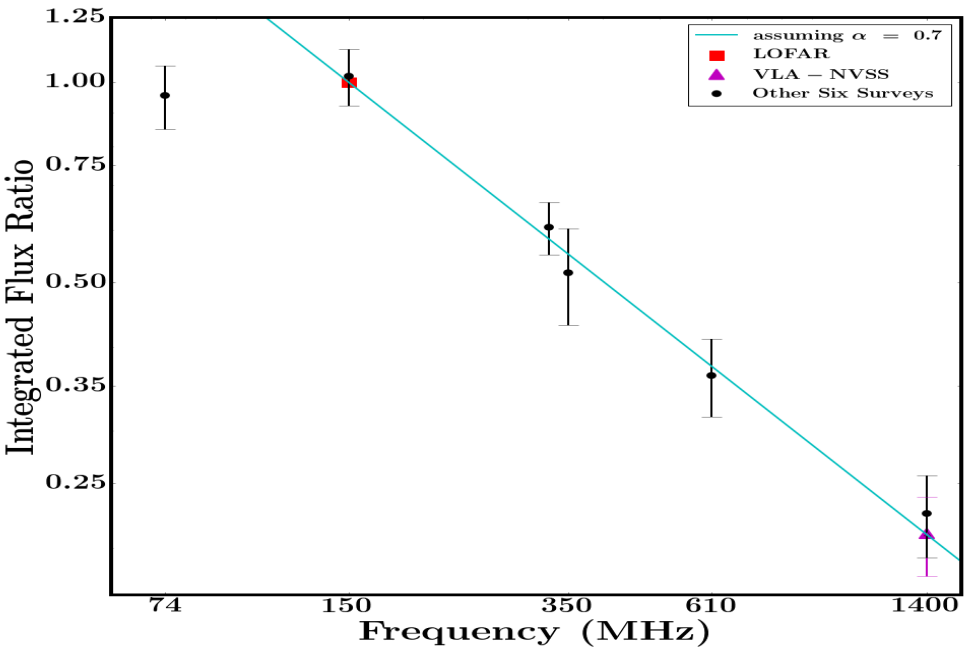

Figure 5.4 *The ratio of the LOFAR flux densities to those of seven other surveys. The line shows the theoretical ratio assuming a spectral index of* $\alpha = 0.7$*. A reasonable conclusion from the chart is that the LOFAR flux densities are accurate at the* $\sim 10\%$ *level.*

adequate. The two uncertainties were combined in quadrature to produce the error bars shown in Figure 5.4. These should be considered to be indicative only of the uncertainty attaching to the ratios.

The results are set out in Table 5.3 and plotted in Figure 5.4. Also shown in the chart is a line that marks the theoretical ratio assuming that the LOFAR flux densities are accurate and that the spectral index is $\alpha = 0.7$. The large error bars and the fact that some curvature in the spectrum is expected still make it difficult to draw definitive conclusions. Nevertheless, the analysis provides solid support for the tentative conclusions that were drawn from Figure 5.1, namely:

- The VLSS flux densities appear to be heavily biased downwards. This, together with the very low number of matches, suggests that they should be disregarded for the purposes of this exercise.
- If there is spectral curvature, then the LOFAR flux densities may be biased slightly high.
- However, the analysis confirms the earlier indication that the LOFAR and

Table 5.3 *The results of the flux density comparisons*

Telescope	Frequency mJy	Flux Density Ratio	Error	Implied Value of α	Error
VLSS	74	0.95	± 0.10	-0.07	± 0.16
TGSS	150	1.02	± 0.10	n.a.	n.a.
GMRT	325	0.60	± 0.05	0.65	± 0.11
WSRT	350	0.52	± 0.09	0.78	± 0.22
GMRT	610	0.36	± 0.05	0.72	± 0.10
VLA-FIRST	1400	0.22	± 0.03	0.67	± 0.07
VLA-NVSS	1400	0.21	± 0.03	0.70	± 0.07

TGSS fluxes are closely aligned and this argues that any mis-calibration of the LOFAR flux densities is not too significant.

- A reasonable conclusion is that the LOFAR flux densities are accurate at the $\sim 10\%$ level and that the analysis gives no strong justification for amending them.

It is now possible to calculate source counts as a function of flux density and this will provide a further test of the accuracy of the flux densities.

5.3 Investigation of the Incompleteness

Before computing the source counts, it is necessary to examine the completeness of the sample. A Monte Carlo simulation is a standard approach to estimate incompleteness levels, by injecting fake sources into the image and attempting to recover them. A drawback with the Monte Carlo method is that a detailed knowledge of source sizes is required in order to be able to produce accurate results; that is not a priori known at small flux densities. A potentially more accurate method of determining the incompleteness was available in this case. Advantage was taken of a deeper data set of 10507 radio sources in the ELAIS-N1 field that had been prepared by Dr Jose Sabater and collaborators in July 2017 as part of ongoing efforts to push the ELAIS-N1 dataset deeper by exploiting the full set of observations.

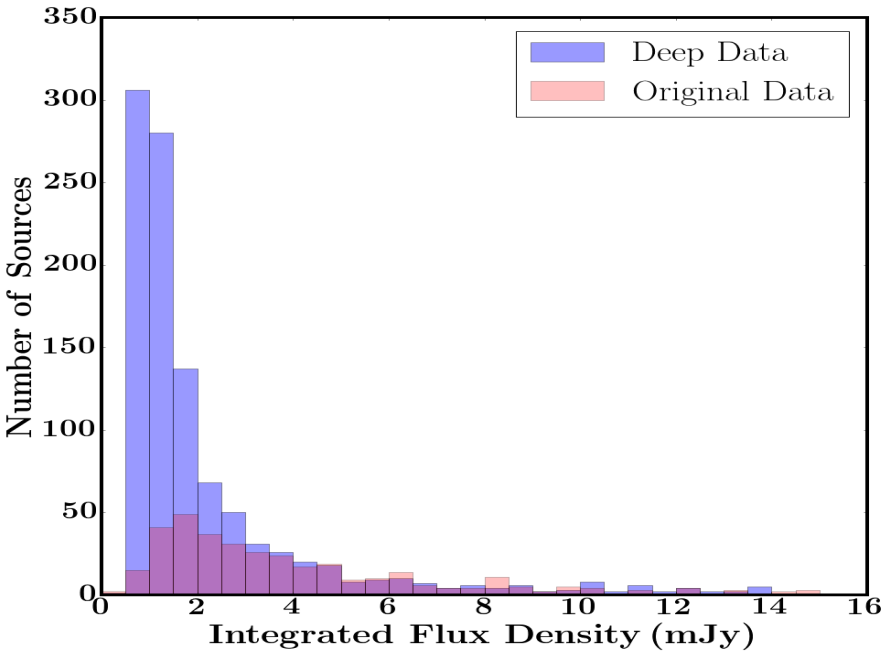

Figure 5.5 *The distribution of flux densities for the deeper set of radio sources (blue histogram) and the dataset used in this work (red histogram). The deep dataset and the original dataset can be considered to be complete down to around 2.0 mJy and between 4.0 mJy and 4.5 mJy respectively.*

The reduction of the deeper image and extraction of the radio sources had been performed using different procedures from those used to produce the sample in this research; they used the KILLMS and DD-Facet techniques developed by Cyril Tasse (in prep.). In particular, the flux calibration was achieved using the standard LOFAR-surveys approach of interpolating between NVSS, WENSS and VLSS flux densities (Shimwell et al., 2017). Given the discussion in Section 5.2, this method may be inappropriate for ELAIS-N1 due to the low VLSS flux densities and a first step, therefore, was to calibrate the flux densities into line with those of the original sample. A positional crossmatch between the original and the new LOFAR catalogues using a search radius of 5 arcseconds generated 1238 matches (note: over the full ELAIS-N1 image and not just the restricted PS1/UKIDSS region), the ratio of the integrated flux densities was recorded and the mean used to adjust the flux densities of the new dataset. The distribution of the flux density ratios was sharply and symmetrically peaked around the mean.

A comparison between the two datasets could now be made. The analysis was restricted to the central region of the image in order to avoid the need for primary

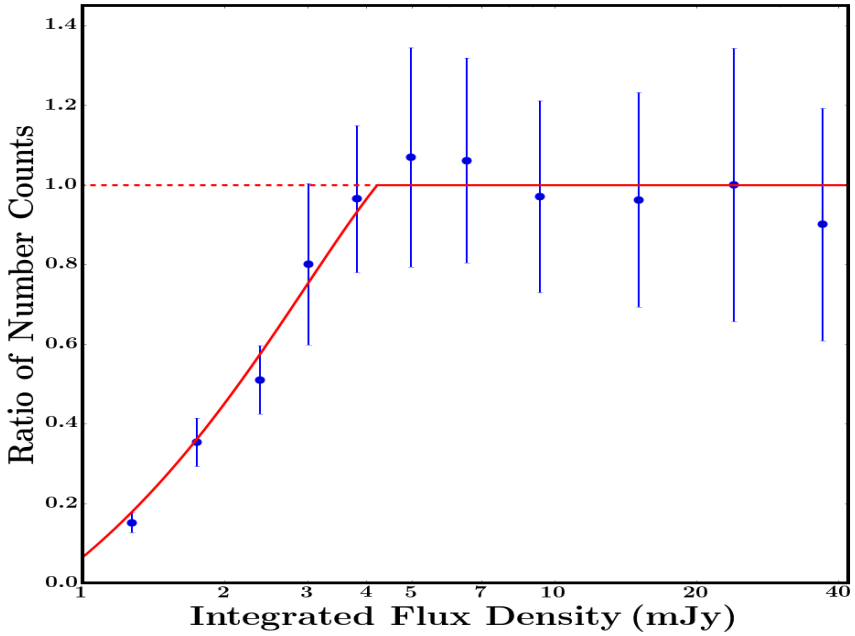

Figure 5.6 *The ratio of number counts (original dataset / deeper dataset) as a function of flux density. The chart shows that the original dataset can be considered to be complete down to 4.25 mJy. The red line shows the best-fitting horizontal line through the datapoints above a flux density of 4.25 mJy and the best-fitting quadratic through the datapoints below 4.25 mJy.*

beam corrections and hence possible distortions to the results. The area chosen was that bounded by RAs of 241.5 and 244.0 and by Decs of 54.2 and 55.7; it contained 425 and 111 sources from the new and original datasets respectively. The distribution of the adjusted total flux densities of the deeper dataset together with the distribution of the original dataset are shown in Figure 5.5. The turn-over point for the deeper data is around a flux density of 1.5 mJy and, for the purposes of this analysis, the assumption was made that the sample can be considered to be essentially complete down to 2.0 mJy. The chart also suggests that the dataset used in this thesis starts to suffer from incompleteness somewhere between 4.0 mJy and 4.5 mJy.

Both samples were then binned by integrated flux density and in each bin the ratio of the number of sources from each dataset was calculated. The results are shown in Figure 5.6. The ratio decreases abruptly at flux densities below 4.25 mJy, suggesting the onset of incompleteness from that point. The error bars shown here have been calculated assuming Poisson errors on the source counts; it

should be noted that, especially at bright fluxes, these will greatly overestimate the true error since both the original and new datasets are observing the same sky area, and thus subject to the same random fluctuations.

A horizontal line was fitted through the ratios for flux densities above 4.25 mJy, confirming a ratio of 1.00. A quadratic was fitted through those ratios for flux densities of 4.25 mJy and below. The curve has the equation:

$$\mathrm{r(f)} = -0.0431\,\mathrm{f}^2 \;+\; 0.5157\,\mathrm{f} - 0.4086 \tag{5.1}$$

where r(f) is the ratio as a function of the flux density, f, which is measured in mJy. The incompleteness factor at a given flux density can then be calculated as 1.0/r(f); this expression will be used in the analysis in the rest of this chapter. Examples of the incompleteness factors are shown in Table 5.4. The incompleteness factors are unreliable below a flux density of 2.0 mJy because of the possibility that the deeper data are then themselves incomplete.

Table 5.4 *Examples of the incompleteness factor*

Flux Density mJy	Incompleteness Factor
4.25	1.000
4.00	1.037
3.50	1.152
3.00	1.333
2.50	1.636
2.00	2.221

5.4 Source Counts

Having calculated the completeness adjustments and the minimum flux density at which the data are reliable, the 150 MHz source counts (that is, the number of sources per unit sky area, as a function of flux density) could now be obtained down to a flux density of 2.0 mJy. There are 1000 LOFAR sources with a flux density above that threshold.

Because of a large variation in the rms across the ELAIS-N1 image, sources

with peak flux densities only slightly above the minimum threshold may not be detectable uniformly across the whole image. Faint sources can be detected only in regions of low noise, mainly in the centre of the image. To allow for this, the following procedure was adopted:

- The rms image was used to determine the limiting flux density at each pixel, based on a signal / noise criterion of 5x.
- For each radio source, a count was made of the number of pixels at which it would have been detectable.
- An adjustment factor was calculated as the total number of pixels divided by the number of pixels at which it could have been detected.
- Each source was weighted by its adjustment factor during the count.

In practice, the minimum flux density threshold was sufficiently high that only 116 out of the 1000 sources required a weighting adjustment of more than 1.3. There were 180 sources that needed no adjustment; that is, they would have been detected anywhere in the image.

An adjustment for incompleteness was made in a similar way. For each source whose integrated flux density is below 4.25 mJy, an adjustment factor was calculated from the formula in equation 5.1 and this weighting was applied during the count.

Note that an adjustment for the effect of smearing, which is sometimes made in calculations of this sort, is not required for the ELAIS-N1 data. Smearing leads to a decrease in the peak flux density without affecting the total flux density. However, when the flux data were originally extracted from the ELAIS-N1 image, no correction was made to the peak flux densities for the effect of smearing: crude calculations using the equations of Bridle and Schwab (1989) show that the maximum distortion to the peak flux density, which assumes a source is located at the edge of the catalogue area, is 2%. The measured peak flux densities are, therefore, the same as the catalogue values, removing the need to adjust for smearing.

There are two other issues that might distort the results, but where no adjustment has been made. Firstly, an extended source has a lower probability of detection than a point source of the same integrated flux density, biasing the source count

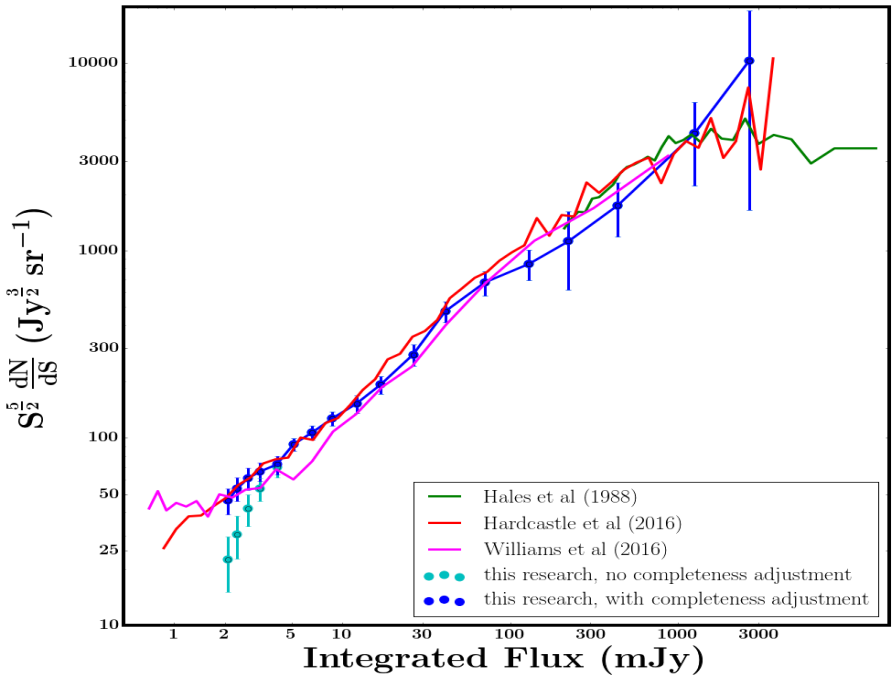

Figure 5.7 *Euclidean-normalised differential source counts at 150MHz. Also shown are other recent count determinations from Williams et al. (2016) and Hardcastle et al. (2016), as well as counts from the shallower 6C survey of Hales et al. (1988).*

towards unresolved sources and penalising extended sources. Resolution bias is a form of incompleteness. Secondly, noise in the estimates of the flux densities may scatter sources into adjacent bins and the net effect is an upwards bias, as discussed by Eddington (1913). In both cases, the effect is obviously most significant for faint sources. Given that a minimum integrated flux density of 2.0 mJy is being imposed in this analysis, then both these potential biases will have a negligible impact on the results and can be safely ignored.

The differential source count could now be calculated. As is standard, the counts are Euclidean-normalised and all are multiplied by $S^{5/2}$ so that the steep slope in the distribution does not obscure features in the chart; a uniform non-evolving population would then show a flat distribution. The results are shown in Figure 5.7. Also shown are the 6C survey source counts of Hales et al. (1988) at the bright end of the distribution, and the more extensive results from Hardcastle et al. (2016) and Williams et al. (2016) based on observations of the H-ATLAS and Bootes fields respectively; in each case, the frequency is consistent with 150

MHz. The distribution from this study is generally in excellent agreement with the other three results. In detail,

- The source counts without an adjustment for incompleteness are also plotted and these tend to confirm that incompleteness does indeed become an issue at flux densities below 4.25 mJy, as found in the previous section.
- At flux densities below 12 mJy, the source counts align very closely with those of Hardcastle et al. (2016).
- At flux densities between 12 mJy and 70 mJy, the source counts are between those found by Hardcastle et al. (2016) and Williams et al. (2016).
- At flux densities between 70 mJy and 1250 mJy, the source counts are lower than those in the other three distributions. It is possible that this is a consequence of the early selection criteria for the ELAIS fields to avoid known bright IRAS sources (Oliver et al., 2000).
- At flux density levels below 1.75 mJy, the source counts of Williams et al. (2016) and Hardcastle et al. (2016) diverge, probably because of their different treatment of the resolution bias. This tends to confirm that it was reasonable to ignore the effect of resolution bias at the flux densities used in this study.

The close agreement with the source counts in the literature provides reassurance that the conclusion from Section 5.2 – that the flux calibration of the LOFAR sources is accurate at the $\sim 10\%$ level – is valid.

5.5 Redshift Estimates

Redshift estimates for the 1180 galaxies in the ELAIS-N1 catalogue were obtained from a number of sources.

The Baryon Oscillation Spectroscopic Survey (BOSS) of the Sloan Digital Sky Survey III (the survey's ninth data release), as described by Bolton et al. (2012), included four special pointings that targeted radio sources within the ELAIS-N1 field. A positional crossmatch using a search radius of two arcseconds identified 293 matches with the ELAIS-N1 sources. BOSS targeted principally galaxies at

redshifts of under 0.8 and so these spectroscopic redshifts are almost all under one.

A further 45 spectroscopic redshifts were obtained from the SERVS Merged Spec-z Catalogue, a compilation of spectroscopic redshifts assembled from several sources by Mattia Vaccari (Vaccari, 2016). Eleven of these were originally obtained from the NASA/IPAC Extragalactic Database. Seven were calculated by Pérez-Fournon et al. (2009) within a sample of 70 infrared-luminous galaxies and quasars targeted by the Infrared Spectrograph (IRS) on board Spitzer. The remaining 27 were obtained from the eleventh and twelfth data releases from the SDSS survey, as described by Alam et al. (2015).

In total, therefore, spectroscopic redshifts were available for 338, or 29% of the galaxies in the ELAIS-N1 sample.

Photometric redshifts were available from three sources. As discussed in Tanaka et al. (2017), a catalogue of photometric redshifts was produced by the Hyper SuprimeCam Subaru Strategic Program (HSC-SSP). The HSC redshift estimates benefit from forced aperture photometry across five optical bands. If a source is detected in any one of the bands, then the flux is recorded through matched apertures in each of the other bands whether or not the fluxes in these bands are above the signal / noise threshold. The additional information so provided can significantly improve the accuracy of a photometric redshift estimate. However, the HSC redshift estimates suffer from the drawback that the photometry is based only on five optical bands, meaning that their reliability is comparatively poor outside a redshift range of 0.3 to 1.5. Within that range, where the observed bands straddle the 4000$\mathring{A}$ break, the photometric redshifts achieve an accuracy of $(|\Delta z|/(1+z) \sim 0.04$ and an outlier rate of about 10% for galaxies down to i = 25. A positional crossmatch with the ELAIS-N1 catalogue using a search radius of 2 arcseconds identified 1029 matches to the HSC catalogue.

A second set of redshifts was generated by Dr Ken Duncan, specifically for the catalogue assembled for this thesis. Where available, magnitudes for the 35 optical and infrared wavebands shown in Table 3.1 were obtained for each of the 1180 galaxies in the ELAIS-N1 catalogue and passed through the fitting process. Three sets of templates were used to analyse each source. Details are given in Duncan et al (2017, in press). The three sets of templates, "EAZY", "XMM-COSMOS" and "ATLAS", were selected in order to encompass the full range of galaxy and AGN types; they are described respectively by Brammer

et al. (2008), Salvato et al. (2009) and Brown et al. (2014). The three resulting photometric estimates were combined using a hierarchical Bayesian procedure in order to obtain the final photo-z. The wide wavelength coverage meant that the photometric estimates had the potential to be accurate over a wider redshift range than is the case for the HSC estimates. However, this advantage was tempered by the fact that apertures were not accurately matched across all datasets and that forced aperture photometry was unavailable where objects were undetected (instead, only a limiting magnitude was used).

Mauduit et al. (2012) calculated redshifts for the subset of sources in the SERVS catalogue via SED fitting with the HyperZ code (Bolzonella et al., 2000) and the Maraston stellar population templates (Maraston, 2005). Like the Duncan photometry, the SERVS photo-zs benefited from wide wavelength coverage – the U, g, r, i, z, Y, J, K, IRAC1[3.5] and IRAC2[4.6] wavebands – but did not have forced aperture photometry. Adjustments were made, however, to aperture correct all magnitudes to the same aperture size. Only one set of templates was used. Also, SERVS does not cover the full area used to construct the ELAIS-N1 catalogue; a positional crossmatch using a search radius of 2 arcseconds generated only 378 matches. Comparisons with known spectroscopic redshifts implied a redshift accuracy for the ELAIS-N1 field of $|\Delta z|/(1+z) = 0.011 \pm 0.072$.

Each of the three sets of photometric redshifts was compared with the BOSS spectroscopic redshifts and the results are shown in Figure 5.8. Also shown is a comparison between the Duncan and HSC photometric redshifts. The outliers in the HSC vs BOSS comparison are marked in red and blue, and these particular sources retain the same colour scheme in the other three charts. The charts make several points.

Firstly, there are 285 sources with both a BOSS and HSC redshift estimate. There is reasonable alignment, with 82% of the sources finding a discrepancy in the two redshift estimates of less than 20%.

Secondly, the fraction of Duncan photometric redshifts within 20% of their BOSS counterpart is very similar at 81% (225 out of a total of 278). The scatter for the "on-trend" sources is a little wider than in the HSC case.

Thirdly, there are only 134 sources with both a BOSS and SERVS redshift estimate. The scatter for the "on-trend" sources is comparatively wide. The proportion of outliers is similar to those for the other two comparisons.

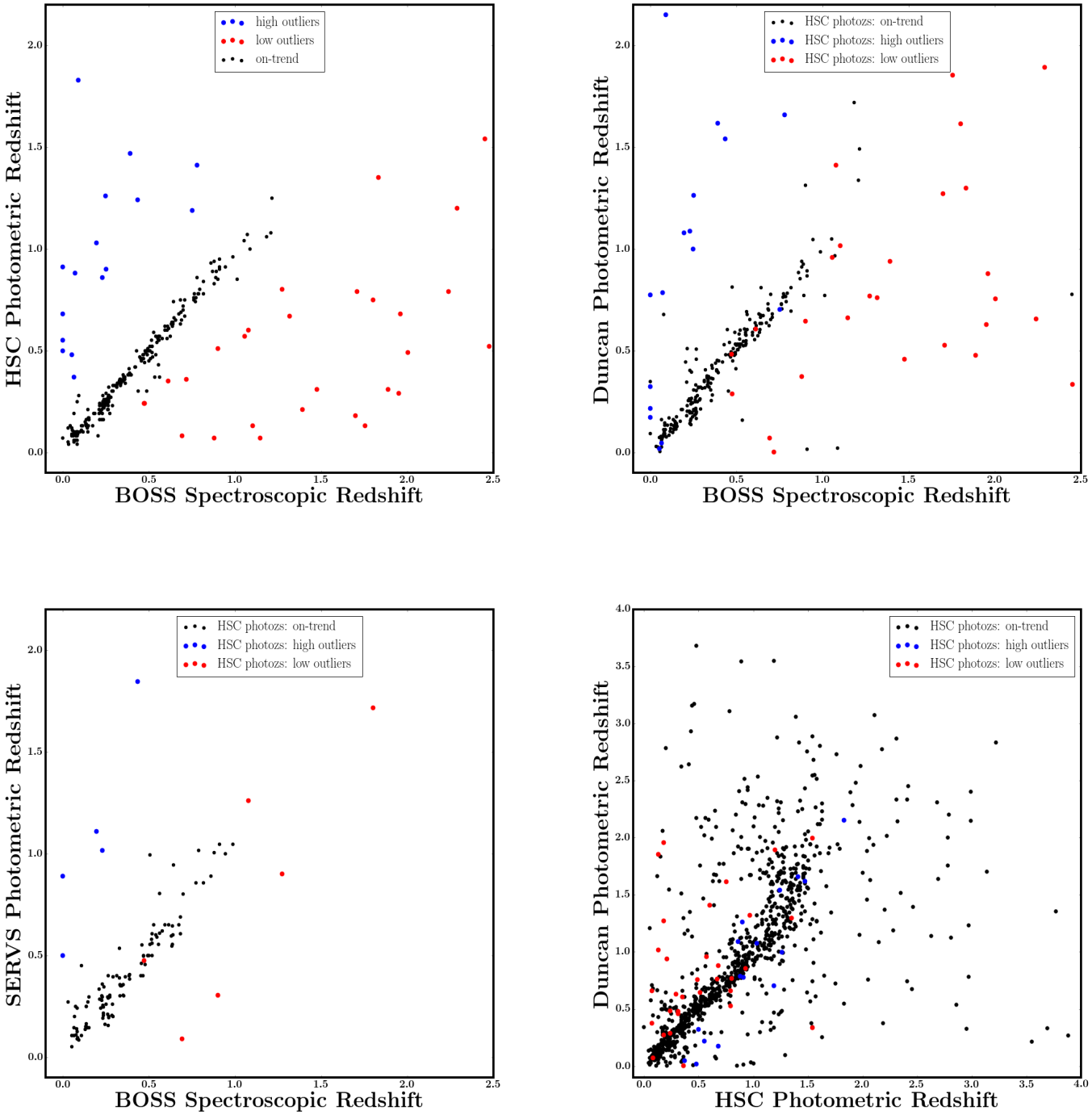

Figure 5.8 *Comparisons of the photometric redshifts produced from the HSC survey (top left chart), by Dr Ken Duncan (top right chart) and from the SERVS survey (lower left chart) against the BOSS spectroscopic redshifts. A comparison between the Duncan and HSC redshift estimates is shown in the lower right chart. The outliers from the HSC vs BOSS comparison are marked by red and blue circles in all four charts.*

Fourthly, where an HSC estimate is much higher or lower than the corresponding BOSS estimate, the other two photometric estimates tend to find a similar discrepancy. That is clearly highlighted in the lower right chart, with a large number of the red and blue circles marking redshift estimates that are consistent with each other. Although the default assumption here is that the photometric estimates are making consistent mistakes, it is possible instead that the spectroscopic redshifts are wrong if, for example, they are based on low signal-to-noise spectra or on a mis-identified single emission line.

Finally, the comparison between the Duncan and HSC redshift estimates shows a clear systematic offset in the redshift range between 1.2 and 1.5. The Duncan estimates benefit from the use of infrared magnitudes and are likely to be the more accurate here.

When allocating redshifts, use was also made of a putative relationship between the K-band magnitude and redshift, the "K-z" relationship that radio AGNs have been long known to follow (for example, Lilly and Longair, 1984). The relationship was derived by comparing the log of the BOSS spectroscopic redshifts against the K-magnitude, binning the sources according to K-magnitude, calculating the mean in each bin after discarding the points in the upper and lower deciles and then finding the best-fitting quadratic. The results are plotted in Figure 5.9 and the expression for the best-fitting quadratic was found to be:

$$log_{10}\, z = -0.01231\, Kmag^2 \;+\; 0.6476\, Kmag \;-\; 7.9766 \qquad (5.2)$$

Note that this is fitted as z(K) rather than the traditional K(z) because this approach minimises biases in redshift estimates (Brookes et al., 2006).

Similar relationships were derived for the i-band and [3.6 micron] magnitudes, although, as described below, less use was made of these. The i-band relationship was found in the same way as for the K-magnitude. and the expression was as follows:

$$log_{10}\, z = -0.01727\, imag^2 \;+\; 0.8964\, imag \;-\; 11.3725 \qquad (5.3)$$

There were too few sources with both a BOSS spectroscopic redshift and [3.6 micron] magnitude to derive a relationship that made physical sense. Accordingly, the K-magnitude relationship was adapted by assuming a typical offset between a detected [3.6 micron] magnitude and an undetected K-band magnitude and also assuming a normalisation adjustment. An optimisation procedure, comparing

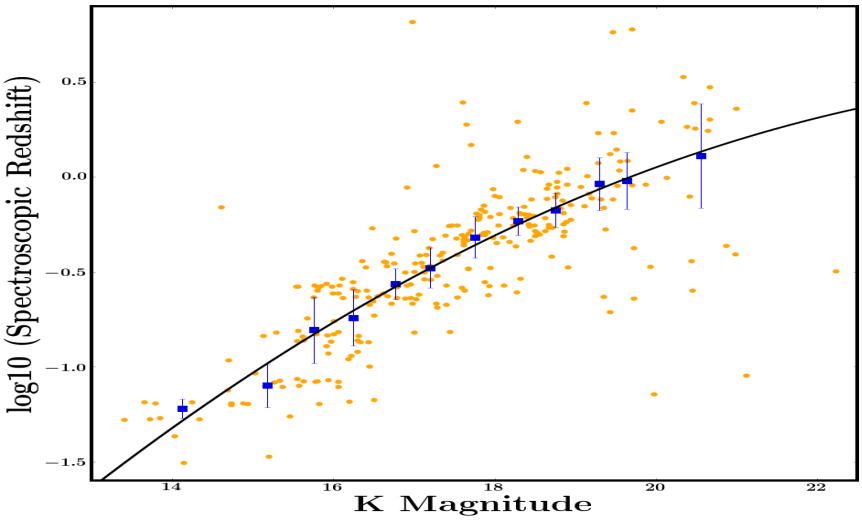

Figure 5.9 *The K-z relation based on a sample of 271 radio sources in the ELAIS-N1 field with spectroscopic redshifts from the Baryon Oscillation Spectroscopic Survey. The individual sources are shown as the orange-coloured points, while the blue squares show the mean redshift in each bin of K-band magnitude after discarding the points in the lowest and highest deciles. The black solid line overlaid shows the resulting best-fit relation, which is detailed in equation 5.2.*

observed and model values for the small number of sources that had both a detected [3.6 micron] magnitude and a spectroscopic redshift, was used to find the best estimates of these two parameters. The offset emerged as 1.47. Given that the mean offset when there are detections in both bands is +1.03, this appears a sensible estimate. The normalisation adjustment was reassuringly small, at +0.07. The expression is therefore:

$$log_{10}\, z = -0.01231\,([3.6] + 1.47)^2 + 0.6476\,([3.6] + 1.47) - (7.9766 - 0.07) \quad (5.4)$$

After taking all the points above into consideration, the procedure used to allocate redshift estimates was as follows (the allocation being made in the order shown):

- The spectroscopic estimates were all accepted, apart from eight of the outliers (see point below) – 285 from BOSS and a further 45 from the Vaccari catalogue.
- Those eight outliers had a warning flag in the BOSS catalogue and, significantly, were all in the red-dot category; that is, the spec-z estimate was much higher than the HSC photo-z estimate. These eight sources were

allocated redshift estimates according to their photometric redshifts, as described below (in fact, in one case, the Duncan photo-z coincided with the BOSS spectroscopic redshift).

- Sources with HSC photometric redshifts in the range 0.3 – 1.2 were accepted. There are 371.

- Duncan redshifts were accepted provided that the estimate was close to either the HSC photometric redshift, the SERVS photometric redshift or the redshift derived from the K-magnitude relationship. The criterion was adopted to avoid catastrophic outliers, given the lack of matched aperture photometry. A discrepancy was deemed to be acceptable if $\Delta z/(1+z) < 0.15$. 326 sources were allocated redshifts in this way.

- SERVS redshifts were accepted provided that they were consistent, using the definition above, with either the HSC estimate or the redshift resulting from the K-magnitude relationship. There are 10 in this category.

- A further 43 HSC redshifts were accepted. These are all outside the 0.3 to 1.2 range, but are consistent with one or both of the other photometric estimates or with the redshift from the K-magnitude relationship.

- 78 sources were given a redshift based purely on their K-magnitudes.

- 9 sources were given a redshift on the basis of their i-magnitudes.

- 13 sources were given a redshift on the basis of their [3.6 micron] magnitudes.

The allocation procedure does introduce some bias into the distribution of redshifts around the edges of the 0.3 – 1.2 redshift range. For example, considering all points with both an HSC and Duncan photo-z between 1.1 and 1.3, then a disproportionate number will be placed into the 1.1 – 1.2 bin at the expense of the 1.2 – 1.3 bin. However, in the analysis that follows, the sources will be allocated into redshift bins of 0.0 – 0.5, 0.5 – 1.0, 1.0 – 1.5, 1.5 – 2.0 and > 2.0 and, given that both cut-off points are in the middle of a bin, there should be no discernible impact on the results.

The distribution of redshifts is shown in Figure 5.10. The number of sources in the five redshift bins that will be used in the following analyses are 402, 318, 244, 135 and 81 respectively.

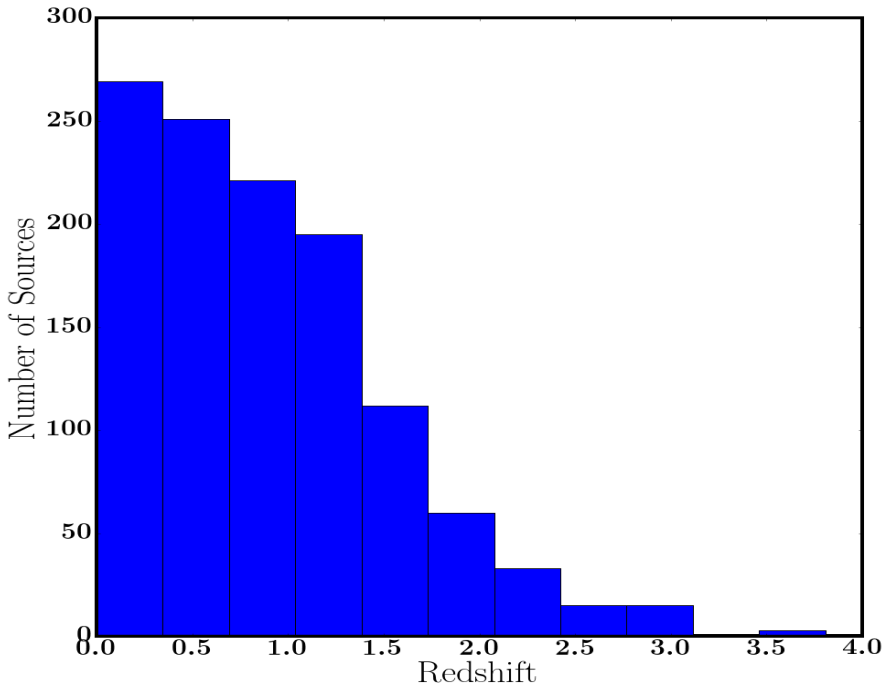

Figure 5.10 *The distribution of redshift estimates for the 1180 radio sources.*

5.6 The Classification of Radio Sources

It is now necessary to separate the radio sources into star-forming galaxies (SFGs), jet-mode AGNs and radiative-mode-AGNs. BOSS spectroscopic data are available for 255 of the sources and this was used by the Portsmouth group (Thomas et al., 2013) to divide the sources into Seyfert, LINERs and SFGs. The classification used the BPT diagnostic tests, described in Section 2.3.3. For 103 sources, however, either no classification was possible or the classification was ambiguous, leaving 152 radio sources, 13% of the total, to be given relatively secure identifications based on their spectral lines.

A number of diagnostic tests were used to place the other 87% of radio sources into their appropriate categories. The theory underlying the different diagnostic tests is first briefly discussed and the diagnostic tests themselves are then described. Each test has its own specific strengths and weaknesses and care was taken to combine the tests in the most efficient way. The procedure used to carry out the classification is set out at the end of this section.

5.6.1 Far-infrared Diagnostics

It has been known for over 40 years (van der Kruit, 1973) that the far-infrared and radio emission of SFGs are tightly correlated. The far-infrared emission is believed to come predominantly from warm dust that has been heated by the energy output from O and B stars to temperatures in the range between 30K and 60K. The radio emission is believed to emanate from synchrotron radiation that is the result of shocks from supernovae. In other words, both the far-IR and radio emission are closely related to star formation within the galaxy, explaining the correlation. The importance of the relationship means that it has been extensively studied in the intervening period; although there are differing conclusions from the many research papers, a consensus appears to be developing that:

- The correlation is very tight in the local universe (Sargent et al., 2010).
- The IR - radio relation is broadly linear in log space for the local universe.
- There is no significant redshift evolution up to z = 0.5 (Smith et al., 2014) and probably none up to a redshift of z = 1.4 (Sargent et al., 2010). At higher redshifts, the relation remains linear, although the slope may change (for example, Murphy, 2009).
- The relation holds for galaxies of different morphological types - ellipticals (Bally and Thronson, 1989), spirals (Hummel et al., 1988) and ultra-luminous infrared galaxies (Bressan et al., 2002).

The IR - radio correlation allows a straightforward means of identifying AGNs. Galaxies with radio emission higher than that predicted by the IR - radio relation are likely to host a radio-loud AGN. The diagnostic test devised by Hardcastle et al. (2016) for 150 MHz radio data is used in this work, in a slightly adapted form, and also a test devised by Bonzini et al. (2013).

5.6.2 Mid-infrared Diagnostics

The spectra of stellar populations are dominated by the composite blackbody curve and peak at approximately 1.6 microns in the rest frame. The spectra dip through the mid-infrared before rising into the far-infrared due to emission from warm dust with a temperature of around 35K that has been heated by star

formation. By contrast, dust surrounding an AGN tends to be warmer, emitting in the mid-infrared, and leading to a power-law spectrum in the ultraviolet to mid-infrared. So, in direct contrast to the situation in the ultraviolet where AGNs tend to be bluer than galaxies which are experiencing the rising portion of the stellar spectra, in the mid-infrared AGNs tend to be redder as galaxies sample the falling part of the blackbody spectra. There is also the considerable advantage that the mid-infrared emission from AGN-heated dust is itself relatively insensitive to intervening obscuration and so mid-infrared selection is capable of identifying many heavily-obscured AGNs. Figure 5.11, taken from Donley et al. (2012), illustrates these points: galaxies with no (red line) or little (yellow line) contribution from an AGN display a dip in their spectra between the 1.6 micron bump and the long-wavelength emission that comes from dust heated by star formation, whereas the spectra of AGNs (blue and purple lines) are flat or rising through the mid-infrared; and the picture does not change due to obscuration (lower panel).

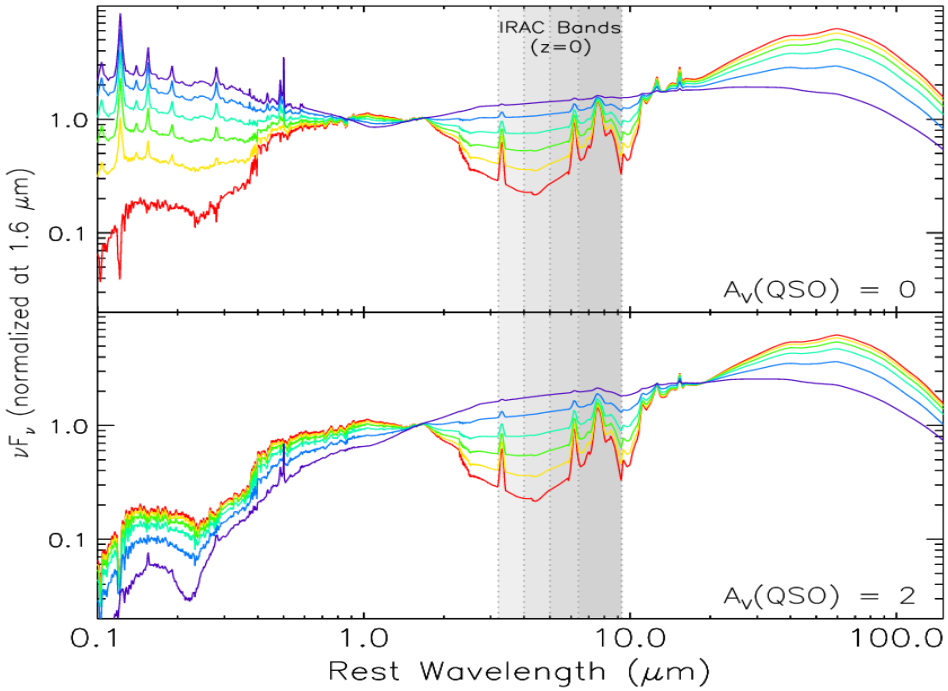

Figure 5.11 *Six composite SEDs, scaled to give 1 - 10 μm AGN contributions ranging from 0% (red line) to 95% (purple line). The top panel applies to unobscured AGNs and the lower panel to obscured AGNs (assuming extinction of $A_V = 2$). Source: Donley et al. (2012).*

There are a number of diagnostic tests in the literature which exploit this in order to separate SFGs from AGNs. Two tests used here are a diagnostic first described by Stern et al. (2005) and later modified by Donley et al. (2012), and

a test developed for this thesis.

5.6.3 Properties of the Radio Sources

There are a number of properties of the radio source that can be exploited. Most obviously, any source that is part of a multi-component system must be an AGN (unless associated with a very nearby and highly resolved SFG). Sources with a large physical size, taken in this analysis to be over 100 kpc, and extended emission are very likely to be AGNs. A source whose emission is extended and consists of multiple Gaussian components is also likely to be an AGN, although this is not clear-cut since a minority of such sources could consist of merging SFGs.

5.6.4 The Diagnostic Tests

The diagnostic tests used flux densities or magnitudes from a number of wavebands. The sources of the data are shown in Table 5.5.

Table 5.5 *The sources of multiband data*

Survey	Waveband
PanSTARRS Medium-Deep	g, r and y bands
UKIDSS	J and K bands
SWIRE	3.6, 4.5, 5.8 and 8.0 microns
MIPS	24 microns
HERMES	24 and 250 microns
LOFAR	150 MHz

In order to test the effectiveness of the diagnostic tests under consideration, a subsample of sources that are highly likely to be AGNs was assembled and the recovery rates calculated from each of the diagnostic tests. The subsample consisted of 289 objects, comprising 57 multi-component sources, 52 sources that had extended emission and a physical size greater than 100 kpc and 180 sources that were classified as AGNs by the Donley et al. (2012) test. As described shortly, this test is highly reliable in selecting AGNs, but suffers from incompleteness. The other statistic that is relevant is the proportion of sources that have the necessary data to allow each test to take place. The results, which are summarised in Table

Table 5.6 *The effectiveness of various diagnostic tests*

Test	Devised by or Properties tested	Number of Sources that can be tested (out of 1180)	289 AGNs identified as AGNs	SFGs	No Decision	No Data
Test 1	Hardcastle et al. (2016)	1153	215	8	57	9
Test 2	Bonzini et al. (2013)	393	95	0	0	194
Test 3	Donley et al. (2012)	760	190	0	99	0
Test 4	Stern et al. (2005)	760	163	8	0	118
Test 5	this study	349	74	8	0	207
Test 6	multi-Gaussian	1180	134	0	155	0
Test 7	physical size	1180	120	0	169	0

5.6, are now discussed in conjunction with a description of each of the diagnostic tests.

The Hardcastle et al. (2016) Test

Figure 5.12 illustrates the test devised by Hardcastle et al. (2016), based on the far-infrared - radio relation. The objects in the subsample of 289 objects are coloured red and the rest are coloured blue. Hardcastle et al. (2016) identified SFGs as those objects with:

$$log_{10}\, L_{250\,\mu m} > log_{10}\, L_{150\,MHz} + log_{10}\,(5.0) \tag{5.5}$$

shown as those above the black line in the diagram. The majority of the 289 objects that are believed to be AGNs are located below the dividing line, but a significant number of the higher-luminosity sources (those with values of $log_{10}\, L_{250\,\mu m}$ above around $25.6\, WHz^{-1}$) lie above the line. These are likely to be radiative-mode AGNs residing in a galaxy with ongoing star formation. In this work, such objects should be classified as AGNs. To reflect that, the diagnostic test was amended so that all objects with excess radio luminosity, those below the black line, were classified as AGNs, those in the region above the black line and below the magenta line were classified as SFGs and those above the magenta line were initially left unclassified.

With that further condition added, the Hardcastle test appears to be effective at

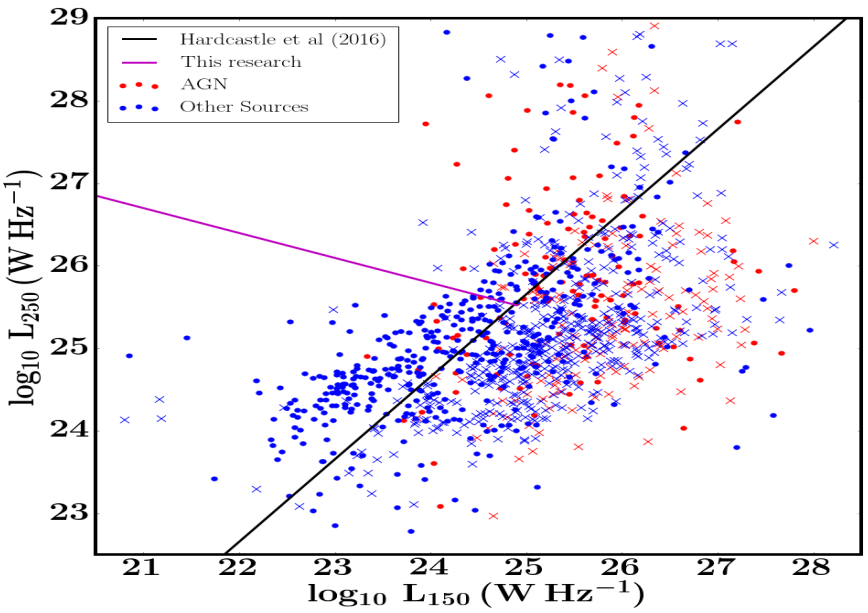

Figure 5.12 *The Hardcastle et al (2016) Diagnostic Test. The subsample of 289 AGNs are coloured red and the remaining objects are coloured blue. Those objects that rely on a limit to calculate L_{250} are marked by crosses. The black and magenta lines are used to classify the sources into AGNs and SFGs – see text.*

correctly identifying AGNs and, to a lesser extent, SFGs. Only eight objects from the subsample of AGNs fall into the SFG region, 215 of the AGNs were correctly identified and 57 of the AGNs were left unclassified.

Just over half of the objects were undetected in the infrared and an upper limit was used to obtain their 250 micron luminosity; they are marked by crosses in the chart. The key point is that very few are likely to be mis-classified as a result, providing reassurance that this test is capable of classifying a very high proportion of the LOFAR sources: only 2% of sources do not have the data to allow the test to be carried out.

The Stern et al. (2005) and Donley et al. (2012) Tests

The test originally devised by Stern et al. (2005) compares the [3.6 μm] - [4.5 μm] colour against the [5.8 μm] - [8.0 μm] colour, with AGNs identified as those lying within the "Stern" wedge, as marked by the black lines in Figure 5.13. Donley et al. (2012) later argued that, while the Stern wedge was suitable for shallow mid-

infrared data, deeper data risked contamination from SFGs at higher redshifts entering the wedge at bluer [5.8 μm] - [8.0 μm] colours. That can be seen in the chart: the radio sources are split into four categories by redshift, showing that a cluster of galaxies with redshifts of over one and [5.8 μm] - [8.0 μm] colour of around zero lie just inside the wedge. In addition, Donley et al. (2012) argued that sources with a [3.6 μm] - [4.5 μm] colour towards the bottom of the Stern wedge could not be definitively classified as AGNs. Accordingly, they proposed a set of stricter criteria. Defining $x = log_{10}\frac{S_{5.8}}{S_{3.6}}$ and $y = log_{10}\frac{S_{8.0}}{S_{4.5}}$, an object should be classified as an AGN only if it fulfilled all of the following conditions:

(i) x $>$ 0.08

(ii) y $>$ 0.15

(iii) y $>$ 1.12x - 0.27

(iv) y $<$ 1.12x + 0.27

(v) $S_{4.5} > S_{3.6}$

(vi) $S_{5.8} > S_{4.5}$

(vii) $S_{8.0} > S_{5.8}$

The reason for the final three conditions – that the fluxes should be rising monotonically across the mid-infrared range – can be easily seen from Figure 5.11, but is a demanding criterion.

The sources that would be classified as AGNs under these criteria (those included in the subsample of AGNs) are marked in Figure 5.13 by triangles. The improved reliability comes at a cost, however. As discussed in their paper, the stricter criteria mean that completeness is poor for AGNs with luminosities below $L_{2-10\,keV} = 10^{44} erg\,s^{-1}$, luminous AGNs with heavy obscuration and those with especially bright host galaxies. Also, as argued by Bonzini et al. (2013), Type 2 Seyfert galaxies are also easily missed. The incompleteness is confirmed by poor recovery rates for the subsample of AGNs. Excluding those selected by the Donley test itself, the strict criteria recover only 10 out of the remaining 109 objects in the subsample. For the purposes of this study, the Donley test was used in order to identify AGNs with a high degree of certainty. At a later stage in the selection process, the Stern test was also used to identify both AGNs and

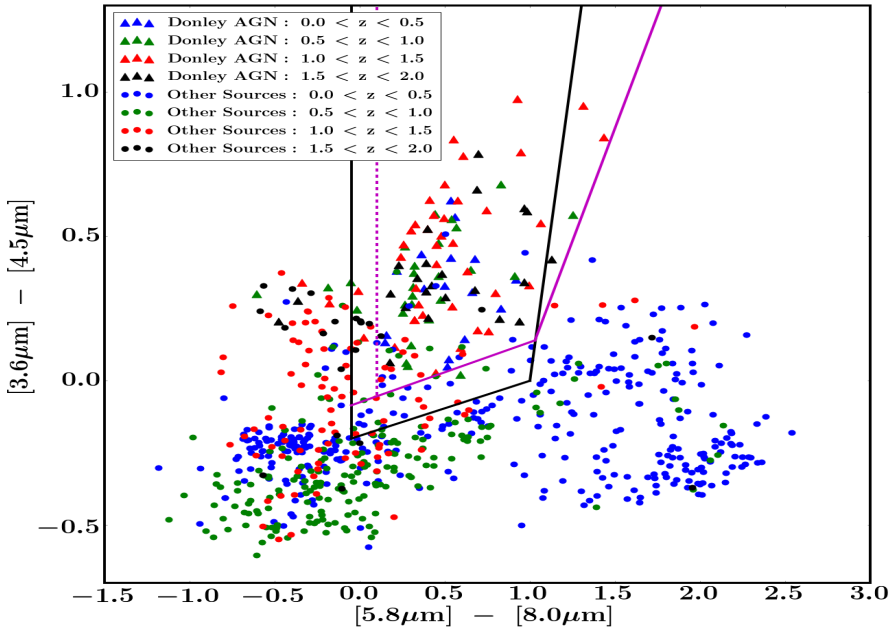

Figure 5.13 *The Stern and Donley Diagnostic Tests. The radio sources are categorised by redshift. The objects classified as AGNs under the Donley test are marked by triangles. The objects classified as AGNs under the Stern test are those within the wedge defined by black lines. The wedge marked by magenta shows the revised Stern test as adapted for use in this thesis.*

SFGs, but amended to minimise the shortcomings identified by Donley et al. (2012). The revised wedge is marked by the solid magenta line in Figure 5.13. A further restriction was placed on sources with a redshift of over 1.0; they also had to be placed to the right of the dashed line in order to avoid wrongly including high-redshift SFGs.

The Donley/Stern tests can also be used to identify SFGs and to separate AGNs into radiative-mode and jet-mode objects. Those objects identified as AGNs by the Donley and Stern tests are likely to be radiative-mode AGNs. Any objects located outside the wedge that have been identified as AGNs by other tests are likely to be jet-mode AGNs. And those low-redshift galaxies clustered in the bottom right-hand side of the diagram are SFGs, as evident from Figure 4 of Donley et al. (2012).

51% of the radio sources have detections in all four wavebands used in these two tests. A further 13% of sources are missing a detection in only one band, allowing

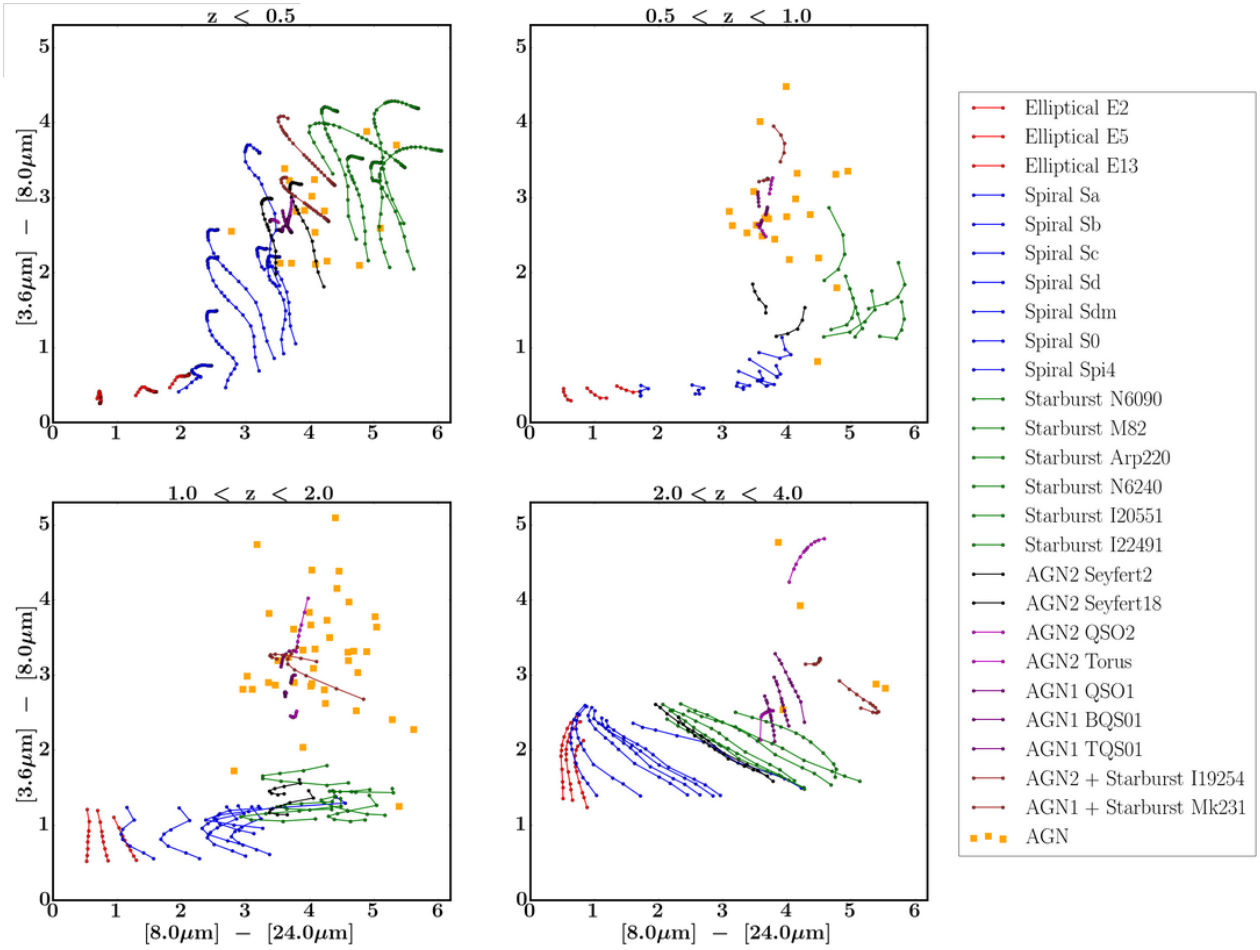

Figure 5.14 *Template tracks from Polletta et al. (2007) have been placed onto a colour-colour diagram and split by redshift. The orange squares are objects drawn from a subsample of 289 "secure" AGNs assembled for this thesis.*

the test to be carried out using an upper limit.

Another Mid-infrared Diagnostic Test

A second test based on mid-infrared magnitudes was developed for this research. A weakness of the Stern and Donley tests is that no allowance is made for redshift. Polletta et al. (2007) constructed a library of 25 templates containing different types of ellipticals, SFGs and AGNs, as shown in the side panel of Figure 5.14. These template tracks were divided into four redshift bins and placed onto a colour-colour diagram. The colours that provide the clearest demarcation between the AGN, elliptical, spiral and starburst galaxies are [3.6 μm] - [8.0 μm] and [8.0 μm] - [24.0 μm]. The results are shown in Figure 5.14.

There is little overlap between the AGNs (purple and brown tracks), starburst galaxies (green tracks), spiral galaxies (blue tracks) and ellipticals (red tracks), although at redshifts below 0.5 the region containing AGNs is tightly bounded between the starburst and spiral galaxies. This diagnostic test has, therefore, the potential to identify AGNs accurately. That does indeed appear to be the case: as can be see in Figure 5.14, 74 of the subsample of AGNs would be correctly identified and 8 would be misclassified. The test, however, suffers from the fact that only 30% of sources can be tested unless limits are employed. The regions containing each type of galaxy, although distinct, tend to be only narrowly separated and there is a risk that relying on limits will lead to a significant proportion of mis-classifications.

The Bonzini et al. (2013) Test

The test of Bonzini et al. (2013) also exploits the infrared - radio correlation, but using the 24 micron flux in place of the 250 micron flux and incorporating redshift information to account for K-corrections. The diagnostic test is based on the ratio of $q = log_{10}\frac{S_{24\mu m}}{S_{1.4\,GHz}}$. The ratio, as a function of redshift, was derived using the SED of M82. Information on the mean value of q(z=0) = 1.31 and the scatter around the mean, $\sigma = 0.35$, for a sample of local galaxies was available from Sargent et al. (2010). q(z) was normalised to this mean value and a diagnostic line set at a level 2σ below q(z). Bonzini et al. (2013) classified all sources under this line as radio-loud AGNs. The sources above the line were classified as radio-quiet AGNs if they satisfied the Donley et al. (2012) test and SFGs otherwise.

In this study, the Bonzini et al. (2013) test was used solely as a means of dividing AGNs into their two sub-categories. It was used at the end of the classification procedure for those sources that had not already been classified by other diagnostic tests. In order to calculate the q-values, 24 micron flux densities were obtained from the MIPS data and 150 MHz flux densities were adjusted onto the 1.4 GHz basis using $\alpha = 0.75$. Figure 5.15 illustrates the situation. Those AGNs that had already been categorised are coloured red (radiative-mode AGNs) and blue (jet-mode AGNs). The sources requiring classification by this test are coloured green; those with an observed 24 micron flux density are marked with circles and those where the flux density is an upper limit are marked by arrows (to make the chart easier to read, the already-classified AGNs are not divided in this way). The diagnostic line used by Bonzini et al. (2013) is shown in black.

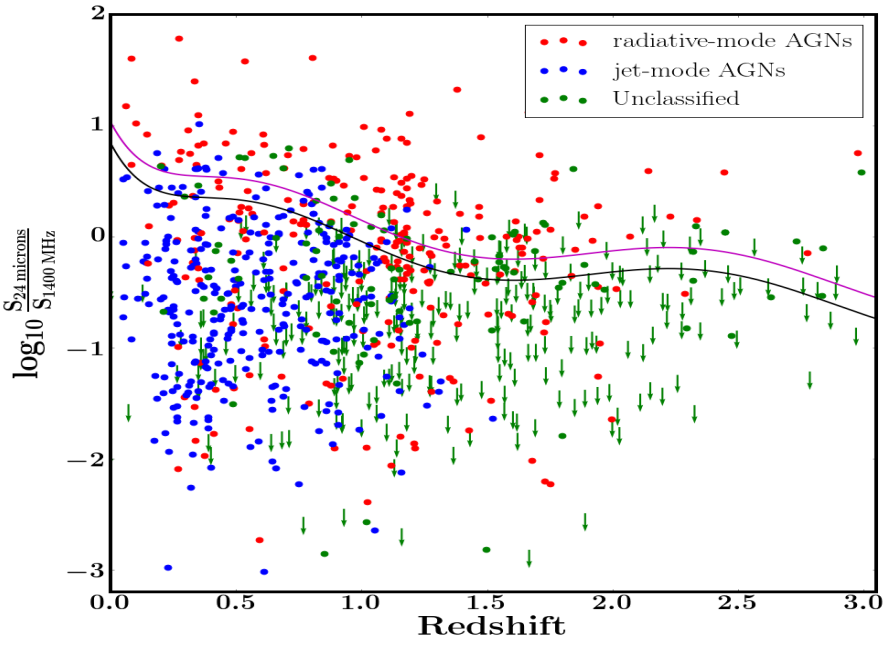

Figure 5.15 *The Bonzini et al. (2013) Diagnostic Test. The AGNs that have been classified by other tests are coloured blue (jet-mode) and red (radiative-mode). Sources classified by this test are coloured green, with circles showing those with observed 24 micron flux densities and arrows denoting those with upper limits. The diagnostic line for AGNs with observed fluxes is shown in black; the diagnostic line for AGNs with flux density limits is shown in magenta.*

The test appears to be reasonably effective in separating radiative-mode and jet-mode AGNs. If, however, the classifications made prior to this test are accurate, then there does appear to be some cross-contamination, especially at redshifts around and above z = 1. The implicit assumption underpinning the test is that the infrared and radio properties of SFGs do not change with redshift since the diagnostic line was calibrated from a set of local galaxies; it is possible that this assumption is challenged at higher redshifts. Another factor may be that, since not all radiative-mode AGNs have extremely strong AGN-torus signatures, then the absence of these signatures does not necessarily guarantee that an object is a jet-mode AGN.

Three-quarters of sources have only a limit as the infrared flux density. For most, this should not affect the classification since they already are located well below the diagnostic line. A second dividing line was drawn as q(z) + 0.2, shown in magenta, and was used as the diagnostic line for those sources with limits.

Given the risk of mis-classification at higher redshifts, those AGNs classified under this test as jet-mode and with a redshift of over one were subjected to a further check, discussed in the next sub-section.

A Diagnostic Test using Optical Colours

A crude division into radiative and jet modes is possible using optical data to separate sources across the "green valley". The test applied to galaxies in the local universe, discussed in Smolčić (2009), finds a separation at a g - r colour of 0.8, although this is not a particularly clean division. Figure 2 in that paper suggests that of the order of 20% of sources may be mis-classified. That is confirmed here: using the g - r test on the 582 HERGs and LERGs identified ahead of the Bonzini et al. (2013) test results in 22% of the sources switching category. Nevertheless, this test was adapted and used as a check on the high-redshift separation effected by the Bonzini test. Those AGNs classified as jet-mode and with a redshift between 1.0 and 1.5 were accepted only if their [y-band] - [J-band] colour exceeded 0.7; those at higher redshifts were accepted only if their [J-band] - [K-band] colour exceeded 0.7. These colours broadly replicate a rest-frame g - r colour and the division at 0.7 ensures that only sources firmly in the radiative-mode regime were re-classified.

The Classification Procedure

The procedure used to categorise the radio sources is now described. The first step was to divide them into AGNs and SFGs, which was carried out as follows:

- The 57 multi-component radio sources were classified as AGNs.
- 52 sources with extended emission and a physical size of more than 100 kpc were classified as AGNs.
- The Hardcastle et al. (2016) test was applied to the remaining 1071 galaxies, with 681 sources identified as AGNs. At this stage, no source was classified as a SFG.
- 94 of the remaining sources had classifications based on BOSS spectroscopic data; the BPT test classified 16 of these as AGNs and 78 as SFGs.

- The Donley test could be performed on 238 of the remaining sources, finding 38 as AGNs.
- The test developed in this thesis was used on the remaining sources and identified a further 11 AGNs - these are objects unambiguously within the regions occupied by the AGN template tracks.
- Having now made comparatively secure identifications of AGNs, the 247 remaining sources were passed again through the Hardcastle et al. (2016) test and the magenta line used to separate SFGs from AGNs. 228 sources were able to be categorised – 103 as SFGs and 125 as AGNs (those located above the magenta line in Figure 5.12).
- The modified Stern test found one further AGN and 4 SFGs.
- That left 14 sources. Four of these were at redshifts of between 0.5 and 1.0 and the remainder at redshifts over one. This is unsurprising since the absence of detections explain why these sources were unable to be diagnosed in the tests above. All of the sources have a physical size of over 60 kpc and the emission from the two smallest comprises multi-Gaussians. All 14 sources were classified as AGNs.

Overall, therefore, 185 SFGs and 995 AGNs were identified. The proportion of radio sources categorised as SFGs of 16% is considerably lower than the 30% found by Hardcastle et al. (2016). There are two reasons for the discrepancy: the survey of Hardcastle et al. (2016) is deeper than that used in this research, allowing a greater number of SFGs at higher redshift to enter their sample; and there is a difference in definition. For the purposes of this study, galaxies exhibiting both star-formation and AGN activity have been classified as AGNs – typically those above the magenta line in Figure 5.12 – whereas Hardcastle et al. (2016) have included those within the SFG category.

The subdivision of the AGNs into HERGs and LERGs proceeded as follows. First, the BPT classifications were adopted, identifying 35 and 50 radiative-mode and jet-mode AGNs respectively. Second, the Stern et al. (2005) test found a further 167 radiative-mode and 256 jet-mode AGNs. Third, the test developed in this study (based on a comparison of the [3.6 μm] - [8.0 μm] and [8.0 μm] - [24.0 μm] colours in four redshift ranges) identified 32 radiative-mode and 19 jet-mode AGNs. Finally, the Bonzini test, with the check using the rest-frame g - r colour, identified 179 radiative-mode AGNs and 247 jet-mode AGNs. There were

10 radio sources that could not be categorised. These were all at redshifts over 2 and are outside the redshift range used to investigate the luminosity functions. These were left unclassified.

In total, the 995 AGNs divided into 413 radiative-mode, 572 jet-mode and 10 unclassified objects. As expected, the proportion of radiative-mode AGNs increased sharply with redshift: the proportions were 22%, 24%, 55%, 66% and 93% for redshifts under 0.5, between 0.5 and 1.0, between 1.0 and 1.5, between 1.5 and 2.0 and over 2.0 respectively.

5.7 Luminosity Functions

Luminosity functions could now be constructed using the standard formalism developed by Schmidt (1968) and Condon (1989), with $\rho = \sum_i \frac{1}{V_{max,i}}$. The calculation of V_{max} was similar to the method used to derive the source count, here calculating the maximum volume to which a source is visible above a given luminosity, and again an allowance for incompleteness was made. Luminosity functions out to a redshift of two were calculated for the whole AGN population and also for the radiative and jet modes separately. Of prime interest in this thesis is the evolution of the jet-mode AGNs.

Care was taken to recognise that the sample is flux restricted which imposes minimum luminosity thresholds at each redshift and, as discussed above, these need to be folded into the calculation of V_{max}. No datapoints below these thresholds are included within the analysis.

The error bars shown in the charts that follow are based simply on Poissonian errors, which will be the principal source of uncertainty in the results. No account has been taken of possible errors in the calculation of the redshifts, in the calculation of the incompleteness function, in the classification of the radio sources and in the extraction of the flux densities from the LOFAR image. The additional uncertainties are unlikely to compromise the conclusions, but when viewing the following Figures, it should be noted that the error bars underestimate the uncertainties.

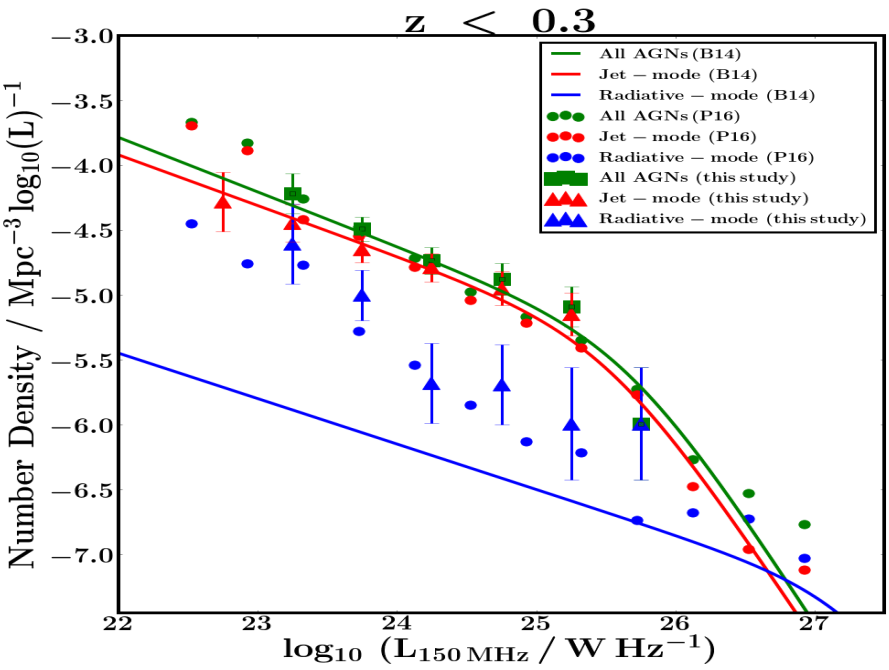

Figure 5.16 *The luminosity functions for the local universe derived in this study for the whole AGN population (green squares), jet-mode AGNs (red triangles) and radiative-mode AGNs (blue triangles). A comparison is made with the functions derived by Best et al. (2014) (solid lines) and the datapoints from Pracy et al. (2016) (circles); error bars are not shown for these latter two sets of data to improve clarity.*

5.7.1 A Comparison with Luminosity Functions in the Literature

The results for the local universe – redshifts below 0.3 – are shown in Figure 5.16. The sample used in this work is not designed to examine accurately the local luminosity functions given its comparatively small areal coverage of 6.8 square degrees, and indeed that is not the focus of this thesis. Nevertheless, this redshift range is useful in allowing a comparison to be made with the results from Best et al. (2014) and Pracy et al. (2016) and providing a sanity check on the calculations underlying the luminosity functions. In order to make the comparison, the luminosity functions derived by Best et al. (2014) and Pracy et al. (2016) have been converted from a frequency of 1.4 GHz onto a frequency of 150 MHz assuming a spectral index of $\alpha = 0.75$. There is close agreement with the literature results.

The luminosity functions for the entire AGN population are shown in green.

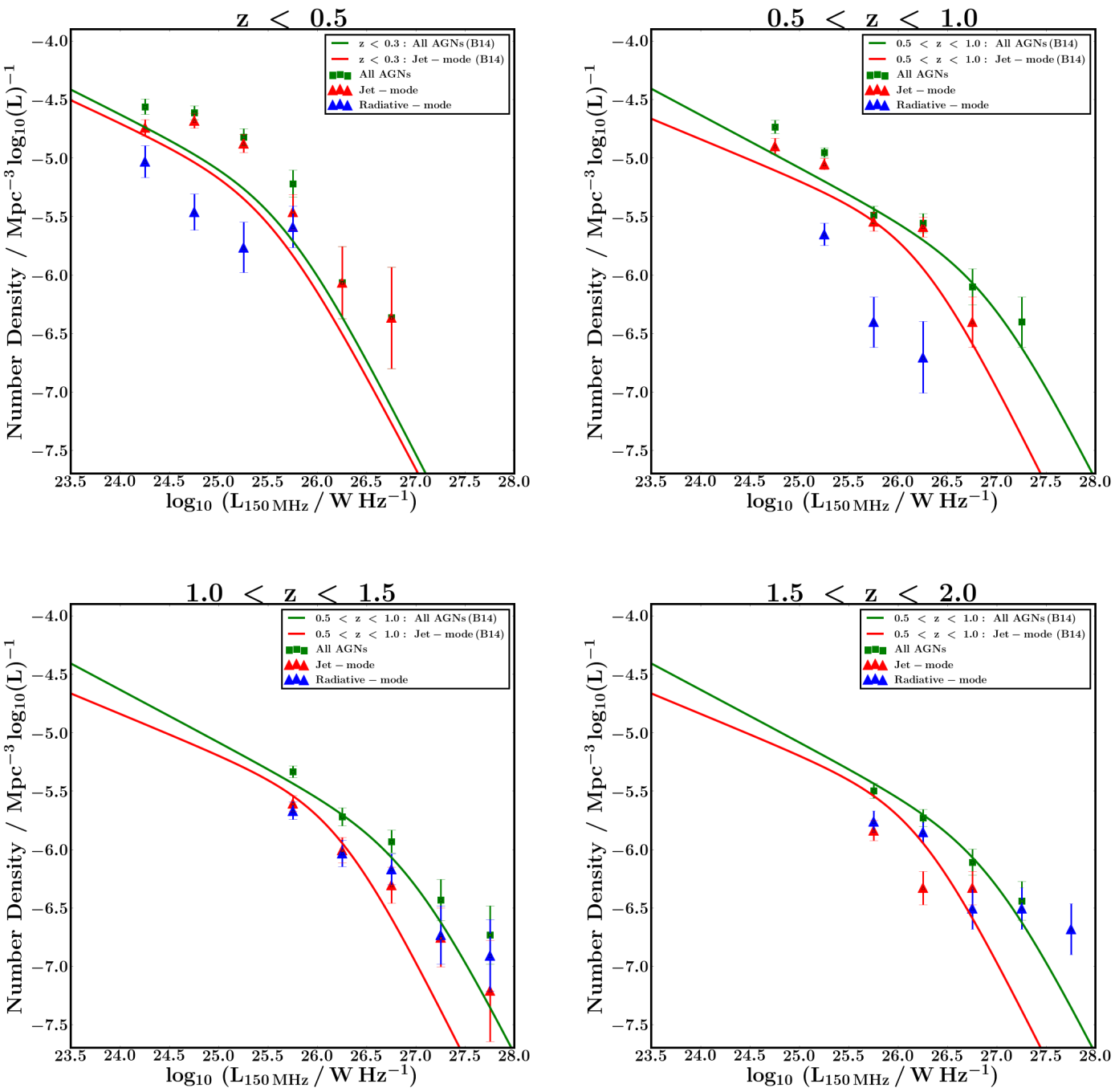

Figure 5.17 *The luminosity functions by redshift range for the whole AGN population (green squares), jet-mode AGNs (red triangles) and radiative-mode AGNs (blue triangles). For comparison, the functions derived by Best et al. (2014) are shown in solid lines.*

The datapoints in this sample (green squares) align closely with the luminosity function found by Best et al. (2014) (green line), although this sample has only one datapoint after the break (and that with a large uncertainty) which means that it is not possible to determine accurately the break point in the function. There are small discrepancies between the results of Best et al. (2014) and Pracy et al. (2016), with the latter finding a steeper slope below the break and a shallower slope thereafter; the results from this investigation align more closely with those of Best et al. (2014).

All three luminosity functions for the jet-mode AGNs align closely (red symbols and line), although there are no data points after the break in this sample. The data points for the radiative-mode AGNs in this sample are consistent, given the large uncertainties, with those of Pracy et al. (2016). Here there is a difference in definition which invalidates a direct comparison with the function found by Best et al. (2014): a larger proportion of galaxies with both star formation activity and radio-quiet AGN activity were placed into the SFG category in that study.

The luminosity functions in four redshift ranges up to z = 2 are shown in Figure 5.17. The functions derived by Best et al. (2014) for redshifts below 0.3 are included in the top left chart and those for redshifts between 0.5 and 1.0 are included in the other three charts. In the redshift range between 0.5 and 1.0, the results from this work find a higher space density at the faintest luminosities than Best et al. (2014) do, but otherwise the results are consistent. This is important. The two sets of results show close enough agreement at redshifts below 1.0 to suggest that the sample constructed for this thesis is capable of testing the set of models hypothesised in Best et al. (2014) out to higher redshifts.

Another point that emerges from Figure 5.17 is that in the highest redshift range at log luminosities between 26.0 and 27.0 the division between the jet-mode and radiative-mode AGNs appears out of line with the pattern elsewhere. The Bonzini test carried out the segregation in this redshift / luminosity parameter space and it is possible that, as briefly mentioned in 5.6.4, this test becomes less effective at higher redshifts.

5.7.2 The Evolution of the Luminosity Functions

Best et al. (2014) derived their luminosity functions using a broken power law

function:

$$\rho = \frac{\rho_0}{(\frac{L}{L_0})^{\beta} \; + \; (\frac{L}{L_0})^{\gamma}} \tag{5.6}$$

where ρ_0 is the space density in units of number per $log_{10}L$ per Mpc^3, L_0 is the luminosity break, and β and γ define the slopes before and after the break respectively.

They found that the luminosity function of the radiative-mode AGNs evolved positively up to z = 0.75. The evolution was constant across the luminosity range, consistent with a pure density evolution model and little or no change in L_0. This analysis broadly supports that conclusion. It is difficult to draw firm conclusions beyond a redshift of 0.75 because of the paucity of datapoints and high uncertainties, but a reasonable interpretation from the right-hand chart in Figure 5.18 is that the evolution continues between z = 1.0 and z = 2.0 and possibly at a broadly similar pace. That would be consistent with derivations of the total luminosity function (for example, Rigby et al., 2011) which at these luminosities and redshifts is dominated by the radiative-mode population.

Best et al. (2014) found that the evolution of the jet-mode AGNs was more

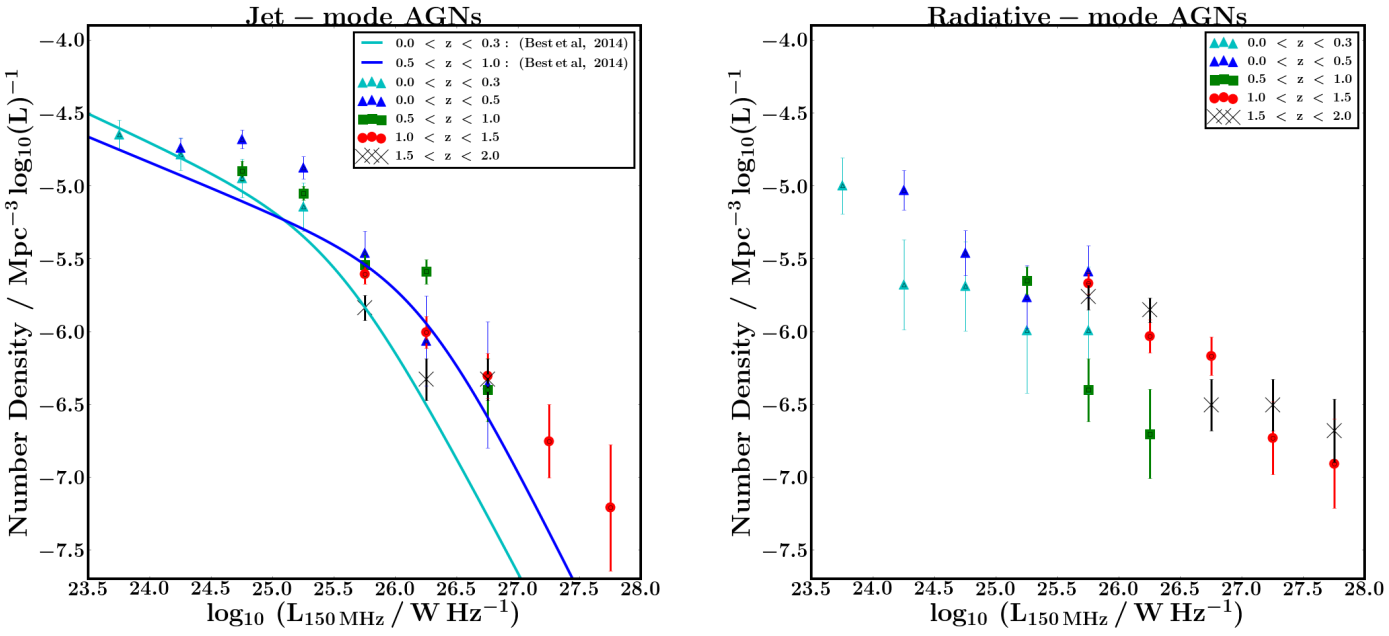

Figure 5.18 *The evolution of the luminosity functions of jet-mode AGNs (left-hand chart) and radiative-mode AGNs (right-hand chart). The datapoints are from this study and the solid lines in the left-hand chart are taken from Best et al. (2014).*

complex. They concluded that at the lowest luminosities the space density remains constant up to z $\sim$ 0.5 and then declines out to z = 1.0, at moderate luminosities the space density increases to z $\sim$ 0.5 and then declines, and at the highest luminosities the space density increases right out to z = 1.0. A visual examination of Figures 5.17 and, in particular, 5.18 broadly confirms these findings. The luminosity function appears to evolve positively between redshifts of 0.3 and 0.5. There is a suggestion that the evolution might be less strong at the lowest luminosities as found by Best et al. (2014), although this is based on just one datapoint. Between redshifts of 0.5 and 1.0, the evolution appears to reverse at luminosities below $10^{26.0} WHz^{-1}$, but to continue at higher luminosities. Beyond a redshift of one, the evolution is negative.

Best et al. (2014) considered three types of hypothetical model to explain the observed pattern. In the first, jet-mode AGNs are assumed to evolve in line with their hosts, massive quiescent galaxies, either with no time delay between when the galaxy becomes passive and the onset of AGN activity (their Model 1a) or with a time delay (their Model 1b). This implies pure density evolution – in equation 5.6, ρ_0 is a function of redshift. The second type of model assumes that radio luminosities increase systematically with redshift. A plausible physical interpretation is that the higher density environments found in the earlier universe boost synchrotron luminosities, as argued by Barthel and Arnaud (1996). This type of model suggests that L_0 is a function of redshift; there may or may not be density evolution as well. Three models were considered. Models 2a and 2b correspond to Models 1a and 1b, but with luminosity evolution added. Model 2c assumes density and luminosity evolution, but with the rate of density evolution treated as a free parameter and modelled as scaling with (1 + z) to some (negative) power. The third type of model considered by Best et al. (2014) is based on the view that the jet-mode population may be contaminated by radiative-mode AGNs whose accretion rates have temporarily fallen below the critical Eddington fraction. The expectation would then be that the jet-mode AGNs evolve with the declining population of their hosts, but modified by a function related to the radiative-mode luminosity function. Three variants of this type of model were considered.

Using data up to a redshift of z = 1.0 meant that Best et al. (2014) were unable to differentiate between these models. It is hoped that by extending the analysis out to redshift z = 2.0 this study might be able to do so, or at least favour one of them.

Table 5.7 *Model parameters for the radio luminosity functions*

Redshift	$log_{10}(\rho_0)$	$log_{10}(L_0)$	β	γ
z < 0.3	-5.30 ± 0.17	25.54 ± 0.18	0.39 ± 0.06	1.61 ± 0.19
z < 0.5	-5.58 ± 0.20	26.00 ± 0.17	0.39 ± 0.05	1.47 ± 0.23
0.5 < z < 1.0	-5.80 ± 0.18	26.30 ± 0.15	0.39 ± 0.08	1.72 ± 0.13
z < 0.5	-5.53 ± 0.14	25.98 ± 0.13	0.39 fixed	1.61 fixed
0.5 < z < 1.0	-5.82 ± 0.12	26.38 ± 0.12	0.39 fixed	1.61 fixed
1.0 < z < 1.5	-6.38 ± 0.18	26.89 ± 0.19	0.39 fixed	1.61 fixed
1.5 < z < 2.0	-6.77 ± 0.23	27.22 ± 0.14	0.39 fixed	1.61 fixed

The first row shows the parameters derived by Best et al. (2014) for the local universe after converting onto a frequency of 150 MHz. Rows 2 and 3 set out the best-fit parameters derived in this work. The final four rows show the parameters adopted in this work, derived by assuming that the two slopes are fixed at the values of 0.39 and 1.61 and the other two parameters are found through a best-fit procedure.

The first step was to find the best-fitting luminosity function for each redshift range. The two lowest redshift ranges had sufficient datapoints to allow the four parameters in equation 5.6 to be found through an optimisation procedure. The values are shown in the second and third rows of Table 5.7. The slopes before and after the break point were consistent with those found by Best et al. (2014) for the local (defined here to mean z < 0.3) universe. The two highest redshift ranges, however, did not show any clear evidence for a luminosity function break, probably because of an absence of datapoints below the likely break location. Because of this and to ensure a consistent approach for all four redshift ranges, the following procedure was adopted:

- It was assumed that the basic shape of the luminosity function derived by Best et al. (2014) for the local universe is valid for the local universe in this dataset. Figure 5.17 illustrates that this is a reasonable assumption. It was assumed that the slopes before and after the break point in the local universe model remain valid up to redshift of 2.0.

- It was assumed that the space density and luminosity both evolve with redshift and so equation 5.6 becomes:

$$\rho(z) = \frac{\rho_0 \, (1 \, + \, z)^a}{(\frac{L}{L_0 \, (1+z)^b})^\beta \; + \; (\frac{L}{L_0 \, (1+z)^b})^\gamma} \tag{5.7}$$

- The values of a and b were found through a minimisation procedure: the two parameters were allowed to vary and chi-squared values calculated for each point in the parameter space. Figure 5.19 shows the chi-squared contour plots for a and b for the four redshift ranges.

The best-fit parameters derived for the luminosity functions are set out the last four rows in Table 5.7. It can immediately be seen that there is a steady positive redshift evolution in luminosity and negative evolution in space density. As illustrated in Figure 5.19, it is interesting to observe that the values found for a and b are very similar in the three highest redshift ranges, at around 4 and 5 respectively. For the lowest redshift range, the evolution being assessed is only from $z < 0.3$ to $z < 0.5$ which introduces greater uncertainty into the values found for a and b.

The luminosity functions themselves are plotted in Figure 5.20, together with the functions derived by Best et al. (2014) for redshift ranges of $z < 0.3$ and $0.5 < z < 1.0$. These latter functions have been converted from a frequency of 1.4 GHz onto a frequency of 150 MHz assuming a spectral index of $\alpha = 0.75$. This work finds a higher density of jet-mode AGNs in the local universe ($z < 0.3$) across all luminosities. For the redshift range 0.5 - 1.0, this work finds a higher density at luminosities below $10^{26}\ WHz^{-1}$. Part of the discrepancy may be due to the choice of spectral index when converting the results of Best et al. (2014) onto a frequency of 150 MHz: it is noted that the luminosity functions for the local universe would coincide if a spectral index of 0.85 rather than 0.75 had been used. A clear evolutionary pattern can be seen. At lower luminosities, the number density of jet-mode AGNs declines with increasing redshift; by contrast, the number density increases with redshift at the higher luminosities.

Having obtained the four radio luminosity function models, it was now possible to test the hypothesised models of Best et al. (2014) and this is discussed in the next section.

5.8 The Jet-mode AGN Heating Rate

It is possible to use these radio luminosity functions to examine the importance of jet-mode AGN feedback as a function of redshift. Radio luminosity can be

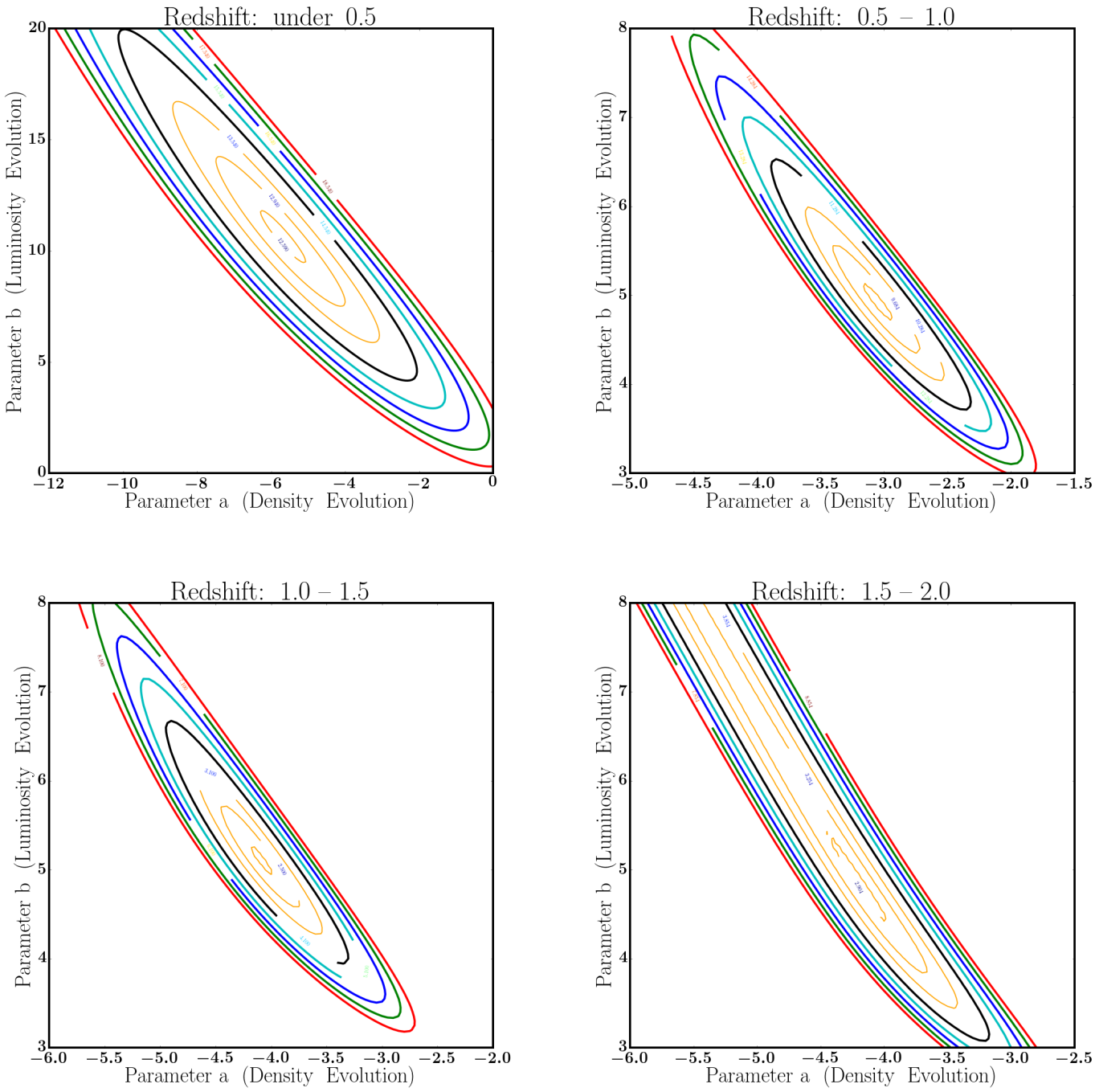

Figure 5.19 *Contours show the chi-square values in the fitting process; the minimum value defines the best-fit values of the parameters a (defining the evolution of the space density) and b (the evolution of the luminosity) – see text. The black, cyan, blue, green and red countour lines correspond respectively to the minimum chi-squared value plus 1, 2, 3, 4 and 5 respectively; the orange contour lines are chosen simply to map out the chi-squared values close to the minimum.*

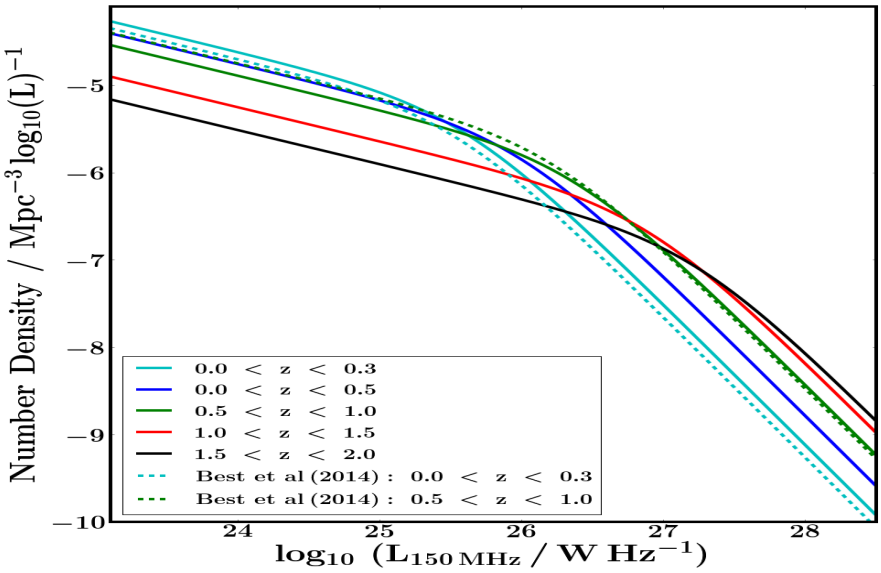

Figure 5.20 *The luminosity functions of jet-mode AGNs for different redshift ranges derived from this work (solid lines) and derived by Best et al. (2014). At lower luminosities, the number density of jet-mode AGNs declines with increasing redshift; by contrast, the number density increases with redshift at the higher luminosities*

approximately converted into jet mechanical luminosity using the expression:

$$P_{mech} = 7 \times 10^{36} f_{cav} \left(\frac{L_{1.4\,GHz}}{10^{25}\,W Hz^{-1}} \right)^{0.68} W \tag{5.8}$$

where f_{cav}, the work done in inflating radio lobes to their pressure and volume, is commonly taken to be equal to 4. The analysis that follows assumes that the value of f_{cav} does not change over the redshift range being considered, although that assumption can be questioned. An explanation of the derivation of this expression is given in Heckman and Best (2014) and references therein. By combining this relation with the radio luminosity function, the heating rate as a function of luminosity is obtained. The results for each redshift range are shown in Figure 5.21. It can be seen that the luminosity that contributes to the peak heating rate increases steadily with redshift, illustrating the point made in the previous section.

The total heating rate for each redshift range can be obtained by integrating these functions. This is the statistic used by Best et al. (2014) to test the three hypothesised models (and variants of these models) and the analysis is repeated

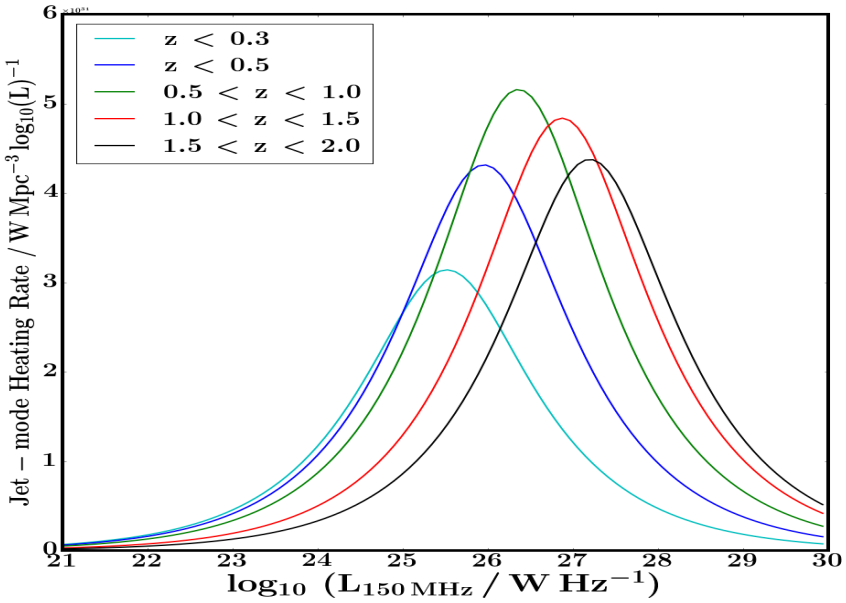

Figure 5.21 *The heating rate, as a function of luminosity for jet-mode AGNs for different redshift ranges. The derivation assumes that the slope of the luminosity function both below and above the break that has been found for the local universe also applies at higher redshifts.*

here, with the results shown in Figure 5.22. The datapoints of Best et al. (2014) were unable to differentiate between the models. The results from this analysis suggest that the heating rate increases up to a redshift of ~ 0.75 and then very gently falls thereafter as the rising luminosities of jet-mode AGNs are outweighed by their declining numbers.

Model 1a assumes that the space density evolves in line with that of the population of host galaxies, as does Model 1b but in this case a delay of 2 Gyr between the formation of a quiescent galaxy and its ability to generate jet-mode AGN activity is built in. Both of these models are heavily disfavoured by this analysis. The three versions of Model 3 assume that samples of jet-mode AGNs are "contaminated" by radiative-mode AGNs whose accretion has temporarily fallen below the Eddington threshold. These models are also disfavoured, even although it is noted that the error bars for the datapoints for the two highest redshift ranges are comparatively large.

Models 2a and 2b replicate Models 1a and 1b, but now also incorporating evolution in luminosity. Neither model fits the data well. The best fit, by far, is provided by Model 2c; in this, luminosity evolution is combined with a simple

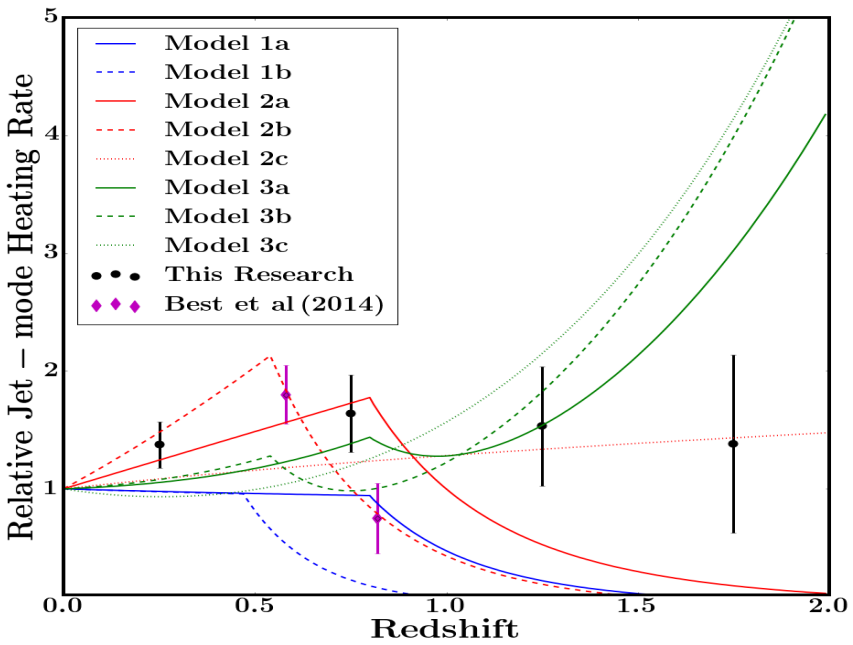

Figure 5.22 *The integrated heating rate at different redshifts compared with the value for the local universe. Also shown are the predictions from the models hypothesised by Best et al. (2014) and described in the text.*

space density parameterised to fit the data of Best et al. (2014). This is, indeed, in line with the pattern suggested by the parameter values in Table 5.7.

Finally, it is noted that models 1, 2 and 3 are discrete. It is possible that a combination of, say, Model 2a and one of the versions of Model 3 could provide a satisfactory fit to the results from this analysis.

5.9 Conclusions

The catalogue of radio sources for the ELAIS-N1 field has allowed radio luminosity functions for all AGNs and also for the sub-categories of jet-mode and radiative-mode AGNs to be estimated up to a redshift of two. The results suggest that the space density of jet-mode AGNs declines steadily with redshift, although not necessarily exactly in line with the space density of available host galaxies. The results also suggest that the luminosity of jet-mode AGNs increases with redshift. A plausible physical explanation is that synchrotron luminosities are higher at

earlier redshifts when both the average density of the universe and the gas fraction are higher. A third conclusion from the analysis is that feedback from jet-mode AGNs peaks at around a redshift of 0.75.

It is believed that these conclusions are robust, but it is recognised that the analysis would have benefited from a wider and, especially, deeper dataset and also from spectroscopic information. With new surveys currently taking place and new facilities being developed, both of these should be available shortly. It is hoped that the analysis in this chapter will provide a useful template for future studies.

Chapter 6

Summary and Conclusions

It is now widely accepted that AGNs divide into two types according to the nature of their accretion flow and that both radiative-mode and jet-mode AGNs play an important role in the evolution of galaxies through different feedback mechanisms. The details are, however, still imperfectly understood. The aim of this thesis is to improve our understanding of jet-mode AGNs and the ways in which they interact with their host galaxies. The key conclusions are described in this chapter together with suggestions on how this work might be taken forward.

6.1 Key Conclusions

The investigation of the Fundamental Plane of black hole activity confirms that the mechanism responsible for the launching of radio jets is scale-invariant. There had been several studies into the Fundamental Plane previously, but all of these had derived the relationship by finding the best fit through a sample containing both AGNs and microquasars. Given the huge difference in magnitude in mass and luminosity between these two sets of objects, an analysis of that type was, in effect, assuming that a Fundamental Plane does exist and, on that assumption, was then calculating what the relationship must be. The important difference in this work is that the relationship was derived solely from a sample of jet-mode AGNs and then verified against a sample of microquasars. In other words, this thesis answered the question for the first time of *whether* a single relationship exists as well as deriving it.

The analysis of the Fundamental Plane provided a number of insights into the activity of jet-mode AGNs:

- Jet-mode AGNs release a significant fraction of their energy into the jets; the fraction averaged over one half for the LINERs in the sample analysed.
- Furthermore, that fraction increases with black hole mass.
- The proportion of galaxies hosting a LINER is a strong function of both stellar mass and black hole mass.
- Hence, not only do larger-mass black hole objects have a higher "on" fraction than their lower-mass counterparts, but they are also more efficient at radio-jet feedback.
- The higher the mass of a black hole, the lower its Eddington ratio is likely to be.
- The LINERs in the sample assembled for this thesis were generally found to have Eddington ratios no higher than 1%, tending to confirm that the dividing threshold between radiative- and jet-mode AGNs is at around that level.

The relationship between black hole mass and velocity dispersion is a critical component of many studies conducted on AGNs. Unsurprisingly, the relationship has been extensively investigated. The fact that recent investigations by Graham and Scott (2013) and McConnell and Ma (2013) have found a much steeper relationship than that previously assumed – a logarithmic slope of around 5.5 compared with around 4.0 – has profound implications. The Fundamental Plane relationship derived in this thesis provides important corroboration for the higher value.

To fully understand jet-mode AGNs and their impact on galaxy evolution, it is necessary to study large samples of these objects across cosmic time. To achieve this, deep surveys are required, not only at radio wavelengths but also across the electromagnetic spectrum in order to identify and classify host galaxies. The difficulty in matching radio sources to their optical counterparts is a known problem: the possibility of mistakenly identifying bright foreground interlopers as host galaxies risks introducing systematic bias into analyses in this area. The development of a likelihood ratio technique that incorporates colour information

into the selection process may prove to be one of the most lasting benefits from this thesis. The selection process developed here allowed a remarkably high fraction, 97%, of radio sources to be matched with a host and, it is believed, with a comparatively high degree of accuracy (based on the visual checking that was subsequently conducted). Given the new radio facilities that have recently, or are about to, come on stream and the wide surveys currently being carried out, an effective means of matching radio sources without the need for visual examination is critical.

Deep observations by LOFAR of the ELAIS-N1 field combined with the wealth of multiband data for that field allowed the construction of a catalogue of radio sources and their host galaxies out to redshifts beyond two. Source counts were derived and found to be consistent with literature values. The radio sources were separated into SFGs, radiative-mode AGNs and jet-mode AGNs, with respective proportions of 16%, 35% and 48% (and 1% representing AGNs that could not be placed into sub-categories).

Radio luminosity functions were calculated for the total population of AGNs and also for the sub-categories of radiative-mode and jet-mode objects; these confirmed functions derived for the local universe and extended the work done by Best et al. (2014) and Pracy et al. (2016) out to a redshift of two. An analysis of the jet-mode luminosity functions led to three key conclusions:

- The space density of jet-mode AGNs declines steadily with redshift, although not necessarily exactly in line with the fall-off in the population of massive quiescent galaxies (their host galaxies).

- The typical luminosity of a jet-mode AGN increases steadily with redshift. A possible explanation is that higher gas fractions and greater densities in the early universe have the effect of boosting synchrotron radiation.

- Feedback from jet-mode AGNs peaks at a redshift of approximately 0.75, but does not evolve strongly with redshift - variations of less than a factor of ~ 2 out to a redshift of two.

6.2 Future Work

This work has developed the techniques, processes and codes required to derive the luminosity function of jet-mode AGNs from the starting point of a sample of radio sources extracted from a radio image. It would be a straightforward exercise to process a larger catalogue through the pipeline. The radio sources used to investigate the evolution of jet-mode AGNs out to a redshift of two were obtained from just 3% of the observations taken by LOFAR of the ELAIS-N1 field. As the remainder of these observations are reduced, the catalogue will increase significantly in depth. The greater depth would extend the investigation out to higher redshifts, would extend it to fainter luminosities and would improve the accuracy of results in the redshift/luminosity range already studied. In particular, an extension to fainter luminosities could be critical in characterising the break of the luminosity function at redshifts of over one and so allowing the density and luminosity evolution to be distinguished more cleanly than was possible in this thesis. A wider areal coverage, which for example will be provided by the LOFAR Two-metre Sky Survey, would allow a fuller investigation in the local universe as well as reducing uncertainties for the higher luminosities at higher redshifts (although different optical and infrared catalogues would then be required to find the host galaxies).

There are three sets of data that would have been useful to have in order to improve on other critical steps within the analysis. Firstly, spectroscopic information was available for 30% of the objects in the ELAIS-N1 catalogue. Information for the whole sample would have provided greater certainty, and possibly accuracy, in estimating the redshift of each object and in separating the AGNs into jet-mode and radiative-mode categories. It is noted that the launch of new facilities, especially the WEAVE multi-object spectrograph on the William Herschel Telescope, will mean that spectroscopic information will more commonly be available for future radio observations.

Secondly, in the absence of spectroscopic information, redshifts were calculated from photometric data. It would have been of benefit had matched-aperture forced photometry data been available; that is, if the optical and infrared catalogues had had fluxes measured through precisely matched apertures on seeing-matched images, with flux densities calculated even if they are below the signal to noise threshold provided that the source had been detected in another band. The PanSTARRS Medium-Deep catalogues do not provide that

information yet, although it is intended that it will be available in the future.

Thirdly, deeper mid-infrared data would have been useful for source classification as many objects were unable to be classified on the most reliable diagnostic tests. However, unlike the spectroscopic and matched-aperture data, it is not obvious that deeper mid-infrared data will be available in the near future.

It would be of interest to undertake follow-up studies of the high-redshift jet-mode AGNs assembled in this thesis in order to investigate the properties of their host galaxies. Are these star-forming lower-mass objects (scaled-down versions of radiative-mode AGNs)? Their stellar masses could be derived from the improved photometric information discussed above.

As the quality of radio and X-ray data improves from respectively LoTSS and, for example, from the ROentgen Survey with an Imaging Telescope Array (eROSITA) (Merloni et al., 2012), it would be interesting to investigate again the Fundamental Plane relationship. It is firmly believed that the relationship derived in this thesis is robust, but the analysis was forced to rely on upper limits for the luminosities of a significant number of sources. Corroboration using deeper datasets would be useful. More critically, it would provide much greater signal to noise in the tests to investigate what is the astrophysical origin of the scatter in the Fundamental Plane.

The work on the Fundamental Plane identified two avenues for future research, both related to the angular momentum of a black hole. It is highly probable that spin plays a role in the launching of jets and that this factor may account for some of the scatter found in the relationship. Also, the analysis discovered hints that the properties of a black hole may change above a mass of approximately 10^8 solar masses, with the spin of the black hole being a possible explanation. It would be interesting to investigate this matter in more detail. Techniques are being developed to estimate the spin of a black hole from the shape of the red wing of the Fe Kα line (for example, Reynolds and Fabian, 2008). This is not an easy exercise and the accuracy of the results is still uncertain, as discussed in Ballantyne (2010), but as the quantity and quality of X-ray data improves, then there will be greater opportunity to incorporate spin information into studies of black holes.

In summary, there are many avenues worth pursuing to investigate jet-mode AGNs and how they impact on their host galaxies. It is extremely exciting that the data to allow these investigations are now starting to emerge.

Appendix A

An Investigation of the Schmidt-Kennicutt Relationship at Higher Redshifts

A.1 Introduction

Stars form out of cold molecular gas. A knowledge of the efficiency of the process is key to our understanding of galaxy evolution and an accurate model of the relationship between the rate of star formation and the mass of molecular gas is a critical component of cosmological simulations. Unsurprisingly, the subject has received much attention over the past sixty years. Schmidt (1959) proposed a relationship between the star formation rate and the mass of interstellar gas by marrying observations of the Milky Way with theoretical considerations. Many papers followed, culminating in research by Kennicutt (1998) that proposed the relationship::

$$\Sigma_{SFR} = A\Sigma_{gas}^{N} \tag{A.1}$$

where $\sum_{SFR}$ and $\sum_{gas}$ are the surface densities of star formation and gas respectively and N is found to lie in the range 1.2–1.5. This relationship was developed empirically through observations of the local universe. It seems to hold both globally for galaxies and internally for star-forming regions within galaxies, at least until the very smallest scales are probed (for example, Kruijssen and Longmore, 2014). Several simulations supported this model, mostly finding

values of N towards the top of that range; examples include Kravtsov (2003), Li et al. (2006), Tasker and Bryan (2006) and Wada and Norman (2007).

Observations at higher redshifts have shown a more dramatic picture than in the contemporary universe, with massive galaxies dominated by gas-rich, turbulent disks and forming stars at prodigious rates (for example, Tacconi et al. (2010), Daddi et al. (2010) and Genzel et al. (2010)). Yet it appears that the Schmidt-Kennicutt relationship also holds good at these higher redshifts. However, observational constraints have meant that the small samples studied at a redshift of around two have, out of necessity, investigated either the most massive galaxies or those that have particularly high star formation rates. It is of interest to investigate whether the Schmidt-Kennicutt relationship remains valid for less massive and more typical galaxies at this redshift. Advantage was taken of radio observations of two carefully-selected galaxies to carry out such an investigation.

A.2 HiZELS 11473 and HiZELS 11551

The Hi-z Emission Line Survey (HiZELS) is an extragalactic survey conducted by the WFCAM instrument on the 3.8-metre UK Infrared Telescope. The survey is described in detail in, for example, Geach et al. (2008), Sobral et al. (2013) and Best et al. (2013). HiZELS uses several narrow-band filters to detect emission line galaxies; in particular, the H2(S1) filter targets H-alpha emitting galaxies at a redshift of z = 2.231 ± 0.016; these are likely to be star-forming systems. Two galaxies were selected from the survey in order to investigate the Schmidt-Kennicutt relationship. They were chosen to be typical galaxies at that redshift: galaxy 11473 has Hα luminosity of 43.15 (log $L_{H\alpha}$, erg/s), a star formation rate of 116 $M_\odot$ / year and stellar mass of 10.43 (log $M/M_\odot$), with respective figures of 42.61, 32 and 10.18 for galaxy 11551. These properties had been calculated by Sobral et al. (2013). The star formation rates were estimated using a standard $L_{H\alpha}$ to SFR conversion rate (Kennicutt (1998)). Multiwavelength data were used to perform a full SED fit and a comparison with model SED templates provided an estimate of the stellar masses; details are in Sobral et al. (2011), Section 2.5. The two galaxies lie within 10 arcseconds of each other, meaning that both were able to be observed with a single pointing of the VLA.

A.3 The Observations

Although H_2 is the most abundant molecule in giant molecular clouds, its symmetry, and hence lack of a permanent dipole moment, renders it largely invisible: the first transition above the ground state is at 171K. The second most abundant molecule, CO, is widely used to trace molecular gas; its first rotationally excited state is 5.5K above the ground state. The rationale and advantages and disadvantages of this approach are discussed in more detail in Glover and Mac Low (2011). The CO_{1-0} molecular line can be used as a tracer for the entire gas reservoir of a galaxy, thus allowing an estimate to be made of the molecular gas mass of each of the two galaxies and hence allowing the Schmidt-Kennicutt relationship to be derived. The rest frequency of the CO_{1-0} line is 115.27 GHz and so, after redshift, the viewing frequency of the line is 35.68 ± 0.18 GHz. Consequently, the Jansky VLA telescope was selected, with observations in the Ka band (27.5 GHz – 40 GHz). The D-configuration was used; this is the smallest configuration, with minimum and maximum baselines of 0.035km and 1.0km respectively, which was intended to maximise sensitivity by not spatially resolving the CO emission. The observations were taken in February 2013. Ten hours of usable observations were completed, of which three-quarters were centred on the target(s) and the remainder on two calibrators. The calibrators were 3C 48 and NGC 1052, which are respectively a quasar with a 5 GHz flux density of 5.8 Jy and a bright galaxy with a 5 GHz flux density of 3.2 Jy. Ten hours were slightly less than half of the observing time that had been hoped for. The data were cleaned by running them through the VLA pipeline software package ("EVLA") to remove interference; additional manual cleaning was also performed.

A.4 The Spectra

Theoretical calculations suggested that a noise level of 0.05 mJy per 6 MHz bandwidth might be attainable. However, partly because the numbers of observations were lower than planned, partly because of poor observing conditions and the necessity for data-flagging and partly because of residual calibration noise, rms noise levels of 0.13 mJy and 0.14 mJy for galaxies 11473 and 11551 respectively were actually achieved. Using the CASA software package, the flux

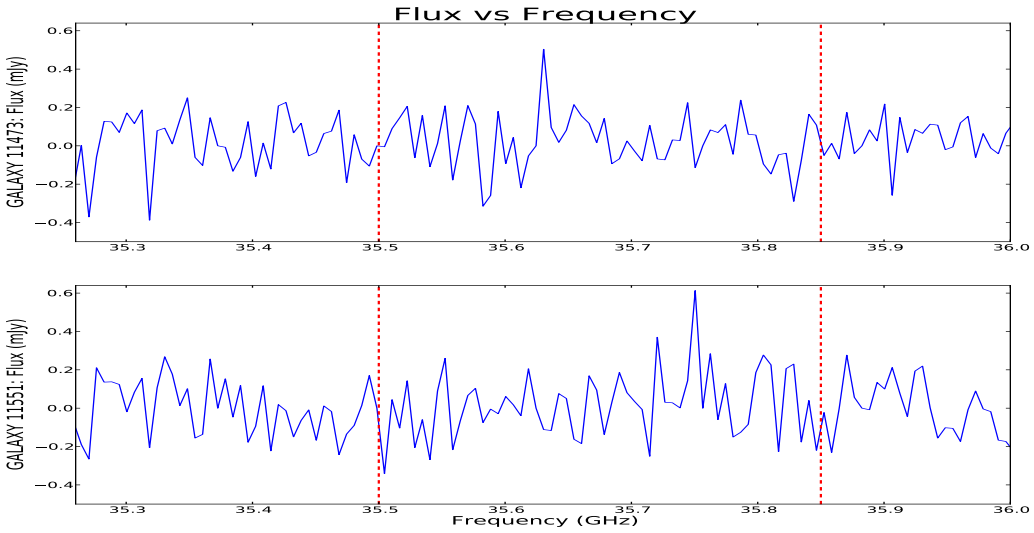

Figure A.1 *A plot of the spectrum for each galaxy. The red vertical lines define the region within which the CO_{1-0} line is expected to reside; the red lines are at frequencies corresponding to 1σ either side of the estimated redshift of the galaxies.*

at each frequency was extracted for the pixel centred on each galaxy. The results are shown in Figure A.1. Although a peak could be found within the appropriate frequency range for both galaxies, the signal-to-noise ratios were low – 3.75 for galaxy 11473 and 4.24 for galaxy 11551. Also, neither peak shows the broadened profile expected of genuine lines. Accordingly, it was decided to view the results as providing an upper limit for the Schmidt-Kennicutt relationship.

The calculations proceeded as follows:

- Gaussian distributions of varying width were fitted at each frequency along the two spectra, with the amplitude of the Gaussian allowed to vary.
- A width of 150 km/s appears appropriate for these galaxies: this is broadly consistent with the velocity width implied by the Tully-Fisher relationship and also with velocity widths for comparable galaxies (see, for example, Table 2 in Ivison et al. (2011)). In fact, an examination of the Gaussian fits indicates that the integrated flux limit is not very sensitive to a choice of width for all sensible values.
- Using a velocity width of 150 km/s, the distribution of best-fit amplitudes at each frequency was produced and an upper limit for the integrated flux taken to be 3σ above the mean. This resulted in upper limits of 80 mJy km/s and 85 mJy km/s for galaxies 11473 and 11551 respectively.

- Solomon et al. (1997) showed that the line luminosity, $L'_{CO_{1-0}}$, can be expressed as a function of the total line flux, leading to the equation:

$$L'_{CO_{1-0}} = \frac{3.25 \times 10^7}{1+z}(\frac{D_L}{\nu_{CO}})^2 \int S_{CO_{1-0}} dv \tag{A.2}$$

  where $L'_{CO_{1-0}}$ is the luminosity of the CO_{1-0} molecular line, D_L is the luminosity distance (in Mpc), ν_{CO} is the rest frame frequency (in GHz) and the final item is the integrated line flux as calculated above. Inserting the numbers gives an upper value for $L'_{CO_{1-0}}$ of 2.0×10^{10} K km s^{-1}pc^2 and 2.1×10^{10} K km s^{-1}pc^2 for galaxies 11473 and 11551 respectively.

- From Kennicutt (1998):

$$SFR = \frac{L_{IR}}{5.8 \times 10^9 \times L_\odot} M_\odot/yr \tag{A.3}$$

  where the infra-red luminosity and the solar luminosity are both in Joules. The relationship was derived assuming an initial mass function (IMF) which is a Salpeter function, with dN(m)/dm = -2.35; in the absence of further information, that IMF should be a defensible choice for the two galaxies under consideration and was also the one adopted for the $L_{H\alpha}$ to star formation rate conversion. Inserting the star formation rate estimated for both galaxies gives values for L_{IR} of $2.6 \times 10^{38} J$ and $7.1 \times 10^{37} J$ for galaxies 11473 and 11551 respectively.

- Finally, these results can be compared with the Schmidt-Kennicutt relationship. Figure A.2, which is based on Figure 2 in Ivison et al. (2011), shows a variant of the Schmidt-Kennicutt relationship, with the infra-red luminosity used as a proxy for the star formation rate and the line luminosity used as a proxy for the mass of the molecular gas. All the points shown are for high-redshift galaxies. The blue arrows represent the two galaxies studied here, with the base of each arrow marking the upper limit for the line luminosity.

A.5 Summary

The upper limit for galaxy 11473 (the higher arrow) rules out a higher $L'_{CO_{1-0}}$ for a given L_{IR}, but values well within the scatter of observations are still allowed. By contrast, the upper limit for galaxy 11551 does not impose much

constraint on the Schmidt-Kennicutt relationship. Longer observation times, and hence deeper data, are needed to provide tighter constraints. Nevertheless, the analysis provides tentative support for the hypothesis that the Schmidt-Kennicutt relationship does indeed provide a realistic basis for estimating star formation efficiency at higher redshifts.

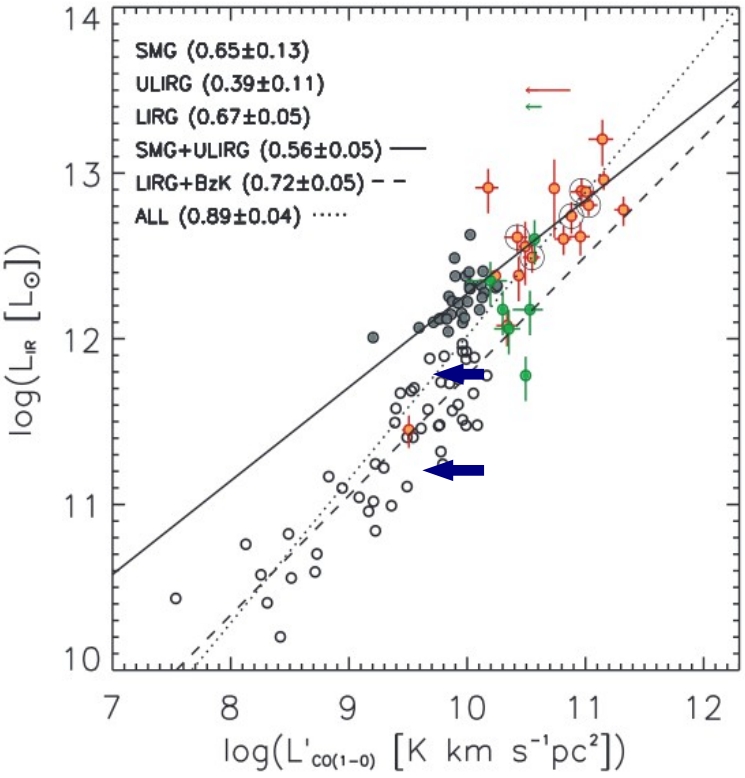

Figure A.2 *The Schmidt-Kennicutt relationship for high redshift galaxies. The blue arrows represent the galaxies studied in this research, with the base of each arrow marking the upper limit for the line luminosity. Adapted from Figure 2 in Ivison et al. (2011). The galaxies from that paper's dataset are divided into sub-millimetre galaxies (SMGs), (ultra) luminous infrared galaxies (ULIRGs and LIRGs) and BzK galaxies (BzKs). Trend lines are fitted to the ULIRGs plus SMGs (solid line) and LIRGs plus BzK galaxies (dashed line); the dotted line shows the trend line for the full sample. The resulting linear slopes are shown in parentheses in the legend. The paper contains a fuller description of the data and trend lines.*

Appendix B

The Catalogue of LINERs

The catalogue of LINERs used in the analysis described in Chapter 2 is set out in the Table on the following pages. The column descriptions are as follows:

(1) Identifier in this sample of LINERs.
(2) Plate identifier for the SDSS source in the SDSS-DR7 catalogue.
(3) MJD identifier for the SDSS source in the SDSS-DR7 catalogue.
(4) Fibre identifier for the SDSS source in the SDSS-DR7 catalogue.
(5) Right Ascension for the SDSS source.
(6) Declination for the SDSS source.
(7) Redshift derived from the SDSS spectra.
(8) Stellar velocity dispersion of the galaxy bulge, derived from SDSS data, in units of km/s.
(9) $\log_{10}$ (M_{BH} in solar masses); black hole mass derived from the velocity dispersion using the McConnell & Ma (2013) relationship.
(10) $\log_{10}$ (M^* in solar masses); stellar mass derived from the SDSS data.
(11) Identifier of X-ray source in the 3XMM-DR4 catalogue.
(12) X-ray flux in the 2.0 - 12.0 keV band, in units of erg/cm^2/s.
(13) X-ray luminosity corresponding to the flux in the 2.0 - 10.0 keV band, in units of erg/s.
(14) Radio flux density at an observing frequency of 1.4 GHz, in units of Jy.
(15) Radio luminosity from an observing frequency of 1.4 GHz (using νL_ν), in units of erg/s. If the radio flux density is under 0.32 mJy (2x the FIRST survey rms), the luminosity is shown as a limit corresponding to a flux density of 0.32 mJy.

Id	SDSS Plate id	SDSS MJD id	SDSS Fibre id	RA ——(J2000)——	Dec	Redshift	Velocity Dispersion km/s	Black Hole Mass —$\log_{10}$ (in solar masses)—	Stellar Mass	3XMM id	Xray Flux erg/cm^2/s	Xray Luminosity erg/s	Radio Flux Density Jy	Radio Luminosity erg/s
(1)	(2)	(3)	(4)	(5)	(6)	(7)	(8)	(9)	(10)	(11)	(12)	(13)	(14)	(15)
121	297	51663	449	201.73746	1.19847	0.083	184.0	7.98	11.10	330017	1.696e-14	41.417	1.955e-03	38.665
122	2112	53534	44	201.82020	32.03071	0.024	186.3	8.01	11.14	330181	1.957e-14	40.377	-6.541e-04	36.781
123	2094	53851	475	205.15107	30.31803	0.040	140.2	7.51	10.73	35611	6.293e-15	40.328	2.425e-05	37.224
124	1321	52764	629	206.29241	56.02928	0.144	236.2	8.42	11.48	324947	1.444e-14	41.858	3.610e-03	39.437
125	2742	54233	459	206.99570	17.41982	0.026	94.1	6.81	10.31	7784	5.163e-14	40.863	2.586e-05	36.845
126	2114	53848	252	207.01872	26.67900	0.117	125.4	7.31	10.64	322751	3.660e-15	41.068	-2.019e-04	38.193
127	2756	54508	168	209.04463	18.27314	0.064	235.1	8.41	11.20	328617	4.869e-15	40.630	1.994e-04	37.635
128	1702	53144	135	209.09589	10.55103	0.124	129.5	7.37	10.74	328059	2.925e-14	42.021	2.129e-04	38.243
129	531	52028	504	210.19407	2.79535	0.136	240.7	8.45	10.97	11249	4.027e-15	41.250	1.513e-04	38.332
130	2784	54529	4	211.54836	22.31630	0.129	139.1	7.50	10.76	343014	2.745e-14	42.030	8.310e-03	39.693
131	2123	53793	48	212.19055	26.25008	0.068	139.9	7.51	10.80	342607	4.285e-15	40.633	6.548e-04	38.004
132	1394	53108	437	213.46970	43.70744	0.088	127.3	7.34	10.71	341562	6.534e-14	42.054	1.330e-04	37.930
133	2128	53800	219	214.14687	23.37063	0.069	94.7	6.82	10.34	35797	4.608e-14	41.673	6.598e-04	38.016
134	2131	53819	455	216.03695	26.63630	0.038	134.4	7.44	10.66	50113	3.602e-15	40.041	-8.096e-05	37.179
135	535	51999	291	217.14969	1.36187	0.101	158.0	7.72	10.52	345954	1.801e-14	41.626	9.161e-05	38.060
136	306	51637	203	217.78785	-0.83054	0.082	174.6	7.89	10.44	346615	2.422e-14	41.560	-1.822e-04	37.867
137	2137	54206	353	217.90452	28.13139	0.032	154.1	7.67	10.63	346538	7.410e-15	40.186	-2.150e-06	37.011
138	537	52027	434	221.13729	2.08229	0.163	173.6	7.88	11.20	41631	7.788e-15	41.708	9.364e-04	38.967
139	609	52339	444	222.24564	63.39760	0.130	170.7	7.85	11.10	337227	9.462e-14	42.576	1.879e-04	38.287
140	2777	54554	50	223.18023	16.90375	0.046	271.9	8.67	11.37	335588	2.661e-15	40.075	1.925e-02	39.123
141	2778	54539	379	223.72210	18.75728	0.063	116.5	7.19	10.69	334906	1.286e-15	40.043	1.600e-03	38.325
142	540	51996	254	227.04074	1.24932	0.035	142.3	7.54	10.87	340339	1.279e-14	40.522	2.367e-04	37.110
143	1817	53851	382	227.51673	7.67699	0.046	140.5	7.51	10.55	338424	2.235e-13	41.997	6.442e-04	37.645
144	1816	53919	545	227.57672	7.70544	0.042	201.4	8.14	11.27	338663	1.315e-13	41.696	6.606e-04	37.586
145	612	52079	255	227.74022	56.36406	0.102	203.3	8.16	10.84	338594	2.287e-14	41.739	4.015e-05	38.069
146	1817	53851	236	227.92548	7.10643	0.043	204.8	8.17	11.28	338040	4.432e-14	41.229	1.630e-03	37.984
147	312	51689	466	229.11249	0.38428	0.053	144.3	7.56	10.64	338957	1.158e-14	40.840	1.880e-03	38.239
148	312	51689	471	229.16759	0.25051	0.053	293.2	8.80	11.15	28382	2.186e-12	43.111	7.557e-01	40.837
149	1833	54561	596	229.57372	6.25247	0.097	139.9	7.51	10.95	207531	3.331e-14	41.848	1.361e-04	38.015
150	1818	54539	546	230.39475	7.57641	0.048	154.5	7.68	11.08	207101	6.523e-14	41.494	2.407e-04	37.373
151	1652	53555	447	233.00930	30.27470	0.065	180.3	7.95	11.07	28550	6.750e-13	42.796	6.118e-02	39.941
152	1835	54563	92	233.03565	4.74766	0.037	185.9	8.00	10.98	207960	1.508e-13	41.638	5.741e-04	37.408
153	614	53437	598	233.69766	55.67085	0.074	205.7	8.18	10.99	206075	1.104e-14	41.120	1.523e-04	37.769
154	616	52442	109	236.02991	53.76656	0.109	178.4	7.93	11.12	48187	2.043e-14	41.749	4.021e-04	38.227
155	1391	52817	147	239.43138	27.46473	0.032	126.5	7.33	10.77	208522	7.659e-15	40.198	7.720e-03	38.392
156	1419	53144	400	241.40777	32.93644	0.053	158.1	7.72	10.68	19777	1.894e-15	40.055	2.338e-04	37.471
157	1393	52824	459	241.77162	27.55151	0.153	112.4	7.12	10.80	201046	7.925e-15	41.657	1.558e-05	38.443
158	2528	54571	540	244.24436	12.81632	0.034	159.6	7.74	10.75	199436	5.408e-14	41.114	3.747e-04	37.145
159	2530	53881	301	244.42080	12.57292	0.073	193.6	8.07	10.98	41792	2.945e-15	40.544	7.102e-04	38.112
160	816	52379	93	247.90797	41.49364	0.030	108.0	7.05	10.70	204676	3.194e-14	40.783	5.554e-04	37.213

Id	SDSS Plate id	SDSS MJD id	SDSS Fibre id	RA ——(J2000)——	Dec	Redshift	Velocity Dispersion km/s	Black Hole Mass —$\log_{10}$ (in solar masses)—	Stellar Mass	3XMM id	Xray Flux erg/cm^2/s	Xray Luminosity erg/s	Radio Flux Density Jy	Radio Luminosity erg/s
(1)	(2)	(3)	(4)	(5)	(6)	(7)	(8)	(9)	(10)	(11)	(12)	(13)	(14)	(15)
1	689	52262	240	7.29344	-0.16375	0.061	144.6	7.56	11.16	113618	7.713e-14	41.789	5.517e-04	37.831
2	393	51794	445	11.01946	1.03133	0.112	218.6	8.28	11.14	28750	1.439e-12	43.619	1.100e-02	39.686
3	454	51908	395	35.96062	-8.39710	0.163	169.1	7.84	11.37	103781	3.227e-14	42.325	-2.458e-04	38.501
4	407	51820	391	37.33730	0.59383	0.132	250.7	8.52	11.43	104810	1.965e-14	41.907	2.973e-05	38.301
5	407	51820	388	37.37939	0.58968	0.132	135.8	7.45	10.97	104735	4.668e-15	41.285	-1.522e-04	38.303
6	889	52663	365	116.59722	31.02186	0.056	211.2	8.22	11.01	78716	1.175e-01	40.890	2.171e-04	37.513
7	889	52663	406	116.63720	31.02268	0.054	162.7	7.77	11.14	78766	1.653e-15	40.006	-7.766e-05	37.481
8	928	52578	162	118.19276	25.09057	0.050	134.2	7.43	10.68	81323	1.865e-14	41.001	1.060e-04	37.424
9	435	51882	11	118.65446	39.17994	0.096	191.0	8.05	11.23	82590	1.507e-13	42.498	4.881e-02	40.193
10	544	52201	127	119.61712	37.78657	0.041	263.2	8.61	11.62	84098	1.669e-13	41.766	2.255e-01	40.086
11	2418	53794	470	120.08741	11.31945	0.015	112.6	7.13	10.29	77652	2.034e-14	39.962	-4.548e-05	36.350
12	2267	53713	209	121.41883	15.55045	0.098	192.1	8.06	11.24	90736	3.744e-15	40.915	8.153e-04	38.438
13	759	52254	418	122.38064	39.80186	0.064	153.9	7.67	10.95	85116	3.248e-14	41.458	6.678e-05	37.639
14	440	51912	73	124.27590	48.45555	0.121	155.3	7.69	11.27	70901	6.942e-15	41.375	2.900e-04	38.221
15	443	51873	513	127.25065	49.98580	0.097	204.2	8.17	10.69	36309	1.535e-13	42.515	1.426e-04	38.018
16	1930	53347	259	129.40408	24.99980	0.029	218.5	8.28	10.84	38438	2.521e-14	40.637	6.993e-05	36.931
17	1930	53347	477	129.60004	25.75454	0.018	150.8	7.64	10.39	304783	1.131e-13	40.880	9.538e-02	38.997
18	896	52592	473	131.21095	43.04681	0.057	257.8	8.57	11.36	309430	1.651e-14	41.059	5.278e-04	37.752
19	1210	52701	108	133.27612	33.37857	0.086	121.1	7.25	10.76	308323	9.739e-14	42.208	4.769e-04	38.083
20	2431	53818	165	133.43382	15.13472	0.071	169.0	7.84	10.91	308490	8.474e-15	40.970	-2.290e-04	37.734
21	471	51924	125	136.60252	0.96556	0.070	166.1	7.81	10.48	298764	2.608e-13	42.450	7.521e-03	39.097
22	553	51999	523	138.35790	52.98131	0.025	220.5	8.30	11.10	51714	8.161e-15	40.027	7.740e-06	36.811
23	1193	52652	3	138.88499	4.50847	0.098	217.5	8.28	11.10	303479	1.291e-14	41.451	5.669e-04	38.278
24	1936	53330	621	138.99367	29.73059	0.187	205.4	8.18	11.18	301504	3.176e-16	40.449	3.025e-04	38.630
25	1941	53386	256	141.57143	30.81864	0.076	96.9	6.87	10.71	318959	5.556e-15	40.845	2.134e-04	37.792
26	486	51910	426	143.82665	61.47545	0.124	231.5	8.39	11.29	317810	6.277e-15	41.358	4.802e-04	38.424
27	570	52266	267	145.19237	3.41278	0.073	189.0	8.03	11.05	321767	2.831e-14	41.522	4.699e-04	37.929
28	2370	53764	299	146.49046	17.43043	0.128	175.3	7.90	11.00	321815	3.790e-13	43.165	2.091e-04	38.274
29	500	51994	503	149.72818	2.35804	0.220	195.6	8.09	11.25	312654	2.600e-15	41.521	6.088e-05	38.787
30	501	52235	341	149.74388	2.24973	0.133	149.1	7.62	10.93	7041	1.357e-13	42.756	9.600e-04	38.787
31	1744	53055	337	149.76370	13.03917	0.036	146.4	7.59	10.71	312635	3.360e-14	40.948	-9.670e-05	37.117
32	500	51994	534	149.77296	2.63608	0.079	182.7	7.97	11.22	13846	4.855e-15	40.826	4.641e-04	37.992
33	501	52235	342	149.93832	2.57759	0.124	137.1	7.47	10.79	312740	1.408e-14	41.704	-2.300e-05	38.243
34	500	51994	597	150.23003	2.39552	0.044	94.3	6.82	10.50	4443	1.927e-14	40.905	-3.484e-05	37.315
35	1953	53358	26	153.06387	29.56709	0.049	148.6	7.61	10.56	315684	6.253e-14	41.496	-1.392e-04	37.393
36	2365	53739	33	155.40693	21.68731	0.039	164.1	7.78	10.70	314289	9.584e-14	41.489	-3.972e-05	37.202
37	1746	53062	194	155.42829	13.11559	0.076	187.8	8.02	11.09	314295	2.043e-14	41.419	1.641e-02	39.510
38	2374	53765	627	156.08466	19.83593	0.166	225.5	8.34	10.82	51938	2.296e-15	41.193	7.953e-05	38.516
39	961	52615	381	156.21366	47.12743	0.143	163.0	7.77	10.90	282248	1.100e-14	41.734	2.091e-04	38.379
40	961	52615	385	156.30686	47.11523	0.060	104.6	7.00	10.32	282107	8.464e-15	40.824	1.694e-04	37.589

Id	SDSS Plate id	SDSS MJD id	SDSS Fibre id	RA ——(J2000)——	Dec	Redshift	Velocity Dispersion km/s	Black Hole Mass —$\log_{10}$ (in solar masses)—	Stellar Mass	3XMM id	Xray Flux erg/cm^2/s	Xray Luminosity erg/s	Radio Flux Density Jy	Radio Luminosity erg/s
(1)	(2)	(3)	(4)	(5)	(6)	(7)	(8)	(9)	(10)	(11)	(12)	(13)	(14)	(15)
41	2349	53734	152	156.97717	24.02124	0.085	150.4	7.63	10.84	281733	4.432e-14	41.851	8.423e-05	37.896
42	1430	53002	135	157.92513	38.12806	0.115	236.3	8.42	11.07	280587	3.200e-15	40.991	2.306e-02	40.032
43	1432	53003	519	159.88386	39.83643	0.068	107.6	7.05	10.55	285446	9.285e-15	40.975	-3.219e-04	37.700
44	2478	54097	391	159.96867	20.84705	0.046	201.7	8.14	11.15	285351	3.018e-14	41.131	5.440e-03	38.576
45	1240	52734	548	160.11822	9.18257	0.019	219.7	8.29	11.12	33271	5.586e-15	39.633	6.467e-02	38.888
46	274	51913	81	160.14434	-0.90941	0.039	134.9	7.44	10.61	284825	2.070e-13	41.819	2.597e-04	37.197
47	1240	52734	558	160.19073	9.36989	0.210	338.3	9.05	11.22	285149	1.494e-15	41.236	6.420e-04	39.045
48	948	52428	532	160.60187	58.45874	0.045	147.9	7.60	10.63	283101	3.849e-15	40.219	1.278e-04	37.327
49	948	52428	640	162.85702	57.59558	0.073	228.5	8.36	11.05	14209	1.740e-15	40.312	5.472e-04	37.996
50	948	52428	35	162.93239	57.49359	0.080	145.4	7.57	10.89	13736	2.818e-15	40.604	1.749e-04	37.845
51	1434	53053	52	163.09802	44.14658	0.092	142.2	7.53	10.73	50856	4.599e-15	40.944	2.074e-02	39.783
52	1002	52646	435	164.11314	7.08687	0.160	257.7	8.57	11.11	26260	7.231e-15	41.657	1.418e-03	39.129
53	949	52427	103	164.25329	57.61380	0.135	197.7	8.11	11.35	274215	3.476e-15	41.182	6.074e-04	38.606
54	508	52366	320	164.46603	1.67770	0.041	193.6	8.07	11.01	278261	2.267e-15	39.911	-2.871e-04	37.250
55	878	52353	323	166.91295	52.11224	0.181	154.2	7.68	10.88	277671	1.819e-13	43.177	3.427e-04	38.630
56	510	52381	271	167.84574	2.39596	0.079	224.6	8.33	11.36	293955	2.256e-13	42.489	1.157e-03	38.385
57	1004	52723	98	167.97660	6.44053	0.075	138.5	7.49	10.84	293909	9.968e-14	42.093	1.639e-04	37.785
58	1012	52649	95	168.94680	53.17979	0.106	139.6	7.50	10.91	292190	1.409e-14	41.560	3.655e-04	38.158
59	2215	53793	468	169.05643	29.38525	0.029	250.7	8.52	11.00	292177	2.880e-14	40.707	1.450e-03	37.599
60	1617	53112	460	169.72410	7.90859	0.127	246.2	8.49	11.18	58510	3.417e-15	41.116	8.190e-03	39.678
61	2497	54154	235	170.69784	24.30820	0.096	241.9	8.46	10.87	296645	1.633e-15	40.532	4.720e-03	39.178
62	328	52282	296	174.12438	-3.59427	0.108	256.2	8.56	10.60	287477	1.044e-15	40.446	-1.612e-04	38.116
63	2504	54179	557	174.47883	21.98550	0.030	146.2	7.58	9.82	287186	1.233e-14	40.359	5.121e-04	37.167
64	2508	53875	277	174.81196	17.14367	0.021	150.2	7.63	10.66	287444	7.675e-13	41.847	5.930e-03	37.926
65	1226	52734	345	175.57287	10.29193	0.117	240.7	8.45	11.68	287870	1.135e-13	42.559	4.563e-03	39.346
66	2506	54179	582	176.26617	19.97368	0.017	173.0	7.88	10.80	54703	2.902e-13	41.224	5.222e-04	36.670
67	2506	54179	558	176.27094	19.60635	0.022	260.0	8.59	11.15	44193	1.160e-12	42.043	5.454e-01	39.906
68	2509	54180	492	176.55077	20.39165	0.023	195.4	8.09	11.17	285706	6.023e-13	41.819	8.890e-03	38.178
69	880	52367	636	176.92368	52.44885	0.048	162.3	7.77	10.80	285755	9.682e-14	41.679	7.877e-04	37.778
70	881	52368	437	177.05076	52.85209	0.050	195.7	8.09	11.10	285821	1.848e-14	40.998	9.140e-03	38.880
71	2222	53799	18	177.71679	28.70579	0.149	117.8	7.21	11.07	286469	1.554e-13	42.923	3.974e-04	38.512
72	1017	52706	194	177.95075	54.92885	0.143	130.7	7.39	10.96	290690	2.482e-14	42.088	3.380e-04	38.403
73	1016	52759	554	177.99043	55.13566	0.080	280.7	8.72	11.16	290666	3.093e-14	41.638	5.362e-04	38.063
74	2514	53882	94	178.86453	23.60707	0.138	148.2	7.61	11.05	14467	3.903e-15	41.247	-4.052e-05	38.342
75	2226	53819	214	179.53133	26.52288	0.023	171.3	7.86	10.34	291007	3.142e-13	41.516	-3.480e-04	36.714
76	2226	53819	217	179.58393	26.35337	0.112	198.5	8.12	11.12	291232	5.636e-14	42.214	6.956e-04	38.489
77	2225	53729	520	180.45550	30.12199	0.080	215.3	8.26	11.29	18814	4.636e-15	40.818	1.307e-02	39.454
78	2225	53729	505	180.46685	30.17658	0.164	183.5	7.98	11.27	19763	2.140e-14	42.151	2.320e-06	38.505
79	2225	53729	506	180.49117	29.99599	0.071	201.6	8.14	10.78	56432	6.665e-15	40.871	3.057e-04	37.739
80	2608	54474	513	180.98328	20.43046	0.022	104.6	7.00	10.13	39109	1.166e-14	40.054	2.458e-04	36.683

Id	SDSS Plate id	SDSS MJD id	SDSS Fibre id	RA ——(J2000)——	Dec	Redshift	Velocity Dispersion km/s	Black Hole Mass —$\log_{10}$ (in solar masses)—	Stellar Mass	3XMM id	Xray Flux erg/cm^2/s	Xray Luminosity erg/s	Radio Flux Density Jy	Radio Luminosity erg/s
(1)	(2)	(3)	(4)	(5)	(6)	(7)	(8)	(9)	(10)	(11)	(12)	(13)	(14)	(15)
81	2609	54476	384	181.04708	20.40984	0.024	206.1	8.18	11.20	17080	2.421e-13	41.452	7.256e-05	36.764
82	2226	53819	589	181.16993	28.03465	0.138	170.9	7.85	11.05	355628	1.928e-15	40.946	2.050e-04	38.347
83	2228	53818	330	181.18834	31.19248	0.025	120.5	7.24	10.27	355607	1.443e-14	40.267	5.859e-04	37.066
84	882	52370	638	181.84068	52.59015	0.062	181.3	7.96	11.08	356451	4.668e-14	41.583	5.427e-04	37.836
85	2656	54484	499	182.02316	25.23732	0.022	252.8	8.54	11.03	356331	1.992e-14	40.315	5.338e-02	38.934
86	1995	53415	205	182.70669	39.47281	0.023	155.2	7.69	11.06	5279	2.267e-13	41.374	2.930e-03	37.677
87	1612	53149	560	182.98412	13.43788	0.057	96.4	6.86	10.41	353457	4.340e-13	42.484	6.158e-04	37.823
88	518	52282	468	183.39903	2.81045	0.133	223.9	8.33	11.10	354616	3.267e-15	41.135	-9.899e-05	38.308
89	1765	53466	64	183.61437	14.24167	0.155	244.6	8.48	11.08	27586	3.777e-15	41.347	1.252e-04	38.455
90	883	52430	557	183.77842	52.46796	0.194	215.0	8.26	11.24	354266	5.448e-14	42.720	6.724e-04	38.989
91	1624	53386	73	184.05854	7.13383	0.084	180.3	7.95	10.97	354467	3.776e-14	41.771	4.144e-04	37.997
92	2232	53827	215	185.24787	29.12478	0.133	234.5	8.41	11.59	359554	1.183e-14	41.695	1.050e-03	38.825
93	2233	53845	480	185.68008	28.07702	0.031	193.3	8.07	10.49	356886	8.114e-14	41.200	2.579e-04	36.986
94	1767	53436	416	185.85531	15.90923	0.080	139.2	7.50	10.79	357067	7.660e-15	41.036	2.108e-04	37.843
95	1626	53472	189	185.99109	7.40828	0.075	222.0	8.31	11.06	356649	4.243e-15	40.717	1.700e-03	38.506
96	1626	53472	171	186.27654	7.40167	0.085	133.2	7.42	11.07	357798	2.832e-14	41.660	-6.963e-05	37.899
97	1615	53166	489	187.35381	12.69216	0.094	173.9	7.89	11.12	32086	5.772e-14	42.059	1.207e-03	38.564
98	1627	53473	459	187.42683	8.22701	0.090	125.3	7.31	10.56	350258	4.069e-15	40.870	8.113e-05	37.950
99	1768	53442	422	187.78722	15.05178	0.204	186.0	8.00	11.23	347603	8.052e-15	41.938	2.610e-04	38.714
100	520	52288	147	188.42648	2.13693	0.082	141.5	7.53	10.80	352614	4.948e-14	41.866	1.981e-03	38.654
101	1616	53169	516	189.19421	12.93608	0.094	186.2	8.00	11.19	351032	7.827e-15	41.191	4.829e-04	38.166
102	1233	52734	174	189.54114	9.49735	0.033	122.1	7.27	10.30	350369	5.734e-14	41.111	6.219e-04	37.336
103	336	51999	345	190.31259	-1.95474	0.065	155.2	7.69	10.32	351135	5.672e-15	40.722	-2.336e-04	37.661
104	1975	53734	321	190.32993	33.18682	0.095	156.0	7.70	10.66	59086	3.891e-15	40.901	3.830e-03	39.079
105	2020	53431	4	190.55888	33.38169	0.038	171.3	7.86	10.94	367722	2.405e-15	39.869	1.429e-04	37.182
106	292	51609	310	191.21775	-0.43045	0.082	145.0	7.57	11.21	368041	1.581e-15	40.375	2.409e-04	37.867
107	292	51609	519	192.61428	0.22934	0.047	196.0	8.09	10.76	366696	2.591e-13	42.079	6.195e-02	39.646
108	2240	53823	129	193.63097	26.34462	0.069	232.1	8.39	11.22	371776	3.671e-14	41.583	3.765e-02	39.781
109	2241	54169	185	194.35521	27.40457	0.016	85.4	6.64	9.61	2263	1.261e-14	39.824	2.110e-03	37.239
110	2240	53823	144	194.40226	27.03137	0.025	111.4	7.11	10.38	29439	9.305e-15	40.059	-2.596e-05	36.786
111	338	51694	502	194.85969	-1.78281	0.083	160.1	7.74	11.18	361620	3.647e-15	40.749	8.389e-05	37.878
112	1039	52707	129	195.92005	53.72325	0.028	135.9	7.46	10.39	361887	1.228e-14	40.285	2.710e-04	36.891
113	2603	54479	426	196.24584	17.91503	0.034	163.4	7.78	10.59	360072	1.218e-13	41.458	-7.462e-05	37.067
114	2603	54479	469	196.33352	17.92298	0.052	149.0	7.62	10.82	359967	4.730e-15	40.432	-9.774e-05	37.451
115	1039	52707	113	196.86303	54.03773	0.030	173.7	7.88	10.60	359878	5.666e-14	41.012	1.785e-04	36.954
116	340	51691	407	197.80665	-1.53998	0.113	220.5	8.30	11.04	364185	2.850e-14	41.925	3.439e-04	38.190
117	2093	53818	102	199.50573	32.76537	0.036	121.8	7.26	10.59	363890	1.209e-14	40.524	1.713e-04	37.136
118	2112	53534	385	200.13274	33.29159	0.035	176.7	7.91	11.10	363613	2.437e-15	39.801	5.599e-05	37.109
119	2110	53467	344	200.93757	31.56576	0.016	193.6	8.07	11.01	331490	2.475e-13	41.117	2.210e-03	37.259
120	2110	53467	380	201.58689	31.72248	0.044	134.3	7.43	10.94	328771	1.950e-14	40.900	8.431e-04	37.725

Id	SDSS Plate id	SDSS MJD id	SDSS Fibre id	RA ——(J2000)——	Dec	Redshift	Velocity Dispersion km/s	Black Hole Mass —$\log_{10}$ (in solar masses)—	Stellar Mass	3XMM id	Xray Flux erg/cm^2/s	Xray Luminosity erg/s	Radio Flux Density Jy	Radio Luminosity erg/s
(1)	(2)	(3)	(4)	(5)	(6)	(7)	(8)	(9)	(10)	(11)	(12)	(13)	(14)	(15)
161	818	52395	392	250.29273	38.83200	0.062	119.5	7.23	10.73	220125	6.103e-14	41.700	2.094e-04	37.607
162	973	52426	519	255.80864	33.51154	0.091	212.4	8.23	10.79	214507	4.198e-14	41.898	4.293e-05	37.965
163	355	51788	590	259.73745	57.85064	0.149	165.2	7.80	11.18	25294	2.189e-15	41.075	4.550e-05	38.420
164	988	52520	167	322.39157	0.02666	0.052	161.9	7.76	10.59	266035	9.068e-15	40.723	-7.441e-05	37.459
165	989	52468	512	324.25989	0.42824	0.051	228.2	8.36	11.35	264461	1.315e-14	40.861	3.804e-05	37.435
166	384	51821	466	353.26755	0.05294	0.058	159.7	7.74	10.91	238430	1.118e-15	39.913	9.130e-06	37.557
167	387	51791	279	359.43375	-0.17493	0.076	275.7	8.69	11.44	56660	7.012e-15	40.949	4.950e-03	38.984
168	392	51793	635	9.82502	0.69980	0.280	259.2	8.58	11.70	116548	1.495e-14	42.520	-4.352e-05	39.021
169	393	51794	449	11.00631	1.19198	0.197	218.1	8.28	11.20	129414	2.388e-15	41.378	5.747e-05	38.682
170	398	51789	356	18.58979	0.17974	0.044	208.9	8.21	10.99	127055	9.871e-15	40.610	-1.109e-04	37.310
171	397	51794	585	18.69559	0.52469	0.045	212.3	8.23	10.93	127287	3.652e-16	39.201	1.323e-04	37.332
172	398	51789	390	18.72592	0.50740	0.044	187.8	8.02	10.73	127179	2.128e-15	39.934	-1.134e-04	37.300
173	398	51789	427	18.78638	0.57601	0.045	235.3	8.41	10.95	127197	7.990e-15	40.541	-3.073e-05	37.332
174	695	52202	499	18.82319	0.16527	0.045	171.8	7.86	10.44	125448	1.793e-15	39.885	-2.663e-04	37.326
175	398	51789	477	18.87353	0.16961	0.044	75.5	6.43	9.93	125498	1.721e-14	40.840	-5.278e-05	37.298
176	398	51789	589	19.76685	0.44177	0.078	192.3	8.06	11.31	126160	2.691e-15	40.554	-3.385e-05	37.815
177	454	51908	252	36.24962	-9.70992	0.142	174.2	7.89	10.78	101891	3.958e-15	41.285	2.067e-01	41.184
178	454	51908	144	37.09111	-8.80243	0.137	226.6	8.35	11.15	106730	6.198e-15	41.442	-3.244e-05	38.337
179	454	51908	603	37.98916	-7.50258	0.179	235.8	8.42	11.45	160581	7.538e-15	41.782	6.153e-04	38.872
180	412	52258	313	46.49724	-0.16648	0.107	214.5	8.25	11.41	156179	1.991e-14	41.720	3.170e-04	38.110
181	411	51873	120	46.57226	-0.14001	0.110	278.3	8.71	11.37	32633	2.924e-15	40.909	2.061e-02	39.941
182	411	51817	112	46.58974	-0.13717	0.108	253.4	8.54	11.04	55945	3.007e-15	40.909	2.902e-04	38.120
183	412	52250	393	46.74466	0.14259	0.075	279.2	8.71	11.25	155800	2.060e-15	40.409	3.535e-04	37.830
184	460	51924	608	51.41343	-6.05954	0.169	210.0	8.21	11.25	157374	1.487e-14	42.022	1.103e-03	39.072
185	541	51959	244	113.62512	31.70024	0.169	220.9	8.30	11.08	85750	9.647e-15	41.836	2.646e-04	38.536
186	1868	53318	379	115.90186	49.66756	0.018	214.4	8.25	10.89	77846	9.905e-15	39.829	1.934e-04	36.529
187	1059	52618	199	116.42288	27.82962	0.202	296.8	8.82	11.39	78553	8.586e-14	42.955	2.583e-02	40.610
188	1920	53314	164	117.69566	17.64849	0.206	221.3	8.31	11.42	62429	1.116e-15	41.093	1.660e-02	40.442
189	1920	53314	180	117.75314	17.63161	0.183	270.2	8.66	11.43	81649	2.688e-15	41.357	2.354e-05	38.611
190	544	52201	462	119.42546	39.40812	0.096	257.7	8.57	11.02	81779	5.034e-15	41.017	1.046e-04	38.005
191	1265	52705	225	121.06886	23.65140	0.263	200.4	8.13	11.48	88118	5.837e-15	42.048	2.514e-03	39.854
192	1205	52670	60	121.27032	24.95598	0.099	240.8	8.45	11.19	88596	2.066e-14	41.662	3.519e-04	38.077
193	2267	53713	201	121.58442	15.52929	0.095	252.3	8.54	11.28	21896	1.302e-15	40.425	4.806e-04	38.177
194	2267	53713	178	121.68290	15.54620	0.094	143.8	7.55	10.76	41975	1.616e-15	40.508	6.680e-05	37.989
195	758	52253	558	122.09308	39.01640	0.196	255.6	8.56	11.26	85328	4.443e-15	41.640	3.962e-02	40.768
196	1927	53321	186	125.09857	21.13147	0.017	192.3	8.06	10.96	53042	2.791e-15	39.207	1.490e-04	36.458
197	1927	53321	163	125.33807	20.86749	0.017	148.7	7.61	10.51	75836	2.275e-15	39.128	-3.664e-05	36.467
198	893	52589	635	126.12095	38.01633	0.102	233.3	8.40	11.07	72784	2.550e-15	40.785	3.676e-04	38.128
199	1267	52932	57	126.50255	26.76060	0.178	166.4	7.81	10.95	71477	3.201e-14	42.407	2.661e-04	38.585
200	442	51882	17	127.14342	50.29422	0.078	241.3	8.46	11.33	71859	5.515e-14	41.875	2.793e-04	37.825

Id	SDSS Plate id	SDSS MJD id	SDSS Fibre id	RA ——(J2000)——	Dec	Redshift	Velocity Dispersion km/s	Black Hole Mass —$\log_{10}$ (in solar masses)—	Stellar Mass	3XMM id	Xray Flux erg/cm^2/s	Xray Luminosity erg/s	Radio Flux Density Jy	Radio Luminosity erg/s
(1)	(2)	(3)	(4)	(5)	(6)	(7)	(8)	(9)	(10)	(11)	(12)	(13)	(14)	(15)
201	827	52312	416	127.56786	38.18935	0.167	206.5	8.19	11.46	74296	3.841e-15	41.422	-3.413e-04	38.522
202	444	51883	200	127.87683	52.75072	0.140	187.7	8.02	11.34	52400	1.072e-14	41.705	1.409e-04	38.362
203	444	51883	192	128.06607	52.69214	0.082	184.6	7.99	10.34	27156	1.795e-15	40.431	9.841e-05	37.868
204	1783	53386	147	128.84953	55.59908	0.243	335.9	9.04	11.64	305966	3.484e-15	41.745	-1.073e-03	38.882
205	828	52317	171	129.56819	38.67165	0.060	128.1	7.35	10.68	304790	2.381e-14	41.266	1.214e-04	37.582
206	828	52317	149	130.04880	38.76244	0.116	180.7	7.95	10.98	305344	1.354e-15	40.628	-4.173e-05	38.185
207	828	52317	151	130.21948	38.57883	0.216	195.1	8.09	11.43	304919	3.415e-14	42.624	6.344e-05	38.772
208	2281	53711	235	133.05141	17.96727	0.185	256.1	8.56	11.59	307163	3.285e-15	41.453	2.256e-02	40.468
209	2282	53683	283	133.60130	20.22479	0.031	210.4	8.22	10.71	25199	4.041e-15	39.909	6.199e-05	36.998
210	935	52643	447	134.12733	37.81007	0.091	181.7	7.96	10.90	300088	2.539e-15	40.676	-8.880e-06	37.962
211	1190	52670	606	134.31488	5.70540	0.152	275.5	8.69	11.56	299707	3.589e-14	42.308	9.466e-05	38.438
212	448	51900	601	134.99654	57.11056	0.183	128.6	7.36	11.27	298440	3.578e-14	42.484	1.294e-04	38.614
213	2434	53826	461	136.19952	14.48732	0.110	206.7	8.19	11.17	299356	1.465e-13	42.608	2.582e-04	38.131
214	1739	53050	334	137.22539	11.06491	0.163	358.1	9.15	11.61	303269	1.250e-15	40.916	1.936e-04	38.504
215	472	51955	440	138.01796	0.42180	0.055	200.4	8.13	10.76	303824	4.478e-15	40.457	-5.570e-05	37.499
216	472	51955	429	138.02212	0.48366	0.164	309.7	8.89	11.64	303813	2.151e-15	41.157	2.565e-04	38.509
217	1200	52668	62	138.52115	40.88007	0.146	251.7	8.53	11.22	303452	1.840e-14	41.980	7.266e-05	38.401
218	1938	53379	286	138.95613	29.83396	0.185	248.0	8.51	11.22	301455	3.906e-16	40.530	6.860e-03	39.953
219	1936	53330	23	139.09985	29.13241	0.196	209.7	8.21	11.34	301710	1.895e-14	42.274	-1.422e-04	38.679
220	2439	53795	205	139.40971	16.44049	0.029	243.2	8.47	11.06	301281	4.185e-14	40.857	1.380e-03	37.565
221	2438	54056	565	139.53873	16.19811	0.030	318.7	8.94	11.39	30398	1.012e-14	40.274	1.931e-04	36.965
222	2581	54085	134	145.04858	14.93490	0.177	221.8	8.31	11.29	321433	7.316e-16	40.761	-3.511e-04	38.581
223	2581	54085	136	145.10039	14.92263	0.013	187.8	8.02	10.78	321447	5.205e-15	39.230	1.583e-04	36.210
224	2369	53733	14	145.81705	16.87182	0.162	264.8	8.62	11.54	55257	2.224e-15	41.158	2.070e-03	39.306
225	1305	52757	494	146.53065	10.01272	0.140	172.3	7.87	11.02	321823	1.225e-15	40.758	-7.570e-05	38.357
226	266	51630	623	147.18007	0.42961	0.063	145.0	7.57	10.80	320128	7.851e-16	39.834	8.942e-05	37.632
227	995	52731	214	149.87087	5.22284	0.122	314.3	8.92	11.38	312592	2.727e-15	40.978	3.200e-03	39.230
228	1744	53055	421	149.93385	12.98858	0.024	187.2	8.01	10.80	312747	4.502e-15	39.717	6.485e-05	36.759
229	501	52235	335	149.99849	2.76911	0.166	266.1	8.63	11.51	22390	3.734e-15	41.405	2.462e-03	39.403
230	995	52731	138	150.03026	5.30021	0.122	200.7	8.14	11.09	310706	2.393e-15	40.922	-7.658e-05	38.231
231	500	51994	114	150.03976	1.61532	0.133	176.1	7.91	10.93	310773	1.103e-14	41.668	2.746e-04	38.312
232	500	51994	555	150.09075	2.00000	0.219	278.9	8.71	11.42	46807	1.536e-15	41.289	4.491e-04	38.930
233	2344	53740	167	150.20724	25.30845	0.075	234.7	8.41	11.20	310790	1.697e-15	40.324	1.072e-04	37.786
234	1950	53436	111	150.32868	28.84364	0.089	245.7	8.49	10.84	310211	2.513e-15	40.650	3.490e-04	37.978
235	500	51994	21	150.42649	1.68275	0.218	184.9	7.99	11.31	25341	4.388e-15	41.739	2.208e-04	38.778
236	1217	52672	18	150.91270	41.05427	0.233	199.9	8.13	11.39	311174	2.358e-14	42.534	5.160e-03	40.049
237	1217	52672	3	151.27424	41.09426	0.092	266.2	8.63	11.36	315286	5.163e-15	40.999	3.790e-03	39.049
238	1744	53055	590	151.80525	12.78699	0.248	232.2	8.39	11.56	315480	5.798e-15	41.988	4.757e-03	40.076
239	1744	53055	38	152.04044	12.17943	0.164	252.0	8.53	11.30	315202	2.448e-16	40.209	9.024e-04	38.955
240	271	51883	358	153.49609	-0.08159	0.090	334.2	9.03	11.56	62039	6.597e-15	41.083	2.731e-05	37.954

Id	SDSS Plate id	SDSS MJD id	SDSS Fibre id	RA ——(J2000)——	Dec	Redshift	Velocity Dispersion km/s	Black Hole Mass —$\log_{10}$ (in solar masses)—	Stellar Mass	3XMM id	Xray Flux erg/cm^2/s	Xray Luminosity erg/s	Radio Flux Density Jy	Radio Luminosity erg/s
(1)	(2)	(3)	(4)	(5)	(6)	(7)	(8)	(9)	(10)	(11)	(12)	(13)	(14)	(15)
241	2365	53739	143	154.37814	21.56517	0.187	239.7	8.45	11.57	313646	3.341e-14	42.474	7.206e-05	38.633
242	944	52614	139	154.90460	44.98227	0.164	202.0	8.15	11.05	314187	5.768e-15	41.586	2.678e-04	38.510
243	772	52375	289	155.27412	61.20079	0.132	187.9	8.02	11.16	314387	2.394e-13	42.995	4.829e-04	38.482
244	1358	52994	504	155.99499	43.85576	0.043	242.8	8.47	11.26	280919	9.075e-15	40.552	1.128e-02	38.835
245	961	52615	421	156.41550	47.08535	0.192	223.2	8.32	11.42	282158	1.848e-15	41.239	2.562e-04	38.654
246	1430	53002	314	156.60534	38.74644	0.061	125.1	7.31	10.70	282371	7.629e-15	40.790	-3.649e-05	37.600
247	2354	53799	368	157.66814	30.85505	0.136	279.5	8.71	11.27	279678	1.231e-14	41.736	2.620e-03	39.245
248	1959	53440	116	157.69842	30.85563	0.140	237.3	8.43	11.20	279721	5.132e-15	41.380	3.069e-05	38.356
249	2354	53799	410	157.75753	30.86198	0.136	319.1	8.95	11.76	279621	4.243e-15	41.273	3.288e-04	38.344
250	1430	53002	368	157.79679	40.33279	0.107	226.3	8.35	11.08	280642	3.103e-15	40.912	1.618e-04	38.109
251	875	52354	321	158.04972	50.54707	0.134	162.0	7.76	10.85	280723	8.711e-14	42.570	-1.821e-04	38.316
252	560	52296	515	158.44314	60.02444	0.229	263.5	8.61	11.38	280521	5.967e-15	41.921	9.752e-04	39.309
253	1432	53003	263	158.47567	39.69634	0.148	250.2	8.52	11.09	57954	1.859e-15	40.995	-5.895e-05	38.411
254	1432	53003	280	158.75907	39.62255	0.150	187.0	8.01	11.10	284706	6.578e-16	40.554	-1.268e-05	38.422
255	1361	53047	277	159.37422	41.87270	0.126	216.0	8.26	11.15	284308	3.724e-15	41.141	1.649e-05	38.258
256	560	52296	14	159.63094	58.78542	0.031	235.3	8.41	10.51	285274	8.682e-16	39.241	1.102e-03	37.535
257	1432	53003	559	160.18200	39.79649	0.043	170.3	7.85	11.12	285069	4.300e-14	41.220	2.826e-04	37.281
258	274	51913	43	160.37646	-1.17617	0.133	252.5	8.54	11.43	282909	5.032e-15	41.323	4.951e-04	38.498
259	1001	52670	312	161.24766	6.62336	0.108	235.5	8.42	11.22	283556	1.650e-15	40.644	-4.118e-05	38.116
260	561	52295	86	162.22627	59.32869	0.198	179.4	7.94	11.24	275642	1.793e-14	42.258	2.768e-04	38.686
261	949	52427	97	163.97761	57.44310	0.073	200.8	8.14	10.67	274042	1.814e-16	39.325	0.000e+00	37.758
262	1002	52646	437	164.18426	7.15136	0.106	308.1	8.88	11.31	274172	2.478e-15	40.805	5.829e-04	38.360
263	508	52366	284	164.38711	1.62141	0.035	148.8	7.61	10.33	278403	3.852e-15	39.998	3.875e-04	37.190
264	508	52366	268	164.71845	1.66931	0.038	158.6	7.73	10.53	278555	1.016e-15	39.490	-1.050e-03	37.178
265	277	51908	126	165.34169	-1.14022	0.074	268.3	8.64	11.52	278205	6.298e-15	40.877	1.320e-04	37.769
266	1011	52652	18	166.79754	52.63218	0.209	245.9	8.49	11.34	277734	7.947e-15	41.959	8.607e-05	38.741
267	774	52286	552	167.09958	61.46913	0.111	211.6	8.23	11.04	277178	6.923e-15	41.298	9.146e-05	38.147
268	1752	53379	258	168.09104	13.46421	0.166	253.1	8.54	11.01	293273	3.657e-15	41.395	1.408e-05	38.517
269	1752	53379	208	168.19481	13.40036	0.068	263.5	8.61	11.48	293590	1.875e-15	40.283	3.500e-03	38.741
270	1752	53379	220	168.19864	13.52043	0.178	237.0	8.43	11.61	293601	8.444e-15	41.826	3.680e-04	38.644
271	1222	52763	358	168.22701	9.51399	0.029	126.6	7.33	10.19	293517	4.288e-13	41.873	-8.468e-05	36.936
272	1752	53379	139	168.24735	13.61483	0.211	213.9	8.25	11.27	294536	1.657e-15	41.286	-9.185e-05	38.748
273	1004	52723	41	168.35362	6.08205	0.152	206.1	8.18	11.08	39972	8.750e-16	40.690	4.410e-04	38.573
274	1752	53379	97	168.40607	13.54308	0.177	251.8	8.53	11.41	294748	2.850e-15	41.352	6.424e-04	38.884
275	1752	53379	99	168.45210	13.52763	0.170	215.4	8.26	11.03	294672	3.906e-15	41.447	-1.177e-04	38.539
276	1004	52723	1	168.46719	6.15263	0.150	325.0	8.98	11.44	40660	1.678e-15	40.962	7.885e-05	38.423
277	1753	53383	289	169.98933	13.42928	0.085	248.5	8.51	11.28	292532	7.954e-15	41.104	-2.275e-05	37.894
278	511	52636	498	170.40672	2.69408	0.049	223.6	8.32	11.04	296926	9.382e-15	40.674	-5.300e-04	37.396
279	2498	54169	159	171.86482	19.13889	0.084	133.0	7.42	10.77	297365	1.385e-13	42.333	2.501e-04	37.883
280	1974	53430	161	172.90035	31.23644	0.202	211.0	8.22	11.30	55617	1.252e-15	41.120	4.246e-04	38.827

Id	SDSS Plate id	SDSS MJD id	SDSS Fibre id	RA ——(J2000)——	Dec	Redshift	Velocity Dispersion km/s	Black Hole Mass —$\log_{10}$ (in solar masses)—	Stellar Mass	3XMM id	Xray Flux erg/cm^2/s	Xray Luminosity erg/s	Radio Flux Density Jy	Radio Luminosity erg/s
(1)	(2)	(3)	(4)	(5)	(6)	(7)	(8)	(9)	(10)	(11)	(12)	(13)	(14)	(15)
281	967	52636	301	173.69398	48.95612	0.032	251.9	8.53	10.99	295690	2.561e-14	40.723	4.277e-02	39.135
282	1309	52762	554	173.69941	56.91083	0.094	185.4	8.00	10.98	295681	2.918e-14	41.767	1.590e-03	38.688
283	1619	53084	166	174.02176	7.19941	0.103	178.6	7.93	10.95	295833	1.179e-14	41.459	7.460e-03	39.445
284	1619	53084	180	174.03486	7.22931	0.102	204.9	8.17	11.45	295841	2.372e-15	40.752	7.962e-05	38.066
285	1619	53084	179	174.09882	7.22709	0.103	231.5	8.39	11.42	287611	3.132e-15	40.881	-1.969e-04	38.075
286	2507	53876	277	174.44079	21.94532	0.208	279.9	8.72	11.34	287202	3.395e-15	41.585	4.438e-04	38.877
287	2504	54179	558	174.46517	21.97424	0.030	221.5	8.31	10.94	41981	3.504e-15	39.821	-8.626e-05	36.972
288	2221	53792	216	175.63688	26.48889	0.030	323.9	8.97	11.38	288173	2.596e-14	40.693	4.467e-02	39.118
289	2506	54179	478	175.75173	20.20852	0.070	224.2	8.33	11.08	288075	2.834e-15	40.485	-3.478e-04	37.724
290	2509	54180	188	176.37477	19.44469	0.021	187.7	8.02	10.73	286234	7.493e-15	39.839	-2.580e-04	36.661
291	514	51994	493	176.40360	2.80297	0.106	212.4	8.23	11.20	286307	1.893e-14	41.688	-2.788e-04	38.100
292	1016	52759	143	177.67741	54.94387	0.228	261.9	8.60	11.43	286417	5.613e-15	41.891	-4.056e-04	38.822
293	1016	52759	120	178.02177	54.99926	0.059	214.4	8.25	10.76	290736	1.190e-14	40.949	-9.507e-05	37.566
294	2513	54141	447	178.78196	23.53943	0.149	208.2	8.20	11.17	59915	3.055e-15	41.216	-3.596e-05	38.416
295	2513	54141	522	178.83753	23.29608	0.144	210.3	8.22	11.01	291504	8.735e-16	40.639	9.552e-04	38.859
296	881	52368	600	179.21082	52.96910	0.199	183.3	7.98	11.36	291672	1.551e-14	42.198	1.753e-04	38.689
297	331	52368	126	180.34374	-3.40450	0.167	213.2	8.24	11.29	288979	4.119e-14	42.457	7.120e-06	38.526
298	2225	53729	566	180.97467	31.12455	0.165	284.0	8.74	11.69	289586	2.793e-14	42.275	-5.058e-05	38.513
299	2227	53820	539	181.52766	28.25634	0.029	182.2	7.97	10.86	355150	2.003e-15	39.556	5.051e-04	37.148
300	2226	53819	606	181.62861	28.13781	0.030	208.9	8.21	10.88	356204	1.533e-15	39.445	5.981e-05	36.955
301	1995	53415	218	182.55612	39.40912	0.160	202.3	8.15	11.17	353799	3.144e-16	40.298	-3.290e-06	38.485
302	969	52442	584	182.75463	50.57553	0.170	226.9	8.35	11.26	353986	4.442e-16	40.505	2.999e-04	38.542
303	969	52442	636	182.89532	50.30501	0.094	168.2	7.83	10.99	353421	2.172e-13	42.636	3.040e-04	37.990
304	1612	53149	489	183.02274	13.20564	0.065	234.1	8.40	11.45	353680	7.618e-15	40.843	1.036e-04	37.653
305	2230	53799	246	183.11203	29.14921	0.013	88.8	6.71	10.27	353580	5.086e-15	39.267	1.615e-05	36.257
306	2228	53818	20	183.33787	29.23708	0.144	218.2	8.28	11.07	354546	1.221e-13	42.783	2.460e-02	40.268
307	1766	53468	300	183.49173	14.06696	0.154	308.2	8.89	11.51	20191	1.612e-15	40.969	2.640e-03	39.363
308	1765	53466	7	183.69772	14.09551	0.081	156.9	7.71	11.23	13012	2.604e-14	41.574	1.511e-04	37.850
309	2230	53799	598	184.80043	29.90890	0.104	140.5	7.51	10.94	358359	7.078e-15	41.242	1.295e-05	38.081
310	844	52378	578	184.98189	5.89252	0.172	173.8	7.88	10.70	50197	2.947e-15	41.340	-3.853e-05	38.555
311	2232	53827	219	185.11411	29.09654	0.132	230.6	8.38	11.15	359255	8.037e-15	41.520	-1.357e-04	38.302
312	2232	53827	172	185.12115	30.06094	0.214	200.8	8.14	11.71	359259	3.954e-14	42.676	2.945e-04	38.760
313	2232	53827	203	185.15512	29.24254	0.170	190.7	8.05	11.02	359235	1.292e-14	41.967	1.849e-04	38.540
314	2233	53845	429	185.29728	28.07831	0.027	140.6	7.51	10.36	359387	1.437e-15	39.347	2.319e-04	36.885
315	2232	53827	150	185.40591	29.95013	0.166	164.1	7.78	11.20	358935	1.821e-14	42.097	7.377e-05	38.521
316	1231	52725	403	186.00430	10.67733	0.131	253.9	8.55	11.14	356659	1.634e-15	40.819	5.517e-04	38.530
317	2612	54480	337	186.33054	20.80280	0.128	201.5	8.14	11.15	357718	3.889e-15	41.177	7.158e-03	39.624
318	1615	53166	421	186.75985	12.86862	0.132	202.5	8.15	11.20	65461	7.226e-16	40.476	5.230e-05	38.304
319	2015	53819	233	186.88616	33.60466	0.104	218.1	8.28	10.95	349457	1.038e-14	41.412	5.000e-05	38.085
320	1768	53442	286	187.22925	13.79083	0.044	242.3	8.46	11.00	349028	2.022e-15	39.912	5.267e-05	37.300

Id	SDSS Plate id	SDSS MJD id	SDSS Fibre id	RA ——(J2000)——	Dec	Redshift	Velocity Dispersion km/s	Black Hole Mass —$\log_{10}$ (in solar masses)—	Stellar Mass	3XMM id	Xray Flux erg/cm^2/s	Xray Luminosity erg/s	Radio Flux Density Jy	Radio Luminosity erg/s
(1)	(2)	(3)	(4)	(5)	(6)	(7)	(8)	(9)	(10)	(11)	(12)	(13)	(14)	(15)
321	2598	54232	504	187.56727	18.02882	0.133	285.3	8.75	11.41	349612	2.702e-15	41.057	6.490e-03	39.619
322	1454	53090	318	187.73130	41.78504	0.174	300.4	8.84	11.57	19220	6.394e-15	41.686	1.515e-02	40.239
323	2647	54495	253	187.80132	21.73617	0.129	138.4	7.49	10.95	347421	2.198e-15	40.937	1.391e-04	38.282
324	1768	53442	165	187.93865	14.77183	0.198	112.5	7.13	10.93	348131	5.304e-14	42.730	-4.631e-05	38.687
325	2659	54498	485	187.98735	25.61054	0.230	230.6	8.38	11.46	347992	9.615e-15	42.134	1.240e-04	38.831
326	1992	53466	10	188.47326	37.54766	0.117	235.4	8.41	11.32	352469	1.653e-14	41.724	3.460e-03	39.228
327	1992	53466	610	188.66732	39.35282	0.123	175.2	7.90	11.31	351910	1.415e-15	40.703	1.742e-04	38.240
328	335	52000	244	188.78791	-3.59709	0.059	235.2	8.41	11.20	353113	6.195e-15	40.675	-4.810e-06	37.576
329	2000	53495	323	188.78907	39.45153	0.092	164.2	7.79	11.35	353179	2.345e-15	40.649	-3.853e-05	37.969
330	2236	53729	293	188.91878	26.64295	0.020	142.9	7.54	10.27	352746	2.209e-15	39.255	4.072e-04	36.711
331	2236	53729	285	188.92164	26.52308	0.022	319.2	8.95	11.38	352759	2.158e-14	40.337	1.494e-03	37.368
332	2659	54498	580	189.05943	25.84010	0.176	183.0	7.97	11.20	350809	7.607e-14	42.773	3.395e-04	38.601
333	1616	53169	518	189.13028	12.99536	0.093	253.6	8.54	11.20	350747	3.434e-15	40.830	1.280e-03	38.587
334	1453	53084	36	189.89271	47.53750	0.131	209.4	8.21	11.20	351531	1.795e-13	42.866	3.599e-04	38.350
335	2600	54243	365	190.20951	18.61338	0.069	254.0	8.55	11.02	351240	1.636e-15	40.228	-3.757e-04	37.707
336	2020	53431	58	190.53954	33.22165	0.159	286.9	8.76	11.50	46930	7.879e-15	41.692	4.757e-03	39.653
337	1769	53502	54	190.55643	14.16185	0.154	234.7	8.41	11.43	367710	2.951e-15	41.235	3.480e-03	39.486
338	521	52326	111	190.55952	2.54996	0.120	260.7	8.59	11.39	367717	9.084e-16	40.488	-2.581e-05	38.218
339	1975	53734	409	190.69563	33.31707	0.244	276.2	8.69	11.65	367427	4.203e-16	40.834	-6.660e-06	38.889
340	1769	53502	66	190.72115	14.32250	0.071	175.1	7.90	10.56	367337	5.226e-16	39.760	2.015e-04	37.733
341	522	52024	176	191.71377	2.29492	0.135	247.7	8.50	11.12	366160	2.617e-15	41.057	-3.589e-05	38.326
342	1038	52673	171	191.82513	54.57993	0.240	229.7	8.37	11.52	366335	8.666e-15	42.130	1.840e-03	39.631
343	1790	53876	602	192.26286	8.52322	0.274	273.5	8.68	11.66	366923	5.408e-15	42.055	2.527e-04	38.999
344	848	52669	348	192.52344	5.24114	0.213	178.7	7.93	11.31	366549	7.927e-16	40.973	-6.919e-05	38.755
345	2238	54205	631	193.04415	27.51749	0.086	136.0	7.46	10.44	370992	4.076e-15	40.823	-6.943e-05	37.904
346	2240	53823	208	193.46048	26.31052	0.172	157.1	7.71	11.05	371528	1.630e-14	42.084	-1.678e-04	38.555
347	1770	53171	605	193.46941	15.87115	0.130	200.1	8.13	11.14	371582	6.329e-14	42.405	-1.817e-04	38.291
348	2240	53823	200	193.92207	27.25076	0.024	251.3	8.53	10.80	371349	1.111e-14	40.104	9.381e-05	36.754
349	2240	53823	478	194.14246	27.53895	0.024	160.9	7.75	10.47	369508	5.048e-15	39.762	2.483e-04	36.754
350	2240	53823	447	194.17857	28.02045	0.021	188.2	8.02	10.56	369547	5.033e-15	39.650	-1.617e-05	36.644
351	2240	53823	179	194.18133	27.17880	0.025	254.2	8.55	11.16	369420	1.123e-14	40.169	1.169e-02	38.377
352	2240	53823	476	194.31994	27.61846	0.024	160.9	7.75	10.11	44084	9.641e-15	40.061	1.847e-04	36.773
353	2240	53823	491	194.35769	27.54613	0.019	169.3	7.84	10.18	369157	2.486e-14	40.240	2.260e-06	36.541
354	2662	54505	311	194.38308	24.21118	0.141	226.3	8.35	11.12	369015	6.229e-12	44.471	1.063e-02	39.884
355	1457	53116	98	194.38512	47.06254	0.131	121.4	7.26	10.78	369082	6.920e-15	41.450	1.065e-04	38.297
356	2240	53823	496	194.38683	27.61035	0.020	238.1	8.43	10.76	2596	6.167e-15	39.706	6.901e-04	36.946
357	2240	53823	153	194.40057	27.48482	0.024	161.6	7.76	10.29	27673	4.452e-15	39.725	2.798e-04	36.772
358	2240	53823	120	194.50652	27.48967	0.025	84.1	6.62	10.46	28026	3.154e-15	39.621	-4.404e-05	36.818
359	2241	54169	121	194.50994	26.85953	0.025	159.8	7.74	10.62	370271	1.627e-15	39.302	-7.972e-05	36.786
360	338	51694	529	194.65942	-1.57486	0.086	222.4	8.32	11.39	369584	2.733e-15	40.657	3.499e-02	39.950

Id	SDSS Plate id	SDSS MJD id	SDSS Fibre id	RA ——(J2000)——	Dec	Redshift	Velocity Dispersion km/s	Black Hole Mass —$\log_{10}$ (in solar masses)—	Stellar Mass	3XMM id	Xray Flux erg/cm^2/s	Xray Luminosity erg/s	Radio Flux Density Jy	Radio Luminosity erg/s
(1)	(2)	(3)	(4)	(5)	(6)	(7)	(8)	(9)	(10)	(11)	(12)	(13)	(14)	(15)
361	2240	53823	68	194.80712	27.40257	0.019	187.8	8.02	10.29	369775	1.234e-14	39.950	-2.193e-04	36.555
362	2240	53823	620	194.99062	28.24667	0.022	192.7	8.06	10.86	4425	2.274e-15	39.366	-3.966e-05	36.705
363	2241	54169	450	195.07470	28.20240	0.028	232.7	8.39	11.21	6238	3.927e-15	39.816	3.222e-04	36.920
364	2241	54169	443	195.12821	28.34638	0.020	159.8	7.74	10.64	4304	1.143e-15	38.963	7.020e-06	36.601
365	2011	53499	118	195.21705	28.36612	0.025	173.1	7.88	10.83	4488	2.244e-15	39.475	-9.907e-05	36.820
366	2241	54169	577	195.44591	28.09500	0.019	180.0	7.95	10.47	362378	4.648e-15	39.549	5.452e-05	36.577
367	2241	54169	585	195.47388	27.62445	0.026	264.0	8.61	11.28	362372	4.917e-15	39.841	3.161e-04	36.845
368	338	51694	113	195.58953	-2.50170	0.080	243.3	8.47	11.19	362317	5.618e-15	40.898	8.387e-04	38.258
369	2242	54153	326	195.67300	28.13631	0.165	220.1	8.30	11.29	362598	3.311e-15	41.346	6.710e-03	39.832
370	1039	52707	179	195.87949	53.99682	0.242	227.9	8.36	11.63	361899	1.919e-14	42.484	1.453e-03	39.536
371	2603	54479	422	196.25931	18.00476	0.088	196.6	8.10	10.52	360084	1.091e-15	40.282	-5.992e-04	37.935
372	2603	54479	485	196.49517	17.96215	0.080	188.8	8.03	10.99	360293	1.775e-15	40.404	-2.681e-04	37.846
373	2603	54479	533	196.64265	18.00070	0.106	137.1	7.47	10.88	359731	2.581e-15	40.825	1.871e-04	38.102
374	2009	53904	465	197.11575	29.40579	0.123	275.3	8.69	11.53	360869	1.425e-15	40.706	1.955e-04	38.240
375	340	51691	392	197.34376	-1.71598	0.143	240.0	8.45	11.18	360516	2.351e-15	41.064	1.017e-04	38.379
376	2029	53819	615	197.40609	32.39536	0.123	227.8	8.36	11.11	360376	1.523e-15	40.731	2.100e-04	38.236
377	2029	53819	603	197.59310	32.23584	0.125	266.8	8.63	11.57	364600	1.367e-14	41.702	1.120e-03	38.798
378	2029	53819	605	197.62524	32.48621	0.186	235.1	8.41	11.29	364652	1.093e-15	40.985	3.575e-04	38.677
379	1795	54507	528	197.65113	8.30091	0.219	227.9	8.36	11.44	364899	4.968e-15	41.797	5.648e-04	39.028
380	2016	53799	69	197.83773	35.26151	0.101	262.4	8.60	11.23	364479	1.147e-14	41.429	2.296e-04	38.058
381	2029	53819	634	197.84136	31.83707	0.146	216.4	8.27	10.92	364491	7.331e-16	40.580	1.075e-04	38.401
382	2650	54505	623	197.86806	22.06998	0.172	288.4	8.77	11.50	364406	6.660e-15	41.692	9.180e-03	40.010
383	2243	53794	373	198.13650	27.95095	0.206	207.5	8.19	11.43	364961	6.343e-14	42.847	3.708e-04	38.791
384	296	51665	215	199.76966	-0.89105	0.085	248.9	8.51	11.29	364018	1.950e-15	40.497	7.805e-04	38.285
385	296	51984	130	199.87437	-1.14550	0.139	280.7	8.72	11.51	363533	7.665e-15	41.551	5.728e-03	39.605
386	296	51984	188	199.96674	-0.73241	0.112	196.8	8.10	10.86	363566	6.614e-15	41.283	2.161e-05	38.151
387	2093	53818	36	200.20425	33.10038	0.035	208.6	8.20	10.77	330739	1.493e-15	39.569	2.333e-04	37.090
388	1799	53556	506	201.36618	7.69703	0.033	122.3	7.27	10.65	329191	1.513e-15	39.522	2.800e-04	37.038
389	297	51663	441	201.68112	1.13769	0.083	196.3	8.10	11.24	328960	8.093e-15	41.098	1.600e-03	38.580
390	1699	53148	235	202.17362	11.60851	0.024	215.8	8.26	10.75	329536	7.469e-15	39.959	-4.871e-04	36.782
391	1699	53148	169	202.37869	11.74583	0.024	239.1	8.44	10.97	329766	4.353e-15	39.715	1.375e-03	37.405
392	1699	53148	157	202.44959	11.70913	0.085	194.4	8.08	11.26	333908	1.819e-15	40.472	3.760e-03	38.972
393	2665	54232	397	202.49105	24.19389	0.166	275.9	8.69	11.54	49790	4.256e-15	41.461	4.312e-04	38.646
394	298	51955	300	202.50520	-0.68173	0.239	280.9	8.72	11.62	333812	6.298e-15	41.988	5.354e-04	39.091
395	2665	54232	375	202.67121	25.02177	0.108	200.9	8.14	11.10	333525	2.247e-15	40.777	6.861e-04	38.446
396	1668	53433	172	202.98382	50.58007	0.109	219.8	8.29	11.17	334868	4.666e-15	41.110	-1.814e-05	38.130
397	1669	53433	318	203.70721	50.40615	0.088	147.2	7.59	10.72	332220	3.324e-15	40.767	1.399e-04	37.935
398	1668	53433	585	204.19634	51.69027	0.068	284.5	8.74	11.26	332159	7.457e-15	40.879	5.067e-04	37.898
399	298	51955	25	204.88978	-0.37321	0.141	331.3	9.01	11.57	324664	5.732e-15	41.439	4.490e-03	39.514
400	299	51671	232	204.89268	-0.27657	0.145	342.7	9.07	11.73	324659	2.549e-14	42.113	2.459e-03	39.279

Id	SDSS Plate id	SDSS MJD id	SDSS Fibre id	RA ——(J2000)——	Dec	Redshift	Velocity Dispersion km/s	Black Hole Mass —$\log_{10}$ (in solar masses)—	Stellar Mass	3XMM id	Xray Flux erg/cm^2/s	Xray Luminosity erg/s	Radio Flux Density Jy	Radio Luminosity erg/s
(1)	(2)	(3)	(4)	(5)	(6)	(7)	(8)	(9)	(10)	(11)	(12)	(13)	(14)	(15)
401	299	51671	181	205.18926	-0.46546	0.143	266.5	8.63	11.30	324779	3.165e-15	41.194	-1.456e-04	38.380
402	2246	53767	512	205.60674	26.21243	0.066	244.0	8.48	11.24	324452	2.264e-15	40.328	1.180e-03	38.232
403	1321	52764	74	205.92486	55.71478	0.136	231.3	8.38	11.24	325609	2.292e-14	42.002	2.047e-04	38.329
404	2115	53535	413	207.10599	26.41081	0.062	233.7	8.40	10.91	55138	1.649e-15	40.143	1.050e-04	37.618
405	2114	53848	186	207.15308	27.02268	0.175	190.6	8.05	11.15	323743	1.422e-14	42.037	-1.275e-04	38.568
406	2114	53848	84	207.34320	26.45532	0.060	246.9	8.50	11.33	61350	3.954e-15	40.483	9.269e-05	37.579
407	2114	53848	98	207.36148	26.46189	0.076	159.7	7.74	10.99	61978	1.128e-14	41.162	3.068e-05	37.801
408	2114	53848	95	207.42204	26.71701	0.067	239.5	8.44	11.38	43361	1.351e-15	40.115	-1.436e-05	37.676
409	2117	54115	426	208.51064	33.85165	0.171	212.7	8.24	11.42	327185	1.714e-15	41.098	1.451e-03	39.204
410	915	52443	428	210.18419	-1.59415	0.146	118.1	7.21	10.70	325800	1.411e-14	41.859	2.511e-04	38.396
411	1347	52823	431	212.23671	41.72541	0.143	239.0	8.44	11.52	58471	4.282e-15	41.322	2.962e-02	40.343
412	2123	53793	145	212.39523	26.49529	0.133	265.8	8.63	11.34	40630	4.034e-16	40.229	-1.656e-04	38.310
413	2123	53793	2	212.46254	26.20911	0.108	140.6	7.51	10.63	342830	2.278e-15	40.784	-2.170e-04	38.116
414	533	51994	399	213.23447	2.30147	0.145	229.5	8.37	11.28	343408	1.574e-15	40.904	3.491e-04	38.431
415	916	52378	53	213.38935	-3.22962	0.079	147.5	7.60	10.32	343590	2.296e-14	41.499	-7.038e-05	37.829
416	1394	53108	421	213.53646	44.09286	0.137	180.8	7.95	10.93	341591	3.818e-14	42.237	1.594e-05	38.342
417	2126	53794	147	213.61296	28.47518	0.140	262.9	8.61	11.36	341439	8.809e-14	42.618	2.534e-02	40.258
418	304	51609	292	213.62168	-0.37475	0.136	261.2	8.60	11.33	341441	9.712e-16	40.633	1.021e-02	39.837
419	1287	52728	284	214.25588	45.09241	0.114	185.4	8.00	11.13	341404	6.293e-14	42.279	3.794e-04	38.242
420	2128	53800	122	214.34995	23.30053	0.172	219.0	8.29	11.33	342329	7.424e-15	41.740	2.449e-04	38.553
421	1045	52725	526	214.59518	52.45246	0.281	260.0	8.59	11.59	342528	6.395e-15	42.154	3.955e-05	39.024
422	1826	53499	485	215.20120	6.71153	0.174	239.6	8.45	11.47	342067	2.031e-13	43.186	1.463e-03	39.223
423	584	52049	251	215.28081	3.24825	0.136	193.1	8.07	10.95	346198	5.411e-15	41.377	4.983e-05	38.330
424	1673	53462	386	215.34654	47.91841	0.073	235.7	8.42	11.40	346162	1.046e-14	41.083	-2.330e-05	37.755
425	1395	52825	253	216.03113	42.23570	0.072	127.2	7.34	10.53	346392	1.036e-14	41.073	4.003e-05	37.749
426	2131	53819	456	216.11733	26.66836	0.171	250.2	8.52	11.47	25273	5.881e-16	40.630	3.703e-04	38.608
427	2131	53819	530	216.29334	26.70559	0.171	199.7	8.13	10.90	42716	4.187e-14	42.485	5.480e-04	38.781
428	2131	53819	616	216.80769	26.58671	0.173	251.6	8.53	11.43	345755	6.975e-16	40.719	4.621e-04	38.719
429	1395	52825	166	216.90192	42.61985	0.143	222.3	8.31	11.17	4359	6.075e-15	41.478	6.880e-03	39.713
430	1673	53462	156	217.11285	47.86113	0.187	257.1	8.57	11.22	345874	1.982e-15	41.248	-4.674e-04	38.634
431	1396	53112	313	217.71212	42.00827	0.140	215.2	8.26	11.07	346561	1.021e-14	41.684	1.355e-04	38.361
432	586	52023	278	218.66665	3.63883	0.146	173.2	7.88	11.05	33102	1.205e-14	41.793	4.289e-04	38.526
433	585	52027	39	218.74680	3.60757	0.146	190.9	8.05	11.08	344848	2.787e-15	41.157	-3.778e-04	38.398
434	1047	52733	226	219.10327	48.81988	0.075	216.3	8.27	11.02	344252	3.095e-14	41.587	3.320e-03	38.804
435	2947	54533	511	219.59145	64.38259	0.141	254.8	8.55	11.34	344337	1.560e-15	40.875	3.245e-03	39.374
436	2947	54533	555	219.66136	64.39091	0.143	217.0	8.27	11.28	344387	6.413e-16	40.497	3.140e-04	38.376
437	586	52023	123	219.86992	2.76874	0.144	293.8	8.80	11.63	345292	1.288e-14	41.811	2.660e-03	39.307
438	307	51663	28	220.83390	-0.66822	0.148	214.4	8.25	11.12	337109	1.290e-14	41.838	1.467e-04	38.413
439	308	51662	273	220.86192	-0.72091	0.150	260.1	8.59	11.55	337112	1.918e-15	41.020	3.315e-05	38.423
440	1829	53494	425	220.97269	6.55540	0.191	217.5	8.28	11.18	337040	1.902e-15	41.251	1.969e-04	38.654

Id	SDSS Plate id	SDSS MJD id	SDSS Fibre id	RA ——(J2000)——	Dec	Redshift	Velocity Dispersion km/s	Black Hole Mass —$\log_{10}$ (in solar masses)—	Stellar Mass	3XMM id	Xray Flux erg/cm^2/s	Xray Luminosity erg/s	Radio Flux Density Jy	Radio Luminosity erg/s
(1)	(2)	(3)	(4)	(5)	(6)	(7)	(8)	(9)	(10)	(11)	(12)	(13)	(14)	(15)
441	537	52027	194	221.18177	1.76770	0.180	149.8	7.62	11.17	13693	1.295e-14	42.025	1.120e-04	38.596
442	537	52027	476	221.39938	2.06318	0.068	230.2	8.38	10.99	25975	1.763e-15	40.243	-2.212e-04	37.689
443	2142	54208	588	222.67818	27.25759	0.251	262.7	8.61	11.53	337538	2.599e-14	42.653	9.400e-03	40.384
444	2777	54554	536	222.78430	19.23224	0.060	104.3	6.99	10.04	337403	6.147e-14	41.679	-5.168e-05	37.583
445	2763	54507	610	223.00656	16.86161	0.118	234.1	8.40	11.25	335301	3.365e-15	41.040	7.201e-05	38.201
446	2777	54554	560	223.43757	18.56837	0.072	158.6	7.73	11.00	335535	1.651e-14	41.269	5.857e-05	37.743
447	540	51996	241	226.88587	1.05003	0.092	244.6	8.48	11.01	340310	5.932e-15	41.057	3.035e-02	39.951
448	310	51990	35	227.12781	-0.24707	0.095	168.5	7.83	10.88	340569	3.442e-15	40.847	5.212e-05	38.000
449	1386	53116	345	227.50332	33.51394	0.109	178.0	7.93	10.81	338408	3.068e-14	41.925	-4.100e-04	38.127
450	1832	54259	484	227.60605	5.84112	0.074	215.5	8.26	11.12	13069	2.084e-15	40.405	3.011e-04	37.778
451	1386	53116	398	227.67132	33.58465	0.114	207.9	8.20	11.53	15777	2.202e-12	43.824	4.520e-03	39.319
452	1833	54561	408	227.78242	5.88462	0.077	191.8	8.06	10.81	18049	2.904e-15	40.584	1.935e-03	38.594
453	1817	53851	475	227.81709	7.46330	0.205	224.6	8.33	11.59	338145	1.867e-14	42.310	5.218e-04	38.933
454	1817	53851	476	227.83972	7.38073	0.044	210.2	8.22	10.92	338152	5.677e-16	39.364	8.068e-05	37.304
455	1817	53851	479	228.00459	7.38955	0.042	180.2	7.95	10.40	338262	1.622e-15	39.782	4.567e-05	37.266
456	612	52079	217	228.24258	56.38280	0.091	112.9	7.13	10.82	338165	5.103e-15	40.981	0.000e+00	37.964
457	1678	53433	310	228.72534	42.01315	0.135	315.4	8.93	11.83	339423	1.682e-15	40.863	5.510e-03	39.560
458	1817	53851	111	229.04137	6.95152	0.032	128.0	7.35	10.53	35101	2.911e-14	40.790	1.526e-04	37.021
459	312	51689	208	229.07079	-0.85092	0.124	231.8	8.39	11.31	339042	3.334e-15	41.082	1.485e-04	38.246
460	1818	54539	433	229.29396	7.20910	0.077	282.1	8.73	11.25	14590	1.994e-15	40.418	-2.040e-05	37.809
461	1649	53149	550	229.53943	31.29341	0.108	274.4	8.68	11.29	207553	2.565e-15	40.840	6.768e-04	38.445
462	1818	54539	608	230.64636	7.72781	0.044	255.7	8.56	11.02	208236	7.497e-15	40.485	1.373e-04	37.304
463	1721	53857	507	230.91332	8.75909	0.034	231.7	8.39	10.87	40628	3.985e-15	39.988	-1.529e-05	37.082
464	1400	53470	50	231.71999	36.01701	0.152	133.2	7.42	11.20	208313	2.016e-14	42.053	4.955e-05	38.434
465	2163	53823	50	233.52701	23.48837	0.164	177.5	7.92	11.11	7626	3.934e-14	42.418	-4.377e-04	38.507
466	1417	53141	302	237.00639	35.15498	0.235	248.5	8.51	11.57	210690	1.756e-16	40.415	2.264e-04	38.850
467	1654	53498	391	237.31735	27.07434	0.126	251.6	8.53	11.28	210122	1.404e-14	41.717	1.237e-04	38.257
468	2520	54584	606	239.14543	11.21706	0.106	252.2	8.53	11.44	53505	4.069e-15	41.022	1.338e-04	38.101
469	1392	52822	274	239.50115	27.30062	0.090	201.7	8.14	11.04	208628	1.145e-14	41.321	1.078e-04	37.952
470	1392	52822	433	239.63135	27.36214	0.100	161.7	7.76	11.04	208660	2.199e-14	41.700	5.683e-04	38.297
471	1391	52817	65	239.76843	27.26856	0.091	193.4	8.07	11.09	209783	3.450e-15	40.808	-9.420e-06	37.961
472	2197	53555	221	240.74493	15.84282	0.032	236.4	8.42	11.02	209486	1.749e-15	39.565	2.697e-04	37.017
473	1170	52756	412	241.32810	43.32309	0.131	224.7	8.33	11.26	59275	4.285e-14	42.245	-8.300e-06	38.300
474	1418	53142	44	241.43772	32.87215	0.116	115.8	7.18	10.81	4223	1.053e-14	41.516	1.118e-04	38.181
475	2528	54571	451	244.09263	12.56277	0.050	103.8	6.99	9.79	199491	3.290e-15	40.247	-1.548e-04	37.424
476	1172	52759	510	247.23855	39.70829	0.031	187.9	8.02	10.54	205099	3.659e-14	40.866	5.578e-05	36.998
477	1172	52759	75	247.31876	39.40104	0.028	197.6	8.11	10.74	205146	2.366e-15	39.586	8.636e-05	36.907
478	817	52381	429	248.00751	41.42518	0.135	172.3	7.87	11.01	204843	2.199e-14	41.981	-7.609e-05	38.326
479	1572	53177	533	248.21847	24.64736	0.220	218.8	8.29	11.63	202438	8.504e-13	44.034	7.440e-03	40.152
480	1339	52767	312	248.24720	34.18560	0.125	174.4	7.89	10.89	202275	4.700e-15	41.236	9.014e-05	38.251

Id	SDSS Plate id	SDSS MJD id	SDSS Fibre id	RA ——(J2000)——	Dec	Redshift	Velocity Dispersion km/s	Black Hole Mass —$\log_{10}$ (in solar masses)—	Stellar Mass	3XMM id	Xray Flux erg/cm^2/s	Xray Luminosity erg/s	Radio Flux Density Jy	Radio Luminosity erg/s
(1)	(2)	(3)	(4)	(5)	(6)	(7)	(8)	(9)	(10)	(11)	(12)	(13)	(14)	(15)
481	817	52381	11	250.69639	39.68293	0.161	211.9	8.23	11.42	217870	3.149e-15	41.301	2.698e-03	39.413
482	1424	52912	147	253.24373	23.60456	0.165	306.6	8.88	11.48	223381	5.510e-14	42.568	5.099e-04	38.714
483	1691	53260	581	254.26749	27.69272	0.181	237.1	8.43	11.34	222126	4.929e-15	41.609	3.581e-04	38.648
484	973	52426	181	255.04678	32.58744	0.102	238.6	8.44	11.32	213776	1.282e-14	41.484	1.075e-02	39.592
485	973	52426	509	255.74878	33.55451	0.085	274.4	8.68	11.27	214585	5.440e-15	40.942	4.352e-04	38.031
486	353	51703	142	258.46591	59.09188	0.129	163.0	7.77	11.20	217086	2.200e-14	41.938	6.200e-06	38.283
487	2974	54592	595	260.59857	32.02453	0.227	281.7	8.73	11.52	18450	1.696e-14	42.367	6.559e-02	41.129
488	636	52176	334	312.68658	-5.58312	0.155	203.1	8.16	11.13	273152	3.114e-14	42.265	6.980e-03	39.796
489	988	52520	451	322.25317	0.18262	0.133	226.8	8.35	11.02	261870	5.516e-15	41.369	1.306e-05	38.314
490	988	52520	168	322.35953	0.09053	0.138	253.3	8.54	11.59	265989	3.342e-15	41.185	5.537e-05	38.348
491	1521	52945	151	322.48074	0.13372	0.234	252.5	8.54	11.35	266193	3.170e-15	41.669	3.038e-03	39.825
492	731	52460	245	323.05575	10.29343	0.077	221.7	8.31	11.24	265775	2.256e-14	41.471	-5.097e-05	37.809
493	989	52468	549	324.29733	0.64552	0.174	191.8	8.06	11.26	264443	3.341e-15	41.401	3.437e-04	38.592
494	716	52203	124	328.98406	-9.34437	0.134	153.2	7.66	11.04	232446	2.566e-14	42.042	-2.722e-04	38.319
495	716	52203	492	329.32013	-7.91403	0.058	205.0	8.17	10.95	232354	5.108e-15	40.565	-4.569e-05	37.549
496	717	52468	311	329.33923	-7.81302	0.059	183.4	7.98	10.90	232415	2.185e-15	40.209	-2.942e-04	37.562
497	716	52203	491	329.34756	-7.97057	0.056	269.8	8.65	11.11	45928	9.403e-16	39.805	-3.864e-04	37.525
498	1104	52912	218	333.47107	-1.07149	0.155	211.3	8.23	11.10	234708	1.318e-13	42.892	1.213e-04	38.457
499	374	51791	215	333.60312	-0.91006	0.260	270.4	8.66	11.71	234932	9.023e-14	43.228	3.750e-03	40.019
500	719	52203	155	334.17215	-9.23731	0.085	295.5	8.81	11.50	235776	6.169e-15	41.000	3.360e-03	38.922
501	382	51816	520	349.63839	0.27933	0.136	162.4	7.77	10.87	242880	1.383e-14	41.783	-6.629e-05	38.329
502	383	51818	553	351.61496	0.16097	0.108	262.8	8.61	10.92	248404	9.350e-16	40.398	6.991e-04	38.455
503	385	51877	596	355.91556	0.42438	0.186	228.3	8.36	11.58	237037	7.736e-14	42.832	3.770e-04	38.697
504	649	52201	176	358.41882	-10.40555	0.074	232.9	8.40	11.24	239604	3.365e-16	39.608	-4.138e-04	37.773
505	398	51789	434	18.81563	0.08818	0.107	136.5	7.46	11.26	125477	2.555e-15	40.827	4.837e-04	38.289
506	460	51924	569	51.33072	-6.20583	0.035	104.0	6.99	10.21	156453	3.681e-14	40.960	-3.455e-04	37.089
507	1927	53321	233	124.96622	20.98497	0.016	221.0	8.30	10.78	372167	1.267e-15	38.833	2.097e-04	36.426
508	553	51999	521	138.35150	52.89876	0.060	145.7	7.58	10.88	303943	2.921e-14	41.358	1.546e-02	39.269
509	1938	53379	48	140.62560	29.85746	0.149	179.7	7.94	11.13	317943	1.375e-13	42.868	3.124e-04	38.415
510	1939	53389	492	141.97012	29.98575	0.027	213.5	8.24	11.27	316969	5.914e-15	39.936	4.875e-05	36.860
511	2345	53757	320	149.34196	27.21681	0.056	102.4	6.96	10.37	311993	8.100e-14	41.731	-2.803e-04	37.516
512	501	52235	354	149.92842	2.59210	0.079	135.1	7.44	10.41	312882	7.698e-15	41.023	1.947e-04	37.828
513	500	51994	594	150.40389	2.50887	0.124	190.4	8.04	11.29	53966	2.787e-15	41.001	-1.012e-04	38.243
514	1949	53433	567	150.77107	33.04726	0.029	126.8	7.33	10.54	311037	2.159e-13	41.567	-6.471e-05	36.927
515	948	52428	357	158.24892	57.88934	0.123	219.3	8.29	11.26	280166	1.007e-14	41.555	1.162e-03	38.800
516	1433	53035	302	159.87682	39.78861	0.093	274.2	8.68	11.52	285452	2.658e-14	41.715	1.698e-02	39.705
517	1000	52643	136	160.22997	5.99141	0.028	108.8	7.07	10.15	284980	1.654e-14	40.417	3.657e-03	37.952
518	2215	53793	472	169.11861	29.28595	0.047	234.4	8.41	11.04	292389	2.821e-15	40.127	8.050e-03	38.771
519	1309	52762	596	174.19093	56.98611	0.067	186.0	8.00	11.23	287798	9.113e-15	40.955	-2.345e-04	37.687
520	2509	54180	432	176.00901	19.97192	0.021	184.4	7.99	10.66	286023	6.233e-15	39.752	1.634e-04	36.653

Id	SDSS Plate id	SDSS MJD id	SDSS Fibre id	RA ——(J2000)——	Dec	Redshift	Velocity Dispersion km/s	Black Hole Mass —$\log_{10}$ (in solar masses)—	Stellar Mass	3XMM id	Xray Flux erg/cm^2/s	Xray Luminosity erg/s	Radio Flux Density Jy	Radio Luminosity erg/s
(1)	(2)	(3)	(4)	(5)	(6)	(7)	(8)	(9)	(10)	(11)	(12)	(13)	(14)	(15)
521	2506	54179	36	176.49483	19.52902	0.018	171.9	7.87	10.34	286183	3.681e-14	40.399	-2.011e-04	36.529
522	1017	52706	391	177.63552	55.05799	0.018	106.5	7.03	10.38	286976	1.015e-14	39.840	5.526e-04	36.767
523	1016	52759	512	177.71268	55.14366	0.019	121.8	7.26	10.57	286476	7.566e-15	39.757	3.110e-03	37.562
524	2224	53815	582	180.19560	30.05983	0.050	154.2	7.68	10.57	60374	8.256e-15	40.634	-2.040e-06	37.411
525	2599	54234	551	189.77139	17.74933	0.065	232.0	8.39	11.36	351569	8.581e-14	41.902	7.090e-02	40.006
526	1975	53734	373	190.46374	33.20452	0.038	71.9	6.34	9.89	351354	9.153e-15	40.453	-3.255e-04	37.186
527	291	51928	593	191.74454	0.11634	0.089	149.9	7.63	11.06	366445	1.859e-14	41.519	5.971e-05	37.940
528	2241	54169	289	193.49631	26.44404	0.024	176.7	7.91	10.80	371568	7.140e-15	39.910	2.040e-03	37.557
529	338	51694	77	195.78102	-2.36532	0.087	122.8	7.28	10.87	361993	5.670e-15	40.979	1.375e-04	37.916
530	2603	54479	420	196.26525	18.08911	0.202	210.9	8.22	11.38	360075	2.671e-14	42.449	4.995e-04	38.898
531	2029	53819	613	197.36916	32.44307	0.068	89.9	6.73	10.76	360353	1.590e-15	40.199	3.025e-04	37.689
532	527	52342	57	202.60598	1.49469	0.083	174.7	7.89	11.15	334001	2.381e-13	42.559	1.230e-03	38.458
533	1993	53762	245	202.68141	33.83842	0.040	94.5	6.82	10.18	333504	2.031e-14	40.829	1.689e-04	37.215
534	1978	53473	428	202.82270	29.36819	0.048	112.1	7.12	11.00	333606	1.922e-13	41.970	2.255e-05	37.380
535	587	52026	268	220.17847	3.46542	0.027	257.2	8.57	11.45	345017	1.580e-14	40.385	2.540e-03	37.782
536	1816	53919	147	227.39068	7.51532	0.078	221.8	8.31	11.12	338469	1.562e-13	42.321	4.320e-03	38.949
537	1833	54561	586	229.69052	6.23225	0.102	296.7	8.82	11.47	207004	5.199e-12	44.093	2.109e-01	40.885
538	1721	53857	471	230.71995	8.74493	0.038	224.6	8.33	10.89	48239	6.641e-15	40.293	-2.527e-04	37.166
539	973	52426	275	254.73481	32.59863	0.064	105.9	7.02	10.90	213577	2.192e-14	41.287	-9.840e-05	37.638
540	353	51703	103	258.53766	58.81843	0.030	96.7	6.86	10.61	54370	8.386e-15	40.186	3.528e-04	37.000
541	731	52460	291	322.92081	10.16095	0.104	203.0	8.16	10.94	265858	4.323e-14	42.029	4.834e-04	38.261
542	373	51788	233	331.36255	-0.53346	0.031	135.6	7.45	10.78	230926	3.708e-15	39.870	6.014e-05	36.996
543	374	51791	554	334.34466	0.35242	0.095	145.8	7.58	10.88	57189	1.561e-15	40.508	-1.891e-04	38.004
544	655	52162	117	10.75688	-9.78948	0.130	253.4	8.54	11.30	115624	1.477e-15	40.772	4.280e-03	39.416
545	663	52145	496	24.98413	-9.24241	0.042	267.3	8.64	11.64	101471	4.018e-15	40.175	2.286e-04	37.265
546	403	51871	204	29.53043	-0.96434	0.081	148.5	7.61	10.66	93651	1.216e-14	41.248	-1.645e-05	37.854
547	412	52258	384	46.68597	-0.02406	0.112	213.3	8.24	11.15	155886	1.552e-14	41.650	4.154e-04	38.261
548	1920	53314	169	117.59539	17.64541	0.064	169.0	7.84	11.31	35638	1.462e-14	41.106	4.349e-04	37.767
549	435	51882	513	119.12673	41.03624	0.072	240.1	8.45	11.26	82536	8.556e-14	41.991	9.800e-03	39.236
550	1783	53386	106	129.24379	55.64578	0.044	228.1	8.36	11.20	306436	1.537e-14	40.807	9.627e-03	38.792
551	448	51900	604	134.91043	56.87890	0.031	114.4	7.15	10.56	300455	1.194e-14	40.369	1.762e-04	36.987
552	2434	53826	98	136.81807	13.84368	0.087	159.0	7.73	10.94	298709	2.150e-14	41.565	3.856e-04	38.004
553	1936	53330	36	139.17128	29.33950	0.036	229.3	8.37	10.96	301554	2.922e-15	39.902	5.775e-05	37.131
554	572	52289	218	149.71828	2.85674	0.072	185.5	8.00	10.76	26438	1.398e-15	40.206	1.531e-04	37.752
555	500	51994	514	150.01336	2.02959	0.079	187.3	8.02	11.00	9541	2.473e-15	40.528	1.711e-04	37.826
556	1217	52672	61	151.24305	41.22276	0.087	136.2	7.46	10.60	315279	1.852e-14	41.500	8.070e-06	37.923
557	1000	52643	178	160.30404	6.36990	0.019	136.2	7.46	10.46	282991	2.534e-14	40.280	9.057e-05	36.572
558	508	52366	242	164.61110	1.38292	0.041	237.9	8.43	11.15	278278	1.819e-14	40.804	-1.043e-04	37.238
559	1988	53469	110	166.34964	38.02031	0.030	192.6	8.06	10.72	276638	4.544e-15	39.922	2.664e-04	36.960
560	2494	54174	327	169.24263	17.81373	0.195	231.1	8.38	11.43	292306	9.187e-15	41.951	3.892e-04	38.755

Id	SDSS Plate id	SDSS MJD id	SDSS Fibre id	RA ——-(J2000)——-	Dec	Redshift	Velocity Dispersion km/s	Black Hole Mass —$\log_{10}$ (in solar masses)—	Stellar Mass	3XMM id	Xray Flux erg/cm^2/s	Xray Luminosity erg/s	Radio Flux Density Jy	Radio Luminosity erg/s
(1)	(2)	(3)	(4)	(5)	(6)	(7)	(8)	(9)	(10)	(11)	(12)	(13)	(14)	(15)
561	2509	54180	428	176.02276	19.99610	0.019	140.0	7.51	10.42	286034	2.855e-15	39.313	9.237e-05	36.554
562	1624	53386	634	184.30795	7.51743	0.130	204.7	8.17	10.90	358445	1.435e-14	41.759	2.202e-03	39.126
563	2013	53818	55	186.63685	31.43131	0.060	307.0	8.88	11.38	47982	7.513e-15	40.760	6.370e-03	38.876
564	2013	53818	43	186.67939	31.26344	0.061	233.0	8.40	11.01	357515	3.145e-15	40.397	7.470e-05	37.592
565	2236	53729	298	188.89959	26.56669	0.023	134.2	7.43	10.18	353274	3.363e-15	39.548	-1.265e-04	36.717
566	2243	53794	397	197.84011	27.50882	0.121	210.6	8.22	11.11	364488	8.143e-15	41.443	7.019e-04	38.562
567	296	51984	203	199.80732	-0.98774	0.082	243.3	8.47	11.44	364008	4.055e-15	40.779	3.576e-04	37.911
568	296	51665	208	199.81911	-0.91701	0.082	330.5	9.01	11.48	364072	1.541e-14	41.361	1.364e-02	39.494
569	2246	53767	437	205.23580	26.48673	0.075	230.6	8.38	11.36	324823	2.143e-15	40.424	2.687e-02	39.709
570	2123	53793	147	212.31830	26.41235	0.056	89.2	6.72	10.62	342883	1.834e-15	40.093	2.660e-04	37.523
571	1816	53919	70	227.88075	7.25197	0.045	334.3	9.03	11.58	337994	7.631e-14	41.510	8.303e-02	39.735
572	595	52023	160	239.78973	2.79958	0.048	218.2	8.28	11.18	209757	5.442e-16	39.419	3.726e-04	37.443
573	817	52381	356	247.43703	40.81166	0.029	276.3	8.69	11.58	205012	1.255e-14	40.348	6.387e-03	38.245
574	974	52427	297	255.63808	33.51666	0.086	319.6	8.95	11.81	214350	2.290e-14	41.582	1.022e-02	39.417
575	383	51818	637	352.63349	0.08103	0.017	169.9	7.85	10.90	246894	7.597e-15	39.659	1.100e-05	36.474
576	649	52201	124	358.52366	-10.30850	0.073	206.5	8.19	11.02	239660	2.901e-15	40.535	5.260e-06	37.764

Appendix C

The Catalogue of ELAIS-N1 Radio Sources

The catalogue of ELAIS-N1 radio sources described in Chapter 3 and used for the analyses in Chapters 4 and 5 is set out in the Table on the following pages. The column descriptions are as follows:

ID: The identifier for this sample of radio sources.

RA, **DEC**: The coordinates of the LOFAR radio source. For those sources with a morphology of "D_centre" (see below) the coordinates are for the host galaxy.

Major Axis, **Minor Axis**: The FWHM of the major and minor axes in arcseconds.

Peak Flux: The peak Stokes I flux density per beam in mJy.

Total Flux: The total, integrated Stokes I flux density per beam in mJy.

Analysis: The method used to find the host galaxy. ML = Maximum Likelihood Ratio analysis; V = Visual examination; MLV = Maximum Likelihood Ratio analysis followed by Visual examination.

LR: The likelihood ratio for those sources sent through the likelihood ratio analysis.

Morph: The morphology of the source. S = isolated, compact source; E = source with extended emission; CD = compact double; D_centre, D_lobe1, D_lobe2 = the central galaxy and its two lobes (note that the entries in the catalogue for the lobes are immediately below the entry for their host galaxy); T_centre, T_lobe1, T_lobe2 = the central galaxy, which was identified as a radio source in its own right, and its two lobes (note that the entries in the catalogue for the lobes are immediately below the entry for their host galaxy); SX = a source whose host galaxy could not be identified.

Type: This item indicates whether the host galaxy was detected in each of the i, K, g or s (= 3.6 micron) bands; an underscore shows no detection in that band. Two additional symbols are shown for those sources analysed by the likelihood ratio method: the number indicates the i - K colour category and the letter indicates whether the galaxy has a blue ("b") or red ("r") g - i colour, both as shown in Table 3.8 and described in the accompanying text.

g-band, **i-band**, **K-band** and **3.6 micron Magnitudes**: Catalogue magnitudes for the host galaxy.

Redshift: Estimate of redshift.

Redshift Source: BOSS = Spectroscopic redshift from BOSS; Vacc = spectroscopic redshift from the SERVS Merged Spec-z Catalogue; HSC = photometric redshift from HSC-SSP; Dunc = photometric redshifts generated specifically for this ELAIS-N1 catalogue by Dr Ken Duncan; SERVS = photometric redshift calculated by Mauduit et al. (2012) for the SERVS catalogue; Kmag = redshift estimated using a K-magnitude / redshift relationship; imag = redshift estimated using a i-magnitude / redshift relationship; smag = redshift estimated using a 3.6 micron-magnitude / redshift relationship.

Galaxy Type: SFG = star-forming galaxy; HERG = radiative-mode AGN; LERG = jet-mode AGN; AGN = an AGN unable to be classified as a radiative-mode or jet-mode object; BLANK = either a lobe or a source for which no host galaxy could be identified.

ID	Properties of Radio Source						Identification Data				Properties of Host Galaxy						
	RA	DEC	Major Axis arcsec	Minor Axis arcsec	Peak Flux mJy	Total Flux mJy	Analysis	LR	Morph	Type	g-band Mag	i-band Mag	K-band Mag	3.6μ m Mag	Redshift	Redshift Source	Galaxy Type
0	244.06906	55.16857	10.38	6.35	1.38	2.01	ML	32.93	S	iKgs8b	24.34	22.87	19.93	19.41	0.89	HSC	LERG
1	244.02984	55.08765	13.68	9.32	3.59	19.64	ML	56.29	S	iKgs9r	25.36	23.44	20.25	19.80	1.24	Dunc	LERG
2	243.97201	55.05909	12.94	8.18	0.95	2.23	ML	0.12	S	iKgs7r	24.05	21.87	19.37	19.64	0.89	Kmag	LERG
3	243.96376	55.12364	13.32	8.98	0.85	2.25	ML	1.88	S	iKgs1b	19.81	19.68	18.90	n.d.	1.10	BOSS	HERG
4	243.82323	55.07514	9.30	8.12	4.11	6.86	ML	111.82	S	iKgs7r	25.43	22.57	20.04	19.82	0.92	HSC	LERG
5	243.81084	54.99322	12.12	9.11	0.93	2.28	ML	180.39	S	iKgs9r	24.81	22.47	19.20	19.19	0.93	HSC	LERG
6	243.74726	55.04063	10.83	10.24	1.19	2.92	ML	51.61	S	iKgs4b	20.43	19.79	17.94	n.d.	0.27	BOSS	SFG
7	243.75301	55.33052	14.31	7.46	0.82	1.93	ML	334.30	S	_Kg_7r	24.36	n.d.	19.45	n.d.	1.18	HSC	HERG
8	243.74777	55.14231	22.01	14.80	0.64	4.59	ML	183.55	S	iKgs3r	20.32	19.05	17.28	n.d.	0.22	BOSS	LERG
9	243.67069	55.03533	15.14	9.54	0.76	2.41	ML	31.88	S	iKgs6b	22.80	22.03	19.71	19.19	6.00	BOSS	HERG
10	243.65659	55.08854	9.26	6.95	0.88	1.25	ML	1359.68	S	iKgs7b	20.21	18.64	16.16	n.d.	0.28	Dunc	SFG
11	243.64590	55.42146	7.89	7.62	2.76	3.67	ML	84.14	S	iKgs9b	24.59	23.73	20.50	20.15	1.18	HSC	HERG
12	243.63571	55.08619	17.36	11.79	0.69	3.13	ML	163.28	S	iKgs9b	24.08	22.73	19.54	19.22	1.08	HSC	HERG
13	243.63469	55.38860	9.01	5.23	1.05	1.10	ML	25.57	S	iK__4r	n.d.	22.70	20.77	n.d.	0.54	HSC	LERG
14	243.63204	55.38582	10.09	5.61	0.84	1.05	ML	347.08	S	iKgs5r	21.89	20.39	18.20	19.05	0.35	HSC	SFG
15	243.60432	55.06296	9.10	8.02	0.94	1.51	ML	120.52	S	iKgs3b	20.48	19.70	18.01	n.d.	0.46	HSC	HERG
16	243.57345	55.06912	10.35	8.31	2.98	5.66	ML	80.14	S	iKgs2b	18.33	17.43	15.80	n.d.	0.08	BOSS	HERG
17	243.57494	55.11750	9.74	7.19	1.27	1.96	ML	61.55	S	_K_s0k	n.d.	n.d.	20.63	20.13	1.06	HSC	HERG
18	243.57190	55.13390	7.56	5.80	0.84	0.81	ML	21.69	S	iKgs4b	23.26	23.29	21.33	20.53	1.38	HSC	HERG
19	243.55439	55.13932	5.68	3.64	0.93	1.17	ML	42.26	S	iKgs0r	28.96	25.30	21.10	20.55	1.77	Dunc	HERG
20	243.55298	55.32039	7.21	6.38	1.10	1.12	ML	4.44	S	_K__8k	n.d.	n.d.	22.15	n.d.	2.12	Kmag	HERG
21	243.53888	55.44240	10.13	7.19	0.91	1.47	ML	89.22	S	iKgs4r	21.84	20.37	18.46	n.d.	0.49	HSC	HERG
22	243.53098	55.25573	10.41	8.40	1.55	2.99	ML	255.26	S	iKgs9r	24.88	21.82	18.65	n.d.	0.87	BOSS	LERG
23	243.52086	55.38826	7.92	5.88	11.34	13.35	ML	39.26	S	_K_s5k	n.d.	n.d.	22.84	20.30	1.83	Dunc	LERG
24	243.51969	55.44388	7.61	5.88	9.87	11.47	ML	59.36	S	iKgs7b	25.14	23.79	21.17	20.65	0.97	HSC	LERG
25	243.51815	55.38104	9.80	6.28	0.83	1.13	ML	68.56	S	iKgs8b	23.79	22.93	20.13	19.45	1.18	HSC	HERG
26	243.51461	55.19505	8.83	6.27	0.84	1.03	ML	102.68	S	iKgs5r	25.48	22.85	20.65	20.59	0.66	HSC	SFG
27	243.49732	55.13029	9.61	6.30	0.90	1.20	ML	58.58	S	iKgs9b	24.60	23.62	20.29	19.92	1.59	Dunc	HERG
28	243.49301	54.99070	9.66	6.36	0.80	1.09	ML	12.08	S	iKgs4b	23.27	22.91	20.98	20.46	1.84	Dunc	HERG
29	243.48160	54.96344	21.63	12.09	1.04	6.04	ML	371.36	S	iKgs8r	23.15	20.58	17.80	n.d.	0.59	BOSS	LERG
30	243.38500	55.14316	9.11	7.12	1.46	2.10	ML	54.74	S	iKgs6b	24.22	23.40	21.10	20.45	1.26	Dunc	HERG
31	243.34150	55.10468	9.19	7.13	1.44	2.08	ML	80.36	S	_K_s0k	n.d.	n.d.	20.03	19.66	1.12	HSC	LERG
32	243.32094	55.15976	9.22	6.93	2.96	4.18	ML	150.05	S	iKgs6r	23.72	21.90	19.63	19.54	0.00	BOSS	LERG
33	243.31578	55.03702	11.33	9.97	0.73	1.81	ML	676.55	S	iKgs7b	20.89	19.43	16.89	n.d.	0.23	BOSS	SFG
34	243.30848	55.26528	8.10	6.62	1.25	1.48	ML	103.99	S	iKgs8r	25.75	23.05	19.95	19.65	0.94	HSC	LERG
35	243.30123	55.55164	8.24	6.26	2.91	3.32	ML	123.12	S	iKgs3r	21.36	19.95	18.12	n.d.	0.27	BOSS	HERG
36	243.25739	55.35633	8.55	6.16	1.93	2.24	ML	2639.05	S	iKgs8b	17.60	16.72	13.77	n.d.	0.01	Vacc	SFG
37	243.24671	55.27243	7.72	6.79	1.09	1.26	ML	119.67	S	iKgs5r	24.10	21.86	19.62	19.14	0.84	HSC	LERG
38	243.23766	55.19007	12.15	8.97	0.71	1.71	ML	319.42	S	iKgs6r	22.79	20.92	18.63	n.d.	0.76	HSC	LERG
39	243.22613	54.92366	14.35	10.31	1.04	3.41	ML	1554.72	S	iKgs7b	18.04	16.87	14.24	n.d.	0.06	BOSS	SFG

ID	Properties of Radio Source						Identification Data				Properties of Host Galaxy						
	RA	DEC	Major Axis arcsec	Minor Axis arcsec	Peak Flux mJy	Total Flux mJy	Analysis	LR	Morph	Type	g-band Mag	i-band Mag	K-band Mag	3.6μm Mag	Redshift	Redshift Source	Galaxy Type
40	243.21960	55.11729	11.95	8.33	1.73	3.80	ML	82.24	S	_K_s0k	n.d.	n.d.	20.38	19.86	1.93	Dunc	LERG
41	243.21230	55.59625	7.80	7.47	1.65	2.13	ML	12.45	S	iKgs1b	18.55	17.78	17.45	n.d.	0.34	Dunc	HERG
42	243.18923	55.46819	9.65	7.86	1.03	1.73	ML	27.76	S	iKgs3b	22.32	21.62	19.96	19.37	0.88	HSC	HERG
43	243.17543	55.49220	8.32	7.10	1.34	1.76	ML	2.42	S	iKg_2b	24.08	23.72	22.17	n.d.	2.14	Dunc	HERG
44	243.16342	54.95590	17.88	14.61	0.77	4.42	ML	26.14	S	iK_s0b	n.d.	25.49	20.49	20.57	1.22	HSC	LERG
45	243.15982	55.00934	10.01	8.36	1.85	3.42	ML	42.22	S	iKgs9b	24.91	23.21	19.92	19.47	1.14	HSC	HERG
46	243.14991	55.56870	11.13	5.51	0.90	2.90	ML	24.23	S	iKg_7b	22.47	21.42	18.89	n.d.	0.97	Dunc	HERG
47	243.13914	54.94109	9.00	5.88	0.68	6.98	ML	70.89	S	iKgs7b	18.71	17.69	15.20	n.d.	0.08	Dunc	SFG
48	243.13813	55.38152	7.61	5.80	3.62	5.19	ML	199.60	S	iKgs8r	25.07	22.34	19.36	19.17	1.02	HSC	LERG
49	243.12070	55.11037	7.92	6.66	47.84	55.72	ML	85.42	S	_K__0k	n.d.	n.d.	20.29	n.d.	1.06	HSC	HERG
50	243.11342	55.19608	11.64	8.77	1.18	2.67	ML	72.59	S	iKgs4b	20.49	20.35	18.44	n.d.	0.71	Vacc	HERG
51	243.11539	55.21283	6.23	5.18	0.79	0.56	ML	16.45	S	iKgs9b	25.48	23.99	20.18	19.68	1.30	Dunc	HERG
52	243.10594	54.91737	8.57	6.61	2.54	3.18	ML	15.80	S	i_gs8b	26.56	25.65	n.d.	21.69	2.84	Dunc	HERG
53	243.10729	55.67202	9.76	6.61	1.14	1.62	ML	355.10	S	iKgs4b	20.53	19.25	17.30	n.d.	0.32	Dunc	SFG
54	243.09831	55.43204	8.37	6.85	59.26	75.05	ML	36.70	S	_K_s0k	n.d.	n.d.	20.61	20.65	1.69	Dunc	LERG
55	243.09065	55.69485	6.94	5.73	7.82	8.00	ML	19.40	S	_K_s9k	n.d.	n.d.	21.30	20.55	2.29	Dunc	HERG
56	243.08537	54.96117	7.40	6.63	1.41	1.53	ML	85.54	S	iK_s9b	n.d.	23.67	19.86	19.40	1.31	Dunc	HERG
57	243.06426	54.92622	9.28	7.48	3.19	4.89	ML	39.25	S	iKgs9b	26.25	24.66	21.51	20.82	1.17	HSC	HERG
58	243.04506	55.21657	7.31	6.34	1.33	1.36	ML	370.02	S	iKgs7r	23.17	21.21	18.55	n.d.	0.72	HSC	SFG
59	243.04095	55.28913	7.99	6.88	3.30	4.00	ML	275.69	S	iKgs7r	24.59	21.70	19.18	19.18	0.82	BOSS	LERG
60	243.03728	55.26798	7.72	5.94	4.40	4.46	ML	313.98	S	iKgs5r	23.77	20.89	18.72	19.00	0.54	BOSS	HERG
61	243.01848	54.91799	15.76	8.91	0.67	2.08	ML	6.59	S	iKgs4b	20.63	19.65	17.64	n.d.	0.38	Dunc	LERG
62	243.00922	54.91415	13.12	6.78	0.77	1.52	ML	7.54	S	iKgs7b	24.83	24.01	21.46	20.77	1.52	Dunc	HERG
63	242.99419	55.53804	13.61	7.60	0.83	1.89	ML	365.10	S	iKgs6b	20.63	19.58	17.27	n.d.	0.56	Dunc	HERG
64	242.97196	55.60079	18.16	9.12	0.92	3.38	ML	70.37	S	iKgs6b	20.96	19.71	17.30	n.d.	0.51	Dunc	HERG
65	242.95340	55.53242	11.55	7.21	0.71	1.30	ML	3.29	S	iKg_9b	24.51	24.13	20.85	n.d.	1.65	Dunc	HERG
66	242.94965	55.75980	7.93	6.60	1.16	1.34	ML	208.07	S	iKgs5b	21.24	19.80	17.61	n.d.	0.37	HSC	SFG
67	242.94603	55.74442	7.90	6.36	1.88	2.09	ML	47.96	S	_K_s5k	n.d.	n.d.	23.48	n.d.	2.76	Kmag	HERG
68	242.94283	55.23121	10.78	6.62	1.04	4.20	ML	1.81	S	iKgs5b	21.25	19.85	17.61	n.d.	0.36	Dunc	SFG
69	242.93995	55.52297	7.40	7.18	2.77	3.25	ML	185.60	S	iKgs5r	24.47	21.79	19.59	19.72	0.66	HSC	LERG
70	242.93608	54.91938	8.02	6.55	1.49	3.60	ML	31.69	S	iK_s8b	n.d.	24.27	21.29	20.35	1.15	Dunc	LERG
71	242.92608	55.47473	6.92	6.61	1.06	1.07	ML	80.21	S	iKgs9b	24.30	23.18	19.98	19.43	1.39	Dunc	HERG
72	242.90922	55.35923	5.72	4.41	1.04	1.74	ML	50.36	S	iKgs9b	24.95	23.69	20.37	19.89	1.16	HSC	LERG
73	242.90482	55.39699	9.24	6.82	2.68	3.72	ML	81.96	S	iKgs6r	23.13	21.01	18.62	n.d.	0.90	HSC	LERG
74	242.88852	55.21019	6.91	5.93	5.18	5.90	ML	1363.14	S	iKgs5b	20.13	18.74	16.50	n.d.	0.22	BOSS	LERG
75	242.86918	55.14266	8.93	5.91	0.77	0.90	ML	6.70	S	iKgs7b	23.20	22.50	20.02	19.81	1.61	Dunc	HERG
76	242.85140	55.57110	10.23	5.86	1.65	2.19	ML	114.04	S	_Kgs4r	19.65	n.d.	16.09	n.d.	0.22	Vacc	LERG
77	242.83694	55.03779	11.44	8.84	1.31	2.92	ML	492.91	S	iKgs7r	23.15	20.98	18.51	n.d.	0.52	BOSS	HERG
78	242.83345	55.53060	6.15	4.82	1.39	2.56	ML	666.20	S	iKgs8b	22.43	20.91	18.08	n.d.	0.81	HSC	LERG
79	242.81239	55.57837	10.63	8.73	9.06	23.39	ML	9.11	S	_K__9k	n.d.	n.d.	21.41	n.d.	0.35	HSC	LERG

ID	Properties of Radio Source						Identification Data				Properties of Host Galaxy						
	RA	DEC	Major Axis arcsec	Minor Axis arcsec	Peak Flux mJy	Total Flux mJy	Analysis	LR	Morph	Type	g-band Mag	i-band Mag	K-band Mag	3.6μm Mag	Redshift	Redshift Source	Galaxy Type
80	242.80281	55.13980	8.28	6.81	2.25	2.81	ML	569.78	S	iKg_8r	23.27	21.57	18.61	n.d.	0.98	HSC	HERG
81	242.79980	55.41810	15.30	10.66	0.79	2.84	ML	566.18	S	iKgs7b	21.75	20.26	17.70	n.d.	0.35	HSC	LERG
82	242.79619	55.44956	8.07	5.19	1.30	1.20	ML	3.95	S	iKgs1b	22.55	21.70	20.97	20.84	0.77	HSC	HERG
83	242.78010	55.48587	9.10	7.48	1.78	2.67	ML	308.11	S	iKgs6b	21.44	20.03	17.71	n.d.	0.37	HSC	HERG
84	242.77244	55.91832	9.07	7.44	4.18	6.24	ML	31.29	S	iKgs9b	26.30	24.81	20.69	20.53	1.86	Dunc	LERG
85	242.76756	55.60592	8.02	7.29	1.25	1.61	ML	46.48	S	iKgs5r	26.91	25.14	22.89	21.25	1.25	Dunc	HERG
86	242.76936	54.92424	9.67	8.12	1.08	1.87	ML	245.48	S	iKgs3r	20.66	18.99	17.21	n.d.	0.29	BOSS	LERG
87	242.75934	54.96653	10.93	9.63	1.95	4.53	ML	1179.04	S	iKgs7r	21.98	19.48	17.01	n.d.	0.52	BOSS	LERG
88	242.75049	55.43257	7.47	6.20	1.23	1.26	ML	42.96	S	iKgs9b	25.83	24.29	20.48	20.12	1.14	HSC	HERG
89	242.74804	55.11906	11.16	7.28	1.36	2.45	ML	76.65	S	_K_s0k	n.d.	n.d.	20.16	19.92	1.92	Dunc	HERG
90	242.74051	55.59108	9.74	7.62	45.84	67.81	ML	400.07	S	iKgs7r	22.27	19.97	17.40	n.d.	0.49	BOSS	HERG
91	242.73107	54.95129	7.79	7.59	1.18	1.55	ML	120.11	S	iKgs7b	23.47	22.52	20.00	19.60	1.18	HSC	HERG
92	242.71687	55.51068	8.66	7.36	1.36	1.91	ML	171.55	S	iKgs9r	25.65	22.72	19.29	19.03	1.10	HSC	LERG
93	242.71911	55.20473	9.07	7.10	0.85	1.21	ML	215.49	S	iKgs6b	22.67	21.33	18.89	19.09	0.58	BOSS	LERG
94	242.69759	55.69429	8.75	7.64	2.58	3.82	ML	34.70	S	iKgs9b	25.97	24.58	20.75	19.84	1.84	Dunc	HERG
95	242.68928	55.34786	7.70	6.22	4.96	5.26	ML	62.88	S	iKgs9r	25.94	23.66	20.07	19.74	1.34	Dunc	LERG
96	242.69099	55.22759	7.19	5.56	0.90	0.79	ML	125.53	S	iKgs9r	24.98	22.58	19.42	19.24	0.68	HSC	SFG
97	242.68911	55.29580	7.66	6.30	1.65	1.76	ML	856.67	S	iKgs6b	20.08	18.87	16.60	n.d.	0.33	Dunc	SFG
98	242.65926	55.44133	8.68	7.35	3.45	4.87	ML	1560.56	S	iKgs5r	20.17	18.47	16.30	n.d.	0.25	BOSS	LERG
99	242.65985	55.47120	6.17	4.21	0.94	0.54	ML	113.94	S	iKgs7b	23.53	22.64	20.11	20.13	0.95	HSC	SFG
100	242.65630	55.40402	9.58	7.44	1.57	2.48	ML	11.31	S	_Kgs1b	19.64	n.d.	17.70	n.d.	1.19	Vacc	HERG
101	242.65526	55.36024	6.78	6.05	0.97	0.88	ML	30.66	S	_K_s5k	n.d.	n.d.	23.57	n.d.	2.45	SERVS	HERG
102	242.63156	55.80539	13.35	11.26	7.89	34.33	ML	42.19	S	iKgs5r	20.32	18.62	16.46	n.d.	0.32	Dunc	LERG
103	242.63647	55.24288	14.71	10.88	0.74	2.61	ML	349.72	S	iKgs6r	22.25	20.20	17.84	n.d.	0.41	HSC	SFG
104	242.62583	55.02609	11.19	7.73	1.85	3.53	ML	1720.67	S	iKgs7b	20.12	18.83	16.19	n.d.	0.11	BOSS	SFG
105	242.61554	55.77721	8.65	6.59	1.71	2.16	ML	77.40	S	_K_s0k	n.d.	n.d.	20.70	20.34	0.89	HSC	LERG
106	242.61133	54.99220	8.67	7.63	2.87	4.19	ML	19.14	S	_K__9k	n.d.	n.d.	21.54	n.d.	1.14	Dunc	LERG
107	242.60567	55.36452	9.79	7.24	0.99	1.56	ML	283.22	S	iKgs5r	22.40	20.44	18.26	n.d.	0.45	HSC	SFG
108	242.59846	55.01675	12.74	10.77	0.94	2.83	ML	98.75	S	iKgs8r	26.22	22.90	20.04	19.96	0.93	HSC	LERG
109	242.58011	55.71069	6.80	5.29	0.97	0.77	ML	17.94	S	iKgs3b	23.12	22.86	21.13	20.63	0.09	BOSS	SFG
110	242.56545	55.56590	11.47	7.90	3.53	10.54	ML	0.27	S	iKgs7r	23.10	21.49	19.02	n.d.	1.17	HSC	LERG
111	242.55749	55.40702	8.17	5.15	1.71	1.59	ML	340.70	S	iKgs5r	23.52	20.73	18.52	n.d.	0.67	HSC	LERG
112	242.56369	54.93591	16.26	12.41	0.85	3.78	ML	46.79	S	i_gs5b	24.47	24.15	n.d.	21.74	0.62	HSC	LERG
113	242.55625	55.37137	7.22	4.54	1.08	1.83	ML	14.36	S	iK_s0b	n.d.	25.66	21.30	20.57	1.54	Dunc	HERG
114	242.55646	55.11306	11.85	9.77	0.91	2.32	ML	131.07	S	iKgs7r	23.02	21.39	18.86	n.d.	0.52	BOSS	HERG
115	242.54208	55.38218	8.33	6.85	0.99	1.25	ML	149.72	S	iKgs6r	24.68	21.98	19.57	19.73	0.78	HSC	LERG
116	242.54219	55.28389	5.90	3.42	0.81	1.78	ML	173.38	S	iKgs7b	22.99	21.88	19.43	19.12	0.19	BOSS	LERG
117	242.51169	55.87866	9.14	8.25	200.91	287.80	ML	8.33	S	iKgs1b	21.34	20.82	20.65	20.06	1.75	BOSS	HERG
118	242.52099	55.37557	7.87	6.27	1.39	1.51	ML	7.80	S	iKgs2b	22.99	22.53	21.37	20.81	1.16	HSC	HERG
119	242.52183	55.16272	10.01	7.95	1.69	2.96	ML	335.06	S	iKgs6r	22.52	20.49	18.24	n.d.	0.56	BOSS	SFG

ID	Properties of Radio Source						Identification Data				Properties of Host Galaxy						
	RA	DEC	Major Axis arcsec	Minor Axis arcsec	Peak Flux mJy	Total Flux mJy	Analysis	LR	Morph	Type	g-band Mag	i-band Mag	K-band Mag	$3.6\mu m$ Mag	Redshift	Redshift Source	Galaxy Type
120	242.50247	55.24574	12.37	9.47	1.07	2.77	ML	50.03	S	iKgs8b	24.55	23.25	20.15	19.78	1.46	Dunc	LERG
121	242.50047	55.28675	9.60	6.46	0.96	1.32	ML	188.65	S	iKgs5b	22.75	21.78	19.62	n.d.	1.14	HSC	HERG
122	242.48295	55.47366	8.20	5.66	7.97	10.04	ML	81.25	S	iKgs9r	25.90	23.39	20.20	19.90	1.22	Dunc	LERG
123	242.47498	55.38005	19.92	18.21	0.92	7.34	ML	0.81	S	_K_s8k	n.d.	n.d.	21.96	21.43	0.89	HSC	LERG
124	242.46851	55.11782	9.95	8.31	2.28	4.18	ML	581.68	S	iKgs6r	21.07	19.07	16.66	n.d.	0.35	BOSS	HERG
125	242.43029	55.81678	10.22	7.77	2.75	4.84	ML	2.93	S	_K__9k	n.d.	n.d.	21.04	n.d.	1.58	Kmag	LERG
126	242.43375	55.35703	16.05	8.80	0.99	3.08	ML	15.03	S	iKgs5b	22.73	21.59	19.47	19.08	0.96	Dunc	HERG
127	242.41382	55.78368	8.48	7.19	8.87	11.94	ML	11.72	S	iKgs4r	28.00	24.88	22.91	n.d.	2.49	Kmag	HERG
128	242.38696	55.33063	16.10	9.58	1.36	4.63	ML	198.86	S	iKgs7r	23.67	21.31	18.78	n.d.	0.83	HSC	LERG
129	242.38543	55.19173	6.10	4.08	0.80	0.44	ML	281.07	S	iKgs5r	22.65	20.86	18.63	n.d.	0.52	BOSS	SFG
130	242.38123	55.04513	12.63	8.70	0.97	2.35	ML	313.81	S	iKgs8b	23.63	22.02	19.06	n.d.	1.06	HSC	LERG
131	242.37100	55.61228	9.23	7.18	2.05	3.00	ML	2.16	S	_K__8k	n.d.	n.d.	22.24	n.d.	0.32	BOSS	HERG
132	242.36911	55.30919	22.13	17.33	0.97	8.24	ML	109.69	S	iKgs5r	23.44	21.27	19.18	19.88	0.49	HSC	LERG
133	242.35969	55.21995	10.47	7.63	1.31	2.32	ML	82.61	S	_K__0k	n.d.	n.d.	19.83	n.d.	0.69	HSC	HERG
134	242.35629	55.34601	10.04	8.68	2.53	4.87	ML	9.45	S	iKgs9b	25.78	25.08	21.75	21.23	2.31	Dunc	HERG
135	242.32750	55.35467	9.60	7.41	3.45	5.43	ML	80.50	S	iKgs6b	23.69	22.60	20.21	19.82	1.17	HSC	LERG
136	242.32112	55.68112	8.75	6.81	4.27	5.62	ML	60.72	S	iKgs7b	24.52	23.70	21.18	20.59	1.64	Kmag	HERG
137	242.30403	55.56554	8.82	7.26	3.14	4.44	ML	13.62	S	_K_s9k	n.d.	n.d.	21.52	20.81	1.68	Dunc	LERG
138	242.30575	55.36170	9.08	6.55	0.77	1.02	ML	50.92	S	iKgs4b	20.31	19.27	17.25	n.d.	0.20	Dunc	SFG
139	242.29287	55.44241	8.79	8.22	12.75	23.37	ML	1513.49	S	iKgs7r	21.34	19.19	16.64	n.d.	0.36	BOSS	HERG
140	242.28487	55.37810	9.90	7.16	1.34	2.10	ML	788.62	S	iKgs4b	19.22	17.98	15.93	n.d.	0.08	BOSS	SFG
141	242.28219	55.40796	13.76	8.90	1.38	3.74	ML	933.44	S	iKgs7b	20.16	18.87	16.20	n.d.	0.07	BOSS	SFG
142	242.25349	55.47848	10.61	7.84	1.33	2.44	ML	1.56	S	iKgs2b	19.79	19.00	17.68	n.d.	0.65	HSC	HERG
143	242.21400	55.43670	6.11	5.14	1.07	2.32	ML	303.98	S	iKgs7r	21.34	19.54	16.98	n.d.	0.34	HSC	SFG
144	242.16581	55.39193	12.17	11.49	0.93	2.88	ML	304.52	S	iKgs3b	18.89	18.00	16.17	n.d.	0.10	Dunc	SFG
145	242.15533	55.39856	11.39	8.76	0.86	1.90	ML	2078.67	S	iKgs7b	19.68	18.24	15.68	n.d.	0.15	Dunc	SFG
146	242.15162	55.23824	10.33	9.15	1.40	2.92	ML	32.31	S	iKgs4b	23.10	22.44	20.46	19.11	0.25	BOSS	HERG
147	242.14258	55.54482	8.03	6.29	24.38	30.82	ML	226.97	S	iKgs9r	25.07	22.51	18.87	n.d.	1.10	HSC	LERG
148	242.13598	55.49073	11.68	6.26	0.91	1.47	ML	1804.91	S	iKgs7b	20.01	18.56	15.99	n.d.	0.07	Vacc	SFG
149	242.13170	55.20645	6.81	4.64	0.79	0.55	ML	120.77	S	iKgs9b	24.62	23.36	19.65	19.50	0.94	HSC	SFG
150	242.10662	55.29837	17.57	11.90	2.00	9.25	ML	44.12	S	iKgs7r	24.80	23.05	20.36	20.18	0.78	HSC	LERG
151	242.07360	55.32949	15.79	10.57	1.07	3.94	ML	826.31	S	iKgs6r	20.61	18.83	16.49	n.d.	0.30	Vacc	HERG
152	243.43837	53.73482	25.11	21.97	0.82	9.59	ML	1.78	S	iKgs5r	20.46	18.65	16.58	n.d.	0.41	HSC	LERG
153	243.35472	53.57782	14.61	9.65	1.31	3.93	ML	1.02	S	iKgs1b	17.98	17.39	17.90	n.d.	0.47	Kmag	LERG
154	243.33549	53.59264	10.55	6.81	2.65	4.04	ML	101.17	S	iKgs8b	24.21	22.74	19.74	19.24	0.96	HSC	HERG
155	243.25532	53.64761	12.59	6.67	1.12	2.00	ML	1.92	S	_K_s8k	n.d.	n.d.	22.10	21.06	2.33	Dunc	HERG
156	243.25339	53.69168	12.88	7.50	1.19	2.43	ML	128.24	S	iKgs5b	22.65	21.24	19.07	n.d.	0.89	BOSS	HERG
157	243.22417	53.40966	8.79	7.17	2.66	3.56	ML	126.28	S	iKgs8b	24.31	22.76	19.96	19.55	1.04	HSC	LERG
158	243.19632	53.91311	11.83	8.33	0.87	1.82	ML	200.34	S	iKgs8r	22.04	20.33	17.38	n.d.	0.37	HSC	SFG
159	243.16764	53.60004	30.70	15.63	37.85	151.64	ML	98.61	S	iKgs5b	18.34	17.11	14.95	n.d.	0.32	HSC	LERG

ID	Properties of Radio Source						Identification Data				Properties of Host Galaxy						
	RA	DEC	Major Axis arcsec	Minor Axis arcsec	Peak Flux mJy	Total Flux mJy	Analysis	LR	Morph	Type	g-band Mag	i-band Mag	K-band Mag	3.6μm Mag	Redshift	Redshift Source	Galaxy Type
160	243.17265	53.53231	9.61	8.05	2.13	3.50	ML	110.97	S	iKgs6r	24.21	21.70	19.32	19.27	0.62	HSC	LERG
161	243.08457	53.43417	8.59	8.41	1.37	2.10	ML	49.77	S	iKgs7b	23.98	22.47	19.99	19.63	1.12	HSC	SFG
162	243.07793	53.53160	9.32	7.67	1.54	2.34	ML	8.54	S	iKgs4b	24.20	23.39	21.49	21.08	0.34	HSC	LERG
163	243.06414	53.55384	10.35	9.28	1.43	2.92	ML	369.21	S	iKgs7b	22.45	21.03	18.58	n.d.	0.77	HSC	HERG
164	243.06390	53.87405	7.38	5.84	0.96	0.88	ML	15.81	S	iKg_8b	26.61	25.28	22.24	n.d.	2.17	Kmag	HERG
165	243.05010	53.62285	9.03	6.73	2.42	3.13	ML	49.59	S	iKg_0b	26.07	24.71	20.39	n.d.	1.35	Dunc	LERG
166	243.04441	53.92455	7.61	6.80	2.88	5.18	ML	20.80	S	iKgs2b	21.69	20.86	19.48	n.d.	1.71	BOSS	HERG
167	243.00889	53.69070	5.68	4.35	1.33	0.70	ML	17.11	S	iKgs7b	23.70	23.15	20.41	19.83	0.87	HSC	HERG
168	242.99756	53.41949	7.55	6.04	1.75	1.70	ML	49.38	S	iKgs4b	22.42	21.24	19.34	n.d.	0.81	HSC	HERG
169	242.98421	53.44175	9.75	6.29	1.78	2.32	ML	9.79	S	iKgs1b	18.77	18.62	17.67	n.d.	0.10	Vacc	HERG
170	242.98345	53.75005	8.60	6.20	1.06	14.08	ML	30.60	S	iKgs6r	25.19	22.27	19.83	19.59	0.94	HSC	LERG
171	242.95855	53.57354	8.00	5.46	4.74	6.23	ML	32.13	S	iKgs4r	24.42	21.66	19.64	19.73	0.69	HSC	LERG
172	242.93160	53.88739	11.68	10.02	1.55	3.86	ML	53.22	S	iKgs7b	24.68	24.03	21.42	20.87	1.15	HSC	LERG
173	242.91511	53.85988	8.52	6.90	4.42	5.52	ML	751.66	S	iKgs6r	20.49	18.85	16.44	n.d.	0.23	BOSS	HERG
174	242.89039	53.61355	11.95	9.83	1.58	3.94	ML	501.65	S	iKgs8r	24.04	21.57	18.74	19.25	0.50	HSC	HERG
175	242.87410	53.45300	10.11	8.13	1697.10	2972.02	ML	29.35	S	iKgs3r	23.12	20.73	18.95	19.16	0.59	BOSS	HERG
176	242.86999	53.96197	10.17	9.20	3.63	7.23	ML	39.73	S	iKgs8b	25.38	24.15	21.21	20.67	1.01	HSC	LERG
177	242.85842	53.75406	13.47	10.60	1.20	3.63	ML	1.48	S	_Kg_2r	24.48	n.d.	21.87	n.d.	1.90	Dunc	LERG
178	242.84727	53.92768	15.04	7.75	1.26	3.11	ML	10.48	S	iKgs9b	26.19	24.81	21.59	21.02	1.85	SERVS	HERG
179	242.81936	53.73893	8.48	7.66	41.64	56.00	ML	34.65	S	iK__7b	n.d.	25.04	22.57	n.d.	2.33	Kmag	HERG
180	242.81686	53.55829	10.57	5.90	1.69	2.23	ML	16.97	S	iKgs7b	25.41	24.48	21.74	21.00	1.04	HSC	HERG
181	242.79773	53.93914	12.00	8.79	15.43	31.15	ML	12.70	S	iK_s0b	n.d.	26.61	21.60	20.83	1.94	Dunc	HERG
182	242.79361	53.68068	7.39	6.37	1.25	1.24	ML	335.42	S	iKgs3r	20.14	18.78	17.01	n.d.	0.15	BOSS	SFG
183	242.78980	53.96868	11.57	7.98	2.16	4.24	ML	3437.47	S	iKgs8b	17.95	16.64	13.80	n.d.	0.06	BOSS	LERG
184	242.78118	53.63022	11.99	8.34	1.26	2.69	ML	1177.22	S	iKgs5b	19.83	18.63	16.50	n.d.	0.43	Dunc	LERG
185	242.77947	53.64241	8.48	5.71	1.07	1.10	ML	54.11	S	iKgs7b	24.33	23.25	20.53	20.21	1.18	HSC	HERG
186	242.76921	53.83210	11.02	7.20	1.80	3.04	ML	4.54	S	iKgs1b	19.44	18.99	18.12	n.d.	0.44	Vacc	HERG
187	242.74365	53.61363	10.10	8.30	1.07	1.90	ML	38.38	S	iKgs9r	26.57	23.83	20.55	20.10	1.15	HSC	HERG
188	242.71327	53.69011	10.32	7.33	1.85	2.98	ML	41.15	S	iKgs9b	25.60	24.76	21.59	21.11	0.73	HSC	HERG
189	242.67487	53.56280	8.14	6.96	4.21	6.48	ML	85.94	S	iKgs8r	24.61	22.74	19.93	19.52	0.97	HSC	LERG
190	242.65946	53.66994	10.26	8.71	1.45	2.76	ML	5.07	S	_K__9k	n.d.	n.d.	21.43	n.d.	1.42	Dunc	LERG
191	242.65936	53.56680	9.12	6.56	1.97	2.50	ML	618.90	S	iKgs4b	19.76	18.61	16.73	n.d.	0.14	Dunc	SFG
192	242.62041	53.73986	10.44	5.85	1.55	3.70	ML	472.62	S	iKgs8b	22.36	20.76	17.99	n.d.	0.62	HSC	LERG
193	242.61741	53.77624	9.59	8.06	3.52	5.77	ML	56.48	S	iK_s9b	n.d.	23.81	19.75	19.32	1.69	Dunc	HERG
194	242.61017	53.70260	17.85	11.30	1.28	5.50	ML	535.33	S	iKgs6b	18.75	17.54	15.18	n.d.	0.09	Vacc	SFG
195	242.60093	53.42878	9.22	7.22	1.81	2.56	ML	669.40	S	iKgs4b	18.50	17.25	15.26	n.d.	0.14	Vacc	LERG
196	242.59080	53.79806	9.95	8.11	1.46	2.50	ML	34.32	S	iKgs8b	25.15	24.45	21.62	21.05	1.12	HSC	LERG
197	242.57137	53.91450	9.34	7.86	3.56	5.55	ML	33.79	S	iKgs8b	24.33	23.23	20.27	20.35	0.95	HSC	LERG
198	242.57134	53.69963	8.39	6.78	2.63	3.19	ML	63.35	S	iKgs3r	22.85	20.70	18.95	n.d.	0.81	HSC	LERG
199	242.55866	53.73166	11.00	6.51	0.96	1.47	ML	529.59	S	iKgs5r	21.26	19.28	17.05	n.d.	0.34	Vacc	LERG

ID	Properties of Radio Source						Identification Data				Properties of Host Galaxy						
	RA	DEC	Major Axis arcsec	Minor Axis arcsec	Peak Flux mJy	Total Flux mJy	Analysis	LR	Morph	Type	g-band Mag	i-band Mag	K-band Mag	$3.6\mu m$ Mag	Redshift	Redshift Source	Galaxy Type
200	242.54965	53.59584	9.78	7.25	2.05	3.09	ML	826.15	S	iKgs8r	23.17	21.10	18.23	n.d.	0.51	HSC	HERG
201	242.54707	53.67155	11.85	7.43	1.13	2.12	ML	36.71	S	iKgs9b	25.23	24.93	21.01	20.30	1.47	HSC	HERG
202	242.53564	53.84191	11.66	8.34	0.95	1.96	ML	9.22	S	iKg_9b	25.40	23.67	19.72	n.d.	1.08	HSC	HERG
203	242.51081	53.52297	8.82	6.73	1.43	1.80	ML	1278.32	S	iKgs7b	20.17	19.02	16.43	n.d.	0.09	Vacc	SFG
204	242.50274	53.87907	9.79	8.29	3.22	5.54	ML	559.38	S	iKgs5r	21.94	19.75	17.66	n.d.	0.46	BOSS	LERG
205	242.49526	53.82268	8.63	7.81	8.77	14.78	ML	10.85	S	iKgs3b	23.88	23.32	21.49	21.53	2.06	Dunc	HERG
206	242.47196	53.74726	8.53	8.05	16.03	23.93	ML	29.15	S	iKgs9b	26.10	24.85	20.74	20.66	1.55	HSC	HERG
207	242.44689	53.58594	9.89	8.43	2.54	4.50	ML	1025.16	S	iKgs6b	19.66	18.54	16.21	n.d.	0.09	Vacc	SFG
208	242.44053	53.82847	21.89	17.08	0.97	7.72	ML	40.14	S	iKgs7r	21.80	20.15	17.55	n.d.	0.55	HSC	SFG
209	242.43199	53.96177	14.32	9.03	11.68	34.22	ML	8.07	S	iKgs1b	21.65	21.19	20.58	19.72	1.37	Kmag	HERG
210	242.39794	53.40818	9.96	5.45	3.72	4.29	ML	57.30	S	iKgs0b	24.72	24.20	19.88	19.64	1.23	HSC	HERG
211	242.39362	53.58097	15.47	8.97	1.03	3.05	ML	2.19	S	iKgs1b	17.48	17.14	16.25	n.d.	0.05	Vacc	SFG
212	242.37697	53.92594	9.25	5.98	4.59	5.40	ML	1.09	S	___s__	n.d.	n.d.	n.d.	21.73	3.09	smag	AGN
213	242.35692	53.69185	12.77	7.03	0.98	1.88	ML	45.47	S	iKgs6r	21.17	19.18	16.78	n.d.	0.39	Dunc	SFG
214	242.28640	53.60039	8.16	6.45	23.48	29.92	ML	35.47	S	iKgs9b	25.80	25.29	21.94	21.64	2.26	Dunc	HERG
215	242.21454	53.42730	13.20	11.47	2.26	7.26	ML	368.86	S	iKgs8r	23.71	21.89	19.00	n.d.	0.86	HSC	HERG
216	242.14838	53.63941	9.11	8.27	32.56	52.11	ML	2378.96	S	iKgs7b	18.70	17.36	14.70	n.d.	0.11	BOSS	LERG
217	242.45075	54.86888	20.04	17.02	0.90	7.05	ML	16.12	S	iKg_6b	25.13	24.09	21.83	n.d.	0.42	HSC	LERG
218	242.44383	54.70189	10.75	9.13	5.59	16.66	ML	547.88	S	iKgs6b	20.29	18.94	16.68	n.d.	0.24	BOSS	LERG
219	242.27630	54.56775	9.80	5.98	1.09	7.14	ML	508.58	S	iK_s8r	n.d.	21.31	18.53	n.d.	0.51	BOSS	HERG
220	242.26810	54.88298	11.02	10.15	10.70	31.32	ML	108.69	S	iKgs9b	24.74	23.46	20.15	19.41	1.35	Dunc	HERG
221	242.24133	54.66231	13.73	10.85	1.69	5.76	ML	43.33	S	iKgs7b	24.53	23.00	20.45	20.03	0.83	HSC	LERG
222	242.20805	54.73967	12.96	10.76	0.86	2.75	ML	380.56	S	iKgs8r	21.99	19.95	17.16	n.d.	0.39	BOSS	SFG
223	242.20306	54.86449	9.13	7.04	0.90	1.33	ML	167.19	S	iKgs6b	21.23	19.88	17.59	n.d.	0.26	BOSS	SFG
224	242.16782	54.36446	19.72	13.71	0.75	4.68	ML	0.99	S	iKgs1b	23.20	23.47	22.58	21.86	2.73	Dunc	HERG
225	242.16193	54.46383	10.27	7.87	4.76	17.32	ML	1.17	S	___s__	n.d.	n.d.	n.d.	22.81	3.62	smag	AGN
226	242.16361	55.07369	11.11	7.08	0.75	1.36	ML	31.91	S	iKgs5b	22.80	21.68	19.53	19.68	0.90	BOSS	SFG
227	242.13461	54.83869	9.45	6.90	7.01	12.28	ML	72.74	S	iKgs0b	26.22	24.78	20.50	20.44	1.54	Dunc	HERG
228	242.11863	54.74755	12.29	10.74	1.55	4.71	ML	71.56	S	iKgs8r	25.11	22.26	19.47	19.46	5.80	BOSS	HERG
229	242.08887	54.50450	12.78	9.56	7.40	26.33	ML	26.94	S	iKgs0b	26.23	24.98	20.50	20.11	1.61	Dunc	LERG
230	242.08964	54.97716	12.83	11.43	1.23	4.15	ML	84.74	S	iKgs7b	23.54	22.51	19.88	19.63	1.12	HSC	LERG
231	242.05796	54.47643	16.32	13.40	1.24	6.23	ML	94.72	S	iKgs6b	19.64	18.65	16.30	n.d.	0.12	BOSS	SFG
232	242.06169	55.06542	12.03	6.32	0.82	1.43	ML	254.38	S	iK__8r	n.d.	21.54	18.44	n.d.	0.52	HSC	HERG
233	242.03636	54.94451	16.51	14.93	0.94	5.34	ML	3.43	S	iKgs9r	24.25	22.02	18.69	n.d.	0.80	HSC	LERG
234	242.01522	54.88367	16.37	13.66	1.32	6.76	ML	977.12	S	iKgs5b	17.38	16.54	14.33	n.d.	0.05	BOSS	LERG
235	241.98864	54.77826	8.37	6.62	3.90	6.47	ML	5.77	S	iKgs2b	23.92	23.30	21.73	21.21	1.56	Dunc	LERG
236	241.98944	55.17102	15.92	14.27	2.55	13.32	ML	12.74	S	iKgs3r	21.38	19.50	17.71	n.d.	0.24	Dunc	LERG
237	241.97468	54.62377	13.94	8.30	1.41	3.75	ML	13.81	S	iKgs4b	25.19	24.07	22.14	21.73	0.44	HSC	LERG
238	241.94748	55.08150	15.65	12.20	0.78	3.44	ML	115.30	S	iKgs6r	23.80	21.65	19.38	19.48	0.53	BOSS	HERG
239	241.93547	54.83939	10.14	7.72	22.13	41.93	ML	55.94	S	iKgs0r	26.53	23.74	18.32	19.99	1.15	HSC	LERG

ID	Properties of Radio Source						Identification Data				Properties of Host Galaxy						
	RA	DEC	Major Axis arcsec	Minor Axis arcsec	Peak Flux mJy	Total Flux mJy	Analysis	LR	Morph	Type	g-band Mag	i-band Mag	K-band Mag	$3.6\mu m$ Mag	Redshift	Redshift Source	Galaxy Type
240	241.91782	54.49706	14.20	8.96	1.12	3.29	ML	4.83	S	iKgs3b	23.38	22.72	20.88	20.14	1.61	Dunc	HERG
241	241.92179	55.03174	23.80	13.30	0.98	7.10	ML	379.38	S	iKgs7b	22.47	21.09	18.45	n.d.	0.46	BOSS	SFG
242	241.90832	54.76697	12.69	9.84	1.59	4.57	ML	200.10	S	iKgs3b	17.97	16.84	15.03	n.d.	0.09	BOSS	SFG
243	241.88334	54.37303	18.54	15.70	0.96	6.41	ML	590.50	S	iKg_8b	22.40	21.23	18.36	n.d.	1.09	BOSS	HERG
244	241.83916	55.06623	13.18	11.25	0.85	2.88	ML	122.02	S	iKgs9r	26.28	23.12	19.74	19.75	1.01	HSC	LERG
245	241.80790	54.36386	29.87	16.76	0.89	10.17	ML	221.30	S	iKgs7r	20.26	18.45	15.94	n.d.	0.20	Dunc	LERG
246	241.80903	54.81652	28.34	18.53	1.34	16.16	ML	2.77	S	iKgs8b	23.97	23.32	20.41	20.61	1.21	Dunc	HERG
247	241.80519	54.46910	18.26	12.55	1.31	6.87	ML	19.64	S	iKg_8r	27.08	23.53	20.60	n.d.	1.39	HSC	LERG
248	241.74040	54.72525	11.75	9.04	10.98	30.29	ML	31.14	S	iKgs8r	24.47	22.05	19.12	19.24	0.90	Dunc	LERG
249	241.67528	54.44485	9.09	4.45	2.73	2.54	ML	16.30	S	iKgs8b	24.19	23.98	21.17	21.15	1.55	SERVS	HERG
250	241.65812	55.34966	18.29	12.06	1.73	8.78	ML	79.54	S	iKgs6r	22.83	21.01	18.56	n.d.	0.62	HSC	LERG
251	241.65070	54.54702	15.18	11.73	22.26	91.93	ML	0.52	S	iKgs9r	26.41	23.84	20.18	19.76	1.43	Dunc	LERG
252	241.64287	54.76220	11.26	10.55	1.71	4.66	ML	0.72	S	___s__	n.d.	n.d.	n.d.	19.19	1.65	smag	LERG
253	241.60907	54.81894	18.48	12.49	2.16	11.44	ML	105.59	S	iKgs7r	24.67	21.94	19.45	19.96	0.70	HSC	LERG
254	241.58742	54.94509	16.49	8.96	4.03	18.66	ML	444.65	S	iKgs7r	23.25	20.35	17.83	n.d.	0.67	BOSS	LERG
255	241.59593	55.19816	26.83	17.45	0.97	10.39	ML	599.45	S	iKgs8b	23.10	21.47	18.32	n.d.	0.81	HSC	LERG
256	241.55622	55.03121	25.55	13.36	1.82	14.27	ML	445.03	S	iKgs8r	24.80	21.63	18.62	n.d.	0.90	HSC	LERG
257	241.53710	54.45248	17.52	9.88	1.40	5.57	ML	149.25	S	iKgs3r	20.01	18.60	16.78	n.d.	0.14	Dunc	LERG
258	241.53174	55.35975	13.23	9.73	74.28	233.94	ML	1345.86	S	iKgs7b	20.82	19.36	16.66	n.d.	0.34	BOSS	HERG
259	241.52367	54.46907	10.34	9.08	25.88	58.59	ML	176.66	S	iKgs6r	24.36	21.57	19.21	19.33	0.77	BOSS	LERG
260	241.52074	54.47736	12.30	8.07	5.94	22.33	ML	13.61	S	iKgs9r	23.84	21.25	17.72	n.d.	0.84	HSC	LERG
261	241.51346	54.99266	16.09	11.16	1.08	4.47	ML	325.50	S	iKgs7r	24.09	21.49	18.95	n.d.	0.85	HSC	LERG
262	241.49989	54.90154	16.07	10.63	290.06	1404.55	ML	378.06	S	iKgs6r	23.12	20.38	17.95	n.d.	0.61	BOSS	LERG
263	241.47088	55.17625	10.38	9.69	18.20	44.12	ML	38.74	S	iKg_5b	26.16	24.94	22.75	n.d.	2.11	HSC	HERG
264	241.47167	54.37330	9.77	6.12	1.00	12.64	ML	26.48	S	iKgs5b	19.79	18.44	16.31	n.d.	0.38	HSC	LERG
265	241.46468	55.06922	18.70	9.78	1.22	5.11	ML	0.25	S	i_g___	24.98	24.28	n.d.	n.d.	0.56	HSC	LERG
266	241.42642	54.77870	9.92	8.53	16.54	35.64	ML	915.16	S	iKgs7r	22.02	19.75	17.23	n.d.	0.47	BOSS	LERG
267	241.41494	54.76301	9.20	6.10	1.89	18.81	ML	124.16	S	iKg_5b	22.62	22.55	20.48	n.d.	0.33	Dunc	HERG
268	241.41031	54.69222	24.27	16.03	2.67	23.89	ML	295.77	S	iKgs5r	20.10	18.38	16.25	n.d.	0.25	Vacc	LERG
269	241.35476	55.22568	14.94	11.67	1.86	7.46	ML	5.61	S	iKgs8r	24.22	22.39	19.52	19.29	1.27	Dunc	HERG
270	241.31251	54.76113	9.81	8.05	5.08	13.34	ML	132.88	S	iKgs8r	25.73	22.63	19.87	19.75	0.93	HSC	LERG
271	241.29533	54.91905	10.94	5.97	1.11	1.66	ML	2.38	S	iKgs4r	20.54	18.64	16.63	n.d.	0.95	HSC	LERG
272	241.27349	55.10750	14.29	11.58	1.50	5.68	ML	2.60	S	iK_s1b	n.d.	24.38	24.22	n.d.	4.37	Dunc	AGN
273	241.26742	54.74336	8.38	7.44	1.40	2.00	ML	97.00	S	iKgs5r	22.55	20.26	18.01	n.d.	0.38	HSC	LERG
274	241.24079	54.95446	15.34	13.48	1.20	5.72	ML	167.66	S	iKgs5b	22.76	21.50	19.43	n.d.	0.73	HSC	HERG
275	241.21492	54.83796	7.40	6.71	1.21	8.60	ML	1342.00	S	iKgs7b	20.84	19.32	16.77	n.d.	0.26	BOSS	SFG
276	241.18121	54.55939	11.50	8.23	1.43	3.11	ML	866.14	S	iKgs8b	21.16	19.60	16.82	n.d.	0.29	Vacc	SFG
277	241.17487	54.72239	13.03	9.52	2.43	6.91	ML	51.82	S	_K_s0k	n.d.	n.d.	20.35	19.88	0.48	HSC	HERG
278	241.17055	54.84715	19.55	13.54	1.25	7.60	ML	25.74	S	iKgs2r	22.62	20.06	18.42	n.d.	0.56	BOSS	LERG
279	241.16915	54.95823	15.01	10.74	1.14	4.21	ML	347.50	S	iKgs6b	21.74	20.21	17.94	n.d.	0.44	HSC	SFG

ID	Properties of Radio Source						Identification Data				Properties of Host Galaxy						
	RA	DEC	Major Axis arcsec	Minor Axis arcsec	Peak Flux mJy	Total Flux mJy	Analysis	LR	Morph	Type	g-band Mag	i-band Mag	K-band Mag	$3.6\mu m$ Mag	Redshift	Redshift Source	Galaxy Type
280	241.15830	55.34830	28.03	19.58	1.26	15.90	ML	268.94	S	iKgs5r	22.42	20.30	18.22	19.31	0.38	HSC	LERG
281	241.14432	55.21681	12.48	9.58	1.61	12.20	ML	9.63	S	_K__9k	n.d.	n.d.	21.74	n.d.	1.92	Kmag	HERG
282	241.14105	54.74244	21.99	15.12	1.29	9.84	ML	509.79	S	iKgs6b	18.08	17.03	14.69	n.d.	0.08	BOSS	SFG
283	241.10932	54.62560	8.79	4.87	1.40	1.38	ML	56.80	S	iKgs7b	19.86	18.52	15.95	n.d.	0.31	Dunc	SFG
284	241.08010	55.18822	14.10	12.59	2.10	8.58	ML	32.84	S	iKgs9b	25.31	24.98	21.37	20.86	1.54	HSC	HERG
285	241.08294	54.38895	8.04	5.42	4.64	5.01	ML	48.20	S	iKgs8r	25.71	23.57	20.43	20.09	1.13	Dunc	LERG
286	241.05552	55.18127	14.30	11.60	2.65	10.09	ML	47.02	S	iKgs9b	24.97	23.79	20.47	20.11	1.74	Dunc	HERG
287	241.05759	54.65973	10.93	8.54	2.05	4.40	ML	79.61	S	iKg_9r	25.55	23.57	20.16	n.d.	1.19	HSC	LERG
288	241.04859	55.21616	9.99	9.16	6.15	18.74	ML	3.34	S	_K__7k	n.d.	n.d.	22.35	n.d.	0.36	HSC	LERG
289	241.04074	55.24898	13.95	10.99	5.84	20.56	ML	93.00	S	iKgs7r	25.03	22.41	19.87	19.67	0.93	HSC	LERG
290	241.03458	54.97033	13.51	9.08	1.74	4.89	ML	1709.77	S	iKgs5b	18.06	17.05	14.89	n.d.	0.06	BOSS	SFG
291	241.03275	54.42552	18.93	17.24	0.90	6.74	ML	7.48	S	iKgs5r	21.09	19.50	17.25	n.d.	0.36	HSC	SFG
292	241.00506	55.25036	8.20	7.61	2.21	6.04	ML	110.75	S	iKgs3b	19.29	18.28	16.51	n.d.	0.31	Dunc	HERG
293	240.95127	54.44046	10.92	8.60	3.08	6.65	ML	1.33	S	_K__7k	n.d.	n.d.	22.47	n.d.	2.28	Kmag	HERG
294	240.90351	54.68943	27.96	18.97	1.06	12.87	ML	129.51	S	iKgs6r	20.44	18.60	16.20	n.d.	0.47	HSC	LERG
295	240.83778	55.11213	12.47	9.64	3.42	16.84	ML	345.18	S	iKgs7r	20.36	18.45	15.76	n.d.	0.27	BOSS	HERG
296	240.84623	54.62723	25.74	20.54	1.21	14.70	ML	5.97	S	iKgs9r	28.72	24.18	20.08	19.56	1.21	Dunc	HERG
297	240.81438	55.22529	9.75	8.30	4.68	12.44	ML	52.66	S	iKgs8b	23.74	23.36	20.21	20.23	1.73	Dunc	HERG
298	240.78774	55.00845	17.50	12.14	1.50	7.31	ML	30.70	S	iKgs9b	25.85	24.65	21.40	21.22	1.13	HSC	LERG
299	240.72845	55.09339	24.81	15.11	1.35	11.62	ML	180.88	S	iKgs5r	22.11	19.75	17.63	n.d.	0.48	BOSS	LERG
300	240.72027	54.99904	17.56	11.10	2.85	12.77	ML	182.06	S	iKgs9r	24.91	21.99	18.50	n.d.	1.07	BOSS	LERG
301	240.71247	54.84940	17.59	12.51	1.08	5.44	ML	12.73	S	iKgs1b	18.79	18.53	18.59	n.d.	1.20	Vacc	HERG
302	240.70109	54.79351	10.63	8.70	5.98	16.35	ML	68.27	S	iKgs9r	25.15	23.26	19.66	19.07	1.12	HSC	HERG
303	240.64521	54.78657	15.84	12.54	1.55	7.05	ML	11.36	S	iKgs5b	23.34	22.32	20.22	19.79	1.11	Dunc	HERG
304	240.62682	54.93808	19.73	13.93	1.52	9.58	ML	48.23	S	iKgs5r	22.81	20.36	18.28	n.d.	0.52	Dunc	LERG
305	240.62410	54.94910	11.23	8.76	12.39	32.02	ML	107.04	S	iKgs6r	24.51	21.73	19.35	19.35	0.89	BOSS	LERG
306	240.51636	54.91182	22.35	11.82	31.13	136.88	ML	49.16	S	iKgs6b	22.81	22.03	19.65	19.03	1.21	BOSS	HERG
307	240.49620	54.62080	15.59	12.80	2.57	11.76	ML	13.36	S	iKgs6r	23.58	20.77	18.43	n.d.	0.67	Dunc	LERG
308	240.39835	54.61649	22.96	17.55	1.22	11.28	ML	2816.35	S	iKgs8b	18.50	17.96	15.15	n.d.	0.05	Vacc	SFG
309	240.36294	54.65882	9.97	7.32	5.35	11.43	ML	18.00	S	iKgs2b	21.65	20.99	19.71	19.65	0.79	HSC	HERG
310	240.34228	54.95277	24.29	16.23	1.22	11.02	ML	1.58	S	iKgs1b	17.29	16.64	17.07	n.d.	0.40	HSC	LERG
311	240.29706	54.76542	20.12	13.75	1.02	6.50	ML	65.94	S	iKgs8r	24.76	23.09	19.98	19.64	0.83	HSC	LERG
312	240.24701	54.73111	32.53	18.38	1.41	19.37	ML	599.71	S	iKgs9b	18.96	18.09	14.04	n.d.	0.04	BOSS	SFG
313	240.16023	54.59719	18.06	11.52	1.84	8.81	ML	14.82	S	_K__9k	n.d.	n.d.	21.47	n.d.	1.79	Kmag	HERG
314	245.50812	54.67180	15.38	15.09	1.09	5.53	ML	165.43	S	iKgs3b	19.14	18.38	16.65	n.d.	0.10	Dunc	SFG
315	245.45435	54.75456	27.68	19.42	1.02	12.06	ML	89.09	S	iKgs4r	22.29	20.14	18.14	n.d.	0.48	Vacc	LERG
316	245.44867	54.65596	12.33	10.62	6.50	35.93	ML	1374.55	S	iKg_8b	18.71	18.45	15.46	n.d.	0.05	BOSS	SFG
317	245.43517	54.68655	12.26	8.45	1.23	13.82	ML	3.69	S	iKgs2b	18.63	17.89	16.40	n.d.	0.21	Kmag	LERG
318	245.43907	54.79000	11.68	9.02	1.98	4.58	ML	19.69	S	iKgs4r	24.47	23.11	21.10	20.61	0.80	HSC	LERG
319	245.43056	54.53980	7.21	5.31	2.72	3.97	ML	39.75	S	_K__5k	n.d.	n.d.	23.49	n.d.	2.76	Kmag	HERG

ID	Properties of Radio Source						Identification Data				Properties of Host Galaxy						
	RA	DEC	Major Axis arcsec	Minor Axis arcsec	Peak Flux mJy	Total Flux mJy	Analysis	LR	Morph	Type	g-band Mag	i-band Mag	K-band Mag	$3.6\mu m$ Mag	Redshift	Redshift Source	Galaxy Type
320	245.33085	54.85332	13.41	8.78	2.59	11.81	ML	236.66	S	iKgs7r	24.52	21.79	19.15	19.17	1.01	BOSS	LERG
321	245.30447	54.65258	15.42	7.37	4.50	16.10	ML	14.33	S	_K__9k	n.d.	n.d.	20.97	n.d.	1.54	Kmag	HERG
322	245.30527	54.83711	14.98	9.30	1.09	3.32	ML	65.91	S	iKgs5b	23.79	23.25	21.08	20.71	2.33	Dunc	HERG
323	245.29347	54.68803	6.85	5.21	1.43	3.03	ML	234.90	S	iKgs3b	19.27	18.27	16.48	n.d.	0.30	Dunc	SFG
324	245.29365	54.82145	15.24	13.36	1.04	4.65	ML	19.47	S	iKgs6r	23.74	21.73	19.37	19.47	0.65	HSC	LERG
325	245.28662	54.76152	9.59	8.28	1.47	2.56	ML	17.41	S	_K_s9k	n.d.	n.d.	21.70	20.91	1.27	Dunc	LERG
326	245.24172	54.61209	8.46	7.47	3.09	4.27	ML	5.75	S	_K_s8k	n.d.	n.d.	22.06	20.75	0.92	HSC	LERG
327	245.22925	54.81512	8.12	7.31	25.61	37.77	ML	11.94	S	iKgs1b	18.61	18.24	17.28	n.d.	1.15	BOSS	HERG
328	245.17701	54.62013	9.44	6.05	1.17	1.47	ML	1174.08	S	iKgs6b	19.51	18.26	15.92	n.d.	0.12	Dunc	SFG
329	245.15846	54.85793	10.23	8.29	29.01	64.27	ML	137.11	S	iKgs7r	25.17	22.44	19.77	19.75	0.90	HSC	LERG
330	245.15460	54.67957	15.61	7.95	8.47	30.94	ML	54.83	S	iKgs5r	24.05	21.44	19.28	19.46	0.95	HSC	LERG
331	245.09968	54.58049	16.86	14.92	0.87	4.78	ML	28.49	S	iKgs7r	24.75	21.99	19.53	19.32	0.83	Dunc	LERG
332	245.08373	54.77205	6.94	5.98	1.04	3.95	ML	23.45	S	_K_s5k	n.d.	n.d.	22.94	n.d.	2.51	Kmag	HERG
333	245.07622	54.83329	8.41	6.85	3.76	7.56	ML	45.82	S	iKgs4b	18.97	17.98	15.98	n.d.	0.14	Dunc	SFG
334	245.02721	54.54229	10.09	8.26	19.40	40.91	ML	10.50	S	iKgs2r	23.16	21.33	19.73	20.42	0.42	BOSS	HERG
335	245.01274	54.71508	7.68	5.97	1.49	1.50	ML	36.43	S	iKg_7b	24.93	24.72	22.08	n.d.	2.20	Dunc	HERG
336	244.96070	54.62096	8.90	7.29	1.88	2.67	ML	1565.90	S	iKgs5b	19.62	18.38	16.25	n.d.	0.13	Dunc	SFG
337	244.94171	54.91546	9.34	5.17	0.91	0.96	ML	142.25	S	iKgs4r	21.58	19.39	17.34	n.d.	0.38	Vacc	LERG
338	244.93511	54.73836	15.35	9.31	1.24	3.88	ML	3.92	S	iKg_5b	24.50	24.22	22.09	n.d.	2.32	Dunc	HERG
339	244.93434	54.85245	15.43	10.09	1.10	3.76	ML	175.92	S	iKgs9b	23.39	22.37	18.42	n.d.	1.08	HSC	LERG
340	244.92406	54.97432	13.68	11.12	1.05	3.51	ML	99.49	S	iKgs4b	20.49	19.26	17.33	n.d.	0.28	Dunc	SFG
341	244.91110	54.64492	12.49	8.06	1.07	2.36	ML	30.78	S	iKgs9b	25.99	24.68	21.20	20.49	1.94	Dunc	HERG
342	244.89043	54.42635	16.49	9.71	1.23	4.33	ML	14.96	S	_K_s9k	n.d.	n.d.	21.65	20.99	1.87	Kmag	LERG
343	244.89099	54.55302	9.71	8.10	1.65	2.84	ML	36.97	S	i_gs4b	22.64	22.41	n.d.	20.52	1.10	imag	HERG
344	244.88913	54.90989	5.82	3.02	0.92	1.37	ML	22.12	S	iKgs3b	21.54	20.60	18.85	19.59	0.36	HSC	LERG
345	244.88493	54.60525	10.13	8.31	1.32	2.43	ML	1070.25	S	iKgs8b	20.95	19.48	16.59	n.d.	0.16	HSC	SFG
346	244.87414	54.24041	9.36	7.94	1.54	2.52	ML	1636.51	S	iKgs5b	19.06	17.70	15.56	n.d.	0.15	BOSS	HERG
347	244.87337	54.31180	10.07	8.68	2.25	4.32	ML	49.67	S	iKgs2r	18.85	17.75	16.46	n.d.	0.10	BOSS	SFG
348	244.86399	54.21435	10.47	5.91	3.10	6.90	ML	610.03	S	iKgs6r	20.55	18.61	16.34	n.d.	0.00	BOSS	SFG
349	244.83403	54.80475	8.15	7.68	149.95	231.03	ML	12.84	S	iKg_1b	19.41	19.08	20.68	n.d.	0.49	HSC	LERG
350	244.82170	54.35871	22.28	16.35	0.91	7.27	ML	173.07	S	iKgs5r	22.55	20.31	18.09	n.d.	0.52	HSC	LERG
351	244.81241	54.37143	14.45	8.77	0.99	2.75	ML	38.40	S	iKgs0r	27.72	25.59	20.82	19.93	0.81	HSC	LERG
352	244.79094	54.86254	9.39	7.92	6.78	11.05	ML	216.99	S	iKgs5r	23.63	21.56	19.47	19.47	0.76	BOSS	LERG
353	244.78801	54.61622	15.10	11.97	1.07	4.22	ML	20.76	S	iKgs4b	24.30	23.49	21.53	21.19	1.57	Dunc	HERG
354	244.77966	54.18835	6.09	5.20	1.87	1.65	ML	8.13	S	iKgs2b	22.97	22.50	20.87	20.81	1.58	Dunc	HERG
355	244.76321	54.87810	10.90	9.55	2.63	6.01	ML	1506.54	S	iKgs5r	20.04	18.51	16.45	n.d.	0.21	BOSS	LERG
356	244.75268	54.49363	23.90	9.57	527.88	1987.76	ML	80.76	S	iKgs6b	23.29	22.62	20.36	19.72	1.02	HSC	HERG
357	244.73662	54.73735	16.89	9.19	1.05	3.58	ML	272.44	S	iKgs5r	22.86	20.35	18.27	n.d.	0.58	HSC	LERG
358	244.73708	54.66913	15.53	8.69	0.92	2.74	ML	0.67	S	iKgs2r	23.66	22.38	21.04	20.26	1.58	Kmag	LERG
359	244.72046	54.55978	6.64	5.76	2.86	4.32	ML	57.71	S	iKg_6b	23.47	22.62	20.28	n.d.	1.09	HSC	HERG

ID	Properties of Radio Source						Identification Data				Properties of Host Galaxy						
	RA	DEC	Major Axis arcsec	Minor Axis arcsec	Peak Flux mJy	Total Flux mJy	Analysis	LR	Morph	Type	g-band Mag	i-band Mag	K-band Mag	3.6μm Mag	Redshift	Redshift Source	Galaxy Type
360	244.70960	54.42530	8.49	6.77	3.55	4.48	ML	319.56	S	iKgs5r	22.68	20.90	18.71	19.14	0.38	BOSS	LERG
361	244.70532	54.67654	16.09	13.29	1.19	5.57	ML	190.56	S	iKgs7r	23.36	20.47	17.87	n.d.	0.71	BOSS	LERG
362	244.68250	54.57808	7.48	6.46	12.51	15.66	ML	14.92	S	_K__9k	n.d.	n.d.	21.80	n.d.	0.95	HSC	LERG
363	244.67560	54.40524	9.69	4.48	0.98	11.70	ML	0.71	S	iKgs5r	22.91	20.37	18.20	n.d.	0.78	HSC	LERG
364	244.65996	54.34177	10.10	8.48	0.92	1.73	ML	174.63	S	iKgs7r	24.04	22.23	19.60	19.19	0.87	HSC	LERG
365	244.64736	54.49296	10.10	8.98	1.65	3.29	ML	879.38	S	iKgs7b	21.22	19.89	17.43	n.d.	0.34	HSC	SFG
366	244.63586	54.56623	8.68	5.89	2.96	3.32	ML	214.82	S	iKgs9r	25.14	22.38	19.07	n.d.	1.04	HSC	LERG
367	244.63055	54.64092	8.71	6.87	13.85	21.10	ML	81.56	S	iKgs3r	22.78	20.31	18.49	n.d.	0.55	BOSS	LERG
368	244.63244	54.85050	9.24	7.72	3.31	5.17	ML	5.21	S	_K__8k	n.d.	n.d.	22.05	n.d.	2.07	Kmag	HERG
369	244.60774	54.42840	9.52	6.86	29.81	48.59	ML	570.52	S	iKgs6r	22.37	19.85	17.43	n.d.	0.55	BOSS	HERG
370	244.60329	54.32427	9.27	7.65	1.81	2.81	ML	246.84	S	iKgs3r	20.56	19.04	17.22	n.d.	0.35	HSC	HERG
371	244.58088	54.31652	8.37	7.34	5.21	12.84	ML	3119.90	S	iKgs8b	18.41	17.24	14.49	n.d.	0.00	BOSS	SFG
372	244.57399	54.28481	10.52	8.31	1.25	2.39	ML	18.61	S	_K_s9k	n.d.	n.d.	21.12	20.69	1.69	Dunc	HERG
373	244.56496	55.01891	12.33	8.29	0.79	1.77	ML	31.96	S	_K_s5k	n.d.	n.d.	23.06	n.d.	2.56	Kmag	HERG
374	244.54936	54.69122	10.27	6.86	1.54	2.38	ML	250.14	S	iKgs6r	22.27	19.79	17.47	n.d.	0.55	BOSS	LERG
375	244.53607	54.56101	14.87	9.37	0.99	3.02	ML	3.68	S	_K_s8k	n.d.	n.d.	22.22	20.96	2.32	Dunc	HERG
376	244.51017	54.79419	15.41	12.21	0.86	3.56	ML	325.60	S	iKgs6b	21.34	19.94	17.57	n.d.	0.57	Dunc	LERG
377	244.50355	54.44638	14.33	6.95	40.80	68.48	ML	47.16	S	iKgs7b	23.41	23.27	20.67	20.28	2.00	Dunc	HERG
378	244.49144	54.58832	7.65	6.20	7.95	9.43	ML	194.19	S	iKgs4r	21.23	19.63	17.62	n.d.	0.44	BOSS	LERG
379	244.47784	54.80026	14.55	8.29	1.06	2.79	ML	8.85	S	iKgs3b	23.89	23.43	21.63	20.98	1.71	Dunc	HERG
380	244.44884	54.51371	8.99	6.93	0.98	1.34	ML	54.87	S	_K_s0k	n.d.	n.d.	20.69	20.06	1.25	HSC	HERG
381	244.43484	54.69146	6.80	6.11	2.71	3.87	ML	946.15	S	iKgs7r	21.42	19.77	17.10	n.d.	0.35	BOSS	LERG
382	244.43147	54.40207	8.21	5.85	0.92	0.97	ML	46.41	S	iKgs0r	29.77	24.46	19.29	19.01	1.18	BOSS	LERG
383	244.42404	54.42932	10.88	6.54	0.89	1.38	ML	4.84	S	i_gs7b	25.03	24.48	n.d.	21.14	1.66	imag	HERG
384	244.41135	54.88639	7.56	4.76	1.04	3.03	ML	33.44	S	iKgs2b	18.54	17.57	16.01	n.d.	0.17	BOSS	SFG
385	244.41158	54.70814	13.65	9.70	1.00	2.91	ML	0.84	S	iK__9b	n.d.	26.24	22.46	n.d.	2.27	Kmag	HERG
386	244.39714	55.00689	15.82	13.99	0.68	3.31	ML	17.79	S	iKgs2r	21.19	19.94	18.53	n.d.	0.35	HSC	LERG
387	244.38581	54.39414	13.09	7.37	1.01	2.15	ML	4.16	S	iKgs8r	24.87	22.71	19.60	19.85	0.97	Kmag	HERG
388	244.37132	54.43953	10.02	5.57	1.03	1.26	ML	52.22	S	iKgs9b	24.98	24.13	20.66	20.57	1.61	HSC	HERG
389	244.33655	54.99924	7.54	7.01	8.04	10.40	ML	360.58	S	iKgs7r	23.96	21.33	18.65	n.d.	0.77	BOSS	LERG
390	244.34398	54.35797	23.97	12.75	0.83	5.59	ML	22.88	S	iKgs4b	23.03	22.47	20.46	n.d.	1.24	HSC	HERG
391	244.33827	54.55527	8.96	7.74	1.48	2.25	ML	94.98	S	iK_s9r	n.d.	23.18	19.73	19.36	0.99	Dunc	LERG
392	244.33207	54.69600	15.42	8.27	0.84	2.35	ML	163.12	S	iKgs5r	23.71	21.17	18.99	n.d.	0.75	HSC	LERG
393	244.32929	54.54534	10.33	7.93	1.01	1.81	ML	9.27	S	iKgs1b	17.19	17.14	16.49	n.d.	0.53	BOSS	HERG
394	244.32598	54.29979	16.89	10.75	1.10	4.39	ML	26.84	S	_K_s5k	n.d.	n.d.	23.79	n.d.	2.89	Kmag	HERG
395	244.31048	54.97351	16.06	9.71	0.86	2.93	ML	936.68	S	iKgs5b	18.91	17.57	15.51	n.d.	0.14	Vacc	LERG
396	244.30473	54.53503	38.16	10.44	4.80	40.09	ML	204.47	S	iKgs6r	24.41	21.53	19.11	19.31	0.70	BOSS	LERG
397	244.31089	54.66082	7.43	6.52	3.62	5.75	ML	275.23	S	iKgs7r	23.60	21.40	18.76	n.d.	0.78	BOSS	LERG
398	244.28822	55.01814	12.70	9.14	1.27	3.23	ML	60.58	S	iKgs5b	22.02	20.60	18.50	19.04	0.49	BOSS	LERG
399	244.29290	54.40706	7.62	6.41	1.07	1.14	ML	127.36	S	iKgs6r	24.36	21.49	19.07	19.13	0.83	HSC	LERG

ID	Properties of Radio Source						Identification Data				Properties of Host Galaxy						
	RA	DEC	Major Axis arcsec	Minor Axis arcsec	Peak Flux mJy	Total Flux mJy	Analysis	LR	Morph	Type	g-band Mag	i-band Mag	K-band Mag	$3.6\mu m$ Mag	Redshift	Redshift Source	Galaxy Type
400	244.26861	54.83983	14.84	6.94	2.29	8.79	ML	634.85	S	iKgs7r	22.25	20.12	17.62	n.d.	0.44	Vacc	LERG
401	244.26627	54.86839	9.65	9.01	1.50	2.87	ML	16.72	S	iKgs2r	21.76	20.32	19.12	19.78	0.00	BOSS	SFG
402	244.25607	54.98142	12.96	9.51	1.29	3.49	ML	311.38	S	iKgs4r	20.58	18.96	17.06	n.d.	0.24	BOSS	LERG
403	244.23286	55.01718	18.78	11.46	0.92	4.36	ML	0.26	S	___s__	n.d.	n.d.	n.d.	21.24	2.82	smag	HERG
404	244.23134	54.73691	11.78	11.15	0.90	2.59	ML	277.05	S	iKgs5r	23.31	20.92	18.68	19.16	0.54	BOSS	LERG
405	244.23171	54.68758	14.27	10.49	0.98	3.22	ML	12.29	S	_K_s9k	n.d.	n.d.	21.01	20.36	1.06	HSC	HERG
406	244.20541	54.82253	9.85	8.22	3.72	6.60	ML	140.63	S	iKg_6r	22.41	20.15	17.70	n.d.	0.00	BOSS	SFG
407	244.21014	54.42176	6.85	6.04	4.99	5.41	ML	36.03	S	iKgs6r	25.41	23.73	21.38	20.83	0.78	HSC	LERG
408	244.20071	54.76625	11.51	6.80	0.70	1.20	ML	24.82	S	iKgs6r	22.11	19.86	17.60	n.d.	0.51	HSC	LERG
409	244.19952	54.38465	9.07	7.95	2.54	4.01	ML	117.41	S	iKgs5r	24.08	22.32	20.14	19.72	0.99	BOSS	LERG
410	244.19111	54.43133	9.02	5.31	0.95	1.00	ML	18.52	S	iKgs2b	19.31	18.24	16.63	n.d.	0.27	Dunc	HERG
411	244.18338	54.69977	7.89	5.92	0.81	0.83	ML	545.20	S	iKgs5r	21.10	19.52	17.35	n.d.	0.34	HSC	SFG
412	244.10356	54.93334	22.38	9.49	6.65	31.03	ML	2.69	S	iKgs0r	29.74	25.86	20.40	19.90	1.23	HSC	HERG
413	244.09763	54.96058	8.89	7.68	44.90	75.39	ML	26.07	S	iKgs6b	24.63	24.11	21.66	21.36	2.00	Dunc	HERG
414	244.09635	54.75815	12.77	7.08	0.85	1.68	ML	46.06	S	iK_s9b	n.d.	24.27	20.78	20.31	1.69	Dunc	HERG
415	244.06430	54.62318	10.71	9.97	1.94	4.55	ML	29.58	S	i_gs6b	22.96	22.55	n.d.	19.76	0.78	BOSS	LERG
416	244.04397	54.71253	8.20	5.57	0.91	0.91	ML	11.49	S	iKgs7b	24.44	23.55	20.91	20.36	1.18	HSC	HERG
417	244.03943	54.99150	9.42	5.29	1.13	6.45	ML	1031.75	S	iKgs8b	21.38	19.91	16.98	n.d.	0.21	BOSS	SFG
418	244.44723	54.18409	12.70	10.34	1.02	2.93	ML	46.38	S	iK_s0b	n.d.	24.53	20.20	19.87	1.45	Dunc	HERG
419	244.35193	54.23326	8.42	7.35	2.93	3.96	ML	38.32	S	_Kg_7r	25.08	n.d.	20.06	n.d.	1.15	Dunc	LERG
420	244.34822	54.23955	10.87	8.32	0.87	1.71	ML	13.26	S	iKg_9r	27.49	24.86	20.92	n.d.	0.82	HSC	HERG
421	244.31917	54.24236	14.19	8.11	3.29	8.28	ML	59.69	S	iKgs9r	26.26	23.24	19.71	19.32	1.14	HSC	LERG
422	244.25359	54.23136	8.46	6.96	4.08	8.28	ML	354.39	S	iKgs8r	25.28	21.95	19.09	n.d.	0.91	HSC	LERG
423	244.13211	53.69449	13.31	7.37	23.02	49.78	ML	2.98	S	iKgs3r	23.24	21.79	19.96	19.94	0.83	HSC	LERG
424	244.12122	53.68901	9.68	5.18	1.31	1.44	ML	0.81	S	__g___	24.86	n.d.	n.d.	n.d.	0.90	HSC	LERG
425	244.11072	54.04788	7.74	5.78	2.40	4.61	ML	27.41	S	iK_s8b	n.d.	25.22	22.40	21.22	1.62	Dunc	LERG
426	244.06757	54.28958	15.14	8.99	17.33	57.32	ML	13.65	S	iKgs5r	23.09	20.84	18.76	n.d.	0.69	Kmag	LERG
427	244.05283	53.88151	12.49	10.11	1.78	4.92	ML	533.75	S	iKgs4b	19.67	18.84	16.95	n.d.	0.19	Vacc	LERG
428	244.04648	54.05481	8.37	5.98	4.71	6.96	ML	115.18	S	iKgs7b	23.98	22.59	19.99	19.35	0.99	HSC	HERG
429	244.02293	53.95334	11.61	8.78	15.96	42.03	ML	40.49	S	iKgs7r	24.74	22.65	20.08	19.91	0.90	HSC	LERG
430	244.02161	53.83710	14.62	10.73	0.98	3.36	ML	211.68	S	iKgs3b	20.00	19.00	17.17	n.d.	0.14	Dunc	SFG
431	244.01559	54.07555	9.32	7.03	17.23	27.90	ML	10.72	S	iKgs3b	24.12	23.47	21.66	21.18	2.79	Dunc	HERG
432	243.99023	54.25127	16.61	13.16	0.71	3.41	ML	420.84	S	iKgs6b	21.35	20.28	17.98	n.d.	0.48	BOSS	SFG
433	243.97345	54.22471	7.56	5.83	1.35	3.30	ML	32.03	S	iKgs5r	22.47	20.17	17.95	19.13	0.37	Dunc	LERG
434	243.96429	54.25988	13.15	10.26	1.22	3.60	ML	1088.33	S	iKgs5b	20.06	18.87	16.73	n.d.	0.21	BOSS	SFG
435	243.95631	53.72100	17.31	14.02	1.35	7.20	ML	12.53	S	_K__0k	n.d.	n.d.	18.66	n.d.	1.57	Dunc	HERG
436	243.95376	54.27145	7.33	4.41	1.04	4.80	ML	79.90	S	iKgs9r	25.33	23.03	19.82	19.44	1.27	Dunc	HERG
437	243.95327	53.90378	13.99	11.48	0.88	3.11	ML	42.26	S	iKgs9b	24.88	23.55	20.13	19.23	1.41	Dunc	HERG
438	243.95139	53.76426	14.54	9.11	1.36	3.93	ML	925.76	S	iKgs4b	18.90	18.02	16.10	n.d.	0.11	Dunc	SFG
439	243.94439	53.89995	10.13	4.70	1.02	5.13	ML	60.14	S	iKgs8b	24.65	23.35	20.31	19.39	1.15	HSC	HERG

ID	Properties of Radio Source						Identification Data				Properties of Host Galaxy						
	RA	DEC	Major Axis arcsec	Minor Axis arcsec	Peak Flux mJy	Total Flux mJy	Analysis	LR	Morph	Type	g-band Mag	i-band Mag	K-band Mag	$3.6\mu m$ Mag	Redshift	Redshift Source	Galaxy Type
440	243.93529	53.98713	32.32	16.70	0.88	10.45	ML	10.00	S	iKgs8r	22.63	20.28	17.36	n.d.	0.69	HSC	LERG
441	243.91851	54.22118	15.26	12.24	1.29	5.27	ML	848.90	S	iKgs4b	19.07	18.31	16.44	n.d.	0.13	BOSS	SFG
442	243.90739	53.77922	33.15	11.99	54.08	368.36	ML	64.45	S	iKgs8r	23.60	21.93	18.80	n.d.	1.05	BOSS	LERG
443	243.91398	54.01883	15.05	9.90	1.00	3.26	ML	62.30	S	iKgs9b	25.40	24.16	20.52	19.69	1.73	Dunc	HERG
444	243.88181	54.16848	8.64	5.53	1.69	3.45	ML	1850.96	S	iKgs7r	20.20	18.58	16.00	n.d.	0.24	BOSS	LERG
445	243.88062	54.10860	12.37	7.05	0.93	1.77	ML	1.13	S	iKgs8b	25.16	24.29	21.34	20.38	1.46	Dunc	LERG
446	243.88150	53.72962	10.29	8.65	2.08	4.05	ML	35.44	S	iKgs9b	25.68	24.38	20.77	20.22	1.58	Dunc	LERG
447	243.87716	54.17840	6.58	4.27	1.18	1.04	ML	23.16	S	iKgs8b	25.99	24.40	21.26	20.99	0.89	HSC	SFG
448	243.86879	54.22195	8.04	6.03	2.15	4.74	ML	6.09	S	_K_s8k	n.d.	n.d.	22.13	21.17	1.98	Dunc	HERG
449	243.86819	53.73477	28.27	14.30	1.05	9.33	ML	55.73	S	_K__0k	n.d.	n.d.	20.59	n.d.	1.66	Dunc	HERG
450	243.85934	54.23376	8.00	6.70	1.87	4.85	ML	49.48	S	iKgs7b	24.46	23.46	20.86	20.21	1.47	Dunc	LERG
451	243.85345	54.01007	19.84	7.31	3.17	13.98	ML	119.50	S	iKgs8r	25.00	21.96	18.88	n.d.	0.94	HSC	LERG
452	243.84401	53.96188	7.68	6.12	1.69	5.60	ML	214.92	S	iKgs4r	21.07	19.15	17.22	n.d.	0.32	HSC	SFG
453	243.74501	54.17126	10.78	5.71	1.19	1.60	ML	66.72	S	iKgs9b	24.38	23.22	20.05	19.60	1.36	Dunc	HERG
454	243.74623	53.91875	8.01	4.98	1.35	3.09	ML	1118.71	S	iKgs6b	19.45	18.31	15.98	n.d.	0.14	BOSS	SFG
455	243.74226	54.14868	14.64	8.26	1.14	3.02	ML	42.27	S	iKgs5b	19.43	18.67	16.61	n.d.	0.61	HSC	HERG
456	243.73436	53.86369	6.91	6.01	1.75	3.38	ML	271.73	S	iKgs6r	23.09	21.04	18.61	n.d.	0.77	HSC	LERG
457	243.72441	53.83346	7.78	5.48	1.49	3.01	ML	11.70	S	iKg_2b	22.53	21.57	19.94	n.d.	0.33	BOSS	SFG
458	243.66456	53.90432	14.68	9.12	1.31	3.84	ML	163.20	S	iKgs7r	25.86	22.28	19.76	19.69	0.89	HSC	LERG
459	243.60626	53.93342	9.07	8.78	1.00	13.39	ML	334.85	S	iKgs6b	19.44	18.68	16.33	n.d.	0.13	BOSS	SFG
460	243.59766	54.06428	12.90	9.37	1.00	2.65	ML	75.44	S	iKgs4b	19.37	18.43	16.54	n.d.	0.13	Dunc	SFG
461	243.59310	54.02980	16.52	12.88	1.14	5.32	ML	118.48	S	_Kg_7r	24.86	n.d.	20.29	n.d.	0.91	HSC	LERG
462	243.56885	53.98045	8.01	4.33	1.04	2.17	ML	30.80	S	iKgs0r	26.24	24.41	20.16	19.82	1.38	HSC	HERG
463	243.55519	54.06972	10.95	8.15	32.95	63.03	ML	78.96	S	iKgs9r	24.26	21.26	17.98	n.d.	0.86	BOSS	LERG
464	243.50139	53.95397	14.13	8.77	14.18	47.55	ML	982.17	S	iKgs6r	20.33	18.51	16.20	n.d.	0.29	Vacc	HERG
465	243.48736	53.97334	11.94	9.61	1.42	3.56	ML	15.66	S	iK_s0b	n.d.	25.69	20.68	21.15	0.84	HSC	HERG
466	243.41468	53.96837	17.88	12.58	0.98	4.83	ML	0.76	S	iKgs6r	24.43	22.08	19.65	20.62	0.99	Kmag	LERG
467	243.36431	53.92957	34.02	29.75	0.84	18.62	ML	39.20	S	iKgs8b	19.27	18.02	15.07	n.d.	0.12	Dunc	SFG
468	243.31582	53.91647	15.33	12.24	1.20	4.94	ML	615.88	S	iKgs4b	18.86	17.66	15.65	n.d.	0.13	Vacc	SFG
469	244.85201	55.85310	11.44	6.83	4.77	13.03	ML	133.37	S	iKgs4r	20.00	18.20	16.25	n.d.	0.28	BOSS	LERG
470	244.78533	55.81363	11.62	9.10	1.80	4.16	ML	512.13	S	iKgs5r	22.53	20.06	17.84	n.d.	0.49	BOSS	LERG
471	244.68467	55.85214	13.68	8.23	1.23	3.03	ML	6.54	S	iKgs1b	20.29	19.94	19.14	19.01	2.45	BOSS	HERG
472	244.68029	55.74231	15.03	9.28	1.38	4.20	ML	792.91	S	iKgs5b	19.15	18.29	16.06	n.d.	0.15	BOSS	SFG
473	244.64401	55.62774	7.10	6.26	1.16	1.13	ML	17.63	S	iKgs9r	26.76	24.03	19.90	19.34	1.47	Dunc	HERG
474	244.63558	55.56897	9.18	7.02	2.42	3.40	ML	383.19	S	iKgs6b	21.46	20.33	18.03	n.d.	0.45	BOSS	LERG
475	244.56561	55.52784	7.94	6.28	8.21	11.76	ML	3.48	S	iKgs1b	20.06	19.30	19.42	19.94	0.28	HSC	LERG
476	244.56134	55.58459	9.90	7.66	4.16	6.89	ML	19.51	S	_K_s9k	n.d.	n.d.	20.91	20.22	1.61	HSC	HERG
477	244.55431	55.68933	9.57	8.19	1.23	2.11	ML	5.02	S	iKgs9b	24.73	23.25	19.53	19.46	1.26	Dunc	HERG
478	244.52706	55.43577	10.20	7.98	1.03	1.82	ML	444.97	S	iKgs7r	22.83	20.81	18.07	n.d.	0.78	BOSS	LERG
479	244.50445	55.53039	18.52	11.34	1.02	4.70	ML	770.55	S	iKgs5r	20.17	18.45	16.24	n.d.	0.26	BOSS	LERG

ID	Properties of Radio Source						Identification Data				Properties of Host Galaxy						
	RA	DEC	Major Axis arcsec	Minor Axis arcsec	Peak Flux mJy	Total Flux mJy	Analysis	LR	Morph	Type	g-band Mag	i-band Mag	K-band Mag	3.6μm Mag	Redshift	Redshift Source	Galaxy Type
480	244.49314	55.74228	8.04	7.07	1.20	1.49	ML	220.38	S	iKgs8b	20.70	19.16	16.16	n.d.	0.19	Kmag	SFG
481	244.45042	55.30871	11.13	8.34	1.23	2.48	ML	774.34	S	iKgs4b	19.42	18.13	16.18	n.d.	0.14	Dunc	SFG
482	244.43195	55.59093	13.39	10.16	2.20	6.55	ML	73.76	S	iKgs9b	24.50	22.95	19.58	19.22	1.12	HSC	LERG
483	244.40467	55.81463	5.57	5.32	1.09	0.70	ML	149.03	S	iKgs6b	22.53	21.62	19.27	19.19	0.95	Dunc	SFG
484	244.38582	55.25992	14.02	8.28	1.21	3.06	ML	16.46	S	iKgs5r	25.29	22.91	20.68	20.38	1.65	HSC	LERG
485	244.33857	55.59809	9.71	5.73	1.16	1.41	ML	50.78	S	iKgs0b	27.45	25.93	21.46	20.74	1.40	Dunc	HERG
486	244.31803	55.26295	9.18	7.72	26.85	41.09	ML	12.69	S	iKgs1b	18.70	18.67	17.61	n.d.	2.48	BOSS	HERG
487	244.31517	55.61119	10.33	7.75	1.12	1.95	ML	38.40	S	iKgs6b	20.38	18.95	16.61	n.d.	0.15	Dunc	SFG
488	244.31261	55.78286	11.39	10.26	1.31	3.35	ML	1444.75	S	iKgs8b	20.01	18.91	15.90	n.d.	0.19	HSC	SFG
489	244.29577	55.14482	20.06	10.45	1.00	4.57	ML	707.96	S	iKgs6b	20.09	18.78	16.41	n.d.	0.29	Dunc	SFG
490	244.28021	55.43716	9.65	6.54	3.23	4.45	ML	34.66	S	iKgs9b	26.39	25.10	21.01	20.95	2.45	Dunc	HERG
491	244.26620	55.46176	8.17	5.21	1.21	1.13	ML	322.20	S	iKgs6r	22.55	20.43	18.02	n.d.	0.49	HSC	LERG
492	244.26076	55.34268	7.85	6.34	10.71	14.80	ML	41.88	S	iKgs4r	23.54	21.36	19.36	19.56	0.69	BOSS	LERG
493	244.25639	56.07317	20.96	9.69	11.59	54.96	ML	14.05	S	iKgs9r	25.63	21.62	18.46	n.d.	0.87	HSC	LERG
494	244.24959	56.00739	7.82	5.11	2.36	4.26	ML	9.10	S	iKgs1b	17.22	16.24	15.82	n.d.	0.06	BOSS	SFG
495	244.21667	55.76946	12.32	9.03	3.01	7.31	ML	1.87	S	iKgs2b	22.22	21.52	20.18	19.12	1.20	Kmag	HERG
496	244.21055	55.64945	14.15	11.18	1.09	3.75	ML	716.40	S	iKgs8r	22.72	20.97	18.13	n.d.	0.47	HSC	SFG
497	244.20732	55.84659	8.21	7.61	3.00	4.09	ML	74.22	S	iKgs9r	25.54	23.63	20.12	19.15	1.55	Dunc	HERG
498	244.18426	55.15203	14.47	9.78	0.94	2.89	ML	34.31	S	iKgs4b	19.48	18.72	16.80	n.d.	0.13	Dunc	SFG
499	244.18148	55.93001	9.08	7.10	1.35	1.90	ML	275.47	S	iKgs6b	20.61	19.59	17.30	n.d.	0.54	Dunc	HERG
500	244.17936	55.88922	10.21	8.71	1.54	2.98	ML	65.46	S	iKgs5b	23.44	22.62	20.39	19.89	1.83	BOSS	LERG
501	244.17317	55.75389	10.60	9.45	4.27	9.34	ML	87.05	S	iKg_9r	25.91	22.67	19.49	n.d.	1.16	Vacc	LERG
502	244.16397	55.75712	7.68	6.30	196.64	228.16	ML	144.14	S	iKgs9r	25.67	22.90	18.99	n.d.	1.16	HSC	LERG
503	244.15040	55.65261	9.25	6.62	1.87	2.50	ML	471.08	S	iKgs6b	20.56	19.47	17.07	n.d.	0.15	Dunc	SFG
504	244.13451	55.20001	13.93	9.65	1.48	4.33	ML	33.84	S	iKgs0b	27.03	25.43	20.65	20.07	1.27	HSC	HERG
505	244.13117	55.89829	8.41	7.91	2.11	3.07	ML	29.48	S	iKgs9b	26.03	24.51	20.42	20.34	1.20	HSC	LERG
506	244.12099	55.27050	13.54	7.08	0.98	2.06	ML	11.84	S	iKgs2r	22.07	20.56	19.36	19.96	0.23	BOSS	HERG
507	244.09896	55.45070	16.54	9.65	10.04	34.38	ML	1400.65	S	iKgs7r	20.32	18.63	16.07	n.d.	0.24	BOSS	LERG
508	244.11587	55.67432	11.84	6.77	1.37	2.40	ML	45.67	S	iKgs3r	22.42	20.39	18.65	n.d.	0.55	Vacc	SFG
509	244.10574	55.19576	13.41	10.88	0.76	2.43	ML	314.34	S	iKgs3b	19.47	18.59	16.75	n.d.	0.11	Dunc	SFG
510	244.09482	56.26384	12.11	7.93	1.48	3.11	ML	72.39	S	iKgs8r	24.64	22.33	19.28	19.21	0.94	HSC	LERG
511	244.08585	55.66125	7.01	4.95	2.41	3.31	ML	69.67	S	iKgs6b	23.68	23.07	20.66	20.61	1.47	Dunc	HERG
512	244.08572	55.86082	7.65	6.55	2.96	3.24	ML	13.61	S	iKgs2r	23.12	20.98	19.57	19.74	0.62	HSC	HERG
513	244.07767	55.57580	6.77	4.51	1.06	0.70	ML	9.01	S	iKgs1b	18.02	17.91	17.63	n.d.	0.81	Vacc	HERG
514	244.06387	56.07333	12.24	8.66	1.70	3.93	ML	673.93	S	iKgs5r	20.36	18.76	16.66	n.d.	0.27	Vacc	LERG
515	244.05323	55.40139	11.46	10.30	1.05	2.71	ML	224.33	S	iKgs3r	20.70	19.01	17.19	n.d.	0.19	Dunc	LERG
516	244.04573	55.24745	12.85	12.05	1.16	3.94	ML	75.21	S	_K_s0k	n.d.	n.d.	20.49	20.19	1.45	HSC	LERG
517	244.04834	55.83114	8.81	6.47	1.63	2.03	ML	173.66	S	iKgs9r	24.50	22.50	19.11	n.d.	1.08	HSC	HERG
518	244.04532	55.83653	6.66	4.43	1.19	2.21	ML	239.23	S	iKgs4b	18.97	18.31	16.41	n.d.	0.08	Dunc	SFG
519	244.04607	55.95118	10.89	8.54	1.36	2.76	ML	76.50	S	iKgs3r	20.80	19.52	17.69	n.d.	1.16	HSC	HERG

ID	Properties of Radio Source						Identification Data				Properties of Host Galaxy						
	RA	DEC	Major Axis arcsec	Minor Axis arcsec	Peak Flux mJy	Total Flux mJy	Analysis	LR	Morph	Type	g-band Mag	i-band Mag	K-band Mag	3.6μm Mag	Redshift	Redshift Source	Galaxy Type
520	244.04360	55.95346	9.36	7.09	1.01	1.47	ML	8.78	S	iKgs7r	26.39	23.58	20.96	20.47	0.89	HSC	HERG
521	244.03893	55.78211	9.41	8.37	1.26	2.17	ML	29.43	S	iKgs9b	25.36	24.40	21.19	20.20	1.13	HSC	HERG
522	244.03613	56.05320	7.57	4.15	1.12	2.77	ML	299.78	S	iKgs8r	24.85	22.02	18.90	n.d.	0.91	BOSS	LERG
523	243.99542	55.41852	13.46	9.11	1.51	4.03	ML	274.86	S	iKgs4r	20.17	18.52	16.62	n.d.	0.24	BOSS	LERG
524	243.97257	55.51294	8.15	6.39	8.72	9.91	ML	7.58	S	iKgs3b	25.73	25.17	23.45	n.d.	1.28	Dunc	LERG
525	243.95653	55.27993	15.20	7.69	38.94	114.18	ML	80.24	S	iKgs9r	26.25	23.20	19.86	19.27	1.14	HSC	HERG
526	243.94932	55.41664	8.64	7.74	1.74	2.54	ML	71.93	S	iKgs8b	24.26	22.86	19.94	19.74	1.39	Dunc	LERG
527	243.93276	55.82857	9.44	7.83	2.94	4.75	ML	200.28	S	iKgs6b	21.96	21.19	18.82	n.d.	0.95	HSC	HERG
528	243.92182	55.81841	15.65	11.46	1.41	5.50	ML	845.97	S	iKgs8r	22.56	20.36	17.35	n.d.	0.67	HSC	LERG
529	243.92204	56.06729	6.91	5.37	5.81	6.62	ML	103.25	S	iKgs7b	24.41	22.92	20.27	20.14	1.02	HSC	LERG
530	243.90121	56.04689	15.29	8.45	16.69	38.43	ML	21.91	S	iKgs9b	25.27	24.67	21.09	20.52	1.94	HSC	HERG
531	243.89915	55.52059	11.82	9.86	1.17	2.99	ML	763.71	S	iKgs4b	19.18	17.87	16.01	n.d.	0.15	BOSS	HERG
532	243.89239	56.20577	23.29	12.81	1.27	8.27	ML	1284.37	S	iKgs7b	20.46	19.39	16.67	n.d.	0.20	HSC	SFG
533	243.88872	55.43832	15.62	10.69	1.72	6.28	ML	7.32	S	_K_s8k	n.d.	n.d.	21.86	21.41	1.91	Dunc	HERG
534	243.87890	55.87971	7.67	6.48	6.39	6.95	ML	55.12	S	iKgs4b	22.25	21.75	19.82	19.57	0.98	HSC	HERG
535	243.87869	55.85165	11.26	7.25	1.24	2.22	ML	40.20	S	iKgs9b	25.66	24.72	21.14	20.83	1.45	Dunc	HERG
536	243.86918	56.04225	10.21	6.65	1.77	2.62	ML	55.65	S	iKgs9b	24.79	24.23	20.86	20.41	1.55	Dunc	HERG
537	243.84090	55.34493	11.87	8.60	1.53	3.41	ML	643.87	S	iKgs4b	19.02	17.77	15.80	n.d.	0.15	BOSS	LERG
538	243.82628	55.93516	12.83	7.51	1.11	2.33	ML	366.97	S	iKgs6b	18.36	17.15	14.72	n.d.	0.06	Dunc	SFG
539	243.81959	55.51294	7.44	6.25	5.47	7.57	ML	881.75	S	iKgs4b	18.57	17.68	15.78	n.d.	0.08	BOSS	SFG
540	243.80099	55.63056	8.98	6.21	1.47	1.79	ML	153.62	S	i_gs6r	23.78	21.81	n.d.	n.d.	0.84	HSC	LERG
541	243.78599	55.84584	9.94	5.91	1.58	2.02	ML	25.75	S	iKgs8r	24.88	23.00	20.17	20.21	1.19	Kmag	HERG
542	243.78171	55.76136	7.49	5.67	776.78	720.27	ML	120.86	S	iK_s9r	n.d.	23.08	19.70	19.32	1.16	HSC	HERG
543	243.73829	55.87316	26.84	14.83	2.97	52.45	ML	278.72	S	iKgs9b	18.18	17.05	13.73	n.d.	0.05	BOSS	LERG
544	243.74465	55.96539	6.72	5.52	4.04	4.79	ML	31.72	S	iKgs9r	27.03	25.06	21.75	20.97	1.69	Dunc	LERG
545	243.71112	55.46334	9.14	8.01	1.78	2.84	ML	0.47	S	___s__	n.d.	n.d.	n.d.	19.35	1.73	smag	LERG
546	243.70306	55.70880	43.21	23.95	1.10	24.84	ML	2070.26	S	iKgs7b	19.04	18.21	15.52	n.d.	0.08	Dunc	SFG
547	243.70447	55.75344	7.48	6.70	4.41	4.83	ML	2413.82	S	iKgs7b	18.72	17.44	14.94	n.d.	0.06	BOSS	HERG
548	243.70083	55.92330	8.30	7.25	2.80	3.68	ML	172.19	S	iKgs3r	20.97	19.55	17.72	n.d.	0.52	BOSS	HERG
549	243.69432	55.49951	7.28	5.60	5.30	6.61	ML	112.98	S	iKgs7b	23.53	22.78	20.05	19.75	1.68	Dunc	HERG
550	243.66812	55.73652	12.18	6.72	1.39	2.48	ML	28.43	S	iKg_8b	24.49	24.18	21.38	n.d.	2.18	HSC	HERG
551	243.66087	55.69670	7.62	5.80	24.31	26.32	ML	61.60	S	iKgs8r	25.45	23.33	20.36	19.97	1.11	HSC	HERG
552	243.65538	55.64893	9.91	6.24	1.82	2.46	ML	226.37	S	iKgs3r	19.92	18.67	16.96	n.d.	0.21	Dunc	SFG
553	243.63924	56.03455	18.84	14.32	1.04	6.14	ML	89.84	S	iK_s8r	n.d.	22.63	19.58	19.51	0.90	HSC	LERG
554	243.62245	56.07528	14.47	10.15	1.04	3.33	ML	147.14	S	iKgs3b	20.49	19.48	17.68	n.d.	0.34	HSC	SFG
555	243.62116	55.55740	11.01	8.26	2.44	4.84	ML	9.14	S	iKgs9r	26.63	23.13	19.88	19.65	0.97	Dunc	LERG
556	243.61000	56.14563	8.50	6.41	17.19	22.85	ML	148.22	S	iKgs8r	24.40	22.71	19.81	19.28	1.15	HSC	HERG
557	243.55955	55.65322	8.12	5.80	4.33	4.45	ML	438.59	S	iKgs7b	22.28	21.15	18.57	n.d.	1.06	BOSS	HERG
558	243.54969	55.69283	11.75	5.52	5.44	7.71	ML	394.51	S	iKgs7r	20.22	18.39	15.80	n.d.	0.25	BOSS	LERG
559	243.55088	55.96063	8.69	5.61	1.10	1.17	ML	66.98	S	iKgs6r	23.63	21.83	19.52	19.30	0.79	HSC	LERG

ID	Properties of Radio Source						Identification Data				Properties of Host Galaxy						
	RA	DEC	Major Axis arcsec	Minor Axis arcsec	Peak Flux mJy	Total Flux mJy	Analysis	LR	Morph	Type	g-band Mag	i-band Mag	K-band Mag	3.6μm Mag	Redshift	Redshift Source	Galaxy Type
560	243.52639	55.78594	8.24	6.06	3.71	4.05	ML	141.48	S	iKgs7r	24.41	22.46	19.75	19.04	0.94	HSC	LERG
561	243.51265	56.13213	12.26	10.11	2.50	6.76	ML	2149.61	S	iKgs8b	18.97	17.71	14.74	n.d.	0.06	BOSS	SFG
562	243.50583	55.52081	8.78	6.49	4.79	5.96	ML	35.56	S	iKgs9r	27.00	24.64	21.07	20.50	1.31	Dunc	LERG
563	243.42099	55.69864	11.80	6.80	7.31	17.75	ML	1.45	S	iKgs7r	21.70	19.74	17.05	n.d.	0.41	HSC	LERG
564	243.41181	55.90888	10.78	6.84	1.36	2.18	ML	6.64	S	_K__8k	n.d.	n.d.	21.93	n.d.	1.03	HSC	LERG
565	243.39864	55.82307	8.22	5.63	1.14	1.15	ML	274.38	S	iKgs8r	24.81	21.91	19.00	19.07	0.92	HSC	LERG
566	243.39539	55.71513	7.51	7.28	2.24	2.67	ML	79.37	S	iKgs9r	25.58	23.61	19.93	19.17	1.09	HSC	HERG
567	243.39345	55.90296	9.25	6.76	2.49	3.39	ML	944.49	S	iKgs5b	20.08	19.13	17.01	n.d.	0.32	BOSS	SFG
568	243.37771	55.61568	10.42	8.58	1.58	3.08	ML	3.02	S	_K__7k	n.d.	n.d.	22.46	n.d.	2.46	HSC	HERG
569	243.37584	55.80096	8.75	7.04	2.96	3.98	ML	109.09	S	iKgs9b	24.70	23.34	20.11	19.90	1.17	HSC	LERG
570	243.36607	55.86616	7.58	6.11	84.38	94.35	ML	62.92	S	iKgs8b	24.59	23.48	20.37	19.89	1.43	Dunc	HERG
571	243.36300	55.72640	13.90	10.72	1.05	3.42	ML	57.33	S	_K_s0k	n.d.	n.d.	20.09	19.35	1.25	HSC	HERG
572	243.32247	56.02143	21.88	16.00	22.15	103.45	ML	55.76	S	iKgs5r	21.96	19.86	17.62	n.d.	0.53	HSC	LERG
573	243.28862	56.05258	6.76	4.25	1.54	3.66	ML	0.79	S	iKgs7b	22.84	21.83	19.36	19.25	0.94	Dunc	LERG
574	243.28189	55.99540	8.38	6.35	49.28	65.16	ML	240.69	S	iKgs8r	24.02	21.60	18.68	n.d.	0.91	BOSS	LERG
575	243.28377	55.92587	8.86	6.27	1.22	1.48	ML	261.11	S	iKgs6r	23.15	20.75	18.31	19.04	1.42	Vacc	LERG
576	243.21958	55.80942	11.78	7.90	1.21	2.46	ML	227.85	S	iKgs3r	20.56	19.12	17.29	n.d.	0.30	BOSS	SFG
577	243.19422	55.83191	41.40	9.81	5.02	45.57	ML	316.14	S	iKgs8r	21.34	19.52	16.74	n.d.	0.30	Vacc	LERG
578	243.18768	55.95582	12.99	11.10	1.12	3.51	ML	295.26	S	iKgs3b	18.93	18.02	16.29	n.d.	0.10	Dunc	SFG
579	243.18950	55.81311	14.84	9.19	1.54	4.58	ML	31.06	S	iKgs9b	26.63	25.66	22.29	21.10	2.07	HSC	HERG
580	243.17707	55.81274	7.99	7.36	2.50	3.22	ML	116.90	S	iKgs4r	20.98	19.19	17.32	n.d.	0.32	HSC	LERG
581	243.13345	56.00640	15.66	10.03	1.12	3.84	ML	155.46	S	iKgs9r	24.88	21.69	18.49	n.d.	0.91	HSC	LERG
582	243.10361	55.91037	8.50	7.14	47.81	72.48	ML	1591.30	S	iKgs7r	20.28	18.47	15.85	n.d.	0.27	BOSS	LERG
583	243.10161	55.97329	8.79	6.88	5.37	7.09	ML	193.66	S	i_gs4b	21.14	19.92	n.d.	n.d.	0.72	BOSS	LERG
584	243.01778	55.89906	17.41	11.25	14.30	58.57	ML	1171.77	S	iKgs7r	20.78	18.88	16.40	n.d.	0.33	BOSS	HERG
585	242.85893	55.93030	12.20	10.19	1.29	3.49	ML	519.91	S	iKgs7b	17.35	16.22	13.61	n.d.	0.06	Vacc	LERG
586	242.32457	55.96610	8.44	5.82	1.54	1.63	ML	5.85	S	iKgs3b	23.20	22.53	20.79	20.51	0.66	HSC	LERG
587	242.29262	55.94137	13.37	10.94	1.65	5.20	ML	334.07	S	iKgs8r	24.53	21.83	18.92	n.d.	0.86	HSC	LERG
588	242.26956	55.87572	18.32	9.18	1.00	3.60	ML	0.64	S	iKgs6r	22.84	21.30	18.88	n.d.	0.56	Dunc	HERG
589	242.17864	55.81620	14.00	9.51	1.54	4.40	ML	422.69	S	iKgs7r	22.83	21.17	18.65	n.d.	0.80	HSC	LERG
590	242.13261	55.75744	13.26	7.61	1.76	3.82	ML	273.77	S	iKgs7r	24.04	21.47	18.93	n.d.	0.78	HSC	HERG
591	242.11065	55.79126	18.26	9.92	0.99	3.86	ML	130.50	S	iKgs3r	21.07	19.34	17.63	n.d.	0.25	BOSS	LERG
592	242.11247	56.09646	10.93	7.51	6.24	11.01	ML	12.88	S	_K_s9k	n.d.	n.d.	21.80	20.64	2.16	Dunc	HERG
593	242.07346	55.71549	13.49	10.01	11.90	34.82	ML	2.57	S	iKgs8r	26.26	24.29	21.27	20.72	2.15	HSC	LERG
594	242.08599	56.23200	9.61	7.71	73.47	129.15	ML	3.27	S	iKgs1b	18.07	17.93	18.29	n.d.	1.95	BOSS	HERG
595	242.04233	56.05944	9.83	9.56	16.30	38.23	ML	1058.71	S	iKgs5r	21.13	18.94	16.72	n.d.	0.39	BOSS	LERG
596	241.99927	56.10404	20.45	10.38	25.82	101.46	ML	1174.40	S	iKgs7r	21.66	19.48	17.02	n.d.	0.41	Vacc	HERG
597	241.99501	55.95411	9.91	6.60	2.87	4.04	ML	40.05	S	_K_s5k	n.d.	n.d.	23.18	n.d.	2.62	Kmag	HERG
598	241.98586	56.43195	41.30	22.71	1.87	37.72	ML	17.92	S	iKgs6r	24.71	22.02	19.62	19.68	1.06	HSC	HERG
599	241.94485	55.93510	10.52	6.18	2.31	3.23	ML	62.01	S	iKgs9b	25.01	24.20	20.45	20.74	1.50	HSC	LERG

ID	Properties of Radio Source						Identification Data				Properties of Host Galaxy						
	RA	DEC	Major Axis arcsec	Minor Axis arcsec	Peak Flux mJy	Total Flux mJy	Analysis	LR	Morph	Type	g-band Mag	i-band Mag	K-band Mag	$3.6\mu m$ Mag	Redshift	Redshift Source	Galaxy Type
600	241.93451	55.70987	10.37	6.69	6.50	9.69	ML	10.93	S	_K__9k	n.d.	n.d.	21.08	n.d.	0.37	HSC	LERG
601	241.93010	55.73765	18.69	9.97	1.51	6.06	ML	146.37	S	iKgs3b	18.63	17.70	15.94	n.d.	0.12	BOSS	SFG
602	241.93178	55.96162	11.87	6.77	1.28	2.21	ML	1546.76	S	iKgs7r	20.98	18.91	16.36	n.d.	0.36	BOSS	LERG
603	241.90930	56.00880	9.05	7.39	1.02	1.47	ML	108.54	S	iKgs7b	23.95	22.74	20.12	19.80	1.17	HSC	HERG
604	241.85757	55.59037	8.89	6.47	16.39	23.56	ML	62.55	S	iKgs3r	22.94	20.58	18.77	n.d.	0.82	BOSS	LERG
605	241.83634	56.00556	8.43	6.11	9.92	13.79	ML	3.94	S	iKg_2b	24.87	23.80	22.33	n.d.	0.46	HSC	LERG
606	241.82475	55.47714	11.21	9.80	1.23	2.90	ML	13.83	S	_K_s9k	n.d.	n.d.	21.69	21.08	2.00	Dunc	LERG
607	241.81233	55.73692	10.22	7.44	1.39	2.28	ML	826.05	S	iKgs7b	20.57	19.33	16.86	n.d.	0.35	HSC	SFG
608	241.80923	56.05248	8.28	7.24	1.80	2.32	ML	81.04	S	iKgs9b	24.63	23.40	20.21	19.67	1.37	Dunc	HERG
609	241.76744	55.62975	9.78	6.84	3.65	5.25	ML	196.54	S	iKgs8b	23.34	22.38	19.56	19.41	1.21	BOSS	HERG
610	241.75271	55.63625	10.61	8.45	1.12	2.17	ML	819.02	S	iKgs5b	18.10	17.29	15.20	n.d.	0.03	BOSS	SFG
611	241.71734	55.87560	20.04	12.26	1.46	7.69	ML	6.45	S	iKgs2r	21.84	20.57	19.04	19.76	0.37	HSC	LERG
612	241.71735	55.62035	8.40	7.15	0.96	1.24	ML	30.27	S	i_gs6b	24.91	24.50	n.d.	21.51	0.52	HSC	LERG
613	241.71062	55.74504	11.79	6.86	1.06	1.84	ML	40.94	S	iKgs0r	30.45	24.92	20.30	19.72	1.62	Dunc	HERG
614	241.71607	56.27656	9.61	7.76	2.47	3.96	ML	64.48	S	iKgs6r	23.86	21.90	19.59	19.29	0.96	Kmag	LERG
615	241.67111	56.02692	16.86	8.39	5.42	19.19	ML	35.14	S	iKgs4r	23.63	21.17	19.25	19.30	0.63	HSC	LERG
616	241.66781	55.77714	9.34	7.93	4.83	7.69	ML	65.17	S	_K_s0k	n.d.	n.d.	19.99	19.50	1.29	Dunc	LERG
617	241.66291	56.13483	9.17	7.00	4.18	5.77	ML	366.93	S	iKgs7r	23.45	20.63	18.01	n.d.	0.79	BOSS	LERG
618	241.61579	55.56761	8.61	6.50	10.74	15.71	ML	51.60	S	iKgs9b	25.35	24.28	20.51	20.32	1.69	Dunc	LERG
619	241.60173	55.47065	19.32	9.86	1.14	4.68	ML	59.62	S	iKgs6r	21.31	19.40	17.05	n.d.	0.41	HSC	LERG
620	241.57346	55.84472	13.46	8.38	0.99	2.39	ML	46.79	S	_K_s0k	n.d.	n.d.	20.42	20.01	1.27	HSC	HERG
621	241.54869	55.46093	11.43	6.64	1.76	6.08	ML	0.15	S	iKgs7r	24.42	21.42	18.76	n.d.	1.01	HSC	LERG
622	241.54548	55.98045	9.74	6.30	5.49	7.24	ML	1239.26	S	iKgs5r	20.16	18.49	16.41	n.d.	0.25	BOSS	LERG
623	241.53571	55.83347	8.14	6.10	14.69	17.86	ML	75.34	S	iKgs3r	22.88	20.47	18.63	n.d.	0.61	BOSS	LERG
624	241.53180	56.12836	8.97	6.46	5.54	6.90	ML	1.52	S	___s__	n.d.	n.d.	n.d.	21.16	2.77	smag	HERG
625	241.52942	55.92091	10.81	6.72	1.96	3.06	ML	16.39	S	iKgs7b	25.03	24.10	21.46	20.68	0.43	HSC	LERG
626	241.52520	55.89991	8.18	5.77	33.27	38.01	ML	77.79	S	iKgs4r	23.07	20.75	18.85	19.33	0.49	BOSS	LERG
627	241.52890	56.33714	11.03	8.88	1.10	2.32	ML	21.95	S	_K_s0k	n.d.	n.d.	20.56	20.14	1.30	HSC	HERG
628	241.51916	56.17901	14.98	13.06	26.34	101.88	ML	55.37	S	iK_s9r	n.d.	21.48	18.06	n.d.	0.64	HSC	LERG
629	241.51933	55.71255	13.04	7.60	0.95	2.02	ML	676.06	S	iKgs5r	21.78	19.53	17.32	n.d.	0.39	BOSS	LERG
630	241.51820	55.98341	9.08	6.81	3.29	4.37	ML	587.44	S	iKgs7r	22.28	20.69	18.23	n.d.	0.69	HSC	LERG
631	241.51745	56.08642	10.02	6.45	5.74	7.97	ML	7.39	S	_K_s8k	n.d.	n.d.	22.02	21.19	2.22	Dunc	HERG
632	241.47111	56.17909	17.22	6.84	3.08	13.83	ML	4.76	S	iKgs5r	24.30	21.60	19.47	19.69	0.92	Kmag	LERG
633	241.44411	55.46829	8.58	6.96	5.29	9.04	ML	163.61	S	iKgs9r	26.12	22.80	19.24	n.d.	1.15	HSC	LERG
634	241.44779	55.98583	9.71	6.53	4.37	5.95	ML	6.68	S	iKgs1b	21.65	21.41	20.35	20.57	1.96	Dunc	HERG
635	241.44648	56.28023	15.98	9.44	1.12	3.64	ML	86.28	S	iKgs6b	23.72	22.40	20.11	20.31	0.57	HSC	LERG
636	241.42266	55.59806	7.89	4.23	0.97	2.29	ML	0.26	S	iKgs2b	23.23	23.14	21.66	n.d.	2.99	HSC	HERG
637	241.39613	55.64140	13.83	8.45	1.02	2.57	ML	31.14	S	iKgs3r	23.06	21.61	19.88	19.49	0.77	HSC	HERG
638	241.39301	55.66551	9.01	5.28	1.74	1.78	ML	109.09	S	iKgs9r	26.72	23.26	19.67	19.31	1.16	HSC	LERG
639	241.37754	55.78741	6.49	5.02	1.14	2.10	ML	714.37	S	iKgs6b	19.36	18.46	16.08	n.d.	0.18	Dunc	SFG

ID	Properties of Radio Source						Identification Data				Properties of Host Galaxy						
	RA	DEC	Major Axis arcsec	Minor Axis arcsec	Peak Flux mJy	Total Flux mJy	Analysis	LR	Morph	Type	g-band Mag	i-band Mag	K-band Mag	$3.6\mu m$ Mag	Redshift	Redshift Source	Galaxy Type
640	241.35650	55.79084	19.54	11.71	0.80	3.94	ML	267.20	S	iKgs4b	19.04	18.21	16.23	n.d.	0.11	BOSS	SFG
641	241.34700	55.70566	8.65	6.04	1.27	1.42	ML	55.74	S	i_gs2b	20.39	19.36	n.d.	n.d.	0.32	imag	SFG
642	241.31433	55.93088	8.48	5.87	46.28	54.85	ML	124.94	S	iKgs7r	25.40	22.56	19.98	19.96	0.07	BOSS	LERG
643	241.31445	56.23437	8.64	5.90	2.54	2.78	ML	55.19	S	iKgs9b	25.21	24.37	20.31	20.25	1.77	Dunc	HERG
644	241.29637	55.64905	8.46	6.48	45.88	60.65	ML	190.29	S	iKgs8b	22.47	21.25	18.28	n.d.	0.25	BOSS	LERG
645	241.26236	55.63258	15.86	9.07	4.50	22.63	ML	53.24	S	iKgs8r	20.70	18.95	16.19	n.d.	0.34	Dunc	LERG
646	241.25567	55.59930	9.05	7.85	1.38	2.11	ML	787.73	S	iKgs8r	20.71	19.01	16.21	n.d.	0.24	Dunc	SFG
647	241.25597	55.76957	7.99	7.61	1.30	1.70	ML	3.46	S	_K_s7k	n.d.	n.d.	22.53	n.d.	2.31	Kmag	HERG
648	241.25285	55.39870	11.93	8.52	2.60	5.67	ML	80.06	S	iKgs0b	26.02	24.69	19.87	19.39	1.94	Dunc	HERG
649	241.24309	55.95783	9.21	5.38	10.67	13.69	ML	23.53	S	iKgs6b	24.61	24.00	21.70	21.21	1.90	Kmag	HERG
650	241.22807	55.99707	9.82	6.36	773.47	1124.25	ML	22.49	S	iKg_9b	25.44	25.25	21.23	n.d.	1.67	Kmag	HERG
651	241.21427	55.71836	10.47	8.99	1.33	2.68	ML	843.25	S	iKgs7r	21.38	19.62	17.10	n.d.	0.34	HSC	LERG
652	241.16928	55.56931	9.87	7.19	3.43	5.23	ML	1578.48	S	iKgs5b	18.76	17.56	15.37	n.d.	0.08	BOSS	SFG
653	241.17179	55.55640	8.89	6.82	1.10	1.43	ML	20.97	S	iK_s4r	n.d.	22.73	20.69	20.17	1.13	HSC	HERG
654	241.14650	55.59662	14.39	9.75	15.89	51.32	ML	787.03	S	iKgs7r	22.76	20.35	17.78	n.d.	0.64	BOSS	LERG
655	241.15215	56.03629	8.89	7.28	2.78	3.87	ML	48.32	S	iKgs2r	20.42	19.19	17.98	n.d.	0.34	Dunc	HERG
656	241.10926	55.67321	11.89	6.81	2.94	10.44	ML	12.00	S	iKgs9r	25.36	23.55	20.08	19.69	1.38	Dunc	LERG
657	241.11096	55.84966	8.37	6.61	4.83	5.74	ML	88.70	S	iKg_3r	21.67	20.30	18.50	n.d.	0.88	Dunc	LERG
658	241.06101	55.41039	9.58	6.96	1.85	6.35	ML	514.90	S	iKgs7b	18.89	17.74	15.16	n.d.	0.08	BOSS	SFG
659	241.05347	55.56458	11.34	5.49	0.96	6.15	ML	85.74	S	_K_s0k	n.d.	n.d.	19.18	n.d.	1.12	Dunc	LERG
660	241.03313	55.83903	8.81	6.51	1.49	1.84	ML	14.01	S	_K_s9k	n.d.	n.d.	20.98	20.51	1.55	Kmag	HERG
661	240.99279	55.45601	35.39	23.87	0.81	14.64	ML	71.85	S	_K_s0k	n.d.	n.d.	16.72	n.d.	0.22	Dunc	LERG
662	240.91126	55.83013	13.05	6.81	1.08	2.06	ML	8.72	S	iKgs9b	25.70	23.99	19.94	19.09	1.34	Dunc	HERG
663	240.88639	55.77309	8.22	6.83	3.52	4.25	ML	43.85	S	_K_s5k	n.d.	n.d.	23.67	n.d.	2.84	Kmag	HERG
664	240.85630	55.72344	9.29	8.80	1.06	1.86	ML	12.84	S	i_gs7b	24.55	23.91	n.d.	20.71	1.55	Dunc	HERG
665	240.79770	55.83375	14.44	5.76	1.06	7.27	ML	0.42	S	iKgs7r	23.46	20.79	18.11	n.d.	0.73	Dunc	LERG
666	240.73843	55.77593	9.03	6.42	2.48	3.09	ML	35.98	S	iKg_7b	26.80	25.26	22.65	n.d.	2.89	Dunc	HERG
667	243.95069	56.34157	55.61	7.66	24.40	102.25	ML	43.22	S	iKgs5r	22.13	20.41	18.23	19.19	0.39	Dunc	LERG
668	243.93153	56.28382	10.10	9.08	8.86	19.82	ML	296.34	S	iKgs5r	22.72	20.30	18.23	n.d.	0.61	BOSS	LERG
669	243.90394	56.26567	11.33	8.06	3.85	8.58	ML	10.41	S	_K__9k	n.d.	n.d.	21.24	n.d.	1.67	Kmag	HERG
670	243.84627	56.27468	14.42	8.47	2.54	7.55	ML	28.80	S	iKg_7r	24.50	21.82	19.27	n.d.	0.90	HSC	LERG
671	243.83289	56.23049	13.22	7.17	1.30	3.00	ML	222.59	S	iKg_8r	25.61	21.93	18.92	n.d.	1.05	HSC	LERG
672	243.75713	56.23962	10.04	6.10	19.87	34.46	ML	3.30	S	iKgs2r	23.19	22.04	20.72	20.49	0.35	HSC	LERG
673	243.74427	56.34850	10.10	6.98	1.19	2.05	ML	19.48	S	iKgs3r	20.30	19.09	17.29	n.d.	0.35	Kmag	LERG
674	243.72270	56.40241	17.03	9.74	2.97	12.01	ML	3512.21	S	iKgs8b	17.70	16.56	13.66	n.d.	0.06	BOSS	SFG
675	243.57524	56.35278	11.59	7.89	1.25	2.78	ML	827.29	S	iKgs7b	19.12	17.95	15.37	n.d.	0.07	Dunc	SFG
676	243.53491	56.45479	9.08	7.39	1.81	2.96	ML	280.61	S	iKgs8r	23.98	22.11	19.21	n.d.	0.81	HSC	LERG
677	243.52587	56.15716	7.85	5.95	24.03	30.87	ML	7.89	S	iKgs1b	21.92	21.07	20.07	19.72	0.68	HSC	HERG
678	243.51466	56.24188	8.66	7.73	1.42	2.33	ML	40.80	S	iKgs4r	23.63	21.00	19.02	19.26	0.61	HSC	LERG
679	243.48396	56.28839	17.38	9.05	1.14	4.38	ML	90.10	S	iKgs7r	23.79	21.36	18.89	19.08	0.74	HSC	LERG

ID	Properties of Radio Source						Identification Data				Properties of Host Galaxy						
	RA	DEC	Major Axis arcsec	Minor Axis arcsec	Peak Flux mJy	Total Flux mJy	Analysis	LR	Morph	Type	g-band Mag	i-band Mag	K-band Mag	3.6μm Mag	Redshift	Redshift Source	Galaxy Type
680	243.46345	56.41995	8.25	6.63	4.10	5.47	ML	3.33	S	_K__7k	n.d.	n.d.	22.55	n.d.	2.20	HSC	HERG
681	243.44677	56.37633	7.35	5.41	27.68	30.46	ML	6.48	S	_K__8k	n.d.	n.d.	22.07	n.d.	1.28	Dunc	LERG
682	243.39873	56.16038	7.95	6.13	21.47	28.89	ML	50.17	S	iK_s0b	n.d.	25.93	21.45	21.41	0.96	HSC	LERG
683	243.37708	56.29825	37.53	17.52	6.43	78.35	ML	262.53	S	iKgs4r	20.70	18.96	16.92	n.d.	0.27	BOSS	LERG
684	243.36553	56.31416	6.81	4.85	2.96	4.20	ML	160.22	S	iKgs7r	23.57	20.56	17.88	n.d.	0.61	Vacc	LERG
685	243.35942	56.35386	7.32	5.15	9.06	10.38	ML	59.46	S	iKgs6b	23.92	23.27	20.89	20.14	1.11	HSC	HERG
686	243.33874	56.30270	8.62	6.67	3.29	4.61	ML	315.92	S	iKgs6r	23.25	20.91	18.55	19.21	0.51	HSC	LERG
687	243.29753	56.14716	7.23	5.89	2.14	2.22	ML	34.34	S	iKgs7b	24.44	23.87	21.27	21.00	1.62	Dunc	HERG
688	243.20989	56.06612	11.22	9.14	7.72	24.41	ML	53.53	S	iKg_4r	22.75	20.55	18.56	n.d.	0.50	BOSS	LERG
689	243.18897	56.34402	6.99	4.38	2.39	1.78	ML	148.06	S	iKgs9b	24.41	23.07	19.60	19.37	1.33	Dunc	HERG
690	243.18881	56.50048	12.01	8.94	1.67	4.37	ML	39.83	S	_K_s5k	n.d.	n.d.	22.89	n.d.	2.48	Kmag	HERG
691	243.17364	56.37841	24.17	12.99	1.20	9.16	ML	0.40	S	iKgs9b	18.84	17.60	14.34	n.d.	0.07	Dunc	SFG
692	243.05680	56.11057	7.41	5.50	6.29	8.40	ML	41.90	S	iKgs7b	25.41	24.59	22.10	21.20	0.97	HSC	LERG
693	243.00947	56.47386	9.13	7.95	1.73	3.06	ML	81.54	S	iKgs9b	24.28	23.46	20.01	19.48	1.13	Kmag	HERG
694	242.98493	56.03645	14.24	7.47	3.00	7.77	ML	259.55	S	iKgs5r	19.74	18.19	16.12	n.d.	0.23	BOSS	LERG
695	242.97900	56.41625	10.54	7.37	1.27	17.58	ML	1.63	S	iKg_1b	22.21	21.27	20.45	n.d.	0.37	HSC	LERG
696	242.97515	56.41097	21.15	14.81	1.63	12.47	ML	49.21	S	iKgs7r	21.84	19.52	17.02	n.d.	0.41	HSC	LERG
697	242.95851	56.32074	7.12	5.26	7.09	8.63	ML	108.04	S	iKgs9r	25.31	23.27	20.06	19.59	1.32	Dunc	HERG
698	242.95084	56.15595	14.52	7.39	0.96	2.52	ML	53.37	S	iKgs0b	24.90	24.20	19.94	19.39	1.28	HSC	HERG
699	242.94758	56.43280	13.28	9.94	1.59	5.13	ML	127.79	S	iKgs3b	18.77	17.79	16.07	n.d.	0.05	Dunc	SFG
700	242.92512	56.33086	7.45	5.24	22.85	25.49	ML	7.68	S	_K_s8k	n.d.	n.d.	21.93	21.05	1.73	Dunc	LERG
701	242.90804	55.99922	14.75	12.07	6.32	37.46	ML	757.76	S	iKgs5r	20.94	19.18	17.13	n.d.	0.31	BOSS	LERG
702	242.89870	56.27032	13.51	8.94	1.18	3.48	ML	15.45	S	_K_s9k	n.d.	n.d.	21.47	21.11	1.64	Dunc	LERG
703	242.89609	56.15897	9.19	6.82	2.51	3.83	ML	18.60	S	_K_s9k	n.d.	n.d.	21.22	20.19	1.63	HSC	HERG
704	242.89571	56.17910	9.91	5.15	1.20	1.50	ML	631.87	S	iKgs7r	22.35	20.37	17.62	n.d.	0.45	HSC	SFG
705	242.88442	56.25231	9.11	8.00	1.54	2.74	ML	197.17	S	iKgs6r	23.42	20.70	18.40	n.d.	0.61	BOSS	LERG
706	242.85535	56.32391	10.61	8.44	2.42	5.29	ML	1791.08	S	iKgs7r	20.61	18.76	16.25	n.d.	0.34	Vacc	LERG
707	242.83642	56.11183	8.27	7.09	3.60	5.16	ML	7.22	S	_K_s8k	n.d.	n.d.	21.97	n.d.	2.03	Kmag	AGN
708	242.83024	56.52402	6.81	5.05	5.99	6.69	ML	6.85	S	iKgs2b	22.77	22.37	21.00	20.66	1.20	HSC	LERG
709	242.83254	56.05602	14.37	8.11	0.87	2.47	ML	72.42	S	iKgs7r	23.19	20.63	18.09	n.d.	0.46	HSC	SFG
710	242.81761	56.28514	5.38	4.51	1.36	0.81	ML	78.21	S	iKgs9r	25.16	23.03	19.68	19.25	1.19	HSC	SFG
711	242.74015	56.41552	11.62	8.78	7.48	20.23	ML	4.11	S	iKgs9b	25.36	23.90	20.22	19.92	1.21	Kmag	LERG
712	242.64769	56.27058	7.85	6.00	11.79	15.93	ML	2202.15	S	iKgs7b	16.98	15.92	13.41	n.d.	0.05	BOSS	LERG
713	242.61362	56.27618	7.37	5.87	1.39	1.47	ML	51.17	S	iKgs4r	22.31	20.51	18.48	n.d.	0.62	BOSS	SFG
714	242.59150	56.45401	6.41	3.55	1.73	2.47	ML	48.35	S	i__s7r	n.d.	23.29	20.84	19.69	1.19	HSC	HERG
715	242.57077	56.20267	16.48	10.35	1.19	4.96	ML	2.71	S	_K_s5k	n.d.	n.d.	22.79	n.d.	2.44	Kmag	HERG
716	242.54764	56.48856	10.06	6.26	20.04	37.26	ML	784.84	S	iKgs7r	23.04	20.33	17.88	n.d.	0.65	BOSS	LERG
717	242.50529	55.99295	11.69	10.10	2.24	6.46	ML	44.23	S	iKgs8b	24.71	24.02	20.97	20.41	1.42	Dunc	LERG
718	242.45821	56.21859	8.27	6.17	7.28	12.45	ML	156.48	S	iKgs5b	23.01	22.02	19.85	19.39	0.69	HSC	HERG
719	242.45129	56.43809	10.03	9.07	4.24	9.41	ML	561.27	S	iKgs8r	24.18	21.34	18.46	n.d.	0.76	BOSS	LERG

ID	Properties of Radio Source						Identification Data				Properties of Host Galaxy						
	RA	DEC	Major Axis arcsec	Minor Axis arcsec	Peak Flux mJy	Total Flux mJy	Analysis	LR	Morph	Type	g-band Mag	i-band Mag	K-band Mag	3.6μm Mag	Redshift	Redshift Source	Galaxy Type
720	242.44766	56.17334	10.23	6.31	1.75	2.76	ML	10.70	S	iKgs1b	19.02	18.36	17.82	n.d.	0.61	BOSS	HERG
721	242.42680	56.04879	7.89	6.18	1.15	1.36	ML	6.27	S	_K_s8k	n.d.	n.d.	22.11	21.65	0.89	HSC	HERG
722	242.38332	56.13753	6.95	6.26	1.42	4.82	ML	45.32	S	iKgs4r	22.69	21.29	19.32	19.23	0.76	BOSS	HERG
723	242.35442	56.01315	8.07	5.08	1.16	1.16	ML	64.07	S	iKgs4b	20.06	19.27	17.26	n.d.	0.31	HSC	SFG
724	242.34452	56.25306	9.06	8.26	65.29	134.01	ML	512.48	S	iKgs7r	22.41	20.10	17.54	n.d.	0.56	BOSS	LERG
725	242.26304	56.22146	12.58	7.99	17.81	46.67	ML	205.13	S	iKgs5r	23.44	21.19	18.94	19.13	0.71	BOSS	LERG
726	242.17328	56.44053	11.01	8.41	3.76	8.50	ML	56.99	S	iKgs4b	22.49	21.67	19.71	n.d.	0.90	BOSS	HERG
727	242.14120	56.33497	6.92	6.46	1.99	6.93	ML	20.92	S	iK_s0b	n.d.	25.75	21.30	20.72	1.60	Dunc	LERG
728	245.54539	55.04847	9.00	7.33	6.70	9.79	ML	2042.87	S	iKgs7b	18.14	16.85	14.15	n.d.	0.03	BOSS	SFG
729	245.47831	55.03466	30.55	23.38	1.24	19.61	ML	640.60	S	iKg_6b	18.70	17.99	15.58	n.d.	0.06	Dunc	SFG
730	245.47294	54.88925	9.00	8.51	39.60	69.78	ML	2.93	S	_K_s7k	n.d.	n.d.	22.51	n.d.	1.34	Dunc	HERG
731	245.45267	55.28231	10.33	7.99	4.96	9.06	ML	7.20	S	iKgs1b	19.13	18.84	18.14	n.d.	0.71	Dunc	HERG
732	245.43169	55.37627	8.55	6.99	41.33	60.01	ML	229.58	S	iKgs7r	24.02	21.90	19.43	19.08	1.32	BOSS	LERG
733	245.42531	55.13582	11.50	8.56	2.24	4.89	ML	264.22	S	iKgs5r	22.41	20.87	18.74	n.d.	0.49	HSC	SFG
734	245.40388	55.32864	9.06	8.11	1.70	2.77	ML	0.98	S	_K_s6k	n.d.	n.d.	22.72	21.40	2.37	Dunc	HERG
735	245.38550	55.21660	8.75	7.49	135.25	210.12	ML	221.15	S	iKgs4r	20.85	19.35	17.40	n.d.	0.27	BOSS	HERG
736	245.23579	55.09359	22.92	13.01	1.19	7.87	ML	102.83	S	_Kg_3r	25.36	n.d.	22.14	n.d.	1.60	Dunc	HERG
737	245.20159	55.26276	9.16	5.83	1.62	1.92	ML	55.68	S	iKgs9r	25.12	22.03	18.73	19.09	0.86	HSC	LERG
738	245.13396	55.17487	12.13	10.68	3.53	10.11	ML	150.52	S	iKgs6r	22.27	19.84	17.49	n.d.	0.53	Vacc	LERG
739	245.12875	55.25308	13.62	9.13	10.99	38.27	ML	37.63	S	iKgs5r	23.87	21.08	18.92	19.11	0.65	Dunc	LERG
740	245.12114	55.19654	9.19	7.48	2.97	4.51	ML	64.66	S	iKgs9b	25.74	24.12	20.11	19.67	1.27	Dunc	HERG
741	245.06875	55.25377	23.80	13.05	1.01	6.97	ML	0.12	S	iKgs9b	25.36	24.31	21.06	20.47	1.75	Dunc	LERG
742	245.02085	54.95568	7.22	6.03	1.05	1.01	ML	0.81	S	iKg_5b	22.56	22.40	20.16	n.d.	1.86	Dunc	HERG
743	245.01198	55.25980	12.23	7.67	1.41	2.93	ML	208.36	S	iKgs6r	23.95	21.09	18.65	n.d.	0.73	HSC	LERG
744	245.00182	55.38319	12.94	7.91	1.13	2.56	ML	38.52	S	iKgs7r	23.96	21.97	19.36	19.28	0.67	Dunc	LERG
745	244.99050	55.00906	18.54	9.30	1.17	4.47	ML	172.03	S	iKgs8r	22.25	20.27	17.28	n.d.	0.48	Dunc	SFG
746	244.98267	55.03769	18.78	8.37	2.43	13.84	ML	1.92	S	iKgs3r	22.28	20.12	18.36	19.17	1.16	HSC	LERG
747	244.95024	55.74494	10.28	9.36	7.42	21.63	ML	49.30	S	iKgs5b	24.95	23.58	21.50	21.63	1.80	Kmag	HERG
748	244.93756	55.57391	9.09	7.75	6.44	10.04	ML	55.81	S	iKgs6b	23.33	23.08	20.82	20.61	1.11	HSC	LERG
749	244.92657	55.71755	8.32	6.95	7.75	13.39	ML	5.89	S	_K_s8k	n.d.	n.d.	21.91	21.08	1.73	Dunc	LERG
750	244.91657	55.71173	14.64	7.72	2.29	5.73	ML	16.78	S	_K_s9k	n.d.	n.d.	21.67	20.92	1.97	Dunc	HERG
751	244.89513	55.08764	22.56	14.91	0.98	7.33	ML	4.83	S	iKgs7b	23.97	23.44	20.79	20.31	0.51	HSC	LERG
752	244.87745	55.33555	5.04	3.83	1.22	1.70	ML	58.92	S	iKgs7r	24.65	22.75	20.01	19.80	0.88	HSC	HERG
753	244.87396	55.22093	8.59	6.76	28.58	40.76	ML	74.55	S	iKgs5b	23.87	23.54	21.43	21.41	1.89	HSC	HERG
754	244.84626	55.31542	31.10	18.27	1.26	15.80	ML	0.12	S	_K__8k	n.d.	n.d.	22.15	n.d.	2.12	Kmag	HERG
755	244.84484	55.29872	9.80	8.09	2.53	4.44	ML	43.06	S	iKgs4r	22.68	20.69	18.67	n.d.	0.56	BOSS	LERG
756	244.81396	55.22945	14.86	10.26	1.56	5.27	ML	88.18	S	iKgs3b	20.44	20.12	18.37	19.29	0.36	HSC	HERG
757	244.79415	55.48425	12.17	6.71	1.21	2.19	ML	4.87	S	iKgs2b	23.10	22.81	21.41	21.49	1.73	Dunc	HERG
758	244.79586	55.31167	9.18	7.57	3.46	5.33	ML	162.80	S	iKgs8r	24.68	22.11	19.34	19.14	0.88	HSC	LERG
759	244.77461	55.04606	24.96	20.94	1.12	12.96	ML	122.72	S	iKgs6b	18.22	17.09	14.73	n.d.	0.34	HSC	LERG

ID	Properties of Radio Source						Identification Data				Properties of Host Galaxy						
	RA	DEC	Major Axis arcsec	Minor Axis arcsec	Peak Flux mJy	Total Flux mJy	Analysis	LR	Morph	Type	g-band Mag	i-band Mag	K-band Mag	$3.6\mu m$ Mag	Redshift	Redshift Source	Galaxy Type
760	244.64716	55.49247	12.12	6.54	1.09	1.92	ML	482.89	S	iKgs8r	25.32	21.71	18.66	n.d.	0.91	HSC	LERG
761	244.64230	55.29767	10.94	7.91	26.55	57.22	ML	1277.38	S	iKgs7r	20.04	18.24	15.56	n.d.	0.26	BOSS	LERG
762	244.63515	55.28039	15.93	10.61	2.69	10.07	ML	1.87	S	iKg_5b	25.28	24.71	22.61	n.d.	2.35	Kmag	HERG
763	244.60800	55.47644	26.65	15.81	1.07	9.99	ML	348.27	S	iKgs5b	19.52	18.77	16.60	n.d.	0.10	Dunc	SFG
764	244.60868	55.37048	11.59	7.95	2.03	4.13	ML	353.61	S	iKgs6r	22.04	20.23	17.91	n.d.	0.51	BOSS	SFG
765	244.59654	55.45603	9.40	8.06	5.68	9.52	ML	758.41	S	iKgs4b	18.23	17.26	15.34	n.d.	0.08	BOSS	SFG
766	244.56675	55.36299	9.62	8.27	3.17	5.59	ML	65.80	S	iKgs2r	19.54	18.09	16.50	n.d.	0.19	BOSS	LERG
767	244.56116	55.19130	20.84	10.55	1.10	5.35	ML	235.64	S	iKgs4r	20.93	19.30	17.30	n.d.	0.34	HSC	SFG
768	244.54777	55.41260	11.07	7.86	1.42	2.74	ML	12.98	S	iKgs9b	24.27	23.76	20.50	20.28	0.99	HSC	LERG
769	244.50911	55.33399	10.08	8.77	3.54	6.93	ML	579.12	S	iKgs7r	23.49	20.70	18.20	n.d.	0.69	BOSS	LERG
770	244.01511	53.57726	12.41	8.49	3.43	30.12	ML	1.62	S	iKgs1b	23.84	23.36	22.48	n.d.	1.27	Dunc	LERG
771	243.98686	53.53563	7.71	5.06	2.74	3.75	ML	65.81	S	iKgs9r	25.62	22.36	19.13	n.d.	0.99	HSC	LERG
772	243.95430	53.53471	8.87	6.50	4.44	8.13	ML	38.66	S	iKgs7b	24.27	23.64	21.18	21.22	1.08	HSC	HERG
773	243.85292	53.60713	12.78	10.70	1.55	4.40	ML	5.47	S	iKgs2r	23.87	21.58	19.94	20.02	0.70	HSC	LERG
774	243.62419	53.71260	9.78	8.04	1.30	4.79	ML	95.00	S	iKgs7b	18.65	17.42	14.74	n.d.	0.09	Dunc	SFG
775	243.59967	53.52683	9.02	7.72	10.72	14.36	ML	4.68	S	iKgs1b	20.93	20.15	19.51	n.d.	1.39	BOSS	HERG
776	243.53946	53.52936	13.66	6.37	2.05	4.57	ML	90.60	S	iKg_7b	19.01	17.67	15.09	n.d.	0.00	Dunc	LERG
777	243.51371	53.71270	17.29	10.37	0.83	3.11	ML	3.07	S	_K_s7k	n.d.	n.d.	22.47	21.34	2.03	Dunc	LERG
778	243.51109	53.51000	10.11	7.48	2.86	10.69	ML	2079.88	S	iKgs7b	18.37	17.41	14.73	n.d.	0.06	BOSS	SFG
779	242.36110	54.18083	8.08	6.64	2.02	2.33	ML	29.34	S	iKgs7b	25.13	23.56	20.94	20.46	1.17	HSC	HERG
780	242.31411	54.23058	10.91	8.63	4.88	13.26	ML	12.29	S	_K_s9k	n.d.	n.d.	21.69	21.37	1.94	Dunc	HERG
781	242.26963	54.28969	17.51	12.97	1.23	6.01	ML	87.97	S	iKgs7b	22.72	21.42	18.78	n.d.	0.94	BOSS	HERG
782	242.24178	54.30484	11.34	10.11	2.61	6.42	ML	1826.74	S	iKgs8b	20.10	18.50	15.54	n.d.	0.26	BOSS	LERG
783	242.19628	54.02096	18.11	13.36	1.13	5.87	ML	7.21	S	_K_s9k	n.d.	n.d.	21.05	20.55	2.02	Dunc	HERG
784	242.16149	54.28163	13.60	9.73	5.42	19.58	ML	74.77	S	iKgs8b	24.70	23.26	20.38	20.48	1.01	HSC	LERG
785	242.15102	54.23855	16.83	10.64	7.59	33.98	ML	1.73	S	i_gs4b	24.47	23.71	n.d.	21.68	1.48	imag	LERG
786	242.14726	53.99321	9.17	8.52	3.63	10.79	ML	17.65	S	iKg_4r	25.24	23.01	21.08	n.d.	0.81	HSC	HERG
787	242.14674	54.27590	21.87	12.61	0.95	5.62	ML	504.69	S	iKgs7r	23.18	20.51	18.06	n.d.	0.64	BOSS	LERG
788	242.11792	54.17507	10.22	8.50	44.35	82.86	ML	355.92	S	iKgs4r	20.00	18.45	16.55	n.d.	0.23	BOSS	LERG
789	242.09860	53.69306	12.99	10.20	2.66	7.57	ML	34.55	S	iKgs4b	23.10	22.92	20.90	20.49	1.58	Dunc	HERG
790	242.01458	54.04083	8.77	7.60	5.29	7.57	ML	155.77	S	iKg_9r	25.43	22.78	19.20	n.d.	1.19	HSC	LERG
791	241.99862	53.90083	10.27	8.11	0.99	1.77	ML	1.22	S	___s__	n.d.	n.d.	n.d.	21.77	3.11	smag	AGN
792	241.98776	53.68172	10.29	9.87	1.41	3.09	ML	16.55	S	iK_s9b	n.d.	25.90	21.76	20.91	2.15	Dunc	LERG
793	241.98474	53.73534	9.86	7.75	3.19	5.25	ML	150.14	S	iKgs8r	24.46	22.72	19.63	19.27	0.86	HSC	LERG
794	241.96631	54.14281	8.75	6.76	3.14	5.90	ML	43.39	S	iKgs9r	25.51	22.66	18.87	n.d.	1.04	Dunc	LERG
795	241.94482	53.69751	20.34	13.66	1.00	5.98	ML	46.85	S	iKgs4b	17.51	16.46	14.60	n.d.	0.05	Dunc	LERG
796	241.94421	53.81028	18.09	13.00	1.12	5.66	ML	5.93	S	_K_s9k	n.d.	n.d.	20.96	20.01	1.73	Dunc	LERG
797	241.94006	53.79043	11.12	9.48	2.67	6.05	ML	47.75	S	iKgs9b	25.24	24.61	20.79	20.11	1.50	SERVS	HERG
798	241.94136	54.20054	10.79	8.69	6.43	15.74	ML	11.36	S	iKgs0r	27.70	25.60	21.18	21.07	1.66	Dunc	LERG
799	241.93534	53.72251	10.40	7.82	1.34	2.34	ML	335.90	S	iKgs7r	23.22	21.29	18.64	n.d.	0.62	HSC	LERG

ID	Properties of Radio Source						Identification Data				Properties of Host Galaxy						
	RA	DEC	Major Axis arcsec	Minor Axis arcsec	Peak Flux mJy	Total Flux mJy	Analysis	LR	Morph	Type	g-band Mag	i-band Mag	K-band Mag	3.6μm Mag	Redshift	Redshift Source	Galaxy Type
800	241.90215	53.95879	21.54	16.17	1.66	12.43	ML	22.06	S	i_gs2b	17.41	16.60	n.d.	n.d.	0.03	BOSS	SFG
801	241.90474	54.17991	22.71	15.72	1.00	7.66	ML	0.76	S	iKgs4r	22.76	20.40	18.36	n.d.	0.48	Dunc	LERG
802	241.89867	54.22948	6.59	4.48	0.93	0.59	ML	52.21	S	iKgs6b	23.77	22.93	20.52	20.05	1.67	Dunc	HERG
803	241.88575	54.20318	11.32	7.04	1.93	8.29	ML	0.27	S	iKgs7r	24.56	21.54	18.89	n.d.	0.87	Dunc	LERG
804	241.85582	53.89814	9.50	8.60	4.84	13.06	ML	0.83	S	___s__	n.d.	n.d.	n.d.	22.93	3.66	smag	AGN
805	241.85243	54.20295	19.23	18.72	1.13	8.73	ML	250.48	S	iKgs6b	19.75	18.70	16.28	n.d.	0.23	BOSS	SFG
806	241.84000	53.77739	9.93	9.16	47.74	91.57	ML	10.72	S	iKgs2b	22.55	21.74	20.49	19.85	1.80	BOSS	HERG
807	241.83525	54.09740	12.13	9.77	1.81	4.60	ML	4.00	S	iKg_1b	22.29	21.86	21.37	n.d.	0.13	Dunc	LERG
808	241.78291	53.94951	13.77	9.10	2.19	5.89	ML	0.78	S	___s__	n.d.	n.d.	n.d.	22.71	3.57	smag	AGN
809	241.76139	53.69117	9.37	8.80	19.95	37.45	ML	51.58	S	iKgs0r	27.14	24.85	20.40	19.95	1.57	Dunc	LERG
810	241.76425	53.95153	15.67	12.15	1.08	4.42	ML	11.07	S	iKgs4b	23.23	23.00	21.09	20.63	1.89	Dunc	HERG
811	241.73993	54.05596	9.15	6.19	1.20	8.00	ML	10.33	S	iKgs2b	18.19	17.73	16.58	n.d.	0.35	HSC	LERG
812	241.70289	53.83980	10.73	8.63	2.18	11.84	ML	19.16	S	iKgs8r	28.86	22.78	19.65	19.27	1.01	Dunc	LERG
813	241.64051	53.93769	9.28	8.16	24.46	41.30	ML	39.81	S	iKgs9b	25.53	24.42	20.67	20.65	1.79	Dunc	LERG
814	241.64013	53.79162	20.04	15.93	0.91	6.25	ML	159.61	S	iKgs6b	20.46	19.05	16.73	n.d.	0.20	Dunc	SFG
815	241.63851	54.11095	9.15	8.77	2.98	5.14	ML	77.97	S	_K_s0k	n.d.	n.d.	19.88	21.19	3.92	SERVS	HERG
816	241.59794	54.09869	9.72	8.88	84.87	157.72	ML	10.18	S	iKgs1b	17.62	17.65	16.91	n.d.	0.88	BOSS	HERG
817	241.59233	54.22663	9.80	8.47	58.92	107.80	ML	53.74	S	iKgs9r	25.61	23.73	20.33	19.86	1.16	Dunc	HERG
818	241.54026	54.05688	9.15	8.20	66.33	110.00	ML	55.36	S	iKgs9b	24.91	23.99	20.44	19.67	1.68	Dunc	HERG
819	241.51259	53.80318	61.05	10.47	89.45	528.45	ML	51.90	S	iKgs9b	24.31	22.75	19.58	19.23	1.12	HSC	HERG
820	241.47266	54.29513	9.32	8.12	6.21	13.05	ML	19.63	S	iKgs9r	26.87	25.04	21.51	20.76	0.82	HSC	LERG
821	241.46976	54.11407	9.78	9.46	11.36	22.57	ML	2330.58	S	iKgs7b	18.91	17.71	15.13	n.d.	0.15	BOSS	SFG
822	241.46809	53.90674	8.80	6.78	2.29	2.94	ML	246.27	S	iKgs7b	23.22	21.84	19.26	n.d.	1.01	HSC	HERG
823	241.44730	54.07526	10.39	8.39	4.53	8.48	ML	547.03	S	iKgs7r	23.87	20.88	18.37	n.d.	0.70	BOSS	LERG
824	241.43438	53.95838	9.23	9.00	3.25	9.68	ML	1.64	S	iKgs9b	25.73	24.94	21.53	20.52	1.63	Dunc	HERG
825	241.40001	54.20665	7.95	6.31	1.49	3.70	ML	33.22	S	iKgs8b	24.96	23.87	20.76	20.44	1.00	HSC	LERG
826	241.38915	54.01777	8.91	8.65	3.02	4.99	ML	11.25	S	iKgs1b	19.98	19.58	19.29	n.d.	1.70	BOSS	HERG
827	241.36511	53.92694	8.35	8.01	12.42	18.70	ML	18.37	S	_K__9k	n.d.	n.d.	21.07	n.d.	1.59	Kmag	HERG
828	241.34528	53.95534	25.78	19.94	1.01	11.14	ML	22.27	S	iKgs8b	24.25	24.11	21.15	20.66	1.60	SERVS	HERG
829	241.34249	53.87866	8.11	7.98	3.47	4.81	ML	18.37	S	_K__9k	n.d.	n.d.	21.46	n.d.	1.78	Kmag	LERG
830	241.32944	54.35017	12.88	10.64	7.53	31.60	ML	68.21	S	iKgs2b	19.74	18.74	17.41	n.d.	0.21	BOSS	LERG
831	241.31650	53.90282	8.23	7.81	4.57	11.12	ML	55.10	S	iKgs2r	19.78	18.57	17.29	n.d.	0.20	BOSS	HERG
832	241.28772	53.89783	14.02	9.75	1.16	3.41	ML	20.71	S	iKg_7b	24.43	23.92	21.20	n.d.	1.45	Dunc	HERG
833	241.26442	54.30512	10.78	9.34	1.11	2.40	ML	186.47	S	iKgs9b	24.72	22.98	19.52	19.21	1.17	HSC	HERG
834	241.25164	54.22541	11.63	9.92	1.63	4.04	ML	126.56	S	iKgs8r	24.80	22.10	19.21	19.18	0.84	HSC	LERG
835	241.22061	54.24780	10.98	10.37	1.37	3.34	ML	14.49	S	iKgs2b	22.48	21.44	20.04	19.43	0.59	HSC	LERG
836	241.16353	54.35749	9.24	7.48	1.06	1.58	ML	32.79	S	iKgs9b	25.63	24.48	20.43	19.86	1.08	HSC	HERG
837	241.11808	54.24976	10.46	8.73	2.40	4.71	ML	533.47	S	iKgs6r	21.84	20.03	17.67	n.d.	0.50	BOSS	LERG
838	241.07861	54.25677	10.88	8.96	1.53	3.20	ML	6.95	S	iKgs1b	18.32	17.97	17.72	n.d.	1.48	BOSS	HERG
839	241.02508	54.34613	10.49	9.79	3.22	7.09	ML	31.93	S	iKgs8b	25.45	24.53	21.45	21.35	1.85	Dunc	LERG

ID	Properties of Radio Source						Identification Data				Properties of Host Galaxy						
	RA	DEC	Major Axis arcsec	Minor Axis arcsec	Peak Flux mJy	Total Flux mJy	Analysis	LR	Morph	Type	g-band Mag	i-band Mag	K-band Mag	$3.6\mu m$ Mag	Redshift	Redshift Source	Galaxy Type
840	241.00466	54.29726	21.75	12.98	1.01	6.15	ML	27.15	S	iKgs3r	21.97	19.80	17.98	n.d.	0.55	HSC	HERG
841	240.99397	54.31108	22.63	19.47	0.86	8.16	ML	25.49	S	iKg_2r	21.65	19.94	18.53	n.d.	0.53	HSC	LERG
842	240.82505	54.22016	8.53	5.39	1.17	4.44	ML	1.01	S	_K__9k	n.d.	n.d.	21.22	n.d.	1.66	Kmag	LERG
843	240.78990	54.35530	26.33	14.67	1.01	8.38	ML	16.12	S	iKg_8b	25.18	24.77	21.90	n.d.	0.65	HSC	LERG
844	240.75024	54.29364	19.65	10.54	0.77	3.41	ML	3524.62	S	iKgs8b	19.06	17.86	15.09	n.d.	0.11	Vacc	SFG
845	240.72454	54.26753	16.40	10.84	1.42	5.40	ML	18.72	S	_K_s9k	n.d.	n.d.	20.94	20.58	1.35	Dunc	LERG
846	244.04295	54.71223	7.94	5.83	1.06	1.19	ML	54.46	S	iKgs7b	24.44	23.55	20.91	20.36	1.18	HSC	HERG
847	244.03156	54.54328	13.18	10.34	1.23	4.06	ML	319.73	S	iKgs6r	23.36	20.77	18.37	n.d.	0.64	BOSS	LERG
848	244.02089	54.79623	9.14	6.74	7.08	10.60	ML	48.60	S	iKgs9r	26.86	24.10	20.67	20.23	1.22	Dunc	LERG
849	243.95725	54.63260	20.04	10.45	0.96	4.89	ML	7.53	S	_K_s9k	n.d.	n.d.	20.99	20.58	0.39	BOSS	LERG
850	243.94631	54.53217	9.25	5.50	1.73	2.13	ML	50.74	S	iKgs9b	25.55	24.39	20.29	19.82	1.39	Dunc	HERG
851	243.87790	54.87522	22.80	18.81	5.49	76.85	ML	0.36	S	iKgs4r	20.97	19.04	17.10	n.d.	0.39	HSC	LERG
852	243.88090	54.75797	8.28	6.37	0.94	1.21	ML	2.06	S	iKgs2b	23.56	23.23	22.03	20.77	0.95	HSC	HERG
853	243.86482	54.45392	9.64	6.61	11.73	22.35	ML	459.46	S	iKgs5r	22.43	20.20	18.11	n.d.	0.48	BOSS	LERG
854	243.86582	54.57039	10.98	8.18	1.49	3.26	ML	1060.83	S	iKgs6b	18.90	17.82	15.55	n.d.	0.14	BOSS	SFG
855	243.86389	54.94323	7.88	6.52	10.17	15.38	ML	119.98	S	iKgs7b	23.70	22.69	20.01	19.69	1.06	HSC	HERG
856	243.86288	54.76494	10.04	7.70	1.01	1.90	ML	27.85	S	iKgs3r	22.07	20.71	18.92	19.68	0.33	BOSS	LERG
857	243.85210	54.39765	7.62	5.40	9.08	11.27	ML	82.12	S	iKgs7b	24.00	23.26	20.59	20.61	0.66	HSC	LERG
858	243.85619	54.70512	5.95	4.21	1.35	1.86	ML	27.69	S	iKgs2r	21.37	19.95	18.44	n.d.	0.55	BOSS	HERG
859	243.85116	54.33533	10.45	7.93	1.07	2.15	ML	218.93	S	iKgs3b	20.26	19.14	17.36	n.d.	0.36	BOSS	SFG
860	243.84030	54.30446	8.31	6.32	6.28	8.01	ML	42.91	S	_K_s5k	n.d.	n.d.	22.87	21.39	1.05	HSC	LERG
861	243.84087	54.53024	8.14	6.06	2.36	17.17	ML	11.32	S	iKgs1b	17.72	17.58	16.78	n.d.	0.47	BOSS	HERG
862	243.84018	54.58853	7.53	6.20	5.73	6.50	ML	115.33	S	iKgs7b	23.76	22.61	19.94	n.d.	1.16	HSC	HERG
863	243.84288	54.97373	8.47	7.18	6.20	12.27	ML	1.26	S	___s__	n.d.	n.d.	n.d.	21.75	3.10	smag	AGN
864	243.83282	54.48855	7.88	6.33	1.18	1.43	ML	14.97	S	_K__9k	n.d.	n.d.	21.21	n.d.	0.83	HSC	LERG
865	243.82993	54.81194	9.72	6.71	2.02	3.21	ML	78.07	S	iK_s0b	n.d.	24.81	20.34	19.98	1.54	Dunc	LERG
866	243.78743	54.31019	13.73	9.42	1.02	3.21	ML	772.76	S	iKgs6b	19.95	19.13	16.73	n.d.	0.29	Vacc	SFG
867	243.77962	54.30917	15.85	8.59	1.12	3.71	ML	24.36	S	iKgs2r	19.96	18.85	17.45	n.d.	0.15	BOSS	SFG
868	243.77337	54.40415	8.86	6.01	0.93	1.20	ML	85.36	S	iKgs2b	19.84	18.79	17.16	n.d.	0.21	Vacc	SFG
869	243.75725	54.86124	9.88	7.23	2.19	3.80	ML	82.99	S	iKgs8b	24.39	23.12	20.07	19.69	1.44	Dunc	HERG
870	243.73761	54.59134	8.86	6.23	2.64	3.54	ML	17.38	S	iKgs4b	24.25	23.56	21.54	20.32	1.80	Dunc	LERG
871	243.72027	54.47359	10.83	7.50	2.97	5.86	ML	151.64	S	iKgs9r	25.81	22.84	19.46	19.22	1.12	HSC	LERG
872	243.72163	54.66502	9.20	6.59	1.15	1.69	ML	416.47	S	iKgs6r	22.11	20.33	17.95	n.d.	0.33	BOSS	SFG
873	243.66054	54.38012	7.34	5.58	17.84	20.17	ML	59.49	S	iKg_8b	24.52	23.58	20.65	n.d.	1.52	Dunc	LERG
874	243.66086	54.60669	8.92	7.61	1.15	1.90	ML	1.32	S	___s__	n.d.	n.d.	n.d.	19.79	1.98	smag	HERG
875	243.65445	54.27621	13.92	8.78	1.58	4.70	ML	628.89	S	iKgs8b	19.93	18.71	15.58	n.d.	0.08	BOSS	SFG
876	243.64778	54.32650	6.98	5.05	7.22	8.07	ML	21.04	S	iKg_6b	25.61	24.92	22.57	n.d.	2.87	Dunc	HERG
877	243.64266	54.64049	6.80	6.12	1.14	1.15	ML	1234.05	S	iKgs7b	20.73	19.45	16.96	n.d.	0.23	BOSS	SFG
878	243.63510	54.43463	7.56	6.37	1.55	1.81	ML	83.69	S	iKgs6b	21.77	20.34	17.93	n.d.	0.24	BOSS	SFG
879	243.63649	54.68212	8.58	7.19	1.13	1.69	ML	50.04	S	iKgs2r	20.78	19.19	17.54	n.d.	0.23	BOSS	LERG

ID	Properties of Radio Source						Identification Data				Properties of Host Galaxy						
	RA	DEC	Major Axis arcsec	Minor Axis arcsec	Peak Flux mJy	Total Flux mJy	Analysis	LR	Morph	Type	g-band Mag	i-band Mag	K-band Mag	3.6μm Mag	Redshift	Redshift Source	Galaxy Type
880	243.63557	54.81566	10.03	6.79	1.00	1.65	ML	411.24	S	iKgs4b	20.04	19.01	16.96	n.d.	0.27	BOSS	HERG
881	243.60784	54.63825	10.13	5.68	1.29	1.80	ML	12.39	S	iKgs3b	21.86	21.37	19.54	19.22	1.08	BOSS	HERG
882	243.60668	54.61137	11.22	10.02	1.48	4.06	ML	398.06	S	iKgs6b	20.16	19.06	16.79	n.d.	0.23	BOSS	SFG
883	243.60060	54.72137	11.40	9.12	5.08	12.83	ML	30.11	S	iKgs6r	21.02	19.08	16.79	n.d.	0.41	HSC	LERG
884	243.58822	54.29493	6.83	5.11	14.82	14.53	ML	113.22	S	iKgs5r	24.32	22.66	20.49	19.35	1.02	HSC	HERG
885	243.58612	54.56652	11.02	7.94	1.69	3.59	ML	53.89	S	iKgs9b	25.41	24.23	20.96	20.47	1.17	HSC	LERG
886	243.56542	54.72459	8.41	6.14	29.43	41.88	ML	20.54	S	iKgs6r	20.80	18.87	16.46	n.d.	0.35	HSC	LERG
887	243.55843	54.73273	9.13	7.04	9.60	14.99	ML	760.75	S	iKgs6r	21.43	19.34	16.96	n.d.	0.33	Vacc	LERG
888	243.53850	54.16496	7.06	5.22	1.25	1.12	ML	56.36	S	i_gs3r	21.51	19.97	n.d.	n.d.	0.45	HSC	SFG
889	243.53309	54.92798	12.23	8.43	0.95	2.38	ML	1565.32	S	iKgs8b	20.34	18.77	15.81	n.d.	0.26	BOSS	SFG
890	243.49666	54.46713	9.94	6.41	1.19	1.84	ML	922.11	S	iKgs5b	20.65	19.32	17.13	n.d.	0.29	BOSS	SFG
891	243.48589	54.66141	8.12	5.34	1.16	1.22	ML	30.48	S	iKgs4b	23.52	22.92	20.88	20.38	0.43	BOSS	SFG
892	243.46939	54.11567	7.97	6.44	5.10	6.37	ML	30.64	S	iKgs4r	25.48	22.30	20.25	20.17	0.75	HSC	LERG
893	243.47091	54.45650	9.28	6.32	1.83	14.97	ML	822.42	S	iKgs7r	20.42	18.61	16.11	n.d.	0.29	BOSS	LERG
894	243.44983	54.23510	29.56	11.79	28.72	134.62	ML	4.65	S	iKg_5b	22.55	22.04	19.84	n.d.	0.00	BOSS	LERG
895	243.43500	54.68860	9.77	8.03	1.13	2.16	ML	48.68	S	iK_s7b	n.d.	24.22	21.52	20.36	1.14	HSC	HERG
896	243.40114	54.21649	8.30	6.40	6.51	8.40	ML	46.21	S	iKgs7r	25.87	24.12	21.48	19.44	1.59	Dunc	HERG
897	243.40015	54.50312	8.01	6.82	2.66	3.53	ML	261.15	S	iKgs6r	23.67	20.86	18.43	n.d.	0.63	BOSS	LERG
898	243.39235	54.21821	7.50	5.58	1.74	1.77	ML	37.93	S	iKg_0r	26.73	24.25	20.10	n.d.	1.66	Dunc	HERG
899	243.38040	54.45502	8.46	6.51	346.64	495.97	ML	62.66	S	iKgs9b	25.32	24.05	20.46	20.14	1.50	Dunc	LERG
900	243.37998	54.27511	11.66	8.35	2.88	6.81	ML	1009.21	S	iKgs6b	18.10	16.93	14.61	n.d.	0.69	BOSS	HERG
901	243.37184	54.24885	18.08	9.53	1.46	6.12	ML	4.82	S	iKgs9b	24.83	23.87	20.65	20.44	0.64	HSC	LERG
902	243.37268	54.62772	9.09	7.10	2.80	4.39	ML	70.91	S	iKgs4r	20.58	18.86	16.81	n.d.	0.27	BOSS	LERG
903	243.37263	54.50669	8.08	6.43	2.59	3.26	ML	923.39	S	iKgs5r	21.27	19.11	17.02	n.d.	0.35	BOSS	HERG
904	243.33427	54.27703	8.72	5.48	6.05	8.11	ML	1267.37	S	iKgs6r	19.65	18.06	15.76	n.d.	0.23	BOSS	LERG
905	243.33015	54.86021	10.64	6.65	1.55	2.67	ML	70.45	S	iKgs2b	18.41	17.81	16.51	n.d.	0.07	BOSS	SFG
906	243.31134	54.29689	7.94	6.50	21.85	31.11	ML	13.52	S	_K__9k	n.d.	n.d.	20.92	n.d.	0.99	HSC	LERG
907	243.31125	54.73796	13.29	11.28	0.88	3.21	ML	430.48	S	iKgs7r	22.18	20.28	17.67	n.d.	0.33	BOSS	HERG
908	243.27544	54.58330	26.51	14.94	0.89	8.52	ML	933.64	S	iKgs7b	19.58	18.63	15.91	n.d.	0.13	BOSS	SFG
909	243.26406	54.53977	25.46	7.18	17.58	75.21	ML	86.28	S	iKgs8r	25.85	23.17	20.10	20.17	1.00	HSC	LERG
910	243.27053	54.00491	21.71	14.18	1.07	8.00	ML	7.23	S	iKgs5r	21.89	19.70	17.60	n.d.	0.53	HSC	LERG
911	243.25481	54.16792	10.55	6.16	1.06	1.67	ML	261.95	S	iKgs4b	19.23	18.24	16.30	n.d.	0.14	BOSS	SFG
912	243.24355	54.47592	10.97	7.29	1.07	2.08	ML	94.69	S	iKgs6r	24.85	22.03	19.63	19.67	0.84	HSC	LERG
913	243.22258	54.68716	14.52	8.19	0.80	2.32	ML	380.32	S	iKgs7b	21.84	20.80	18.32	19.13	0.29	BOSS	SFG
914	243.21258	53.99293	9.93	8.35	9.58	23.49	ML	1.81	S	iKgs6r	21.84	19.82	17.49	n.d.	0.43	Dunc	LERG
915	243.20623	54.14349	14.99	11.35	1.67	6.92	ML	2115.17	S	iKgs7b	19.15	17.88	15.29	n.d.	0.15	BOSS	LERG
916	243.20011	54.58799	8.37	6.34	2.39	3.08	ML	39.66	S	iK_s0b	n.d.	25.27	20.34	20.00	1.55	Dunc	LERG
917	243.18746	54.47319	10.93	6.63	1.95	3.44	ML	545.12	S	iKgs5r	22.37	20.01	17.88	n.d.	0.49	BOSS	LERG
918	243.18413	54.57884	8.84	7.65	1.12	1.85	ML	21.10	S	iKgs8b	24.17	23.93	20.88	21.04	1.73	SERVS	HERG
919	243.15446	53.96850	24.47	14.44	1.21	10.41	ML	2397.36	S	iKg_8b	17.89	16.77	13.86	n.d.	0.05	BOSS	SFG

ID	Properties of Radio Source						Identification Data				Properties of Host Galaxy						
	RA	DEC	Major Axis arcsec	Minor Axis arcsec	Peak Flux mJy	Total Flux mJy	Analysis	LR	Morph	Type	g-band Mag	i-band Mag	K-band Mag	3.6μm Mag	Redshift	Redshift Source	Galaxy Type
920	243.15332	54.31212	7.16	5.53	7.70	9.82	ML	5.15	S	_K_s8k	n.d.	n.d.	22.09	21.39	2.28	Dunc	HERG
921	243.14658	54.48820	5.97	5.25	1.21	0.92	ML	176.40	S	iKgs9r	25.52	22.74	19.12	n.d.	1.01	HSC	HERG
922	243.12666	54.85239	11.27	10.52	4.08	11.75	ML	700.92	S	iKgs5r	21.28	19.19	17.07	n.d.	0.39	BOSS	LERG
923	243.12861	54.86969	8.74	6.70	1.60	2.28	ML	857.54	S	iKgs5r	21.24	19.26	17.12	n.d.	0.33	BOSS	HERG
924	243.11537	53.96253	10.56	8.38	2.37	5.11	ML	66.54	S	iKgs9r	26.72	23.78	20.10	19.73	1.24	Dunc	LERG
925	243.11185	54.04262	10.52	6.38	1.70	2.77	ML	0.94	S	_K_s6k	n.d.	n.d.	22.67	21.22	2.78	Dunc	HERG
926	243.10039	54.65147	9.81	5.62	0.93	1.25	ML	64.71	S	iKgs4r	22.31	20.84	18.86	n.d.	0.56	BOSS	SFG
927	243.09585	54.64420	5.94	5.03	3.81	3.74	ML	19.43	S	_K_s9k	n.d.	n.d.	21.15	21.07	0.63	HSC	LERG
928	243.09623	54.01719	18.98	8.97	10.61	50.97	ML	312.92	S	iKg_6r	22.16	20.07	17.62	n.d.	0.45	BOSS	LERG
929	243.09294	54.87273	9.30	7.04	4.85	7.72	ML	12.78	S	iKgs1b	18.58	17.81	17.65	n.d.	1.89	BOSS	HERG
930	243.08809	54.78008	13.54	6.45	2.04	7.79	ML	82.70	S	iKgs4r	22.46	20.22	18.18	18.99	0.46	BOSS	LERG
931	243.08936	54.09538	9.06	7.51	3.27	5.41	ML	18.34	S	_K_s9k	n.d.	n.d.	21.08	20.55	1.68	Dunc	LERG
932	243.07882	54.16086	11.08	6.35	1.28	2.19	ML	702.61	S	iKgs5b	19.24	17.83	15.63	n.d.	0.14	BOSS	LERG
933	243.05877	54.08008	17.78	11.43	1.80	8.87	ML	7.61	S	iKgs0r	26.97	24.61	19.61	19.95	1.54	Dunc	LERG
934	243.02921	54.32742	9.58	6.50	1.78	2.70	ML	142.60	S	iKgs3r	20.61	19.32	17.52	n.d.	0.47	BOSS	LERG
935	243.02003	54.69681	12.51	9.72	1.03	3.05	ML	14.64	S	_K_s9k	n.d.	n.d.	21.68	20.18	0.93	HSC	HERG
936	243.01912	54.58017	7.39	5.15	0.95	0.88	ML	70.28	S	iKgs6b	22.18	21.15	18.82	n.d.	0.68	BOSS	SFG
937	243.01293	54.75921	7.53	5.65	6.16	8.35	ML	243.70	S	iKgs6b	22.44	21.09	18.78	n.d.	0.88	BOSS	HERG
938	242.99668	54.73823	8.40	6.91	4.34	6.12	ML	54.16	S	iKgs0b	26.53	25.31	21.02	20.69	1.54	Dunc	LERG
939	242.99612	54.40366	9.56	5.82	1.04	1.41	ML	823.71	S	iKgs6r	20.86	19.04	16.76	n.d.	0.35	BOSS	HERG
940	242.97933	54.52148	8.68	6.76	4.51	6.43	ML	141.64	S	iKgs7r	23.97	22.35	19.86	19.42	0.92	HSC	LERG
941	242.97171	54.14513	10.82	8.21	1.00	2.16	ML	49.00	S	iKgs9b	25.26	24.00	20.45	19.83	1.13	HSC	LERG
942	242.96818	54.02575	9.34	7.68	3.55	6.18	ML	66.50	S	iKgs6b	24.01	23.17	20.79	20.40	1.18	Dunc	HERG
943	242.95794	54.78826	8.52	6.31	4.25	5.56	ML	45.33	S	_K_s5k	n.d.	n.d.	23.06	21.53	2.22	Dunc	HERG
944	242.93163	54.27482	8.46	6.48	1.41	8.24	ML	712.25	S	iKgs7r	21.46	19.68	17.20	n.d.	0.34	BOSS	LERG
945	242.93129	54.11867	8.84	6.98	2.71	4.06	ML	20.41	S	iKg_9r	27.56	25.73	21.69	n.d.	2.63	Dunc	HERG
946	242.91689	54.74141	10.05	8.73	0.85	1.81	ML	1.82	S	iKgs4b	20.15	19.40	17.48	n.d.	0.55	Dunc	HERG
947	242.90877	53.99221	11.91	8.21	39.36	93.54	ML	47.88	S	iKgs8r	24.03	22.10	19.05	19.00	0.99	HSC	LERG
948	242.90663	54.22058	8.36	6.22	3.66	4.62	ML	98.23	S	iKgs8r	25.21	23.12	20.23	19.59	0.97	HSC	LERG
949	242.87312	54.76847	7.95	5.95	20.45	26.84	ML	38.73	S	iKgs7b	25.40	24.81	22.34	21.83	1.09	HSC	LERG
950	242.87740	54.27639	11.96	9.22	6.32	23.24	ML	13.69	S	iKgs5r	21.39	19.41	17.31	n.d.	0.33	Dunc	LERG
951	242.87255	54.50291	12.78	8.75	1.41	3.83	ML	19.05	S	_K__9k	n.d.	n.d.	21.72	n.d.	1.04	HSC	LERG
952	242.86395	54.37695	8.59	5.91	2.39	2.95	ML	36.45	S	iKgs9r	26.39	24.51	20.69	20.66	1.29	Dunc	LERG
953	242.85796	54.64145	9.84	7.03	2.21	3.71	ML	6.78	S	iKgs2r	23.05	21.75	20.43	20.15	0.79	BOSS	LERG
954	242.85227	54.28557	16.91	12.23	1.11	5.59	ML	0.38	S	iKgs2r	23.10	21.18	19.64	20.44	0.98	Kmag	LERG
955	242.82247	54.27476	10.71	7.36	2.41	4.61	ML	1911.45	S	iKgs7b	19.47	18.29	15.62	n.d.	0.14	BOSS	SFG
956	242.81474	54.69495	7.88	6.44	1.18	1.46	ML	28.41	S	iKgs6b	24.95	23.99	21.59	21.15	2.23	Dunc	HERG
957	242.81741	54.42178	10.04	6.62	1.63	2.63	ML	162.48	S	iKgs8r	24.43	22.61	19.81	19.84	0.96	HSC	LERG
958	242.81638	54.10909	15.43	11.70	1.09	4.79	ML	1.02	S	___s__	n.d.	n.d.	n.d.	21.89	3.18	smag	AGN
959	242.78876	54.78297	8.91	5.58	1.36	1.64	ML	24.55	S	iKgs9r	28.63	25.04	21.05	19.80	1.64	Dunc	HERG

ID	Properties of Radio Source						Identification Data				Properties of Host Galaxy						
	RA	DEC	Major Axis arcsec	Minor Axis arcsec	Peak Flux mJy	Total Flux mJy	Analysis	LR	Morph	Type	g-band Mag	i-band Mag	K-band Mag	3.6μm Mag	Redshift	Redshift Source	Galaxy Type
960	242.76030	54.26265	8.26	5.72	2.78	3.19	ML	693.60	S	iKgs8r	24.00	21.31	18.41	n.d.	1.27	BOSS	LERG
961	242.75990	54.39199	10.52	6.23	1.06	1.68	ML	42.45	S	iKgs9b	25.56	24.61	20.83	19.97	1.75	Dunc	HERG
962	242.75147	54.70112	11.09	7.76	53.25	142.56	ML	251.03	S	iKgs5r	22.60	20.91	18.85	19.03	0.64	BOSS	LERG
963	242.72818	54.54921	18.31	14.03	0.83	5.16	ML	398.52	S	iKgs6r	22.25	19.87	17.60	n.d.	0.49	BOSS	HERG
964	242.70065	54.78447	11.15	6.79	0.92	1.69	ML	29.40	S	i__s5b	n.d.	25.72	n.d.	23.01	1.80	imag	HERG
965	242.68868	54.60306	9.59	7.82	0.93	1.69	ML	9.39	S	iKgs2b	19.58	19.31	17.91	n.d.	0.47	Kmag	SFG
966	242.69175	54.39092	10.67	6.80	1.18	2.08	ML	125.11	S	iKgs9b	24.42	22.78	19.11	19.09	1.20	Dunc	HERG
967	242.67260	54.49731	11.60	6.80	0.98	1.88	ML	17.12	S	iKgs8b	25.24	24.01	20.88	20.46	1.16	HSC	HERG
968	242.67192	54.17539	12.03	9.08	1.10	2.91	ML	77.62	S	iKgs2b	19.35	18.49	17.03	n.d.	0.23	BOSS	SFG
969	242.65283	54.68531	10.58	6.14	8.79	17.10	ML	5.03	S	iKgs9b	25.76	24.23	20.19	19.77	1.20	Kmag	HERG
970	242.63119	54.71779	8.51	6.65	1.42	1.96	ML	565.95	S	iKgs7r	22.92	20.28	17.82	n.d.	0.63	BOSS	LERG
971	242.61450	54.21264	22.19	7.98	6.21	38.42	ML	829.33	S	iKgs6r	20.30	18.50	16.07	n.d.	0.27	BOSS	LERG
972	242.61017	54.60771	8.73	6.73	2.76	3.94	ML	370.93	S	iKgs6r	22.64	20.31	17.87	n.d.	0.51	BOSS	HERG
973	242.58676	54.65024	8.91	6.76	17.36	23.87	ML	97.77	S	iKgs7r	24.19	22.56	19.94	n.d.	0.48	HSC	LERG
974	242.59727	54.05782	10.18	7.93	2.13	4.17	ML	252.60	S	iKgs9r	24.72	21.79	17.93	n.d.	0.91	HSC	LERG
975	242.58032	54.36508	12.88	8.93	1.18	3.31	ML	1110.00	S	iKgs8r	22.51	20.48	17.68	n.d.	0.33	BOSS	HERG
976	242.57508	54.39216	8.94	7.21	1.00	1.57	ML	62.33	S	iKgs9b	24.97	23.80	20.45	20.21	1.18	HSC	HERG
977	242.57903	54.05290	11.57	8.34	1.81	4.25	ML	1018.52	S	iKgs5r	20.65	18.88	16.79	n.d.	0.26	BOSS	LERG
978	242.55569	54.82499	13.45	7.71	0.95	2.38	ML	0.14	S	iKgs9r	22.60	20.23	16.57	n.d.	0.63	HSC	LERG
979	242.55301	54.59184	8.65	7.23	3.36	5.10	ML	3.03	S	iKgs1b	19.13	18.49	19.02	19.82	0.21	HSC	LERG
980	242.55539	54.07371	9.37	7.68	5.04	8.82	ML	4.36	S	iKgs3r	24.70	23.19	21.50	21.36	0.89	HSC	LERG
981	242.53555	54.13230	31.01	8.08	3.10	24.03	ML	71.69	S	iKgs9r	25.64	22.77	19.52	19.35	1.12	Dunc	HERG
982	242.52675	54.17357	37.48	26.71	0.89	21.72	ML	0.12	S	_K__0k	n.d.	n.d.	20.38	n.d.	1.28	Kmag	LERG
983	242.50967	54.27711	15.17	7.77	23.93	56.79	ML	85.25	S	iKgs9r	24.28	21.53	18.26	n.d.	1.26	HSC	LERG
984	242.45565	54.14150	12.78	7.26	5.26	15.42	ML	16.62	S	_K_s0k	n.d.	n.d.	20.49	20.03	1.30	SERVS	HERG
985	242.42864	54.25228	5.85	4.85	1.00	0.69	ML	19.42	S	iKgs8b	25.93	24.53	21.68	21.25	0.59	HSC	LERG
986	242.40623	54.21606	7.43	5.78	1.20	8.21	ML	1054.16	S	iKgs7b	19.43	18.09	15.56	n.d.	0.09	BOSS	SFG
987	242.38108	54.32184	11.99	6.44	2.45	9.71	ML	0.47	S	___s__	n.d.	n.d.	n.d.	22.45	1.11	HSC	LERG
988	242.38150	54.30751	12.37	9.12	1.34	3.68	ML	69.16	S	i_gs2r	19.63	18.36	n.d.	n.d.	0.08	BOSS	SFG
989	240.92118	55.43676	14.84	8.59	1.10	3.03	ML	128.70	S	iKgs4b	19.00	17.94	15.93	n.d.	0.15	BOSS	HERG
990	240.86578	55.44643	12.50	9.26	2.11	5.28	ML	738.09	S	iKgs8r	23.88	21.06	18.27	n.d.	0.43	BOSS	HERG
991	240.75157	55.29535	11.48	8.90	0.95	2.09	ML	274.79	S	iKgs5r	21.42	19.94	17.88	n.d.	0.28	BOSS	SFG
992	240.73160	55.24819	26.65	18.51	0.82	8.70	ML	14.03	S	iKgs9b	25.62	24.13	20.84	20.52	1.13	HSC	LERG
993	240.67003	55.36374	7.00	3.12	1.18	1.44	ML	179.89	S	iKgs7r	22.84	20.58	18.13	n.d.	0.44	HSC	LERG
994	240.64444	55.23325	10.81	6.80	1.00	1.59	ML	25.79	S	iKgs4r	22.08	20.69	18.83	19.65	0.36	HSC	HERG
995	240.64476	55.37925	11.59	6.05	1.20	1.81	ML	800.19	S	iKgs8r	23.00	21.07	17.96	n.d.	0.48	HSC	SFG
996	240.54908	55.26979	20.23	9.26	3.05	16.70	ML	1.51	S	iKgs0r	25.63	23.42	19.17	19.23	1.28	Dunc	LERG
997	240.51843	55.24007	21.97	15.54	0.98	7.24	ML	26.83	S	iKgs8b	23.64	22.70	19.72	19.05	1.17	HSC	HERG
998	240.50634	55.31429	7.91	6.86	1.47	4.62	ML	8.86	S	iKgs5r	21.68	19.53	17.42	n.d.	0.36	Dunc	LERG
999	240.48895	55.30390	11.32	10.44	3.65	16.24	ML	12.88	S	iKgs5r	21.30	19.29	17.06	n.d.	0.39	HSC	LERG

ID	Properties of Radio Source						Identification Data				Properties of Host Galaxy						
	RA	DEC	Major Axis arcsec	Minor Axis arcsec	Peak Flux mJy	Total Flux mJy	Analysis	LR	Morph	Type	g-band Mag	i-band Mag	K-band Mag	3.6μm Mag	Redshift	Redshift Source	Galaxy Type
1000	240.24794	55.20966	27.52	15.26	1.57	14.22	ML	72.88	S	iKgs9r	25.43	23.16	19.38	19.17	1.15	HSC	LERG
1001	240.24293	55.15289	21.03	12.33	1.29	7.22	ML	34.72	S	iKgs6r	21.41	19.26	16.97	n.d.	0.48	Dunc	LERG
1002	240.23803	55.22553	8.74	6.92	21.43	32.48	ML	38.36	S	iKgs9r	27.03	24.04	20.09	19.69	1.16	Dunc	LERG
1003	240.21548	55.01191	14.60	12.02	1.09	4.15	ML	214.34	S	iKg_3b	20.21	19.14	17.48	n.d.	0.20	HSC	HERG
1004	240.18795	55.29369	24.26	15.33	1.79	14.35	ML	252.97	S	iKgs5r	21.64	19.52	17.36	n.d.	0.40	BOSS	LERG
1005	240.16702	55.21507	9.93	7.69	45.52	82.32	ML	71.22	S	iKgs8r	24.77	22.94	19.87	19.60	1.10	HSC	HERG
1006	240.16134	55.17191	16.38	10.40	1.27	4.67	ML	214.95	S	iKgs3b	19.32	18.14	16.31	n.d.	0.14	BOSS	SFG
1007	240.07336	55.22345	18.87	15.11	1.40	8.64	ML	466.42	S	iKgs7b	21.11	19.72	17.13	n.d.	0.24	Dunc	LERG
1008	240.06370	55.04467	9.62	7.83	33.19	61.28	ML	396.91	S	iKgs7r	23.45	20.83	18.31	n.d.	0.65	BOSS	LERG
1009	240.03060	54.89661	17.63	12.08	1.33	6.13	ML	8.36	S	iKgs2b	18.03	17.06	15.64	n.d.	0.09	Dunc	SFG
1010	244.70264	54.36184	11.15	9.50	0.93	2.08	ML	119.41	S	iKgs7r	25.45	22.66	19.92	19.53	0.82	HSC	LERG
1011	244.36552	55.58548	23.92	8.40	1.71	7.24	ML	30.02	S	iKgs9r	26.64	23.41	20.05	19.80	1.16	HSC	LERG
1012	243.82896	54.55067	10.70	8.56	1.05	2.03	ML	56.68	S	iKgs8r	25.24	22.39	19.26	19.10	1.03	HSC	LERG
1013	243.55002	55.06199	18.01	9.64	0.66	2.44	ML	881.82	S	iKgs6b	19.60	18.79	16.49	n.d.	0.12	Dunc	SFG
1014	243.30854	55.26502	10.93	6.33	1.21	1.77	ML	76.44	S	iKgs8r	25.75	23.05	19.95	19.65	0.94	HSC	LERG
1015	243.21191	56.13761	9.48	5.86	0.91	1.06	ML	354.92	S	iKgs6r	21.30	19.70	17.38	n.d.	0.36	HSC	SFG
1016	242.84744	54.86617	10.58	7.32	0.94	1.54	ML	1312.29	S	iKgs5b	19.49	18.26	16.07	n.d.	0.08	BOSS	SFG
1017	242.60107	53.42854	16.12	9.07	1.32	4.08	ML	490.96	S	iKgs4b	18.50	17.25	15.26	n.d.	0.14	Vacc	LERG
1018	242.41274	56.34965	12.34	9.09	1.11	2.62	ML	346.39	S	iKgs6r	22.39	20.63	18.27	n.d.	0.46	HSC	SFG
1019	241.88347	54.37960	18.98	9.35	1.33	5.00	ML	704.58	S	iKg_6r	21.73	19.44	17.19	n.d.	0.42	BOSS	LERG
1020	241.76148	56.28740	19.27	14.44	1.01	5.95	ML	104.32	S	iKgs8r	23.08	21.18	18.25	n.d.	1.12	HSC	LERG
1021	241.51025	54.04259	18.32	9.45	1.34	4.88	ML	43.15	S	iKgs2b	18.97	18.19	16.59	n.d.	0.12	Dunc	SFG
1022	241.25195	54.23058	10.10	8.36	0.96	1.71	ML	222.17	S	iKgs6r	22.85	20.63	18.33	n.d.	0.64	BOSS	LERG
1023	243.14059	56.22224	10.91	6.06	6.89	15.55	ML	0.31	S	_K_s6k	n.d.	n.d.	22.70	20.71	2.29	Dunc	HERG
1024	241.99101	54.27606	26.48	9.72	7.47	39.23	ML	0.18	S	iKgs9r	27.11	24.31	20.47	19.86	1.38	Dunc	LERG
1025	243.00656	54.00158	13.68	7.05	1.17	2.74	ML	0.36	S	iKgs1r	18.49	16.80	16.42	n.d.	0.85	HSC	LERG
1026	244.16115	54.78294	9.75	7.23	0.88	1.36	ML	0.34	S	_K__6k	n.d.	n.d.	22.60	n.d.	1.71	HSC	LERG
1027	243.54490	54.02712	10.74	6.15	0.99	1.43	ML	11.26	S	_K_s5k	n.d.	n.d.	23.11	n.d.	2.35	HSC	HERG
1028	243.47705	55.72764	14.53	6.78	5.31	11.24	ML	1.52	S	___s__	n.d.	n.d.	n.d.	21.51	2.97	smag	HERG
1029	244.50469	54.45168	5.48	4.58	1.20	0.66	ML	0.62	S	i_g___	23.62	23.33	n.d.	n.d.	1.37	imag	HERG
1030	243.62105	54.98231	13.59	10.40	0.85	2.66	V	n.a.	E	i_gs	25.28	24.44	n.d.	23.10	0.08	BOSS	SFG
1031	243.54345	55.18767	13.55	10.82	0.69	2.22	V	n.a.	E	_Kg_	24.24	n.d.	18.63	n.d.	0.44	HSC	SFG
1032	243.29075	55.37067	9.86	6.81	1.99	4.16	V	n.a.	E	iKgs	19.71	18.75	16.70	n.d.	0.24	SERVS	SFG
1033	242.87136	55.86314	27.64	15.99	6.23	36.50	V	n.a.	E	_Kgs	20.19	n.d.	16.17	n.d.	0.40	HSC	LERG
1034	242.82465	55.56299	32.41	12.26	19.73	117.27	V	n.a.	E	_Kgs	19.87	n.d.	16.05	n.d.	0.18	Kmag	LERG
1035	242.66245	55.13794	14.71	8.78	0.97	2.77	V	n.a.	E	iKgs	25.83	24.75	20.89	20.32	1.49	Dunc	HERG
1036	242.49260	55.00582	57.13	15.54	30.39	133.07	V	n.a.	E	iKgs	23.86	23.77	20.58	20.67	1.37	Kmag	LERG
1037	242.45267	55.28911	12.58	8.84	1.62	3.98	V	n.a.	E	iKgs	20.99	19.13	16.89	n.d.	0.31	BOSS	LERG
1038	242.14299	55.40171	24.45	12.55	0.33	2.25	V	n.a.	E	iKgs	21.65	20.01	18.05	n.d.	0.32	Dunc	LERG
1039	242.06154	55.45019	20.92	9.62	3.10	22.76	V	n.a.	E	iKgs	24.53	20.99	18.29	n.d.	0.80	HSC	LERG

ID	Properties of Radio Source						Identification Data				Properties of Host Galaxy						
	RA	DEC	Major Axis arcsec	Minor Axis arcsec	Peak Flux mJy	Total Flux mJy	Analysis	LR	Morph	Type	g-band Mag	i-band Mag	K-band Mag	3.6μm Mag	Redshift	Redshift Source	Galaxy Type
1040	242.04046	54.78292	48.08	14.02	2.48	57.52	V	n.a.	E	iKgs	21.87	19.68	17.54	n.d.	0.39	BOSS	LERG
1041	241.90197	54.59305	14.39	9.95	9.09	32.49	V	n.a.	E	iKgs	23.33	22.32	19.83	19.72	0.92	Dunc	HERG
1042	241.81775	55.31264	28.71	26.08	0.98	16.92	V	n.a.	E	iKgs	23.55	22.19	19.45	19.11	1.02	Dunc	LERG
1043	241.64695	54.58363	35.99	14.11	6.90	72.63	V	n.a.	E	iKgs	19.66	18.03	15.45	n.d.	0.39	HSC	LERG
1044	241.47141	54.76313	22.62	10.91	3.11	39.04	V	n.a.	E	iKg_	24.16	22.83	22.31	n.d.	2.20	Kmag	HERG
1045	241.40963	54.65621	15.62	9.48	369.23	1445.16	V	n.a.	E	iKgs	20.05	17.25	15.95	n.d.	0.66	HSC	LERG
1046	241.17056	54.64166	19.16	10.66	45.87	172.00	V	n.a.	E	iKgs	26.05	23.49	19.58	19.32	1.13	Dunc	HERG
1047	241.16673	54.52816	14.70	12.44	35.55	133.56	V	n.a.	E	iKg_	20.48	18.65	16.83	n.d.	0.40	HSC	LERG
1048	241.14444	54.57072	18.56	10.91	8.54	43.00	V	n.a.	E	iKgs	20.34	18.55	16.38	n.d.	0.31	Dunc	LERG
1049	241.07616	54.83296	18.72	8.99	11.28	59.05	V	n.a.	E	_K_s	n.d.	n.d.	21.76	21.09	2.02	SERVS	HERG
1050	240.88964	54.48564	25.23	10.15	10.62	69.76	V	n.a.	E	i_g_	21.77	21.84	n.d.	n.d.	0.92	imag	LERG
1051	240.63586	54.90176	13.51	9.36	16.69	50.97	V	n.a.	E	iKgs	24.92	24.23	20.15	19.82	1.52	Dunc	HERG
1052	240.34725	54.89094	14.16	8.94	17.74	66.75	V	n.a.	E	iKgs	24.15	23.39	21.49	20.74	1.62	Dunc	HERG
1053	244.96912	54.92684	21.49	16.36	0.89	6.83	V	n.a.	E	iKg_	20.30	19.31	17.42	n.d.	0.30	Dunc	LERG
1054	244.88657	54.39755	11.40	6.90	7.42	19.43	V	n.a.	E	iKgs	23.52	21.83	19.65	19.71	0.99	Kmag	LERG
1055	244.74758	54.87899	47.89	11.44	26.21	93.92	V	n.a.	E	iKgs	21.63	20.08	18.83	19.61	0.71	Kmag	LERG
1056	244.62730	54.29924	31.49	21.25	1.21	17.74	V	n.a.	E	iKgs	24.26	21.30	18.66	n.d.	0.76	Dunc	LERG
1057	244.53160	54.71003	17.41	8.84	9.55	32.75	V	n.a.	E	iKgs	25.46	23.08	20.36	20.41	1.27	Kmag	HERG
1058	244.52445	54.76069	11.11	7.77	0.91	1.73	V	n.a.	E	iKgs	24.25	22.94	20.11	19.48	1.29	Dunc	HERG
1059	244.48825	54.85373	43.91	11.41	10.75	158.84	V	n.a.	E	iKgs	21.93	21.01	19.29	n.d.	0.79	HSC	HERG
1060	244.46020	54.61309	23.91	9.31	11.42	46.89	V	n.a.	E	iKgs	23.20	20.59	18.29	n.d.	0.69	HSC	LERG
1061	244.19198	55.04252	11.53	9.78	3.97	14.43	V	n.a.	E	iKgs	18.16	17.07	15.63	n.d.	0.08	BOSS	LERG
1062	244.41874	54.20843	19.50	10.13	13.06	74.19	V	n.a.	E	_K__	n.d.	n.d.	20.94	n.d.	1.52	Dunc	LERG
1063	243.75319	54.08400	20.31	13.65	0.45	2.70	V	n.a.	E	iK__	n.d.	18.11	16.57	n.d.	0.07	Vacc	SFG
1064	244.63464	55.61861	10.29	7.80	5.99	10.49	V	n.a.	E	iKgs	26.23	23.28	19.16	n.d.	1.38	Dunc	HERG
1065	244.41519	55.47191	10.42	8.67	1.11	2.19	V	n.a.	E	iKgs	20.18	19.32	17.56	n.d.	0.71	HSC	HERG
1066	244.29221	55.29624	8.76	7.17	70.64	99.47	V	n.a.	E	_K__	n.d.	n.d.	21.13	n.d.	1.62	Kmag	HERG
1067	243.91063	55.33752	17.41	12.36	6.61	33.26	V	n.a.	E	iKgs	22.15	19.93	17.70	n.d.	0.45	HSC	LERG
1068	241.84500	55.51627	47.45	12.09	8.27	96.22	V	n.a.	E	iKgs	24.70	21.79	19.04	19.02	0.83	HSC	LERG
1069	241.84934	55.83527	17.86	5.94	0.65	3.48	V	n.a.	E	iKgs	20.35	18.82	16.07	n.d.	0.20	Dunc	SFG
1070	241.13706	55.51076	15.52	9.71	2.67	15.84	V	n.a.	E	iKgs	19.26	17.45	17.03	n.d.	0.13	Dunc	LERG
1071	240.79934	55.65355	18.25	8.68	4.26	15.98	V	n.a.	E	iKgs	23.73	22.15	19.44	19.14	1.05	Dunc	HERG
1072	243.32013	56.13802	21.97	6.66	17.00	35.77	V	n.a.	E	i_g_	24.29	23.41	n.d.	n.d.	1.40	imag	LERG
1073	243.14639	56.47425	14.61	8.46	667.75	1554.81	V	n.a.	E	_K__	n.d.	n.d.	19.27	n.d.	0.85	Kmag	LERG
1074	242.83531	55.96691	22.12	6.39	1.74	11.91	V	n.a.	E	iKgs	23.80	22.35	19.59	19.24	1.15	Dunc	HERG
1075	245.30945	55.39691	18.42	7.25	274.03	526.77	V	n.a.	E	_K_s	n.d.	n.d.	21.94	21.35	1.89	Dunc	HERG
1076	244.83219	55.59904	22.54	10.36	42.23	160.59	V	n.a.	E	iKgs	19.07	18.39	16.49	n.d.	0.38	Dunc	HERG
1077	242.12772	53.73936	33.05	24.87	5.04	136.06	V	n.a.	E	iKg_	21.19	19.33	17.32	n.d.	1.02	HSC	HERG
1078	241.79675	54.10196	30.79	8.63	3.50	15.07	V	n.a.	E	iKgs	25.13	21.72	18.43	n.d.	0.86	HSC	LERG
1079	241.41399	53.92312	11.58	4.72	1.47	6.32	V	n.a.	E	iKg_	24.25	22.70	22.39	n.d.	2.24	Kmag	AGN

ID	Properties of Radio Source						Identification Data				Properties of Host Galaxy						
	RA	DEC	Major Axis arcsec	Minor Axis arcsec	Peak Flux mJy	Total Flux mJy	Analysis	LR	Morph	Type	g-band Mag	i-band Mag	K-band Mag	$3.6\mu m$ Mag	Redshift	Redshift Source	Galaxy Type
1080	243.64007	54.24009	16.88	8.12	3.37	16.86	V	n.a.	E	iK_s	n.d.	23.71	20.12	19.63	1.18	HSC	LERG
1081	243.55344	54.71252	21.98	7.94	5.76	34.81	V	n.a.	E	iKgs	20.85	19.31	17.73	n.d.	0.36	Dunc	LERG
1082	243.51019	54.73905	28.45	10.74	30.65	174.86	V	n.a.	E	iKgs	21.33	19.35	16.99	n.d.	6.54	BOSS	LERG
1083	243.33149	54.17670	21.14	7.69	3.37	17.35	V	n.a.	E	iKgs	24.30	22.00	20.88	21.52	1.57	HSC	HERG
1084	243.12954	54.30081	10.21	5.80	40.84	63.59	V	n.a.	E	iKgs	29.99	24.81	20.72	20.13	1.60	Dunc	LERG
1085	242.66771	54.10844	19.78	8.32	5.54	19.97	V	n.a.	E	iKgs	22.29	20.03	17.13	n.d.	0.40	HSC	LERG
1086	242.43498	54.62973	12.59	8.35	7.33	23.72	V	n.a.	E	iKgs	24.11	21.57	18.52	n.d.	0.86	Dunc	LERG
1087	240.64867	55.77778	10.12	9.35	44.19	88.36	V	n.a.	E	iKgs	24.61	23.46	21.96	20.83	2.03	Kmag	HERG
1088	244.72831	55.14577	12.05	8.39	0.98	2.08	V	n.a.	E	_K__	n.d.	n.d.	21.80	n.d.	1.20	Dunc	LERG
1089	241.32599	54.87778	10.69	5.44	1.29	1.58	V	n.a.	E	iKgs	24.37	23.88	20.81	20.55	2.14	Dunc	HERG
1090	241.28270	55.19448	26.05	20.17	0.98	10.85	V	n.a.	E	iKgs	24.06	21.31	18.26	n.d.	0.76	Dunc	LERG
1091	240.91810	55.72543	38.19	12.85	3.60	42.21	V	n.a.	E	iKgs	26.98	25.35	20.03	18.17	1.31	Dunc	LERG
1092	243.28858	55.36904	9.86	6.81	1.99	4.16	V	n.a.	E	iKgs	18.40	17.59	16.07	n.d.	0.08	BOSS	HERG
1093	242.83021	55.56525	32.41	12.26	4.93	29.32	V	n.a.	E	iKgs	20.05	18.60	16.06	n.d.	0.28	Dunc	HERG
1094	242.14285	55.40039	24.45	12.55	0.33	2.25	V	n.a.	E	_K_s	n.d.	n.d.	19.20	19.97	0.34	HSC	LERG
1095	244.18852	55.04193	11.53	9.78	0.99	3.61	V	n.a.	E	iKgs	19.04	17.65	15.26	n.d.	0.08	BOSS	SFG
1096	243.75037	54.08182	20.31	13.65	0.30	1.80	V	n.a.	E	iKgs	20.45	19.00	17.11	n.d.	0.19	Dunc	SFG
1097	241.84225	55.83459	17.86	5.94	0.65	3.48	V	n.a.	E	iKgs	20.58	19.19	17.00	n.d.	0.23	Dunc	SFG
1098	241.13825	55.50656	15.52	9.71	1.33	7.92	V	n.a.	E	iKgs	22.03	21.10	19.85	20.50	0.36	HSC	LERG
1099	244.71288	55.14181	12.05	8.39	0.98	2.08	V	n.a.	E	iKg_	21.43	19.95	17.77	n.d.	0.35	HSC	HERG
1100	242.69191	56.54966	10.90	6.21	1.70	2.80	V	0.11	E	i_gs	19.99	19.58	n.d.	n.d.	2.98	Vacc	HERG
1101	241.12224	54.72652	9.80	5.15	1.36	1.57	V	n.a.	E	iKgs1b	18.94	18.60	18.15	n.d.	0.61	Dunc	HERG
1102	244.87902	54.52277	19.38	5.45	2.87	3.09	V	n.a.	E	iKgs8r	24.45	22.22	19.14	n.d.	0.99	Dunc	LERG
1103	244.39959	55.71555	11.67	10.31	1.71	4.49	V	n.a.	E	iKgs7r	23.66	21.10	18.58	n.d.	0.74	Dunc	LERG
1104	242.00873	55.89916	18.36	12.46	0.91	4.45	V	n.a.	E	i_____	n.d.	21.07	n.d.	n.d.	0.70	imag	LERG
1105	241.27124	55.87222	24.49	13.52	0.89	6.32	V	n.a.	E	iKgs9b	25.87	25.03	21.40	21.30	1.75	Kmag	HERG
1106	241.02141	55.77225	20.75	14.19	1.21	26.37	V	n.a.	E	iKgs4r	22.11	19.95	17.99	n.d.	0.42	Dunc	LERG
1107	243.03434	56.00723	8.87	6.16	1.27	8.36	V	n.a.	E	iKgs4b	19.93	19.33	17.41	n.d.	0.38	HSC	LERG
1108	245.46344	55.05446	16.70	11.24	3.33	24.48	V	n.a.	E	iKg_5r	20.58	18.74	16.60	n.d.	0.27	Dunc	LERG
1109	243.49481	53.63582	17.70	9.20	0.97	3.27	V	n.a.	E	iKg_2r	25.19	23.58	21.99	n.d.	2.04	Kmag	LERG
1110	242.42895	55.57916	5.84	2.91	0.77	1.24	V	n.a.	E	i_gs4b	24.76	24.20	n.d.	n.d.	1.14	Dunc	HERG
1111	243.33970	53.71821	16.80	10.05	4.26	22.55	V	n.a.	E	iKgs6r	22.04	19.82	17.47	n.d.	0.38	Dunc	LERG
1112	244.67208	54.26807	19.36	11.21	1.16	5.49	V	n.a.	E	iKgs1r	21.49	19.00	18.11	n.d.	0.41	Dunc	LERG
1113	243.32713	55.78962	7.67	6.60	6.12	6.76	V	n.a.	E	iKgs1r	22.42	20.06	19.20	19.59	0.83	Kmag	LERG
1114	241.03033	55.57267	14.66	7.44	3.91	14.36	V	n.a.	E	iKgs5b	20.97	20.56	18.49	n.d.	0.61	Kmag	HERG
1115	243.39737	54.18715	22.99	9.64	3.38	22.94	V	n.a.	E	iKgs2r	21.75	20.07	18.43	19.29	0.60	Kmag	LERG
1116	243.05111	53.88519	12.26	3.38	0.82	2.09	V	n.a.	E	_K__8k	n.d.	n.d.	22.05	n.d.	1.24	Dunc	LERG
1117	243.47646	55.30904	22.39	21.12	0.98	10.28	V	n.a.	E	iKgs	22.96	21.74	19.61	19.68	0.72	Dunc	LERG
1118	244.35364	55.55935	10.13	6.57	1.09	4.36	V	n.a.	E	iKg_	26.11	23.06	20.95	n.d.	0.79	HSC	LERG
1119	240.24973	54.81510	30.95	15.91	1.06	11.98	V	n.a.	E	iKgs	24.68	22.41	19.33	19.36	1.00	Dunc	HERG

ID	Properties of Radio Source						Identification Data				Properties of Host Galaxy						
	RA	DEC	Major Axis arcsec	Minor Axis arcsec	Peak Flux mJy	Total Flux mJy	Analysis	LR	Morph	Type	g-band Mag	i-band Mag	K-band Mag	3.6μm Mag	Redshift	Redshift Source	Galaxy Type
1120	242.02652	56.06119	20.83	10.99	1.07	5.25	V	n.a.	E	iKgs	24.38	23.34	19.34	n.d.	0.69	HSC	HERG
1121	241.22138	55.77566	12.95	8.16	1.18	8.18	V	n.a.	E	iKgs	22.56	21.40	19.86	19.98	0.60	HSC	LERG
1122	243.36585	55.26311	26.14	11.17	18.18	96.59	V	n.a.	CD	iKgs	24.01	21.25	18.76	n.d.	0.68	BOSS	LERG
1123	243.20476	55.04423	13.42	8.63	12.48	39.72	V	n.a.	CD	iKgs	22.22	19.84	17.54	n.d.	0.49	Vacc	HERG
1124	242.96281	55.01491	63.14	11.41	3.40	25.54	V	n.a.	CD	iKgs	19.74	18.20	16.00	n.d.	0.38	HSC	LERG
1125	242.83209	55.47959	13.34	6.19	76.87	123.81	V	n.a.	CD	_K_s	n.d.	n.d.	21.31	20.51	1.21	Dunc	HERG
1126	242.54382	55.59794	7.76	6.05	0.91	0.94	V	n.a.	CD	iKgs	25.70	22.98	20.08	19.98	1.11	HSC	HERG
1127	242.33508	53.61410	18.09	8.33	23.54	66.83	V	n.a.	CD	iKgs	22.52	22.21	21.35	20.38	1.18	HSC	HERG
1128	242.23628	53.57996	17.49	8.71	8.56	28.97	V	n.a.	CD	iKgs	24.94	21.87	19.03	n.d.	0.90	Dunc	LERG
1129	242.33450	54.72998	22.31	6.68	1.16	10.01	V	n.a.	CD	iKgs	24.33	22.65	19.45	19.20	1.11	Dunc	HERG
1130	242.20913	54.89741	15.97	9.10	1.49	14.68	V	n.a.	CD	iKgs	25.23	21.99	19.40	19.25	0.85	Dunc	LERG
1131	241.34193	54.49087	19.41	9.18	10.10	36.57	V	n.a.	CD	iKgs	21.46	19.39	17.36	n.d.	0.33	HSC	LERG
1132	241.27149	55.01262	27.18	12.69	51.32	480.89	V	n.a.	CD	iKgs	24.86	22.22	19.14	19.19	0.93	HSC	LERG
1133	240.41941	54.92199	49.30	27.44	15.26	568.27	V	n.a.	CD	iKgs	22.91	20.69	19.02	19.77	0.77	Kmag	LERG
1134	240.11920	54.60967	23.75	11.09	4.78	31.42	V	n.a.	CD	iKgs	20.77	18.95	17.05	n.d.	0.21	Dunc	LERG
1135	245.19659	54.84357	47.70	11.31	16.39	137.05	V	n.a.	CD	iKgs	23.39	22.32	19.39	n.d.	0.89	Kmag	HERG
1136	244.63755	54.52960	26.37	8.93	85.10	293.01	V	n.a.	CD	iKgs	24.08	21.26	18.84	n.d.	0.75	BOSS	LERG
1137	244.61896	54.90460	7.95	6.47	1.84	2.08	V	n.a.	CD	iK_s	n.d.	24.75	20.03	19.47	1.13	Kmag	HERG
1138	244.30761	55.13689	20.23	11.60	1.23	6.34	V	n.a.	CD	_K_s	n.d.	n.d.	19.85	19.25	1.06	Kmag	LERG
1139	244.18088	56.05932	21.58	12.33	7.19	48.26	V	n.a.	CD	iKgs	21.10	19.17	16.99	n.d.	0.34	Dunc	LERG
1140	244.16936	55.67132	29.93	9.92	28.05	157.22	V	n.a.	CD	iKgs	20.59	18.57	16.35	n.d.	0.33	Dunc	LERG
1141	243.58979	55.61425	20.90	8.91	50.29	206.10	V	n.a.	CD	iKgs	25.39	23.19	19.60	19.29	0.40	HSC	LERG
1142	242.99939	55.95555	27.59	15.09	9.41	100.68	V	n.a.	CD	iKgs	20.51	18.63	16.24	n.d.	0.22	Dunc	LERG
1143	242.22361	55.93725	68.15	15.65	6.31	59.40	V	n.a.	CD	iKgs	20.70	18.92	16.35	n.d.	0.25	Dunc	LERG
1144	240.95224	55.71134	44.21	16.52	5.95	66.25	V	n.a.	CD	iKgs	24.87	22.22	19.19	19.02	0.93	Dunc	LERG
1145	240.91803	55.72543	37.52	10.77	3.11	36.16	V	n.a.	CD	iKgs	26.98	25.35	21.88	21.00	1.99	Kmag	LERG
1146	242.70470	56.29016	20.16	7.98	1.55	13.61	V	n.a.	CD	iKgs	20.76	18.97	17.08	n.d.	0.33	Dunc	LERG
1147	242.19933	54.08864	38.94	15.30	17.72	126.83	V	n.a.	CD	iKg_	26.03	23.07	19.37	n.d.	0.89	Kmag	LERG
1148	242.59564	54.50267	20.20	7.05	20.09	49.09	V	n.a.	CD	iKg_	26.36	25.74	20.79	n.d.	1.28	HSC	HERG
1149	240.59361	55.51785	17.98	6.92	1.77	17.03	V	n.a.	CD	iKgs	23.53	21.10	19.44	19.54	0.91	Kmag	LERG
1150	243.47463	55.03146	19.36	17.18	2.88	26.41	V	n.a.	D_centre	iKgs	22.54	20.23	17.97	n.d.	0.54	Vacc	LERG
1151	243.49230	55.03948	19.36	17.18	1.65	12.10	V	n.a.	D_lobe1	n.a.	n.d.	n.d.	n.d.	n.d.	n.a.	n.a.	BLANK
1152	243.45609	55.02877	26.45	19.78	1.24	14.31	V	n.a.	D_lobe2	n.a.	n.d.	n.d.	n.d.	n.d.	n.a.	n.a.	BLANK
1153	243.05121	55.38490	8.15	6.75	2431.75	2987.45	V	n.a.	D_centre	iKgs	23.73	22.39	19.73	19.76	0.23	BOSS	LERG
1154	243.05185	55.38570	8.15	6.75	1788.91	2228.82	V	n.a.	D_lobe1	n.a.	n.d.	n.d.	n.d.	n.d.	n.a.	n.a.	BLANK
1155	243.04987	55.38056	7.70	6.93	642.84	758.63	V	n.a.	D_lobe2	n.a.	n.d.	n.d.	n.d.	n.d.	n.a.	n.a.	BLANK
1156	242.93091	55.79503	23.66	15.80	17.16	70.59	V	n.a.	D_centre	iKgs	25.45	22.99	19.83	19.63	1.08	HSC	LERG
1157	242.93698	55.80457	23.66	15.80	1.25	10.36	V	n.a.	D_lobe1	n.a.	n.d.	n.d.	n.d.	n.d.	n.a.	n.a.	BLANK
1158	242.92830	55.79088	14.44	9.94	15.91	60.24	V	n.a.	D_lobe2	n.a.	n.d.	n.d.	n.d.	n.d.	n.a.	n.a.	BLANK
1159	242.34111	55.71591	10.79	7.38	25.52	49.33	V	n.a.	D_centre	iKgs	26.17	25.73	21.85	21.08	1.85	Dunc	LERG

ID	Properties of Radio Source						Identification Data				Properties of Host Galaxy						
	RA	DEC	Major Axis arcsec	Minor Axis arcsec	Peak Flux mJy	Total Flux mJy	Analysis	LR	Morph	Type	g-band Mag	i-band Mag	K-band Mag	3.6μm Mag	Redshift	Redshift Source	Galaxy Type
1160	242.34935	55.71657	10.79	7.38	18.70	36.69	V	n.a.	D_lobe1	n.a.	n.d.	n.d.	n.d.	n.d.	n.a.	n.a.	BLANK
1161	242.33588	55.71598	10.13	8.28	6.82	12.64	V	n.a.	D_lobe2	n.a.	n.d.	n.d.	n.d.	n.d.	n.a.	n.a.	BLANK
1162	242.24023	53.59511	19.29	14.38	6.05	37.05	V	n.a.	D_centre	iKgs	24.80	21.78	18.92	n.d.	0.91	HSC	LERG
1163	242.25528	53.59430	19.29	14.38	1.92	11.30	V	n.a.	D_lobe1	n.a.	n.d.	n.d.	n.d.	n.d.	n.a.	n.a.	BLANK
1164	242.22896	53.59665	15.74	10.28	4.14	25.74	V	n.a.	D_lobe2	n.a.	n.d.	n.d.	n.d.	n.d.	n.a.	n.a.	BLANK
1165	242.14067	54.58137	16.87	10.69	19.33	69.83	V	n.a.	D_centre	iKg_	23.48	21.89	19.88	n.d.	0.91	BOSS	LERG
1166	242.14959	54.57230	16.87	10.69	8.79	44.61	V	n.a.	D_lobe1	n.a.	n.d.	n.d.	n.d.	n.d.	n.a.	n.a.	BLANK
1167	242.12736	54.59374	50.75	9.07	10.54	25.22	V	n.a.	D_lobe2	n.a.	n.d.	n.d.	n.d.	n.d.	n.a.	n.a.	BLANK
1168	241.88290	54.85258	10.71	7.43	4.18	22.36	V	n.a.	D_centre	iKgs	25.70	25.28	21.96	21.02	1.14	HSC	LERG
1169	241.88354	54.85351	10.71	7.43	2.90	9.87	V	n.a.	D_lobe1	n.a.	n.d.	n.d.	n.d.	n.d.	n.a.	n.a.	BLANK
1170	241.87976	54.84864	22.17	19.19	1.28	12.49	V	n.a.	D_lobe2	n.a.	n.d.	n.d.	n.d.	n.d.	n.a.	n.a.	BLANK
1171	241.89263	56.41245	9.69	7.43	189.74	405.61	V	n.a.	D_centre	iKgs	25.28	24.30	20.19	19.65	1.73	Dunc	HERG
1172	241.90224	56.41178	9.69	7.43	68.51	120.02	V	n.a.	D_lobe1	n.a.	n.d.	n.d.	n.d.	n.d.	n.a.	n.a.	BLANK
1173	241.88505	56.41203	15.06	12.54	121.23	285.59	V	n.a.	D_lobe2	n.a.	n.d.	n.d.	n.d.	n.d.	n.a.	n.a.	BLANK
1174	241.71153	55.97044	18.34	14.03	7.02	13.78	V	n.a.	D_centre	iKgs	22.16	21.36	20.45	21.13	0.36	BOSS	LERG
1175	241.71178	55.97364	18.34	14.03	1.09	6.01	V	n.a.	D_lobe1	n.a.	n.d.	n.d.	n.d.	n.d.	n.a.	n.a.	BLANK
1176	241.70988	55.96817	9.45	6.45	5.94	7.77	V	n.a.	D_lobe2	n.a.	n.d.	n.d.	n.d.	n.d.	n.a.	n.a.	BLANK
1177	240.64959	55.17382	18.20	13.48	3.70	26.69	V	n.a.	D_centre	iKgs	20.32	18.48	15.99	n.d.	0.26	BOSS	LERG
1178	240.66305	55.17353	18.20	13.48	2.45	27.77	V	n.a.	D_lobe1	n.a.	n.d.	n.d.	n.d.	n.d.	n.a.	n.a.	BLANK
1179	240.63067	55.17345	15.54	13.61	2.56	11.68	V	n.a.	D_lobe2	n.a.	n.d.	n.d.	n.d.	n.d.	n.a.	n.a.	BLANK
1180	244.81853	55.08234	20.99	10.42	28.78	106.97	V	n.a.	D_centre	iKgs	23.56	21.79	19.31	n.d.	0.88	BOSS	HERG
1181	244.82473	55.07525	20.99	10.42	16.33	58.02	V	n.a.	D_lobe1	n.a.	n.d.	n.d.	n.d.	n.d.	n.a.	n.a.	BLANK
1182	244.81495	55.08631	14.19	10.88	12.45	48.96	V	n.a.	D_lobe2	n.a.	n.d.	n.d.	n.d.	n.d.	n.a.	n.a.	BLANK
1183	241.67264	55.86801	9.26	6.76	29.60	42.98	V	n.a.	D_centre	iKgs	24.21	23.81	21.79	21.40	1.03	HSC	LERG
1184	241.67792	55.86972	9.26	6.76	19.68	29.41	V	n.a.	D_lobe1	n.a.	n.d.	n.d.	n.d.	n.d.	n.a.	n.a.	BLANK
1185	241.66599	55.86345	8.19	6.32	9.92	13.57	V	n.a.	D_lobe2	n.a.	n.d.	n.d.	n.d.	n.d.	n.a.	n.a.	BLANK
1186	242.41933	56.03599	8.41	7.38	4.58	14.68	V	n.a.	D_centre	iKgs	24.63	21.76	18.93	19.11	0.84	HSC	LERG
1187	242.36835	56.04987	14.49	9.39	2.02	10.80	V	n.a.	D_lobe1	n.a.	n.d.	n.d.	n.d.	n.d.	n.a.	n.a.	BLANK
1188	242.46569	56.02939	8.41	7.38	2.56	3.88	V	n.a.	D_lobe2	n.a.	n.d.	n.d.	n.d.	n.d.	n.a.	n.a.	BLANK
1189	241.70066	54.25226	16.33	12.50	7.90	53.08	V	n.a.	D_centre	iKgs	27.24	24.28	20.35	19.97	1.57	Dunc	LERG
1190	241.71280	54.24783	16.33	12.50	2.38	17.51	V	n.a.	D_lobe1	n.a.	n.d.	n.d.	n.d.	n.d.	n.a.	n.a.	BLANK
1191	241.69479	54.25284	17.40	11.28	5.52	35.57	V	n.a.	D_lobe2	n.a.	n.d.	n.d.	n.d.	n.d.	n.a.	n.a.	BLANK
1192	243.37903	54.06688	15.71	12.16	5.26	29.17	V	n.a.	D_centre	iKg_	26.00	23.25	20.26	n.d.	1.19	HSC	LERG
1193	243.38449	54.06494	15.71	12.16	3.41	15.83	V	n.a.	D_lobe1	n.a.	n.d.	n.d.	n.d.	n.d.	n.a.	n.a.	BLANK
1194	243.36548	54.06822	20.62	14.40	1.85	13.34	V	n.a.	D_lobe2	n.a.	n.d.	n.d.	n.d.	n.d.	n.a.	n.a.	BLANK
1195	243.51282	55.67991	10.50	7.60	20.99	47.35	V	n.a.	D_centre	iKgs	19.57	19.73	18.50	n.d.	0.62	Kmag	HERG
1196	243.51310	55.68205	10.50	7.60	13.59	29.20	V	n.a.	D_lobe1	n.a.	n.d.	n.d.	n.d.	n.d.	n.a.	n.a.	BLANK
1197	243.50521	55.67791	10.25	7.87	7.40	18.16	V	n.a.	D_lobe2	n.a.	n.d.	n.d.	n.d.	n.d.	n.a.	n.a.	BLANK
1198	242.58688	54.02890	14.00	9.96	3.39	6.15	V	n.a.	D_centre	___s	n.d.	n.d.	n.d.	20.81	0.41	HSC	LERG
1199	242.61967	54.02377	14.00	9.96	1.33	3.94	V	n.a.	D_lobe1	n.a.	n.d.	n.d.	n.d.	n.d.	n.a.	n.a.	BLANK

ID	Properties of Radio Source						Identification Data				Properties of Host Galaxy						
	RA	DEC	Major Axis arcsec	Minor Axis arcsec	Peak Flux mJy	Total Flux mJy	Analysis	LR	Morph	Type	g-band Mag	i-band Mag	K-band Mag	3.6μm Mag	Redshift	Redshift Source	Galaxy Type
1200	242.56909	54.02917	8.45	5.97	2.06	2.21	V	n.a.	D_lobe2	n.a.	n.d.	n.d.	n.d.	n.d.	n.a.	n.a.	BLANK
1201	242.00292	54.36451	11.63	9.06	3.12	14.09	V	n.a.	D_centre	iKgs	22.07	19.83	17.62	n.d.	0.47	BOSS	LERG
1202	242.00392	54.36172	11.63	9.06	2.20	10.40	V	n.a.	D_lobe1	n.a.	n.d.	n.d.	n.d.	n.d.	n.a.	n.a.	BLANK
1203	241.99927	54.36972	14.94	11.71	0.92	3.69	V	n.a.	D_lobe2	n.a.	n.d.	n.d.	n.d.	n.d.	n.a.	n.a.	BLANK
1204	244.60006	54.50455	11.84	7.65	4.71	18.37	V	n.a.	D_centre	iKgs	22.68	20.14	17.58	n.d.	0.52	HSC	LERG
1205	244.61340	54.50990	11.84	7.65	2.66	10.97	V	n.a.	D_lobe1	n.a.	n.d.	n.d.	n.d.	n.d.	n.a.	n.a.	BLANK
1206	244.58979	54.50138	14.03	11.78	2.04	7.39	V	n.a.	D_lobe2	n.a.	n.d.	n.d.	n.d.	n.d.	n.a.	n.a.	BLANK
1207	244.23232	54.92947	36.66	20.11	2.16	20.57	V	n.a.	D_centre	iKgs	21.92	21.31	19.86	20.02	1.07	Kmag	LERG
1208	244.26981	54.93109	36.66	20.11	0.95	15.32	V	n.a.	D_lobe1	n.a.	n.d.	n.d.	n.d.	n.d.	n.a.	n.a.	BLANK
1209	244.19900	54.92790	17.05	11.64	1.21	5.26	V	n.a.	D_lobe2	n.a.	n.d.	n.d.	n.d.	n.d.	n.a.	n.a.	BLANK
1210	243.65345	55.70640	7.42	6.33	6.58	11.75	V	n.a.	D_centre	iKgs	23.16	21.59	18.60	n.d.	0.90	HSC	LERG
1211	243.67851	55.70486	7.42	6.33	2.67	3.11	V	n.a.	D_lobe1	n.a.	n.d.	n.d.	n.d.	n.d.	n.a.	n.a.	BLANK
1212	243.64164	55.70835	12.03	7.21	3.91	8.64	V	n.a.	D_lobe2	n.a.	n.d.	n.d.	n.d.	n.d.	n.a.	n.a.	BLANK
1213	242.15525	55.75345	23.14	14.86	5.14	30.28	V	n.a.	D_centre	iKgs	22.85	20.36	18.05	n.d.	0.55	BOSS	HERG
1214	242.15928	55.74544	23.14	14.86	1.68	12.39	V	n.a.	D_lobe1	n.a.	n.d.	n.d.	n.d.	n.d.	n.a.	n.a.	BLANK
1215	242.15215	55.75925	18.19	9.41	3.46	17.89	V	n.a.	D_lobe2	n.a.	n.d.	n.d.	n.d.	n.d.	n.a.	n.a.	BLANK
1216	245.31067	55.30483	19.23	11.89	15.55	118.82	V	n.a.	D_centre	iKgs	23.27	20.81	18.90	19.12	0.59	HSC	LERG
1217	245.31777	55.29985	19.23	11.89	13.66	88.96	V	n.a.	D_lobe1	n.a.	n.d.	n.d.	n.d.	n.d.	n.a.	n.a.	BLANK
1218	245.28246	55.32575	28.87	24.74	1.89	29.86	V	n.a.	D_lobe2	n.a.	n.d.	n.d.	n.d.	n.d.	n.a.	n.a.	BLANK
1219	245.16691	55.28826	8.57	7.76	20.21	35.69	V	n.a.	D_centre	iKgs	25.42	24.56	21.15	20.79	0.86	HSC	HERG
1220	245.16829	55.29735	8.57	7.76	14.46	25.31	V	n.a.	D_lobe1	n.a.	n.d.	n.d.	n.d.	n.d.	n.a.	n.a.	BLANK
1221	245.16461	55.28340	10.11	8.06	5.76	10.39	V	n.a.	D_lobe2	n.a.	n.d.	n.d.	n.d.	n.d.	n.a.	n.a.	BLANK
1222	243.59188	54.53836	24.29	18.02	1.88	29.15	V	n.a.	D_centre	iKgs	20.23	18.55	15.91	n.d.	0.27	BOSS	LERG
1223	243.60602	54.53837	24.29	18.02	0.82	8.69	V	n.a.	D_lobe1	n.a.	n.d.	n.d.	n.d.	n.d.	n.a.	n.a.	BLANK
1224	243.58759	54.53827	36.31	25.05	1.07	20.45	V	n.a.	D_lobe2	n.a.	n.d.	n.d.	n.d.	n.d.	n.a.	n.a.	BLANK
1225	242.81558	54.54368	16.92	7.85	13.96	48.80	V	n.a.	D_centre	iKgs	19.67	17.77	17.31	n.d.	0.19	Dunc	LERG
1226	242.83682	54.52950	18.06	7.79	8.83	28.49	V	n.a.	D_lobe1	n.a.	n.d.	n.d.	n.d.	n.d.	n.a.	n.a.	BLANK
1227	242.80322	54.55479	16.92	7.85	5.12	20.31	V	n.a.	D_lobe2	n.a.	n.d.	n.d.	n.d.	n.d.	n.a.	n.a.	BLANK
1228	242.26592	56.17881	13.86	9.16	121.15	417.58	V	n.a.	D_centre	iKgs	21.21	20.38	19.30	n.d.	1.02	Dunc	HERG
1229	242.26592	56.17881	13.86	9.16	29.98	106.81	V	n.a.	D_lobe1	n.a.	n.d.	n.d.	n.d.	n.d.	n.a.	n.a.	BLANK
1230	242.19766	56.18839	23.01	10.97	91.17	310.77	V	n.a.	D_lobe2	n.a.	n.d.	n.d.	n.d.	n.d.	n.a.	n.a.	BLANK
1231	242.42394	54.60656	19.45	15.77	2.14	8.05	V	n.a.	D_centre	iKgs	23.58	21.04	20.30	20.93	0.78	HSC	LERG
1232	242.43094	54.61201	19.45	15.77	0.82	6.10	V	n.a.	D_lobe1	n.a.	n.d.	n.d.	n.d.	n.d.	n.a.	n.a.	BLANK
1233	242.41424	54.60155	9.96	7.04	1.32	1.95	V	n.a.	D_lobe2	n.a.	n.d.	n.d.	n.d.	n.d.	n.a.	n.a.	BLANK
1234	243.46923	56.26653	7.10	5.14	11.74	30.43	V	n.a.	T_centre	iKgs	19.84	17.93	15.68	n.d.	0.18	BOSS	LERG
1235	243.51569	56.33059	20.07	17.41	1.30	11.04	V	n.a.	T_lobe1	n.a.	n.d.	n.d.	n.d.	n.d.	n.a.	n.a.	BLANK
1236	243.42262	56.19823	18.42	15.59	1.26	8.82	V	n.a.	T_lobe2	n.a.	n.d.	n.d.	n.d.	n.d.	n.a.	n.a.	BLANK
1237	242.81661	55.62896	7.80	6.23	1.30	1.39	MLV	0.00	SX	i_g_	30.27	25.26	n.d.	n.d.	n.a.	n.a.	BLANK
1238	242.41192	55.82553	13.08	11.31	4.60	15.03	MLV	0.00	SX	iKgs	27.51	22.88	20.59	20.72	n.a.	n.a.	BLANK
1239	242.40224	55.45123	18.58	10.34	15.61	51.30	MLV	n.a.	SX	___s	n.d.	n.d.	n.d.	19.79	n.a.	n.a.	BLANK

ID	Properties of Radio Source						Identification Data				Properties of Host Galaxy						
	RA	DEC	Major Axis arcsec	Minor Axis arcsec	Peak Flux mJy	Total Flux mJy	Analysis	LR	Morph	Type	g-band Mag	i-band Mag	K-band Mag	$3.6\mu m$ Mag	Redshift	Redshift Source	Galaxy Type
1240	242.18336	55.30524	11.46	7.56	1.39	2.65	MLV	0.00	SX	i___	n.d.	25.65	n.d.	n.d.	n.a.	n.a.	BLANK
1241	243.23796	53.42025	8.21	7.16	6.79	11.14	MLV	0.00	SX	i_g_	24.85	24.45	n.d.	n.d.	n.a.	n.a.	BLANK
1242	241.09133	55.09593	10.29	9.46	80.49	199.71	MLV	0.00	SX	i_g_	24.24	23.82	n.d.	n.d.	n.a.	n.a.	BLANK
1243	240.91704	54.85744	7.88	7.66	2.62	9.63	MLV	0.01	SX	i___	n.d.	25.65	n.d.	n.d.	n.a.	n.a.	BLANK
1244	240.81656	54.53327	11.65	10.42	21.61	64.61	MLV	0.01	SX	i_gs	26.94	24.21	n.d.	21.03	n.a.	n.a.	BLANK
1245	245.14008	54.72343	7.79	6.86	13.65	20.22	MLV	0.00	SX	iKgs	21.22	20.18	19.23	19.94	n.a.	n.a.	BLANK
1246	245.06112	54.59257	8.98	8.51	2.68	4.48	MLV	0.00	SX	iKgs	19.57	18.30	18.17	n.d.	n.a.	n.a.	BLANK
1247	244.84432	54.49590	9.18	6.78	2.05	2.80	MLV	0.00	SX	iKgs	21.08	19.80	17.82	n.d.	n.a.	n.a.	BLANK
1248	244.14148	54.59192	9.42	5.08	0.82	0.85	MLV	0.00	SX	i_g_	25.53	24.30	n.d.	n.d.	n.a.	n.a.	BLANK
1249	243.85372	54.24355	7.71	5.12	1.40	2.65	MLV	0.00	SX	iKgs	21.38	18.88	17.92	n.d.	n.a.	n.a.	BLANK
1250	243.54259	54.06438	12.77	10.14	15.64	48.04	MLV	0.01	SX	iKgs	25.30	22.48	20.17	19.98	n.a.	n.a.	BLANK
1251	244.57431	55.71960	7.88	6.25	12.23	15.92	MLV	0.00	SX	_K_s	n.d.	n.d.	22.52	21.19	n.a.	n.a.	BLANK
1252	244.27992	55.46586	9.50	6.78	1.54	2.17	MLV	0.00	SX	iKg_	23.47	22.37	21.53	n.d.	n.a.	n.a.	BLANK
1253	244.11416	55.60182	9.82	6.01	2.69	3.47	MLV	0.01	SX	iKg_	24.26	23.10	22.03	n.d.	n.a.	n.a.	BLANK
1254	243.91715	55.50894	6.32	6.00	2.04	1.69	MLV	0.00	SX	i_g_	25.26	24.59	n.d.	n.d.	n.a.	n.a.	BLANK
1255	243.84502	55.74764	11.61	7.08	2.28	4.09	MLV	0.00	SX	i___	n.d.	26.14	n.d.	n.d.	n.a.	n.a.	BLANK
1256	243.35416	55.65814	8.74	6.88	22.98	30.16	MLV	0.00	SX	i_g_	25.25	24.47	n.d.	n.d.	n.a.	n.a.	BLANK
1257	241.93658	55.81138	8.65	6.20	41.51	54.56	MLV	0.00	SX	iKgs	19.95	17.42	16.46	n.d.	n.a.	n.a.	BLANK
1258	241.25332	55.49794	11.95	8.61	1.40	3.10	MLV	0.00	SX	i_g_	28.14	25.47	n.d.	n.d.	n.a.	n.a.	BLANK
1259	243.29742	56.30086	8.03	6.02	1.44	1.70	MLV	0.02	SX	iKg_	23.17	22.34	21.35	n.d.	n.a.	n.a.	BLANK
1260	242.72334	56.52983	10.90	6.21	1.70	2.80	MLV	0.11	SX	_K__	n.d.	n.d.	21.96	n.d.	n.a.	n.a.	BLANK
1261	244.82195	55.65129	9.69	8.33	4.77	8.53	MLV	0.00	SX	i_g_	25.70	24.13	n.d.	n.d.	n.a.	n.a.	BLANK
1262	242.00695	54.34090	16.60	12.41	11.56	59.15	MLV	0.00	SX	iKgs	24.94	21.90	18.95	n.d.	n.a.	n.a.	BLANK
1263	243.79731	54.58848	13.57	7.83	1.53	3.94	MLV	0.00	SX	iKg_	24.23	22.96	21.72	n.d.	n.a.	n.a.	BLANK
1264	243.62762	54.42763	10.57	7.40	2.24	8.48	MLV	0.00	SX	iKg_	22.42	21.05	20.08	n.d.	n.a.	n.a.	BLANK
1265	243.54584	54.19382	5.93	5.10	1.03	0.76	MLV	0.19	SX	_K__	n.d.	n.d.	21.60	n.d.	n.a.	n.a.	BLANK
1266	242.38635	54.34119	15.46	7.91	1.05	15.59	MLV	0.00	SX	__g_	25.51	n.d.	n.d.	n.d.	n.a.	n.a.	BLANK
1267	240.73067	55.38897	7.92	4.48	1.14	0.87	MLV	0.01	SX	i_g_	25.31	24.18	n.d.	n.d.	n.a.	n.a.	BLANK
1268	240.62177	55.32889	15.89	10.09	1.55	5.36	MLV	0.01	SX	iKgs	25.70	25.35	21.75	21.21	n.a.	n.a.	BLANK

Bibliography

Abadi, M. G., Navarro, J. F., Steinmetz, M., and Eke, V. R. (2003). Simulations of Galaxy Formation in a Λ Cold Dark Matter Universe. II. The Fine Structure of Simulated Galactic Disks. , 597:21–34.

Abazajian, K. N., Adelman-McCarthy, J. K., Agüeros, M. A., Allam, S. S., Allende Prieto, C., An, D., Anderson, K. S. J., Anderson, S. F., Annis, J., Bahcall, N. A., and et al. (2009). The Seventh Data Release of the Sloan Digital Sky Survey. , 182:543–558.

Aird, J., Coil, A. L., Moustakas, J., Blanton, M. R., Burles, S. M., Cool, R. J., Eisenstein, D. J., Smith, M. S. M., Wong, K. C., and Zhu, G. (2012). PRIMUS: The Dependence of AGN Accretion on Host Stellar Mass and Color. *ApJ*, 746:90.

Alam, S., Albareti, F. D., Allende Prieto, C., Anders, F., Anderson, S. F., Anderton, T., Andrews, B. H., Armengaud, E., Aubourg, É., Bailey, S., and et al. (2015). The Eleventh and Twelfth Data Releases of the Sloan Digital Sky Survey: Final Data from SDSS-III. , 219:12.

Allen, S. W., Dunn, R. J. H., Fabian, A. C., Taylor, G. B., and Reynolds, C. S. (2006). The relation between accretion rate and jet power in X-ray luminous elliptical galaxies. , 372:21–30.

Antonucci, R. (1993). Unified models for active galactic nuclei and quasars. , 31:473–521.

Bañados, E., Hung, L.-W., De Propris, R., and West, M. J. (2010). The Faint End of the Galaxy Luminosity Function in A1689: A Steep Red Faint End Upturn at z = 0.18. , 721:L14–L18.

Baldwin, J. A., Phillips, M. M., and Terlevich, R. (1981). Classification parameters for the emission-line spectra of extragalactic objects. *PASP*, 93:5–19.

Ballantyne, D. R. (2010). The Integrated Relativistic Iron Line from Active Galactic Nuclei: Chasing the Spin Evolution of Supermassive Black Holes. , 716:L27–L30.

Bally, J. and Thronson, Jr., H. A. (1989). Infrared and radio emission from S0 galaxies. , 97:69–78.

Barthel, P. D. and Arnaud, K. A. (1996). Anomalous radio-loudness of Cygnus A and other powerful radio galaxies. , 283:L45–L49.

Baugh, C. M. (2006). A primer on hierarchical galaxy formation: the semi-analytical approach. *Reports on Progress in Physics*, 69:3101–3156.

Becker, R. H., White, R. L., and Helfand, D. J. (1995). The FIRST Survey: Faint Images of the Radio Sky at Twenty Centimeters. *ApJ*, 450:559.

Behroozi, P. S., Conroy, C., and Wechsler, R. H. (2010). A Comprehensive Analysis of Uncertainties Affecting the Stellar Mass-Halo Mass Relation for 0 z 4. , 717:379–403.

Bennert, V. N., Auger, M. W., Treu, T., Woo, J.-H., and Malkan, M. A. (2011). The Relation between Black Hole Mass and Host Spheroid Stellar Mass Out to z ˜ 2. , 742:107.

Benson, A. J. and Babul, A. (2009). Maximum spin of black holes driving jets. , 397:1302–1313.

Benson, A. J., Bower, R. G., Frenk, C. S., Lacey, C. G., Baugh, C. M., and Cole, S. (2003). What Shapes the Luminosity Function of Galaxies? *ApJ*, 599:38–49.

Best, P., Smail, I., Sobral, D., Geach, J., Garn, T., Ivison, R., Kurk, J., Dalton, G., Cirasuolo, M., and Casali, M. (2013). HiZELS: The High Redshift Emission Line Survey with UKIRT. In Adamson, A., Davies, J., and Robson, I., editors, *Thirty Years of Astronomical Discovery with UKIRT*, volume 37 of *Astrophysics and Space Science Proceedings*, page 235.

Best, P. N., Arts, J. N., Röttgering, H. J. A., Rengelink, R., Brookes, M. H., and Wall, J. (2003). CENSORS: A Combined EIS-NVSS Survey Of Radio Sources - I. Sample definition, radio data and optical identifications. , 346:627–683.

Best, P. N. and Heckman, T. M. (2012). On the fundamental dichotomy in the local radio-AGN population: accretion, evolution and host galaxy properties. *MNRAS*, 421:1569–1582.

Best, P. N., Kauffmann, G., Heckman, T. M., Brinchmann, J., Charlot, S., Ivezić, Ž., and White, S. D. M. (2005). The host galaxies of radio-loud active galactic nuclei: mass dependences, gas cooling and active galactic nuclei feedback. *MNRAS*, 362:25–40.

Best, P. N., Ker, L. M., Simpson, C., Rigby, E. E., and Sabater, J. (2014). The cosmic evolution of radio-AGN feedback to z = 1. , 445:955–969.

Best, P. N., von der Linden, A., Kauffmann, G., Heckman, T. M., and Kaiser, C. R. (2007). On the prevalence of radio-loud active galactic nuclei in brightest cluster galaxies: implications for AGN heating of cooling flows. , 379:894–908.

Bieri, R., Dubois, Y., Silk, J., Mamon, G. A., and Gaibler, V. (2016). External pressure-triggering of star formation in a disc galaxy: a template for positive feedback. , 455:4166–4182.

Bîrzan, L., Rafferty, D. A., McNamara, B. R., Wise, M. W., and Nulsen, P. E. J. (2004). A Systematic Study of Radio-induced X-Ray Cavities in Clusters, Groups, and Galaxies. , 607:800–809.

Bolton, A. S., Schlegel, D. J., Aubourg, É., Bailey, S., Bhardwaj, V., Brownstein, J. R., Burles, S., Chen, Y.-M., Dawson, K., Eisenstein, D. J., Gunn, J. E., Knapp, G. R., Loomis, C. P., Lupton, R. H., Maraston, C., Muna, D., Myers, A. D., Olmstead, M. D., Padmanabhan, N., Pâris, I., Percival, W. J., Petitjean, P., Rockosi, C. M., Ross, N. P., Schneider, D. P., Shu, Y., Strauss, M. A., Thomas, D., Tremonti, C. A., Wake, D. A., Weaver, B. A., and Wood-Vasey, W. M. (2012). Spectral Classification and Redshift Measurement for the SDSS-III Baryon Oscillation Spectroscopic Survey. , 144:144.

Bolzonella, M., Miralles, J.-M., and Pelló, R. (2000). Photometric redshifts based on standard SED fitting procedures. , 363:476–492.

Bonchi, A., La Franca, F., Melini, G., Bongiorno, A., and Fiore, F. (2013). On the radio luminosity distribution of active galactic nuclei and the black hole fundamental plane. *MNRAS*, 429:1970–1980.

Bondi, H. (1952). On spherically symmetrical accretion. , 112:195.

Bonzini, M., Padovani, P., Mainieri, V., Kellermann, K. I., Miller, N., Rosati, P., Tozzi, P., and Vattakunnel, S. (2013). The sub-mJy radio sky in the Extended Chandra Deep Field-South: source population. , 436:3759–3771.

Borgani, S., Murante, G., Springel, V., Diaferio, A., Dolag, K., Moscardini, L., Tormen, G., Tornatore, L., and Tozzi, P. (2004). X-ray properties of galaxy clusters and groups from a cosmological hydrodynamical simulation. , 348:1078–1096.

Brammer, G. B., van Dokkum, P. G., and Coppi, P. (2008). EAZY: A Fast, Public Photometric Redshift Code. , 686:1503–1513.

Brandt, W. N. and Alexander, D. M. (2015). Cosmic X-ray surveys of distant active galaxies. The demographics, physics, and ecology of growing supermassive black holes. *A&A*, 23:1.

Bressan, A., Silva, L., and Granato, G. L. (2002). Far infrared and radio emission in dusty starburst galaxies. , 392:377–391.

Bridle, A. H. and Schwab, F. R. (1989). Wide Field Imaging I: Bandwidth and Time-Average Smearing. In Perley, R. A., Schwab, F. R., and Bridle, A. H., editors, *Synthesis Imaging in Radio Astronomy*, volume 6 of *Astronomical Society of the Pacific Conference Series*, page 247.

Brinchmann, J., Charlot, S., Heckman, T. M., Kauffmann, G., Tremonti, C., and White, S. D. M. (2004). Stellar masses, star formation rates, metallicities and AGN properties for 200,000 galaxies in the SDSS Data Release Two (DR2). *ArXiv Astrophysics e-prints, astro-ph/0406220*.

Brookes, M. H., Best, P. N., Rengelink, R., and Röttgering, H. J. A. (2006). CENSORS: A Combined EIS-NVSS Survey of Radio Sources - II. Infrared imaging and the K-z relation. , 366:1265–1288.

Brown, M. J. I., Moustakas, J., Smith, J.-D. T., da Cunha, E., Jarrett, T. H., Imanishi, M., Armus, L., Brandl, B. R., and Peek, J. E. G. (2014). An Atlas of Galaxy Spectral Energy Distributions from the Ultraviolet to the Mid-infrared. , 212:18.

Cattaneo, A., Faber, S. M., Binney, J., Dekel, A., Kormendy, J., Mushotzky, R., Babul, A., Best, P. N., Brüggen, M., Fabian, A. C., Frenk, C. S., Khalatyan, A., Netzer, H., Mahdavi, A., Silk, J., Steinmetz, M., and Wisotzki, L. (2009). The role of black holes in galaxy formation and evolution. , 460:213–219.

Cavagnolo, K. W., McNamara, B. R., Nulsen, P. E. J., Carilli, C. L., Jones, C., and Bîrzan, L. (2010). A Relationship Between AGN Jet Power and Radio Power. *ApJ*, 720:1066–1072.

Chambers, K. C., Magnier, E. A., Metcalfe, N., Flewelling, H. A., Huber, M. E., Waters, C. Z., Denneau, L., Draper, P. W., Farrow, D., Finkbeiner, D. P., Holmberg, C., Koppenhoefer, J., Price, P. A., Saglia, R. P., Schlafly, E. F., Smartt, S. J., Sweeney, W., Wainscoat, R. J., Burgett, W. S., Grav, T., Heasley, J. N., Hodapp, K. W., Jedicke, R., Kaiser, N., Kudritzki, R.-P., Luppino, G. A., Lupton, R. H., Monet, D. G., Morgan, J. S., Onaka, P. M., Stubbs, C. W., Tonry, J. L., Banados, E., Bell, E. F., Bender, R., Bernard, E. J., Botticella, M. T., Casertano, S., Chastel, S., Chen, W.-P., Chen, X., Cole, S., Deacon, N., Frenk, C., Fitzsimmons, A., Gezari, S., Goessl, C., Goggia, T., Goldman, B., Grebel, E. K., Hambly, N. C., Hasinger, G., Heavens, A. F., Heckman, T. M., Henderson, R., Henning, T., Holman, M., Hopp, U., Ip, W.-H., Isani, S., Keyes, C. D., Koekemoer, A., Kotak, R., Long, K. S., Lucey, J. R., Liu, M., Martin, N. F., McLean, B., Morganson, E., Murphy, D. N. A., Nieto-Santisteban, M. A., Norberg, P., Peacock, J. A., Pier, E. A., Postman, M., Primak, N., Rae, C., Rest, A., Riess, A., Riffeser, A., Rix, H. W., Roser, S., Schilbach, E., Schultz, A. S. B., Scolnic, D., Szalay, A., Seitz, S., Shiao, B., Small, E., Smith, K. W., Soderblom, D., Taylor, A. N., Thakar, A. R., Thiel, J., Thilker, D., Urata, Y., Valenti, J., Walter, F., Watters, S. P., Werner, S., White, R., Wood-Vasey, W. M., and Wyse, R. (2016). The Pan-STARRS1 Surveys. *ArXiv e-prints*.

Chambers, K. C. and Pan-STARRS Team (2017). The Pan-STARRS1 Survey Data Release. In *American Astronomical Society Meeting Abstracts*, volume 229 of *American Astronomical Society Meeting Abstracts*, page 223.03.

Chaudhuri, A., Majumdar, S., and Nath, B. B. (2013). Active Galactic Nucleus Feedback and Entropy Injection in Galaxy Cluster Cores. , 776:84.

Ciliegi, P., Zamorani, G., Hasinger, G., Lehmann, I., Szokoly, G., and Wilson, G. (2003). A deep VLA survey at 6 cm in the Lockman Hole. , 398:901–918.

Cohen, A. S., Lane, W. M., Cotton, W. D., Kassim, N. E., Lazio, T. J. W., Perley, R. A., Condon, J. J., and Erickson, W. C. (2007). The VLA Low-Frequency Sky Survey. , 134:1245–1262.

Comastri, A., Mignoli, M., Ciliegi, P., Severgnini, P., Maiolino, R., Brusa, M., Fiore, F., Baldi, A., Molendi, S., Morganti, R., Vignali, C., La Franca, F., Matt, G., and Perola, G. C. (2002). The HELLAS2XMM Survey. II. Multiwavelength Observations of P3: An X-Ray-bright, Optically Inactive Galaxy. *ApJ*, 571:771–778.

Condon, J. J. (1989). The 1.4 gigahertz luminosity function and its evolution. , 338:13–23.

Condon, J. J. (1997). Errors in Elliptical Gaussian FITS. , 109:166–172.

Condon, J. J., Cotton, W. D., Greisen, E. W., Yin, Q. F., Perley, R. A., Taylor, G. B., and Broderick, J. J. (1998). The NRAO VLA Sky Survey. , 115:1693–1716.

Cowie, L. L., Songaila, A., Hu, E. M., and Cohen, J. G. (1996). New Insight on Galaxy Formation and Evolution From Keck Spectroscopy of the Hawaii Deep Fields. , 112:839.

Croton, D. J., Springel, V., White, S. D. M., De Lucia, G., Frenk, C. S., Gao, L., Jenkins, A., Kauffmann, G., Navarro, J. F., and Yoshida, N. (2006). The many lives of active galactic nuclei: cooling flows, black holes and the luminosities and colours of galaxies. , 365:11–28.

Daddi, E., Elbaz, D., Walter, F., Bournaud, F., Salmi, F., Carilli, C., Dannerbauer, H., Dickinson, M., Monaco, P., and Riechers, D. (2010). Different Star Formation Laws for Disks Versus Starbursts at Low and High Redshifts. , 714:L118–L122.

Dalton, G., Trager, S. C., Abrams, D. C., Carter, D., Bonifacio, P., Aguerri, J. A. L., MacIntosh, M., Evans, C., Lewis, I., Navarro, R., Agocs, T., Dee, K., Rousset, S., Tosh, I., Middleton, K., Pragt, J., Terrett, D., Brock, M., Benn, C., Verheijen, M., Cano Infantes, D., Bevil, C., Steele, I., Mottram, C., Bates, S., Gribbin, F. J., Rey, J., Rodriguez, L. F., Delgado, J. M., Guinouard, I., Walton, N., Irwin, M. J., Jagourel, P., Stuik, R., Gerlofsma, G., Roelfsma, R., Skillen, I., Ridings, A., Balcells, M., Daban, J.-B., Gouvret, C., Venema, L., and Girard, P. (2012). WEAVE: the next generation wide-field spectroscopy facility for the William Herschel Telescope. In *Ground-based and Airborne Instrumentation for Astronomy IV*, volume 8446 of , page 84460P.

de Gasperin, F., Merloni, A., Sell, P., Best, P., Heinz, S., and Kauffmann, G. (2011). Testing black hole jet scaling relations in low-luminosity active galactic nuclei. *MNRAS*, 415:2910–2919.

Dekel, A. and Birnboim, Y. (2008). Gravitational quenching in massive galaxies and clusters by clumpy accretion. , 383:119–138.

Ding, X., Treu, T., Suyu, S. H., Wong, K. C., Morishita, T., Park, D., Sluse, D., Auger, M. W., Agnello, A., Bennert, V. N., and Collett, T. E. (2017). H0LiCOW VII. Cosmic evolution of the correlation between black hole mass and host galaxy luminosity. *ArXiv e-prints*.

Donley, J. L., Koekemoer, A. M., Brusa, M., Capak, P., Cardamone, C. N., Civano, F., Ilbert, O., Impey, C. D., Kartaltepe, J. S., Miyaji, T., Salvato, M., Sanders, D. B., Trump, J. R., and Zamorani, G. (2012). Identifying Luminous Active Galactic Nuclei in Deep Surveys: Revised IRAC Selection Criteria. , 748:142.

Dunlop, J. S. and Peacock, J. A. (1990). The Redshift Cut-Off in the Luminosity Function of Radio Galaxies and Quasars. , 247:19.

Eddington, A. S. (1913). On a formula for correcting statistics for the effects of a known error of observation. , 73:359–360.

Eke, V. R., Baugh, C. M., Cole, S., Frenk, C. S., and Navarro, J. F. (2006). Galaxy groups in the 2dF Galaxy Redshift Survey: the number density of groups. , 370:1147–1158.

Fabian, A. C. (1994). Cooling Flows in Clusters of Galaxies. , 32:277–318.

Fabian, A. C. (2012). Observational Evidence of Active Galactic Nuclei Feedback. , 50:455–489.

Fall, S. M. and Romanowsky, A. J. (2013). Angular Momentum and Galaxy Formation Revisited: Effects of Variable Mass-to-light Ratios. , 769:L26.

Ferrarese, L. and Ford, H. (2005). Supermassive Black Holes in Galactic Nuclei: Past, Present and Future Research. , 116:523–624.

Ferrarese, L. and Merritt, D. (2000). A Fundamental Relation between Supermassive Black Holes and Their Host Galaxies. , 539:L9–L12.

Finoguenov, A., Borgani, S., Davis, D. S., Mulchaey, J. S., Osmond, J. P. F., Ponman, T. J., and Zimer, M. (2004). XMM-Newton survey of IGM: news for the modified entropy scaling. In Dettmar, R., Klein, U., and Salucci, P., editors, *Baryons in Dark Matter Halos*, page 28.1.

Fleuren, S., Sutherland, W., Dunne, L., Smith, D. J. B., Maddox, S. J., González-Nuevo, J., Findlay, J., Auld, R., Baes, M., Bond, N. A., Bonfield, D. G., Bourne, N., Cooray, A., Buttiglione, S., Cava, A., Dariush, A., De Zotti, G., Driver, S. P., Dye, S., Eales, S., Fritz, J., Gunawardhana, M. L. P., Hopwood,

R., Ibar, E., Ivison, R. J., Jarvis, M. J., Kelvin, L., Lapi, A., Liske, J., Michałowski, M. J., Negrello, M., Pascale, E., Pohlen, M., Prescott, M., Rigby, E. E., Robotham, A., Scott, D., Temi, P., Thompson, M. A., Valiante, E., and van der Werf, P. (2012). Herschel-ATLAS: VISTA VIKING near-infrared counterparts in the Phase 1 GAMA 9-h data. , 423:2407–2424.

Gallo, E., Fender, R. P., and Pooley, G. G. (2003). A universal radio-X-ray correlation in low/hard state black hole binaries. *MNRAS*, 344:60–72.

Garn, T., Green, D. A., Riley, J. M., and Alexander, P. (2008). A 610-MHz survey of the ELAIS-N1 field with the Giant Metrewave Radio Telescope - observations, data analysis and source catalogue. , 383:75–85.

Gaskell, C. M. (2011). Accurate black hole mass measurements for thermal AGNs and the origin of the correlations between black hole mass and bulge properties. In Alecian, G., Belkacem, K., Samadi, R., and Valls-Gabaud, D., editors, *SF2A-2011: Proceedings of the Annual meeting of the French Society of Astronomy and Astrophysics*, pages 577–582.

Gaspari, M., Ruszkowski, M., and Oh, S. P. (2013). Chaotic cold accretion on to black holes. , 432:3401–3422.

Geach, J. E., Smail, I., Best, P. N., Kurk, J., Casali, M., Ivison, R. J., and Coppin, K. (2008). HiZELS: a high-redshift survey of Hα emitters - I. The cosmic star formation rate and clustering at z = 2.23. , 388:1473–1486.

Genzel, R., Tacconi, L. J., Gracia-Carpio, J., Sternberg, A., Cooper, M. C., Shapiro, K., Bolatto, A., Bouché, N., Bournaud, F., Burkert, A., Combes, F., Comerford, J., Cox, P., Davis, M., Schreiber, N. M. F., Garcia-Burillo, S., Lutz, D., Naab, T., Neri, R., Omont, A., Shapley, A., and Weiner, B. (2010). A study of the gas-star formation relation over cosmic time. , 407:2091–2108.

Georgakakis, A., Nandra, K., Laird, E. S., Aird, J., and Trichas, M. (2008). A new method for determining the sensitivity of X-ray imaging observations and the X-ray number counts. *MNRAS*, 388:1205–1213.

Glover, S. C. O. and Mac Low, M.-M. (2011). On the relationship between molecular hydrogen and carbon monoxide abundances in molecular clouds. , 412:337–350.

Graham, A. W. and Scott, N. (2013). The M $_{BH}$-L $_{spheroid}$ Relation at High and Low Masses, the Quadratic Growth of Black Holes, and Intermediate-mass Black Hole Candidates. , 764:151.

Gultekin, K., Cackett, E. M., King, A. L., Miller, J. M., and Pinkney, J. (2014). Low-Mass AGN and Their Relation to the Fundamental Plane of Black Hole Accretion. *ArXiv e-prints:1405.6986*.

Gültekin, K., Cackett, E. M., Miller, J. M., Di Matteo, T., Markoff, S., and Richstone, D. O. (2009). The Fundamental Plane of Accretion onto Black Holes with Dynamical Masses. *ApJ*, 706:404–416.

Hales, S. E. G., Baldwin, J. E., and Warner, P. J. (1988). The 6C survey of radio sources. II - The zone delta = 30-51 deg, alpha = 08h30m-17h30m. , 234:919–936.

Hardcastle, M. J., Gürkan, G., van Weeren, R. J., Williams, W. L., Best, P. N., de Gasperin, F., Rafferty, D. A., Read, S. C., Sabater, J., Shimwell, T. W., Smith, D. J. B., Tasse, C., Bourne, N., Brienza, M., Brüggen, M., Brunetti, G., Chyży, K. T., Conway, J., Dunne, L., Eales, S. A., Maddox, S. J., Jarvis, M. J., Mahony, E. K., Morganti, R., Prandoni, I., Röttgering, H. J. A., Valiante, E., and White, G. J. (2016). LOFAR/H-ATLAS: a deep low-frequency survey of the Herschel-ATLAS North Galactic Pole field. , 462:1910–1936.

Häring, N. and Rix, H.-W. (2004). On the Black Hole Mass-Bulge Mass Relation. , 604:L89–L92.

Hart, Q. N., Stocke, J. T., and Hallman, E. J. (2009). X-ray Point Sources and Radio Galaxies in Clusters of Galaxies. *ApJ*, 705:854–867.

Heald, G. H., Pizzo, R. F., Orrú, E., Breton, R. P., Carbone, D., Ferrari, C., Hardcastle, M. J., Jurusik, W., Macario, G., Mulcahy, D., Rafferty, D., Asgekar, A., Brentjens, M., Fallows, R. A., Frieswijk, W., Toribio, M. C., Adebahr, B., Arts, M., Bell, M. R., Bonafede, A., Bray, J., Broderick, J., Cantwell, T., Carroll, P., Cendes, Y., Clarke, A. O., Croston, J., Daiboo, S., de Gasperin, F., Gregson, J., Harwood, J., Hassall, T., Heesen, V., Horneffer, A., van der Horst, A. J., Iacobelli, M., Jelić, V., Jones, D., Kant, D., Kokotanekov, G., Martin, P., McKean, J. P., Morabito, L. K., Nikiel-Wroczyński, B., Offringa, A., Pandey, V. N., Pandey-Pommier, M., Pietka, M., Pratley, L., Riseley, C., Rowlinson, A., Sabater, J., Scaife, A. M. M., Scheers, L. H. A., Sendlinger, K., Shulevski, A., Sipior, M., Sobey, C., Stewart, A. J., Stroe, A., Swinbank, J., Tasse, C., Trüstedt, J., Varenius, E., van Velzen, S., Vilchez, N., van Weeren, R. J., Wijnholds, S., Williams, W. L., de Bruyn, A. G., Nijboer, R., Wise, M., Alexov, A., Anderson, J., Avruch, I. M., Beck, R., Bell, M. E., van Bemmel, I., Bentum, M. J., Bernardi, G., Best, P., Breitling, F., Brouw, W. N., Brüggen, M., Butcher, H. R., Ciardi, B., Conway, J. E., de Geus, E., de Jong, A., de Vos, M., Deller, A., Dettmar, R.-J., Duscha, S., Eislöffel, J., Engels, D., Falcke, H., Fender, R., Garrett, M. A., Grießmeier, J., Gunst, A. W., Hamaker, J. P., Hessels, J. W. T., Hoeft, M., Hörandel, J., Holties, H. A., Intema, H., Jackson, N. J., Jütte, E., Karastergiou, A., Klijn, W. F. A., Kondratiev, V. I., Koopmans, L. V. E., Kuniyoshi, M., Kuper, G., Law, C., van Leeuwen, J., Loose, M., Maat, P., Markoff, S., McFadden, R., McKay-Bukowski, D., Mevius, M., Miller-Jones, J. C. A., Morganti, R., Munk, H., Nelles, A., Noordam, J. E., Norden, M. J., Paas, H., Polatidis, A. G., Reich, W., Renting, A., Röttgering, H., Schoenmakers, A., Schwarz, D., Sluman, J., Smirnov, O., Stappers, B. W., Steinmetz, M., Tagger, M., Tang, Y., ter Veen, S., Thoudam, S., Vermeulen, R., Vocks, C., Vogt, C., Wijers, R. A. M. J., Wucknitz, O., Yatawatta, S., and Zarka, P. (2015). The LOFAR Multifrequency Snapshot Sky Survey (MSSS). I. Survey description and first results. , 582:A123.

Heckman, T. M. (1980). An optical and radio survey of the nuclei of bright galaxies - Activity in normal galactic nuclei. *A&A*, 87:152–164.

Heckman, T. M. and Best, P. N. (2014). The Coevolution of Galaxies and Supermassive Black Holes: Insights from Surveys of the Contemporary Universe. *ARA&A*, 52:589–660.

Heckman, T. M. and Kauffmann, G. (2004). The Host Galaxies of 23,000 AGN. In Mújica, R. and Maiolino, R., editors, *Multiwavelength AGN Surveys*, pages 365–372.

Heinz, S. and Sunyaev, R. A. (2003). The non-linear dependence of flux on black hole mass and accretion rate in core-dominated jets. *MNRAS*, 343:L59–L64.

Ho, L. C. (2008). Nuclear Activity in Nearby Galaxies. *ARA&A*, 46:475–539.

Ho, L. C. (2009). Origin and Dynamical Support of Ionized Gas in Galaxy Bulges. *ApJ*, 699:638–648.

Ho, L. C., Filippenko, A. V., Sargent, W. L. W., and Peng, C. Y. (1997). A Search for Low-Luminosity "Type 1" AGNs. In *AAS Meeting Abstracts #189*, volume 29 of *BAAS*, page 122.09.

Huber, M., PS1 Science Consortium, and Pan-STARRS IPP Team (2017). Pan-STARRS1 Medium Deep Survey. In *American Astronomical Society Meeting Abstracts*, volume 229 of *American Astronomical Society Meeting Abstracts*, page 237.06.

Hummel, E., Davies, R. D., Pedlar, A., Wolstencroft, R. D., and van der Hulst, J. M. (1988). The radio continuum, far-infrared and optical emission from SBC galaxies and their relation to star formation. , 199:91–104.

Intema, H. T., Jagannathan, P., Mooley, K. P., and Frail, D. A. (2017). The GMRT 150 MHz all-sky radio survey. First alternative data release TGSS ADR1. , 598:A78.

Intema, H. T., van der Tol, S., Cotton, W. D., Cohen, A. S., van Bemmel, I. M., and Röttgering, H. J. A. (2009). Ionospheric calibration of low frequency radio interferometric observations using the peeling scheme. I. Method description and first results. , 501:1185–1205.

Iqbal, A., Majumdar, S., Nath, B. B., Ettori, S., Eckert, D., and Malik, M. A. (2017). Excess entropy and energy feedback from within cluster cores up to r_200. *ArXiv e-prints*.

Israel, F. P. and Mahoney, M. J. (1990). Low-frequency radio continuum evidence for cool ionized gas in normal spiral galaxies. , 352:30–43.

Ivezić, Ž., Connelly, A. J., VanderPlas, J. T., and Gray, A. (2014). *Statistics, Data Mining, and Machine Learningin Astronomy*.

Ivison, R. J., Papadopoulos, P. P., Smail, I., Greve, T. R., Thomson, A. P., Xilouris, E. M., and Chapman, S. C. (2011). Tracing the molecular gas in distant submillimetre galaxies via CO(1-0) imaging with the Expanded Very Large Array. , 412:1913–1925.

Jahnke, K. and Macciò, A. V. (2011). The Non-causal Origin of the Black-hole-galaxy Scaling Relations. , 734:92.

Janssen, R. M. J., Röttgering, H. J. A., Best, P. N., and Brinchmann, J. (2012). The triggering probability of radio-loud AGN. A comparison of high and low excitation radio galaxies in hosts of different colors. *A&A*, 541:A62.

Jenkins, A., Frenk, C. S., White, S. D. M., Colberg, J. M., Cole, S., Evrard, A. E., Couchman, H. M. P., and Yoshida, N. (2001). The mass function of dark matter haloes. , 321:372–384.

Kauffmann, G., Heckman, T. M., Tremonti, C., Brinchmann, J., Charlot, S., White, S. D. M., Ridgway, S. E., Brinkmann, J., Fukugita, M., Hall, P. B., Ivezić, Ž., Richards, G. T., and Schneider, D. P. (2003a). The host galaxies of active galactic nuclei. *MNRAS*, 346:1055–1077.

Kauffmann, G., Heckman, T. M., White, S. D. M., Charlot, S., Tremonti, C., Brinchmann, J., Bruzual, G., Peng, E. W., Seibert, M., Bernardi, M., Blanton, M., Brinkmann, J., Castander, F., Csábai, I., Fukugita, M., Ivezic, Z., Munn, J. A., Nichol, R. C., Padmanabhan, N., Thakar, A. R., Weinberg, D. H., and York, D. (2003b). Stellar masses and star formation histories for 10^5 galaxies from the Sloan Digital Sky Survey. *MNRAS*, 341:33–53.

Kauffmann, G., Heckman, T. M., White, S. D. M., Charlot, S., Tremonti, C., Peng, E. W., Seibert, M., Brinkmann, J., Nichol, R. C., SubbaRao, M., and York, D. (2003c). The dependence of star formation history and internal structure on stellar mass for 10^5 low-redshift galaxies. *MNRAS*, 341:54–69.

Kay, S. T., Pearce, F. R., Frenk, C. S., and Jenkins, A. (2002). Including star formation and supernova feedback within cosmological simulations of galaxy formation. , 330:113–128.

Kennicutt, Jr., R. C. (1998). The Global Schmidt Law in Star-forming Galaxies. , 498:541–552.

Kennicutt, Jr., R. C., Tamblyn, P., and Congdon, C. E. (1994). Past and future star formation in disk galaxies. , 435:22–36.

Kewley, L. J., Groves, B., Kauffmann, G., and Heckman, T. (2006). The host galaxies and classification of active galactic nuclei. *MNRAS*, 372:961–976.

Kewley, L. J., Heisler, C. A., Dopita, M. A., and Lumsden, S. (2001). Optical Classification of Southern Warm Infrared Galaxies. *ApJS*, 132:37–71.

Kocevski, D. D., Faber, S. M., Mozena, M., Koekemoer, A. M., Nandra, K., Rangel, C., Laird, E. S., Brusa, M., Wuyts, S., Trump, J. R., Koo, D. C., Somerville, R. S., Bell, E. F., Lotz, J. M., Alexander, D. M., Bournaud, F., Conselice, C. J., Dahlen, T., Dekel, A., Donley, J. L., Dunlop, J. S., Finoguenov, A., Georgakakis, A., Giavalisco, M., Guo, Y., Grogin, N. A., Hathi, N. P., Juneau, S., Kartaltepe, J. S., Lucas, R. A., McGrath, E. J., McIntosh, D. H., Mobasher, B., Robaina, A. R., Rosario, D., Straughn, A. N., van der Wel, A., and Villforth, C. (2012). CANDELS: Constraining the AGN-Merger Connection with Host Morphologies at z ˜ 2. , 744:148.

Kodama, T., Yamada, T., Akiyama, M., Aoki, K., Doi, M., Furusawa, H., Fuse, T., Imanishi, M., Ishida, C., Iye, M., Kajisawa, M., Karoji, H., Kobayashi, N., Komiyama, Y., Kosugi, G., Maeda, Y., Miyazaki, S., Mizumoto, Y., Morokuma, T., Nakata, F., Noumaru, J., Ogasawara, R., Ouchi, M., Sasaki, T., Sekiguchi, K., Shimasaku, K., Simpson, C., Takata, T., Tanaka, I., Ueda, Y., Yasuda, N., and Yoshida, M. (2004). Down-sizing in galaxy formation at z˜ 1 in the Subaru/XMM-Newton Deep Survey (SXDS). , 350:1005–1014.

Körding, E., Falcke, H., and Corbel, S. (2006). Refining the fundamental plane of accreting black holes. *A&A*, 456:439–450.

Kormendy, J. and Ho, L. C. (2013). Coevolution (Or Not) of Supermassive Black Holes and Host Galaxies. , 51:511–653.

Kravtsov, A. V. (2003). On the Origin of the Global Schmidt Law of Star Formation. , 590:L1–L4.

Kruijssen, J. M. D. and Longmore, S. N. (2014). An uncertainty principle for star formation - I. Why galactic star formation relations break down below a certain spatial scale. , 439:3239–3252.

Laing, R. and Jones, D. (1985). The Isaac Newton Group. *Vistas in Astronomy*, 28:483–503.

Lawrence, A., Warren, S. J., Almaini, O., Edge, A. C., Hambly, N. C., Jameson, R. F., Lucas, P., Casali, M., Adamson, A., Dye, S., Emerson, J. P., Foucaud, S., Hewett, P., Hirst, P., Hodgkin, S. T., Irwin, M. J., Lodieu, N., McMahon, R. G., Simpson, C., Smail, I., Mortlock, D., and Folger, M. (2007). The UKIRT Infrared Deep Sky Survey (UKIDSS). , 379:1599–1617.

Li, C. and White, S. D. M. (2009). The distribution of stellar mass in the low-redshift Universe. , 398:2177–2187.

Li, Y., Mac Low, M.-M., and Klessen, R. S. (2006). Star Formation in Isolated Disk Galaxies. II. Schmidt Laws and Efficiency of Gravitational Collapse. , 639:879–896.

Lilly, S. J. and Longair, M. S. (1984). Stellar populations in distant radio galaxies. , 211:833–855.

Longair, M. S. (1966). On the interpretation of radio source counts. , 133:421.

Madau, P. and Dickinson, M. (2014). Cosmic Star-Formation History. , 52:415–486.

Magorrian, J., Tremaine, S., Richstone, D., Bender, R., Bower, G., Dressler, A., Faber, S. M., Gebhardt, K., Green, R., Grillmair, C., Kormendy, J., and Lauer, T. (1998). The Demography of Massive Dark Objects in Galaxy Centers. , 115:2285–2305.

Maraston, C. (2005). Evolutionary population synthesis: models, analysis of the ingredients and application to high-z galaxies. , 362:799–825.

Marscher, A. P., Jorstad, S. G., D'Arcangelo, F. D., Smith, P. S., Williams, G. G., Larionov, V. M., Oh, H., Olmstead, A. R., Aller, M. F., Aller, H. D., McHardy, I. M., Lähteenmäki, A., Tornikoski, M., Valtaoja, E., Hagen-Thorn, V. A., Kopatskaya, E. N., Gear, W. K., Tosti, G., Kurtanidze, O., Nikolashvili, M., Sigua, L., Miller, H. R., and Ryle, W. T. (2008). The inner jet of an active galactic nucleus as revealed by a radio-to-γ-ray outburst. *Nature*, 452:966–969.

Martin, D. C., Fanson, J., Schiminovich, D., Morrissey, P., Friedman, P. G., Barlow, T. A., Conrow, T., Grange, R., Jelinsky, P. N., Milliard, B., Siegmund, O. H. W., Bianchi, L., Byun, Y.-I., Donas, J., Forster, K., Heckman, T. M., Lee, Y.-W., Madore, B. F., Malina, R. F., Neff, S. G., Rich, R. M., Small, T., Surber, F., Szalay, A. S., Welsh, B., and Wyder, T. K. (2005). The Galaxy Evolution Explorer: A Space Ultraviolet Survey Mission. , 619:L1–L6.

Mauduit, J.-C., Lacy, M., Farrah, D., Surace, J., Jarvis, M., Oliver, S., Maraston, C., and SERVS Team (2012). The Spitzer Extragalactic Representative Volume Survey (SERVS). In *American Astronomical Society Meeting Abstracts #219*, volume 219 of *American Astronomical Society Meeting Abstracts*, page 446.19.

McAlpine, K., Smith, D. J. B., Jarvis, M. J., Bonfield, D. G., and Fleuren, S. (2012). The likelihood ratio as a tool for radio continuum surveys with Square Kilometre Array precursor telescopes. , 423:132–140.

McConnell, N. J. and Ma, C.-P. (2013). Revisiting the Scaling Relations of Black Hole Masses and Host Galaxy Properties. *ApJ*, 764:184.

McLure, R. J., Jarvis, M. J., Targett, T. A., Dunlop, J. S., and Best, P. N. (2006). On the evolution of the black-hole/spheroid mass ratio. *Astronomische Nachrichten*, 327:213–216.

McNamara, B. R. and Nulsen, P. E. J. (2007). Heating Hot Atmospheres with Active Galactic Nuclei. , 45:117–175.

McNamara, B. R., Wise, M., Nulsen, P. E. J., David, L. P., Sarazin, C. L., Bautz, M., Markevitch, M., Vikhlinin, A., Forman, W. R., Jones, C., and Harris, D. E. (2000). Chandra X-Ray Observations of the Hydra A Cluster: An Interaction between the Radio Source and the X-Ray-emitting Gas. , 534:L135–L138.

Merloni, A. and Heinz, S. (2007). Measuring the kinetic power of active galactic nuclei in the radio mode. *MNRAS*, 381:589–601.

Merloni, A., Heinz, S., and di Matteo, T. (2003). A Fundamental Plane of black hole activity. *MNRAS*, 345:1057–1076.

Merloni, A., Predehl, P., Becker, W., Böhringer, H., Boller, T., Brunner, H., Brusa, M., Dennerl, K., Freyberg, M., Friedrich, P., Georgakakis, A., Haberl, F., Hasinger, G., Meidinger, N., Mohr, J., Nandra, K., Rau, A., Reiprich, T. H., Robrade, J., Salvato, M., Santangelo, A., Sasaki, M., Schwope, A., Wilms, J., and German eROSITA Consortium, t. (2012). eROSITA Science Book: Mapping the Structure of the Energetic Universe. *ArXiv e-prints*.

Mirabel, I. F. and Rodriguez, L. F. (1995). Superluminal Motions in Our Galaxy. In Böhringer, H., Morfill, G. E., and Trümper, J. E., editors, *Seventeeth Texas Symposium on Relativistic Astrophysics and Cosmology*, volume 759 of *Annals of the New York Academy of Sciences*, page 21.

Mo, H., van den Bosch, F. C., and White, S. (2010). *Galaxy Formation and Evolution*.

Mohan, N. and Rafferty, D. (2015). PyBDSM: Python Blob Detection and Source Measurement. Astrophysics Source Code Library.

Mortlock, A., Conselice, C. J., Hartley, W. G., Duncan, K., Lani, C., Ownsworth, J. R., Almaini, O., Wel, A. v. d., Huang, K.-H., Ashby, M. L. N., Willner, S. P., Fontana, A., Dekel, A., Koekemoer, A. M., Ferguson, H. C., Faber, S. M., Grogin, N. A., and Kocevski, D. D. (2015). Deconstructing the galaxy stellar mass function with UKIDSS and CANDELS: the impact of colour, structure and environment. , 447:2–24.

Murphy, E. J. (2009). The Far-Infrared-Radio Correlation at High Redshifts: Physical Considerations and Prospects for the Square Kilometer Array. , 706:482–496.

Mushotzky, R., Figueroa-Feliciano, E., Loewenstein, M., and Snowden, S. L. (2003). Groups and the Entropy Floor- XMM-Newton Observations of Two Groups. *ArXiv Astrophysics e-prints*.

Narayan, R. and Yi, I. (1995). Advection-dominated accretion: Self-similarity and bipolar outflows. , 444:231–243.

Netzer, H. (2015). Revisiting the Unified Model of Active Galactic Nuclei. , 53:365–408.

Nisbet, D. M. and Best, P. N. (2016). The mass fraction of AGN and the Fundamental Plane of black hole activity from a large X-ray-selected sample of LINERs. , 455:2551–2566.

Noordam, J. E. (2004). LOFAR calibration challenges. In Oschmann, Jr., J. M., editor, *Ground-based Telescopes*, volume 5489 of , pages 817–825.

Nulsen, P. E. J., Jones, C., Forman, W. R., David, L. P., McNamara, B. R., Rafferty, D. A., Bîrzan, L., and Wise, M. W. (2007). AGN Heating Through Cavities and Shocks. In Böhringer, H., Pratt, G. W., Finoguenov, A., and Schuecker, P., editors, *Heating versus Cooling in Galaxies and Clusters of Galaxies*, page 210.

Oliver, S., Rowan-Robinson, M., Alexander, D. M., Almaini, O., Balcells, M., Baker, A. C., Barcons, X., Barden, M., Bellas-Velidis, I., Cabrera-Guerra, F., Carballo, R., Cesarsky, C. J., Ciliegi, P., Clements, D. L., Crockett, H., Danese, L., Dapergolas, A., Drolias, B., Eaton, N., Efstathiou, A., Egami, E., Elbaz, D., Fadda, D., Fox, M., Franceschini, A., Genzel, R., Goldschmidt, P., Graham, M., Gonzalez-Serrano, J. I., Gonzalez-Solares, E. A., Granato, G. L., Gruppioni, C., Herbstmeier, U., Héraudeau, P., Joshi, M., Kontizas, E., Kontizas, M., Kotilainen, J. K., Kunze, D., La Franca, F., Lari, C., Lawrence, A., Lemke, D., Linden-Vørnle, M. J. D., Mann, R. G., Márquez, I., Masegosa, J., Mattila, K., McMahon, R. G., Miley, G., Missoulis, V., Mobasher, B., Morel, T., Nørgaard-Nielsen, H., Omont, A., Papadopoulos, P., Perez-Fournon, I., Puget, J.-L., Rigopoulou, D., Rocca-Volmerange, B., Serjeant, S., Silva, L., Sumner, T., Surace, C., Vaisanen, P., van der Werf, P. P., Verma, A., Vigroux, L., Villar-Martin, M., and Willott, C. J. (2000). The European Large Area ISO Survey - I. Goals, definition and observations. , 316:749–767.

Peacock, J. A. (2010). *Growth of structure in the Universe*, page 102.

Peng, C. Y. (2007). How Mergers May Affect the Mass Scaling Relation between Gravitationally Bound Systems. , 671:1098–1107.

Pérez-Fournon, I., Hernán-Caballero, A., and ELAIS-Irs Team (2009). Spitzer IRS Spectroscopy of Infrared-Luminous Galaxies at z
0.5-3. In Onaka, T., White, G. J., Nakagawa, T., and Yamamura, I., editors, *AKARI, a Light to Illuminate the Misty Universe*, volume 418 of *Astronomical Society of the Pacific Conference Series*, page 479.

Peterson, J. R., Kahn, S. M., Paerels, F. B. S., Kaastra, J. S., Tamura, T., Bleeker, J. A. M., Ferrigno, C., and Jernigan, J. G. (2003). High-Resolution X-Ray Spectroscopic Constraints on Cooling-Flow Models for Clusters of Galaxies. , 590:207–224.

Planck Collaboration, Adam, R., Ade, P. A. R., Aghanim, N., Akrami, Y., Alves, M. I. R., Argüeso, F., Arnaud, M., Arroja, F., Ashdown, M., and et al. (2016). Planck 2015 results. I. Overview of products and scientific results. , 594:A1.

Polletta, M., Tajer, M., Maraschi, L., Trinchieri, G., Lonsdale, C. J., Chiappetti, L., Andreon, S., Pierre, M., Le Fèvre, O., Zamorani, G., Maccagni, D., Garcet, O., Surdej, J., Franceschini, A., Alloin, D., Shupe, D. L., Surace, J. A., Fang, F., Rowan-Robinson, M., Smith, H. E., and Tresse, L. (2007). Spectral Energy Distributions of Hard X-Ray Selected Active Galactic Nuclei in the XMM-Newton Medium Deep Survey. , 663:81–102.

Ponman, T. J., Cannon, D. B., and Navarro, J. F. (1999). The thermal imprint of galaxy formation on X-ray clusters. , 397:135–137.

Ponman, T. J., Sanderson, A. J. R., and Finoguenov, A. (2003). The Birmingham-CfA cluster scaling project - III. Entropy and similarity in galaxy systems. , 343:331–342.

Pracy, M. B., Ching, J. H. Y., Sadler, E. M., Croom, S. M., Baldry, I. K., Bland-Hawthorn, J., Brough, S., Brown, M. J. I., Couch, W. J., Davis, T. M., Drinkwater, M. J., Hopkins, A. M., Jarvis, M. J., Jelliffe, B., Jurek, R. J., Loveday, J., Pimbblet, K. A., Prescott, M., Wisnioski, E., and Woods, D. (2016). GAMA/WiggleZ: the 1.4 GHz radio luminosity functions of high- and low-excitation radio galaxies and their redshift evolution to z = 0.75. , 460:2–17.

Qiao, E. and Liu, B. F. (2009). Dependence of Spectral State Transition and Disk Truncation on Viscosity Parameter α. *PASJ*, 61:403–.

Rauch, M., Becker, G. D., Haehnelt, M. G., Carswell, R. F., and Gauthier, J.-R. (2013). A z = 3.045 Lyα emitting halo hosting a QSO and a possible candidate for AGN-triggered star formation. , 431:L68–L72.

Reig, P., Belloni, T., and van der Klis, M. (2003). Does GRS 1915+105 exhibit "canonical" black-hole states? *A&A*, 412:229–233.

Rengelink, R. B., Tang, Y., de Bruyn, A. G., Miley, G. K., Bremer, M. N., Roettgering, H. J. A., and Bremer, M. A. R. (1997). The Westerbork Northern Sky Survey (WENSS), I. A 570 square degree Mini-Survey around the North Ecliptic Pole. , 124.

Renzini, A. (2006). Stellar Population Diagnostics of Elliptical Galaxy Formation. , 44:141–192.

Reynolds, C. S. and Fabian, A. C. (2008). Broad Iron-Kα Emission Lines as a Diagnostic of Black Hole Spin. , 675:1048–1056.

Rieke, G. H., Young, E. T., Engelbracht, C. W., Kelly, D. M., Low, F. J., Haller, E. E., Beeman, J. W., Gordon, K. D., Stansberry, J. A., Misselt, K. A., Cadien, J., Morrison, J. E., Rivlis, G., Latter, W. B., Noriega-Crespo, A., Padgett, D. L., Stapelfeldt, K. R., Hines, D. C., Egami, E., Muzerolle, J., Alonso-Herrero, A., Blaylock, M., Dole, H., Hinz, J. L., Le Floc'h, E., Papovich, C., Pérez-González, P. G., Smith, P. S., Su, K. Y. L., Bennett, L., Frayer, D. T., Henderson, D., Lu, N., Masci, F., Pesenson, M., Rebull, L., Rho, J., Keene, J., Stolovy, S., Wachter, S., Wheaton, W., Werner, M. W., and Richards, P. L. (2004). The Multiband Imaging Photometer for Spitzer (MIPS). , 154:25–29.

Rigby, E. E., Best, P. N., Brookes, M. H., Peacock, J. A., Dunlop, J. S., Röttgering, H. J. A., Wall, J. V., and Ker, L. (2011). The luminosity-dependent high-redshift turnover in the steep spectrum radio luminosity function: clear evidence for downsizing in the radio-AGN population. , 416:1900–1915.

Romero, G. E., Boettcher, M., Markoff, S., and Tavecchio, F. (2017). Relativistic Jets in Active Galactic Nuclei and Microquasars. , 207:5–61.

Rosen, S. R., Webb, N. A., Watson, M. G., Ballet, J., Barret, D., Braito, V., Carrera, F. J., Ceballos, M. T., Coriat, M., Della Ceca, R., Denkinson, G., Esquej, P., Farrell, S. A., Freyberg, M., Grisé, F., Guillout, P., Heil, L., Koliopanos, F., Law-Green, D., Lamer, G., Lin, D., Martino, R., Michel, L., Motch, C., Nebot Gomez-Moran, A., Page, C. G., Page, K., Page, M., Pakull, M. W., Pye, J., Read, A., Rodriguez, P., Sakano, M., Saxton, R., Schwope, A., Scott, A. E., Sturm, R., Traulsen, I., Yershov, V., and Zolotukhin, I. (2016). The XMM-Newton serendipitous survey. VII. The third XMM-Newton serendipitous source catalogue. , 590:A1.

Sabater, J., Best, P. N., and Heckman, T. M. (2015). Triggering optical AGN: the need for cold gas, and the indirect roles of galaxy environment and interactions. , 447:110–116.

Saikia, P., Körding, E., and Falcke, H. (2015). The Fundamental Plane of black hole activity in the optical band. *MNRAS*, 450:2317–2326.

Salomé, Q., Salomé, P., and Combes, F. (2015). Jet-induced star formation in 3C 285 and Minkowski's Object. , 574:A34.

Salvato, M., Hasinger, G., Ilbert, O., Zamorani, G., Brusa, M., Scoville, N. Z., Rau, A., Capak, P., Arnouts, S., Aussel, H., Bolzonella, M., Buongiorno, A., Cappelluti, N., Caputi, K., Civano, F., Cook, R., Elvis, M., Gilli, R., Jahnke, K., Kartaltepe, J. S., Impey, C. D., Lamareille, F., Le Floc'h, E., Lilly, S., Mainieri, V., McCarthy, P., McCracken, H., Mignoli, M., Mobasher, B., Murayama, T., Sasaki, S., Sanders, D. B., Schiminovich, D., Shioya, Y., Shopbell, P., Silverman, J., Smolčić, V., Surace, J., Taniguchi, Y., Thompson, D., Trump, J. R., Urry, M., and Zamojski, M. (2009). Photometric Redshift and Classification for the XMM-COSMOS Sources. , 690:1250–1263.

Sargent, M. T., Schinnerer, E., Murphy, E., Aussel, H., Le Floc'h, E., Frayer, D. T., Martínez-Sansigre, A., Oesch, P., Salvato, M., Smolčić, V., Zamorani, G., Brusa, M., Cappelluti, N., Carilli, C. L., Carollo, C. M., Ilbert, O., Kartaltepe, J., Koekemoer, A. M., Lilly, S. J., Sanders, D. B., and Scoville, N. Z. (2010). The VLA-COSMOS Perspective on the Infrared-Radio Relation. I. New Constraints on Selection Biases and the Non-Evolution of the Infrared/Radio Properties of Star-Forming and Active Galactic Nucleus Galaxies at Intermediate and High Redshift. , 186:341–377.

Schawinski, K., Urry, C. M., Simmons, B. D., Fortson, L., Kaviraj, S., Keel, W. C., Lintott, C. J., Masters, K. L., Nichol, R. C., Sarzi, M., Skibba, R., Treister, E., Willett, K. W., Wong, O. I., and Yi, S. K. (2014). The green valley is a red herring: Galaxy Zoo reveals two evolutionary pathways towards quenching of star formation in early- and late-type galaxies. , 440:889–907.

Schawinski, K., Urry, C. M., Virani, S., Coppi, P., Bamford, S. P., Treister, E., Lintott, C. J., Sarzi, M., Keel, W. C., Kaviraj, S., Cardamone, C. N., Masters, K. L., Ross, N. P., Andreescu, D., Murray, P., Nichol, R. C., Raddick, M. J., Slosar, A., Szalay, A. S., Thomas, D., and Vandenberg, J. (2010). Galaxy Zoo: The Fundamentally Different Co-Evolution of Supermassive Black Holes and Their Early- and Late-Type Host Galaxies. , 711:284–302.

Schaye, J., Crain, R. A., Bower, R. G., Furlong, M., Schaller, M., Theuns, T., Dalla Vecchia, C., Frenk, C. S., McCarthy, I. G., Helly, J. C., Jenkins, A., Rosas-Guevara, Y. M., White, S. D. M., Baes, M., Booth, C. M., Camps, P., Navarro, J. F., Qu, Y., Rahmati, A., Sawala, T., Thomas, P. A., and Trayford, J. (2015). The EAGLE project: simulating the evolution and assembly of galaxies and their environments. , 446:521–554.

Schmidt, M. (1959). The Rate of Star Formation. , 129:243.

Schmidt, M. (1968). Space Distribution and Luminosity Functions of Quasi-Stellar Radio Sources. , 151:393.

Shimwell, T. W., Röttgering, H. J. A., Best, P. N., Williams, W. L., Dijkema, T. J., de Gasperin, F., Hardcastle, M. J., Heald, G. H., Hoang, D. N., Horneffer, A., Intema, H., Mahony, E. K., Mandal, S., Mechev, A. P., Morabito, L., Oonk, J. B. R., Rafferty, D., Retana-Montenegro, E., Sabater, J., Tasse, C., van Weeren, R. J., Brüggen, M., Brunetti, G., Chyży, K. T., Conway, J. E., Haverkorn, M., Jackson, N., Jarvis, M. J., McKean, J. P., Miley, G. K., Morganti, R., White, G. J., Wise, M. W., van Bemmel, I. M., Beck, R., Brienza, M., Bonafede, A., Calistro Rivera, G., Cassano, R., Clarke, A. O., Cseh, D., Deller, A., Drabent, A., van Driel, W., Engels, D., Falcke, H., Ferrari, C., Fröhlich, S., Garrett, M. A., Harwood, J. J., Heesen, V., Hoeft, M., Horellou, C., Israel, F. P., Kapińska, A. D., Kunert-Bajraszewska, M., McKay, D. J., Mohan, N. R., Orrú, E., Pizzo, R. F., Prandoni, I., Schwarz, D. J., Shulevski, A., Sipior, M., Smith, D. J. B., Sridhar, S. S., Steinmetz, M., Stroe, A., Varenius, E., van der Werf, P. P., Zensus, J. A., and Zwart, J. T. L. (2017). The LOFAR Two-metre Sky Survey. I. Survey description and preliminary data release. , 598:A104.

Silk, J. and Nusser, A. (2010). The Massive-black-hole-Velocity-dispersion Relation and the Halo Baryon Fraction: A Case for Positive Active Galactic Nucleus Feedback. , 725:556–560.

Sirothia, S. K., Dennefeld, M., Saikia, D. J., Dole, H., Ricquebourg, F., and Roland, J. (2009). 325-MHz Observations of the ELAIS-N1 Field. In Saikia, D. J., Green, D. A., Gupta, Y., and Venturi, T., editors, *The Low-Frequency Radio Universe*, volume 407 of *Astronomical Society of the Pacific Conference Series*, page 27.

Skrutskie, M. F., Cutri, R. M., Stiening, R., Weinberg, M. D., Schneider, S., Carpenter, J. M., Beichman, C., Capps, R., Chester, T., Elias, J., Huchra, J., Liebert, J., Lonsdale, C., Monet, D. G., Price, S., Seitzer, P., Jarrett, T.,

Kirkpatrick, J. D., Gizis, J. E., Howard, E., Evans, T., Fowler, J., Fullmer, L., Hurt, R., Light, R., Kopan, E. L., Marsh, K. A., McCallon, H. L., Tam, R., Van Dyk, S., and Wheelock, S. (2006). The Two Micron All Sky Survey (2MASS). , 131:1163–1183.

Smith, D. J. B., Best, P. N., Duncan, K. J., Hatch, N. A., Jarvis, M. J., Röttgering, H. J. A., Simpson, C. J., Stott, J. P., Cochrane, R. K., Coppin, K. E., Dannerbauer, H., Davis, T. A., Geach, J. E., Hale, C. L., Hardcastle, M. J., Hatfield, P. W., Houghton, R. C. W., Maddox, N., McGee, S. L., Morabito, L., Nisbet, D., Pandey-Pommier, M., Prandoni, I., Saxena, A., Shimwell, T. W., Tarr, M., van Bemmel, I., Verma, A., White, G. J., and Williams, W. L. (2016). The WEAVE-LOFAR Survey. In Reylé, C., Richard, J., Cambrésy, L., Deleuil, M., Pécontal, E., Tresse, L., and Vauglin, I., editors, *SF2A-2016: Proceedings of the Annual meeting of the French Society of Astronomy and Astrophysics*, pages 271–280.

Smith, D. J. B., Jarvis, M. J., Hardcastle, M. J., Vaccari, M., Bourne, N., Dunne, L., Ibar, E., Maddox, N., Prescott, M., Vlahakis, C., Eales, S., Maddox, S. J., Smith, M. W. L., Valiante, E., and de Zotti, G. (2014). The temperature dependence of the far-infrared-radio correlation in the Herschel-ATLAS. , 445:2232–2243.

Smolčić, V. (2009). The Radio AGN Population Dichotomy: Green Valley Seyferts Versus Red Sequence Low-Excitation Active Galactic Nuclei. , 699:L43–L47.

Sobral, D., Best, P. N., Smail, I., Geach, J. E., Cirasuolo, M., Garn, T., and Dalton, G. B. (2011). The dependence of star formation activity on environment and stellar mass at z
1 from the HiZELS-Hα survey. , 411:675–692.

Sobral, D., Smail, I., Best, P. N., Geach, J. E., Matsuda, Y., Stott, J. P., Cirasuolo, M., and Kurk, J. (2013). A large Hα survey at z = 2.23, 1.47, 0.84 and 0.40: the 11 Gyr evolution of star-forming galaxies from HiZELS. , 428:1128–1146.

Soker, N. (2006). The source of mass accreted by the central black hole in cooling flow clusters. , 12:38–46.

Solomon, P. M., Downes, D., Radford, S. J. E., and Barrett, J. W. (1997). The Molecular Interstellar Medium in Ultraluminous Infrared Galaxies. , 478:144–161.

Somerville, R. S. and Davé, R. (2015). Physical Models of Galaxy Formation in a Cosmological Framework. , 53:51–113.

Springel, V. (2011). Feedback in Cosmological Simulations. accessible at http://astro.ucsc.edu/ nng/webtalks/springel.pdf.

Stern, D., Eisenhardt, P., Gorjian, V., Kochanek, C. S., Caldwell, N., Eisenstein, D., Brodwin, M., Brown, M. J. I., Cool, R., Dey, A., Green, P., Jannuzi, B. T., Murray, S. S., Pahre, M. A., and Willner, S. P. (2005). Mid-Infrared Selection of Active Galaxies. , 631:163–168.

Strauss, M. A., Weinberg, D. H., Lupton, R. H., Narayanan, V. K., Annis, J., Bernardi, M., Blanton, M., Burles, S., Connolly, A. J., Dalcanton, J., Doi, M., Eisenstein, D., Frieman, J. A., Fukugita, M., Gunn, J. E., Ivezić, Ž., Kent, S., Kim, R. S. J., Knapp, G. R., Kron, R. G., Munn, J. A., Newberg, H. J., Nichol, R. C., Okamura, S., Quinn, T. R., Richmond, M. W., Schlegel, D. J., Shimasaku, K., SubbaRao, M., Szalay, A. S., Vanden Berk, D., Vogeley, M. S., Yanny, B., Yasuda, N., York, D. G., and Zehavi, I. (2002). Spectroscopic Target Selection in the Sloan Digital Sky Survey: The Main Galaxy Sample. *AJ*, 124:1810–1824.

Sturm, E., Rupke, D., Contursi, A., Kim, D.-C., Lutz, D., Netzer, H., Veilleux, S., Genzel, R., Lehnert, M., Tacconi, L. J., Maoz, D., Mazzarella, J., Lord, S., Sanders, D., and Sternberg, A. (2006). Mid-Infrared Diagnostics of LINERS. , 653:L13–L16.

Surace, J. A., Shupe, D. L., Fang, F., Evans, T., Alexov, A., Frayer, D., Lonsdale, C. J., and SWIRE Team (2005). Data Processing and Validation of the SWIRE Survey. In *American Astronomical Society Meeting Abstracts*, volume 37 of *Bulletin of the American Astronomical Society*, page 1246.

Sutherland, W. and Saunders, W. (1992). On the likelihood ratio for source identification. , 259:413–420.

Tacconi, L. J., Genzel, R., Neri, R., Cox, P., Cooper, M. C., Shapiro, K., Bolatto, A., Bouché, N., Bournaud, F., Burkert, A., Combes, F., Comerford, J., Davis, M., Schreiber, N. M. F., Garcia-Burillo, S., Gracia-Carpio, J., Lutz, D., Naab, T., Omont, A., Shapley, A., Sternberg, A., and Weiner, B. (2010). High molecular gas fractions in normal massive star-forming galaxies in the young Universe. , 463:781–784.

Tanaka, M., Coupon, J., Hsieh, B.-C., Mineo, S., Nishizawa, A. J., Speagle, J., Furusawa, H., Miyazaki, S., and Murayama, H. (2017). Photometric Redshifts for Hyper Suprime-Cam Subaru Strategic Program Data Release 1. *ArXiv e-prints*.

Tasker, E. J. and Bryan, G. L. (2006). Modelling the Galaxy: Simulating Star Formation and Feedback in Galactic Disc Models. In *American Astronomical Society Meeting Abstracts #208*, volume 38 of *Bulletin of the American Astronomical Society*, page 102.

Tasse, C. (2014). Applying Wirtinger derivatives to the radio interferometry calibration problem. *ArXiv e-prints*.

Thomas, D., Steele, O., Maraston, C., Johansson, J., Beifiori, A., Pforr, J., Strömbäck, G., Tremonti, C. A., Wake, D., Bizyaev, D., Bolton, A., Brewington, H., Brownstein, J. R., Comparat, J., Kneib, J.-P., Malanushenko, E., Malanushenko, V., Oravetz, D., Pan, K., Parejko, J. K., Schneider, D. P., Shelden, A., Simmons, A., Snedden, S., Tanaka, M., Weaver, B. A., and Yan, R. (2013). Stellar velocity dispersions and emission line properties of SDSS-III/BOSS galaxies. , 431:1383–1397.

Tornatore, L., Borgani, S., Springel, V., Matteucci, F., Menci, N., and Murante, G. (2003). Cooling and heating the intracluster medium in hydrodynamical simulations. , 342:1025–1040.

Tremaine, S., Gebhardt, K., Bender, R., Bower, G., Dressler, A., Faber, S. M., Filippenko, A. V., Green, R., Grillmair, C., Ho, L. C., Kormendy, J., Lauer, T. R., Magorrian, J., Pinkney, J., and Richstone, D. (2002). The Slope of the Black Hole Mass versus Velocity Dispersion Correlation. *ApJ*, 574:740–753.

Trump, J. R., Impey, C. D., Taniguchi, Y., Brusa, M., Civano, F., Elvis, M., Gabor, J. M., Jahnke, K., Kelly, B. C., Koekemoer, A. M., Nagao, T., Salvato, M., Shioya, Y., Capak, P., Huchra, J. P., Kartaltepe, J. S., Lanzuisi, G., McCarthy, P. J., Maineri, V., and Scoville, N. Z. (2009). The Nature of Optically Dull Active Galactic Nuclei in COSMOS. *ApJ*, 706:797–809.

Vaccari, M. (2016). HELP: The Herschel Extragalactic Legacy Project and The Coming of Age of Multi-wavelength Astrophysics. *The Universe of Digital Sky Surveys*, 42:71.

van der Kruit, P. C. (1973). High-resolution Radio Continuum Observations of Bright Spiral Galaxies at 1415 MHz: A General Discussion. , 29:263.

van Dokkum, P. G., Whitaker, K. E., Brammer, G., Franx, M., Kriek, M., Labbé, I., Marchesini, D., Quadri, R., Bezanson, R., Illingworth, G. D., Muzzin, A., Rudnick, G., Tal, T., and Wake, D. (2010). The Growth of Massive Galaxies Since z = 2. , 709:1018–1041.

van Haarlem, M. P., Wise, M. W., Gunst, A. W., Heald, G., McKean, J. P., Hessels, J. W. T., de Bruyn, A. G., Nijboer, R., Swinbank, J., Fallows, R., Brentjens, M., Nelles, A., Beck, R., Falcke, H., Fender, R., Hörandel, J., Koopmans, L. V. E., Mann, G., Miley, G., Röttgering, H., Stappers, B. W., Wijers, R. A. M. J., Zaroubi, S., van den Akker, M., Alexov, A., Anderson, J., Anderson, K., van Ardenne, A., Arts, M., Asgekar, A., Avruch, I. M., Batejat, F., Bähren, L., Bell, M. E., Bell, M. R., van Bemmel, I., Bennema, P., Bentum, M. J., Bernardi, G., Best, P., Bîrzan, L., Bonafede, A., Boonstra, A.-J., Braun, R., Bregman, J., Breitling, F., van de Brink, R. H., Broderick, J., Broekema, P. C., Brouw, W. N., Brüggen, M., Butcher, H. R., van Cappellen, W., Ciardi, B., Coenen, T., Conway, J., Coolen, A., Corstanje, A., Damstra, S., Davies, O., Deller, A. T., Dettmar, R.-J., van Diepen, G., Dijkstra, K., Donker, P., Doorduin, A., Dromer, J., Drost, M., van Duin, A., Eislöffel, J., van Enst, J., Ferrari, C., Frieswijk, W., Gankema, H., Garrett, M. A., de Gasperin, F.,

Gerbers, M., de Geus, E., Grießmeier, J.-M., Grit, T., Gruppen, P., Hamaker, J. P., Hassall, T., Hoeft, M., Holties, H. A., Horneffer, A., van der Horst, A., van Houwelingen, A., Huijgen, A., Iacobelli, M., Intema, H., Jackson, N., Jelic, V., de Jong, A., Juette, E., Kant, D., Karastergiou, A., Koers, A., Kollen, H., Kondratiev, V. I., Kooistra, E., Koopman, Y., Koster, A., Kuniyoshi, M., Kramer, M., Kuper, G., Lambropoulos, P., Law, C., van Leeuwen, J., Lemaitre, J., Loose, M., Maat, P., Macario, G., Markoff, S., Masters, J., McFadden, R. A., McKay-Bukowski, D., Meijering, H., Meulman, H., Mevius, M., Middelberg, E., Millenaar, R., Miller-Jones, J. C. A., Mohan, R. N., Mol, J. D., Morawietz, J., Morganti, R., Mulcahy, D. D., Mulder, E., Munk, H., Nieuwenhuis, L., van Nieuwpoort, R., Noordam, J. E., Norden, M., Noutsos, A., Offringa, A. R., Olofsson, H., Omar, A., Orrú, E., Overeem, R., Paas, H., Pandey-Pommier, M., Pandey, V. N., Pizzo, R., Polatidis, A., Rafferty, D., Rawlings, S., Reich, W., de Reijer, J.-P., Reitsma, J., Renting, G. A., Riemers, P., Rol, E., Romein, J. W., Roosjen, J., Ruiter, M., Scaife, A., van der Schaaf, K., Scheers, B., Schellart, P., Schoenmakers, A., Schoonderbeek, G., Serylak, M., Shulevski, A., Sluman, J., Smirnov, O., Sobey, C., Spreeuw, H., Steinmetz, M., Sterks, C. G. M., Stiepel, H.-J., Stuurwold, K., Tagger, M., Tang, Y., Tasse, C., Thomas, I., Thoudam, S., Toribio, M. C., van der Tol, B., Usov, O., van Veelen, M., van der Veen, A.-J., ter Veen, S., Verbiest, J. P. W., Vermeulen, R., Vermaas, N., Vocks, C., Vogt, C., de Vos, M., van der Wal, E., van Weeren, R., Weggemans, H., Weltevrede, P., White, S., Wijnholds, S. J., Wilhelmsson, T., Wucknitz, O., Yatawatta, S., Zarka, P., Zensus, A., and van Zwieten, J. (2013). LOFAR: The LOw-Frequency ARray. , 556:A2.

van Weeren, R. J., Williams, W. L., Hardcastle, M. J., Shimwell, T. W., Rafferty, D. A., Sabater, J., Heald, G., Sridhar, S. S., Dijkema, T. J., Brunetti, G., Brüggen, M., Andrade-Santos, F., Ogrean, G. A., Röttgering, H. J. A., Dawson, W. A., Forman, W. R., de Gasperin, F., Jones, C., Miley, G. K., Rudnick, L., Sarazin, C. L., Bonafede, A., Best, P. N., Bîrzan, L., Cassano, R., Chyży, K. T., Croston, J. H., Ensslin, T., Ferrari, C., Hoeft, M., Horellou, C., Jarvis, M. J., Kraft, R. P., Mevius, M., Intema, H. T., Murray, S. S., Orrú, E., Pizzo, R., Simionescu, A., Stroe, A., van der Tol, S., and White, G. J. (2016). LOFAR Facet Calibration. , 223:2.

Wada, K. and Norman, C. A. (2007). Density Structure of the Interstellar Medium and the Star Formation Rate in Galactic Disks. , 660:276–287.

Walter, F., Carilli, C., Bertoldi, F., Menten, K., Cox, P., Lo, K. Y., Fan, X., and Strauss, M. A. (2004). Resolved Molecular Gas in a Quasar Host Galaxy at Redshift z=6.42. , 615:L17–L20.

White, S. D. M. and Rees, M. J. (1978). Core condensation in heavy halos - A two-stage theory for galaxy formation and clustering. *MNRAS*, 183:341–358.

Williams, W. L., van Weeren, R. J., Röttgering, H. J. A., Best, P., Dijkema, T. J., de Gasperin, F., Hardcastle, M. J., Heald, G., Prandoni, I., Sabater, J., Shimwell, T. W., Tasse, C., van Bemmel, I. M., Brüggen, M., Brunetti,

G., Conway, J. E., Enßlin, T., Engels, D., Falcke, H., Ferrari, C., Haverkorn, M., Jackson, N., Jarvis, M. J., Kapińska, A. D., Mahony, E. K., Miley, G. K., Morabito, L. K., Morganti, R., Orrú, E., Retana-Montenegro, E., Sridhar, S. S., Toribio, M. C., White, G. J., Wise, M. W., and Zwart, J. T. L. (2016). LOFAR 150-MHz observations of the Boötes field: catalogue and source counts. , 460:2385–2412.

Wright, E. L., Eisenhardt, P. R. M., Mainzer, A. K., Ressler, M. E., Cutri, R. M., Jarrett, T., Kirkpatrick, J. D., Padgett, D., McMillan, R. S., Skrutskie, M., Stanford, S. A., Cohen, M., Walker, R. G., Mather, J. C., Leisawitz, D., Gautier, III, T. N., McLean, I., Benford, D., Lonsdale, C. J., Blain, A., Mendez, B., Irace, W. R., Duval, V., Liu, F., Royer, D., Heinrichsen, I., Howard, J., Shannon, M., Kendall, M., Walsh, A. L., Larsen, M., Cardon, J. G., Schick, S., Schwalm, M., Abid, M., Fabinsky, B., Naes, L., and Tsai, C.-W. (2010). The Wide-field Infrared Survey Explorer (WISE): Mission Description and Initial On-orbit Performance. , 140:1868–1881.

Wu, X.-B., Wang, F., Fan, X., Yi, W., Zuo, W., Bian, F., Jiang, L., McGreer, I., Wang, R., Yang, J., Yang, Q., Thompson, D., and Beletsky, Y. (2015). Discovery of a 12 billion solar mass black hole at redshift 6.3 and its challenge to the black hole/galaxy co-evolution at cosmic dawn. *IAU General Assembly*, 22:2251223.

Yaqoob, T., Edelson, R., Weaver, K. A., Warwick, R. S., Mushotzky, R. F., Serlemistos, P. J., and Holt, S. S. (1995). The Iron K Line Profile in NGC 4151 and the Evidence for a Relativistic Accretion Disk. In *American Astronomical Society Meeting Abstracts*, volume 27 of *Bulletin of the American Astronomical Society*, page 1359.

York, D. G., Adelman, J., Anderson, Jr., J. E., Anderson, S. F., Annis, J., Bahcall, N. A., Bakken, J. A., Barkhouser, R., Bastian, S., Berman, E., Boroski, W. N., Bracker, S., Briegel, C., Briggs, J. W., Brinkmann, J., Brunner, R., Burles, S., Carey, L., Carr, M. A., Castander, F. J., Chen, B., Colestock, P. L., Connolly, A. J., Crocker, J. H., Csabai, I., Czarapata, P. C., Davis, J. E., Doi, M., Dombeck, T., Eisenstein, D., Ellman, N., Elms, B. R., Evans, M. L., Fan, X., Federwitz, G. R., Fiscelli, L., Friedman, S., Frieman, J. A., Fukugita, M., Gillespie, B., Gunn, J. E., Gurbani, V. K., de Haas, E., Haldeman, M., Harris, F. H., Hayes, J., Heckman, T. M., Hennessy, G. S., Hindsley, R. B., Holm, S., Holmgren, D. J., Huang, C.-h., Hull, C., Husby, D., Ichikawa, S.-I., Ichikawa, T., Ivezić, Ž., Kent, S., Kim, R. S. J., Kinney, E., Klaene, M., Kleinman, A. N., Kleinman, S., Knapp, G. R., Korienek, J., Kron, R. G., Kunszt, P. Z., Lamb, D. Q., Lee, B., Leger, R. F., Limmongkol, S., Lindenmeyer, C., Long, D. C., Loomis, C., Loveday, J., Lucinio, R., Lupton, R. H., MacKinnon, B., Mannery, E. J., Mantsch, P. M., Margon, B., McGehee, P., McKay, T. A., Meiksin, A., Merelli, A., Monet, D. G., Munn, J. A., Narayanan, V. K., Nash, T., Neilsen, E., Neswold, R., Newberg, H. J., Nichol, R. C., Nicinski, T., Nonino, M., Okada, N., Okamura, S., Ostriker, J. P., Owen, R., Pauls, A. G., Peoples, J., Peterson, R. L., Petravick, D., Pier, J. R.,

Pope, A., Pordes, R., Prosapio, A., Rechenmacher, R., Quinn, T. R., Richards, G. T., Richmond, M. W., Rivetta, C. H., Rockosi, C. M., Ruthmansdorfer, K., Sandford, D., Schlegel, D. J., Schneider, D. P., Sekiguchi, M., Sergey, G., Shimasaku, K., Siegmund, W. A., Smee, S., Smith, J. A., Snedden, S., Stone, R., Stoughton, C., Strauss, M. A., Stubbs, C., SubbaRao, M., Szalay, A. S., Szapudi, I., Szokoly, G. P., Thakar, A. R., Tremonti, C., Tucker, D. L., Uomoto, A., Vanden Berk, D., Vogeley, M. S., Waddell, P., Wang, S.-i., Watanabe, M., Weinberg, D. H., Yanny, B., Yasuda, N., and SDSS Collaboration (2000). The Sloan Digital Sky Survey: Technical Summary. *AJ*, 120:1579–1587.

Zavala, J., Frenk, C. S., Bower, R., Schaye, J., Theuns, T., Crain, R. A., Trayford, J. W., Schaller, M., and Furlong, M. (2016). The link between the assembly of the inner dark matter halo and the angular momentum evolution of galaxies in the EAGLE simulation. , 460:4466–4482.